ACKNOWLEDGEMENTS

First and foremost, I would like to thank my supervisor, Prof K Mark Thomas, for giving me the opportunity to study in NCRL. His continual support and guidance throughout my postgraduate career has been invaluable for me. Without his direction and great expertise, I would not have been able to complete much of this thesis. I would also like to thank the Royal Thai government for granting me a scholarship and Mahasarakham University for allowing me to pursue a PhD in the United Kingdom.

I sincerely thank both Dr X Zhao and Dr A J Fletcher who spent countless time teaching me how to use the Intelligent Gravimetric Analyser (IGA) from the first day of my studies till the end for their advice as well as friendly, kind and understanding attitude towards me.

Special thanks also go to Dr R W Harrington for all his help, especially with X-ray crystallographic determination. I would like to thank Prof Banglin Chen from University of Texas-Pan American for providing mixed metal organic framework (M'MOF 1). I thank to Dr. Kath Liddell, former member of Advanced Materials Division, for her kind assistance on PXRD determination. I also have to thank Dr Jon Bell for proof reading parts of this thesis and for his continuing assistance when I had technical difficulties.

I would also like to thank the past and present members of NCRL, Dr Mark Kennedy, Mr Nykky Allen, Miss Rachel Gill, Miss Jayne Knotts and Mr Augustine Umukolo for their assistance, friendliness, and delightful conversations which made me smile every day.

I would like to thank my family for their patience, love and support. Therefore, I dedicate this thesis to them. Last but not least, I like to thank Miss Ajchara Imkum for her unconditional love, patience and unique understanding.

ABSTRACT

Recently, porous metal organic framework materials (MOFs) have attracted considerable attention due to the wide range of possible applications of the materials in 1) gas storage, purification and separation; 2) as catalysts and catalyst supports; and 3) for adsorption of environmentally unfriendly species. This study has involved the synthesis, characterisation and determination of the adsorption/desorption characteristics of functionalised porous metal organic framework materials. The overall objective was to increase understanding of the role of surface functional groups and framework flexibility in determining the adsorption characteristics of gases and vapours and assess the possible applications of these materials for gas storage and separation.

In this study, two new metal organic frameworks NEW-1 ($C_{12}H_8CuN_2O_4 \cdot C_3H_7NO$) and NEW-2 ($C_6H_{10}O_6Zn$) were synthesised by solvothermal and solvent diffusion methods, respectively**.** Single crystal X-ray crystallographic determination revealed that NEW-1 had a monoclinic space group $P2_1/c$ and the 3-D framework is constructed via two square pyramidal copper atoms bonded with four isonicotinate ligands. The overall framework of NEW-1 gives rise to a uni-directional channel-like porous structure with window size of 6.092 x 6.092 Å (van der Waals surfaces) where guest dimethylformamide molecules reside. NEW-2 had a monoclinic space group *C2/c* and the framework is connected via hexagonal building block of ZnO_6 and fumarate ligands to form a non-porous structure.

The dynamic responses of flexible metal organic framework NEW-1 to adsorption of a series of probe molecules were investigated and thermodynamic and kinetic parameters were determined. The series of probe molecules comprised of

i) H_2O and C_1-C_4 *n*-alcohols (methanol, to *n*-butanol) varying length and hydrophilic to hydrophobic character,

ii) C_1-C_9 alkanes (methane to *n*-nonane) vapours with similar cross-sectional area,

iii) chloro- species (methyl chloride, dichloromethane and chloroform) where the cross-sectional area increases systematically

iv) planar molecules (benzene and toluene) and

v) a range of permanent gases (N_2, CO_2, Ar).

The results showed that most of the adsorption isotherms were Type I in the IUPAC classification scheme, but some deviations occurred. In the case of adsorption of longer *n*-alkanes, at low pressure, convex isotherm curvatures were observed and at high relative pressure, steep uptakes corresponding to pore filling were observed. The adsorption isotherms of small hydrophilic alcohol molecules (methanol, ethanol and *n*-propanol) exhibited a stoichiometric ratio for amount adsorbed and formula unit of NEW-1. This indicates that hydrogen bonding between the hydroxyl group of alcohols with carboxylate non-coordinated oxygen in the pore wall of NEW-1. In contrast, a stoichiometric relationship was not observed for the adsorption isotherms of *n*-butanol. It is reasonable to conclude that the dominant interaction for *n*-butanol is the hydrophobic surface rather than OH-surface oxygen interaction. Thermodynamic and kinetics parameters for vapour adsorption were also investigated and compared in order to understand the role of functional groups on surface diffusion and framework flexibility. Nitrogen, carbon dioxide, argon and methane adsorption showed that the total pore volume was ~35% that obtained from the adsorption of vapours (alcohol, alkane etc). The structural change produced by thermal activation to give the desolvated framework with lower pore volume can be expanded by adsorption of both hydrophilic and hydrophobic adsorptives. These differences were attributed to differences in isosteric enthalpies of adsorption, which influence framework flexibility and adsorption characteristics. Both specific H-bonding and non-specific interactions expand the collapsed desolvated pore structure to similar values to the crystallographic pore volume. This is likely to involve recovery of the long range order by the gas sorption. The adsorption kinetics for each isotherm pressure step were analysed by a stretched exponential model. The activation energies for diffusion of chloroform into the porous structure as a function of surface coverage and the isotherm show that the pore structure expansion occurs at low relative pressure rather than at high relative pressure as in the case of other adsorptives. Comparison of the isosteric enthalpies and activation energies for adsorption show that the site-to-site hopping mechanism mainly controls diffusion into the porous structure rather than diffusion through narrow constrictions in the porous structure.

Adsorption of hydrogen, nitrogen, oxygen and argon were studied in order to investigate the possible applications of metal organic framework NEW-1 in gas storage and air separation. In case of the air separation, adsorption characteristics of O_2, N_2, and Ar on metal organic framework NEW-1, mixed-zinc/copper organic framework (M'MOF-1) and a carbon based molecular sieve (CMS-40) were compared. The crucial factors such as molecular size and shape in relation to pore structure in determining the adsorption characteristics on materials were investigated. Selected kinetic models i.e. stretched exponential model (SE), double stretched exponential model (DSE) were used to determine the kinetic adsorption parameters. Also, the isosteric enthalpies of gases adsorption at zero surface coverage were determined. The results show that very narrow pores are required in metal organic frameworks to achieve kinetic selectivity similar to CMS-40.

TABLE OF CONTENTS

CHAPTER 1 - POROUS MATERIALS

CHAPTER 2 – THE ADSORPTION OF VAPOURS AND GASES INTO POROUS MATERALS

CHAPTER 3 - AIR SEPARATION AND GAS STORAGE

CHAPTER 4 – OBJECTIVES

CHAPTER 5 – EXPERIMENTAL

CHAPTER 6 – CHARACTERISATION OF METAL ORGANIC FRAME WORKS AND CMS-40

CHAPTER 7 – EFFECT OF OXYGEN SURFACE FUNCTIONAL GROUPS ON GAS/VAPOUR ADSORPTION ON POROUS METAL ORGANIC FRAMEWORK NEW-1

LIST OF TABLES

LIST OF FIGURES

CHAPTER 1

CHAPTER 2

CHAPTER 3

CHAPTER 5

CHAPTER 6

CHAPTER 7

LIST OF FIGURES

CHAPTER 8

LIST OF FIGURES

CHAPTER 1

Porous materials

1.1 Terminology of porous materials and pore size

The International Union of Pure and Applied Chemistry (IUPAC)[1, 2] has defined a porous material (or porous solid) as a solid with pores i.e. cavities, channels or interstices, which are deeper than they are wide. Porous materials can be formed by a variety of production processes *e.g.* carbonization process to produce porous carbon which may be activated further by physical and chemical processes, formation of a crystalline structure in the synthesis of metal organic frameworks from which the template/solvent can be removed to form a stable porous structure, and templating techniques used for some zeolites.

Pores can be classified by their availability to an external fluid as shown in Figure 1.1. Open pores may be open only at one end and are described as dead-end or blind pores while the other pores may be open through pores. However, pores may also be classified by their shape, for example, the pore shape can be described as cylinders for activated alumina, prisms for some fibrous zeolites, cavities and windows for other zeolites and metal organic frameworks. Different types of pores may also be pictured as apertures, channels or cavities within a porous structure.[2, 3]

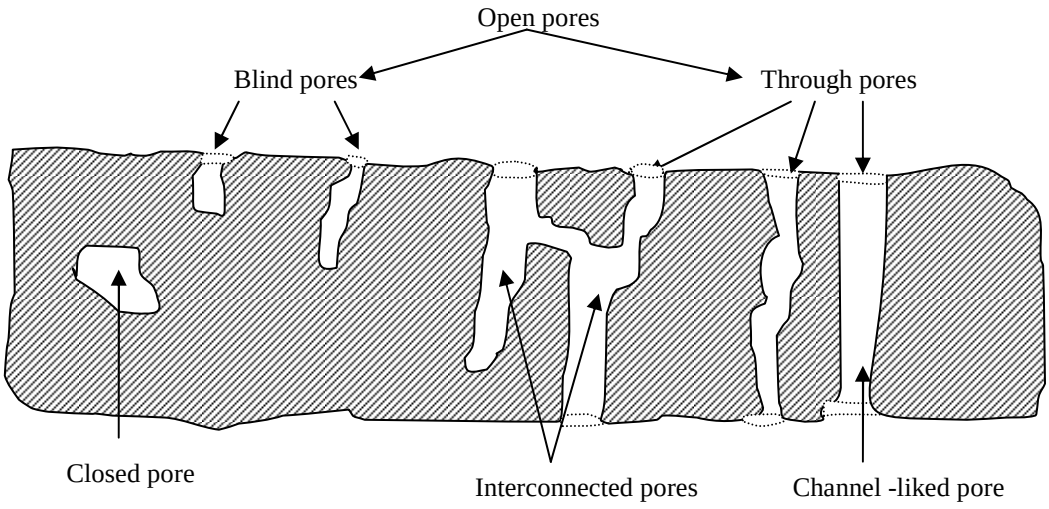

Figure 1.1 Types of pores

According to the International Union of Pure and Applied Chemistry (IUPAC), pores are generally classified into three categories, namely:

(1) Micropores, which have diameters smaller than 2 nm (< 20 Å). These are sometimes called nanopores.
(2) Mesopores, which have diameters between 2 and 50 nm (20-500 Å)
(3) Macropores, which have diameters larger than 50 nm (>500 Å)

To date, porous materials have attracted the attention of many researchers due to their potential application in gas/liquid separation, heterogeneous catalysis and gas storage. Applications of porous coordination polymers (or metal organic frameworks) and porous carbons are reviewed below.

1.2 Coordination polymer

The use of inorganic and organic molecules building new porous materials has become an attractive application. These possible applications are trapping guest molecules, chemical sensing and gas separation and storage.[4-9] Ferey[10, 11] has classified these new porous inorganic and organic materials in to four different categories. The first category is a pure inorganic framework, which has the templated organic molecules inside each cavity, as shown in Figure 1.2a. For the next two categories, templated organic molecules form the pillar between inorganic 2-D layers (Figure 1.2b) or act as a linker between 1-D inorganic chain (Fig 1.2c). Both 1-D and 2-D inorganic layers linked by organic molecules are usually referred to as hybrid inorganic-organic materials. The final category is coordination polymer where organic ligands may be arranged around a discrete molecule, containing one or more metal ion, as shown in Figure 1.2d.

Coordination polymers are also known as metal organic frameworks (MOFs) or metal-organic coordination networks (MOCNs). For reasons of clarity, Ulrich *et al.*[12] suggested that the term coordination polymer should be used to describe any extended structure based on metals and organic bridging ligands, where metal organic framework is typically used for structures that exhibit porosity.

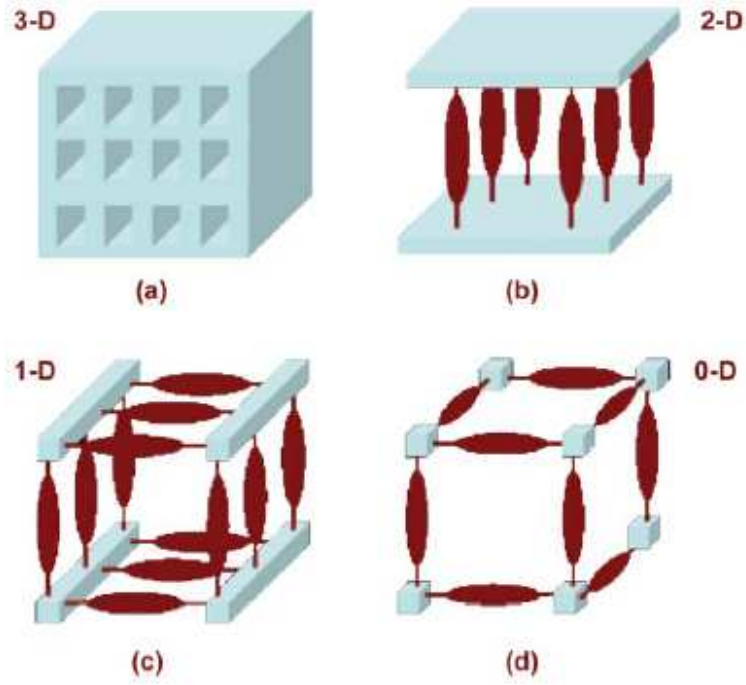

Figure 1.2 Four different categories of porous inorganic and organic materials.[11]

These coordination polymers are often crystalline materials that consist of metal ions (known as the connecter) and organic molecules (known as the linkers) connected to produce an infinite 1, 2, or 3-dimensional framework via more or less covalent metal-ligand bonding. In addition, the ligand must be a bridging organic group. However, these coordination polymers could have other auxiliary components such as counter ions and non binding guest in their structures.[5, 6, 13, 14]

1.3 Synthesis concepts

Synthesis of coordination polymers is normally based on supramolecular approach. These polymers are self assembled from metal ions or cluster that are linked to each metal by organic linking molecules to generate infinite framework structure as shown in Figure 1.3.[14-17] Compared to microporous zeolites and mesoporous silicate/aluminosilicate e.g. MCM-type materials, the coordination polymers are connected through coordination bonds weaker in energy than the strong Si/Al-O bonds in zeolites and molecular sieves. However,

the relatively weak bond energies lead to diverse and flexible coordination spheres of metal ions/metal clusters, which produce coordination frameworks with different topology, such as honeycomb (a), ladder (b), octahedral (c), hexagonal diamondoid (d), square grid (e), and zigzag chain (f) as shown in Figure 1.4.

In principle a wide variety of framework topologies ranging from simple chains to ladders (1-D), sheets or brick wall or bilayers (2-D) and framework (3-D) can be obtained by the selection of reaction-influencing factors. This includes using different metal coordination geometries and experimental variables, such as the metal to organic ligand ratio and synthesis temperature. Moreover, by choosing the appropriate organic linker, it is possibly to control pore sizes and functionality of the open frameworks.[5, 6, 17] Some of the metal ligands and organics bridging molecule are discussed in the following sections.

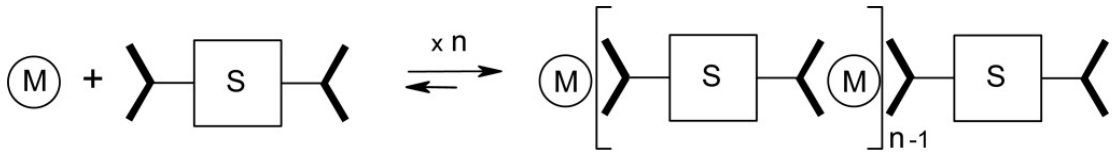

Figure 1.3 Schematic representation of a coordination polymer, with the metal ion (M) and the organic spacer (S) equipped with two donor units (bold).[16]

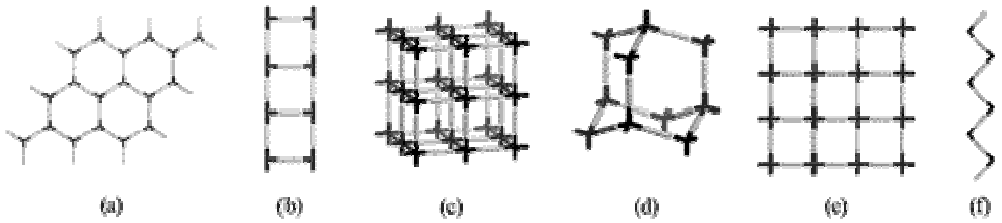

Figure 1.4 Some network structures of metal organic frameworks.[17]

1.3.1 Metal ions in coordination polymers

Transition-metal or lanthanide ions are mostly used in the construction of coordination polymers. Additionally, most of these metals are based on nitrates, phosphates, sulfates, sulfides, halides, and cyanides.[6, 11, 12] However, these transitional metals are also used in the form of metal clusters or secondary building unit (SBU). The secondary building units are metal ions that are chelated by organic bridging ligand molecules, which lock their metal position into M-O-C clusters. Furthermore, the SBU may contain two or more metal centres. For instance, metal organic framework (MOF-5) contains four Zn_4O tetrahedral or secondary building units, which are joined together by carboxylate bridging linker molecules as shown in Figure 1.5. These SBU can help enhance structural stability and rigidity of the MOFs. However, specific SBUs can be generated in situ under the correct chemical conditions.[6, 18-20] In term of coordination number of metal, metal ions that have higher coordination number tend to generate 3-dimensional crystal structures, while the lower coordination number metal ions tend to generate 1- and 2-dimensionl crystal structures.[21]

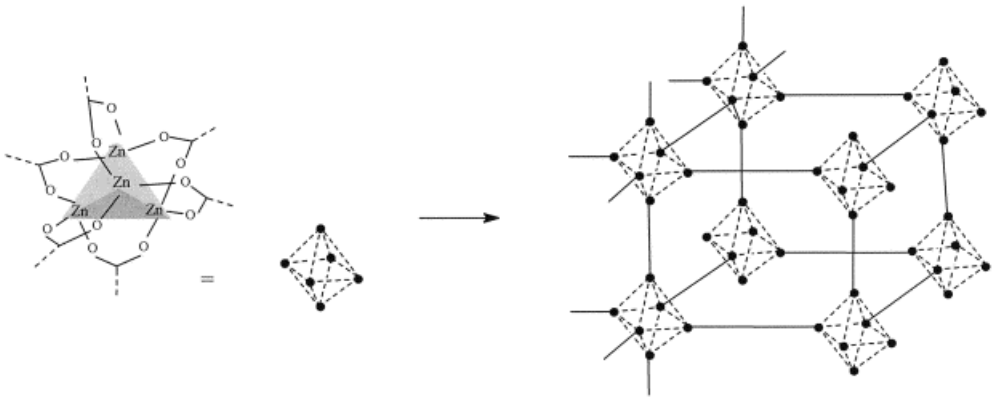

Figure 1.5 Representative geometries of secondary building blocks for the synthesis of porous Zn frameworks.[22]

Recently, mixed-metal organic frameworks have been synthesised with interesting properties. For example, mixed Ni-Co and 1,4-di-(1-imidaxolyo-methyl)-benzene which has potential to be a molecular magnetic alloy material.[23] De Lill *et al.*[24] reported that mixed lanthanide (Eu, Tb) organic framework exhibited luminescence spectra and the strong Eu^{3+} luminescence is enhanced by the present of Tb incorporated into the same

structure. The enhanced luminescence property of this mixed lanthanide organic framework demonstrates the potential application as light-emitting diode.

Some applications of mixed metal organic frameworks in adsorption have been studied by Chen *et al.*[25] This report showed that the mixed zinc/copper metal organic frame work material (M'MOF-1) was solvothermal synthesised and the single X-ray crystallographic determination lead to the chemical formula of $Zn_3(BDC)_3[Cu(Pyen)]\cdot(DMF)_5(H_2O)_5$ where H_2BDC = 1,4 benzenedicarboxylic acid and $PyenH_2$ = 5-methyl-4-oxo-1,4-dihydro-pyridine-3-carbaldehyde. The desolvation form of this M'MOF-1 contained two types of pores e.g. the pore of cross-section 5.6 x 12.0 Å in the direction of the *c* crystallographic axis (Figure 1.6a) and narrower irregular ultramicropores in the direction of the *b* crystallographic axis (Figure 1.6b). The crystallographic pore volume of M'MOF-1 determined using PLATON[26] is about 0.286 $cm^3\ g^{-1}$. The copper sites, in the structure, have four of six possible coordination sites bound by Schiff base N and O, so that there are two potential open sites either side of the CuN_2O_2 plane for binding of hydrogen molecules or other species. The authors also reported that the M'MOF-1 displayed a kinetic isotope quantum molecular sieving of H_2 and D_2. Quantum molecular sieving in microporous M'MOF 1 is due to the larger zero-point energy for the lighter H_2, resulting in higher amplitudes of vibration and slower adsorption kinetics compared with the heavier D_2.

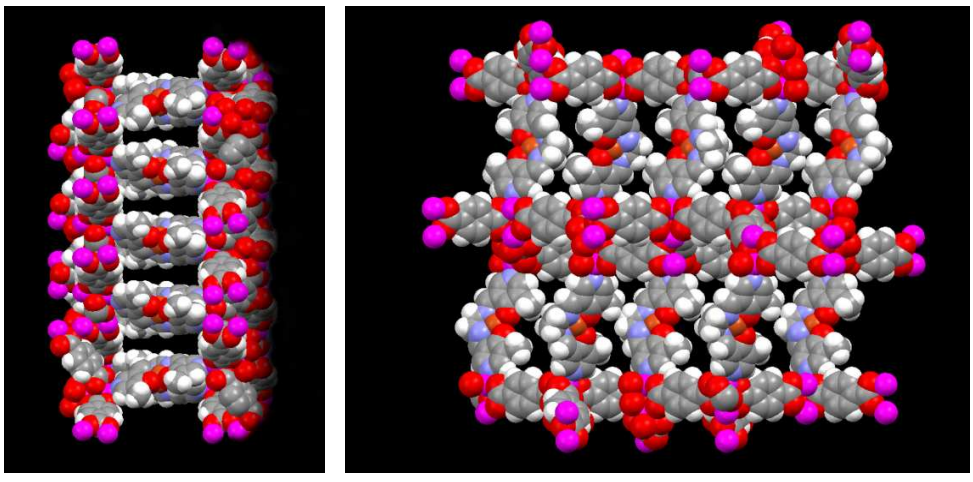

(a) (b)

Figure 1.6 X-ray crystal structure of M'MOF **1** (a) the pores of about 5.6 x 12.0 Å along *c* axis and (b) the irregular ultramicropores along *b* axis, respectively. Legend: Zn (Purple), Cu (orange), O (red) , N (blue), C (grey), H (white).

1.3.2 Organic bridging molecules in coordination polymers

Organic linker molecules used in the synthesis of coordination polymers have to bridge between metal ions. Therefore, multi dentate organic molecules with two or more donor atoms are normally required to construct these coordination polymers. Currently, multidentate nitrogen- and oxygen-donor organic ligands are preferred in the synthesis of coordination polymers due to their thermal stability and perhaps help prevent structural collapse after removal of guest molecules.[5, 6, 11] The first two parts of the following topic are discussion about the construction concepts of coordination polymers with a single species of organic molecules, encompassing nitrogen and oxygen-donor molecules. The last topic discusses the use of hybrid species of organic molecules to generate coordination polymers.

1.3.3 Nitrogen–donor organic molecules

There are a wide variety of heterocyclic nitrogen-organic bridging molecules as shown in Figure 1.7. In the self-assembly process, N-donor sites can bond to metal ions and generate T-shaped secondary building units (SBU). Generally, this T-shaped secondary building unit often produces only 1- or 2- dimensional structures. It should be noted that the long chain of nitrogen-organic bridging molecules e.g. 1,4-bis(3-pyridyl)-2,3-diaza-1,3-butadiene, tends to produce interpenetration frameworks or polycatenation structures leading to the production of 3-dimensional frameworks. However, the structure of the interpenetration framework usually collapses after guest molecules in the cavities are removed.[27-30] The shorter chain of nitrogen-organic bridging molecules, such as 4,4'-bipyridine, tends to produce 3-dimensional frameworks without interpenetration, for example, the desolvated phase of porous framework material Ni_2(4,4'-bipyridine)$_3(NO_3)_4$ exhibited porosity and also showed the reversible guest exchange property.[31] Noro *et al.*[32] reported the rigid framework $CuSiF_6$(4,4'-bipyridine)$_2\}_n$ showed a high degree of porosity with a surface area of 1337 $m^2 g^{-1}$. The frameworks based on this 4,4′-bipyridine have been studied extensively using gas adsorption methods.[32, 33] Some of the N-donor ligands which can produce 3-D frameworks are shown in Figure 1.8.

Most of these 3-D structures are synthesised under low/room temperature, using layering or diffusion methods. However, this is not universal since 2,5-bis(3-pyridyl)-3,4-diaza-2,4-hexadiene ($b_3$pdahd) which is a framework generated by refluxing. The metal organic ligand mole ratio for synthesizing these 3-D polymers ranges from 1.2-1.5. It has been shown that the frameworks produced from refluxing may exhibit high thermal stability.[22, 27-30, 34]

1.3.4 Oxygen–donor organic molecules

A wide range of carboxylic acids have been used to construct coordination polymers, including carboxylate, oxalate, aliphatic and aromatic poly-carboxylate. Some oxygen – carboxylate donor organic molecules, which can produce 3-D frameworks are present in Figure 1.9 and some ligand are discussed herein. Compared with bi-dentate N-donor molecules, bi-dentate carboxylate molecules have the flexibility to chelate metal ions in different ways. This flexibility can be used to generate a wide variety of the polymer framework structures (Figure 1.10). Carboxylate molecules do not only coordinate with metal ions as mono dentate (a) chelating ligand but also coordinate with two to five metal ions (b).[35] Strong metal-oxygen bonding of carboxylate ions gives 3-D coordination frameworks with high stability.

Generally, there are two conventional methods to completely deprotonate the carboxylate group. Firstly, adding some strong base (e.g. triethylamine) is normally sufficient for complete deprotonation. However, pure crystals may not be obtained, due to this base producing a mixture of both framework and byproduct.[36, 37] The other methods are hydrothermal or solvothermal synthesis at high temperature. For entropic reasons, these high temperature synthesis methods can completely deprotonate carboxylate ligands and perhaps promote the formation of framework with high dimensionality. Furthermore, these methods are normally generate pure materials.[38]

Example of metal organic frameworks based on bi-dentate and tri-dentate are $Zn_4O(BDC)_3$ (BDC = 1,4-benzenedicarboxylate):MOF-5 and $[Cu_3(TMA)_2(H_2O)_3]_n$ (TMA = benzene-1,3,5-tricarboxylate):HKUST-1, respectively. Both MOF-5 and HKUST-1 framework are widely produced and studied in various aspects, especially in adsorption/desorption of gases. MOF-5 consists of four Zn_4O clusters in octahedral subunit that are connected to each other by terephthalate groups, while HKUST-1 consist of

$Cu_2(COO)_4$ with four copper connectors and bond with three benzene-1,3,5-tricarboxylate groups. In term of cavity size, HKUST-1 has cavity dimensions of 9 Å x 9 Å. whilst MOF-5 has smaller cavities of 5 Å x 5 Å. This may be because the length of terephthalate ligands, which are contained in the MOF-5 frameworks are shorter than benzene-1,3,5-tricarboxylate groups.[18, 38] This indicates that length of organic molecules is a major influence on pores size and surface area of coordination polymers.

Lin *et al.*[39] reported that pore size and pore volume of metal organic framework materials can be controlled by varying the length of the carboxylic ligand. In this study, $Cu(NO_3)_2.2.5H_2O$ was solvothermally synthesized with three difference length of carboxylate ligands. Quaterphenyl-3,3‴,5,5‴-tetracarboxylic acid (H_4L^3), the longest carboxylic ligand, gave the largest pore size and volume with values of 8.3 Å and 1.284 cm^3g^{-1}, respectively. While, the shorter ligands, biphenyl-3,3′,5,5′-tetracarboxylic acid (H_4L^1) and biphenyl-3,3′,5,5′-tetracarboxylic acid (H_4L^2), gave the smaller pore size and volumes (H_4L^1 ; 6.5 Å and 0.683 cm^3g^{-1}, H_4L^2 7.3 Å and 0.886 cm^3g^{-1}).

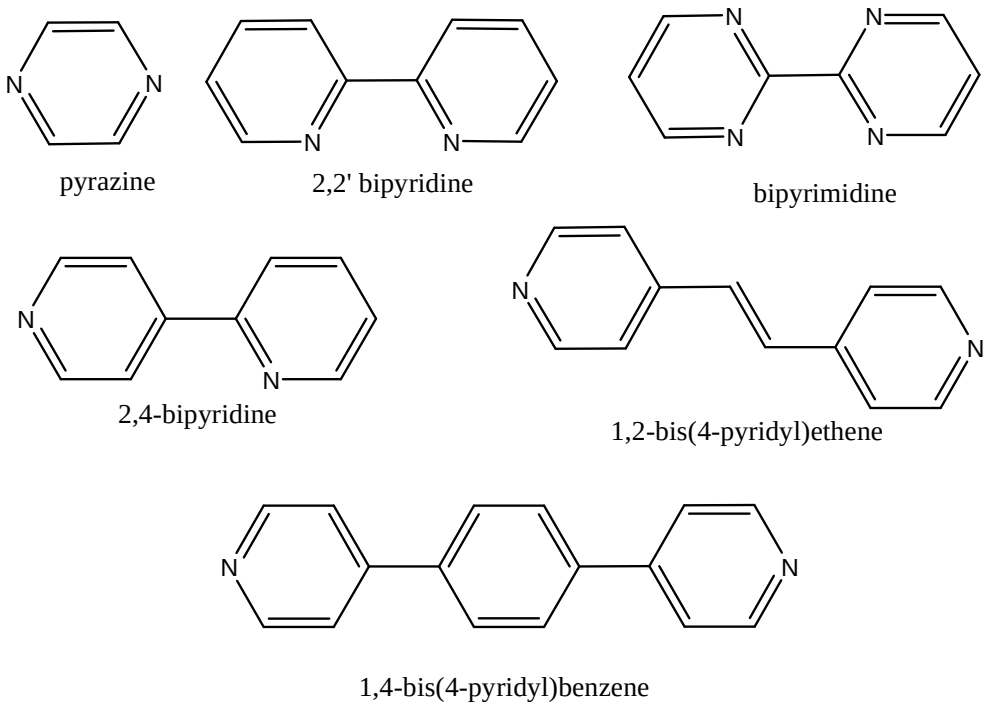

Figure 1.7 N-donor ligands which are preferred in coordination polymer synthesis often generate 1-D or 2-D structure.

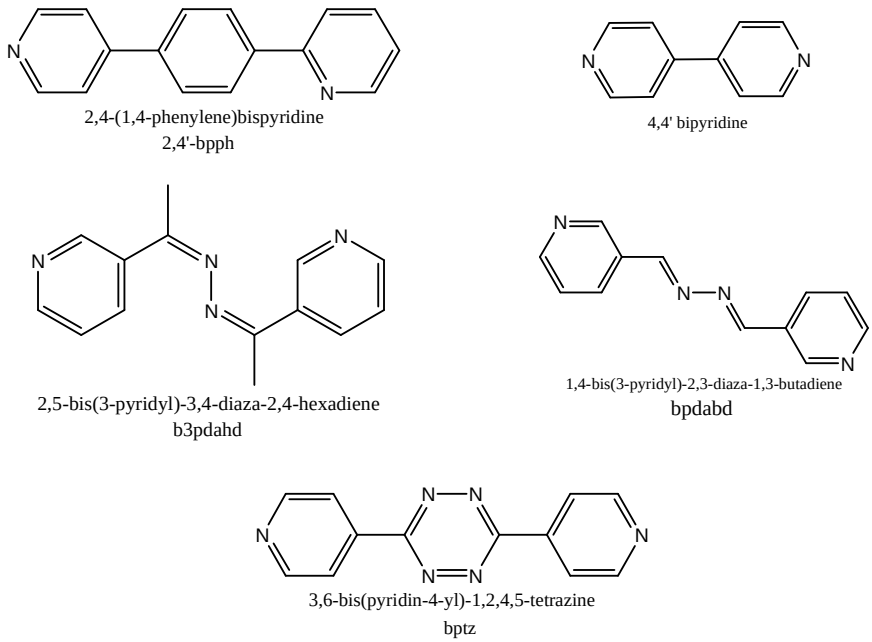

Figure 1.8 N-donor ligands that generate 3-D framework structures.

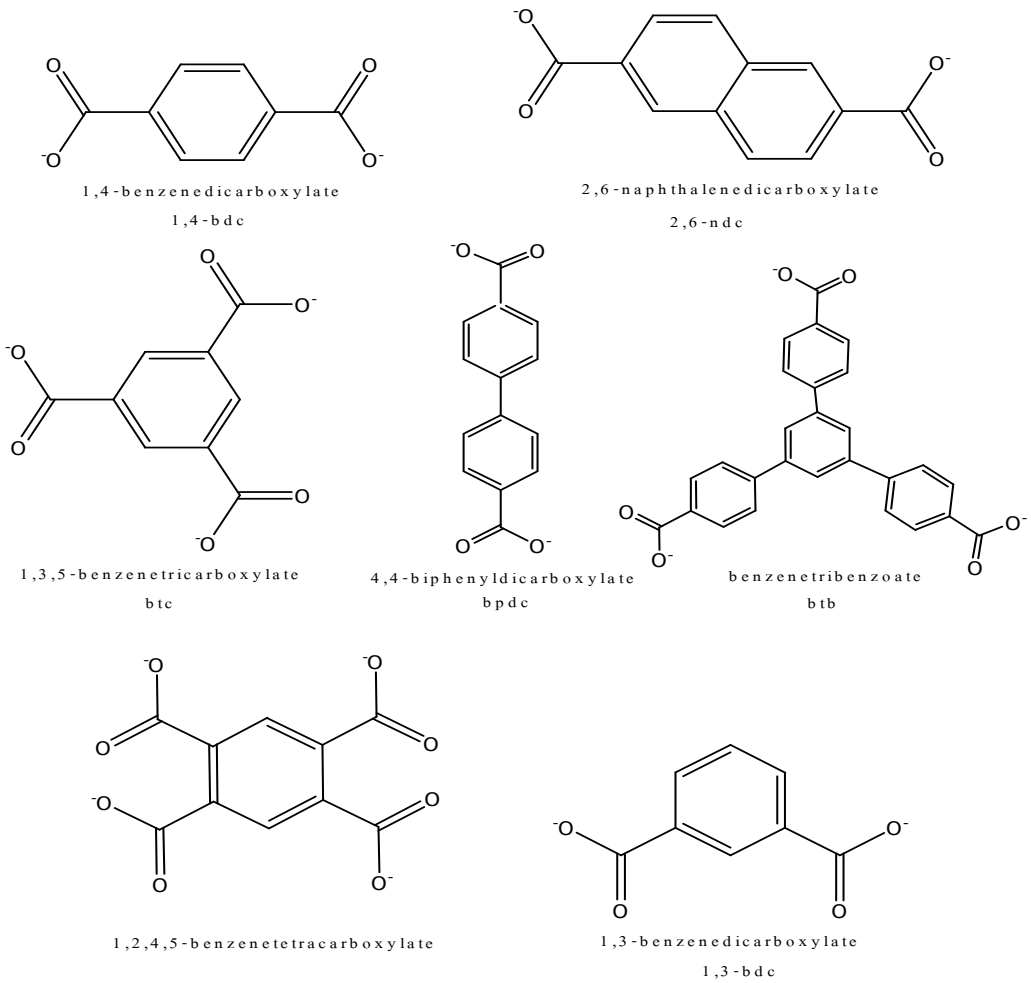

Figure 1.9 Some oxygen – donor organic molecules that produce 3-D frameworks

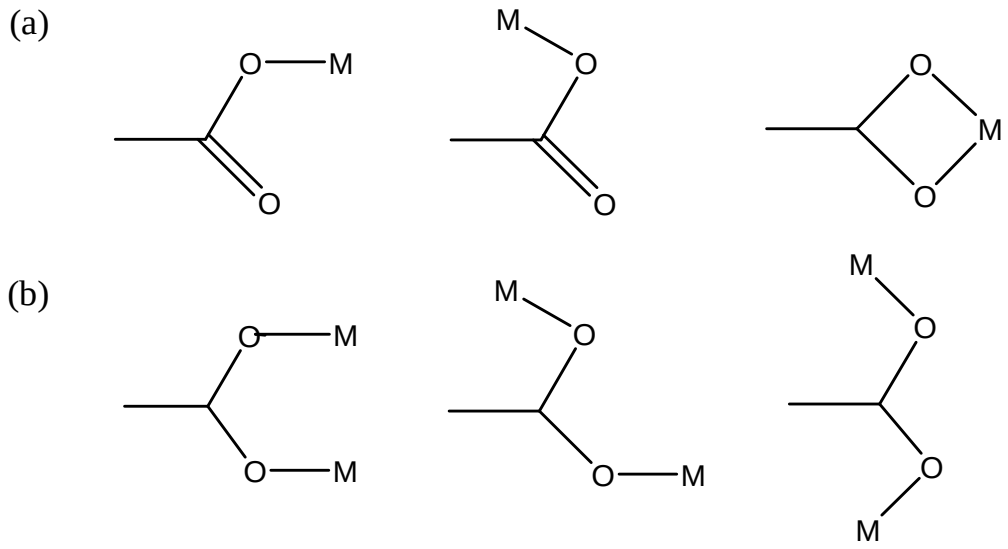

Figure 1.10 Modes of coordination of the carboxylate ions.[35]

1.3.5 Hybrid organic molecules

It has been shown that both nitrogen-and oxygen-donor molecules are effective for construction of 3-D coordination polymers with large pores. Theoretically, the concept of the synthetic method is based on 2 reaction steps. The first step provides the two dimensioned sheet layer, which is composed of metal ions or cluster bonding with organic molecules. Then, another organic ligand is added to form a pillar layer and bond all 2-dimensional sheets together. This organic pillar layer can be constructed via H-bonding or coordination bonding. However, coordination polymer bonding via H-bond usually generates an unstable structure in the absence of guest molecules. In comparison, a coordination network provides a more stable framework structure. [40-43]

Kondo *et al.*[41, 42] synthesised channel-liked porous metal organic frameworks via the direct mixing method under room temperature conditions. These porous metal organic frameworks are composed of two dimensional sheets of Cu (pyrazine-2,3-dicarboxylate) and these sheets coordinate with pillar organic ligands as shown in Figure 1.11. The pillar organic ligands are pyrazine (pyz), 4,4′- bipyridine (bpy), 1,2-dipyridylglycol (dpyg) and N-(pyridine-4-yl)isonicotimamide (pia) and these ligands form pillars between the 2-dimensional sheets of Cu (pyrazine-2,3-dicarboxylate).

Choi *et al.*[44] hydrothermal and solvothermal synthesised of $[Co_3(ndc)_3$-(bipyen)1.5]$\cdot H_2O$(1) and $[Co_2(ndc)_2(bipyen)]\cdot C_6H_6\cdot H_2O$(2), respectively; where bipyen = trans-1,2-bis(4-pyridyl)ethylene and H_2ndc = 2,6-naphthalenedicarboxylic acid). Both

structures are composed of 2-D sheets of $Co_2(O_2CR)_{4/2}$(R= naphthalene group) with these sheets interconnecting with the bipyen group, acting as a pillar, leading to 3-D framework. Structure (1) and (2) has the pore dimension 4.4 Å x 3.5 Å and 6.6 Å x 6.2 Å, respectively. As another example, Takamizawa *et al.*[45] solvothermal synthesised of Cu(bza)(pyz) where bza(benzoate) formed 2-D layer and pyz (pyrazine) interlinked those 2-D layers to form a porous metal organic framework.

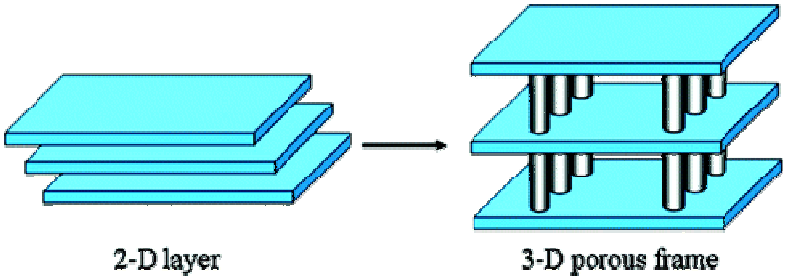

Figure 1.11 Schematic representation of the construction of a 3-D framework by a pillar insertion strategy.[41]

1.4 Classification of Metal organic frameworks

Kitagawa *et al.* [6] were first classified MOFs in to the three categories, 1st, 2nd and 3rd generation. Basically, the framework structures in these three categories contain guest molecules inside their cavities or channels, hence the name host-guest complex. The 1st generation frameworks lose their crystallinity and collapse when guest molecules have been removed (Fig. 1.12). The 2nd generation frameworks can retain their crystallinity and do not collapse even when guest molecules have been removed. Additionally, these 2nd generation frameworks exhibit true porosity, which can be used for gas/vapour storage. Finally, the 3rd generation frameworks have dynamic responses to external stimuli, light and host guest host exchange for instance. Furthermore, the 3rd generation frameworks may exhibit a new crystal phase when their guest has been removed. Furthermore, pore size of these frameworks can be expanded, collapsed or form a densely packed system after host guest exchange. [6, 46, 47] Horike *et al.*[47]suggested that the 3rd generation frameworks may be called as soft porous crystals. Example of soft porous crystal is CU-SIP-3.3H2O $[Cu_2(OH)(C_8H_3O_7S)(H_2O) \cdot 2H_2O]$ where SIP is 5-sulfoisophthalic acid) which is selectively adsorbed only NO above the gate-opening pressure of ~275 mbar.[48] Metal

organic framework Zn(TCNQ–TCNQ)bpy constructed from Zn(ii) centres and two ligands—4,4′-bipyridyl (bpy) and 7,7,8,8-tetracyano-*p*-quinodimethane(TCNQ). This flexible structure exhibited gate opening and closing mechanism in order to accommodated O_2 and NO in to the pores.[49] Bourrelly *et al.*[50] reported that porous chromium(III) terephthalate MIL-53(Cr) hydrogen-bonding network between methanol/ethanol along the tunnel of MIL-53 lead to structural transition.

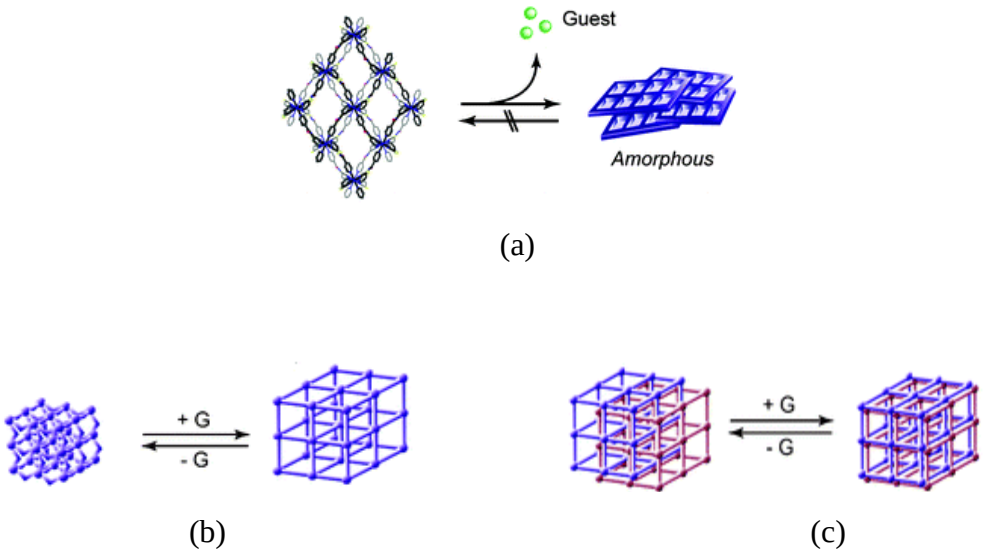

Figure 1.12 Schematic representation of dynamic and flexible MOFs a) the 1st generation frameworks; crystal to amorphous transition b) expanding or shrinking of MOFs c) densely packing during guest exchange.[46]

1.5 Synthetic methods

Coordination polymers are crystalline materials and these materials need a crystal growth technique in order to produce a suitable crystal for X-ray diffraction analysis. Generally, the favoured methods for synthesis of crystalline coordination polymers are solvent diffusion and hydro(solvo)thermal synthesis. These two methods are discussed as the following sections.

1.5.1 Diffusion methods

Basically**,** this method can be divided in two main techniques: solvent diffusion and vapour pressure diffusion techniques. These techniques depend on different properties of the solutions to grow the crystal.

- Solvent Diffusion (Layering Technique). A small amount of solution (solution of metal compound) is place in a tube and solution of organic ligand is carefully layered on the top of the solution. The tube is sealed and left undisturbed. In the passage of time, some crystals grow by diffusion of the ligand into a metal ion solution. However, solvent diffusion can be adapted by using an H-tube instead of the straight tube type. It should be noted that the mixture of organic ligand solution should be less dense than the metal ion solution and a suitable volume ratio metal solution/organic solution is typically 1:4 or 1:5. Typically, water/ethanol, water/mixture of water and ethanol are commonly used for growing crystals.

- Vapor Diffusion. This technique basically has the same principle as the previous technique but the precipitant is allowed to diffuse into the solution from the vapour as shown in figure 1.13. An advantage of these two techniques is a small amount of material may be used and it is possible to set up many experiments by varying solvent and experimental conditions at one time. However, these techniques are time consuming experiments due to slow diffusion and crystal growth with the process taking a few days up to several months.[51, 52]

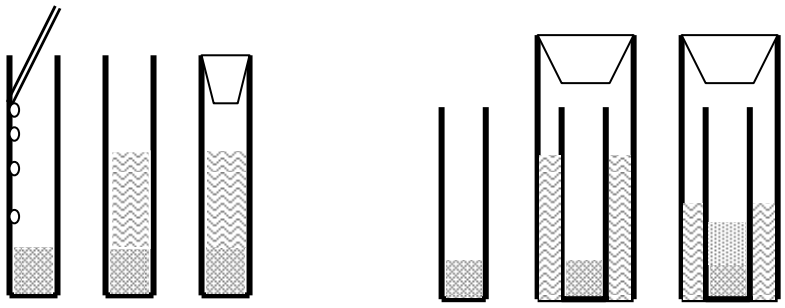

(a) (b)

Figure 1.13 Schematic representations of a) layering technique and b) vapour diffusion technique.

1.5.2 Hydrothermal or solvothermal synthesis

Hydro(solvo)thermal synthesis was firstly introduced for the synthesis of zeolites. Nowadays, this method is widely used for synthesis of several organic framework coordination polymers. Hydrothermal synthesis is typically employed in the temperature range 110-240 ºC in a Teflon-line autoclave under autogenous pressure. Under these

conditions, the solvent temperature can be increased above its atmospheric pressure boiling point while the solvent viscosity and dielectric constant of the solvent are reduced. Reduction of viscosity and dielectric constant also enhances the diffusion process and crystal growth.[52, 53] Schematic of hydrothermal vessel is shown in Figure 1.12.

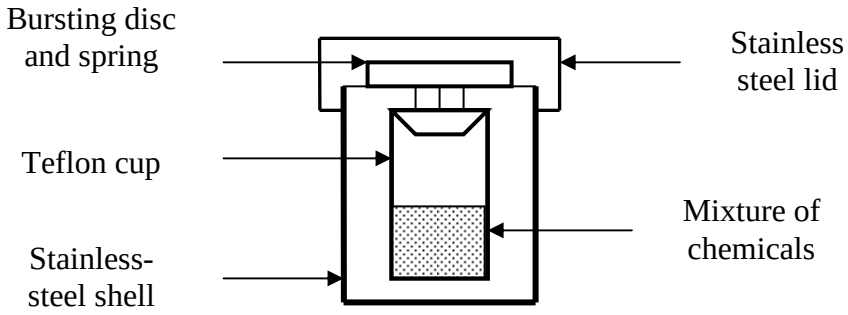

Figure 1.14 A schematic of a Teflon TM-lined, stainless autoclave typically use in the laboratory to perform solvothermal synthesis.

1.6 Porous carbon materials

1.6.1 Activated carbon

European Council of Chemical Manufacturers' Federation defined[54] activated carbon as non-hazardous, processed, carbonaceous products which have a porous structure and large internal surface. In addition, the internal surface area and volume of pores of activated carbons is generally greater than ~ 400 m^2 g^{-1} and 0.2 mL g^{-1}, respectively. Activated carbons are a generic name for a group of porous carbon materials produced by carbonization followed by physical or chemical activation of carbon-rich organic precursors. These activation processes produce a high porosity and surface area which is suitable for removal of impurities from gases and liquid, gas storage and separation processes.[55, 56]

Activated carbons adsorb species from both gaseous and liquid phases and the adsorption process is influenced by the pore size distribution of the activated carbon and size, structure and properties of adsorbate. The usage of carbon adsorbents depends on their surface area, pore size distribution and surface chemical characteristics. In adsorption

from the liquid phase and gas phase, both macro porous and mesoporous carbons are used while microporous carbon is used in gas adsorption processes. Normally, both marcroporous and mesoporous activated carbons have been employed in waste-water treatment[57-59], drinking water purification[60-62], pharmaceutical and chemical industries,[63] *etc*. On the other hand, most of microporous carbons are used for odour treatment[64], gases storage[65, 66] and both agricultural and industrial exhaust gases control.[64, 66] The properties of activated carbons are directly related to the nature of the starting material, the type of production method and the temperature of production. More details on production methods are described in section 1.6.6.1.

Stoeckli[67] described the structure of activated carbon as consisting of aromatic sheets and strips often bent, resembling a mixture of wood shavings or crumpled sheets of paper with a variety of pores size between them. The variety of different gaps between the sheets represents the makeup of the micropores. A schematic structure of activated carbon is shown in Figure 1.15.

In term of physical chemistry, activated carbons are an amorphous and non-graphitic form of carbon. Carbon atoms within the structure of activated carbon are bonding with other carbon atoms forming hexagonal pattern similar to graphene sheet.[55, 68] However, X-ray diffraction studies revealed that these graphene sheets stack on the top of each other layer and each layer often has an irregular shape, randomly oriented, and lack any directional relationship. So, the structure of activated carbon is much more disordered than graphite. In addition, some heteroatoms and inorganic minerals such as metal oxides originating from the precursors and activation method are normally present in the structure of activated carbon. The heteroatom and impurities in activated carbon depend on the nature of the precursor and the activation process.

Figure 1.15 A schematic structure of activated carbon

The heteroatoms, which are mainly oxygen, hydrogen, nitrogen and sulfur, are usually located at the edges of graphene sheets. The presences of surface functional groups determine either acidic or basic properties of the activated carbon. Additionally, carbons with acidic surface or basic functional groups may exhibit cation and anion exchange characteristics, respectively. The adsorption characteristic of activated carbon is not only determined by its pore structure but it is also determined by surface functional groups.[69-71] In addition, these surface functional groups play a significant role in chemisorption and may enhance adsorption of some species.[70, 72-74] Several structures of acid and basic surface functional groups have been proposed as shown in Figure 1.16.

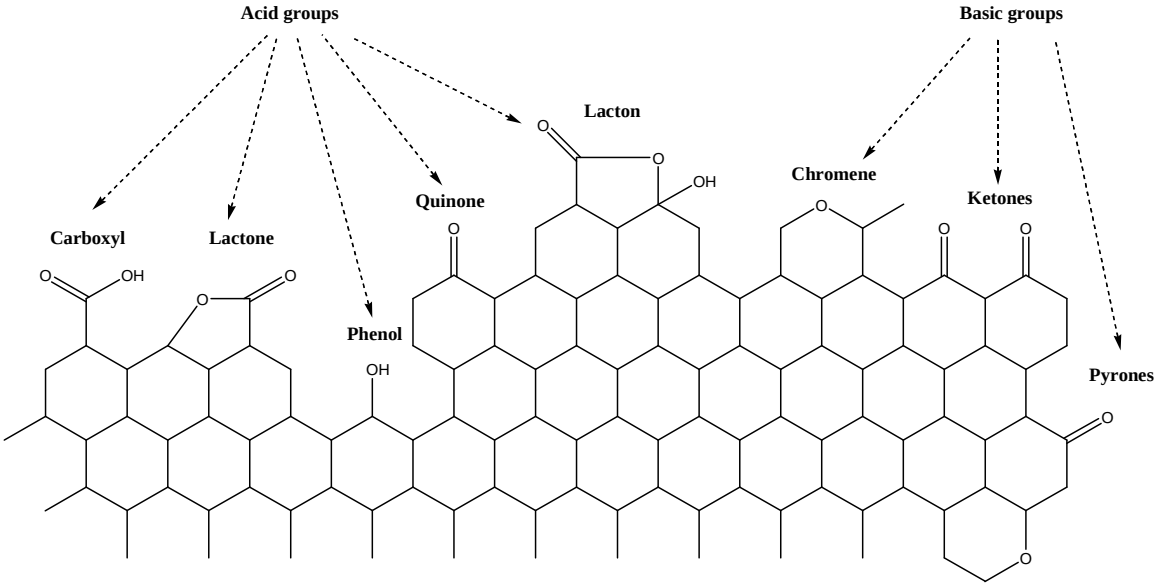

Figure 1.16 Possible acid and basic surface functional groups on activated carbon.

1.6.1.1 Production of activated carbon

Production of activated carbon can be accomplished by the following processes; preparation of raw materials, carbonisation and activation.[71] Originally, typical raw materials for producing activated carbon were coal, peat and lignite, wood, palm and coconut shell. Recently, production of activated carbon from agriculture by-products and waste water treatment residue has gained attention due to its abundance, by-products availability, and inexpensiveness. Agricultural by-products, for example, are saw dust, rich

husk, fruit stones, fruit seed, shell and kernels.[75-77] There are four basic criteria for selecting raw materials that should be considered; a) availability and cost b) a possibility of yielding a good quality of activated carbon c) low content of volatile organic matter and ash d) high stability during storage. Raw materials, which have low volatile organic content, normally give high yields of activated carbon. In addition, raw material with high lignocelluloses (around 40% upward) are suitable for commercial production.[56] Typical fixed carbon contents of raw materials commonly used in the production of activated carbon are shown in table 1.1.

Table 1.1 Fixed carbon content of raw materials commonly used in the production of activated carbon[56]

Raw materials	Approximate carbon content, %
Soft wood	40
Hard wood	40
Coconut shell	40
Lignite	60
Bituminous coal	75
Anthracite	90

Raw materials are usually crushed, milled and sieved to particle size about 1-2 mm before passing it through the cabonisation and activation steps. A particle size of ~ 1-2 mm is appropriate for handling and yields good properties such as high surface area.[78-80] Sentorun-Shalaby and co-workers[81] determined the effect of particle size of raw materials on the properties of the activated carbon. Three particle size ranges were examined which were 0.85-1.7, 1.7-3.35 and 3.35-4.00 mm. Results showed that the coarser particles gave the smaller surface area of activated carbons. However, the coarser particles gave slightly high percentage of the microporosity.

The next process involves carbonization of the materials. In this step, the materials is heated at temperatures normally below 800 ^{o}C with slow heating rate under inert gas (N_2, Ar or very low O_2 condition) to eliminate non carbon species and give materials with enriched carbon contents (chars) with some porosity.[71, 82]

Activation increases porosity and helps to improve the accessibility of the pore structure by opening the closed porosity. Activation can be divided into two categories; physical activation and chemical activation. In physical activation, the char is gasified in steam, air or CO_2. The activation temperature is normally in range 600-900˚C for steam and carbon dioxide. For oxygen activation, however, much lower temperature was employed (300-500 ˚C) to avoid combustion.[83, 84]

Gasification of the char with steam and carbon dioxide are endothermic reactions as described by the following equations;[56]

$$C + H_2O \rightleftharpoons CO + H_2 \qquad (\Delta H = +118.5\ kJmol^{-1}) \qquad (1.1)$$

$$C + CO_2 \rightleftharpoons 2CO \qquad (\Delta H = +159\ kJmol^{-1}) \qquad (1.2)$$

Reaction of CO produced by equation (1.1) with steam by the following reaction:

$$CO + H_2O \rightleftharpoons CO_2 + H_2 \qquad (\Delta H = -42.3\ kJmol^{-1}) \qquad (1.3)$$

During this physical activation, char gasification leads to the formation of meso- and micropores, which form the porous structure of activated carbon. Activation with CO_2 is often used on a laboratory scale whereas steam activation is preferred for larger scale production of most activated carbons with the industrial importance of lower cost. However, steam activation of activated carbon exhibits lager meso- and macropore volumes than a carbon dioxide activated carbon. Additionally, longer reaction times at constant temperature give larger total pore volumes and higher surface areas.[85] A schematic representing the general steps for physical activation is shown as Figure 1.22.

In chemical activation, an activation reagent is used prior to carbonisation. The process involves impregnation of the materials with the chosen chemical agent. Commonly, H_2SO_4, $ZnCl_2$, H_3PO_4, NaOH and KOH have been used as activation reagents.[86] The activation reagents help to develop the porosity, by means of dehydration, degradation of volatile organic compounds and also help remove inherent minerals from the carbon. The interaction between the activation reagent and the carbonised carbon normally occurs during soaking and heating the precursor material prior to carbonization at high temperature.[87, 88] Major advantages of chemical activation, compared to physical activation, are the higher yield, lower temperature of activation (less energy costs), less activation time, and higher surface area activated carbons can be obtained.[89] However, some disadvantages do appear which include high cost of the activating agents, equipment corrosion, and need to perform an additional cleaning step to remove the residue activation reagent on products. [90] A schematic representing the general steps for chemical activation is shown as Figure 1.23.

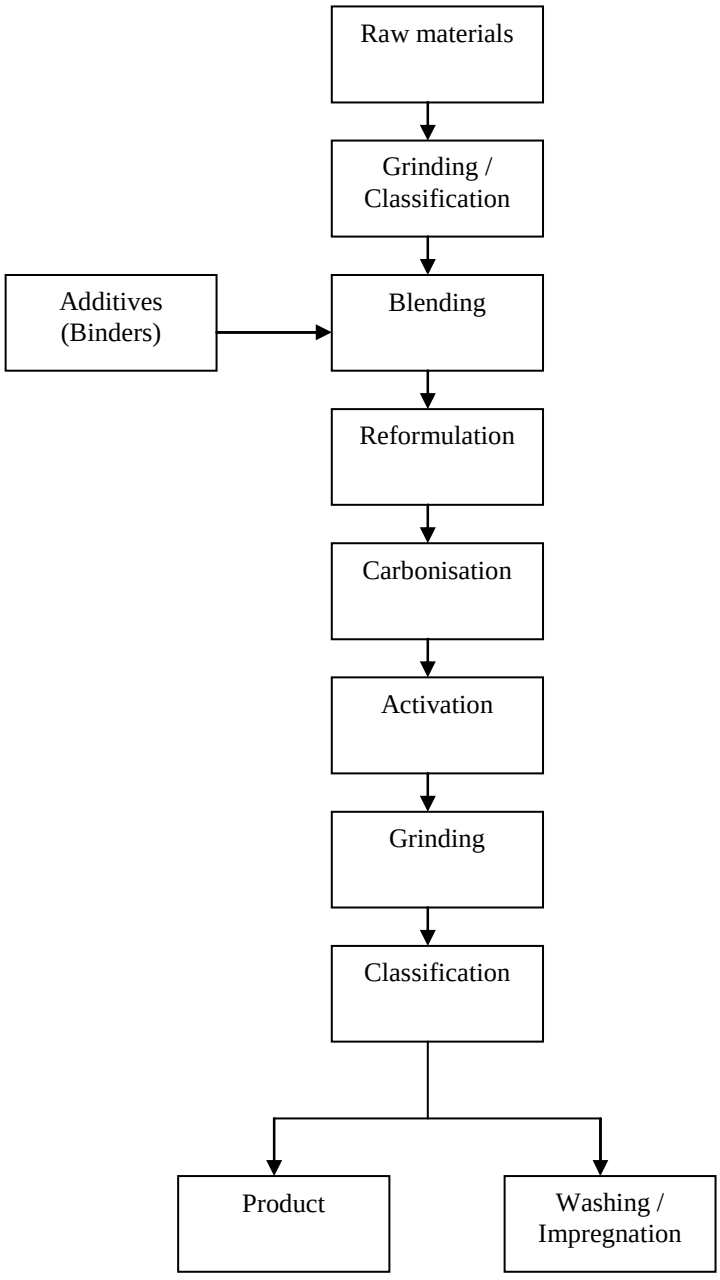

Figure 1.22 Schematic representing the general steps for physical activation

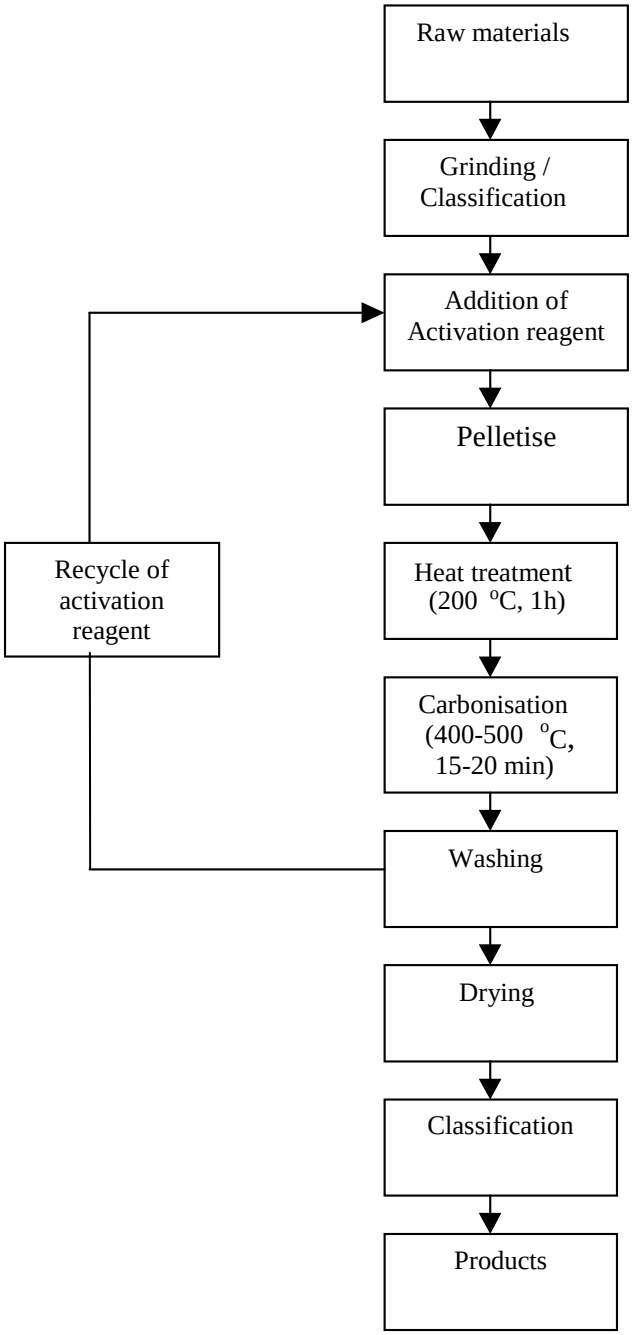

Figure 1.23 Schematic representing the general steps for chemical activation.

1.6.2 Carbon molecular sieves

In 1949, Franklin[91] proposed the first report that fluids were excluded from heat-treated coals in the order of their molecular size. Walker *et al.*[92],[93] reviewed the molecular sieving effect for carbons etc. In 1973, Juntgen *et al.*[94] prepared a black coal-based adsorbent, which separated oxygen from nitrogen. Since then, the molecular sieving effect has been studied extensively in both basic fundamental and industrial applications. Carbon molecular sieves have been produced commercially and widely used in the production of nitrogen from air and gas purification processes.[71] More details on applications of carbon molecular sieves on air and gases separation are discussed in Chapter 3.

The term molecular sieve was originally introduced by J W McBain [95, 96] to describe the selective adsorption of molecules on a zeolite. Bekkum *et. al.*[97] defined the term molecular sieve as porous solid materials with a pore size equivalent to molecular dimensions 0.3 - 2.0 nm in diameter. Examples of crystalline molecular sieves are zeolites and amorphous forms are carbon molecular sieves.

In general, carbon molecular sieves (CMS) are a subgroup of activated carbon with almost homogenous micropores of a few angstroms in diameter, and are able to selectively separate molecules on the basis of their size and shape.[98, 99] Nguyen and Do[100] gave a qualitative description of the structure of carbon molecular sieves as a bimodal structure adsorbent with only a small contribution of meso- and macropores to the total equivalent surface area. Additionally, the surface of CMS is hydrophobic. In comparison, the micropore size distribution of CMS is much narrower than in conventional activated carbon. CMS have slit-shaped pores with pore sizes in the range 0.3 to 1.2 nm, and pore volumes from 0.2 to 0.5 cm^3g^{-1}. The surface area may range from 300 to 1,500 m^2g^{-1}.[68, 101] Compared to zeolite molecular sieves, CMS have some superior properties, such as high hydrophobicity, high thermal stability, resistance in both alkaline/acid media and less expensive than zeolites.[102] Furthermore, CMS generally have a larger pore volume and their pore size can be adjusted to the right pore width by means of relatively simple methods by controlling of carbon deposition.[68]

A variety of raw materials have been used to prepare CMS such as coal, nut shell, coconut shell, palm shell, *etc*. However, bituminous coal and coconut shells have proved to be suitable raw materials for industrial production.[103, 104] Figure 1.24 shows the production process of CMS. In general, this quite similar to activated carbon but the CMS needs to treated by more specific approaches.[71]

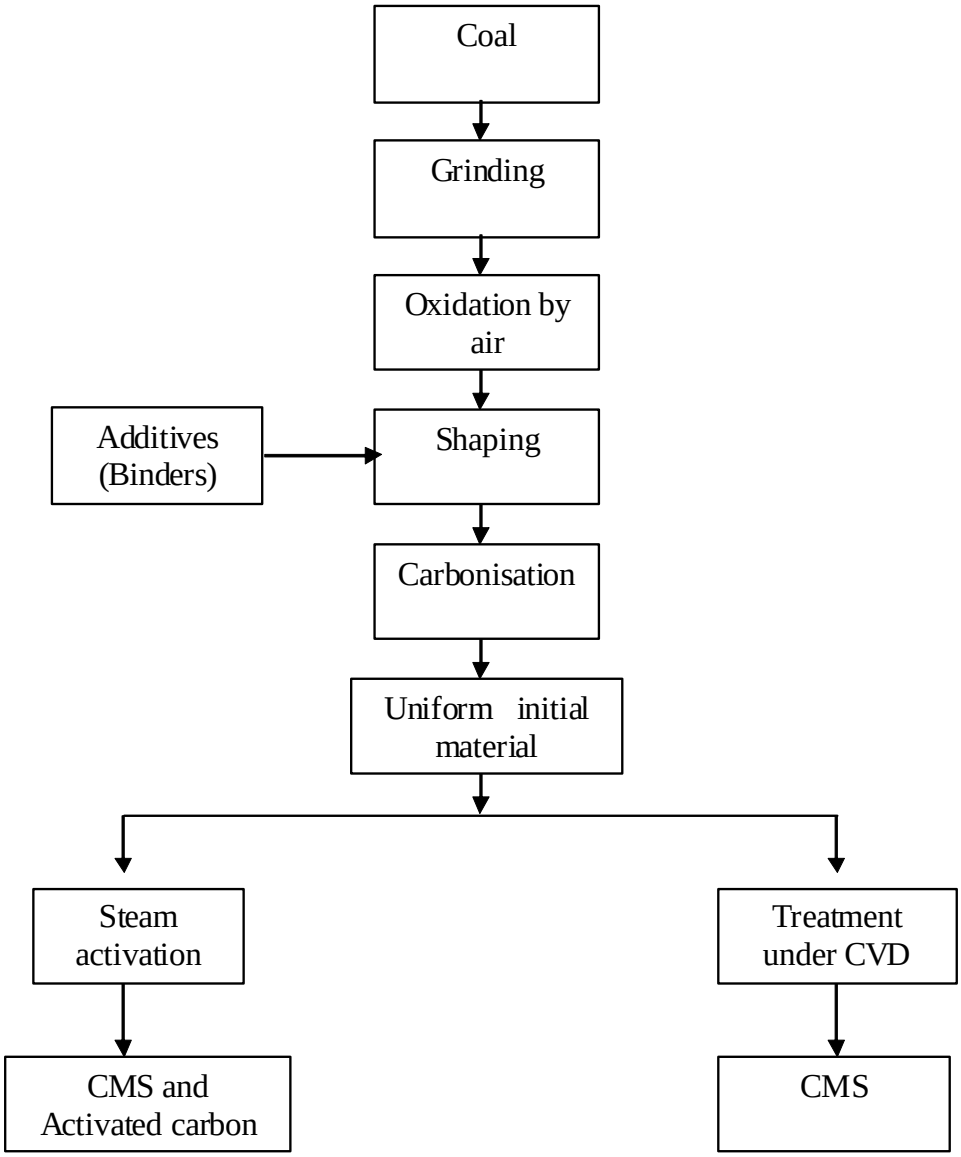

Figure 1.24 Procedure for the manufacture of molecular sieve carbon.

Conventionally, there are two major approaches to produce CMS; the first approach is the synthesis of CMS from carbonaceous precursors under specified carbonization conditions that give pores of the appropriate dimensions. The other approach for preparing CMS is the modification of pore size of an existing porous carbon by chemical vapour deposition (CVD). The first approach may be divided in to four sub preparation methods;

i) Pyrolysis method; a selected carbonaceous precursor is pyrolysed under suitable carbonization temperature and inert environment.[105, 106]
ii) Contraction method; the carbonized material is treated at a temperature greater than 1000°C to shrink the pores of the source material.[99, 107]
iii) Co-carbonisation method; a mixture of the carbonized material and organic additive such as pitch, phenol–formaldehyde resin or other chemicals are pyrolysed under rigidly controlled conditions. The pore size of the CMS may be controllable by changing amount of organic additives.[108, 109]
iv) Covering method; a carbonized porous material is mixed with a chemical species and the mixture is further pyrolyzed to reduce the pore size by decreasing the size of the pores with pyrolytic carbon.

The second approach is chemical vapour deposition (CVD), which is the major methods to control pore structure in selectivity in carbon molecular sieves.[110] In this method, a microporous substrate with narrow pore size distribution is usually used as the starting material. CVD involves a decomposition (cracking) of a volatile hydrocarbon above the surface of activated carbon, which causes deposition as a thin film on the surface.[111-113] A variety of hydrocarbon sources have been used as the deposition agents, such as pyridine, pyrrole, benzene, acetylene, methane and cyclohexane. Benzene has often been in used in CVD as it does not produce the intermediate by-product during the decomposition process and this increases the control of the deposition process.[114] Previous research also showed that controlling pore size can be achieved under temperature and pressure ranging from 300- 900 ˚C and 1 torr to atmosphere, respectively.[100, 115, 116]

There are three possibilities for volatile hydrocarbon deposition into/on a pore of activated carbon have been proposed as shown in Figure 1.25.[117, 118,119] Long exposure times for hydrocarbon deposition may cause blocked pores (b). According to case (c), volatile hydrocarbon may be deposited uniformly over the entire surface of the pore when the molecular size of hydrocarbon is small enough to diffuse into the pore. In this case, deposition of hydrocarbon along the pore can decrease the pore volume of activated carbon and it will also slow the gas diffusion rate, which is not desirable for gas separation processes. The problem in case (c) may be avoided by i) controlling the suitable exposure time for deposition and ii) using a hydrocarbon with a molecular size larger than pore of activated carbon.[117] In the last case (d), hydrocarbon is deposited on the pore mouth of activated carbon. This (d) case produces a desirable CMS as the pore size can be reduced without reducing the pore volume.

Nguyen and Do[100] proposed the block and reopening method to yield a CMS with a small narrow pore size distribution. This method involves three steps: carbonization, reduction of pore size by carbon deposition, and finally reopening of the pores by controlled gasification.

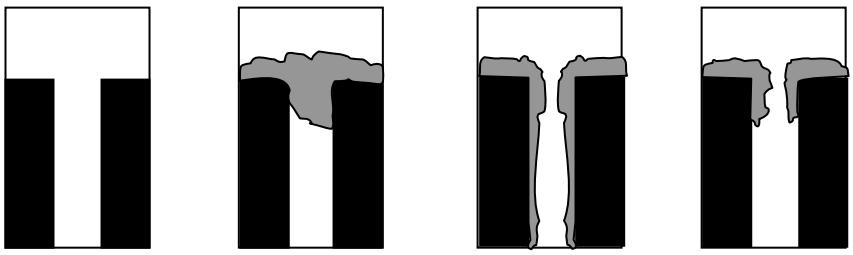

Figure 1.25 Schematic representation of carbon deposition under different regimes: (a) clean pore, (b) blocked pore, (c) deposition entirely on pore surface, and (d) deposit around pore mouth.

1.7 Applications of porous materials

1.7.1 Separation of unfriendly environmentally species.

In recent years, there has been significant public and scientific concern over the potential risks of industrial, flue gas emissions and also impurities in wastewater streams. These emissions may contribute to poor environmental quality and also, pose a threat human health. Thus, as the regulatory limits on environmental emissions become more stringent, industries have developed separation technologies that could remove contaminants and pollutants from process waste streams. Adsorption processes and membrane separations are two dominant technologies that have been applied in industrial waste treatment. Commercial available meso- and macro-porous activated carbons have been applied to waste water treatment system in order to remove contaminants e.g. heavy metal ions, dye, and organic molecules.[120-122] While, micro-porous (nano-porous) activated carbon is typically used as an adsorbent for removal of gaseous species. The surface functionality of micro-and nanoporous activated carbon can be modified for removal various flue gases such as SO_2, NO_x, and volatile organic carbons (VOCs).[123-125] Furthermore, both micro-and nanoporous activated carbon also have possible applications in removal of polychlorinated dibenzo-p-dioxins (PCDDs), dibenzofurans (PCDFs), and various forms of mercury species.[126-129] Metal organic frameworks also show their potential application in flue gas treatment such as CO_2.[130-132] Britt and co-workers[133] conducted research on harmful gas adsorption, e.g. dichloromethane and sulfur dioxide, on six metal organic frameworks and activated carbon. They reported that MOF-199, with open (unsaturated) metal centres, showed superior harmful gases adsorption compare to activated carbon.

1.7.2 Clean energy storage.

Energy is an important part of our daily life. Cars and other internal combustion engines need the energy from fossil fuel combustion to function. However, fossil fuel combustion leads to some environmental problems, for instance acid rain, stratospheric ozone depletion, development of the greenhouse effect and air pollution. These environmental problems also have a negative effect on public health. Furthermore, the supply of oil is limited and supplies are likely to become scarce in the foreseeable future. As a result, a number of solutions have been proposed. One potential solution is using

hydrogen as an alternative energy carrier. In the future, hydrogen may be the dominant fuel, for use in vehicles generating only water as a product.[134, 135] However, at present there are no systems for hydrogen storage that meet all the requirements of safety, capacity, and refuelling distance. Therefore considerable research is being undertaken to develop new porous materials for hydrogen storage application.

1.7.3 Catalysis

In 1995, the global catalyst market was estimated to about 8,600 million US$, with a significant growth in 2001, to a value of 10.7 million US$. Catalyst marketing has growing dramatically because of the remarkable property of catalyst to increase accelerating the rate of a chemical reaction without being part of the final products. Over 80% of the industrial chemical processes in use nowadays rely on one or more catalytic reactions and these industrial chemical processes include, oil refining, petrochemical processing, and the manufacturing of commercial chemicals (olefins, ethylene glycol, methanol, etc.).[136, 137] Porous materials are used as either heterogeneous catalysts or a heterogeneous catalyst support. Zeolites and activated carbons is also used as an inert porous carrier material for distributing metal catalysts on the large internal surface, thus making metal catalyst much more accessible to reactants. Furthermore, precious metal catalyst, e.g. gold, can be easily recovered by burning off the activated carbon support catalyst.[138] The applications of activated carbon supported catalyst in fuel cell, environmental issues and industrial processes are well established.[123, 139-141] Attempts to use MOFs as the catalyst are in an initial stage. In principle, MOFs can be synthesis in a systematic route to funtionalise their structures. In addition, each functional groups may be act as an active site and may be a catalytic centre.[6] An example of a functionalized metal organic framework which exhibits selective sorption and catalysis properties is [Cd(4-btapa)$_2$(NO_3)$_2$]. 6H_2O.2DMF where 4-btapa = 1,3,5-benzene tricarboxylic acid tris [N-(4-pyridyl)amide]).[142] Amine surface functional groups of this 3-D structure only binding selectively with short-chain alcohols e.g. methanol, ethanol, *n*-propanol and *n*-butanol. This Cd(4-btapa)$_2$(NO_3)$_2$ was also used as the catalyst in the reaction of benzaldehyde with methelene compounds and gave the malononitrile product 98%. Metal organic frameworks with unsaturated metal centres may be a highly active and selective Lewis acid catalyst in some chemical reactions.[143-145] Llabrés and co-workers[146] showed that combinations of the

two catalysts containing 10 wt% $Cu(2\text{-pymo})_2$; (2-pymo = 2-hydroxypyrimidinolate) and 90 wt % $Co(PhIM)_2$;(PhIM = phenylimidazolate) yields the best performance in terms of activity, selectivity for the oxidation of tetralin. In the tetralin oxidation process, $Cu(2\text{-pymo})_2$ was used for the activation of tetralin in order to produce tetralinhydroperoxide (TOOH). Once the TOOH was formed, $Co(PhIM)_2$ rapidly oxidised TOOH into tetralone.

1.7.4 Sensors

Many gas detectors developed for portable applications are based on the change in electric resistivity with varying gas concentration and the sensitivity is normally dependent on surface area. Therefore, nanoparticle metal oxides and porous materials with large specific surface areas, and high sensitivity to slight changes in environments (temperature, atmosphere, humidity, and light) are being developed and applied as detectors of combustible gases, humidity, ethanol, and hydrocarbons. The most widely preferred for this application are nanoparticle metal oxides such as SnO_2, TiO_2, ZrO_2, and ZnO oxides.[147] However, recent studies revealed that metal organic frameworks have the potential for sensor application. Wong *et al*.[148] and Chen *et al.*[149] reported that microporous $Tb_2(Municate)_3$ and Eu(benzene-1,3,5-tricarboxylate) showed the reversible sensing of anions and this sensing is controlled by a molecular sieve property. Small molecules are allowed to pass while large molecules are excluded from both microporous MOFs. Additionally, Chen *et al.* gave further suggestion that the open metal centre in Eu(BTC) structure may lead to highly sensitive sensors for small molecules and ions. Yeom *et al.*[150] reported that the electrical signal from the toxic gas sensor can be enhanced by coating the gas preconcentrator with IRMOF-1.

1.8 References

1. Sing, K. S. W.; Everett, D. H.; Haul, R. A. W.; Moscou, L.; Rouquerol, J., Reporting physisorption data for gas/solid systems with special reference to the determination of surface area and porosity. *Pure Appl. Chem.* **1985,** 57, (4), 603-19.

2. Rouquerol, J.; Avnir, D.; Fairbridge, C. W.; Everett, D. H.; Haynes, J. M.; Pernicone, N.; Ramsay, J. D. F.; Sing, K. S. W.; Unger, K. K., Recommendations for the characterization of porous solids (Technical Report). *Pure Appl. Chem.* **1994,** 66, (8), 1739-58.

3. McCusker, L. B.; Liebau, F.; Engelhardt, G., Nomenclature of structural and compositional characteristics of ordered microporous and mesoporous materials with inorganic hosts. *Pure Appl. Chem.* **2001,** 73, (2), 381-94.

4. Bu, X.-H.; Feng, P. Y., *The chemistry of nanostructured materials*. World Scientific Publishing London, 2003.

5. Janiak, C., Engineering coordination polymers towards applications. *Dalton Transactions* **2003**, (14), 2781 - 804.

6. Kitagawa, S.; Kitaura, R.; Noro, S., Functional Porous Coordination Polymers. *Angew. Chem. Int. Ed.* **2004,** 43, (18), 2334-75.

7. Leea, J. Y.; Li, J.; Jagiello, J., Gas sorption properties of microporous metal organic frameworks. *J. Solid State Chem.* **2005**, (178), 2527–32.

8. Rowsell, J. L. C.; Yaghi, O. M., Strategies for Hydrogen Storage in Metal Organic Frameworks. *Angew. Chem. Int. Ed.* **2005,** 44, 4670-9.

9. Fletcher, A. J.; Thomas, K. M.; Rosseinsky, M. J., Flexibility in metal-organic framework materials: Impact on sorption properties *J. Solid State Chem.* **2005,** 178, (8), 2491-510

10. Ferey, G., Microporous Solids: From Organically Templated Inorganic Skeletons to Hybrid Frameworks...Ecumenism in Chemistry. *Chem. Mater.* **2001,** 13, (10), 3084-98.

11. Maspoch, D.; Ruiz-Molina, D.; Veciana, J., Magnetic nanoporous coordination polymers. *J. Mater. Chem.* **2004,** 14, 2713-23.

12. Schubert, U.; Husing, N., *Synthesis of Inorganic Materials*. 2 ed.; Wiley-VCH Weinheim 2004; p 429.

13. Uemuraa, K.; Matsudab, R.; Kitagawa, S., Flexible microporous coordination polymers. *J. Solid State Chem.* **2005**, (178), 2420-9.

14. Papaefstathiou, G. S.; MacGillivray, L. R., Inverted metal-organic frameworks: solid-state hosts with modular functionality. *Coord. Chem. Rev.* **2003,** 246, 169-84.

15. Steed, J. W.; Atwood, J. L., *Supramolecular Chemistry* John Wiley and Sons Ltd Chichester, 2000; p 772.

16. Dobrawa, R.; Würthner, F., Metallo supramolecular approach toward functional coordination polymers *Journal of Polymer Science Part A: Polymer Chemistry* **2005,** 43, (21), 4981-95.

17. Moulton, B.; Zaworotko, M. J., From Molecules to Crystal Engineering: Supramolecular Isomerism and Polymorphism in Network Solids *Chem. Rev.* **2001,** 101, (6), 1629 -58.

18. Li, H.; Eddaoudi, M.; O'Keeffe, M.; Yaghi, O. M., Design and synthesis of an exceptionally stable and highly porous metal-organic framework *Nature* **1999,** 402, 276 - 9.

19. Kim, J.; Chen, B.; Reineke, T. M.; Li, H.; Eddaoudi, M.; Moler, D. B.; O'Keeffe, M.; Yaghi, O. M., Assembly of Metal-Organic Frameworks from Large Organic and Inorganic Secondary Building Units: New Examples and Simplifying Principles for Complex Structures. *J. Am. Chem. Soc.* **2001,** 123, (34), 8239 -47.

20. Blake, A. J.; Champness, N. R.; Khlobystov, A. N.; Parsons, S.; Schröder, M., Controlled Assembly of Dinuclear Metallacycles into a Three-Dimensional Helical Array. *Angew. Chem. Int. Ed.* **2000,** 39, (13), 2317 - 20.

21. Yaghi, O. M.; O'Keeffe, M.; Ockwig, N. W.; Chae, H. K.; Eddaoudi, M.; Kim, J., Reticular synthesis and the design of new materials. *Nature* **2003,** 423, 705-14

22. Erxleben, A., Structures and properties of Zn(II) coordination polymers *Coord. Chem. Rev.* **2003,** 246, (1-2), 203-28

23. Zeng, M.-H.; Wang, B.; Wang, X.-Y.; Zhang, W.-X.; Chen, X.-M.; Gao, S., Chiral Magnetic Metal-Organic Frameworks of Dimetal Subunits; Magnetism Tuning by Mixed-Metal Compositions of the Solid Solutions. *Inorg. Chem.* **2006,** 45, (18), 7069-76.

24. de Lill, D. T.; de Bettencourt-Dias, A.; Cahill, C. L., Exploring Lanthanide Luminescence in Metal-Organic Frameworks: Synthesis, Structure, and Guest-Sensitized Luminescence of a Mixed Europium/Terbium-Adipate Framework and a Terbium-Adipate Framework. *Inorg. Chem.* **2007,** 46, (10), 3960-5.

25. Chen, B.; Zhao, X.; Putkham, A.; Hong, K.; Lobkovsky, E. B.; Hurtado, E. J.; Fletcher, A. J.; Thomas, K. M., Surface Interactions and Quantum Kinetic Molecular Sieving for H_2 and D_2 Adsorption on a Mixed Metal Organic Framework Material. *J. Am. Chem. Soc.* **2008,** 130, (20), 6411-23.

26. Spek, A., Single-crystal structure validation with the program PLATON. *J. Appl. Crystallogr.* **2003,** 36, (1), 7-13.

27. Barnett, S. A.; Champness, N. R., Structural diversity of building-blocks in coordination framework synthesis-combining $M(NO_3)_2$ junctions and bipyridyl ligands. *Coord. Chem. Rev.* **2003,** 246, (1-2), 145-68

28. Gudbjartson, H.; Biradha, K.; Poirier, K. M.; Zaworotko, M. J., Novel Nanoporous Coordination Polymer Sustained by Self-Assembly of T-Shaped Moieties. *J. Am. Chem. Soc.* **1999,** 121, (11), 2599 -600.

29. Dong, Y.-B.; Smith, M. D.; Loye, H.-C. z., New Inorganic/Organic Coordination Polymers Generated from Bidentate Schiff-Base Ligands. *Inorg. Chem.* **2000,** 39, (21), 4927 -35.

30. Withersby, M. A.; Blake, A. J.; Champness, N. R.; Cooke, P. A.; Hubberstey, P.; Schröder, M., Assembly of a Three-Dimensional Polyknotted Coordination Polymer. *J. Am. Chem. Soc.* **2000,** 122, (17), 4044 - 6.

31. Kepert, C. J.; Rosseinsky, M. J., Zeolite-like crystal structure of an empty microporous molecular framework. *Chem. Commun.* **1999,** 4, 375-6.

32. Noro, S.; Kitagawa, S.; Kondo, M.; Seki, K., A New, Methane Adsorbent, Porous Coordination Polymer *Angew. Chem. Int. Ed.* **2000,** 39, (12), 2081-4.

33. Fletcher, A. J.; Cussen, E. J.; Prior, T. J.; Rosseinsky, M. J.; Kepert, C. J.; Thomas, K. M., Adsorption Dynamics of Gases and Vapors on the Nanoporous Metal Organic Framework Material $Ni_2(4,4'\text{-Bipyridine})_3(NO_3)_4$: Guest Modification of Host Sorption Behavior *J. Am. Chem. Soc.* **2001,** 123, (41), 10001 -11.

34. Dong, Y.-B.; Smith, M. D.; Layland, R. C.; Loye, H.-C. z., A Novel Noninterpenetrating Polycyclohexane Network: A New Inorganic/Organic Coordination Polymer Structural Motif Generated by Self-Assembly of "T-Shaped" Moieties. *Chem. Mater.* **2000,** 12, (4), 1156 - 61.

35. Kumagai, H.; Kepert, C. J.; Kurmoo, M., Construction of Hydrogen-Bonded and Coordination-Bonded Networks of Cobalt(II) with Pyromellitate: Synthesis, Structures, and Magnetic Properties *Inorg. Chem.* **2002,** 41, (13), 3410-22.

36. Yaghi, O. M.; Davis, C. E.; Li, G.; Li, H., Selective Guest Binding by Tailored Channels in a 3-D Porous Zinc(II)-Benzenetricarboxylate Network *J. Am. Chem. Soc.* **1997,** 119, (12), 2861-8.

37. Panella, B.; Hirscher, M.; Pütter, H.; Müller, U., Hydrogen Adsorption in Metal-Organic Frameworks: Cu-MOFs and Zn-MOFs Compared. *Adv. Funct. Mater.* **2006,** 16, (4), 520-4.

38. Chui, S. S.-Y.; Lo, S. M. F.; Charmant, J. P. H.; Orpen, A. G.; Williams, I. D., A Chemically Functionalizable Nanoporous Material $[Cu_3(TMA)_2(H_2O)_3]_n$ *Science* **1999,** 19, 1148-50.

39. Lin, X.; Jia, J.; Zhao, X.; Thomas, K. M.; Alexander, J. B.; Gavin, S. W.; Neil, R. C.; Hubberstey, P.; Schröder, M., High H_2 Adsorption by Coordination-Framework Materials. *Angew. Chem. Int. Ed.* **2006,** 45, (44), 7358-64.

40. Kitaura, R.; Fujimoto, K.; Noro, S.; Kondo, M.; Kitagawa, S., A Pillared-Layer Coordination Polymer Network Displaying Hysteretic Sorption. *Angew. Chem. Int. Ed.* **2002,** 41, (1), 133-5.

41. Kondo, M.; Okubo, T.; Asami, A.; Noro, S.; Yoshitomi, T.; Kitagawa, S.; Ishii, T.; Matsuzaka, H.; Seki, K., Rational Synthesis of Stable Channel-Like Cavities with Methane Gas Adsorption Properties. *Angew. Chem. Int. Ed.* **1999,** 38, (1-2), 140-3.

42. Russell, V. A.; Evans, C. C.; Li, W.; Ward, M. D., Nanoporous Molecular Sandwiches: Pillared Two-Dimensional Hydrogen-Bonded Networks with Adjustable Porosity *Science* **1997,** 276, (5312), 575 - 9.

43. Zimmerman, S. C., Enhanced: Putting Molecules Behind Bars. *Science* **1997,** 276, (5312), 543 - 4.

44. Choi, E.-Y.; Park, K.; Yang, C.-M.; Kim, H.; Son, J.-H.; Lee, S. W.; Lee, Y. H.; Kwon, D. M. Y.-U., Benzene-Templated Hydrothermal Synthesis of Metal-Organic Frameworks with Selective Sorption Properties *Chem.--Eur. J.* **2004,** 10, (21), 5535-40.

45. Takamizawa, S.; Takasaki, Y.; Miyake, R., Host-guest transformational correlations for a gas inclusion co-crystal on changing gas pressure and temperature. *Chemical Communications* **2009**, (43), 6625-7.

46. Kitagawa, S.; Uemura, K., Dynamic porous properties of coordination polymers inspired by hydrogen bonds. *Chem. Soc. Rev.* **2005,** 34, 109.

47. Horike, S.; Shimomura, S.; Kitagawa, S., Soft porous crystals. *Nat Chem* **2009,** 1, (9), 695-704.

48. Xiao, B.; Byrne, P. J.; Wheatley, P. S.; Wragg, D. S.; Zhao, X.; Fletcher, A. J.; Thomas, K. M.; Peters, L.; EvansJohn, S. O.; Warren, J. E.; Zhou, W.; Morris, R. E., Chemically blockable transformation and ultraselective low-pressure gas adsorption in a non-porous metal organic framework. *Nat Chem* **2009,** 1, (4), 289-94.

49. Shimomura, S.; Higuchi, M.; Matsuda, R.; Yoneda, K.; Hijikata, Y.; Kubota, Y.; Mita, Y.; Kim, J.; Takata, M.; Kitagawa, S., Selective sorption of oxygen and nitric oxide by an electron-donating flexible porous coordination polymer. *Nat Chem* **2010,** 2, (8), 633-7.

50. Bourrelly, S.; Moulin, B. a.; Rivera, A.; Maurin, G.; Devautour-Vinot, S.; Serre, C.; Devic, T.; Horcajada, P.; Vimont, A.; Clet, G.; Daturi, M.; Lavalley, J.-C.; Loera-Serna, S.; Denoyel, R.; Llewellyn, P. L.; Ferey, G., Explanation of the Adsorption of Polar Vapors in the Highly Flexible Metal Organic Framework MIL-53(Cr). *J. Am. Chem. Soc.* **2010,** 132, (27), 9488-98.

51. Jones, P. G., Crystal Growing. *Chemistry in Britain* **1981**, 222-5

52. Hulliger, J., Chemistry and Crystal Growth. *Angew. Chem. Int. Ed.* **1994,** 33 (2), 143 - 62.

53. Walton, R. I., Subcritical solvothermal synthesis of condensed inorganic materials. *Chemical Society Reviews* **2002,** 31, 230 - 8.

54. *Test Methods for Activated Carbon*. European Council of Chemical Manufacturers' Federations/CEFIC: Brussels 1986; Vol. 7.

55. Marsh, H., *Introduction to Carbon Science* Butterworth: 1989; p 346.

56. McDougall, G. J., The physical nature and manufacture of activated carbon *Journal of The Southern African Institute of Mining and Metallurgy* **1991,** 91, (4), 109-20.

57. Phan, N. H.; Rio, S.; Faur, C.; Le Coq, L.; Le Cloirec, P.; Nguyen, T. H., Production of fibrous activated carbons from natural cellulose (jute, coconut) fibers for water treatment applications. *Carbon* **2006,** 44, (12), 2569-77.

58. Amin, N. K., Removal of reactive dye from aqueous solutions by adsorption onto activated carbons prepared from sugarcane bagasse pith. *Desalination* **2008,** 223, (1-3), 152-61.

59. Santhy, K.; Selvapathy, P., Removal of reactive dyes from wastewater by adsorption on coir pith activated carbon. *Bioresour. Technol.* **2006,** 97, (11), 1329-36.

60. Otowa, T.; Nojima, Y.; Miyazaki, T., Development of KOH activated high surface area carbon and its application to drinking water purification. *Carbon* **1997,** 35, (9), 1315-9.

61. Abe, I.; Fukuhara, T.; Maruyama, J.; Tatsumoto, H.; Iwasaki, S., Preparation of carbonaceous adsorbents for removal of chloroform from drinking water. *Carbon* **2001,** 39, (7), 1069-73.

62. Dastgheib, S. A.; Karanfil, T.; Cheng, W., Tailoring activated carbons for enhanced removal of natural organic matter from natural waters. *Carbon* **2004,** 42, (3), 547-57.

63. Roy, G. M., *Activated carbon applications in the food and pharmaceutical industries*. CRC Press: 1994; p 193.

64. Jiang, X.; Yan, R.; Tay, J. H., Reusing H_2S-exhausted carbon as packing material for odor biofiltration. *Chemosphere* **2008,** 73, (5), 698-704.

65. Xu, W. C.; Takahashi, K.; Matsuo, Y.; Hattori, Y.; Kumagai, M.; Ishiyama, S.; Kaneko, K.; Iijima, S., Investigation of hydrogen storage capacity of various carbon materials. *Int. J. Hydrogen Energy* **2007,** 32, (13), 2504-12.

66. Esteves, I. A. A. C.; Lopes, M. S. S.; Nunes, P. M. C.; Mota, J. P. B., Adsorption of natural gas and biogas components on activated carbon. *Sep. Purif. Technol.* **2008,** 62, (2), 281-96.

67. Stoeckli, H. F., Microporous carbons and their characterization: The present state of the art. *Carbon* **1990,** 28, (1), 1-6.

68. Rodríguez-reinoso, F., The role of carbon materials in heterogeneous catalysis. *Carbon* **1998,** 36, (3), 159-75.

69. Benaddi, H.; Bandosz, T. J.; Jagiello, J.; Schwarz, J. A.; Rouzaud, J. N.; Legras, D.; Béguin, F., Surface functionality and porosity of activated carbons obtained from chemical activation of wood. *Carbon* **2000,** 38, (5), 669-74.

70. Figueiredo, J. L.; Pereira, M. F. R.; Freitas, M. M. A.; Órfão, J. J. M., Modification of the surface chemistry of activated carbons. *Carbon* **1999,** 37, (9), 1379-89.

71. Yang, R. T., *Adsorbents: Fundamentals and Applications*. Wiley-Interscience 2003; p 424.

72. Lahaye, J., The chemistry of carbon surfaces. *Fuel* **1998,** 77, (6), 543-7.

73. Boehm, H. P., Surface oxides on carbon and their analysis: a critical assessment. *Carbon* **2002,** 40, (2), 145-9.

74. Montes-Morán, M. A.; Suárez, D.; Menéndez, J. A.; Fuente, E., On the nature of basic sites on carbon surfaces: an overview. *Carbon* **2004,** 42, (7), 1219-25.

75. Heschel, W.; Klose, E., On the suitability of agricultural by-products for the manufacture of granular activated carbon. *Fuel* **1995,** 74, (12), 1786-91.

76. Kim, T. Y.; Baek, I. H.; Jeoung, Y. D.; Park, S. C., Manufacturing Activated Carbon using Various Agricultural Wastes. *Journal of Industrial and Engineering Chemistry* **2003,** 9, (3), 254-60.

77. Dias, J. M.; Alvim-Ferraz, M. C. M.; Almeida, M. F.; Rivera-Utrilla, J.; Sánchez-Polo, M., Waste materials for activated carbon preparation and its use in aqueous-phase treatment: A review. *J. Environ. Manage.* **2007,** 85, (4), 833-46.

78. Encinar, J. M.; Beltrán, F. J.; Ramiro, A.; González, J. F., Pyrolysis/gasification of agricultural residues by carbon dioxide in the presence of different additives: influence of variables. *Fuel Processing Technology* **1998,** 55, (3), 219-33.

79. Toles, C. A.; Marshall, W. E.; Wartelle, L. H.; McAloon, A., Steam- or carbon dioxide-activated carbons from almond shells: physical, chemical and adsorptive properties and estimated cost of production. *Bioresour. Technol.* **2000,** 75, (3), 197-203.

80. Lua, A. C.; Guo, J., Preparation and characterization of activated carbons from oil-palm stones for gas-phase adsorption. *Colloids Surf., A* **2001,** 179, (2-3), 151-62.

81. Sentorun-Shalaby, Ç.; Uçak-AstarlIoglu, M. G.; Artok, L.; SarIcI, Ç., Preparation and characterization of activated carbons by one-step steam pyrolysis/activation from apricot stones. *Microporous Mesoporous Mater.* **2006,** 88, (1-3), 126-34.

82. Wolff, W. F., A Model of Active Carbon. *J. Phys. Chem.* **1959,** 63, (5), 653-9.

83. Eddaoudi, M.; Kim, J.; Rosi, N.; Vodak, D.; Wachter, J.; O'Keeffe, M. l.; Yaghi, O. M., Systematic Design of Pore Size and Functionality in Isoreticular MOFs and Their Application in Methane Storage *Science* **2002,** 295, (5554), 469 - 72.

84. Li, W.; Yang, K.; Peng, J.; Zhang, L.; Guo, S.; Xia, H., Effects of carbonization temperatures on characteristics of porosity in coconut shell chars and activated carbons derived from carbonized coconut shell chars. *Industrial Crops and Products* **2008,** 28, (2), 190-8.

85. Molina-Sabio, M.; Gonzalez, M. T.; Rodriguez-Reinoso, F.; Sepúlveda-Escribano, A., Effect of steam and carbon dioxide activation in the micropore size distribution of activated carbon. *Carbon* **1996,** 34, (4), 505-9.

86. Henning, K. D.; Schäfer, S., Impregnated activated carbon for environmental protection. *Gas Sep. Purif.* **1993,** 7, (4), 235-40.

87. Illan-Gomez, M. J.; Garcia-Garcia, A.; Salinas-Martinez de Lecea, C.; Linares-Solano, A., Activated Carbons from Spanish Coals. 2. Chemical Activation. *Energy Fuels* **1996,** 10, (5), 1108-14.

88. Hsu, L.-Y.; Teng, H., Influence of different chemical reagents on the preparation of activated carbons from bituminous coal. *Fuel Processing Technology* **2000,** 64, (1-3), 155-66.

89. Soleimani, M.; Kaghazchi, T., Agricultural Waste Conversion to Activated Carbon by Chemical Activation with Phosphoric Acid. *Chemical Engineering & Technology* **2007,** 30, (5), 649-54.

90. Teng, H.; Lin, H.-c., Activated carbon production from low ash subbituminous coal with CO_2 activation. *AIChE Journal* **1998,** 44, (5), 1170-7.

91. Franklin, R. E., *Trans. Faraday Soc.* **1945,** 45, 668.

92. Walker, P. L.; Austin, L. G.; Nandi, S. P., *Chemistry and Physics of Carbon* Marcel Dekker: New York, 1996; Vol. 2, p 440.

93. Koresh, J.; Soffer, A., Study of molecular sieve carbons. Part 1.—Pore structure, gradual pore opening and mechanism of molecular sieving. *J. Chem. Soc., Faraday Trans.* **1980,** 76, 2457 - 71.

94. Patzelová, V.; Kadlec, O.; Seidl, P., The so-called carbon molecular sieves in gas chromatography. *Journal of Chromatography* **1974,** 91, 313-20.

95. Breck, D. W., *Zeolite molecular sieves : structure, chemistry, and use*. Wiley: New York 1984; p 771.

96. Szostak, R., *Molecular Sieves: Principles of Synthesis and Identification.* . 2 ed.; Springer: London, 1998; p 359.

97. Bekkum, H. v.; Flanigen, E. M.; Jansen, J. C., *Introduction to Zeolite Science and Practice*. Elsevier: 1991; p 1062.

98. Vyas, S. N.; Patwardhan, S. R.; Vijayalakshmi, S.; Ganesh, K. S., Adsorption of Gases on Carbon Molecular Sieves. *J. Colloid Interface Sci.* **1994,** 168, (2), 275-80.

99. Mochida, I.; Yatsunami, S.; Kawabuchi, Y.; Nakayama, Y., Influence of heat-treatment on the selective adsorption of CO2 in a model natural gas over molecular sieve carbons. *Carbon* **1995,** 33, (11), 1611-9.

100. Nguyen, C.; Do, D. D., Preparation of carbon molecular sieves from macadamia nut shells. *Carbon* **1995,** 33, (12), 1717-25.

101. Foley, H. C. In *Perspectives in Molecular Sieve Science* 195th natinal meeting of the American Chmical Society, Toronto, 1988; Flank, H. W., Ed. American Chemical Society: Toronto, 1988; p 650.

102. Rosseinsky, M. J., Recent developments in metal-organic framework chemistry: design, discovery, permanent porosity and flexibility. *Microporous Mesoporous Mater.* **2004,** 73, (1-2), 15-30.

103. Schröter, H. J., Carbon molecular sieves for gas separation processes. *Gas Sep. Purif.* **1993,** 7, (4), 247-51.

104. Ahmad, M. A.; Wan Daud, W. M. A.; Aroua, M. K., Adsorption kinetics of various gases in carbon molecular sieves (CMS) produced from palm shell. *Colloids Surf., A* **2008,** 312, (2-3), 131-5.

105. Nandi, S. P.; Walker Jr, P. L., Carbon molecular sieves for the concentration of oxygen from air. *Fuel* **1975,** 54, (3), 169-78.

106. Jüntgen, H.; Knoblauch, K.; Harder, K., Carbon molecular sieves: production from coal and application in gas separation. *Fuel* **1981,** 60, (9), 817-22.

107. Verma, S. K.; Walker Jr, P. L., Alteration of molecular sieving properties of microporous carbons by heat treatment and carbon gasification. *Carbon* **1990,** 28, (1), 175-84.

108. Miura, K.; Hayashi, J.; Hashimoto, K., Production of molecular sieving carbon through carbonization of coal modified by organic additives. *Carbon* **1991,** 29, (4-5), 653-60.

109. Nakagawa, H.; Watanabe, K.; Harada, Y.; Miura, K., Control of micropore formation in the carbonized ion exchange resin by utilizing pillar effect. *Carbon* **1999,** 37, (9), 1455-61.

110. Kyotani, T., Control of pore structure in carbon. *Carbon* **2000,** 38, (2), 269-86.

111. Ohring, M., Chemical vapor deposition. In *Materials Science of Thin Films (Second Edition)*, Academic Press: San Diego, 2002; pp 277-355.

112. Kawabuchi, Y.; Oka, H.; Kawano, S.; Mochida, I.; Yoshizawa, N., The modification of pore size in activated carbon fibers by chemical vapor deposition and its effects on molecular sieve selectivity. *Carbon* **1998,** 36, (4), 377-82.

113. Villar-Rodil, S.; Navarrete, R.; Denoyel, R.; Albiniak, A.; Paredes, J. I.; Martínez-Alonso, A.; Tascón, J. M. D., Carbon molecular sieve cloths prepared by chemical vapour deposition of methane for separation of gas mixtures. *Microporous Mesoporous Mater.* **2005,** 77, (2-3), 109-18.

114. Becker, A.; Hüttinger, K. J., Chemistry and kinetics of chemical vapor deposition of pyrocarbon -- III pyrocarbon deposition from propylene and benzene in the low temperature regime. *Carbon* **1998,** 36, (3), 201-11.

115. Verma, S. K., Development of molecular sieving properties in microporous carbons. *Carbon* **1991,** 29, (6), 793-803.

116. Kang, H. U.; Kim, W.-g.; Kim, S. H., Pore size control through benzene vapor deposition on activated carbon. *Chemical Engineering Journal* **2008,** 144, (2), 167-74.

117. Hu, Z.; Vansant, E. F., Carbon molecular sieves produced from walnut shell. *Carbon* **1995,** 33, (5), 561-7.

118. Freitas, M. M. A.; Figueiredo, J. L., Preparation of carbon molecular sieves for gas separations by modification of the pore sizes of activated carbons. *Fuel* **2001,** 80, (1), 1-6.

119. Verma, S. K.; Walker Jr, P. L., Preparation of carbon molecular sieves by propylene pyrolysis over microporous carbons. *Carbon* **1992,** 30, (6), 829-36.

120. Crini, G., Non-conventional low-cost adsorbents for dye removal: A review. *Bioresour. Technol.* **2006,** 97, (9), 1061-85.

121. Tan, I. A. W.; Ahmad, A. L.; Hameed, B. H., Fixed-bed adsorption performance of oil palm shell-based activated carbon for removal of 2,4,6-trichlorophenol. *Bioresour. Technol.* **2009,** 100, (3), 1494-6.

122. Sison, N. F.; Hanaki, K.; Matsuo, T., Denitrification with external carbon source utilizing adsorption and desorption capability of activated carbon. *Water Research* **1996,** 30, (1), 217-27.

123. Tseng, H.-H.; Wey, M.-Y.; Liang, Y.-S.; Chen, K.-H., Catalytic removal of SO_2, NO and HCl from incineration flue gas over activated carbon-supported metal oxides. *Carbon* **2003,** 41, (5), 1079-85.

124. Alhamed, Y. A.; Bamufleh, H. S., Sulfur removal from model diesel fuel using granular activated carbon from dates' stones activated by ZnCl2. *Fuel* **2009,** 88, (1), 87-94.

125. Tamon, H.; Okazaki, M., Influence of acidic surface oxides of activated carbon on gas adsorption characteristics. *Carbon* **1996,** 34, (6), 741-6.

126. Nagano, S.; Tamon, H.; Adzumi, T.; Nakagawa, K.; Suzuki, T., Activated carbon from municipal waste. *Carbon* **2000,** 38, (6), 915-20.

127. Kilgroe, J. D., Control of dioxin, furan, and mercury emissions from municipal waste combustors. *J. Hazard. Mater.* **1996,** 47, (1-3), 163-94.

128. Chi, K. H.; Chang, S. H.; Huang, C. H.; Huang, H. C.; Chang, M. B., Partitioning and removal of dioxin-like congeners in flue gases treated with activated carbon adsorption. *Chemosphere* **2006,** 64, (9), 1489-98.

129. Ho, T. C.; Lee, Y.; Chu, H. W.; Lin, C. J.; Hopper, J. R., Modeling of mercury desorption from activated carbon at elevated temperatures under fluidized/fixed bed operations. *Powder Technology* **2005,** 151, (1-3), 54-60.

130. Wang, Q. M.; Shen, D.; Bülow, M.; Lau, M. L.; Deng, S.; Fitch, F. R.; Lemcoff, N. O.; Semanscin, J., Metallo-organic molecular sieve for gas separation and purification *Microporous Mesoporous Mater.* **2002,** 55, (2), 217-30.

131. Ramsahye, N. A.; Maurin, G.; Bourrelly, S.; Llewellyn, P. L.; Loiseau, T.; Serre, C.; Ferey, G., On the breathing effect of a metal-organic framework upon CO_2 adsorption: Monte Carlo compared to microcalorimetry experiments. *Chem. Commun.* **2007**, (31), 3261-3.

132. Pianwanit, A.; Kritayakornupong, C.; Vongachariya, A.; Selphusit, N.; Ploymeerusmee, T.; Remsungnen, T.; Nuntasri, D.; Fritzsche, S.; Hannongbua, S., The optimal binding sites of CH_4 and CO_2 molecules on the metal-organic framework MOF-5: ONIOM calculations. *Chemical Physics* **2008,** 349, (1-3), 77-82.

133. Britt, D.; Tranchemontagne, D.; Yaghi, O. M., Metal-organic frameworks with high capacity and selectivity for harmful gases. *Proc. Natl. Acad. Sci. U. S. A.* **2008,** 105, (33), 11623-7.

134. Barreto, L.; Makihira, A.; Riahi, K., The hydrogen economy in the 21st century: a sustainable development scenario. *Int. J. Hydrogen Energy* **2003,** 28, (3), 267-84.

135. Penner, S. S., Steps toward the hydrogen economy. *Energy* **2006,** 31, (1), 33-43.

136. Zamaraev, K. I., Catalytic science and technology for environmental issues. *Catalysis Today* **1997,** 35, (1-2), 3-13.

137. Gallei, E.; Schwab, E., Development of technical catalysts. *Catalysis Today* **1999,** 51, (3-4), 535-46.

138. Auer, E.; Freund, A.; Pietsch, J.; Tacke, T., Carbons as supports for industrial precious metal catalysts. *Applied Catalysis A: General* **1998,** 173, (2), 259-71.

139. Cole-Hamilton, D. J., Homogeneous Catalysis--New Approaches to Catalyst Separation, Recovery, and Recycling. *Science* **2003,** 299, (5613), 1702-6.

140. Guha, A.; Lu, W.; Zawodzinski Jr, T. A.; Schiraldi, D. A., Surface-modified carbons as platinum catalyst support for PEM fuel cells. *Carbon* **2007,** 45, (7), 1506-17.

141. Zielinski, M.; Wojcieszak, R.; Monteverdi, S.; Mercy, M.; Bettahar, M. M., Hydrogen storage in nickel catalysts supported on activated carbon. *Int. J. Hydrogen Energy* **2007,** 32, (8), 1024-32.

142. Hasegawa, S.; Horike, S.; Matsuda, R.; Furukawa, S.; Mochizuki, K.; Kinoshita, Y.; Kitagawa, S., Three-Dimensional Porous Coordination Polymer Functionalized with Amide Groups Based on Tridentate Ligand; Selective Sorption and Catalysis. *J. Am. Chem. Soc.* **2007,** 129, (9), 2607-14.

143. Zou, R.-Q.; Sakurai, H.; Han, S.; Zhong, R.-Q.; Xu, Q., Probing the Lewis Acid Sites and CO Catalytic Oxidation Activity of the Porous Metal-Organic Polymer [Cu(5-methylisophthalate)]. *J. Am. Chem. Soc.* **2007,** 129, (27), 8402-3.

144. Jiang, D.; Mallat, T.; Krumeich, F.; Baiker, A., Copper-based metal-organic framework for the facile ring-opening of epoxides. *J. Catal.* **2008,** 257, (2), 390-5.

145. Alaerts, L.; Séguin, E.; Poelman, H.; Thibault-Starzyk, F.; Jacobs, P. A.; E. De Vos, D., Probing the Lewis Acidity and Catalytic Activity of the Metal-Organic Framework $[Cu_3(btc)_2]$ (BTC=Benzene-1,3,5-tricarboxylate). *Chem.--Eur. J.* **2006,** 12, (28), 7353-63.

146. Llabrés i Xamena, F. X.; Casanova, O.; Galiasso Tailleur, R.; Garcia, H.; Corma, A., Metal organic frameworks (MOFs) as catalysts: A combination of Cu^{2+} and Co^{2+} MOFs as an efficient catalyst for tetralin oxidation. *J. Catal.* **2008,** 255, (2), 220-7.

147. Moseley, P. T., Solid state gas sensors. *Measurement Science and Technology* **1997,** 8, (3), 223-37.

148. K. L. Wong; G. L. Law; Y. Y. Yang; W. T. Wong, A Highly Porous Luminescent Terbium-Organic Framework for Reversible Anion Sensing. *Advanced Materials* **2006,** 18, (8), 1051-4.

149. Chen, B.; Yang, Y.; Zapata, F.; Lin, G.; Qian, G.; Lobkovsky, E. B., Luminescent Open Metal Sites within a Metal-Organic Framework for Sensing Small Molecules. *Adv. Mater.* **2007,** 19, (13), 1693-6.

150. Yeom, J.; Oh, I.; Field, C.; Radadia, A.; Ni, Z.; Bae, B.; Han, J.; Masel, R. I.; Shannon, M. A. In *Enhanced toxic gas detection using a MEMS preconcentrator coated with the metal organic framework absorber*, Micro Electro Mechanical Systems, 2008. MEMS 2008. IEEE 21st International Conference on, 2008; 2008; pp 232-5.

Contents

CHAPTER 2

The adsorption of vapours and gases into porous materials

2.1 General

The term adsorption was introduced to the literature by Kayser in 1881[1, 2] to refer to the condensation of gases on bare surfaces. Kayser also introduced the terms isotherm and isotherm curve to explain the results of adsorption experiments. In 1909, McBain[3] proposed the term sorption for adsorption and absorption in the case of phenomena which cannot be distinguished precisely. In this particular case, the terms sorption, sorbent, sorbate and sorbent should be used.[4-6]

The term adsorption is used to denote the enrichment or accumulation of one or more components, whether molecules, atoms or ions, in an interfacial layer between two bulk phases. In dealing with adsorption at gas-vapour/porous solid interfaces, it is customary to call the components in the adsorbed state the adsorbate, and to refer to the same species in the bulk gas phase as the adsorptive. Additionally, the adsorbing solid is called adsorbent. Adsorption is distinguished from absorption, which involves bulk penetration of the gas/vapour into a mass of the adsorbing solid or liquid.[6, 7]

As mentioned previously, when a gas is introduced into a solid, an adsorbed phase bonded to adsorbent surfaces, may form. When the conditions are changed, gas molecules may desorb. Adsorption of a gas/vapour on a porous solid is a spontaneous process, which means that it involves a decrease in free energy (ΔG) due to the passing of the free gas to the adsorbed film. There is a decrease in entropy (ΔS), because the gas adsorbed on the surface of the adsorbent is more ordered than in the gas phase. The thermodynamic relationship of the adsorption process is shown as the following equation.[8, 9]

$$\Delta G = \Delta \mathrm{H} - T\Delta S \qquad (1)$$

It is evident that ΔH of the adsorption of gases and vapours on porous solids is always an exothermic process for physisorption. Thus the amount of gas adsorption increases with decreasing temperature. Heat of adsorption can be measured by direct calorimetric methods or determined from isotherm studies.

2.2 Physical and chemical adsorption

There are two broad types of adsorption processes: physical adsorption and chemical adsorption. These are both characterized by the strength and nature of the bond between the adsorbate and substrate.[7] The distinction between physical and chemical adsorption is very important as the process and the behaviour of the adsorbed layers are quite different.

Physical adsorption, or physisorption, involves intermolecular bonds between atoms or molecules being adsorbed and the substrate is due to dipole induced dipole interactions (London dispersive force), and other relatively weak interactions. In chemical adsorption, or chemisorption, a chemical bond is formed between the adsorbate and the substrate. Such bonds, which involve the exchange or sharing of electrons between the adsorbate and the substrate, are much stronger. Typical physisorption binding energies are about 20-70 $kJmol^{-1}$ and those of chemisorption are typically higher than physisorption.

In discussing the characteristics of physisorption and chemisorption it best to use the analogy of condensation and chemical reaction. Some significant differences between physisorption and chemisorption are summarized in Table 2.1.[5, 10, 11]

- Reversibility:. Physisorption is reversible, i.e., the adsorbate will desorb (become unbound from the substrate) when the porous material temperature is raised, and return to its original condition in the gas phase. Chemisorption is usually not reversible; i.e., raising the porous material temperature may not result in the adsorbate returning to its original form in the gas phase. Additionally, the physisorption rate at (273 K) is normally faster than the chemisorption rate. This is because chemisorption normally has to overcome the activation energy for breaking chemical bonds while there is at most a small activation energy involved in the physisorption of gases/vapours.

- Enthalpy of adsorption: Enthalpy of chemisorption, in general, is much larger than enthalpy of physical adsorption and generally higher than 80 $kJmol^{-1}$.

Meanwhile, enthalpy of physical adsorption is typically in the range of 20-70 $kJmol^{-1}$ and is larger than the enthalpy of condensation.

- Specificity: Physisorption is non-specific and does not result in the dissociation of adsorbed molecules. Chemisorption is very specific due to the involvement of chemical reactions between gas molecules and surface groups of the porous material. Chemisorption, furthermore, often results in the dissociation of molecules during the adsorption/chemical reaction process.
- Chemisorption: This is typically characterized by the formation of a single layer of adsorbate on the surface of porous materials, but in physisorption, multiple layers of the adsorbate can form on the porous materials.
- Conditions of adsorption: Chemisorption typically occurs over a wide range of temperatures, often exceeding temperatures at which the adsorbate will condense from the gas phase to the liquid phase. Physisorption occurs when the temperature is close to temperature at which the adsorbate will condense from the gas phase to the liquid phase. In physisorption, the uptake is generally favoured at low temperature while the uptake caused by chemisorption is favoured at high temperature.

Table 2.1 Comparison of physical and chemical adsorption[12, 13]

	Physical Adsorption	**Chemical Adsorption**
Rate of adsorption	Fast	Slow
Enthalpy of Adsorption	Usually 20 - 40 kJ mol^{-1}	Usually > 80 kJ mol^{-1}
Origin of interactions force and specificity	van der Waals forces, non-specific adsorption, easy for desorption	Chemical bond forces, highly specific adsorption, difficult for desorption due to the need to break bonds
Monolayer coverage	Monolayer and multilayer formation depending on environment	Limited to mono layer coverage
Dependence of the temperature	Decrease with increasing temperature	Increase with increasing temperature

2.3 Forces of Physical adsorption

There are two major combinations of forces involved in physical adsorption. The first force is the long-rang attractive dispersive (or van der Waals) interactions and the other is the short range repulsive interaction between the adsorbent and the adsorbate molecule.[14, 15]

The force of attraction between adsorbate and solid adsorbent is due to instantaneously fluctuating electric dipole moments in either atoms or molecules of the adsorbate and the surface of the adsorbent. Even in an atom or molecule with no permanent electric dipole moment, fluctuations in the electron charge distribution will give it an instantaneous (short lived, but averaging to zero over a longer time interval) dipole moment which will induce a further dipole moment in a nearby atom or molecule. The interaction between the original and induced dipole moments results in an attractive force between these two moments. These dipole-dipole forces are known as van der Waals forces. The repulsive force arises from the penetration or overlap of the electron cloud between adjacent molecules and surfaces. At short distances, the repulsion force is significant and increases rapidly.

Both attractive dispersive and repulsive forces of the two isolated atoms can be expressed as potential energy in the following equations.[4, 10]

$$\varepsilon_D(r) = -C_1 r^{-6} - C_2 r^{-8} - C_3 r^{-10} \qquad (2)$$

where $\varepsilon_D(r)$ is the potential equation for dispersive force and r is a distance between two isolated atoms. The coefficients C_1, C_2, C_3 are the dispersion constants associated with instantaneous dipole-dipole, dipole-quadrupole and quadrupole- quadrupole, etc. interactions respectively. The terms in r^{-8} and r^{-10} are relatively small and usually omitted. So the equation thus simplifies to (3). The repulsive force can be expressed as the equation (4). B is an empirical constant and the exponent m is usually found to be in the range 9 to 14 in order to fit the data, but m = 12 is commonly used. The dispersion and repulsive interactions are frequently combined to give the total potential energy or Lennard-Jones (6-12) potential as shown in equation (5)

$$\varepsilon_D(r) = -C_1 r^{-6} \quad (3)$$

$$\varepsilon_R(r) = Br^{-m} \quad (4)$$

$$\varepsilon\ (r) = -C_1 r^{-6} + Br^{-12} \quad (5)$$

To apply the Lennard-Jones (6-12) potential equation to the adsorption of gases or vapours, which involves adsorbate atoms or ions, thus the equation becomes

$$\phi_i(z) = B_{ij} \sum_j r_{ij}^{-12} - C_{ij} \sum_j r_{ij}^{-6} \quad (6)$$

where $\phi_i(z)$ is the potential energy for the molecule *i*, expressed as a function of its distance z from the plane of the centre of atoms or ions in the surface layer. From the surface plane; r_{ij} is the distance between *i* and an atom *j*, in the solid and B_{ij} and C_{ij} are characteristic repulsion and attraction constants for the gas-solid system.

Figure 2.1 shows that the potential energy of a physisorbed atom or ion varies as a function of the distance z from the surface of the adsorbent. With a larger z, the potential energy reduces as the attractive force decreases. With a smaller z, the potential energy increases rapidly due to the adsorbate-adsorbent force becoming repulsive. Once the atom or ion moves closer to the surface of the adsorbent, the balance between the attractive and repulsive forces may be established at distance z_e. At this distance z_e the potential energy of the atom or ion is at a minimum.

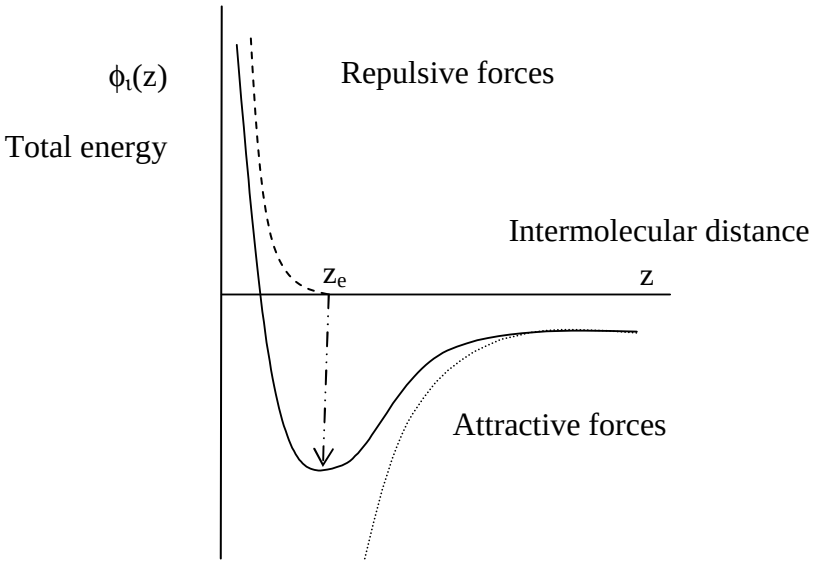

Figure 2.1 Potential energy ϕ_t of a molecule *i* versus its distance *z* from the adsorbing surface.

2.4 Adsorption Isotherms

The quantity of gas taken up by a sample of solid is proportional to the mass *m* of the sample, the temperature T, the pressure *p* of the gas and the nature of both the solid and the gas. This can be expressed as *n*, the quantity of gas adsorbed in moles per gram of solid:

$$n = f\,(p,T,gas,solid) \qquad (7)$$

For a given gas adsorbed on a particular solid kept at a fixed temperature, equation (7) simplifies to

$$n = f\,(p)_{T,\,gas,\,solid} \qquad (8)$$

If the temperature is below the critical temperature of the gas, the alternative form (9) is more useful, p^0 being the saturation vapour pressure of the adsorptive at the temperature of the measurement.

$$n = f(p/p^0)_{T,\,gas,\,solid} \qquad (9)$$

The parameter (p/p^0) is described as the relative pressure. A graph reflecting the amount of adsorbed against pressure or relative pressure at constant temperature is called the adsorption isotherm. This is usually expressed as the amount of adsorbate per gram (or volume) of adsorbent to each equilibrium pressure of the gas at a constant temperature. When a porous material is exposed in a closed space with some definite pressure of gas, it begins to adsorb the gas. The process is accompanied by an increase in the weight of the solid and a decrease in the pressure of the gas. After a time, the pressure becomes constant at the value P, and correspondingly, the weight ceases to increase any further. The amount of gas adsorbed can thus be calculated.

In summary, by studying the adsorption isotherms, one can: 1) estimate the surface area/pore volumes, 2) estimate the pore size distribution, 3) assess the surface chemistry of the adsorbents, and 4) determine the fundamentals of the adsorption process.

The majority of physisorption isotherms may be grouped into the six types shown in Figure 2.2. The five types of physisorption isotherm were originally proposed by Brunauer, Deming, Deming and Teller (B.D.D.T). These can also be referred to as the B.D.D.T classification.[16, 17] The type six isotherm was proposed later by Sing *et al*.[4, 7] Each isotherm is discussed in more detail below.

Type I isotherm

Type I isotherm shows a rapid increase in the amount of gas adsorbed over the low relative pressure range and then reaches a plateau in the high pressure range. Type I isotherms are sometimes referred to as Langmuir isotherms and are often obtained when adsorption is restricted to a monolayer. Therefore, chemisorption isotherms are approximate to this shape.

Type I isotherms have been found for physical adsorption on solids containing very narrow or slit pore structures, e.g. activated carbons, molecular sieve zeolites, a metal organic framework and a certain porous oxide. A rapid increase in the amount of gas adsorbed over the low pressure is often attributed to micropore filling in porous solids and then a subsequent horizontal or near horizontal plateau indicates that the micropores are filled and no further adsorption will take place. So, the limiting uptake is governed by the accessible micropore volume rather than by internal surface area. Examples of type I isotherms are usually obtained from nitrogen and carbon dioxide adsorption on activated carbon at 77 K and 195 K, respectively.[5, 18]

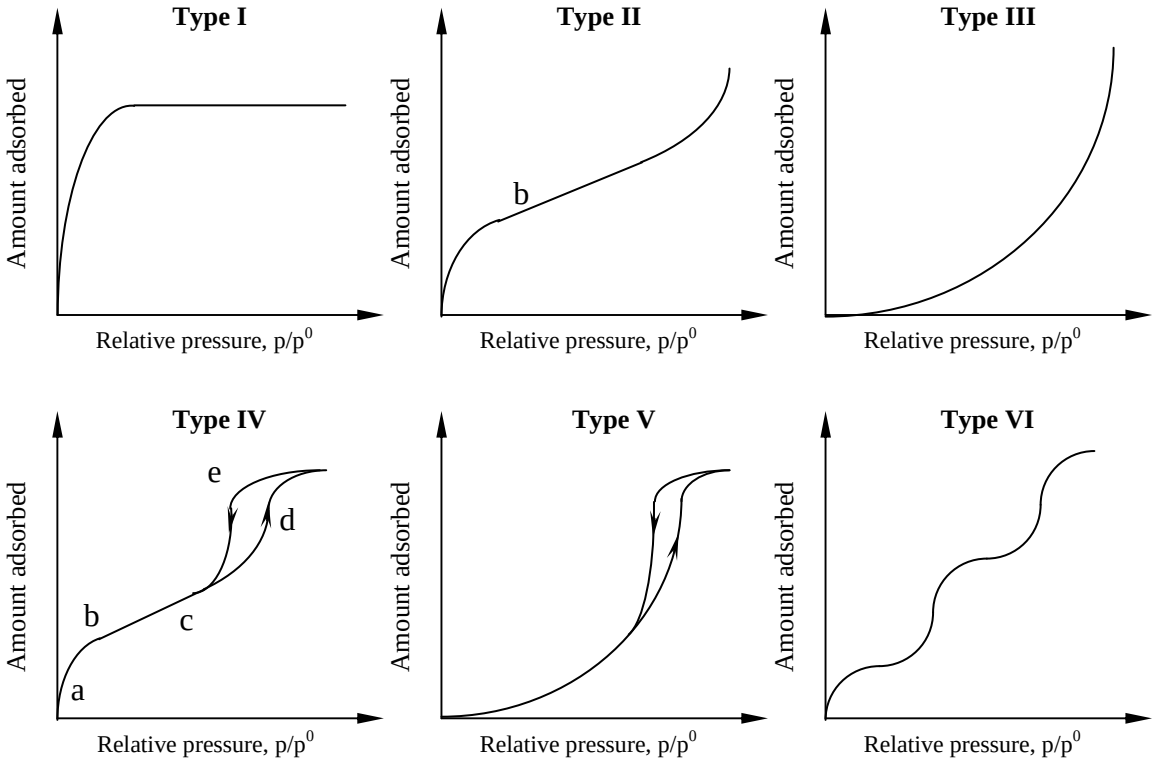

Figure 2.2 The six basic types of adsorption isotherms

Type II isotherm

The Type II isotherms are typically produced by solids which are non-porous or macroporous and the isotherms represent unrestricted monolayer-multilayer adsorption on a heterogeneous adsorbent. These are often referred to as the sigmoid isotherm. The practice is to take point **b** as the point of completion of a monolayer and multilayer adsorption. Consequently, multilayer adsorption increases progressively with rising pressure. Brunauer–Emmett-Teller (BET) originally developed a multi layer adsorption theory and mathematical model to describe the Type II isotherms as described in Section 2.5.3. Examples of type II adsorption isotherm are nitrogen adsorption on non-porous silica at 77 K and *n*-butane adsorption on graphitized carbon black P90 at 298 K.[19,20]

Type III isotherms

Type III isotherms are distinguished from Type II isotherms by a convexity towards the relative pressure axis entire range of the isotherm and do not exhibit a point **b**. At low relative pressure region, Type III isotherms demonstrate very low uptake of adsorbate due to the forces of adsorption in the first monolayer being relatively small. Adsorbate-adsorbent interactions are also found to be weak. In other words, the adsorbate-adsorbate interactions are stronger than adsorbate-adsorbent interactions. However, the uptake at high relative pressure is much higher due to the adsorbate-adsorbate interactions being much stronger and this increases the driving force of the adsorption process. Type III isotherms most commonly occur in both non-porous and microporous adsorbents. Examples include the adsorption of water molecules on carbon and single wall nanotubes.[21-23]

Type IV Isotherm

The Type IV isotherms are found in many mesoporous solids. A characteristic feature is that the adsorption branch of the isotherm is not the same as the desorption branch of the isotherm and hysteresis is observed. Generally, the hysteresis loop occurs due to the capillary condensation taking place in mesopores and the limiting uptake at high relative pressure. The hysteresis process is demonstrated in Figure 2.3 Type IV. At this initial state, adsorption of molecules on to the walls of porous material occurs at a very low relative pressure until a monolayer (a to b) is formed. Then, the multilayer adsorption occurs as pressure increases (b to c) and follows by capillary condensation at high relative pressure below p/p^0 (c to d). In the capillary condensation process, gas/vapour molecules tend to form a liquid-like layer with a curved meniscus at pore entrances (d). As pressure decreases, the angle of the curve of the meniscus also changes. The liquid meniscus blocks the liquid condensed in pores from evaporating. This blocking by the liquid meniscus results in a high mass of adsorbate remaining in the porous material which then creates the hysteretic loop (e). Examples of Type IV adsorption isotherm are: water adsorption on silica[24], activated carbon[25] at 298 K and nitrogen adsorption on mesoporous MCM-41 at 77 K.[26]

Type V isotherms

Type V isotherms, unlike Type III, occurs during the hysteresis loop and exhibits a point of inflection at a higher relative pressure. Subsequently, the Type V isotherms reach a plateau in the multilayer region of the isotherm where the capillary condensation occurs. Type V isotherms occur most often with mesoporous adsorbents. Examples include the water vapours adsorption on carbon in which the adsorbate-adsorbent interactions are very weak and water adsorption on mesoporous alumina at 298 K.[24, 27]

Type VI isotherm

The Type VI isotherm represents the step-like nature of the adsorption process. The steps result from sequential multilayer adsorption on a uniform non-porous surface. Each step-height represents the monolayer capacity for each adsorbed layer. The best examples were obtained with argon or krypton on graphitised carbon blacks at 77 K.

During the desorption process, the amount of adsorbed molecule on the porous surface should be the same as the amount of adsorbed molecule in the adsorption process. In other words, the adsorption process should be reversible. However, some deviations can occur. The phenomena wherein the amount of adsorbed material in the desorption process is higher than in the adsorption process is called hysteresis.[7] To put it more simply, the curve of the desorption isotherm deviates from the adsorption isotherm. Originally, the classification of hysteresis loops was first proposed by de Boer[28] and it has been modified by the IUPAC[7] which recommended four types of hysteresis isotherm as illustrated in Figure 2.3. Type H_1 consists of a steep parallel adsorption and desorption hysteresis curve and these hysteresis loops appear at high relative pressure close to unity. The type H_1 is normally given by porous media with narrow mesopores distribution. However, porous materials with pores with an ink-bottle shape and narrow channel open at both ends and pore with a modulating surface can cause type H_1 hysteresis. Type H_2 is often associated with a solid composed of irregular size and shape (e.g. many silica gel or cracking catalysis).The H_2 hysteresis loop borders the H_1 type which indicates that the adsorbed molecules are easily trapped in the porous material.

Type H_3 and H_4 do not plateau at high relative pressures. Therefore, it is more difficult to distinguish where the limiting desorption boundary curve is. These loops do not close until the equilibrium pressure is reached at the saturation pressure or very close to the saturation vapour pressure. Type H_3 is often observed in the adsorbent as slit shaped pores and also found in the metal oxide aggregate of sheet like shapes. Type H_4 is associated with a Type I isotherm which is characteristic for microporous adsorbents.

Capillary condensation refers to the change of the gas/vapour state into a liquid layer with the curved meniscus at a lower pressure than the saturated pressure. The term is also widely used to describe the hysteresis isotherms in mesoporous materials. But recently much evidence indicates that capillary condensation is not the only reason for causing the hysteresis loop. Some reports reveal that both micro and meso-porous media with pore networking, ink-bottle shape pores or even modulation of pore structure can also trap adsorbates.[29, 30] Zhao *et al.*[31] and Fletcher *et al.*,[32] showed that the structural flexibility of a microporous metal organic framework can provide a kinetics-based trapping mechanism which leads to a hysteretic loop.

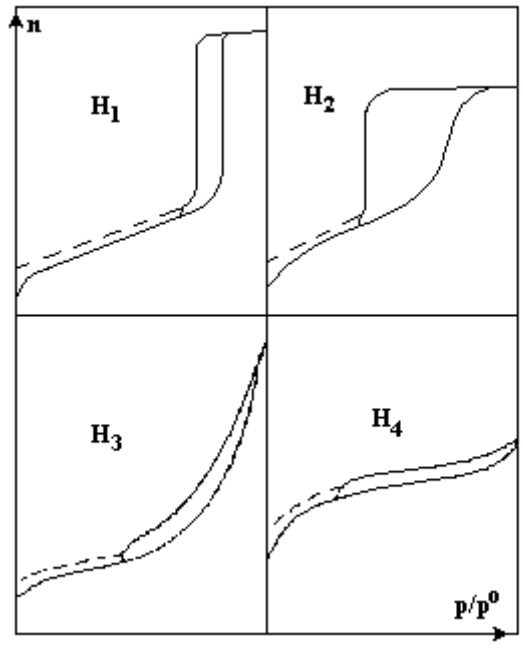

Figure 2.3 The IUPAC classifications of hysteresis loops[7]

2.5 Adsorption Equations

The shape of an adsorption isotherm reflects interactions between the adsorbed molecules and the surface of the porous media. Therefore, for the purpose of inspecting the shape of the isotherm, it is useful to identify the adsorption mechanism and then decide which mathematical model should be used to evaluate the characteristics of the porous material. Thus numerous attempts have been made at developing mathematical expressions to describe adsorption/desorption phenomena observed for various experimental isotherm curves. There are many isotherm equations, for example, Henry's law, virial, Langmuir, Freundlich, Brunauer–Emmett-Teller (BET) and Dubinin–Radushkevich (DR) equations. Firstly, the plot of Langmuir equation generates curves that fit the Type I isotherm shape and the monolayer capacity can also be obtained from the equation. Secondary, the isotherm plot of the BET equation corresponds to Type II isotherms. The Dubinin–Radushkevich model allows an estimation of the micropore volume from the low to medium-relative pressure parts of the Type I isotherm. Further details are discussed in the following sections.

2.5.1 Henry's law and virial equations

Henry's law is based on the assumption that there is no interaction among the adsorbed molecules at very low surface coverage. Henry's law is defined by the following equation.[5]

$$n = k_H\, p \qquad (10)$$

where n is the specific surface excess amount and k_H is the Henry's law constant. It is possible to obtain the differential enthalpy of adsorption at zero coverage ($\Delta_{ads}h_0$) by plotting the variation of Henry's law constant against *1/*temperature. Then, the $\Delta_{ads}h_0$ may be calculated from;

$$\Delta_{ads}h_0 = RT^2(\partial(\ln k_H)/\partial T)_n \qquad (11)$$

The Henry's law equation implies that the specific surface excess amount (n) should vary linearly with the equilibrium gas pressure at sufficiently low pressure and sufficiently high temperature (generally known as Henry's law region). Kiselev and his co-worker[33] applied the virial treatment using the equation below:

$$p = n\exp(C_1 + C_2 n + C_3 n^2 + C_4 n^3 + ...) \qquad (12)$$

where n is the amount of adsorption at pressure p and C_i are virial parameters which depends on temperature. Cole *et al.* [34] proposed that the virial equation may be expressed in the following form:

$$\ln(n/p) = A_0 + A_1 n + A_2 n^2 + ... \qquad (13)$$

where the A_0 and A_1 parameters of the equations (13) are related to adsorbate-adsorbent interaction at zero surface coverage and adsorbate-adsorbate interaction, respectively. Under condition of low surface coverage, the higher order of the virial parameters (A_2….) can be ignored.[33, 35, 36] The values of A_0 can be obtained from the graphs of $ln(n/p)$ versus n at different temperatures T. Also, the isosteric enthalpy of adsorption at zero surface coverage can be estimated from the slope of the plot of ln A_0 against $1/T$. Additionally, Henry's law constant may be calculated by using the equation (14)

$$K_H = \exp(A_0) \qquad (14)$$

Typically, the virial equation is used to compare isotherms when the adsorptives are above their critical temperature.[35, 37, 38]

2.5.2 Langmuir Equation

One of the initial models for the adsorption of a species onto bare surfaces was proposed by Irving Langmuir.[39, 40] The assumptions of the Langmuir equation are as follows and a schematic diagram of the processes is shown in Figure 2.4:

- The molecules are adsorbed at definite equivalent sites without dissociation.

- Each site can only accommodate one adsorbate molecule. In other words, only monolayer adsorption can take place.
- The heat of adsorption is constant and independent of the amount of surface coverage.

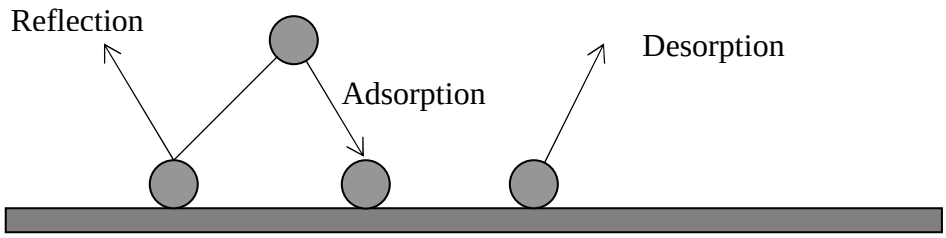

Figure 2.4 Schematic demonstration of Langmuir adsorption on a flat surface

The processes of adsorption and desorption are dynamic and the Langmuir model can be derived from the kinetics of an equilibrium state of the adsorption/desorption. The rate of adsorption depends on the pressure of adsorbate, p, and the fraction of available surface area for adsorption, θ_0 where $\theta_0 = 1 - \theta_1$ and θ_1 is the area covered by a monolayer of adsorbate molecules. Then the adsorption rate is,

$$\text{rate of adsorption} = k_a p \theta_0 = k_a p(1-\theta_1) \qquad (15)$$

The rate of desorption, on other hand, depends on the amount of adsorbed gas/vapours and is proportional to the fraction of the occupied surface area (θ_1) and the activation energy (E_1).

$$\text{rate of desorption} = k_d \theta_1 exp(-E_1/RT) \qquad (16)$$

where k_a and k_d are the rate constants for adsorption and desorption steps. In the equilibrium state, the rate of adsorption and desorption is equal. Therefore the combination of equation (15) and (16) is

$$k_a p(1-\theta_1) = k_d \theta_1 exp(-E_1/RT) \quad (17)$$

$$\frac{\theta_1}{(1-\theta_1)} = \frac{k_a p}{k_d \exp(-E_1/RT)} \quad (18)$$

Where K is defined by

$$K = \frac{k_a}{k_d(\exp - E_1/RT)} \quad (19)$$

If n (in moles) is the amount adsorbed on 1 g of adsorbent, then $\theta_1 = n/n_m$, where n_m is the monolayer capacity. Insertion into (18) leads to the Langmuir equation

$$\frac{n}{n_m} = \frac{Kp}{1+Kp} \quad (20)$$

p = equilibrium pressure (mbar)

n = amount adsorbed (mmol g^{-1})

n_m = amount in monolayer (mmol g^{-1})

K = adsorption coefficient,

For convenience in testing experiment data, the Langmuir equation may be rewritten in the linear form:

$$\frac{p}{n} = \frac{1}{Kn_m} + \frac{p}{n_m} \quad (21)$$

The plot of $\frac{p}{n}$ against p should therefore yield a straight line with slope $\frac{1}{n_m}$. Pressure (p) can also be plotted in form of the relative pressure (p/p^0) which is the ratio of

the actual gas pressure to the saturation pressure. Furthermore, the specific surface area of the solid can be calculated by the standard relation as shown in (22).[4]

$$A = n_m . L . a_m \quad (22)$$

where A = specific surface area ($m^2 g^{-1}$)

a_m = a molecular cross sectional area (nm^2)

L = Avogadro constant (6.02214×10^{23} molecules mol^{-1})

Cross sectional area of some adsorbed molecules are given by British Standard BSI 4359-1[41], McClellan *et al.*[42], Gray *et al.*[43] and Carrott *et al.*[44] is shown in Table 2.2.

Table 2.2 Cross-sectional areas of some adsorbents.

Adsorbed molecules	molecular cross sectional area (nm^2)
Nitrogen	0.162
Argon	0.138
Carbon Dioxide	0.210
Oxygen	0.141
Methanol	0.219
Ethanol	0.283
n-Propanol	0.328
n-Butanol	0.354
Chloroform	0.275
Dichloromethane	0.398
n-Heptane	0.573
n-Pentene	0.450
n-Hexane	0.510
Benzene	0.400
Toluene	0.460

2.5.3 Brunauer Emmett Teller (BET) Theory

The Langmuir equation has been extended by Brunauer, Emmett and Teller to include a multilayer adsorption mechanism giving the equation now known as the BET equation. The kinetic derivation of the BET equation is an extension of the Langmuir isotherm equation. The adsorption can be multilayer and the Langmuir equation can be applied to each layer. Additionally, at equilibrium, the distribution of adsorbate between the different layers is constant and there is no interaction among adsorbed molecules.

Let the surface areas θ_0, θ_1, θ_2, θ_3,…, θ_i be uncovered surface and the surface covered monolayer, two layers, three layers and the *i* layers of adsorbate molecules, respectively (Figure 2.5).

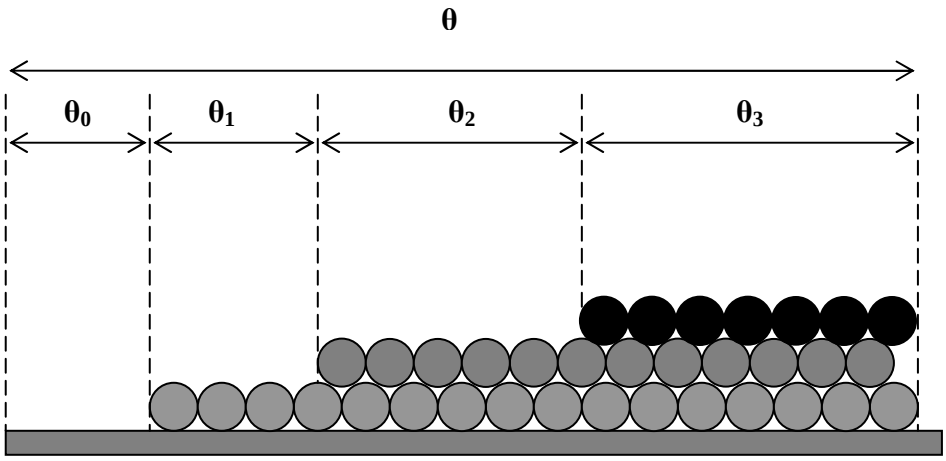

Figure 2.5 Multiple layering on surface in BET theory.

For the first layer, the rate of adsorption onto the bare surface and the desorption form the first layer are equal to each other, therefore

rate of adsorption on θ_0 = rate of desorption from θ_1

$$a_1 p \theta_0 = b_1 \theta_1 \exp\left(-\frac{E_1}{RT}\right) \qquad (23)$$

where a_1 and b_1 are adsorption and desorption constants for the first layer and E_1 is the enthalpy of desorption in the first layer which is expected to be higher than the heat of vaporization.

Similarly, the rate of adsorption onto the first layer must be the same as the rate of desorption from the second, third and … *i* layer, that is

$$a_2 p\theta_1 = b_2\theta_2 \exp\left(-\frac{E_2}{RT}\right) \tag{24}$$

$$a_3 p\theta_2 = b_3\theta_3 \exp\left(-\frac{E_3}{RT}\right) \tag{25}$$

$$a_i p\theta_{i-1} = b_i\theta_i \exp\left(-\frac{E_i}{RT}\right) \tag{26}$$

The total surface area of the adsorbent is the sum of all individual areas which is given by

$$\theta = \sum_{i=0}^{\infty} \theta_i \tag{27}$$

Therefore, the amount of gas adsorbed on the surface covering one to i layer is

$$n = \frac{n_m}{\theta} \sum_{i=0}^{\infty} i\theta_i \tag{28}$$

Hence, the total amount of gas adsorbed at a given pressure is the sum of all amounts. Therefore, the combination of equation (27) and (28) become;

$$n = n_m \frac{\sum_{i=0}^{\infty} i\theta_i}{\sum_{i=0}^{\infty} \theta_i} \tag{29}$$

In order to obtain the amount of gas adsorbed as a function of the pressure, two simplified assumptions are included. Firstly, the heat of adsorption of the second and subsequent layers is the same and equal to the heat of liquefaction (E_L). Therefore;

$$E_2 = E_3 = E_4 \ldots\ldots = E_i = E_L \tag{30}$$

The second assumption is that the ratio of the rate constant of the second layer and the higher layer is equal to each other, then it gives

$$\frac{b_2}{a_2} = \frac{b_3}{a_3} = \ldots \frac{b_i}{a_i} = g \tag{31}$$

where g is assumed constant due to all the layers (except the first) possessing the same properties. It should be noted that no assumptions have been made for the values of E_1 and b_1/a_1 for the first layer. This is because the first layer has direct interaction between the surface of adsorbent and adsorbate. From both assumptions, the surface area of layer one to *i* layer ($\theta_1, \theta_2, \theta_3, \ldots, \theta_i$) can now be expressed as the following equations:

$$\theta_1 = y\theta_0 \text{ where } y = \frac{a_1}{b_1} p \exp\left(\frac{E_1}{RT}\right) \tag{32}$$

$$\theta_2 = x\theta_1 \text{ where } x = \frac{p}{g} \exp\left(\frac{E_L}{RT}\right) \tag{33}$$

$$\theta_3 = x\theta_2 = x^2\theta_1 \tag{34}$$

and so on for other layer while for the general case (i^{th} layer);

$$\theta_i = x^{i-1}\theta_1 = yx^{i-1}\theta_0 \tag{35}$$

Assume that C is a constant parameter, therefore:

$$C = \frac{y}{x} = \frac{a_1}{b_1} g \exp\left(\frac{E_1 - E_L}{RT}\right) \tag{36}$$

Substituting (35) into equation (29) gives:

$$\frac{n}{n_m} = \frac{C\theta_0 \sum_{i=1}^{\infty} i x^i}{\theta_0 \left\{1 + C\sum_{i=1}^{\infty} x^i\right\}} \tag{37}$$

By using the Abramowitz and Stegun's formulas:

$$\sum_{i=1}^{\infty} x^i = \frac{x}{1-x}; \text{ and } \sum_{i=1}^{\infty} i x^i = \frac{x}{(1-x)^2} \tag{38}$$

So, equation (37) can be simplified to the following form

$$\frac{n}{n_m} = \frac{Cx}{(1-x)(1-x+Cx)} \tag{39}$$

It should be noted that at the saturation vapour pressure and finite number of layers can adsorbed the total amount. So, when $p = p^0$ then $n = \infty$ and $x = p/p^0$, therefore;

$$x_{(p=p^0)} = 1 = \frac{p}{g}\exp\left(\frac{E_L}{RT}\right) \tag{40}$$

$$\frac{p}{p^0} = \frac{\frac{p}{g}\exp\left(\frac{E_L}{RT}\right)}{\frac{p^0}{g}\exp\left(\frac{E_L}{RT}\right)} \tag{41}$$

$$\frac{p}{p^0} = \frac{\frac{p}{g}\exp\left(\frac{E_L}{RT}\right)}{1} = x \tag{42}$$

Substituting p / p^0 into (39), we obtain the BET isotherm equation

$$n = \frac{n_m C p}{(p^0 - p)\{1 + (C-1)(p/p^0)\}} \tag{43}$$

The BET equation can be rearranged as follows;

$$\frac{p}{n(p^0 - p)} = \frac{1}{n_m C} + \frac{(C-1)}{n_m C} \cdot \frac{p}{p^0} \qquad (44)$$

where p^0 = saturation vapour pressure (mbar)

n = the amount adsorbed at pressure p (mmol g^{-1})

n_m = the monolayer capacity (mmol g^{-1})

The parameter C is given by

$$C = e^{(q_1 - q_L)/RT} \qquad (45)$$

where q_1 = the heat of adsorption in the first layer

q_L = the heat of condensation

$q_1 - q_L$ = the net heat of adsorption

A plot of $\frac{p}{n(p^0 - p)}$ against $\frac{p}{p^0}$ should therefore be a straight line if the experimental data follows the BET isotherm. The gradient $\frac{C-1}{n_m C}$ and intercept $\frac{1}{n_m C}$ can be determined from the linear graph. Once n_m is obtained from the slope and intercept, the surface area can also be calculated from equation (20). The plots of n/n_m against p/p^0 are shown in Figure (2.6) together with their differences. Lower C values correspond to weak interaction between adsorbent and adsorbate and it also gives a Type III isotherm. When C is larger there is strong interaction between adsorbent and adsorbate and the BET equation gives Isotherm Type II. Very high C values are not always indicative of micropore filling.

Testing the Type II isotherm data against the linear form of BET equation normally yields a good linear plot in the relative pressure range 0.05-0.3. At a higher relative pressure, the plot usually deviates from linearity. So, the linear BET plot will be valid if the intercept is not negative and the C value is in the range 100-200.

The BET equation is widely used to interpret isotherms obtained using nitrogen adsorption at 77 K and is usually applied for surface area analysis of macro-and mesoporous materials. The equation is not applicable in the case of micro-porous materials and very high C values. This is because micropore filling at low relative pressure regions can lead to an overestimation of the surface area.

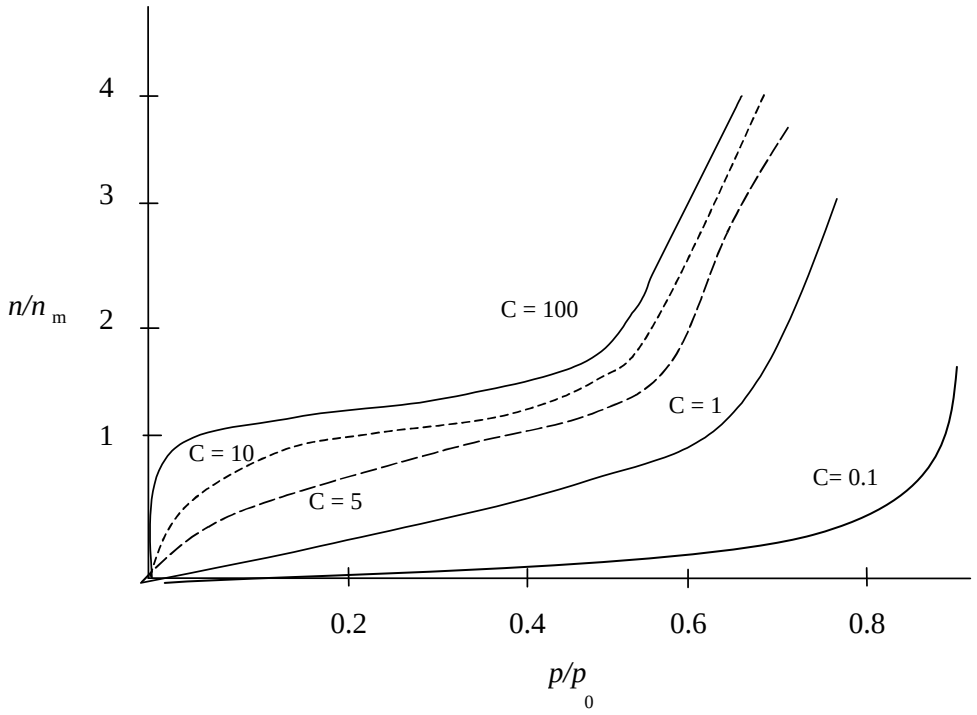

Figure 2.6 Schematic diagram of isotherms for a range of C values obtained from the BET equation.

2.5.4 Dubinin – Radushkevich (D-R) Model

Dubinin and Radushkevich[13,14] proposed an equation for the estimation of the micropore volume from the low- and medium-relative pressure parts of Type I adsorption isotherms. Their equation was adapted from the potential theory of Polanyi[15], and an essential parameter of this theory is the quantity *A*, which is defined by

$$A = RT\ln(\frac{p^0}{p}) \tag{46}$$

where *A is* an adsorption affinity which is also known as Polanyi's adsorption potential. Dubinin assumed that the adsorption process in microporous materials involves the volume filling of the micropores rather than layer-by-layer adsorption on the pore walls. So the degree of pore filling of the micropores (θ) may be defined by:

$$\theta = \frac{V}{V_0} \tag{47}$$

where V_0 is the total volume of the micropore system and V the volume that has been filled when the relative pressure is p/p^0. The fundamental postulate in the development of this theory is that θ is a function of the differential molar work of adsorption A such that;

$$\theta = f(\frac{A}{\beta}) \tag{48}$$

where β is termed the similarity constant which brings the 'characteristic curves' of θ against A for different adsorptives into coincidence with the curve for an arbitrary standard (benzene was chosen where β = 1). Another assumption is that the pore size distribution is Gaussian, so the mathematical model may be expressed as

$$\theta = \exp\left[-k\left(\frac{A}{\beta}\right)^2\right] \tag{49}$$

By combining equations (47), (48) and (49), we obtain

$$V = V_0 \exp\left[-\frac{k}{\beta^2}\left(RT\ln p^0/p\right)^2\right] \tag{50}$$

or

$$\frac{V}{V_0} = \exp\left[-B\left(\frac{T}{\beta}\right)^2 \log^2\left(p^0/p\right)\right] \tag{51}$$

where $B = (2.303R)^2 k$ and k is another characteristic parameter. Equation (51) can be rewritten as equation (52) for linear graph plotting:

$$\log_{10}(V) = \log_{10}(V_0) - D\log_{10}^2\left(p^0/p\right) \qquad (52)$$

Equation (52) can also be written in the form:

$$\ln(n) = \ln(n_0) - D\ln^2(p^0/p) \qquad (53)$$

where

$$D = B\left(\frac{T}{\beta}\right)^2 \qquad (54)$$

where n_0 is the amount of adsorbate which fills the micropores and n the amount at the relative pressure p/p^0.

According to equation (52) the linear D-R plot should be obtained by plotting of log V against $\log_{10}^2(p^0/p)$. An intercept of this D-R plot is equal to the total micropore volume (V_0). However, D-R graphs may be non linear for solids having micropores and ultramicropores.[45] These non linear graphs have been explained by Marsh and Rand[46-48] and the relationships between these deviations from linearity and the associated pore-size distributions are shown in Figure 2.7.

Isotherm A shows that the adsorption process occurs continuously in the microporous material which has the narrow Gaussian distribution of pore size. The adsorption is finished when all the porosity is filled at a relative pressure of $[\log_{10}^2(p^0/p) = 0]$ which means the partial pressure is equal to the total pressure $(p^0/p = 1)$.

Isotherm B shows the linearity of plot from the initial stages of adsorption (low values of (p^0/p) followed by a horizontal part at high p^0/p which indicates that either the micropores are filled at a partial pressure less than the total pressure or the larger size of pores does not exist. The position of the cut off on the p/p^0 scale indicates the width of the pore size distribution. The lower p/p^0 for the cut off position indicates narrower and

smaller pore size distribution. However, extrapolation of the D-R plots to $\log_{10}^2(p^0/p) = 0$ may give a value of micropore volume too large to be realised, which would be erroneous.

Isotherm C shows that the plot has an upward deviation from linearity at high p/p^0. This upward deviation indicates additional adsorption capacity, which could be caused by the filling of supermicropores or filling of mesopores or multilayer adsorption on surface of non-porous materials. In this case, the micropore volume can be calculated by extrapolation of the linear part of the D-R plot.

Isotherm D exhibits negative deviation from the D-R relationship at high $\log_{10}^2(p^0/p)$ (low p/p^0) which could be due to activated diffusion or molecular sieve effects.

Isotherm E shows a non-linear D-R relationship. The upward curve may be related to the volume filling in very narrow micropores. Furthermore, the curve could also be associated with the adsorption process not reaching the adsorption equilibrium. So, the D-R equation should not be used to determine micropore volume in this case.

In summary, the D-R equation generally applies to adsorption isotherms in the low relative pressure (p/p^0 <0.03). The adsorption of CO_2 molecules on microporous carbon at temperature 273 K, where the activated diffusion effects are minimal, is an example of the D-R equation being frequently used to determine the micropore volume.[49, 50]

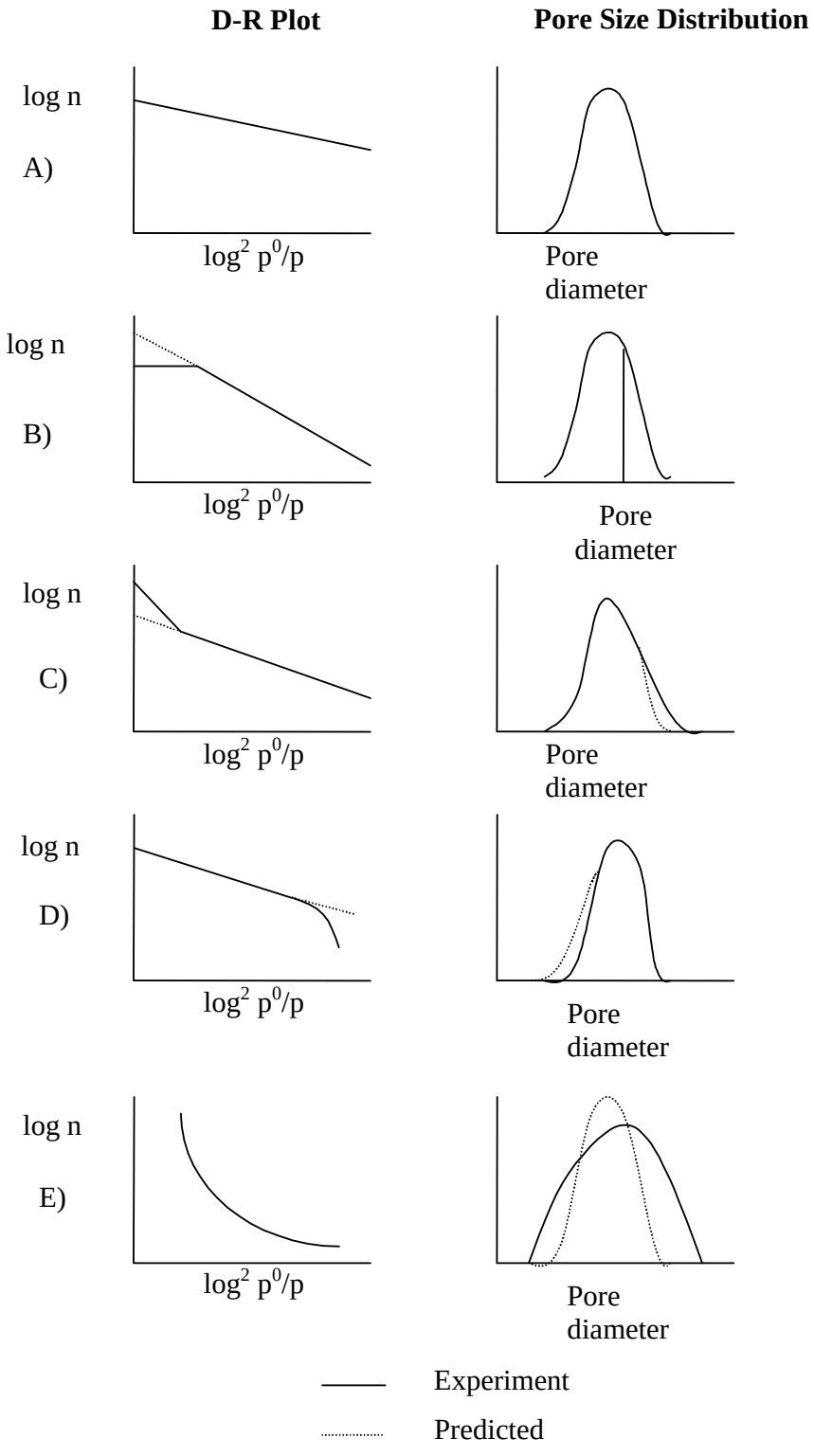

Figure 2.7 Schematic diagram of the deviation in D-R plots explained in terms of distributions of site energy (after Marsh[48])

2.6 Adsorption Kinetics

In general, the kinetics of adsorption processes (also called atom or molecular mass transport) involves the following basic processes. These are 1) diffusion of adsorbate molecules from bulk fluid to the surface of adsorbent, 2) diffusion of the molecules in the pore structure of the adsorbent and 3) diffusion along pore surfaces and 4) diffusion through constrictions in the porosity. The rates of adsorption and desorption in porous adsorbents are often controlled by transport within the pore network, rather than by the intrinsic kinetics of sorption at the surface.

When the system pressure is uniform, the diffusion of gases and vapours through porous materials can occur by several different mechanisms depending on the pore size. These mechanisms include free-gas diffusion, Knudsen diffusion, viscous flow, and surface diffusion. All of these mechanisms may contribute to the flux of gas through the pores of the solid. D. D. Do [22] classify the transport regimes in porous materials as they relate to their pore diameter. This convenient classification is shown as Table 2.3.

Table 2.3 Transport regimes in porous media. Adapted from Do *et al.*[22].

Transport type	Pore diameter (nm)	IUPAC classification scheme
viscous flow or free gas diffusion	>20	macropores and mesopores
molecular diffusion	>10	mesopores
Knudsen diffusion	2-100	
Micropore (configurational) diffusion	<1.5	mircopores and ultramicropores

To classify the different types of diffusion more precisely, Knudsen number (K_n) should take in to account and this is defined as (55)

$$K_n = \frac{\lambda}{d} \qquad (55)$$

where λ is the mean free path (MFP) and *d* is the characteristic pore diameter. The mean free path is the average distance between collisions for a gas molecule and can be expressed by the following equation.[22, 51-53]

$$\lambda = \frac{RT}{\sqrt{2}\pi d^2 N_A P} \qquad (56)$$

where ***d*** is the collision diameter, $\boldsymbol{N_A}$ is Avogadro's number, ***P*** is the gas pressure, ***R*** is the universal gas constant, and ***T*** is the gas temperature (K).

According to the magnitude of K_n, three main diffusion regimes can be defined as follows:[54]

Free gas diffusion	$K_n << 1$
Knudsen diffusion	$K_n = 1$
Surface diffusion	$K_n >> 1$

Within the Knudsen number can be distinguished four different types of diffusion mechanisms as shown in Figure 2.8. Firstly, free-gas diffusion, also known as bulk or molecular diffusion, generally occurs when pore diameter is large relative to the mean free path and at high system pressures (see Figure 2.8a). In this free–gas diffusion, collision between diffusing molecules occurs far more frequently than collisions between the molecule and the pore wall. Under these conditions, the influence of the pore wall is negligible and diffusion occurs by the same mechanism as in the bulk fluid.

Knudsen diffusion (or flow) of gas is the predominant mechanism when pore diameter is comparable with the mean free path of gas molecules and is often encountered with high surface area materials at moderate pressures. Hence molecules are more prone to collision with the pore wall due to difficulties with diffusion into the narrow pore size. The driving force for this diffusion is the concentration gradient, thus the light weight molecule diffuses in to the pores faster than the heavy molecule.

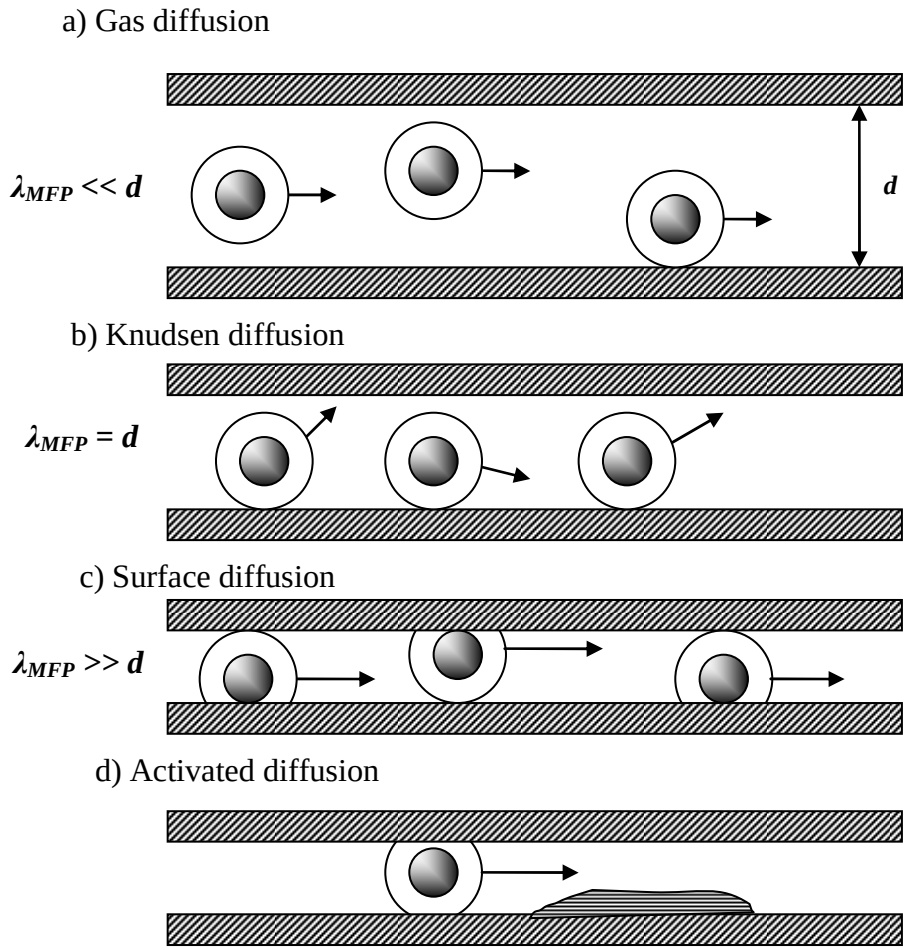

Figure 2.8 Diagrammatic representations of different types of diffusion.

As the diameter of pores decrease, the dominant mechanism of diffusion changes to surface diffusion. Surface diffusion is a site-to-site hopping process and takes place on an open surface as well in pores. Activated diffusion is observed when the dimensions of the adsorbate molecules are slightly smaller than or approaching the size of the pore diameter. Activated diffusion occurs during the adsorption of molecules in micropores, which have the highest energy. At low temperatures, the gas molecules may not have sufficient kinetic energy to enter these pores and the activation energy of diffusion is such that, at low adsorption temperature, rates of adsorption become so slow that equilibrium may not be reached in a reasonable time scale. Surface or activated diffusion becomes dominant for microporous materials, such as zeolites or microporous carbons, and for strongly adsorbed species. Diffusion in micropores is generally known to be dominated by the interactions between the diffusing molecule and the pore walls. In microporosity, the effects associated

with the proximity of the pore walls become crucial and micropore diffusion is an activated process. This is because the diffusing molecules are within the force field of the pore walls.

2.6.1 Empirical equation

Thermodynamically, diffusion is a mass transport process generated by gradients in chemical potential. Empirical mass diffusion is described by the equation below.[55-57]

$$\frac{M_t}{M_e} = kt^n \qquad (57)$$

where M_t = amount uptake at time t (μg)

M_e = amount uptake at equilibrium (μg)

k = constant

t = time (sec)

n = diffusion exponent

Plotting of $\ln(M_t/M_e)$ against $\ln(t)$ should yield the linear line and the diffusion exponent can be obtained from the slope of this plot. Differences in diffusion behaviour can be distinguished by such an exponent. When n = 0.5, the dominant diffusion mechanism is Fickian where it is related to the concentration gradient. While, if n = 1 may be described as a non-Fickian diffusion mechanism and the adsorption is proportional to time t. For an intermediate value of n from 0.5 to 1 represent anomalous diffusion which is combines the transition region between both two cases.[55, 58, 59]

Rao and co-workers[60] proposed that there are two processes involved in the adsorption of the diffusing species in carbon molecular sieves: 1) diffusion along the pores and 2) diffusion through the barrier at the pore entrances. These two processes are schematically illustrated in Figure 2.9. The Fickian diffusion model is followed when diffusion along the pore controls the kinetics while the linear driving force model is followed when diffusion through the barrier is the rate-determining step.

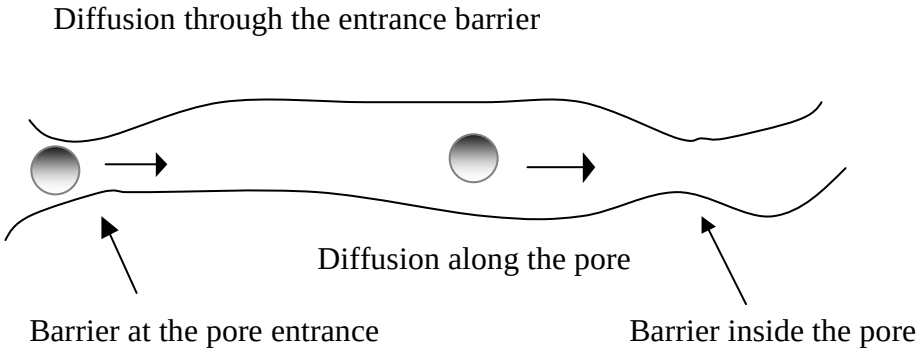

Figure 2.9 Diagrammatic representation of diffusion process

When both processes are significant, a combined barrier resistance/diffusion model (CRBD), stretched exponential model (SE), double exponential model (DE) or double stretched exponential model (DSE) are used to described the adsorption kinetics. The models have been used to examine the adsorption kinetics of various gases/static vapours on carbon molecular sieves (CMS),[35-37, 61] and activated carbons,[23, 62-67] and metal organic frameworks.[38, 68, 69] More details on these models are discussed in the following sections.

2.6.2 Fickian Diffusion

In 1855, Fick proposed his First Law describing a linear relationship between the diffusing of solute per unit area (J_i : flux of component i at time t) with respect to concentration gradient as the driving force.[55, 70-72]

$$J_i = -D_i\left(\frac{\partial C_i}{\partial a}\right) \qquad (58)$$

where D_i is the diffusion coefficient, C_i is the concentration and a is its diffusion distance. Fickian diffusion is a concentration gradient dependent process as represented schematically in Figure 2.10:

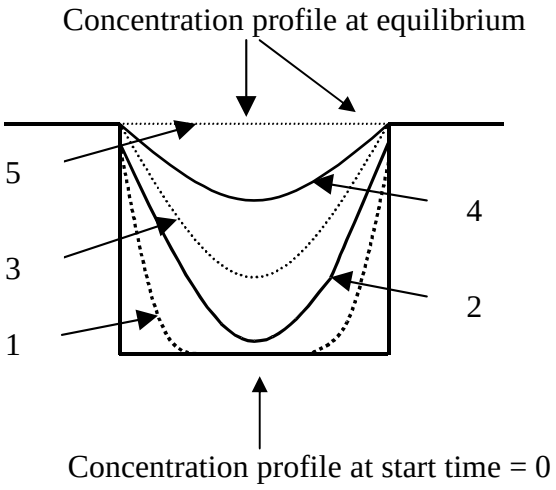

Figure 2.10 Schematic representation of pore filling in the Fickian model

The modification of Flick's First Law equation for describing diffusion behaviour in a homogenous sphere of radius *a* can be expressed as;

$$\frac{\partial C}{\partial t} = D\left(\frac{\partial^2 C}{\partial a^2}\right) + \left(\frac{2}{a}\right)\left(\frac{\partial C}{\partial a}\right) \qquad (59)$$

an analytical solution to this ordinary partial equation is given by;

$$\frac{M_t}{M_e} = 1 - \frac{6}{\pi^2}\sum_{n=1}^{\infty}\frac{1}{n^2}\exp\left(\frac{-Dn^2\pi^2 t}{a^2}\right) \qquad (60)$$

where M_t = the adsorbate uptake at time t

M_e = the adsorbate uptake at equilibrium

D = the gas diffusion coefficient in $cm^2\ s^{-1}$

a = the radius of the particle

For short time scale an alternative equation of (60) may be written as:

$$\frac{M_t}{M_e} = 6\left(\frac{Dt}{a^2}\right)^{\frac{1}{2}} - \left[\pi^{-\frac{1}{2}} + 2\sum_{n=1}^{\infty} ierfc\frac{na}{t\sqrt{D}}\right] - \frac{3Dt}{a^2} \qquad (61)$$

At an initial state of adsorption, the second and the higher term may be neglected and gives:

$$\frac{M_t}{M_e} = 6\left(\frac{Dt}{\pi a^2}\right)^{1/2} - 3\frac{Dt}{a^2} \qquad (62)$$

$$\frac{M_t}{M_e} = \frac{6}{\sqrt{\pi}} \times \frac{\sqrt{D}\sqrt{t}}{a} \qquad (63)$$

As a result, at this short times scale (M_t/M_e < 20%) plotting of M_t/M_e against $t^{1/2}$ should give a straight line with a slope of $\frac{6D^{\frac{1}{2}}}{(\pi)^{\frac{1}{2}}a}$. However, the series in equation (63) converges rapidly since the higher term becomes very small at longer timescales. So, the second and higher term can both be ignored. Therefore, for values of M_t/M_e> 50% the expression can be written thus:

$$\frac{M_t}{M_e} = 1 - \frac{6}{\pi^2}\left[\exp\left(\frac{-D\pi^2 t}{a^2}\right)\right] \qquad (64)$$

So that:

$$\frac{M_e - M_t}{M_e} = \frac{6}{\pi^2}\left[\exp\left(\frac{-D\pi^2 t}{a^2}\right)\right] \qquad (65)$$

In this long-time scale, a plot of $\ln[1-M_t/M_e]$ versus time will yield a straight line with a slope and an intercept equal to $\frac{-\pi^2 D}{a^2}$ and $\ln\frac{6}{\pi^2}$, respectively. So, the diffusion constant can be determined from such a plot.

2.6.3 Linear driving force equation

Linear driving force (LDF) equation was originally derived by Gleuckauf and Coates[73, 74] for determining the adsorption kinetics of species on chromatography. The LDF describes the adsorption rate using the following dimensionless form:

$$\frac{dM_t}{dt} = k(M_e - M_t) \qquad (66)$$

the simpler explicit form can be written by

$$\frac{M_t}{M_e} = 1 - e^{-kt} \qquad (67)$$

where M_t = the amount adsorbed (μg) at time t (s)

M_e = the equilibrium uptake, (μg)

k = the rate constant, (s^{-1})

t = time (s)

Therefore a plot of $\ln(1-M_t/M_e)$ versus time will be linear with a gradient equal to the rate constant. This rate constant k is comparable to $\frac{-\pi^2 D}{a^2}$ in the Fickian equation (when $M_t/M_e > 50\%$).

The basic assumption of the LDF is based on the average concentration of adsorbate inside the particle as it directly relates with the concentration in the fluid phase as represented in Figure 2.11 Adsorption into the particle takes place in the order 1, 2, 3, 4, 5… with the concentration uniform throughout the particle. The model is frequently used for mathematical simulation of breakthrough curves, desorption behaviour and cyclic gas separation processes such as pressure swing adsorption or thermal swing adsorption (PSA or TSA). The simplicity of the LDF equation means that it can be solved analytically.[75]

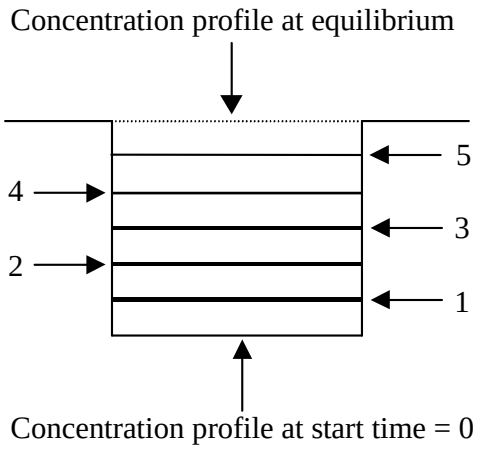

Figure 2.11 Diagrammatic representation of the LDF model

2.6.4 Combined Barrier Resistance/ Diffusion Model

A combined barrier resistance/diffusion model is based on the assumption that the gas diffusion was controlled by the existence of a barrier resistant at the surface and subsequent diffusion in a spherical microporous system by Fick's First Law.[55] The relevant equations for isothermal diffusion into a spherical particle with this model are:

$$\frac{\partial C}{\partial t} = D\left(\frac{\partial^2 C}{\partial r^2}\right) + \left(\frac{2}{r}\right)\left(\frac{\partial C}{\partial r}\right) \qquad (68)$$

and

$$D = \frac{\delta C(r_c t)}{\delta r} = k_b \{C^*(t) - C(\mathrm{r,t})\} \qquad (69)$$

where D = the crystallite diffusivity ($cm^2\ s^{-1}$)

C = the sorbate concentration (mmol cm^{-3})

C^* = The surface concentration in equilibrium with gas phase (mmol cm^{-3})

r = radial coordinate (cm)

t = time (sec)

k_b = The barrier resistance rate constant($cm\ s^{-1}$)

r_c = the radius of the particle (cm)

The parameters derived from the model are $k_{b,}$ the barrier resistance constant (cm s^{-1}) and k_d, the diffusion constant which is equal to D/r_c^2 (s^{-1}). The model has successfully been used to describe the adsorption of various gases/vapours. However, using this model is not simple to use since the finite difference method needs to be used.

A comparison graph of Fickian model, linear driving force and combined barrier resistance is shown in Figure 2.12

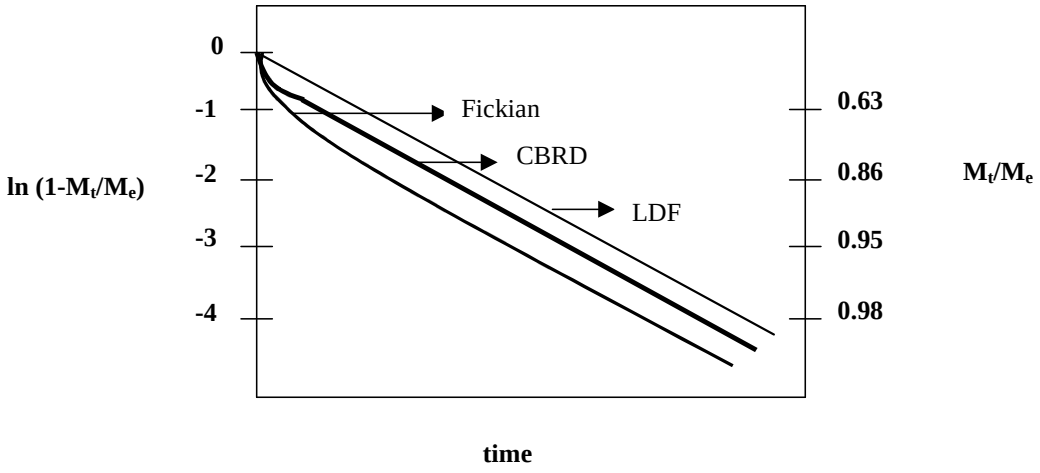

Figure 2.12 Comparison of Combined Barrier Resistance Diffusion, Fickian diffusion and LDF models,

2.6.5 Stretched Exponential (SE) Model

In 1970, Williams and Watts [76, 77] found an empirical dielectric decay function that fitted data for dielectric relaxation between glassy and polymeric materials, including polyethylacrylate and propylene oxide. Klafter *et al.*[78] have shown that there is a common underlying mathematic structure relating the Forster direct-transfer mechanism which is an example of relaxation via parallel channels using hierarchically constrained dynamics. This stretched exponential function, is given by;

$$\phi(t) = \exp\left[\left(\frac{-t}{\tau}\right)^{\beta}\right],\ 0 < \beta < 1 \qquad (70)$$

where the exponent β and the constant ***T*** depend on material and can be fixed as the external conditions such as temperature and pressure while $\phi(t)$ is the relaxation function.

The stretched exponential model is one dimension when β = 0.5 and exhibit three dimensional when β = 1. Presumably an intermediate value of β = 0.75 describes a two dimensional process. The concept of parallel and serial channels is physically feasible for diffusion into a porous material. In order to apply the stretched exponential model to adsorption and desorption kinetics for a specific increment/decrement, the equation was used in the following form:

$$y = A\left[1 - exp\left(-(kt)^{\beta}\right)\right] \qquad (71)$$

where A is a constant, k is the rate constant, β the exponential parameter and t is the time. When the data are normalised to fractional uptake, A is equal to 1 and for adsorption, the equation can be rewritten as:

$$\frac{M_t}{M_e} = 1 - e^{-(kt)^{\beta}} \qquad 0 < \beta < 1 \qquad (72)$$

where M_t is the mass at time t, M_e is the mass at the equilibrium, k is the rate constant and β is the exponential parameter. The value of β is within the range 0.5 – 1. When β = 1 the stretched exponential model is identical with the linear driving force model with a 3-dimensional process and a single relaxation time. When β = 0.5 the process is one dimensional and there is a distribution of relaxation times.

Interestingly, Avrami also proposed his model, known as Kolmogorov-Johnson-Mehl-Avrami or KJMA equation, for describing the kinetics of crystallization. It is apparent that the model has a form related to the stretched exponential model. The equation is given below:[79-82]

$$\frac{M_t}{M_e} = 1 - e^{\left(-kt^{\beta}\right)} \qquad (73)$$

where M_t is the mass at time t, M_e is the mass at the equilibrium, t is time k is the rate constant and is temperature dependent while β is named as the Avrami exponent. Although the stretched exponential and Avrami equations are quite similar to each other, the Avrami exponent,(β) should be an integer from 1 to 4 and k is independent of β, while in the stretched exponential equation $0 < \beta < 1$. If β varies as in the Avrami equation, then the units of k will vary and this makes comparisons difficult.

2.6.6 Double Stretched Exponential (DSE) and Double Exponential (DE) Models

Normalized kinetic profiles for small pressure increments in the adsorption on porous media can be described using a series of models based on a DSE model which describes two kinetic processes each with a distribution of relaxation times. The DSE model is described as follows:

$$\frac{M_t}{M_e} = A_1\left(1 - e^{(-k_1 t)^{\beta_1}}\right) + A_2\left(1 - e^{(-k_2 t)^{\beta_2}}\right) \qquad (74)$$

where $A_1 + A_2 = 1$

M_t = the uptake at time t,

M_e = the equilibrium uptake,

k_1 and k_2 = the rate constants,

β_1 and β_2 = the exponents, describe the distribution of relaxation times.

A_1 and A_2 are the fractional contributions for process mechanisms corresponding to adsorption rate constants k_1 and k_2, respectively.

The double exponential (DE) model is a nested model of the DSE model with $\beta_1 = \beta_2 = 1$ and in this case the equation (74) becomes:

$$\frac{M_t}{M_e} = A_1\left(1 - e^{-k_1 t}\right) + \left(1 - A_1\right)\left(1 - e^{-k_2 t}\right) \qquad (75)$$

The kinetics can be described by two processes each with single relaxation times: (a) slow diffusion through windows with high activation energy and (b) fast diffusion along pore cavities with low activation energy.[69, 83]

The criterion for an acceptable fit of the experimental data to the kinetic model is that 99% of residuals should be within ± 0.02 for the normalized kinetic profiles for the model with the least number of variables. The most appropriate model was selected on the basis of the lowest number of variables, which fitted the experimental data with the criteria outlined above and was consistent with the pore structure and surface chemistry.

2.7 References

1. Kayser, H., *Wied. Ann.* **1881,** 14, 450.
2. Sameshima, J., The sorption of gas by charcoal as a dissolution phenomenon. *Bull. Chem. Soc. Jpn.* **1927,** 2 (1), 1-10.
3. McBain, J. W., *Phil. Mag.* **1909,** 18, 916.
4. Gregg, J. S.; Sing, K. S. W., *Adsorption, Surface Area and Porosity;*. 2nd ed.; Academic Press: London, 1982; p 303.
5. F. Rouquerol; Rouquerol, J.; Sing, K. S. W., *Adsorption by Powders, Porous Solids*. Academic Press: London, 1999; p 467.
6. Dabrowski, A., Adsorption - from theory to practice. *Adv. Colloid Interface Sci.* **2001,** 93, (1-3), 135-224.
7. Sing, K. W.; Everett, D. H.; Haul, R. A. W.; Moscou, L.; Pierotti, R. A.; Rouquerol, J.; Siemieniewska, T., Reporting physisorption data for gas/solid systems with special reference to the determination of surface area and porosity. *Pure Appl. Chem.* **1985,** 57, (4), 603-19.
8. Shaw, D. J., *Introduction to colloid and surface chemistry*. 3rd ed.; Butterworths: London, 1980; p 273.
9. McCash., E. M., *Surface chemistry*. Oxford University Press: Oxford 2001; p 177.
10. Young, D. M.; Crowell, A. D., *Physical adsorption of gases* Butterworths: London 1962; p 426.
11. Adamson, A. W.; Gast, A. P., *Physical chemistry of surfaces*. 6th ed.; Wiley: New York, 1997; p 764.
12. Atkins, P. W., *Physical chemistry*. 5 ed.; Oxford University Press: Oxford, 1998.
13. Attard, G.; Barnes, C., *Surfaces*. Oxford University press: Oxford, 2008; p 96.
14. Polanyi, M., Theories of the adsorption of gases. A general survey and some additional remarks. Introductory paper to section III. *Trans. Faraday Soc.* **1932,** 28, 316 - 33.
15. Flood, E. A., *The solid-gas interface*. Edward Arnold: London, 1967; Vol. 1, p 514.
16. Brunauer, S.; Emmett, P. H.; Teller, E., Adsorption of Gases in Multimolecular Layers. *J. Am. Chem. Soc.* **1938,** 60, (2), 309 - 19.
17. Brunauer, S.; Deming, L. S.; Deming, W. S.; Teller, E., On a Theory of the van der Waals Adsorption of Gases. *J. Am. Chem. Soc.* **1940,** 62, 1723 - 32.

18. Hassan, N. M.; Ghosh, T. K.; Hines, A. L.; Loyalka, S. K., An isotherm model for adsorption of gases and vapours on heterogeneous adsorbents. *Gas Sep. Purif.* **1992,** 6, (4), 229-34.

19. Bhambhani, M. R.; Cutting, P. A.; Sing, K. S. W.; Turk, D. H., Analysis of nitrogen adsorption isotherms on porous and nonporous silicas by the BET and [alpha]s methods. *J. Chem. Phys.* **1972,** 38, (1), 109-17.

20. Tóth, J.; Berger, F.; Dékány, I., Separation of the First Adsorbed Layer from Others and Calculation of the BET Compatible Surface Area from Type II Isotherms. *J. Colloid Interface Sci.* **1999,** 212, (2), 411-8.

21. Kim, P.; Agnihotri, S., Application of water-activated carbon isotherm models to water adsorption isotherms of single-walled carbon nanotubes. *J. Colloid Interface Sci.* **2008,** 325, (1), 64-73.

22. Do, D. D., *Absorption Analysis: Equilibria and Kinetics*. Imperial College Press: 1998; p 892.

23. Fletcher, A. J.; Thomas, K. M., Compensation Effect for the Kinetics of Adsorption/Desorption of Gases/Vapors on Microporous Carbon Materials. *Langmuir* **2000,** 16, (15), 6253-66.

24. Komarneni, S.; Pidugu, R.; Menon, V. C., Water adsorption and desorption isotherms of silica and alumina mesoporous molecular sieves. *J. Porous Mater.* **1996,** 3, (2), 99-106.

25. Cossarutto, L.; Zimny, T.; Kaczmarczyk, J.; Siemieniewska, T.; Bimer, J.; Weber, J. V., Transport and sorption of water vapour in activated carbons. *Carbon* **2001,** 39, (15), 2339-46.

26. Mody, H.; Kannan, S.; Bajaj, H.; Manu, V.; Jasra, R., A simple room temperature synthesis of MCM-41 with enhanced thermal and hydrothermal stability. *J. Porous Mater.* **2008,** 15, (5), 571-9.

27. Qi, N.; LeVan, M. D., Adsorption equilibrium modeling for water on activated carbons. *Carbon* **2005,** 43, (11), 2258-63.

28. De Boer, J. H., *The Structure and Properties of Porous Materials*. Butterworths: London, 1958; p 382.

29. Ball, P. C.; Evans, R., Temperature dependence of gas adsorption on a mesoporous solid: capillary criticality and hysteresis. *Langmuir* **1989,** 5, (3), 714-23.

30. Yang, P.; Zhao, D.; Margolese, D. I.; Chmelka, B. F.; Stucky, G. D., Generalized syntheses of large-pore mesoporous metal oxides with semicrystalline frameworks. *Nature* **1998,** 396, (6707), 152-5.

31. Zhao, X.; Xiao, B.; Fletcher, A. J.; Thomas, K. M.; Bradshaw, D.; Rosseinsky, M. J., Hysteretic Adsorption and Desorption of Hydrogen by Nanoporous Metal-Organic Frameworks. *Science* **2004,** 306, (5698), 1012-5.

32. Fletcher, A. J.; Thomas, K. M.; Rosseinsky, M. J., Flexibility in metal-organic framework materials: Impact on sorption properties. *J. Solid State Chem.* **2005,** 178, (8), 2491-510.

33. Avgul, N. N.; Bezus, A. G.; Dobrova, E. S.; Kiselev, A. V., The similarity of gas adsorption by nonporous and microporous crystalline adsorbents. *J. Chem. Phys.* **1973,** 42, (3), 486-95.

34. Cole, J. H.; Everett, D. H.; Marshall, C. T.; Paniego, A. R.; Powl, J. C.; Rodriguez-Reinoso, F., Thermodynamics of the high temperature adsorption of some permanent gases by porous carbons. *Journal of the Chemical Society, Faraday Transactions* **1974,** 70, 2154 - 69.

35. O'Koye, I. P.; Benham, M.; Thomas, K. M., Adsorption of Gases and Vapors on Carbon Molecular Sieves. *Langmuir* **1997,** 13, (15), 4054-9.

36. Reid, C. R.; O'Koye, I. P.; Thomas, K. M., Adsorption of Gases on Carbon Molecular Sieves Used for Air Separation. Spherical Adsorptives as Probes for Kinetic Selectivity. *Langmuir* **1998,** 14, (9), 2415-25.

37. Reid, C. R.; Thomas, K. M., Adsorption Kinetics and Size Exclusion Properties of Probe Molecules for the Selective Porosity in a Carbon Molecular Sieve Used for Air Separation. *J. Phys. Chem. B* **2001,** 105, (43), 10619-29.

38. Chen, B.; Zhao, X.; Putkham, A.; Hong, K.; Lobkovsky, E. B.; Hurtado, E. J.; Fletcher, A. J.; Thomas, K. M., Surface Interactions and Quantum Kinetic Molecular Sieving for H_2 and D_2 Adsorption on a Mixed Metal-Organic Framework Material. *J. Am. Chem. Soc.* **2008,** 130, (20), 6411-23.

39. Langmuir, I., The constitution and fundamental properties of solids and liquids *J. Am. Chem. Soc.* **1916,** 38, (11), 2221 - 95.

40. Langmuir, I., The adsorption of gases on plane surfaces of glass, mica and platimum. *J. Am. Chem. Soc.* **1918,** 40, (9), 1361 - 403.

41. *BS 4359-4:1995 Determination of the specific surface area of powders. Recommendations for methods of determination of metal surface area using gas adsorption techniques* BS 4359-4:1995; British Standards Institution: 1995; p 24.

42. McClellan, A. L.; Harnsberger, H. F., Cross-sectional areas of molecules adsorbed on solid surfaces. *J. Colloid Interface Sci.* **1967,** 23, (4), 577-99.

43. Gray, M. J.; Mebane, R. C.; Womack, H. N.; Rybolt, T. R., Molecular Mechanics and Molecular Cross-Sectional Areas: A Comparison with Molecules Adsorbed on Solid Surfaces. *J. Colloid Interface Sci.* **1995,** 170, (1), 98-101.

44. Carrott, P. J. M.; Ribeiro Carrott, M. M. L.; Cansado, I. P. P., Reference data for the adsorption of dichloromethane on carbon materials. *Carbon* **2001,** 39, (3), 465-72.

45. Brunauer, S., Some remarks about micropore analysis. *J. Colloid Interface Sci.* **1972,** 39, (2), 435-6.

46. Marsh, H.; Rand, B., The characterization of microporous carbons by means of the dubinin-radushkevich equation. *J. Colloid Interface Sci.* **1970,** 33, (1), 101-16.

47. Rand, B., On the empirical nature of the Dubinin--Radushkevich equation of adsorption. *J. Colloid Interface Sci.* **1976,** 56, (2), 337-46.

48. Marsh, H., Adsorption methods to study microporosity in coals and carbons--a critique. *Carbon* **1987,** 25, (1), 49-58.

49. Cazorla-Amoros, D.; Alcaniz-Monge, J.; Linares-Solano, A., Characterization of Activated Carbon Fibers by CO_2 Adsorption. *Langmuir* **1996,** 12, (11), 2820-4.

50. Lozano-Castelló, D.; Cazorla-Amorós, D.; Linares-Solano, A., Usefulness of CO_2 adsorption at 273 K for the characterization of porous carbons. *Carbon* **2004,** 42, (7), 1233-42.

51. Pollard, W. G.; Present, R. D., On Gaseous Self-Diffusion in Long Capillary Tubes. *Physical Review* **1948,** 73, (7), 762.

52. Weller, K. R.; Stenhouse, N. S.; Watts, H., Diffusion of Gases in Porous Solids. I. Theoretical Background and Experimental Method. *Canadian Journal of Chemistry* **1974,** 52, (15), 2684-91.

53. Ho, F. G.; Strieder, W., A mean free path kinetic theory of void diffusion in a porous medium with surface diffusion. Asymptotic expansion in the Knudsen number. *J. Chem. Phys.* **1981,** 74, (8), 4742-4.

54. Thomson, W. J., *Introduction to transport phenomena* Prentice Hall: Upper Saddle River, NJ 2000; p 509.

55. Crank, J., *The mathematics of diffusion*. 2nd ed.; Oxford science publications: Oxford 1979; p 414.

56. Sparks, D. L., *Rates of soil chemical processes*. Soil Science Society of America: Madison, 1991; p 302.

57. Lee, W.-F.; Yeh, Y.-C., Studies on preparation and properties of NIPAAm/hydrophobic monomer copolymeric hydrogels. *European Polymer Journal* **2005,** 41, (10), 2488-95.

58. Alfrey, T.; Gurnee, E. F.; Lloyd, W. G., Diffusion in glassy polymers. *Journal of Polymer Science Part C: Polymer Symposia* **1966,** 12, (1), 249 - 61.

59. Gao, P.; Mackley, M. R., A General Model for the Diffusion and Swelling of Polymers and its Application to Ultra-High Molecular Mass Polyethylene. *Proceedings: Mathematical and Physical Sciences* **1994,** 444, (1921), 267-85.

60. Rao, M. B.; Jenkins, R. G.; Steele, W. A., Potential functions for diffusive motion in carbon molecular sieves. *Langmuir* **1985,** 1, (1), 137-41.

61. Reid, C. R.; Thomas, K. M., Adsorption of Gases on a Carbon Molecular Sieve Used for Air Separation: Linear Adsorptives as Probes for Kinetic Selectivity. *Langmuir* **1999,** 15, (9), 3206-18.

62. Foley, N. J.; Thomas, K. M.; Forshaw, P. L.; Stanton, D.; Norman, P. R., Kinetics of Water Vapor Adsorption on Activated Carbon. *Langmuir* **1997,** 13, (7), 2083-9.

63. Harding, A. W.; Foley, N. J.; Norman, P. R.; Francis, D. C.; Thomas, K. M., Diffusion Barriers in the Kinetics of Water Vapor Adsorption/Desorption on Activated Carbons. *Langmuir* **1998,** 14, (14), 3858-64.

64. Fletcher, A. J.; Thomas, K. M., Adsorption and Desorption Kinetics of n-Octane and n-Nonane Vapors on Activated Carbon. *Langmuir* **1999,** 15, (20), 6908-14.

65. Fletcher, A. J.; Uygur, Y.; Thomas, K. M., Role of Surface Functional Groups in the Adsorption Kinetics of Water Vapor on Microporous Activated Carbons. *J. Phys. Chem. C* **2007,** 111, (23), 8349-59.

66. Fletcher, A. J.; Thomas, K. M., Kinetic Isotope Quantum Effects in the Adsorption of H_2O and D_2O on Porous Carbons. *J. Phys. Chem. C* **2007,** 111, (5), 2107-15.

67. Lee, J. W.; Shim, W. G.; Moon, H., Adsorption equilibrium and kinetics for capillary condensation of trichloroethylene on MCM-41 and MCM-48. *Microporous Mesoporous Mater.* **2004,** 73, (3), 109-19.

68. Fletcher, A. J.; Cussen, E. J.; Prior, T. J.; Rosseinsky, M. J.; Kepert, C. J.; Thomas, K. M., Adsorption Dynamics of Gases and Vapors on the Nanoporous Metal Organic Framework Material Ni2(4,4'-Bipyridine)3(NO3)4: Guest Modification of Host Sorption Behavior. *J. Am. Chem. Soc.* **2001,** 123, (41), 10001-11.

69. Fletcher, A. J.; Cussen, E. J.; Bradshaw, D.; Rosseinsky, M. J.; Thomas, K. M., Adsorption of Gases and Vapors on Nanoporous Ni_2(4,4'-Bipyridine)$_3(NO_3)_4$ Metal-Organic Framework Materials Templated with Methanol and Ethanol: Structural Effects in Adsorption Kinetics. *J. Am. Chem. Soc.* **2004,** 126, (31), 9750-9.

70. Günther Heinz, F., Mass Transport in Solids. *Angew. Chem. Int. Ed.* **1974,** 13, (6), 384-98.

71. Ruthven, D. M., *Encyclopedia of separation technology* Wiley: New York 1997; Vol. 1, p 1707.

72. Gupta, D., *Diffusion Processes in Advanced Technological Materials*. William Andrew Publishing: Noyes, 2005; p 541.

73. Glueckauf, E.; Coates, J. I., Theory of chromatography. Part IV. The influence of incomplete equilibrium on the front boundary of chromatograms and on the effectiveness of separation. *Journal of Chemical Society* **1947**, 1315 - 21.

74. Glueckauf, E., Theory of chromatography. Part 10.—Formulæ for diffusion into spheres and their application to chromatography. *Trans. Faraday Soc.* **1955,** 51, 1540 - 51.

75. Yang, R. T., *Gas Separation by Adsorption Processes* Imperial College Press: 1997; p 352.

76. Williams, G.; Watts, D. C., Non-symmetrical dielectric relaxation behaviour arising from a simple empirical decay function. *Trans. Faraday Soc.* **1970,** 66, 80 - 5.

77. Shlesinger, M. F.; Montroll, E. W., On the Williams-Watts function of dielectric relaxation. *Proc. Natl. Acad. Sci. U. S. A.* **1984,** 81, (4), 1280-3.

78. Klafter, J.; Shlesinger, M. F., On the relationship among three theories of relaxation in disordered systems. *Proc. Natl. Acad. Sci. U. S. A.* **1986,** 83, (4), 848-51.

79. Melvin, A., Kinetics of Phase Change. I General Theory. *J. Chem. Phys.* **1939,** 7, (12), 1103-12.

80. Melvin, A., Kinetics of Phase Change. II Transformation-Time Relations for Random Distribution of Nuclei. *J. Chem. Phys.* **1940,** 8, (2), 212-24.

81. Melvin, A., Granulation, Phase Change, and Microstructure Kinetics of Phase Change. III. *J. Chem. Phys.* **1941,** 9, (2), 177-84.

82. Ikuya, K.; Hiroki, Y.; Yukinori, S.; Shu, T.; Yoichiro, M., Inhomogeneous decomposition of ultrathin oxide films on Si(100): Application of Avrami kinetics to thermal desorption spectra. *J. Chem. Phys.* **2008,** 128, (16), 164712.

83. Zhao, X.; Villar-Rodil, S.; Fletcher, A. J.; Thomas, K. M., Kinetic Isotope Effect for H_2 and D_2 Quantum Molecular Sieving in Adsorption/Desorption on Porous Carbon Materials. *J. Phys. Chem. B* **2006,** 110, (20), 9947-55.

CHAPTER 3

Air separation and gas storage on porous materials

3.1 Air separation

Nitrogen, oxygen, and argon are three of the most widely used chemicals in the world. In 1990, nitrogen, oxygen, and argon production in the USA was approximately 22, 13, and 0.36 billion cubic metres respectively. In addition, the production of these gases tends to be increased continuously.[1] Figure 3.1 shows the global market share (percentage of sales) of industrial gases in 2008.[2] The major shared market is oxygen (29%), nitrogen (17%), argon (10%) with the total share of oxygen, nitrogen and argon together is 56% of the global gas market. The largest markets for oxygen are in primary metals production, chemical petroleum refineries and gasification. The production needed and the requirement of the use of medical oxygen is also causing increasing demand. Gaseous nitrogen is used in the chemical and petroleum industries and it is also used extensively by the electronics and metals industries for its inert properties. Liquid nitrogen is used in applications ranging from cryogenic grinding of plastics to food freezing. Argon, the third major component of air, finds uses as an inert material primarily in welding, steelmaking, heat treating, and in manufacturing processes for electronics.[3]

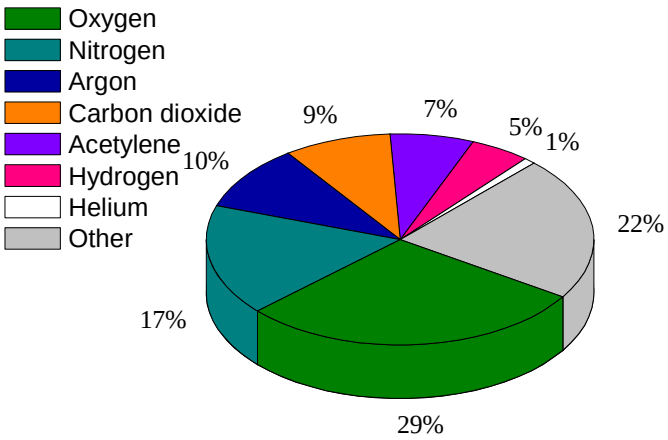

Figure 3.1 The global market shared of industrial gas in 2008

Industrial gas suppliers have an advantage over other suppliers due to the fact that air (raw material) is free. Air is mainly composed of nitrogen (78.09%), oxygen (20.95%), argon (0.93%), and other minority components such as carbon dioxide and rare gases as shown in Table 3.1. Thus, production of nitrogen, oxygen, and argon may be carried out by the separation from air. Two main separation systems were introduced; cryogenic and non-cryogenic systems. The cryogenic system is the dominant air separation system for large scale application with high purity. Non-cryogenic systems for air separation provide gas products with lower purity than cryogenic systems. Some more details of both separation systems are discussed in the following sections.[1, 4]

Table 3.1 Typical composition of dry air at sea level.[5]

Component	**Symbol**	**Volume %**
Nitrogen	N_2	78.084
Oxygen	O_2	20.946
Argon	Ar	0.9340
Carbon Dioxide	CO_2	0.03697 (variable)
Neon	Ne	0.00182
Helium	He	0.00052
Methane	CH_4	0.00016
Krypton	Kr	0.00011
Ozone	O_3	Variable
Nitrous oxide	N_2O	0.00003
Hydrogen	H_2	0.00005
Xenon	Xe	Trace

3.1.1 Air separation by cryogenic systems

Cryogenic systems are currently the most efficient and cost-effective technology for producing large quantities of either gases or liquid products from nitrogen, oxygen, and argon with high purity. On site cryogenic production plants, typically, can supply gas products greater than 400 m^3/h. However, the cryogenic air separation system is carried out at a very low temperature, thus these gas separation systems require a great deal of energy as a result of the cryogenic temperature. These energy intensive systems result in high operating costs as well as high price of the products.[6]

The basic concept of cryogenic separation is to cool air to a very low temperature to liquefy it, and then allow the liquid air to warm up and vaporise. Cryogenic separation relies on the fact that different gases in air have different boiling points, thus each gas can be separated by a distillation process. There are five major unit operations required to separate air into useful products including air compression, impurity removal, heat exchange, cryogenic separation and distillation as shown in Figure 3.2.[7]

a) air compression : pre-treated air is compressed to a high pressure in order to provide energy needed for separation then,
b) air is compressed, cooled, and cleaned by passing if through a molecular sieve to remove impurities such as;
    i) moisture and carbon dioxide which could freeze and cause blockage of piping and equipment at low temperatures, and
    ii) hydrocarbons which could combust in an oxygen rich environment.
c) the cleaned air is then cooled down by a heat exchanger while the excess heat from the cooled air can be used for re-heating the gaseous products.
d) cooled air is then further cooled down to a cryogenic temperature of around -170 ˚C to -180 ˚C, close to the temperature at which air becomes a liquid,
e) then the cooled air is passed through a series of distillation columns to separate it into useful products. The products can also be re-heated by the excess air from the heat exchanger as mentioned above.

Typically, cryogenic systems can produce an oxygen product better than 99.5 % oxygen, a nitrogen product with < 10 ppm oxygen and argon products which contains < 10 ppm impurities. Additionally, nitrogen gas containing between 10 and 0.1 ppm oxygen is classified as high purity nitrogen, while ultra high purity nitrogen only contains parts per billion levels. Requirements for the purity of gas product vary amongst types of industries. High purity of gases is only required for some specific industrial processes where impurities can affect either safety or quality of the process, for example, the presence of oxygen in nitrogen used in gas atomisation will oxidise the metal powder.[6, 8] In order to avoid high cost of gases supplied, gas products from other air separation processes such as

pressure swing adsorption where the purity requirement is not stringent may fit this requirement.

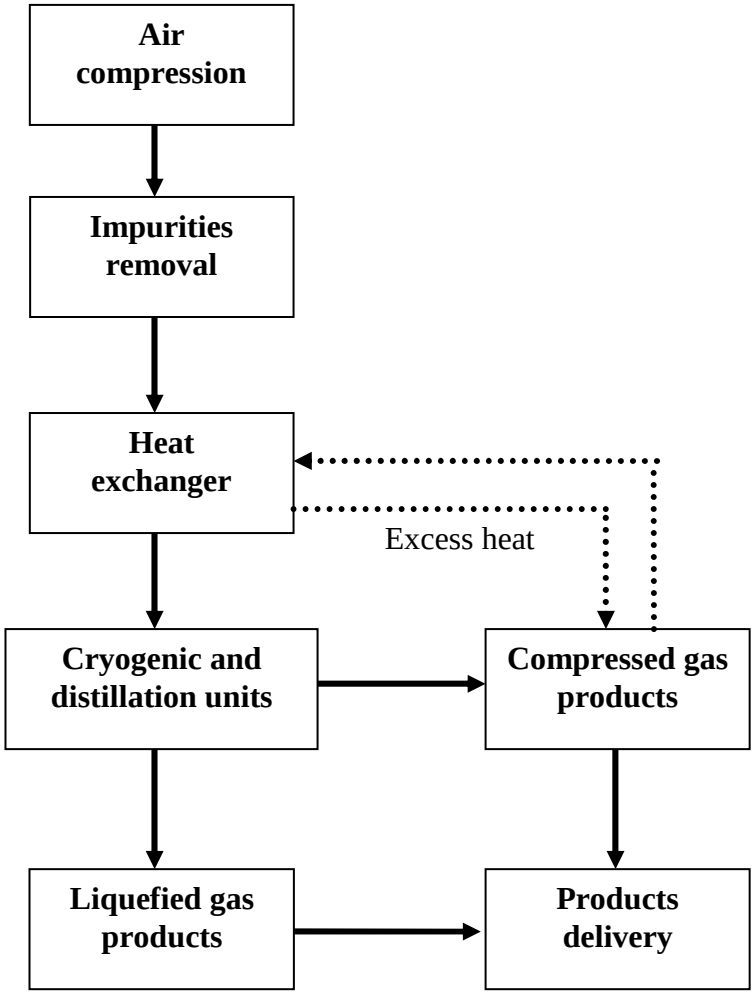

Figure 3.2 Simplified flow diagrams of the cryogenic air separation units.

3.1.2 Non- cryogenic air separations

Non-cryogenic air separation systems are typically carried out at ambient temperatures and mainly based on membrane technology and pressure swing adsorption (PSA). Compared to cryogenic systems, both membrane technology and pressure swing adsorption are the most economical processes for air separation due to the fact that these systems do not require energy to reduce temperature of the gases. However, there are some disadvantages when compared with non-cryogenic systems. Firstly, the capabilities of these non-cryogenic systems to produce gases are in low to moderate volume in the range of 25-400 m^3/h which is much lower than cryogenic systems. Secondly, the purity of the

product gases is also slightly lower. Some more details are discussed in the following sections.

3.1.2.1 Air separation by membrane technology

Air separation using membranes is a pressure-driven process where the separation is obtained as a result of differences in the rate of permeation of each gas species. Permeation rates are generally controlled by one of four transport mechanisms:[9-11]

a) Knudsen diffusion is dominant when mean membrane pore sizes of membranes are smaller than the mean free path of the gases.
b) Partial condensation of some components of a gas mixture in the pores with exclusion of others and subsequent transport of the condensed molecules across the pore. This normally occurs when using a mesoporous membrane (> 300 nm) so that the condensation can take place.
c) Selective adsorption of the more strongly adsorbed components of a gas mixture on porous materials.
d) Kinetic molecular sieving involves separation on the basis of differences in the rate of molecular sieving caused by the passing of smaller molecules with faster kinetic speed through the porous membrane while larger molecules with slower kinetic speed are obstructed.

The technology of separation of nitrogen from air by membranes has been available commercially for about 15 years, although production of oxygen by this technology is still in the research stage.[12] Commercially available membrane systems use polymeric hollow fibre membranes fabricated from polyimides, polysulfones and polycarbonates. These hollow fibre membranes generally consist of a thin layer of nanoporous material with pore diameter of < 7 nm and supported with another mesoporous material such as alumina-graphite.

Membrane separation units are capable of producing nearly 600 tonnes of nitrogen per day, with a purity range of 90-99%. However, the purity of oxygen obtained by this method is in the range of 25-50% oxygen. Additionally, the costs of membranes are high and their durability is uncertain. Major benefits of membrane systems are their simple

operation and that they normally operate at near ambient conditions.[1, 13, 14] A simplified diagram of single stage membrane process is shown in Figure 3.3. Air is compressed and passed to the series of filters for removal of impurities e.g. particulate matter, moisture, hydrocarbon and carbon dioxide. This is followed by heating the purified air up to 40-50 °C and the then feeding the heated gas to the membrane unit. The oxygen permeates faster than nitrogen passes through the membrane and the nitrogen product can be obtained from the retained gas outlet of the membrane unit.

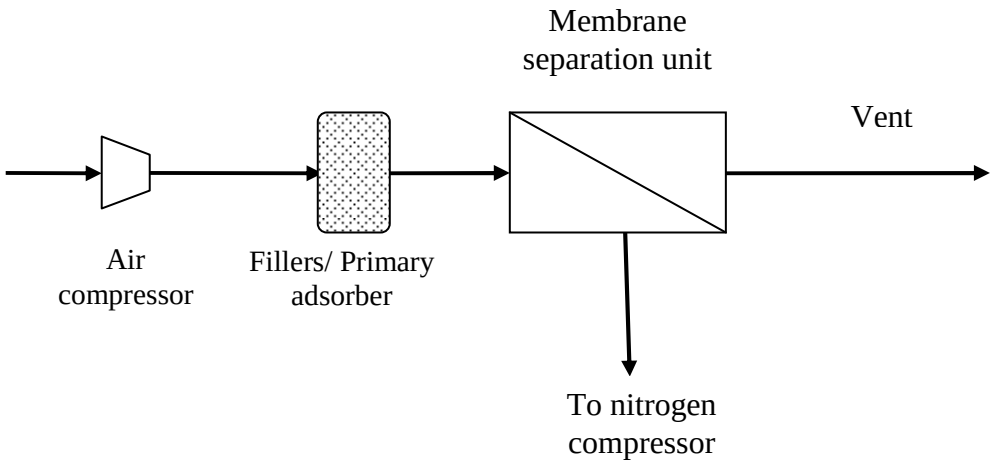

Figure 3.3 A simplified diagram of single stage membrane process.

3.1.2.2 Pressure swing adsorption (PSA)

Pressure swing adsorption (PSA) is a gas separation process, which has attracted increasing interest because of its low energy requirements and low capital investment costs in comparison to traditional separation processes. It is employed in a broad range of industrial applications including the recovery and purification of hydrogen, the separation of oxygen and nitrogen from air, the separation of normal and iso-alkanes , and a variety of drying operations.[15]

Pressure swing adsorption was invented by Skarstrom in 1960. It is also known as the adiabatic adsorption process. At about the same time, a similar process was also introduced by Guerin and Domine but this latter process is known as vacuum swing adsorption in the present state.[10, 16] A typical flow sheet of nitrogen separation from air by PSA is shown in Figure 3.4.

Essentially, nitrogen-pressure swing adsorption requires at least two adsorption beds. Firstly, pressurised air enters a vessel which normally contains a carbon molecular sieve. Then, oxygen is adsorbed more quickly than nitrogen and a nitrogen product stream is produced until the bed has been saturated with oxygen. At this point, the feed air is switched to a second adsorption bed while the first bed is regenerated by reducing the pressure to atmospheric pressure in which the adsorption capacity of oxygen in the carbon molecular sieve is reduced. Regeneration can also be accomplished by depressurisation at high temperature or depressurisation to the vacuum stage. These two regeneration processes may specifically refer to temperature swing adsorption (TSA) and vacuum swing adsorption (VSA), respectively.

Purities available of nitrogen and oxygen product are 98-99.8% and 93-95%, respectively. For many applications of oxygen and nitrogen, ultra high purity of these gases is not required and the daily requirement is not large. Some of these applications are biological treatment of waste water, basic oxygen furnaces in steel making, pulp and paper industry, and medical applications.[1, 15, 17-19] Under these circumstances, pressure swing adsorption processes are commercial because of the simple design.

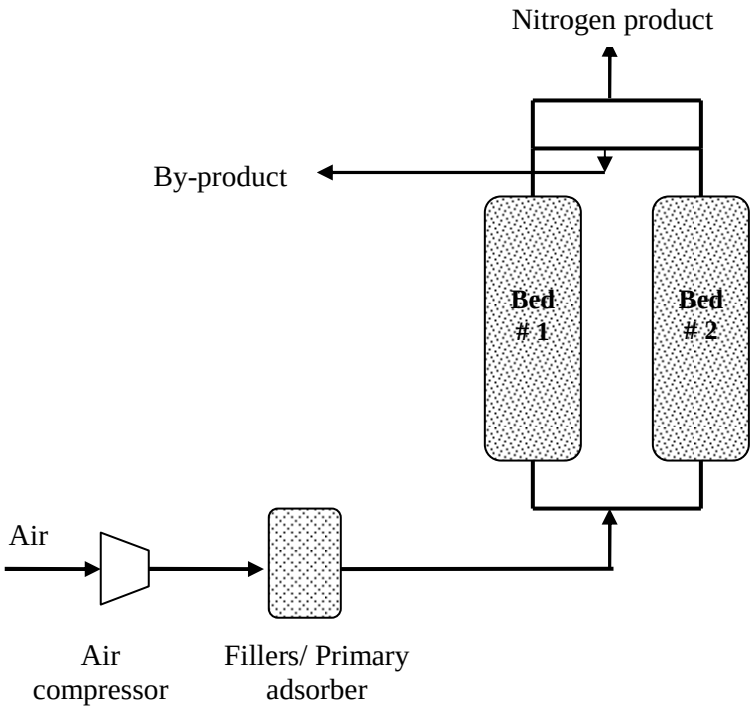

Figure 3.4 A typical flow sheet of nitrogen separation from air by PSA.

3.2 Porous materials for air separation

Typically, either carbon molecular sieves or zeolites have been used in pressure swing adsorption to separate oxygen and nitrogen from air.[20] Both porous materials are suitable for the separation of such gases because they can sustain severe conditions such as high pressure, chemical corrosion, and high temperatures. These materials can be classified in two groups which are oxygen selective adsorbents and nitrogen selective adsorbents as discussed in the following section.

3.2.1 Nitrogen selective adsorbents

3.2.1.1 Zeolites

Zeolites are ordered porous crystalline materials with cavities of molecular sizes connected by windows. Pores, channels, or cages in zeolites can also accommodate ions or large molecules such as water molecules and ammonia and even small organic molecules to be adsorbed or desorbed [21, 22]. In general, zeolites are alumino-silicates, crystalline materials with empirical chemical formula $\mathbf{M_{2/n}[O.Al_2O_3.}\boldsymbol{y}\mathbf{SiO_2]}.\boldsymbol{w}\ \mathbf{H_2O}$, where **M** denotes as an exchangeable cation of valence ***n***, ***w*** is the number of water molecules contained in the cavities of zeolites and ***y*** is the number of aluminium and silicon tetrahedral, respectively. Types of zeolite may be classified by their structure and the letter in their names (e.g., A, X, Y, Z) normally refers to the structure. The basic building units in zeolites are tetrahedral SiO_4 and AlO_4, and each SiO_4 tetrahedron is electrically neutral while each AlO_4 unit has one excess negative charge which is balanced by an exchangeable cation. Typical cations are alkali metals, alkaline earth metals, and the proton H^+. Possible sites of exchanged cations in zeolites are shown in Figure 3.5. Cations in zeolites A (left) and X, Y at sites **II** and **III** are able to adsorb molecules while site **I** is not accessible.[10, 23]

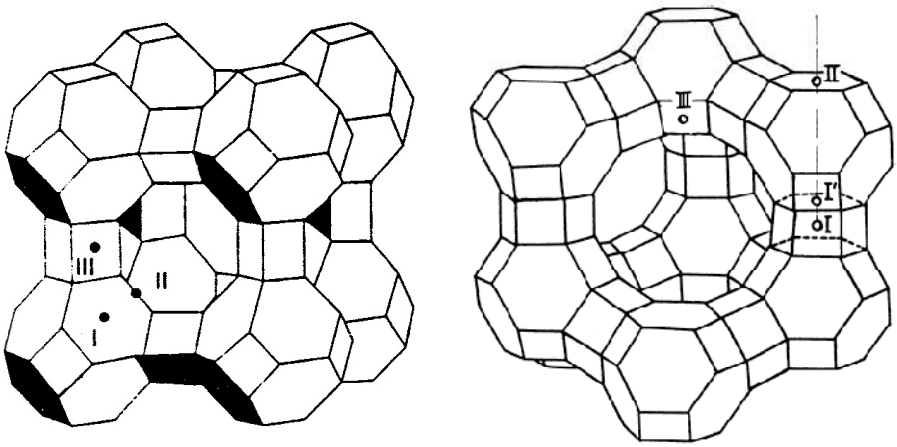

Figure 3.5 Possible sites of exchanged cations in Zeolites A (left) and X, Y types (right)

Zeolites are ionic materials and therefore have large electrostatic field gradients within their cavities. These strong electrostatic fields result in strong adsorbate-adsorbent interaction between adsorbate molecules with polar/quadrupole moments and surfaces of zeolites. This electrostatic property leads to zeolites being used as selective adsorbents for the separation of compounds.

Synthetic zeolites A, X, and Y are mainly applied in the pressure swing adsorption process to produce oxygen from air.[24, 25] These zeolites are nitrogen selective because nitrogen is more polarisable than oxygen and therefore nitrogen molecules are selectively adsorbed on zeolite surfaces while allowing the oxygen-rich stream to exit the adsorber. Generally, oxygen selectivity over nitrogen is approximately 1.5.[10, 23]

3.2.2 Oxygen selective adsorbents

3.2.2.1 Carbon molecular sieves

Carbon molecular sieves (CMS) are a unique class of material in which the selective porosity is incorporated by carbon deposition on a nanoporous substrate with pore sizes of approximately 0.5 nm. These materials are used commercially for nitrogen and oxygen separation from air by pressure swing adsorption (PSA). The adsorption isotherms of both N_2 and O_2 are approximately similar with both gases adsorbed in the CMS pores by non-specific van der Waals forces. The PSA process is based on the difference in the rates

of adsorption of oxygen and nitrogen with nitrogen being faster. Nitrogen, with a kinetic diameter of 364 pm, being slightly larger than that of oxygen (346 pm) is responsible for the kinetic selective of oxygen in the very narrow pore size in CMS.[26] The smaller O_2 kinetic diameter allows faster diffusion through the narrow pores than the bigger N_2 kinetic diameter (see Figure 3.6). Generally, kinetic selectivity of nitrogen over oxygen ranges from 5-25 due to the different pore structure of the CMSs.[27-29]

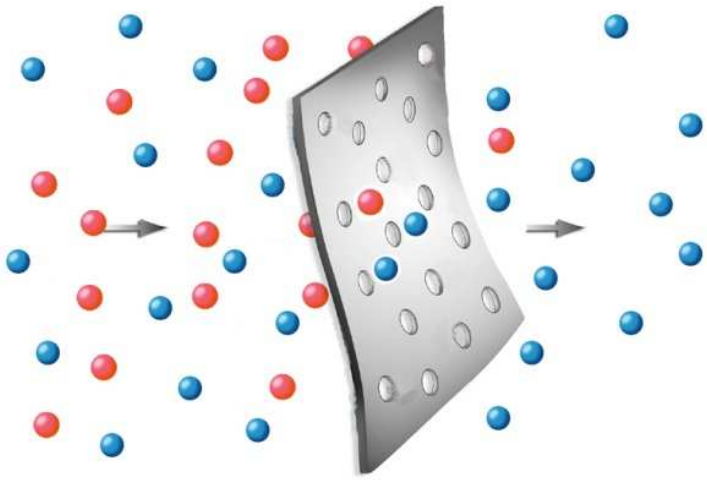

Figure 3.6 Schematic representing the molecular sieving effect in oxygen (blue) and nitrogen (red) separation

3.2.2.2 Metal organic frame works

Recent work on microporous metal organic frameworks has drawn very interesting adsorption properties and has exhibited their possible use in a broad range of applications. However, research on gas separation using metal organic framework is quite rare. Some of these research papers are summarised here.

Quin *et al*[30] conducted adsorption studies of various pure gases on the metal organic framework HKUST-1 or Cu-BTC. As shown in Figure 3.7(a), the HKUST-1 sample is composed of dimeric cupric tetracarboxylate building blocks, $[Cu_3(BTC)_2(H_2O)_x]_n$, and these building blocks are covalent together to form a three dimensional porous structure. The window size of its pores is approximately 0.9 x 0.9 nm with a surface area of 692.2 m^2g^{-1} and single-point total pore volume of 0.333 cm^3g^{-1}.[30] The pure component adsorption isotherms were performed at 295 K using a gravimetric system. Figure 3.7(b) shows the isotherms of CO_2 and N_2O adsorption on HKUST-1 and

both CO_2 and N_2O had strong preferential adsorption over N_2 and O_2. This is also the case for adsorption of these gases on microporous carbons. [27-29] In addition, they gave a further suggestion that HKUST-1 can be used in air-prepurification units for the purpose of removing impurities. However, this paper does not give their comment on the possibility of either oxygen or nitrogen separation from air.

Li and Yang[31] observed gas adsorption and storage in metal organic framework MOF-177. This MOF-177 were synthesised via a hydrothermal route by using a carboxylate derivative, 1,3,5-benzenetribenzoate (BTB), as an organic linker and zinc nitrate as the metal centre. The crystal data showed that the basic structure of this MOF is composed of zinc (II) carboxylate clusters, $Zn_4O(CO_2)_6$, forming a three dimensional structure which can accommodate spheres of diameters of 1.18 and 1.08 nm as shown in Figure 3.8(a). Additionally, a D-R pore volume is 1.59 cm^3g^{-1} and Langmuir surface area is 4,500 m^2g^{-1}. The adsorption isotherms of N_2 and O_2 were performed at 298 K on the MOF-177 as shown in Figure 3.8(b). At pressure above 300 mmHg, it can be noted that O_2 was adsorbed more favourably than N_2 and it showed O_2 selectivity approximately 1.8 over N_2. They further suggested that the O_2/N_2 selectivity could be caused by the higher magnetic susceptibility of O_2 compared with that of N_2, which indicates a lack of electric charges on the surfaces of MOF-177. Furthermore, higher O_2/N_2 selectivity could be obtained at higher pressure.

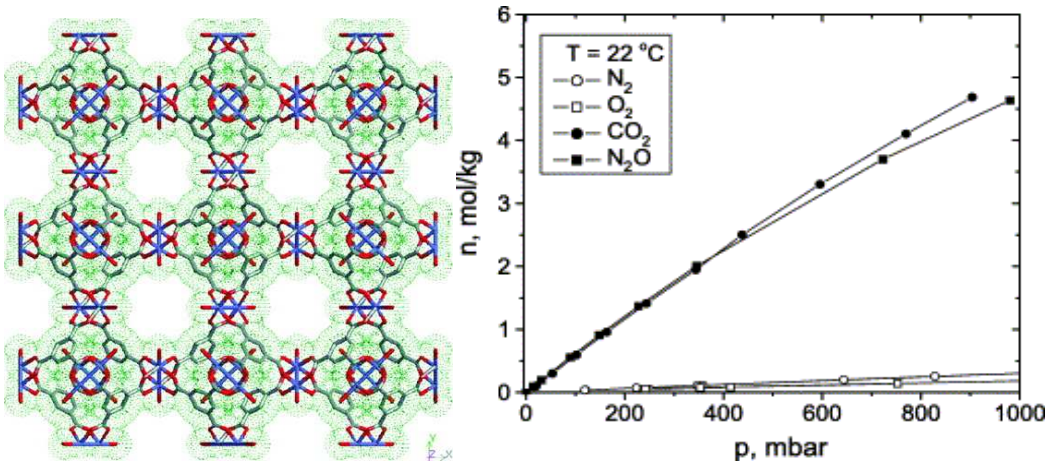

(a) (b)

Figure 3.7 (a) crystal structure of HKUST-1 [32]

(b) adsorption isotherms of N_2, O_2, CO_2 and N_2O on HKU[2]ST-1 at 295 K.[30]

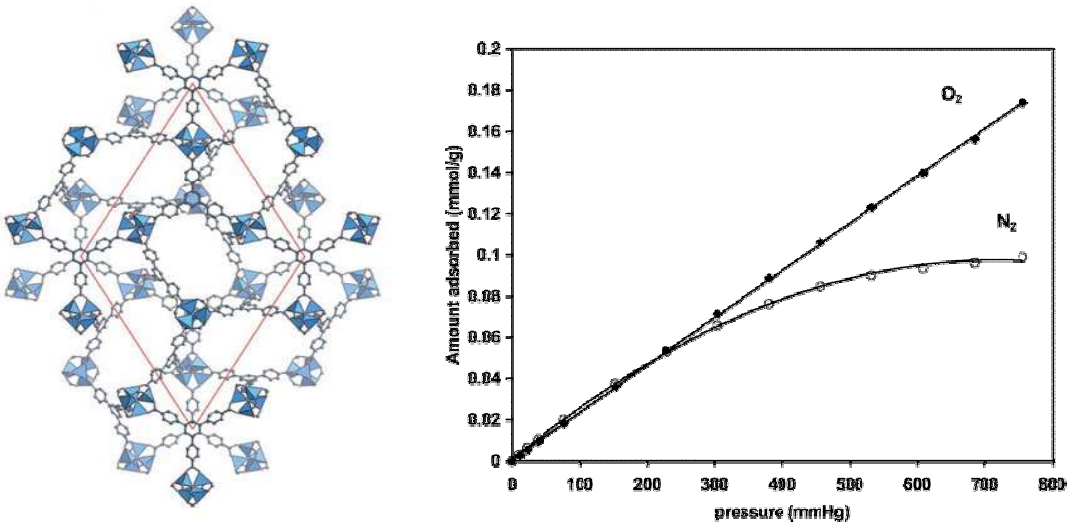

(a) (b)

Figure 3.8 (a) crystal structure of MOF-177 and (b) N_2, O_2 adsorption isotherms on MOF-177 at 298 K and pressures up to 1 atm.[31]

3.3 Recent hydrogen storage methods and problems

A main obstacle for using hydrogen as a non polluting fuel for vehicles is the lack of a safe, efficient system for on-board storage. One possible method to overcome this obstacle is a system based on hydrogen adsorption on porous materials such as carbon based materials, metal organic frameworks, and complex hydride materials. Some aspects of these porous materials are discussed below. Environmentally friendly hydrogen has the potential to be used as a future alternative fuel in vehicles. Hydrogen needs to be stored in a safe on-board system. The operating requirements for effective hydrogen storage for transportation include the following:[33]

- Appropriate thermodynamics, which is favourable enthalpies of hydrogen absorption and desorption,
- Fast kinetics (quick uptake and release),
- High storage capacity (specific capacity to be determined by vehicle range and fuel cell efficiency),
- Effective heat transfer,

• High gravimetric and volumetric densities (light weight and occupying as small a space as possible),
• Long cycle lifetime for hydrogen absorption/desorption,
• High mechanical strength and durability, and
• Safety under normal use and acceptable risk under abnormal conditions.

At present, high pressure storage methods are widely used for storing gases. This is the simplest method to store hydrogen up to ~690 bar in the storage tank, but the energy content is relatively low: approximately 4.4 MJ/L for hydrogen compared with 31.6 MJ/L for gasoline. There is also the issue of safety for on-board vehicle storage. In terms of liquefaction, hydrogen in cryogenic tanks has a much higher energy content than in the gas phase. The energy content of hydrogen in cryogenic systems can reach 8.4 MJ/L or approximately twice that of the compression methods. However, the energy density of liquid hydrogen is still lower than gasoline. Furthermore, a large quantity of energy is required for liquefaction, which is about one third of the energy for storing hydrogen. Also, the insulation system may not be able to maintain the liquid hydrogen at a cryogenic temperature (-252 ºC) due to unavoidable evaporation loss. [34-36]

3.3.1 Physisorption on porous materials

Porous materials can potentially adsorb hydrogen on their porous surface via weak intermolecular interactions (e.g. van der Waals force or physisorption). At a given temperature, the amount of hydrogen adsorbed is a function of pressure and is released when pressure decreases so this process is reversible. Thus, this adsorbed hydrogen can be released more easily than chemical hydrides. However, due to weak interactions, physical adsorption is normally conducted at a low temperature (77 K).[37-40] Moreover, conducting hydrogen adsorption experiments at high pressure and ambient temperature leads to greater error. This is because the buoyancy corrections for gravimetric systems need to be done much more carefully. Furthermore, at high pressures, experiment impurities in hydrogen gas may possibly adsorb on the surfaces and lead to error.[40] Carbon based porous materials, such as activated carbon and nanotubes, are some of the more promising materials for storing hydrogen. This is because of their low density, high surface area and good thermal stability.

For activated carbon, numerous studies have been done both at 77 K and at room temperature (see table 3.2). These results revealed that hydrogen adsorption capacity depends on the total pore volume of activated carbon at 77 K and the pressure up to 20 bar are in range the of 0.6-6.9 weight %. Hydrogen adsorption capacity at room temperature and pressure up to 90 bar is just in the range of 0.2-1.2 weight %. This is because the physical adsorption of hydrogen based on weak van der Waals forces and these forces are very weak at room temperature.[36-38, 41] Zhao *et al.*[40], Jin *et al.*[42] and Nijkamp *et al.*[43] studied the hydrogen adsorption on activated carbon with various nanopore volumes. These reports have shown that high hydrogen adsorption capacities were observed on activated carbon with a high nanopore volume which indicates that hydrogen fills the micropore volume (see Figure 3.9). Smaller pore size plays an important role in hydrogen storage than the larger pores due to the fact that pore walls are in close proximity which results in overlap of potential energy fields. Consequently, the adsorption potential is higher than that found in larger pores.[44, 45]

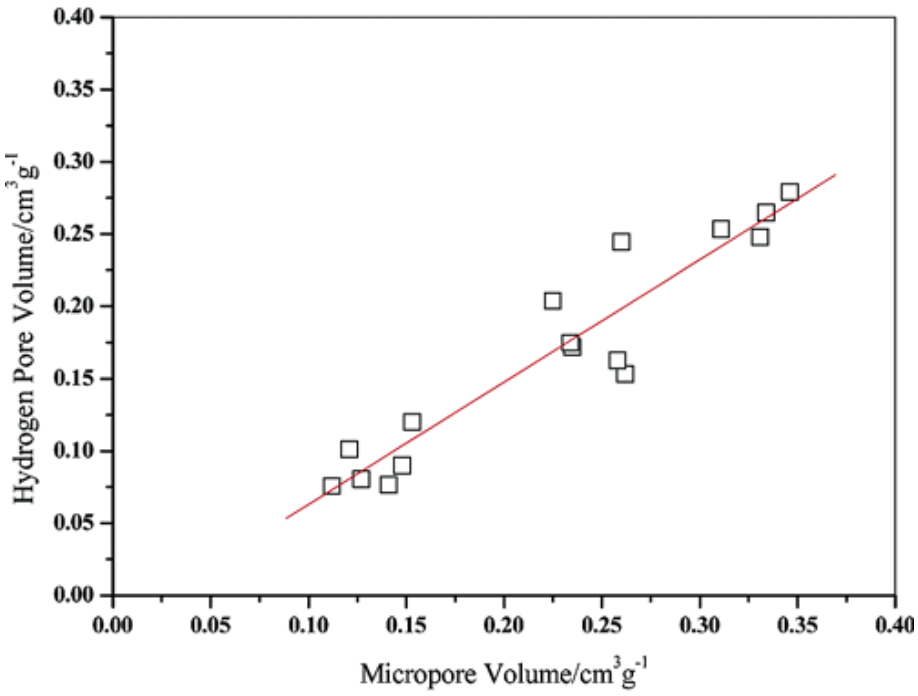

Figure 3.9 The variation of H_2 adsorption capacity at 77 K with micropore volume for carbon adsorbents.[40]

Table 3.2 Characterisations of hydrogen uptake in various MOFs (adapted from Thomas[41])

MOFs and porous carbons	Surface Area ($m^2 g^{-1}$)	Amount Adsorbed at 77K (wt%)	Amount Adsorbed at ambient temperature (wt%)
Porous Carbons			
- **NORIT**[46]	1300	-	0.75 (120 bar, 296 K)
- **AC-15**[42]	-	-	0.85 (100 bar, 298 K)
- **PAN carbon series**[40]	-	0.58-1.95 (1 bar)	-
- **PAN carbon series**[40]	-	1.18-2.15 (1 bar)	-
- **Various porous carbons**[47]	1815–2711	2.6–4.2 (50 bar)	0.25 (50 bar)
MOFs			
- **$Ni_2(bpy)_3(NO_3)_4$ (M)**[48]	-	0.8 (1 bar)	-
- **$Ni_2(bpy)_3(NO_3)_4$ (E)**[48]	-	0.7 (1 bar)	-
- **$Mg_3(NDC)_3$**[49]	190	0.6 (1 bar)	-
- **$Ni_3(btc)_2(3\text{-}pic)_6(pd)_3$**	-	2.1 (14 bar)	-
- **$Cu_3(btc)_2$,(HKUST-1)**[50]	1154	3.6 (30 bar)	0.35 (65 bar)
- **$Zn_4O(bdc)_3$,(MOF-5, IRMOF-1)**[51]	4171	5.2 (48 bar)	-
	3080	4.3 (30 bar)	0.45 (60 bar)
- **$Zn_4O(cbbdc)_3$,(IRMOF-6)**[51]	3305	4.8 (50 bar)	-
- **$Zn_4O(ndc)_3$,(IRMOF-8)**[51]	1818	3.6 (10–15 bar)	0.4 (30 bar)
- **Zn4O(btb), (MOF-177)**	5640[51]	7.5 (70 bar)	-
	3100[31]	-	0.62 (100 bar, 298 K)
- **$Cr_3OF(btc)_2$, (MIL-100(Cr))**[52]	2700	3.28 (26.5 bar)	0.15 (73.3 bar)
- **$Cr_3OF(bdc)_3$, (MIL-101b(Cr))**[52]	5500	6.1 (60 bar)	0.43 (80 bar)
$Zn_3(bdc)_3Cu(pyen)$, (M'MOF1)[53]	-	1.25 (10 bar)	-

Where
bdc = benzene-l,4-dicarboxylate, R6-bdc = 1 ,2-dihydrocyclobutylbenzene-3,6-dicarboxylate, bpy=4,4'-bipyridine, btcc= benzene-l ,3,5-tricarboxylate, ndc = naphthalene-2,6-dicarboxylate, btb = benzene-l ,3,5-tribenzoate.

3.3.2 Hydrogen adsorption in Metal organic frameworks

Physisorption of hydrogen on porous metal organic frameworks is one of the more promising methods for hydrogen storage. Metal organic frameworks with various window and pore sizes can be tailor made by changing their metal nodes and organic spacers. However, not all metal organic frameworks exhibit porosity.[54] The method herein is focused on porous metal organic frameworks (MOFs) which can adsorb hydrogen on their porous surface. Hydrogen adsorption experiments can be undertaken by either volumetric or gravimetric methods. Ultra pure dry hydrogen is required for use in these experiments. In addition, the H_2 adsorption is normally conducted at a low temperature (77 K) with various pressures ranging from 1 to 20 bar. However, some H_2 adsorption experiments have been conducted at room temperature. Table 3.2 shows that the high adsorption capacity of H_2 can be found only at 77 K. This is because of the limited interaction between MOFs and poorly polarisable hydrogen molecules, which lead to strong temperature dependence on hydrogen physisorption bonding via a weak van der Waals force.[60, 61] Schmitz *et. al.*[55] and McKeown *et. al.*[56] reported that MOFs and polymers of intrinsic microporosity (PIMs) with ultramicropores, respectively, beneficially increased the interaction between hydrogen molecules and pore wall at low pressure. However, the relationship between maximum hydrogen uptake at high pressure with the BET specific surface area of the porous materials is approximately linear.[40] Latroche *et. al.*[52] reported that metal organic frameworks with large specific surface area MIL-100 (with cage diameters of 25 and 29 Å) and MIL-101 (with cage diameters of 29 and 34 Å) provide a high hydrogen adsorption capacity at high pressure.[52] MOF-177 with two cage diameters of 10.8 and 11.8 Å shows the highest hydrogen adsorption of 7.5 weight % at 77 K and at 70 bar.[51] However, hydrogen adsorption on MOF-177 at an ambient temperature and at 100 bar decreased significantly to 0.62 weight %.[31] This is because the enthalpies of hydrogen adsorption on MOFs are quite low (4-12 kJ mol^{-1}).[41, 57] A theoretical study showed that an adsorption enthalpy of 15.1 kJ mol^{-1} is required for hydrogen adsorption at ambient temperature.[58] Thus, weak interactions between hydrogen and MOFs are a limit for hydrogen storage. Chen *et. al.*[53] showed that interaction between hydrogen and open metal centre of mixed metal organic frame work (M'MOF 1) so far gave the highest enthalpy of adsorption with the value of 12.3 kJ mol^{-1}. Schmitz *et. al.* further suggested that it will be necessary to synthesis the MOFs with large surface areas whilst maintaining an ultra microporous structure.[59]

3.4 References

1. Thorogood, R. M., Developments in air separation. *Gas Sep. Purif.* **1991,** 5, (2), 83-94.
2. Air separation technology. *Chemical & Engineering News* 2009, p 10.
3. Air-Products Gases and equipment online fact book. http://www.airproducts.com/Products/fastfacts/factbook.htm. (26 October 2009),
4. Castle, W. F., Air separation and liquefaction: recent developments and prospects for the beginning of the new millennium. *International Journal of Refrigeration* **2002,** 25, (1), 158-72.
5. Brimblecombe, P., *Air Composition & Chemistry*. Cambridge University Press: Cambridge 1996; p 253.
6. Rakesh, A., Separations: Perspective of a process developer/designer. *AIChE Journal* **2001,** 47, (5), 967-71.
7. Nakaiwa, M.; Akiya, T.; Owa, M.; Tanaka, Y., Evaluation of an energy supply system with air separation. *Energy Conversion and Management* **1996,** 37, (3), 295-301.
8. Agrawal, R.; Thorogood, R. M., Production of medium pressure nitrogen by cryogenic air separation. *Gas Sep. Purif.* **1991,** 5, (4), 203-9.
9. Koros, W. J.; Fleming, G. K., Membrane-based gas separation. *Journal of Membrane Science* **1993,** 83, (1), 1-80.
10. Rao, M. B.; Sircar, S., Nanoporous carbon membrane for gas separation. *Gas Sep. Purif.* **1993,** 7, (4), 279-84.
11. Yang, R. T., *Adsorbents: Fundamentals and Applications*. Wiley-Interscience 2003; p 424.
12. Smith, A. R.; Klosek, J., A review of air separation technologies and their integration with energy conversion processes. *Fuel Processing Technology* **2001,** 70, (2), 115-34.
13. Feng, X.; Y.Chuen; Ivory, P. J., Pressure swing permeation: Novel process for gas separation by membranes. *AIChE Journal* **2000,** 46, (4), 724-33.
14. Ismail, A. F.; David, L. I. B., A review on the latest development of carbon membranes for gas separation. *Journal of Membrane Science* **2001,** 193, (1), 1-18.
15. Haselden, G. G., Gas separation fundamentals. *Gas Sep. Purif.* **1989,** 3, (4), 209-15.

16. Ruthven, D. M.; Farooq, S., Air separation by pressure swing adsorption. *Gas Sep. Purif.* **1990,** 4, (3), 141-8.

17. Hassan, M. M.; Ruthven, D. M.; Raghavan, N. S., Air separation by pressure swing adsorption on a carbon molecular sieve. *Chemical Engineering Science* **1986,** 41, (5), 1333-43.

18. Wiessner, F. G., Basics and industrial applications of pressure swing adsorption (PSA), the modern way to separate gas. *Gas Sep. Purif.* **1988,** 2, (3), 115-9.

19. Kawai, M.; Kaneko, T., Present state of PSA air separation in Japan. *Gas Sep. Purif.* **1989,** 3, (1), 2-6.

20. Gaffney, T. R., Porous solids for air separation. *Current Opinion in Solid State and Materials Science* **1996,** 1, (1), 69-75.

21. Bekkum, H. v.; Flanigen, E. M.; Jansen, J. C., *Introduction to Zeolite Science and Practice*. Elsevier: 1991; p 1062.

22. Szostak, R., *Molecular Sieves: Principles of Synthesis and Identification.* . 2 ed.; Springer: London, 1998; p 359.

23. Yoshida, S.; Ogawa, N.; Kamioka, K.; Hirano, S.; Mori, T., Study of Zeolite Molecular Sieves for Production of Oxygen by Using Pressure Swing Adsorption. *Adsorption* **1999,** 5, (1), 57-61.

24. Jayaraman, A.; Yang, R. T.; Cho, S.-H.; Bhat, T. S. G.; Choudary, V. N., Adsorption of Nitrogen, Oxygen and Argon on Na-CeX Zeolites. *Adsorption* **2002,** 8, (4), 271-8.

25. Ackley, M. W.; Rege, S. U.; Saxena, H., Application of natural zeolites in the purification and separation of gases. *Microporous and Mesoporous Materials* **2003,** 61, (1-3), 25-42.

26. Hu, Z.; Vansant, E. F., Carbon molecular sieves produced from walnut shell. *Carbon* **1995,** 33, (5), 561-7.

27. Chagger, H. K.; Ndaji, F. E.; Sykes, M. L.; Thomas, K. M., Kinetics of adsorption and diffusional characteristics of carbon molecular sieves. *Carbon* **1995,** 33, (10), 1405-11.

28. Reid, C. R.; Thomas, K. M., Adsorption of Gases on a Carbon Molecular Sieve Used for Air Separation: Linear Adsorptives as Probes for Kinetic Selectivity. *Langmuir* **1999,** 15, (9), 3206-18.

29. Boniface, H. A.; Ruthven, D. M., Selectivity of some zeolites for adsorption of atmospheric gases. *Gas Sep. Purif.* **1993,** 7, (3), 183-4.

30. Qing, M. W.; Dongmin, S.; Martin, B.; Miu, L. L.; Shuguang, D.; Frank R, F.; Norberto O., L.; Jessica, S., Metallo-organic molecular sieve for gas separation and purification. *Microporous and Mesoporous Materials* **2002,** 55, (2), 217-30.

31. Li, Y.; Yang, R. T., Gas Adsorption and Storage in Metal-Organic Framework MOF-177. *Langmuir* **2007,** 23, (26), 12937-44.

32. Chui, S. S. Y.; Lo, S. M. F.; Charmant, J. P.; nbsp; H; Orpen, A. G.; Williams, I. D., A Chemically Functionalizable Nanoporous Material $[Cu_3(TMA)_2(H_2O)_3]n$. *Science* **1999,** 283, (5405), 1148-50.

33. In *Basic research needs for hydrogen energy*, Report on the Basic Energy Sciences Workshop on Hydrogen Production, Storage, and Use, Rockville, Maryland USA, 2004; US Department of Energy Rockville, Maryland USA, 2004.

34. Schlapbach, L.; Zuettel, A., Hydrogen-storage materials for mobile applications. *Nature* **2001,** 414, 353.

35. Ritter, J. A.; Ebner, A. D.; Wang, J.; Zidan, R., Implementing a hydrogen economy. *Materials Today* **2003,** 6, (9), 18.

36. Zhou, L., Progress and problems in hydrogen storage methods. *Renewable and Sustainable Energy Reviews* **2005,** 9, 359-408.

37. David, E., An overview of advanced materials for hydrogen storage. *Journal of Materials Processing Technology* **2005,** 162-163, (15), 169-77.

38. Züttel, A.; Wenger, P.; Sudan, P.; Mauron, P.; Orimo, S., Hydrogen density in nanostructured carbon, metals and complex materials *Materials Science and Engineering B* **2004,** 108, (1-2), 9-18

39. Gadiou, R.; Saadallah, S.-E.; Piquero, T.; David, P.; Parmentier, J.; Vix-Guterl, C., The influence of textural properties on the adsorption of hydrogen on ordered nanostructured carbons *Microporous and Mesoporous Materials* **2005,** 79, (1-3), 121-8

40. Zhao, X. B.; Xiao, B.; Fletcher, A. J.; Thomas, K. M., Hydrogen Adsorption on Functionalized Nanoporous Activated Carbons *J. Phys. Chem. B* **2005,** 109, (18), 8880 -8.

41. Thomas, K. M., Adsorption and desorption of hydrogen on metal-organic framework materials for storage applications: comparison with other nanoporous materials. *Dalton Transactions* **2009**, (9), 1487-505.

42. Jin, H.; Lee, Y. S.; Hong, I., Hydrogen adsorption characteristics of activated carbon. *Catalysis Today* **2007,** 120, (3-4), 399-406.

43. Nijkamp, M. G.; Jong, K. P. d., Hydrogen storage using physisorption- materials demands. *Applied physics A* **2005,** 72, 619-23.

44. Rouquerol, F.; Rouquerol, J.; Sing, K. S. W., *Adsorption by Powders, Porous Solids*. Academic Press: London, 1999; p 467.

45. Gregg, J. S.; Sing, K. S. W., *Adsorption, Surface Area and Porosity;*. 2nd ed.; Academic Press: London, 1982; p 303.

46. Ströbel, R.; Jörissen, L.; Schliermann, T.; Trapp, V.; Schütz, W.; Bohmhammel, K.; Wolf, G.; Garche, J., Hydrogen adsorption on carbon materials. *Journal of Power Sources* **1999,** 84, (2), 221-4.

47. Panella, B.; Hirscher, M.; Roth, S., Hydrogen adsorption in different carbon nanostructures. *Carbon* **2005,** 43, (10), 2209-14.

48. Zhao, X. B.; Xiao, B.; Fletcher, A. J.; Thomas, K. M.; Bradshaw, D.; Rosseinsky, M. J., Hysteretic Adsorption and Desorption of Hydrogen by Nanoporous Metal-Organic Frameworks. *Science* **2004,** 306, 1012-5.

49. Dinca, M.; Long, J. R., Strong H_2 Binding and Selective Gas Adsorption within the Microporous Coordination Solid $Mg_3(O_2C\text{-}C_{10}H_6\text{-}CO_2)_3$. *J. Am. Chem. Soc.* **2005,** 127, (26), 9376 - 7.

50. Chui, S. S.-Y.; Lo, S. M. F.; Charmant, J. P. H.; Orpen, A. G.; Williams, I. D., A Chemically Functionalizable Nanoporous Material $[Cu_3(TMA)_2(H_2O)_3]_n$ *Science* **1999,** 19, 1148-50.

51. Wong-Foy, A. G.; Matzger, A. J.; Yaghi, O. M., Exceptional H_2 Saturation Uptake in Microporous Metal Organic Frameworks. *J. Am. Chem. Soc.* **2006,** 128, (11), 3494-5.

52. Latroche, M.; Surblé, S.; Serre, C.; Mellot-Draznieks, C.; L. Llewellyn, P.; Lee, J.-H.; Chang, J.-S.; Jhung, S. H.; Férey, G., Hydrogen Storage in the Giant-Pore Metal-Organic Frameworks MIL-100 and MIL-101. *Angew. Chem. Int. Ed.* **2006,** 45, (48), 8227-31.

53. Chen, B.; Zhao, X.; Putkham, A.; Hong, K.; Lobkovsky, E. B.; Hurtado, E. J.; Fletcher, A. J.; Thomas, K. M., Surface Interactions and Quantum Kinetic Molecular Sieving for H_2 and D_2 Adsorption on a Mixed Metal Organic Framework Material. *J. Am. Chem. Soc.* **2008,** 130, (20), 6411-23.

54. Kitagawa, S.; Kitaura, R.; Noro, S., Functional Porous Coordination Polymers. *Angew. Chem. Int. Ed.* **2004,** 43, (18), 2334-75.

55. Schmitz, B.; Müller, U.; Trukhan, N.; Schubert, M.; Férey, G.; Michael, H., Heat of Adsorption for Hydrogen in Microporous High-Surface-Area Materials. *ChemPhysChem* **2008,** 9, (15), 2181-4.

56. McKeown, N. B.; Gahnem, B.; Msayib, K. J.; Budd, P. M.; Tattershall, C. E.; Mahmood, K.; Tan, S.; Book, D.; Langmi, H. W.; Walton, A., Towards Polymer-Based Hydrogen Storage Materials: Engineering Ultramicroporous Cavities within Polymers of Intrinsic Microporosity *Angew. Chem. Int. Ed.* **2006,** 45, (11), 1804-7.

57. Morris, Russell E.; Wheatley, P. S., Gas Storage in Nanoporous Materials. *Angew. Chem. Int. Ed.* **2008,** 47, (27), 4966-81.

58. Bhatia, S. K.; Myers, A. L., Optimum Conditions for Adsorptive Storage. *Langmuir* **2006,** 22, (4), 1688-700.

59. Ash, R.; Baker, R. W.; Barrer, R. M., Sorption and Surface Flow in Graphitized Carbon Membranes. I. The Steady State. *Proceedings of the Royal Society of London. Series A, Mathematical and Physical Sciences (1934-1990)* **1967,** 299, (1459), 434-54.

CHAPTER 4

Objectives

4.1 Introduction

Porous materials, such as activated carbons and zeolites, are widely used for gas storage, purification and separation, as catalysts and catalyst supports, and for adsorption of environmentally unfriendly species. Recently, porous framework materials or metal organic frameworks (MOF) have attracted attention due to the wide range of structural topologies and surface chemistries that can be designed. Structures of the metal organic frameworks may be flexible and distort during the adsorption/desorption process, and possible effects include molecular sieving by exclusion of molecules on the basis of size, kinetic molecular sieving and quantum kinetic molecular sieving. Some MOFs also exhibit fluorescence, luminescence and magnetic properties. The basic characteristic requirements of MOFs for specific applications includes i) well defined cavities and frameworks ii) thermal stability suitable for removal of template molecules without losing framework integrity iii) small window dimensions may be required for gas/vapour separation purposes iv) appropriate surface chemistry. As mentioned in section 1.3, MOFs prepared from rod-like organic ligands typically exhibited strong framework rigidity. Short rod-like organic ligands include furmaric acid and pyridine-4-carboxylic acid were used to synthesize MOFs in this research.

4.2 Overall objective

The overall objective of the research was the synthesis, characterisation and determination of the adsorption/desorption characteristics of functionalised porous metal organic frame work materials in order to increase understanding of the effect of surface functional groups and framework flexibility on adsorption characteristics of gases and vapours and to assess the possible applications of these materials for gas storage and separation.

4.3 Specific objectives

4.3.1 Synthesis and characterise the functionalised porous metal organic frameworks

i. To prepare nano-porous metal organic framework materials.
ii. To determine the molecular structure, chemical compositions and physical characteristic of the metal organic frameworks.
iii. To classify the adsorption/desorption isotherms of selected gases/vapours on metal organic framework according to the IUPAC classification scheme.
iv. To determine surface area, micropore and total pore volumes of the adsorbents for a range of adsorptives.

4.3.2 Effect of the oxygen surface functional groups of NEW-1 on adsorption characteristics

i. To determine the characteristic of adsorption/desorption isotherm of selected vapours on metal organic framework NEW-1 over a ranges of temperatures.
ii. To determine isosteric enthalpies for the vapours adsorption on metal organic framework as a function of surface coverage.
iii. To determine the kinetics of adsorption for selected vapours on metal organic framework NEW-1.
iv. To model the adsorption kinetics of the vapours adsorption for selected vapours on metal organic framework using appropriate models.
v. To evaluate the activation energies for adsorption of a range of gases/vapours on metal organic framework NEW-1.
vi. To compare and contrast the isotherm, thermodynamic, kinetics and activation energy of the adsorption of vapours in order to formulate general principles and correlations for understanding the effect of oxygen surface functional groups on adsorption characteristic of gases and vapours on NEW-1.
vii. To increase the scientific understanding of the role of surface chemistry and framework flexibility on adsorption characteristics.

4.3.3 Gas storage and separation

i. To determine the adsorption capacity of the hydrogen on the metal organic framework at 77 K and 1000 mbar.
ii. To determine the isotherms of oxygen, nitrogen and argon adsorption on metal organic framework (NEW-1 and M'MOF-1) and a carbon molecular sieve (CMS-40).
iii. To evaluate and compare the isosteric enthalpies of adsorption for oxygen, nitrogen and argon adsorption on metal organic framework (NEW-1 and M'MOF-1) and carbon molecular sieve (CMS-40).
iv. To evaluate and compare the kinetics of oxygen, nitrogen and argon adsorption on metal organic framework (NEW-1 and M'MOF-1) and carbon molecular sieve (CMS-40).

CHAPTER 5

Experimental

5.1 Materials used

5.1.1 Gases and volatile organic compounds

The gases used were supplied by BOC Ltd, London, U.K. and had the following purities: nitrogen (99.999%), oxygen (99.999%), argon (99.999%), carbon dioxide (99.999%), hydrogen (ultra pure grade 99.9999%), methane (99.95%), ethane (99%), propane (99.5%), *n*-butane (99.5%) and chloromethane (99.9%). The volatile organic compounds used in adsorption/desorption studies include; benzene (anhydrous, 99.8%), toluene (anhydrous, 99.8%), methanol (anhydrous, 99.8%), ethanol (anhydrous, 99.8%), *n*-propanol (anhydrous, ≥99.7%), *n*-butanol (anhydrous, ≥99.8%), chloroform (≥99.0%), dichloromethane (≥99.6%), *n*-pentane (≥99.0%), *n*-hexane (≥99.0%), *n*-heptane (≥99.0%), *n*-octane (≥99.0%), and *n*-nonane (≥99.0%) were supplied by Aldrich Chemical Co., Gillingham-Dorset, U.K.

5.1.2 Adsorbents used

5.1.2.1 Carbon molecular sieve-40 (CMS-40)

Carbon molecular sieve 40 (CMS-40) is a commercial sample supplied by Air Products and Chemical, Inc., Allentown, PA, U.S. CMS-40 was prepared from a microporous substrate on which carbon was deposited to produce a material that was kinetically selective for oxygen and nitrogen. The particle size fraction of this carbon was 1-2 mm.

5.1.2.2 Mixed metal organic framework (M'MOF-1)

Mixed metal organic framework ($Zn_3(BDC)_3[Cu(Pyen)]\cdot(DMF)_5(H_2O)_5$) was supplied by Prof. Banglin Chen, University of Texas-Pan American, Edinburgh, Texas, USA. The synthetic method was as follows. A mixture of $Zn(NO_3)_2\cdot 6H_2O$ (1.2116 g, 4.07 mmol), 1,4 benzenedicarboxylic acid:H_2BDC (0.6732 g, 4.06 mmol) 5-methyl-4-oxo-1,4-dihydro-pyridine-3-carbaldehyde: $Cu(PyenH_2)(NO_3)_2$ (0.600 g, 1.24 mmol) and was

dissolved in the mixture of DMF (306 mL) and H_2O (30.6 mL), and heated in a vial (400 mL) at 373 K for 24 hrs.

5.1.2.3 Metal organic frameworks NEW-1 and NEW-2

In this study, two new metal organic frameworks were synthesised. These two metal organic frameworks were named as NEW-1 and NEW-2. The prefix NEW is a term dedicated to Newcastle University. Their synthesis routes are described as the following section.

Commercial availability of the starting chemicals from Sigma-Aldrich were used without further purification to synthesise both metal organic frameworks NEW-1 and NEW-2.These starting chemicals include; fumaric acid ($C_4H_4O_4$, ≥ 99.5%), dimethylamine solution (C_2H_6NH 2 M in methanol), zinc chloride ($ZnCl_2$, ≥ 98%), pyridine-4-carboxylic acid ($C_6H_5NO_2$, ≥ 99.0%), copper (II) nitrate hemi-pentahydrate, $Cu(NO_3)_2 \cdot 2.5H_2O$, ≥ 98% and *N*,*N*-dimethylformamide or DMF (C_3H_7NO, ≥ 99.0%).

a) Synthesis of metal organic framework NEW-1

The synthesis procedure for NEW-1 was as follows; the compound was synthesised solvothermally in a 20 mL bomb. $Cu(NO_3)_2 \cdot 2.5H_2O$. (0.154 mg, 1.25 mmol) was placed into the solution of isonicotinic acid (0.121 mg, 0.5 mmol) in 15 mL DMF. The mixture was then stirred for 15 minutes before placing it in a 20 mL bomb. The bomb was heated at 160 ^{o}C under autogenous pressure in an autoclave for 48 hours. After 2 days, the bomb vessel was allowed to cool down to room temperature. Dark blue micro crystalline samples were filtered from the products. The filtered sample was washed with DMF and then air dried at room temperature in a desiccator.

b) Synthesis of metal organic framework NEW-2

The synthesis procedure for NEW-2 is as follows; 5 mL of fumaric acid solution $(5\ M)_{aq}$ which contained 0.5 ml of dimethylamine was placed in the bottom of the vial as shown in Figure 5.1a. This was followed by a layer of 2 mL of methanol as an interface layer above the fumaric acid solution (Fig.5.1b). Then a layer of 8 mL of zinc

chloride (0.17 mg, 1.25 mmol) in 8 mL of methanol was added above the interface layer (Fig5.1c). The sealed vial was left undisturbed at room temperature (Fig.5.1d). Crystal samples were harvested after a week.

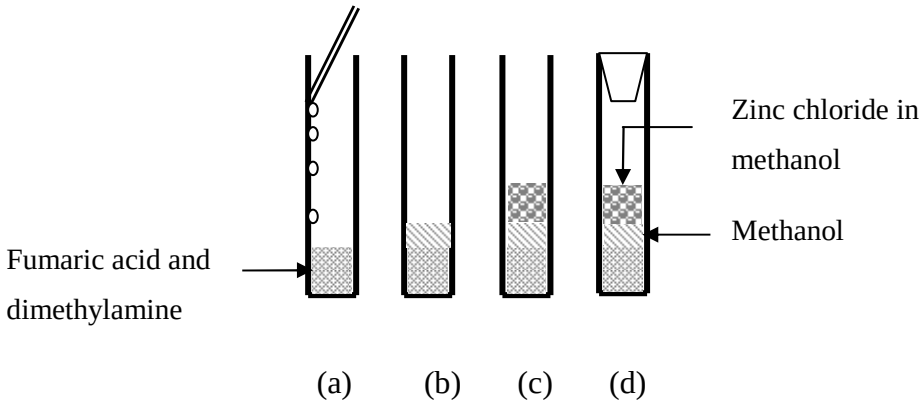

Figure 5.1 Schematic representing the layering synthesis of NEW-2

5.2 Characterisation of adsorbents

5.2.1 X-ray Crystallography

a) Single-Crystal Studies

In this study, crystal data and structure refinement for both NEW- 1 and NEW-2 were collected using a Nonius KappaCCD diffractometer with ϕ and ω scans (MoK_{α}, 0.71073 Å) and a Bruker APEX2 CCD diffractometer with thin-slice ω scans (synchrotron, 0.69430 Å) in a cold nitrogen stream, respectively. Structures were solved by direct methods and refined by full-matrix least squares, using SHELXL. All non-hydrogen atoms were refined anisotropically. The electron density contribution of the diffused scattering of the disordered guest molecules (DMF) and void space of the structure was handled using the SQUEEZE procedure in the PLATON software suite. These single crystal studies were carried out by Dr. R. W. Harrington of the X-ray crystallography research group, School of Chemistry Newcastle University.

b) Powder X- ray Diffraction Studies (PXRD)

The Powder X- ray Diffraction technique was used to determine the purity phase of the bulk sample by comparing the PXRD pattern with the simulated pattern from single crystal X-ray diffraction. In this study, PXRD patterns were obtained with a PANalytical X'Pert Pro MPD (multipurpose diffractometer), fitted with an X'Celerator which can accelerate the scan speed. The diffractometer profiles were recorded using CuK_{α} radiation with a fixed divergent slit (0.38 mm) and with a voltage of 40 kV. For analyses, powder samples were dispersed on glass slides and the continuous scans were set to cover the range 2-70 deg. The Powder X-ray diffraction was carried out by Dr. Kath Liddell of Materials Analytical Unit, Newcastle University.

5.2.2 Adsorbents morphology and elemental analysis

a) Scanning electron microscope (SEM)

Size and sample morphology were obtained by using a scanning electron microscope called JEOL 5300 LV fitted with Rontec and Si(Li) energy dispersive X-ray detector (EDX). Both detectors were cooled by liquid nitrogen. The EDX instrument was run with an operating voltage of 25 kV under vacuum for qualitative elemental analysis. The samples were coated with gold and images with secondary electrons in high vacuum mode. This scanning electron microscopy was carried out by the Materials Analytical Unit, Newcastle University.

b) Determination of C, H, N

A Carlo Erba 1108 elemental analyser was used to determine the C, H, N contents of the porous samples and also used as a tool for establishing the purity of the sample. Roughly 1 mg of each sample was weighed into a tin capsule and placed it in the auto sampler. Then the tin capsule is dropped into a vertical quartz reactor tube maintained about 1,000 ºC. The concentration of each elemental species was determined from the integral of the signals in comparison with that of the analogous organic chemical standard. This determination was also carried out by the Materials Analytical Unit, Newcastle University.

c) Fourier Transform Infra-Red (FTIR) Spectroscopy

FTIR spectra (400-4000 cm^{-1}) of the samples were recorded using a Digilab SCIMITAR series FTIR spectrophotometer. Samples were finely ground in an agate mortar. Approximately 2 mg of finely ground sample was mixed with 300 mg of KBr powder (99.95% purity). The mixture was ground in an agate mortar until the sample was well dispersed and then transferred to the mechanical disk press assembly where it was subjected to a pressure of ~ 10 tons.

5.2.3 Thermogravimetric (TGA) Studies

Thermogravimetric (TGA) Studies were carried using Stanton Redcroft STA 780 thermobalance to determine thermal stability of the samples. The thermobalance consists of an electronic microbalance with a platinum hangdown and ceramic container suspended from it, down the centre of a furnace. The sample mass was monitored by computerised control unit. The Pt v 13% Rh-Pt thermocouple measuring system is also located under the sample container in order to monitor the temperature. For analysis, roughly 20 mg of adsorbent was placed in a ceramic sample bucket. Then, the sample was heated with a furnace heating rate of 5 ºC min^{-1} under a constant flow (50 cm^3 min^{-1}) of nitrogen and the weight loss was recorded. The mass loss m_L, expressed as a percentage, was calculated using the equation as shown in equation (1);

$$m_L = \frac{m_s - m_f}{m_s} x100 \qquad (1)$$

where

m_s is the mass, in milligrams, before heating

m_f is the mass, in milligrams, at the final stage

5.3 Adsorption studies

5.3.1 Intelligent Gravimetric Analyser

In this study, isotherms and adsorption/desorption kinetics properties of all gases and vapours were measured using an Intelligence Gravimetric Analyser (IGA) model 002. The instrument was supplied by Hiden Isochema Ltd., Warrington U.K. A schematic diagram of the IGA is shown in Figure 5.2. The IGA system consists of four main compartments; temperature regulation system, microbalance system, pressure control system, and reactor chamber.

A platinum resistance thermometer (PRT) is installed in the IGA in order to determine the sample temperature throughout the experiment. The accuracy of measurement is about ± 0.1 ºC over a temperature range of -270 to 1000 ºC.[1] Secondly, the microbalance system is a fully computerised microbalance system which automatically measures the mass change of the sample as a function of time, pressure and temperature. The microbalance is connected with the counter weight in the left hand side and a sample bucket via tungsten fixing hooks and hangdown on the right hand side. The microbalance has 5 gram capacity and has a long term stability of ± 1 μg with a weighing resolution of 0.2 μg.

In the pressure control system, the pressure was monitored by three pressure transducers with ranges of 0 – 0.2 kPa, 0 – 10 kPa and 0 – 100 kPa. The accuracy of the set-point pressure regulation was about ± 0.02 %. Cylinders of each adsorbent gas were directly connected to the admit valve for feeding gas to the reactor chamber. Volatile organic liquids stored in a glass vapour reservoir were used to generate the vapour and this reservoir was connected to the admit valve via pipework. The reactor chamber housed the sample bucket. Adsorption in diverse temperature ranges can be done using two different techniques; circulating liquid thermostirrer bath and cryogenic liquid Dewar vessel. The thermostirrer bath is normally used for temperature adsorption experiment in the range of 0-80 ºC. A thermostirrer is controlled by the computer system resulting in the set-sample temperature being stable within ± 0.05 ºC. The thermostirrer comprising of a water heating/cooling device and a jacket containing 2:1 mixture of water and ethylene glycol (Figure.5.3). Adsorption experiments at 77 K are set by immersing the reaction chamber in 5 litres insulated – Dewar vessel which is filled with liquid nitrogen. An acetone/dry ice

mixture was used to set the sample temperature to 195 K while ice/ water was used to control the adsorption temperature at 0 ºC.

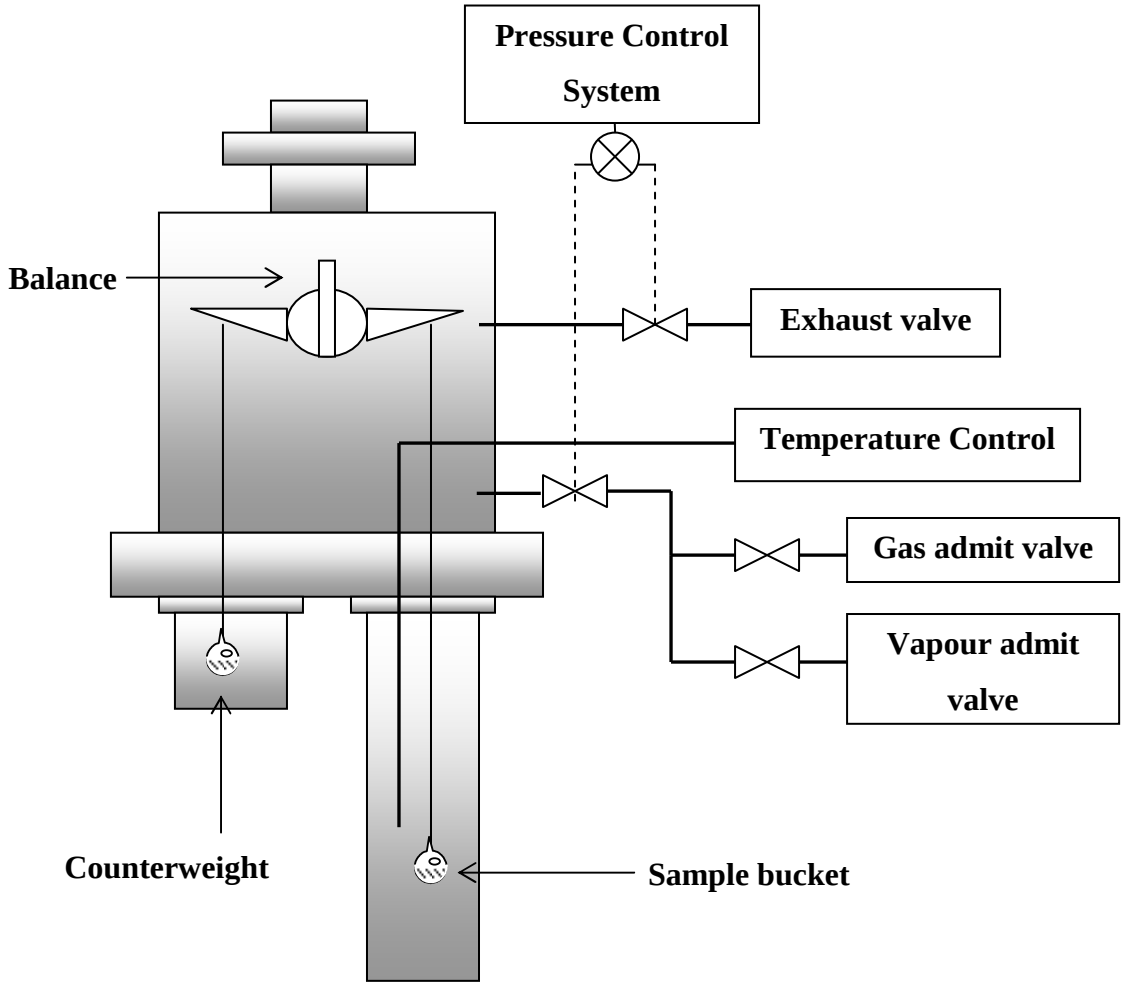

Figure 5.2 A schematic diagram represents the Intelligent Gravimetric Analyser (IGA)

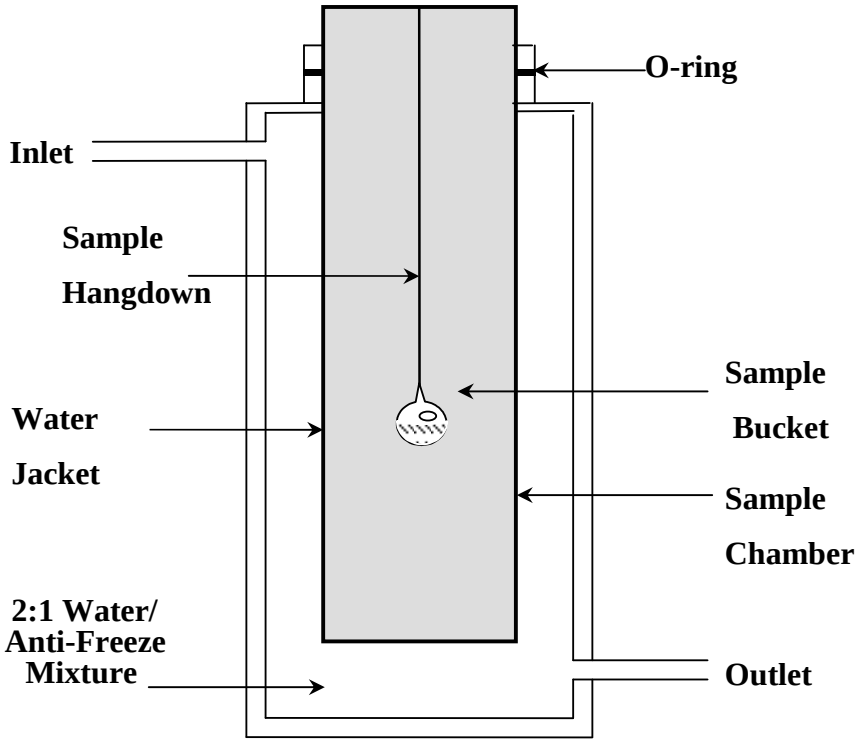

Figure 5.3 Schematic representation of a circulating liquid thermostirrer

5.3.2 Isotherm and kinetic measurements

Adsorption studies were carried out under the British standard procedure BS 4535-1[2] which are described as shown below. Prior to determining any adsorption study, the sample (approximately 20-50 mg) was exposed in an ultra high vacuum condition in order to remove physisorbed molecules or guest molecules from the porous material. Then, heating was normally applied to the sample. The maximum heating temperature which did not affect the sample was determined from thermogravimetric studies. In this study, carbon molecular sieved – 40 (CMS-40) was outgassed at 180 ºC while mixed metal organic framework-1 (M'MOF-1) and NEW-1 were outgassed at 70 ºC and 110 ºC respectively. Degassing was complete when the sample mass was constant over a period of 45-60 minutes as shown in Figure 5.4. The sample was then cooled down to the adsorption temperature under ultra-high vacuum conditions.

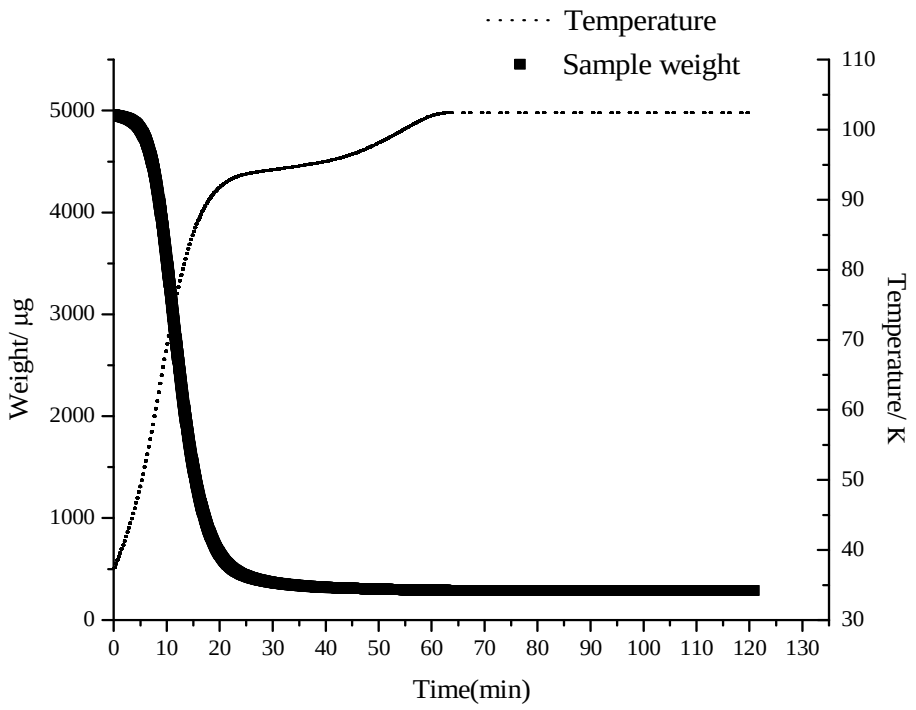

Figure 5.4 Typical thermogavimetric profile for outgas is complete when no further mass loss occurs

In adsorption experiments, the mass of gas or vapour uptake on the adsorbent was measured as a function of time and pressure. The approach to equilibrium was monitored in real time with a computer algorithm of the IGA system. After equilibrium was reached, the pressure of the adsorptive was increased over a period of 20 – 30 seconds to the next pressure step and the uptake of the adsorbent was monitored until equilibrium was established, as shown in Figure 5.5. The equilibrium uptake was established when 99.99 % of the predicted mass uptake value, which is calculated by a real time computer, was archived.

In the desorption measurements, the reverse method of the adsorption process was followed. The pre-adsorbed gas or vapour was desorbed stepwise at constant temperature. The adsorptive pressure was decreased over a timescale of 20 – 30 seconds until the desired value was obtained. The pressure was maintained at the set point by active computer control of the inlet/outlet valves throughout the duration of the experiment. The decrease in mass uptake was measured as a function of time and the approach to equilibrium was monitored in real time with a computer algorithm the same as with the

adsorption process. After the equilibrium was reached, the adsorptive pressure was decreased to the next pressure step as shown in Figure 5.6. The adsorption/desorption isotherms for each gas/vapour were done at least twist in order to check their repeatability.

In order to calculate the kinetic parameters for adsorption, the increase in weight versus time profile due to the adsorbate uptake for each pressure step was used. This data was fitted to the appropriate kinetic model (the kinetic models were discussed in section 2.6). The residuals for the difference between the calculated and observed values for the normalised profiles were typically less than ± 0.02 % for the whole profiles.

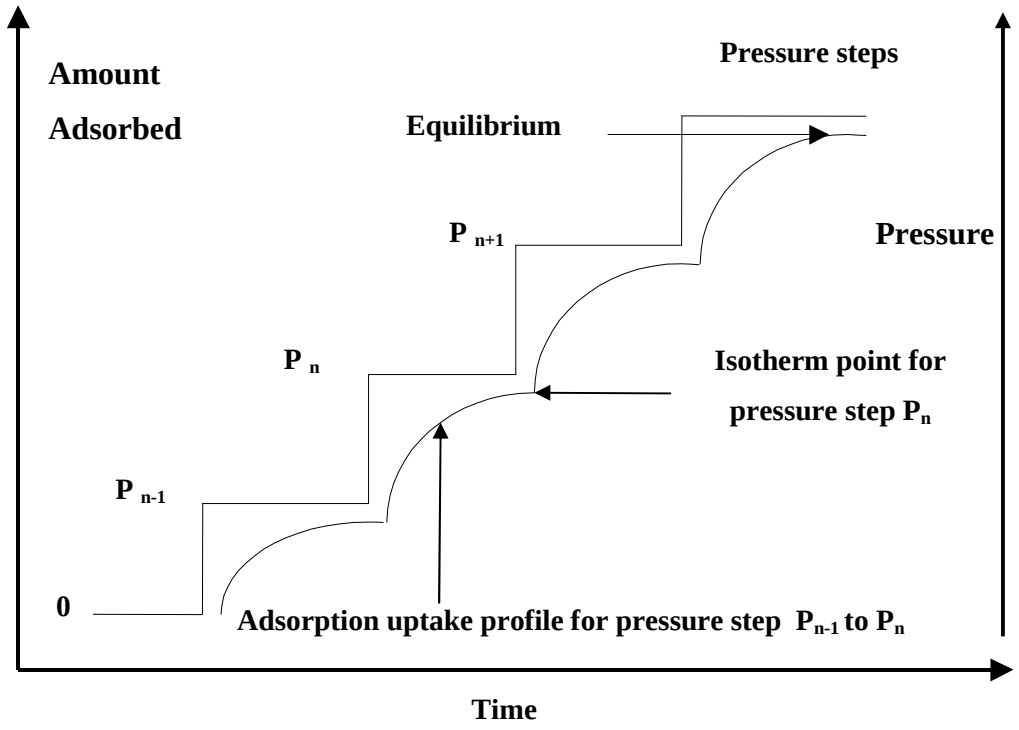

Figure 5.5 Schematic diagram showing sequential pressure steps and corresponding kinetics profiles for an adsorption isotherm

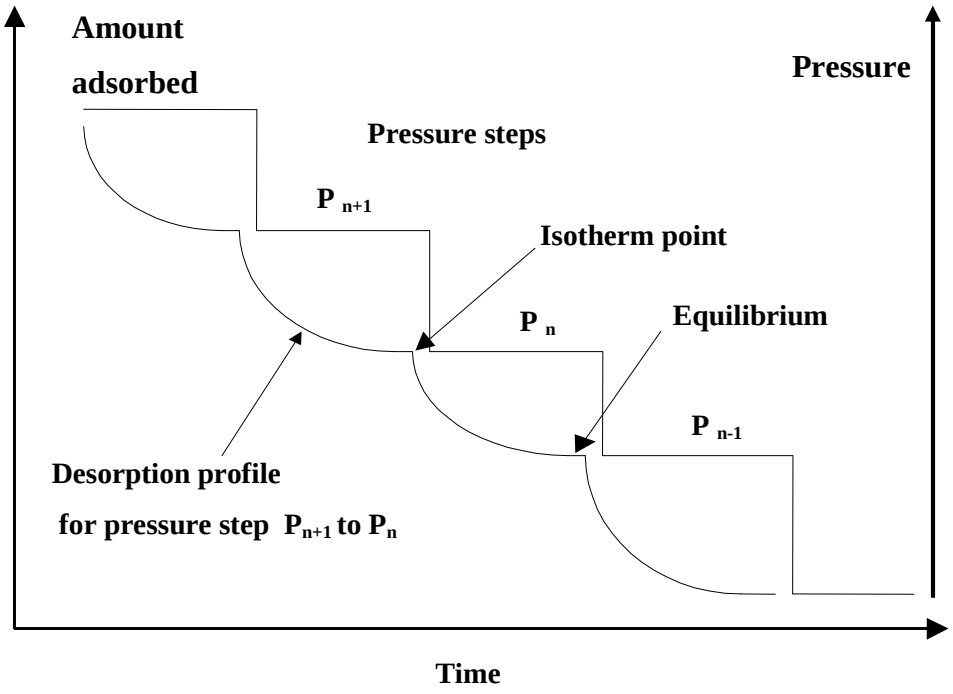

Figure 5.6 Diagram showing sequential pressure steps and corresponding kinetics profiles for a desorption isotherm

5.3.3 Calculation of saturated vapour pressure

The saturated vapour pressures were calculated using the following Antoine equations:[3]

$$\log_{10} p^0 = A - \frac{B}{T + C} \qquad (5.1)$$

where p is the saturated vapour pressure (mmHg), T is the temperature in degrees Celsius, A, B and C are constants of the adsorbates. The constants for the adsorbates used and corresponding temperature ranges over which they are valid, are given in the table 5.1.

Table 5.1 Antoine parameters and density of the adsorbates used in this study.[3-5]

Adsorbate	Temperature range (ºC)	A	B	C	Density (g cm^{-3})
Argon	-189.37 to -122.29	6.84064	340.271	271.801	1.38
Carbon dioxide	-56.57 to 31.04	7.58828	861.82	271.883	1.032
Hydrogen	-259.2 to -239.97	6.14858	80.948	277.532	0.797
Nitrogen	-210 to -147.05	6.72531	285.573	270.087	0.808
Oxygen	-218.8 to -118.57	6.83706	339.209	268.702	1.149
Water	0.01 to 373.97	8.05573	1723.64	233.076	0.997
Ethanol	-114.1 to 243.1	8.13484	1662.48	238.131	0.789
Methanol	-97.68 to 239.43	8.09126	1582.91	239.096	0.791
***n*-Propanol**	-73.15 to 263.56	7.77374	1518.16	213.76	0.803
***n*-Butanol**	-37 to 289.9	7.29062	1282.85	173.247	0.809
Methyl chloride	-140.2 to 143.1	6.99771	870.17	235.586	0.917
Dichloromethane	-95.14 to 236.85	7.11464	1152.41	232.442	1.326
Chloroform	-63.52 to 263.25	7.11148	1232.79	230.213	1.489
Methane	-182.48 to -82.57	6.84566	435.621	271.361	0.466
Ethane	-182.8 to 32.27	6.95335	699.106	260.264	0.572
Propane	-187.69 to 96.67	7.01887	889.864	257.084	0.585
***n*-Butane**	-138.29 to 152.03	7.00961	1022.48	248.15	0.600
***n*-Pentane**	-129.73 to 196.5	7.00877	1134.15	238.678	0.626
***n*-Hexane**	-218.8 to 118.57	6.9895	1216.92	227.451	0.660
***n*-Heptane**	-90.58 to 267.11	7.04605	1341.89	223.733	0.684
***n*-Octane**	-53.52 to 322.5	7.14462	1498.96	225.874	0.702
***n*-Nonane**	-56.77 to 295.68	7.1884	1607.74	222.414	0.717
Benzene	5.53 to 289.01	7.06437	1296.93	229.916	0.865
Toluene	-94.97 to 318.64	7.1362	1457.29	231.827	0.866

5.3.4 Determination of pore volume and surface area of porous materials

Gases and vapours adsorption were firstly used to characterise adsorbent porosity and secondly to investigate the effects of surface chemistry on the adsorption characteristics, e.g. adsorption capacity, type of isotherm, adsorption kinetics, molecular sieve effects, isosteric enthalpy of adsorption, and surface functional groups.

The total pore volume was estimated by adsorption of nitrogen at 77 K from the uptake at the maximum relative pressure used or by extrapolation using a suitable isotherm equation. Carbon dioxide was measured at both 273 K and 195 K in order to estimate micropore volume using the Dubinin-Radushkevich (D-R) equation and total pore volume of the sample, respectively. The shape and type of adsorption isotherms were investigated for a range of probe molecules which varied from hydrophobic to hydrophilic in character.

5.3.5 Hydrogen adsorption

The main problem of studies on hydrogen adsorption is the small mass of hydrogen adsorbed and if the hydrogen gas is not pure enough it may lead to non reliable adsorption isotherms. For example, many researchers reported that water impurity in hydrogen gas is preferentially adsorbed on the sample rather than hydrogen gas itself.[6, 7] So, ultra pure hydrogen was used in this adsorption/desorption study. Additionally, a purification system was constructed by Dr. Xuebo Zhao and Prof. Mark Thomas[8] in order to further purify hydrogen as shown in Figure 5.7. This was necessary for the highest repeatability results even when ultra pure hydrogen was used. The purification system is comprised of the 30 g calcium aluminosilicate zeolite and 40 g activated carbon in a stainless steel tube. The purification system was evacuated then heated at 700 K overnight and then cooled down in order to degas all adsorbed species, especially water, from the zeolite. Then hydrogen gas was filled to about 0.8 MPa in the purification system. Hydrogen was kept for a minimum of 24 hours to remove water. After that, the system was cooled down to 195 K for another 12 hours to remove other impurities such as O_2, N_2, and hydrocarbon by adsorption on the activated carbon. A secondary purification system was also installed on the right arm of the IGA machine. 30 g of zeolite was added in the secondary purification system in order to remove a very small quantity of water remaining in the apparatus. This was necessary for accurate hydrogen adsorption kinetic results.

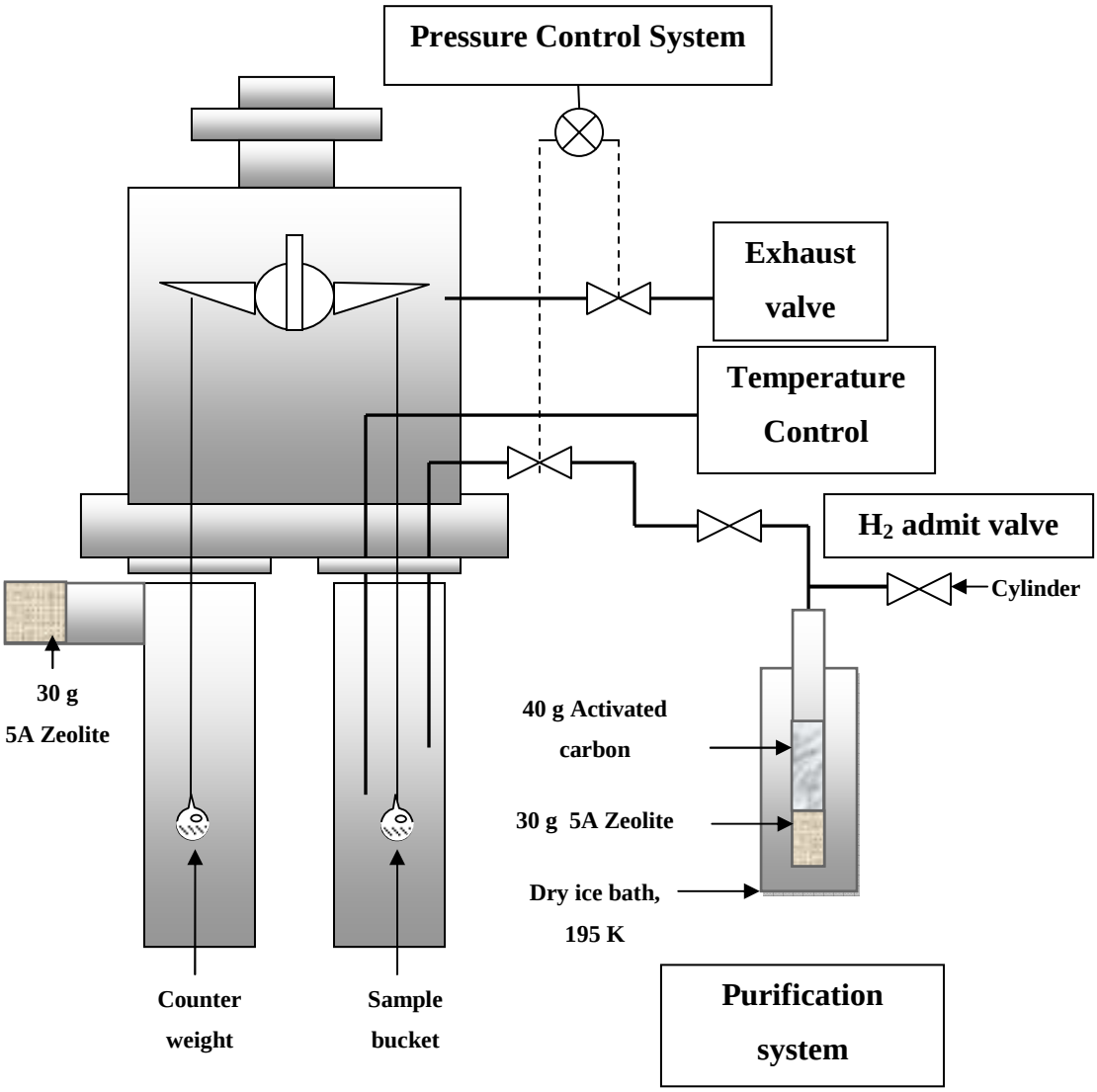

Figure 5.7 Intelligent Gravimetric Analyser with purification system

5.3.6 Oxygen, nitrogen and argon adsorption study

Adsorption of oxygen, argon and nitrogen NEW-1 and M'MOF-1, and CMS-40 were carried out at 195, 273 and 298 K. While CMS-40 was measured at a higher temperature range of 273, 288 and 298 K in order to avoid the very slow adsorption kinetics at 195 K. The adsorption temperatures for oxygen, argon and nitrogen were chosen as mentioned before due to the fact that adsorption kinetics were in range which could be continuously measured over a reasonable timescale. The isotherms and isosteric enthalpies of adsorption of these gases were used to determine the potential of air separation of both metal organic frameworks and carbon molecular sieves.

5.4 References

1. *IGA gravimetric analysers: Guide*; Hiden Isochema Ltd Warrington 1996; p 150.

2. *BS 4359-4 Determination of the specific surface area of powders. BET method of gas adsorption for solids (including porous materials)* British Standards Institution: 1996; p 24.

3. Rodgers, R. C.; Hill, G. E., Equations for vapour pressure versus temperature: derivation and use of the Antoine equation on a hand-held programmable calculator. *Br. J. Anaesth.* **1978,** 50, (5), 415-24.

4. Yaws, C.; Prasad, K.; Gabbula, C., *Yaws' Handbook of Antoine Coefficients for Vapor Pressure*. 2 ed.; Gulf Publishing Company Houston, Tex., 2005; p 200

5. Webster, C. E.; Drago, R. S.; Zerner, M. C., Molecular Dimensions for Adsorptives. *Journal of the American Chemical Society* **1998,** 120, (22), 5509-16.

6. Darkrim, F. L.; Malbrunot, P.; Tartaglia, G. P., Review of hydrogen storage by adsorption in carbon nanotubes. *International Journal of Hydrogen Energy* **2002,** 27, (2), 193-202.

7. Cheng, H. M.; Yang, Q. H.; Liu, C., Hydrogen storage in carbon nanotubes. *Carbon* **2001,** 39, 1447-54.

8. Zhao, X. Adsorption of pollutants and hydrogen storage on nanoporous materials. Newcaslte upon Tyne, Newcastle upon Tyne, 2005.

CHAPTER 6

Characterisation of metal organic frame works and CMS-40

Two new three-dimensional metal organic frameworks, named NEW-1 and NEW-2, were successfully synthesised from $Cu(NO_3)_2$ with isonicotinic acid and $Zn(NO_3)_2$ with fumaric acid, respectively. Their structures were determined by single crystal X-ray diffraction and were also characterised by means of chemical composition and physical properties. The results revealed that NEW-1 was a porous MOF, while NEW-2 was a non porous MOF. The total pore volume of NEW-1, calculated from gases adsorption, indicated that the desolvated structure of NEW-1 was partly collapsed. However, the total pore volume of NEW-1, determined by adsorption of a series of vapours, showed that the partly collapsed desolvated structure of NEW-1 increased in total pore volumes to a value similar to that obtained from the PLATON calculation from crystallographic data. This recovery of pore volume is due to framework flexibility which is driven by the isosteric enthalpy of vapour adsorption.

6.1 Characterisation of metal organic frameworks

The suitable samples of either NEW-1 or NEW-2 were filtered and washed by their mother liquor two times. The samples were dried in a vacuum in a desciccator for 48 hours. Then, the air dried samples were weighed. NEW-1 and NEW-2 gave 0.168 mg (a yield of 55 % based on isonicotinic acid) and 0.0106 mg (a yield of 58 % based on fumaric acid). Results of their crystal morphology and their chemical composition are described herein.

6.1.1 Crystal data and structure refinement of MOFs

6.1.1.1 Structure description of NEW-1

The X-ray crystallographic charaterisation of blue single crystal of NEW-1 was carried out by Dr. R. W. Harrington of the X-ray crystallography research group, School of Chemistry, Newcastle University. The result showed that NEW-1 has the assignment of the formula $C_{12}H_8CuN_2O_4 \cdot C_3H_6NO$ and has a monoclinic space group $P2_1/c$. The final refinement results are $R_1 = 0.0399$, $wR_2 = 0.0920$ [$F^2 > 2\sigma$] and residual density 0.42 and

–0.85 e $Å^{-3}$. The refined crystal data and the standard CIF file are shown in table 6.1 and Appendix A, respectively.

The asymmetric building block in the structure is composed of two square pyramidal copper atoms bonding with four isonicotinate ligands, as shown in Figure 6.1a. Cu atoms are bonded with three carboxylate oxygen atoms from three isonicotinate ligands (O_1, O_2 and O_3) leading to the formation of eight membered rings. The eight membered rings are interlinked via another four pyridyl groups of isonicotinate (N_1, N_2) to form the layers along a crystallographic *a* and *c*-axis. Consequently, linking these building blocks leads to the formation of three dimensional frameworks with the DMF molecules occupying the void. Interestingly, the oxygen atom (O_4) of the isonicotinate carboxylic group is uncoordinated. This uncoordinated oxygen atom (O_4) gives the distance between each uncoordinated oxygen atom along the *c* axis of about 11.57 Å (8.53 Å Van der Waals surface considered). The O(4) is in close proximity to square pyramidal copper centres in the pore walls leading to a formed Cu(1)-O(3)-C(12)-O(4) planar region (see Figure 6.1b).

In the square pyramidal copper, the longest bond lengths around the copper centre are Cu_1-O_1, 2.2578(16) Å, which is similar to the bond lengths found in the literature.[1-6] The longest bond length most likely results from a Jahn-Teller effect.[7-9] The shorter bond lengths are found in Cu1-O2, 1.9702(15) Å and Cu1-O3, 1.9889(15) Å which are comparable to the bond length found in the previous studies.[3-6, 10] The bond lengths of Cu-N_1 and N_2 are 2.0017(18) Å and 1.9946(18) Å, which are in a typical range of values 1.991-2.026.[1, 2, 10, 11] The distance between Cu-Cu in the eight membered rings formation is 4.596 Å, which is much longer than the Cu-Cu distance found in Lu *et. al.*[4] 2.601(2) Å and the Cu-Cu interaction found in the other metal organic frameworks HKUST[3] 2.628(2) Å, Cu-SIP-3-pyridine[11] 2.947(2) Å, and Tran *et. al.*[1] 2.965(2) Å. However, this Cu-Cu distance is shorter than those distances found in $Cu(HCO_2)_2.4H_20$[12, 13]; 5.8 Å. Bond lengths around pyramidal copper in the NEW-1 structure compare with the selected structure from literatures as shown in Table 6.2.

Table 6.1 Crystal data and refinement of NEW-1

Parameters	Crystal data and refinement
Chemical formula (moiety)	$C_{12}H_8CuN_2O_4 \cdot C_3H_7NO$
Chemical formula (total)	$C_{15}H_{15}CuN_3O_5$
Formula weight	380.84 (307.79 without moiety)
Crystal system, space group	monoclinic, $P2_1/c$
Unit cell parameters	a = 11.579(2) Å $\alpha = 90°$
	b = 12.292(3) Å $\beta = 117.871(2)°$
	c = 12.318(3) Å $\gamma = 90°$
Cell volume	1549.8(6) $Å^3$
Void volume (PLATON)	551.4 $Å^3$ (35.6%)
Calculated Porosity	0.269 cm^3g^{-1}
Z	4
Calculated density	1.632 g/cm^3 (1.319 g/cm^3 without moiety)
Crystal colour and size	blue, $0.02 \times 0.02 \times 0.00$ mm^3
Temperature	120(2) K
Radiation, wavelength	synchrotron, 0.69430 Å
Absorption coefficient (μ)	1.441 mm^{-1}
Reflections for cell refinement	977 (θ range 2.5 to 27.1°)
Data collection method	Bruker APEX2 CCD diffractometer
	thin-slice ω scans
θ range for data collection	2.5 to 29.8°
Index ranges	h –15 to 16, k –17 to 17, l –16 to 17
Completeness to θ = 26.0°	99.6 %
Reflections collected	15631
Independent reflections	4515 (R_{int} = 0.0453)
Reflections with $F^2>2\sigma$	3521
Absorption correction	semi-empirical from equivalents
Min. and max. transmission	0.9718 and 0.9986
Structure solution	direct methods
Refinement method	Full-matrix least-squares on F^2
Weighting parameters a, b	0.0512, 0.1354
Data / restraints / parameters	4515 / 0 /230
Final R indices [$F^2>2\sigma$]	R_1 = 0.0399, wR_2 = 0.0920
R indices (all data)	R_1 = 0.0564, wR_2 = 0.0985
Goodness-of-fit on F^2	1.031
Largest and mean shift/su	0.000 and 0.000
Largest diff. peak and hole	0.42 and –0.85 e $Å^{-3}$

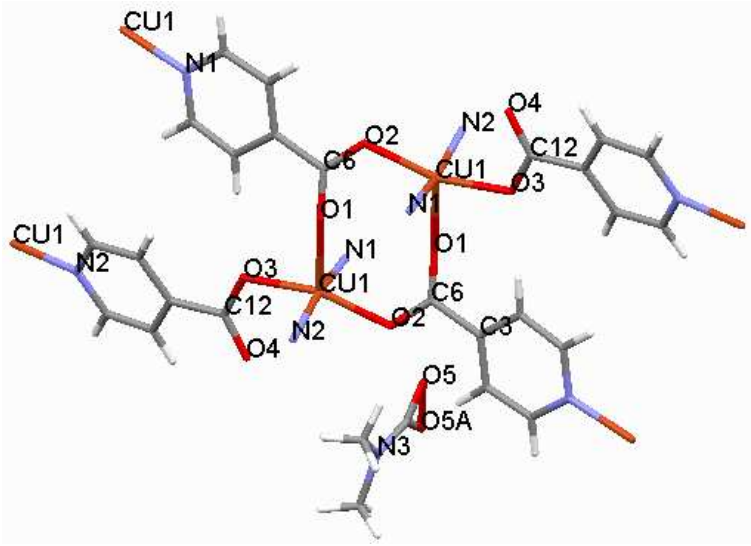

(a)

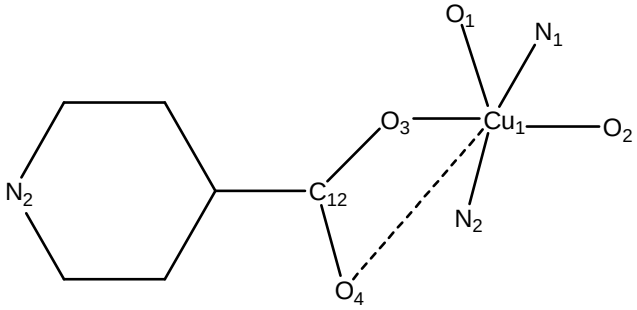

(b)

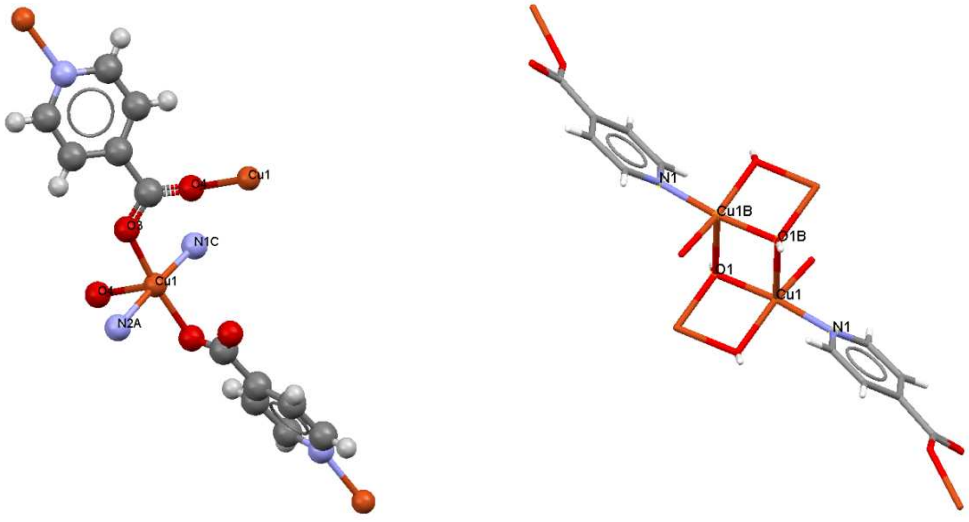

(c) (d)

Figure 6.1 Showing a) structure of NEW-1 with numbering scheme of two Cu metal centre binding with isonicotinate ligand b) the planar structure in the wall of NEW-1 c) framework formed by spiral isonicotinate ligand (CCD-UFUMUD) d) framework with rod-like secondary building (CCD-UGEPEB01)

The simulated structure obtained using Mercury software version 2.2 (build CR5)[14] showed that the framework exhibits a one dimension channel along the *a*-axis after the disordered DMF molecules are removed (Fig.6.2b). The Mercury-Void was used to simulate probe molecules with Van der Waals radius 1.5 Å in the void space of NEW-1 in order to make the one dimension channel more clearly visible (see Figure 6.2 c-d). Additionally, the O(4) atoms on the surface of NEW-1 pores are displayed in ball and stick mode for the purposes of clarity. It can be seen that the framework exhibits an open-ended channel along the *a* axis. These channels have a dimension of approximately 8.892 x 8.892 Å (distance from centre Cu to Cu cross section) or approximately 6.092 x 6.092 Å (Van der Waals surfaces considered). In addition, results from the PLATON[15] software indicated that the void volume of this channel is about 35.6 % (551.4 $Å^3$) of its cell volume. The calculated density (in the absence of guests) and calculated porosity of the NEW-1 sample are 1.319 g cm^{-3} and 0.269 cm^3 g^{-1}, respectively. Furthermore, simulated results from the PLATON-CAVITY[15] showed that the void radius in the framework is in the range of 1.74 - 2.24 Å.

Previously, some metal organic frameworks synthesised from copper and isonicotinate ligand were reported. Lu and Babb[10] hydrothermal synthesized their MOF at 140 º C for three days and reported that their structure consisted of a square pyramidal Cu centre which linked together with five isonicotinate ligands which made the framework exhibit the one-dimensional channel along the *a* axis, as shown in Figure 6.1c. Tran and co-workers[1] also published their Cu-isonicotinate structure, which was hydrothermal synthesised at 150 º C for four days, and revealed that the framework was formed via the coordination of the isonicotinate ligands and rod-like secondary building units of copper centre as shown in Figure 6.1d. The PLATON results show that the void volumes of Lu's and Tran's frameworks are about 2.7% (37.1 $Å^3$) and 17.8% (130 $Å^3$) of the corresponding cell volume respectively. In comparison, the void spaces of these samples are much lower than NEW-1. This may be because larger DMF molecule in the NEW-1 structure can support and form a larger pore than smaller water molecules. Similar effects of various sizes of guest molecule on pore structure were reported. Wang *et. al.*[16] reported that room temperature synthesis of $Mn(HCOO)_3$ with large amines molecular size, such as diethylamine and triethylamine, produced a framework topology with larger unit cell volume rather than the framework synthesised with smaller amine molecular sizes, e.g. methylamine and ethylamine. This report also showed that unit cell volume increases from

841 $Å^3$ to 1873 $Å^3$. Lu *et. al.*[10] reported that solvent inclusion of metal organic framework $(Cu(Isonicotinate))_2$ in a series of solvents with different molecular sizes resulted in a unit cell volume change from 1,326 to 1,431 $Å^3$ with the β angles varying from 96.920(1) to101.229(2)º. Senkovska *et. al.*[17] reported that solvothermal synthesis of $Mg(maphthalenedicarboxlylate)_3$ with larger solvent molecule size, e.g. DMF, produces larger pore diameters of MOF rather than hydrothermal synthesis.

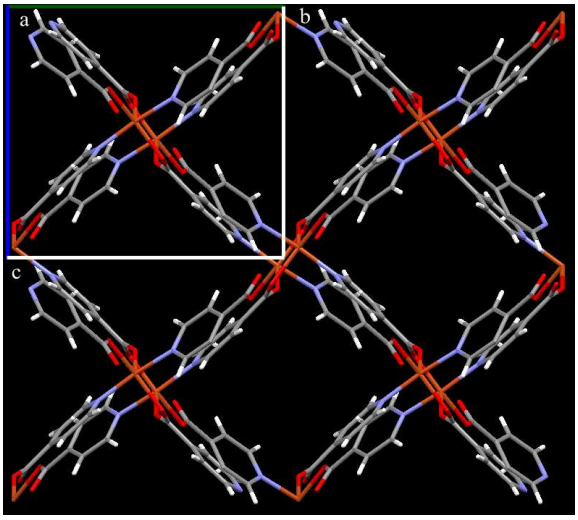

(a)

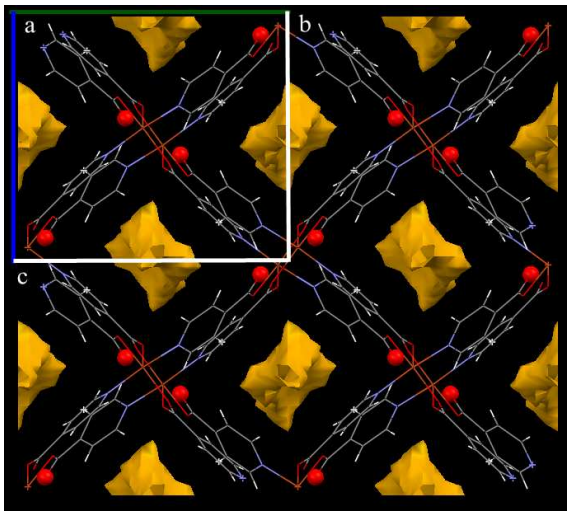

(b)

Figure 6.2 a) simulated structure of NEW-1 after guest molecules were removed, showing a channel along the *a* axis (blue:N, gray:C, red:O, orange;Cu, and O_4 shown in ball and stick mode for clarity) and b) Simulated structure with probe molecules of van der Waals radius 1.5 Å (yellow) along *a* axis.

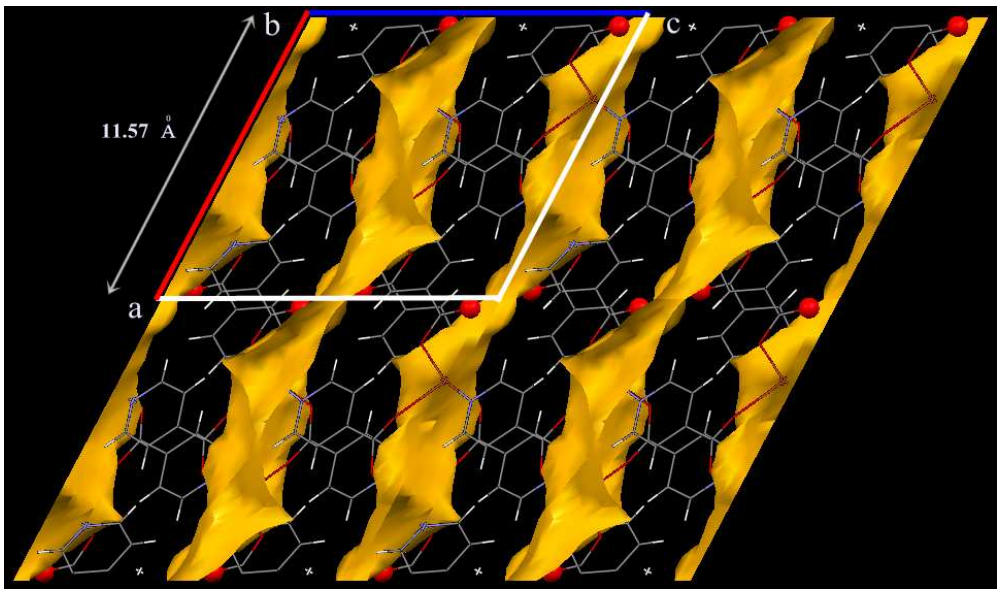

(c)

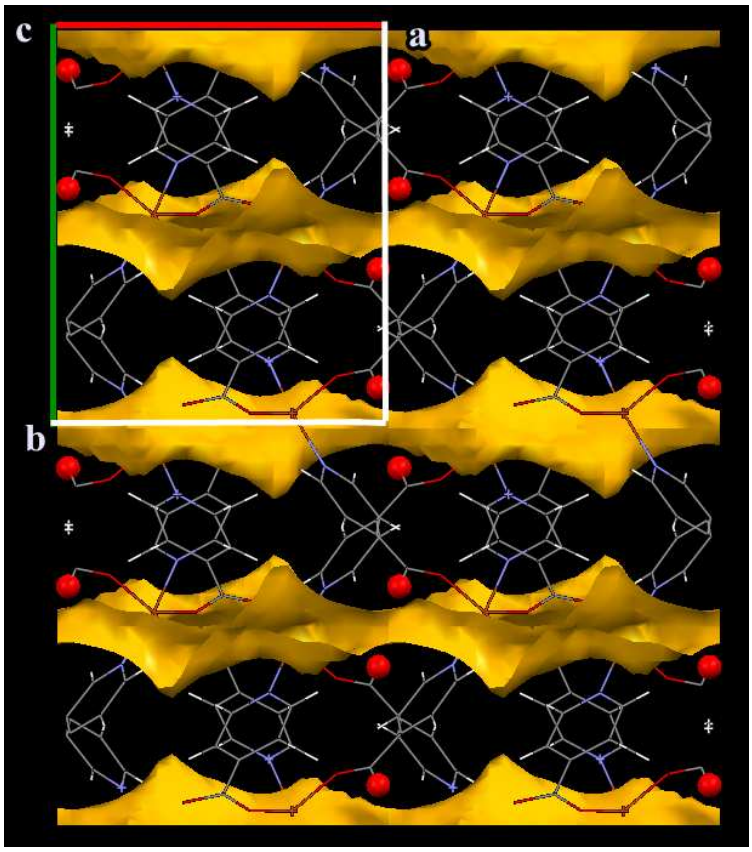

(d)

Figure 6.2 cont. Simulated structure of NEW-1 with probe molecules (orange) of van der Waals radius 1.5 Å along c) *b* axis and d) *c* axis.

6.1.1.2 Structure description of NEW-2

Single X-ray diffraction studies revealed that the colourless crystalline of NEW-2 is a three dimensional framework. It has the chemical formula as $C_6H_{10}O_6Zn$ with a monoclinic space group *C2/c*. The final refinement results are $R_1 = 0.0171$, $wR_2 = 0.0428$ [$F^2>2\sigma$] and residual density 0.44 and –0.20 e $Å^{-3}$. The refined crystal data and the standard CIF file are shown in table 6.3 and Appendix B respectively.

Basically, the structure consisted of the single independent zinc atom (Zn1) which is bonded to four fumarate ligands (O1 and O3) and two methanol (O2) via oxygen atoms (Fig. 6.3a). This bonding leads to the formation of hexagonal building blocks of ZnO_6. The bond distances between Zn and oxygen range from 2.0669(15) to 2.1564(14) Å. These bond distances are comparable with the Zn(terephthalate)(4,4-bipy)[18], 1.998(2)-2.617(2) Å, and $[Zn(H_2O)_4(bpy)]$succinate[19], 2.066(2)-2.166(2) Å, but are quite a lot longer than those found in diamond-like metal organic framework[20], 1.929(7) Å and Zn coordinate polymers,[21] (1.935(2)-1.996(2) Å.

The X-ray structural characterisation revealed that the structure has cell volume 822.3(8) $Å^3$ and has no accessible void space, i.e. it is a non porous framework. NEW-2 formed the dense structure either on the *a*, *b* or *c* axis, as shown in figure 6.3 *b* and 6.3 *c* respectively. The dense structure results from two methanol molecules strongly bonded with Zn, which could not be removed without decomposing the framework structure. It should be noted that a series of solvents, e.g. ethanol, DMF, H_2O, and a mixture of H_2O and methanol, were also used to synthesise a metal organic framework from $Zn(NO_3)_2$ and fumaric acid. However, suitable crystalline samples could not be obtained from these further experiments.

Table 6.3 Crystal data and refinement of NEW-2

Parameters	Crystal data and refinement
Chemical formula (moiety)	$C_6H_{10}O_6Zn$
Chemical formula (total)	$C_6H_{10}O_6Zn$
Formula weight	243.51
Crystal system, space group	monoclinic, C2/c
Unit cell parameters	a = 15.747(7) Å $\alpha = 90°$
	b = 7.047(6) Å $\beta = 116.31(8)°$
	c = 8.266(3) Å $\gamma = 90°$
Cell volume	822.3(8) $Å^3$
Void volume	No accessible void
Calculated Porosity	Non porous
Z	4
Calculated density	1.967 g/cm^3
Crystal colour and size	colourless, $0.20 \times 0.20 \times 0.10$ mm^3
Temperature	150(2) K
Radiation, wavelength	MoKα, 0.71073 Å
Absorption coefficient μ	2.982 mm^{-1}
Reflections for cell refinement	54 (θ range 2.5 to 27.5°)
Data collection method	Nonius KappaCCD diffractometer, ϕ and ω scans
θ range for data collection	4.6 to 27.5°
Index ranges	h –20 to 20, k –9 to 8, l –10 to 10
Completeness to θ = 26.0°	99.6 %
Reflections collected	7363
Independent reflections	944 (R_{int} = 0.0247)
Reflections with $F^2>2\sigma$	845
Absorption correction	semi-empirical from equivalents
Min. and max. transmission	0.5869 and 0.7547
Structure solution	direct methods
Refinement method	Full-matrix least-squares on F^2
Weighting parameters a, b	0.0212, 1.5563
Data / restraints / parameters	944 / 0 / 81
Final R indices [$F^2>2\sigma$]	R_1 = 0.0171, wR_2 = 0.0428
R indices (all data)	R_1 = 0.0219, wR_2 = 0.0451
Goodness-of-fit on F^2	1.036
Largest and mean shift/su	0.000 and 0.000
Largest diff. peak and hole	0.44 and –0.20 e $Å^{-3}$

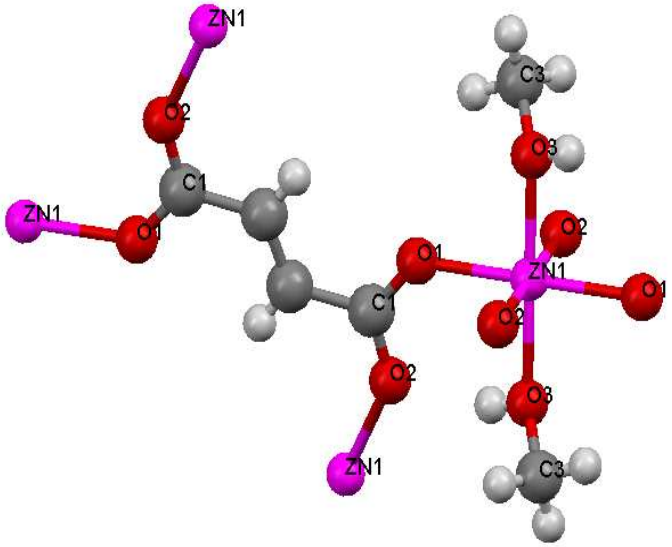

(a)

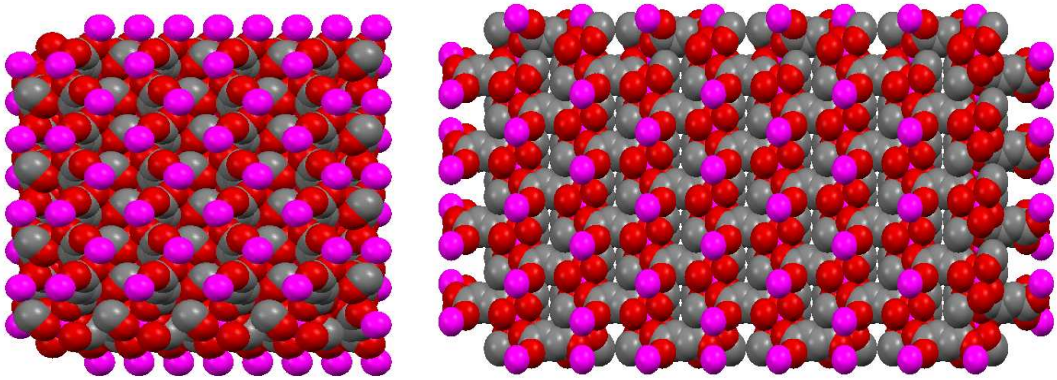

(b) (c)

Figure 6.3 View of NEW-2 structure a) showing numbering scheme of hexagonal ZnO_6 centre bonding with fumarate ligand b) dense framework along the *a* axis and c) along the *c* axis.

6.1.2 Elemental analysis of MOFs

Both NEW-1 and NEW-2 samples were dried in desiccator overnight, labeled as air dried samples, and were used to determine their CHN composition. The CHN values of air dried NEW-1 are consistent with the calculated values for the sample without guest molecule, indicating facile loss of DMF molecules as shown in Table 6.4. The carbon and hydrogen composition for air dried samples of NEW-2 agreed well with calculated values (Table 6.5).

Table 6.4 Comparison of CHN analytical data for NEW-1 by calculated and experimental determination.

Elements (%)	**Calculated values for sample without guest molecules $C_{12}H_8CuN_2O_4$**	**Experimental (air dried sample)**
C	46.82	46.21
H	2.62	2.87
N	9.10	9.33

Table 6.5 Comparison of CHN analytical data for NEW-2 by calculated and experimental determination.

Elements (%)	**Calculated values for Fresh sample ($C_6H_{10}O_6Zn$)**	**Experimental (air dried sample)**
C	29.58	29.22
H	4.13	4.02
N	-	-

6.1.3 Fourier Transform Infrared Spectroscopy (FTIR)

The IR spectra of commercial raw materials of both isonicotinic acid and fumaric acid were recorded and are also presented in Figures 6.4 and 6.5 respectively. The vibrational bands and proposed assignments from the previous studied[22-26]on the isonicotinate complexes were used as guidelines to classify the functional groups and assign infrared absorption bands for both NEW-1 and NEW-2 structures. Generally, observation values of the bands in range 3421-3427 cm^{-1} can be assigned to the O-H group, which showed the presence of water in the sample. The absorption bands in range 3061-3115 cm^{-1} and the strong bands between 1550-1670 cm^{-1} are attributed to the bending vibrations of the C-H in aromatic ring, C=C aromatic stretching, and were indicative of the carboxyl group (C=O) stretching vibrations in the structure. Additionally, unsaturated oxygen ν(C-O) in the structure can be observed in range 1410-1437 cm^{-1}. Furthermore, coordination through N-O is normally demonstrated by the band in ranges 1209-1290 cm^{-1} and 827-870 cm^{-1}.

Figure 6.4 and Figure 6.5 show the FTIR spectra of 48-hours air dried NEW-1, desolvated NEW-1 and 48-hours air dried NEW-2 samples. For comparison, the FTIR spectra of the commercial raw materials, e.g. isonicotinic acid and fumaric acid, are also presented in the Figures mentioned before. The vibrational bands around 1713 and 1717 cm^{-1} observed for both air dried NEW-1 and desolvated NEW-1 confirmed the presence of ν(C=O) in the isonicotinic acid. The presence of pyridine (CC+CN) in isonicotinic acid also found in the vibration bands around 1555 and 1605 cm^{-1} for air dried NEW-1 and 1554, and 1609 cm^{-1}found in desolvated sample. The strong band 1676 and 1507 cm^{-1} presenting C=O and C-N stretching mode[27, 28] respectively in DMF, do not appear in both FTIR spectra of the air dried and desolvated sample of NEW-1. This indicates DMF molecules' facile loss from the NEW-1 framework.

In the case of the FTIR spectrum for NEW-2, the vibration bands 1404, 1450 and 1543 found in air dried NEW-2 confirmed the presence of ν_{as}(COO) and ν_{s}(COO) in the fumaric acid. The vibrational wavenumbers and proposed assignments taken from the literature for both NEW-1 and NEW-2 are listed in Table 6.6 and 6.7 respectively.

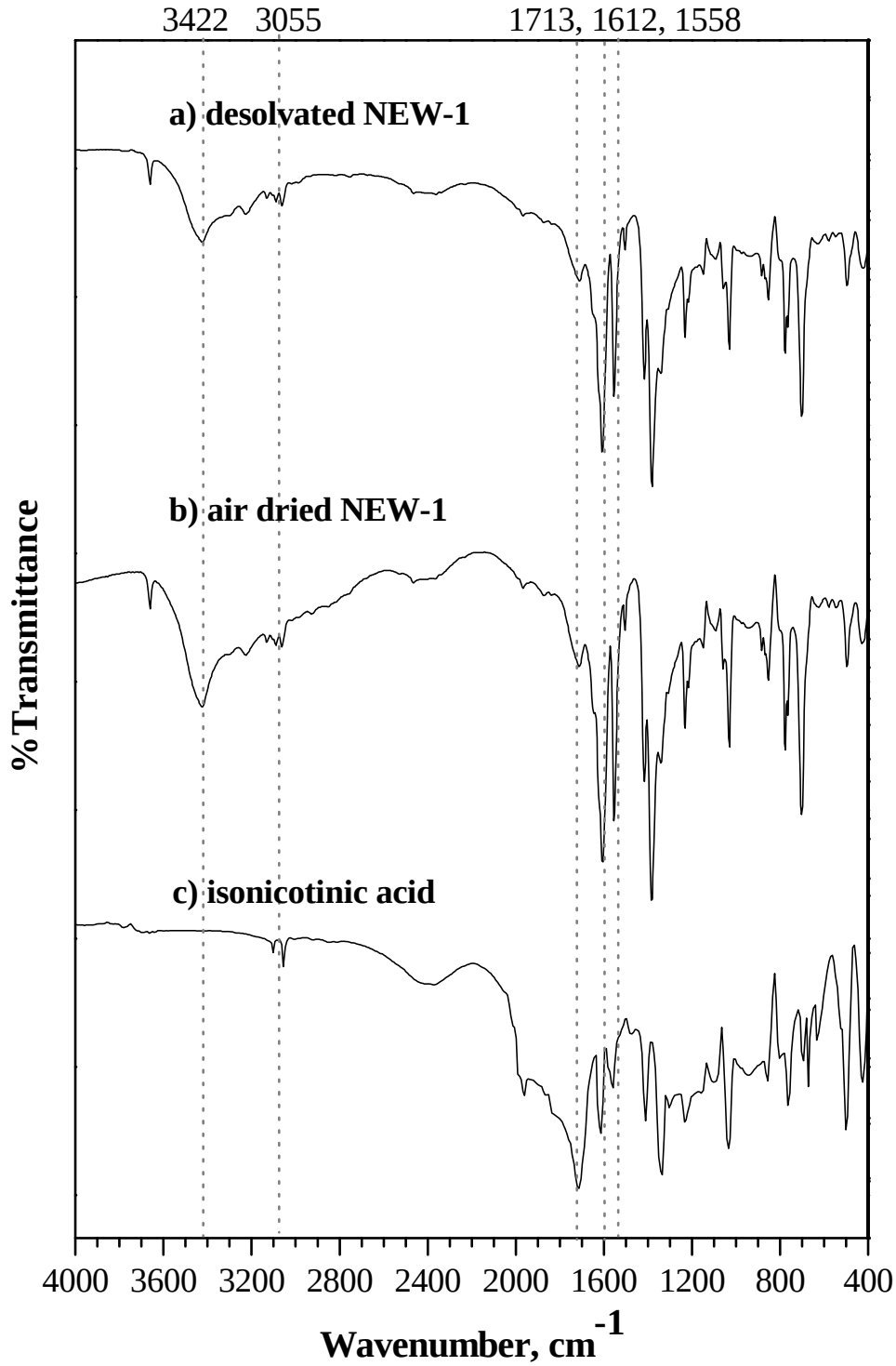

Figure 6.4 Fourier Transform Infrared spectra for desolvated NEW-1, airdried NEW-1 and free isonicotinic acid.

Table 6.6 The infrared spectra (cm^{-1}) of free isonicotinic acid (IN) and NEW-1 sample with their assignments

IN[29]	IN[30]	IN (this study)	$Cu(IN)I_2$ complex[31]	Desolvated NEW-1	Air dried NEW-1	Assignments[29]
3440w	3436m		3418m	3422bw	3426mb	ν(OH)
3052vw	3104w	3055w	3060m	3063vw	3063vw	ν(CH)
1711s	1712vs	1713vs	1699vs	1717w	1713w	ν(C=O)
1616m	1616w	1612s	1597m	1609vs	1605vs	Pyridine(CC+CN)
1563w	1597w	1558m	1554s	1554vs	1555vs	Pyridine(CC+CN)
1338s	1305s	1335s	1327m	1381vs	1385vs	ν(C-O)
1231s		1234m	1236w	1231s	1231s	CHO
1027vs		1034vs	1035vw	1030s	1030s	Ring deformation

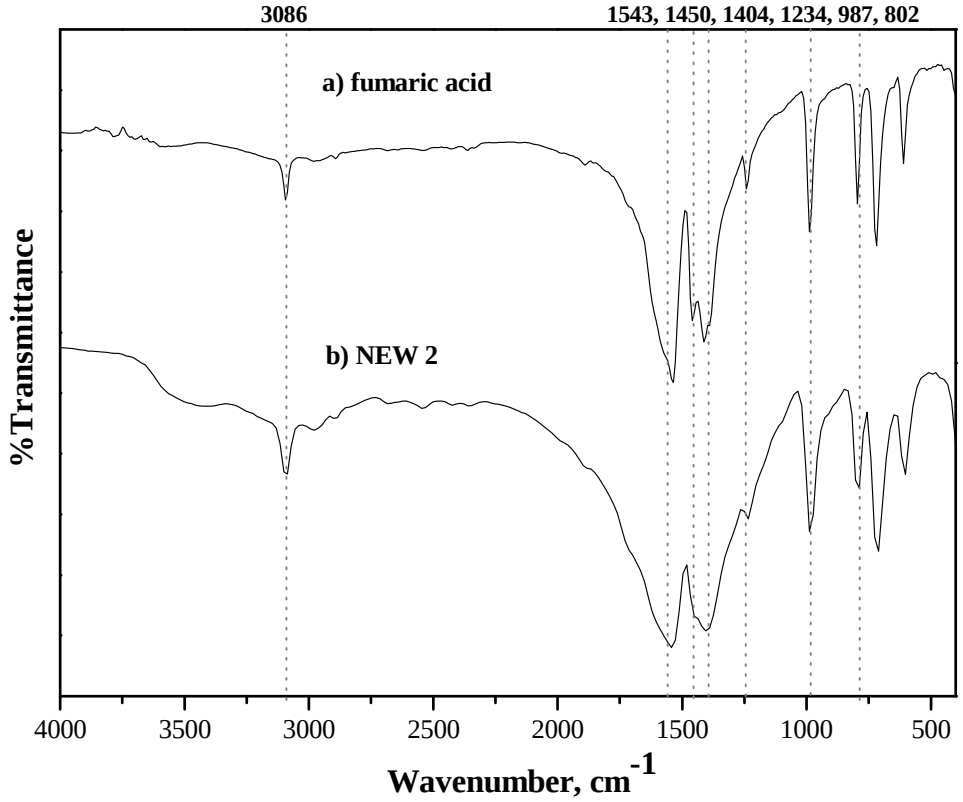

Figure 6.5 Fourier Transform Infrared spectra for NEW-2

Table 6.7 The infrared spectra (cm^{-1}) of free fumaric acid (Fum) and NEW- 2 sample with their assignments

$Ni(Fum)^{32}$	$Ln_2(Fum)_2(oxalate)^{33}$	Dimethyl Fumarate[34]	Fumaric acid (this study)	NEW-2	Assignments
3066w	3804vw	3080vw	3093w	3086w	ν(CH)
1553vs	1558s		1535vs	1543vs	ν_{as}(COO)
1424m		1450s	1458m	1450m	ν_s(COO)
1413s	1401s	1439m	1411s	1404s	ν_s(COO)
	1222m	1230m	1242m	1234m	ν (C-O)
	986m	990m	987vs	987vs	ν (CH)
	880m		794vs	802vs	COO, deformation

6.1.4 Powder X-ray diffraction (PXRD)

In order to establish the presence of the pure phase of the MOFs, the PXRD pattern of both MOFs is compared with the simulated pattern of the single crystal structure produced by Mercury software. Before determining the XRD pattern of the sample, the NEW-1 sample was prepared by heating at 110 ºC under ultrahigh vacuum conditions for 3 hours and labelled as a desolvated sample. Additionally, the NEW-1 sample was also dried in desiccator for 48 hours and labelled as air dried.

Figure 6.6 shows four PXRD patterns of NEW-1 samples. There are four main peaks appearing in the simulated PXRD pattern of both the fresh sample and the desolvated sample (see Figure 6.6a and b). These fours peaks are located at 2θ = 10.84º, 11.26º, 17.36º and 21.78º. However, simulated - desolvated pattern at 2θ = 17.36º and 27.38º appeared in a very low intensity, which is possibly due to contributions from DMF molecules removed from the framework.[35]

Comparing to the air dried sample (Fig.6.6c), the PXRD profile matched well with the simulated - desolvated pattern which indicates that the air dried sample was similar to the single crystal. However, all four strongest peaks of the air dried sample moved to a slightly lower angle compared to the simulated - desolvated pattern, for example, the intense peak at 10.84° in the simulated pattern has moved to 10.74° in the air dried sample. There was a new peak occurred at 18.96° on the PXRD profile of air dry

sample. This and other small changes in peak position suggest that there was a small change in structure. Li and Yang[36] also found small changes in the peak positions of MOF-177 and proposed that these small changes were due to rotation of the unit cell to allow the guests molecule to pass.

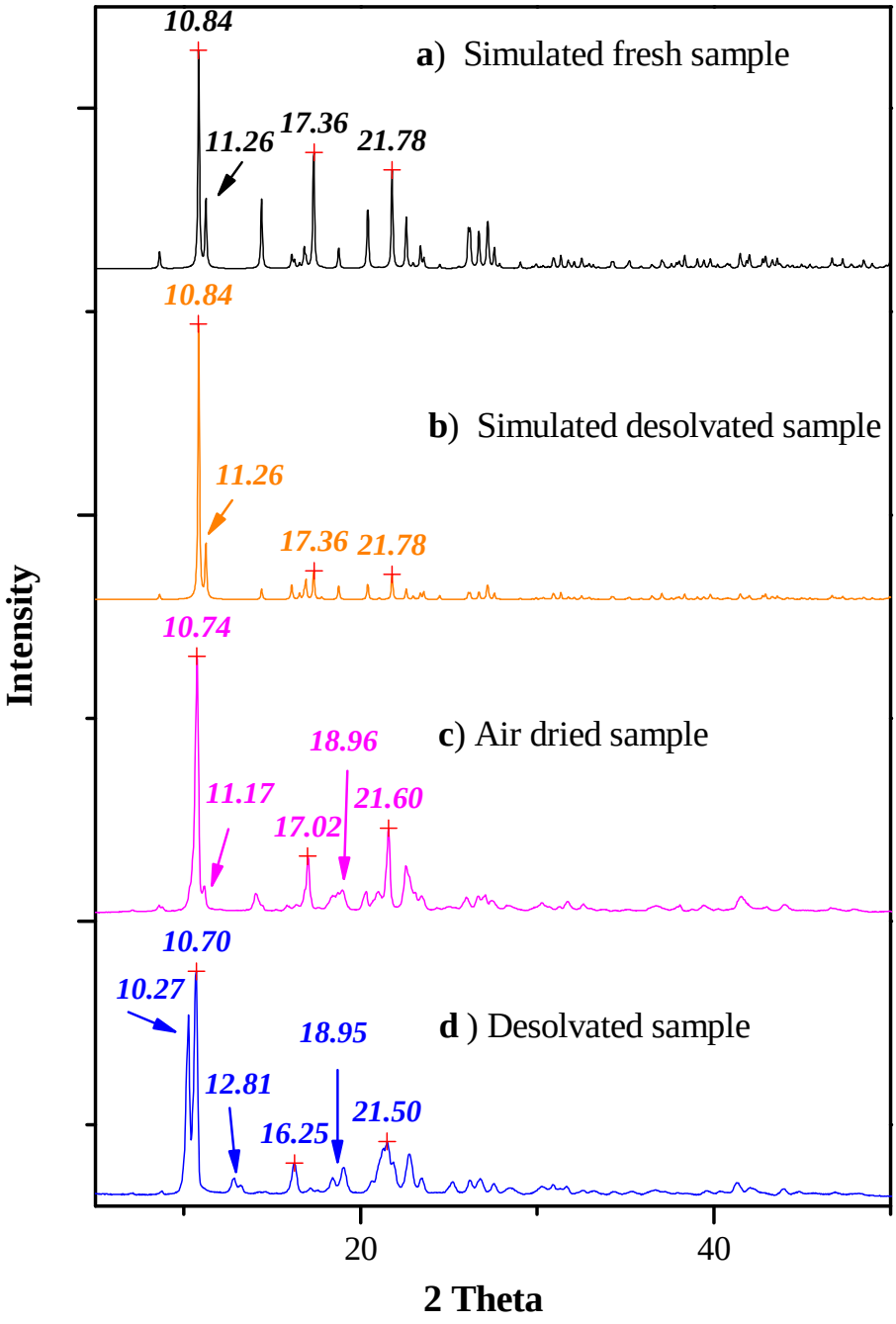

Figure 6.6 Powder X-ray diffraction profiles for NEW-1

As shown in Figure 6.6d, the PXRD pattern after desolvation of the NEW-1 showed significant differences from the simulated pattern due to the fact that there is no peak at 2θ = 11.26° and two new peaks at 10.27° and 12.81° are appeared. Although, four main peaks still remained, however, these three peaks are moved considerably to the lower angle far from the simulated pattern. These changes in peak positions suggest that the framework was collapsed after the sample was desolvated.

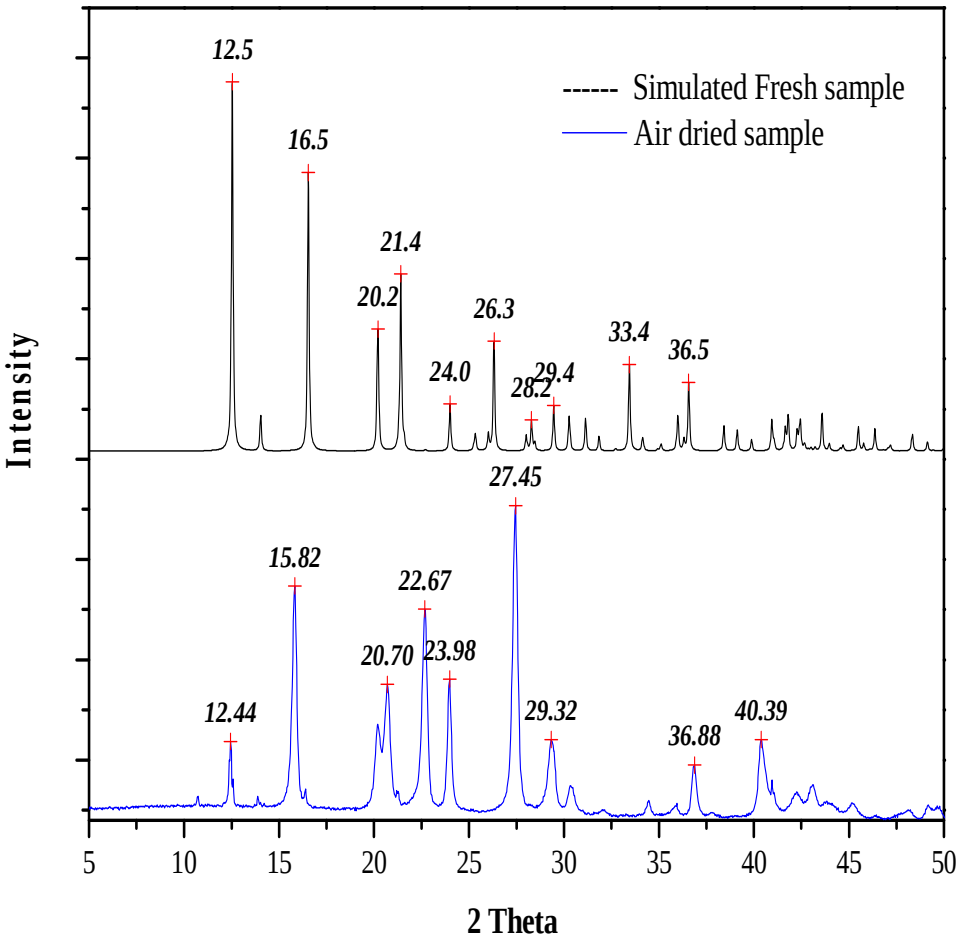

Figure 6.7 Powder X-ray diffraction profiles for NEW- 2

As showed in Figure 6.7, PXRD pattern of NEW-2 changed significantly after exposure to air in a desiccator for 1 day. The intensity of the peak at 2θ = 12.44º decreased markedly while the highest intensity was a new peak which appeared at 2θ = 27.45º. Furthermore, there are new peaks appeared for example at position 2θ = 40.38º and also appeared as a shoulder of the peak at 2θ = 22.70º. This indicated that the simulated pattern does not match the PXRD pattern obtained for NEW-2 sample which is probably due to there was some impurity in the sample.

6.1.5 Thermal stability

Figure 6.7a-b shows the TGA profiles of 12-hours air dried NEW-1 and as-synthesised NEW-1, respectively. It is apparent that both profiles exhibited two distinct steps of weight loss. For as-synthesised sample, the first step of 45.4 % weight loss is attributed to the gradual loss of both DMF molecules on the outer surface of the sample and also in the void of the structure. While, the TGA profiles of air-dried NEW-1 shows weight loss of 18.7 % on heating from 50 to 140 ºC. This weight loss is in agreement with calculated one molecule of DMF loss (18.9%) per formula unit. This profile also indicates that the NEW-1 sample is stable from room temperature up to approximately 250 ºC and then gradually decomposes with the loss of isonicotinate ligand.

Thermogavimetric analysis of 12 hours air-dried NEW-2 indicates two stages of weight loss (Fig. 6.9). An initial weight loss occurred between 25 to 170 ºC, immediately followed by the second decomposition of the framework started approximately at 290 ºC. The first weight loss of the air dried sample is about 5.97 %, which does not agree with the calculated weight loss of two methanol molecules (26.3%) in the void of the corresponding crystal structure. This disagreement indicated that both methanol molecules are strongly bond with the framework and cannot be removed without collapsing of the structure.

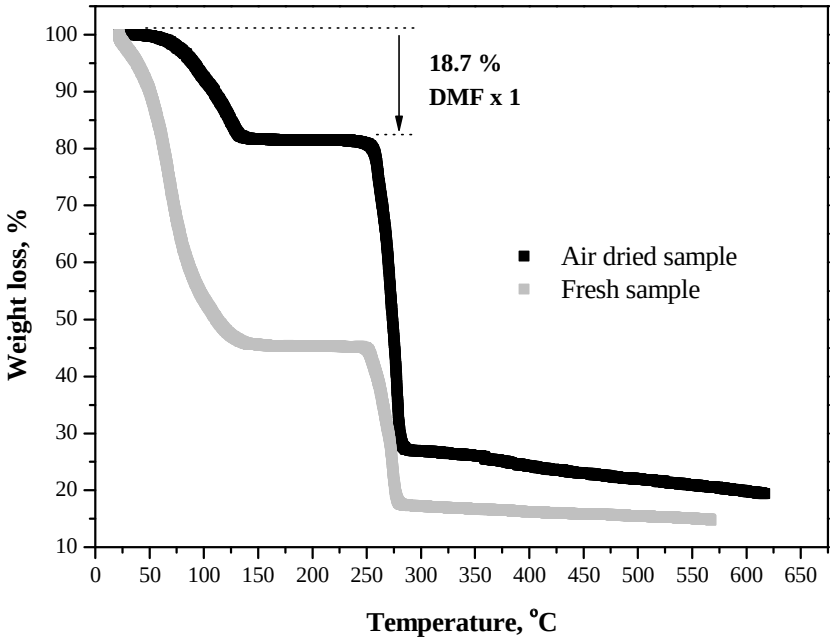

Figure 6.8 Thermogravimetric analysis of air-dried NEW-1 over the temperature range 25 to 700 ºC at a heating rate of 5 ºC min^{-1} under N_2 atmosphere.

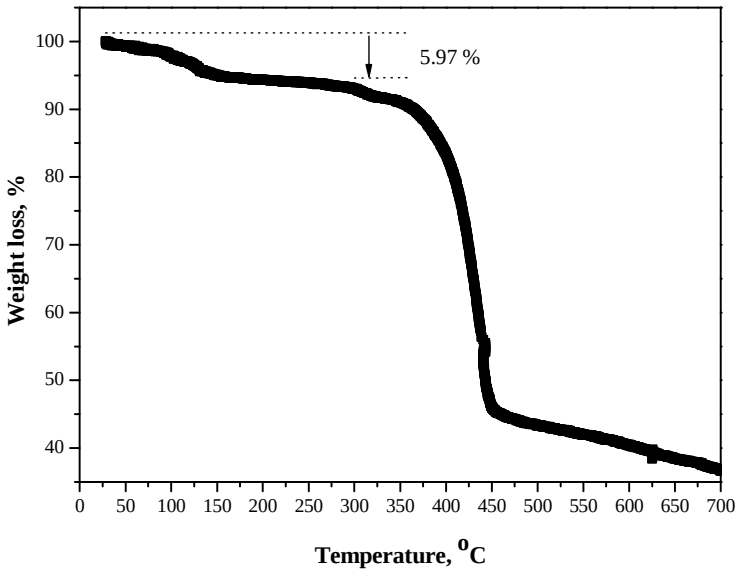

Figure 6.9 Thermogravimetric analysis of air-dried NEW-2

6.1.6 Particle size and crystal morphology

The Scanning Electron Microscope images of NEW-1 sample after drying in a desiccator for 1 and 18 days are shown in figure 6.10a-b, respectively. It is apparent that the both crystals samples dried for 1 and 18 days had the irregular shape and the distribution of their particle size was variable. Typical particles were in the size range approximately from 5 to 60 µm. It is evident that the NEW-1 sample has long term stability.

6.2 Characterisation of CMS - 40

For CMS-40, the CHN analysis found that the carbon is the major composition in the sample was 96.55% while 0.54 % is nitrogen and as expected there is no hydrogen in the sample.

The FTIR spectra for CMS-40 shown in Figure 6.11. There are five major bands appeared which were 956 cm^{-1}, 1290 cm^{-1}, 1543 cm^{-1}, 2021 cm^{-1}, and 3672 cm^{-1}.

Fig.6.12 shows the Scanning Electron Microscope images of CMS-40 sample. Microscope image (a) show the particle size of the CMS-40 which has an average size in range about 1-2 mm. Microscope image (b) shows the rough surface texture of the CMS-40 after magnified x 750.

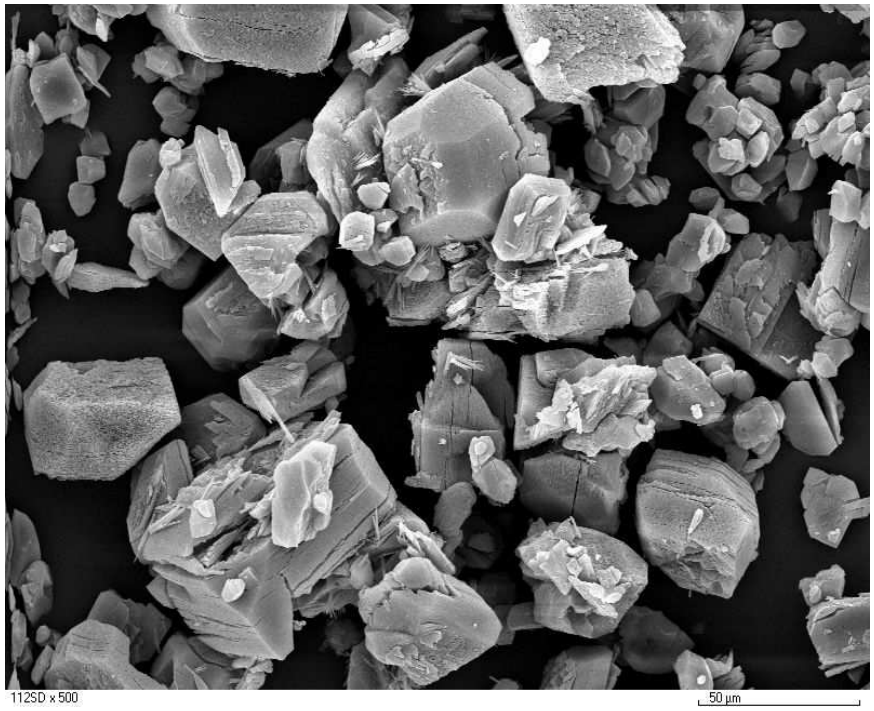

(a)

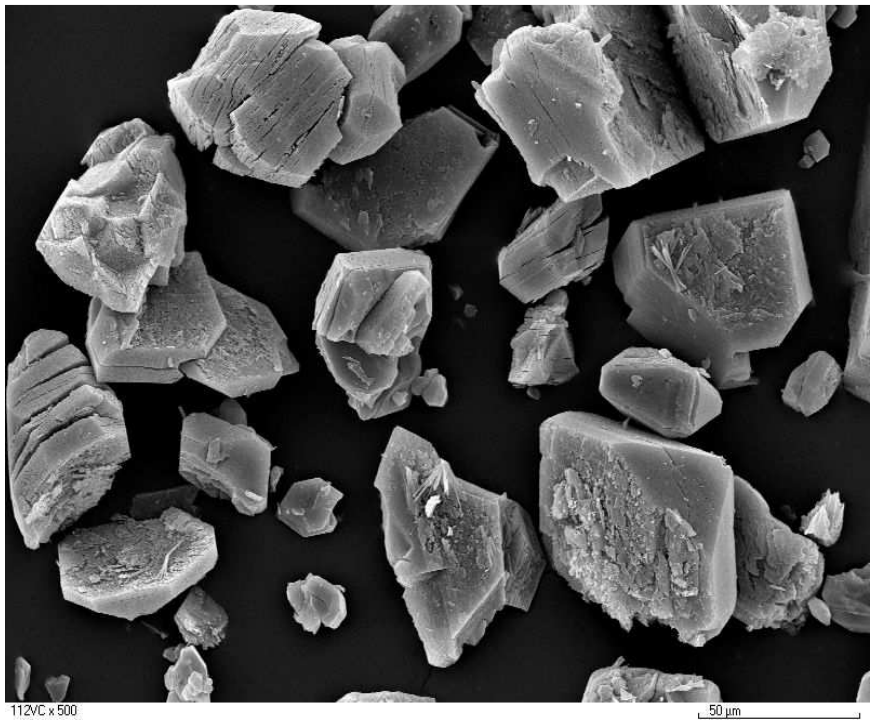

(b)

Figure 6.10 Images of NEW-1 sample dried in desiccator for a) 1 day and b) 18 days.

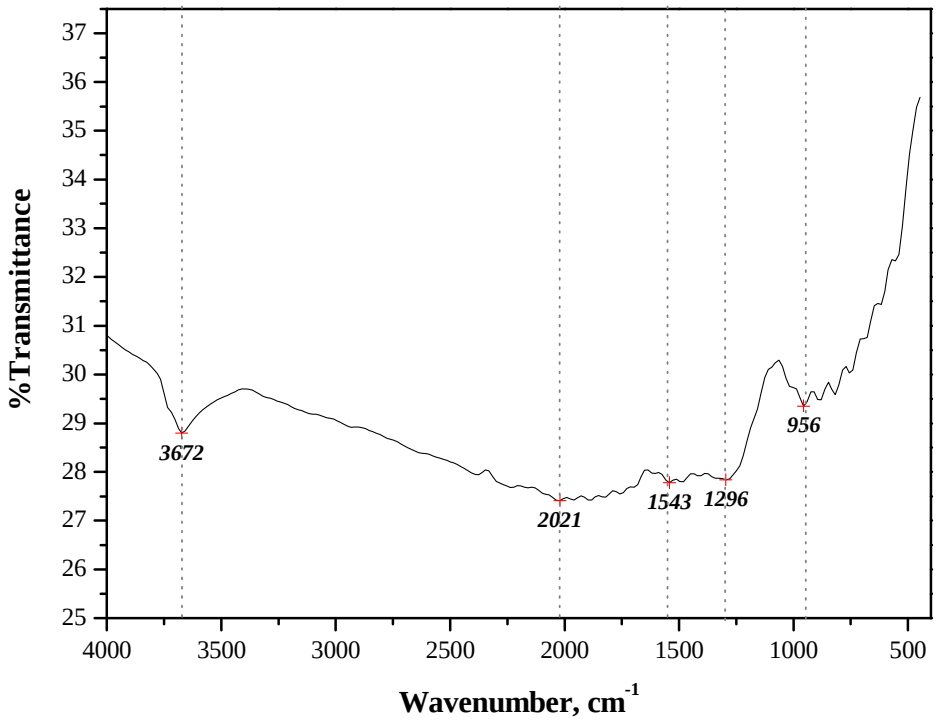

Figure 6.11 Fourier Transform Infrared spectrum for CMS-40

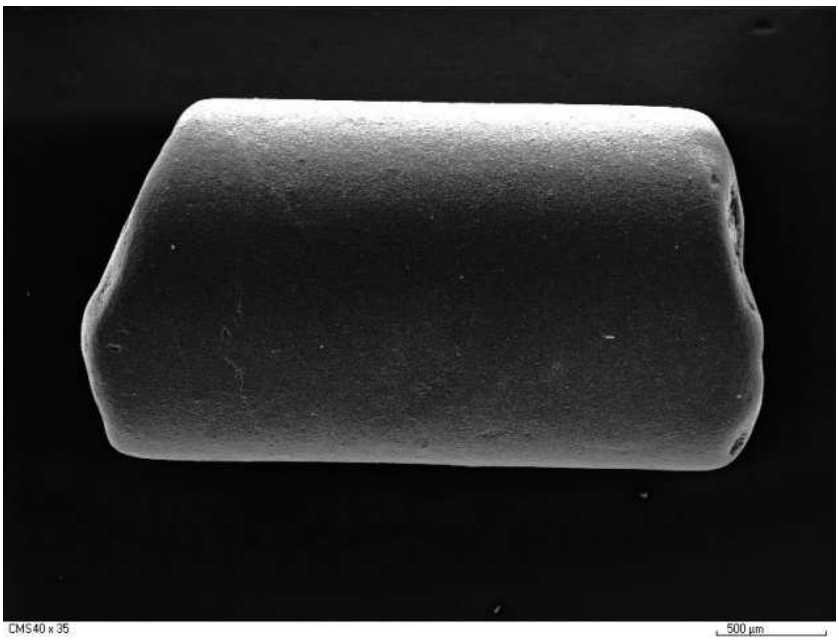

(a)

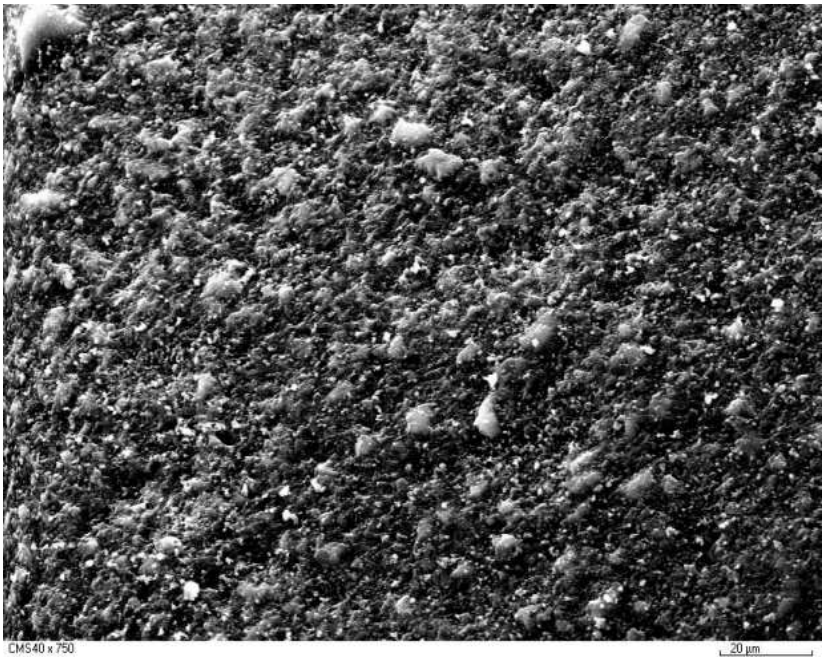

(b)

Figure 6.12 Images of CMS-40 a) magnified x 35 b) magnified x 750

6.3 Surface area and pore volume determination

6.3.1 Adsorption of Gases and vapours on NEW-1 sample

6.3.1.1 Gas adsorption

Gas and vapour adsorption on the NEW-1 sample were studied in order to determine the surface area and pore volume. The adsorption characteristics of both N_2 and Ar on the NEW-1 sample were investigated at 77 K, while the adsorption of CO_2 was also studied at 195 K and 273 K. High pressure adsorption of CO_2 and CH_4 on NEW-1 at 303 K were also investigated.

Figure 6.13 shows that the nitrogen adsorption isotherm is a typical type I as defined by the IUPAC classification scheme, but has an upward curvature due to pore filling at high relative pressure.[37] The argon adsorption isotherm is intermediate between types I and type II and does not reach a plateau.[37, 38] Both isotherms are very steep at $p/p^0 \sim 0.03$ due to rapid filling of the pores. A small amount of hysteresis is observed at the upper part of the adsorption branch, possibly indicating condensation in larger pores formed by deflects in the crystal structure. The maximum N_2 uptake at 978 mbar ($p/p^0 = 0.97$) was 2.876 mmol g^{-1}, while the maximum Ar uptake at 288 mbar ($p/p^0 = 0.90$) was 3.112 mmolg^{-1}. These uptake values and densities of N_2 (0.808 g cm^{-3})[39] and Ar (1.38 g cm^{-3})[40] were used to calculate the total pore volume, which was 0.099 $cm^3\,g^{-1}$ and 0.090 $cm^3\,g^{-1}$ for N_2 and Ar respectively. The Langmuir and BET equations were used to calculate the pore volume and surface area from both N_2 and Ar isotherms. Langmuir and BET graphs are shown in Appendix C, while their related parameters are summarised in Table 6.8. The surface areas determined from Ar adsorption from both Langmuir and BET plots are slightly higher than that of N_2. Also, the total pore volume obtained from Langmuir plots of N_2 and Ar were 0.072 $cm^3\ g^{-1}$ and 0.093 $cm^3\ g^{-1}$ respectively. The Langmuir pore volume of Ar is consistent with those values calculated from the maximum uptake. The Langmuir pore volume of N_2 is slightly lower than the value obtained from the maximum uptake due to the upward curvature of isotherm at high relative pressure, which is possible due to condensation in the pores.[37, 38] However, these calculated pore volumes are much lower than the crystallographic data (0.269 $cm^3\ g^{-1}$, section 6.1.1.1), and this indicates partial collapse of pores.

Figure 6.14 shows the isotherms of CO_2 adsorption/desorption on NEW-1 at 293 and 195 K, respectively. Both isotherms were type I behaviour, and desorption branches were reversible. The Dubinin-Radushkevich (D-R) plot for adsorption isotherm at 273 K gave a calculated micro pore volume of approximately 0.213 $cm^3 g^{-1}$ (assuming a density of CO_2 of 1.107 g cm^{-3}).[41] The pore structural characterisation data are given in table 6.8. The Langmuir plot of the adsorption isotherm at 195 K gave a calculated total pore volume 0.116 $cm^3 g^{-1}$. The surface area calculated from the BET plot was 241 $m^2 g^{-1}$ (195 K). The total pore volume value obtained from CO_2 adsorption at 195 K was slightly larger than the corresponding values obtained from nitrogen and argon adsorption. However, the values are still well below the crystallographic pore volume and indicate that there is partial pore collapse. The NEW-1 sample used in the water vapour adsorption experiments were label as decomposed NEW-1. The adsorption capacity of CO_2 on decomposed NEW-1 at 195 K was markedly decreased and this isotherm gave Langmuir pore volume 0.0835 $m^2 g^{-1}$.

High pressure isotherms of CO_2 and CH_4 adsorption on NEW-1 at 303 K are shown in Figure 6.15. Both isotherms were type I and the total pore volume calculated from the plateau of CO_2 and CH_4 high pressure adsorption isotherms were 0.0979 $cm^3 g^{-1}$ (2.384 mmol g^{-1}, ρ CO_2 = 1.070 g cm^{-3}) and 0.074 $cm^3 g^{-1}$ (2.146 mmol g^{-1}, ρ CH_4 = 0.4660 g cm^{-3}), respectively. These calculated pore volumes are consistent with those total pore volumes calculated from N_2, Ar and CO_2 adsorption isotherm at very low temperature. However, the density of the adsorbed phase for methane is uncertain because the measurements are well above the critical temperature. Therefore, the system is not undergoing a thermally activated phase change.

Table 6.8 shows Langmuir and BET Parameters of gases adsorption on NEW-1. The C parameters of the BET obtained from Ar, N_2 and CO_2 (195 K) adsorption on NEW-1 are larger than 200, indicative of the presence of micropores in NEW-1 sample. This result is consistent with the pore size determined by the X-ray crystallographic method. However, a BET graph with the C above 200 represents micropore volume filling, which may lead to an unrealistic value of the surface area.[37, 38, 42, 43] So the BET surface areas are only used as the primary data in this study.

6.3.1.2 Vapour adsorption

Four series of organic probe molecules and water were also used in this adsorption study to provide some more adsorption characteristics of the NEW-1 sample. These four types were alcohols (methanol, ethanol, *n*-propanol and *n*-butanol), chloromethane compounds (methyl chloride, chloroform and dichloromethane), alkanes (methane, ethane, propane, *n*-butane, *n*-pentane, *n*-hexane, *n*-heptane and *n*-nonane) and aromatics (benzene and toluene).

The adsorption isotherms of methanol, ethanol, *n*-propanol and *n*-butanol at 298 K, are shown in Figure 6.16a-b and 6.17 a-b, respectively. All alcohol isotherms were very steep at low relative pressure, a fact attributed to strong adsorbent-adsorbate interactions[44], and then followed by plateaus above ~ p/p^0 0.023, 0.025, 0.06 and 0.36 for methanol, ethanol, *n*-propanol and *n*-butanol respectively. The plateau was followed by another steep uptake for methanol and ethanol due to the pore filling which occurred at a relative pressure close to 1. The *n*-propanol adsorption isotherm exhibited a second plateau, attributed to structural change of NEW-1 to accommodate more adsorbate molecules. In the case of *n*-butanol, its adsorption isotherm showed smaller upward curvature than other alcohols after reaching the plateau. The adsorption isotherm of methyl chloride at 195K is shown in Figure 6.18. The isotherm had a steep uptake at very low pressure followed by the plateau (~3.09 mmol g^{-1} with p/p^0 ~0.197) and upward curvature at high relative pressure. The latter is a consequence of pore filling. Isotherms of chloroform and dichloromethane adsorption at 298 K are shown in Figure 6.19 a-b. The chloroform isotherm was convex towards the relative pressure axis at the initial point of adsorption (p/p^0 up to 0.015), while dichloromethane showed steep uptake at very low relative pressure. This small convex part of the chloroform isotherm can be attributed to an opening up of the desolvated pore structure. A small amount of hysteresis was also observed during desorption.

Adsorption isotherms for methane, ethane and propane adsorption at 195 K are shown in Figure 6.20 and 6.21, respectively. Both methane and ethane isotherms were type I in the IUPAC classification scheme while propane exhibited and intermediate type between type I and Type II. All methane, ethane and propane adsorption isotherm showed a steep uptake at very relative pressure. Methane adsorption reached a plateau at 298 mbar while ethane and propane reached the plateau at ~ p/p^0 0.083 and ~ p/p^0 0.132,

respectively. Isotherms for *n*-butane adsorption on NEW-1 at 273 K is shown in Figure 6.22 a. *n*-Butane isotherms was type I in the IUPAC classification scheme but has a upward curvature at high relative pressure. *n*-Butane reached the plateau at ~ p/p^0 0.139 with the amount adsorbed ~ 1.94 mmol g^{-1}.

Isotherms for *n*-pentane, *n*-hexane, *n*-heptane, *n*-heptane and *n*-nonane adsorption on NEW-1 at 298 K are shown in Figure 6.22- 6.24. All these adsorption isotherms showed initial convex curvature to the pressure axis followed by a steep uptake adsorption stage of adsorption, a plateau at p/p^0 ~ 0.01 (*n*-pentane), 0.06 (*n*-hexane), 0.03 (*n*-heptane), 0.10 (*n*-octane) and 0.08 (*n*-nonane), then a gradual uptake due to pores filling (see Table 6.9 and 6.10). All alkane adsorption isotherms also exhibited a small amount of hysteresis in the desorption branches. The steepest part of the toluene adsorption isotherm was in relative pressure range 0.05-0.2 and this was followed by a point of inflection (~ p/p^0 0.27) and another gradual uptake. Similarly, a small amount of hysteresis is observed during the desorption process (Figure 6.25). The benzene adsorption isotherms were similar.

Comparison of all vapour isotherms shows that methanol, ethanol, chloroform, *n*-butane, *n*-pentane, *n*-hexane, *n*-heptane *n*-octane, *n*-nonane and toluene isotherms are type I, according to the IUPAC classification scheme, but have deviations at both low pressure due to framework flexibility and high relative pressure due to pore filling. The curvature at low pressure becomes increasingly apparent with increasing temperature (see Chapter 7). Additionally, these isotherms can also be classified as sub-class H4 hysteresis loop. In the same way, the step isotherm of *n*-propanol is type VI. NEW-1 sample has a uniform channel pore as shown by crystallographic results. Additionally, all desorption isotherms of these vapour exhibited a small amount of hysteresis in the desorption braches at high relative pressure. These hysteresis branches contributed to the capillary condensation of vapour in the larger pores of NEW-1 sample formed by structural defects. The step adsorption isotherm found in *n*-propanol revealed that two adsorption processes possibly occurred, hydrogen bonding with the framework and then filling of the pores. More details on these two processes are discussed in Chapter 7. The isotherms of both benzene and toluene have an initial convex curvature with lower uptake at low relative pressure. This is attributed to framework structural change induced by the aromatic molecules with the larger second cross-sectional dimension molecule (see Table 6.11)

Table 6.9 and 6.10 showing the Langmuir parameters, Langmuir pore volume and total pore volumes. The total pore volumes were calculated from the maximum adsorption capacity of the adsorbates at high relative pressure. The total pore volume calculated for adsorption of the series of alcohols on NEW-1 decreased with increasing molecular dimensions in the order of methanol 0.263 $cm^3 g^{-1}$ > ethanol 0.262 $cm^3 g^{-1}$ > *n*-propanol 0.244 $cm^3 g^{-1}$ > *n*-butanol 0.200 $cm^3 g^{-1}$. Total pore volume obtained for methyl chloride, chloroform and dichloromethane were 0.231 cm^3g^{-1}, 0.267 cm^3g^{-1}, and 0.253 cm^3g^{-1}, respectively. In case of the alkane series, the pore volume increased with increasing of the molecular dimension of molecule with the order of methane < ethane < propane, *n*-butane < *n*-pentane < *n*-hexane < *n*-heptane. Total pore volume of benzene and toluene were 0.254 cm^3g^-1 and 0.193 cm^3g^{-1}, respectively. As seen in Table 6.9 and Table 6.10, the pore volume calculated from the Langmuir plots is usually lower than those values obtained from the maximum adsorption capacity due to the Langmuir model estimating the plateau of the isotherm rather than the pore-filling effect at high relative pressure.[38, 43, 44] As will be discussed in chapter 7, the isotherm plateaus usually have a stoichiometric relationship with the crystallographic formula unit.

Figure 6.26 shows the adsorption isotherms of water on NEW-1 at 298. All isotherms were type V in the IUPAC classification scheme. Initially, the amount adsorbed at low relative pressure is low due to weak adsorbate-adsorbent interaction. However, the significant uptake occurred at higher pressure (p/p^0 0.15-0.3). This significant uptake was followed by the plateau and the second uptake due to pore filling. Calculated pore volume at the plateau of water adsorption isotherm of the 1st run was 0.085 cm^3g^{-1}, which is consistent with the total pore volume calculated from N_2, Ar and CO_2 adsorption on NEW-1. However, the total pore volumes calculated for 2nd and 3rd water adsorption isotherms are similar to the total pore volumes of 0.115 cm^3g^{-1} and 0.178 cm^3g^{-1} at the plateau and at the second uptake at high relative pressure respectively. The total pore volume calculated from the 2nd and 3rd water adsorption isotherm runs were significantly higher than those values calculated from the 1st run of water and N_2, Ar and CO_2 adsorption, indicating that the structure of NEW-1 had increased slightly after adsorbing the water vapour.

Gurvitsch's rule states that the amount adsorbed at relative pressure close 1 represent complete filling of the pores with liquid adsorbate provided the isotherm is parallel to the relative pressure axis. Typically, total pore volumes obtained for a range of adsorbates agree within ± 5%. The calculated total pore volumes from many of the

adsorbates agree with Gurvitsch's rule and the crystallographic value obtained from PLATON. This is evidence that the pore structure of NEW-1 was recovered after adsorption of some species. The role of framework flexibility in NEW-1 is discussed in detail in Chapter 7 in relation to molecular dimensions and isosteric enthalpies of adsorption.

6.3.2 Gases adsorption on CMS-40 sample

Nitrogen adsorption on CMS-40 at 77 K was very slow due to activated diffusion effects. Therefore, the porous structure of CMS-40 was characterized, using CO_2 adsorption, at 298 K. As seen in Figure 6.27, the CO_2 isotherm at 298 K is a type I adsorption isotherm as defined by the IUPAC classification scheme, confirming the present of uniform micropores in the sample. Furthermore, it is apparent that no hysteresis occurred. The Dubinnin-Radushkevich (D-R) equation was used to analyse the isotherm and to characterise the micropore volume of CMS-40, which was 0.312 $cm^3\ g^{-1}$ and the correlation is 0.9978.

Table 6.11 Comparison of physical parameters for the probe molecules used in this study.[39, 41, 45-49]

Molecule	Polarisability x 10^{25}/cm^3	Kinetic diameter (pm)	Molecular dimensions x, y, z (pm)
O_2	15.812	346.7	298.5, 293.0, 405.2
N_2	17.403	368.0	305.4, 299.1, 404.6
Ar	16.411	354.2	363, 351
CO_2	29.11	330.0	333.9, 318.9, 536.1
H_2O	82.3-95.0	264.1	322.6, 291.7, 388.8
Alcohol series			
Methanol	32.3-33.2	362.6	381.0 418.0 495.0
Ethanol	51.1-54.5	453.0	416.0, 427.0, 633.0
n-Propanol	65	498.0	n/a
n-Butanol	89.9	540.0	416, 446, 891
Chloromethane series			
Methyl chloride	47.2-53.5	418.2	n/a
Chloroform	82.3-95.0	538.9	618.1, 571.3, 461.3
Dichloromethane	64.8-79.3	489.8	n/a
Alkane series			
Methane	25.93	375.8	382.9, 410.1, 394.2
Ethane	44.3-44.7	443	380.9, 407.9, 482.1
Propane	33.3-39.3	430-511	660.6, 451.6, 402.0
n-butane	82.0	468.7	785.5, 451.9, 401.4
n-Pentane	99.9	450.0	910.1, 452.2, 401.4
n-Hexane	119	430.0	1034.4, 453.6, 401.4
n-Heptane	136.1	430.0	1158.9, 452.3, 401.4
n-Octane	159	430.0	1283.3, 401.4, 452.4
n-Nonane	174	n/a	1407.6, 401.4, 453.7
Aromatic series			
Benzene	100-107.4	534.9	662.8, 733.7, 327.7
Toluene	118-123	525.0	662.5, 401.2, 825.2

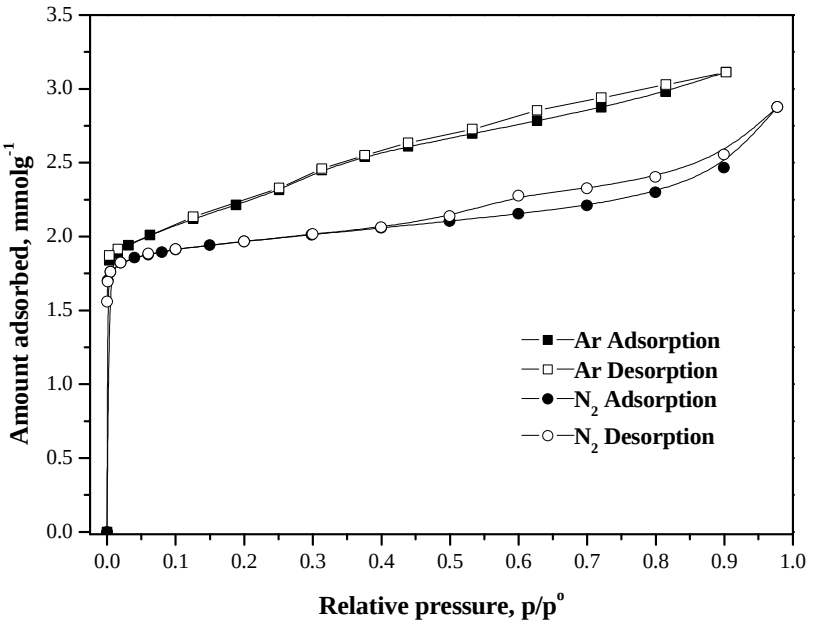

Figure 6.13 Nitrogen and argon adsorption/desorption isotherms for NEW-1 at 77 K

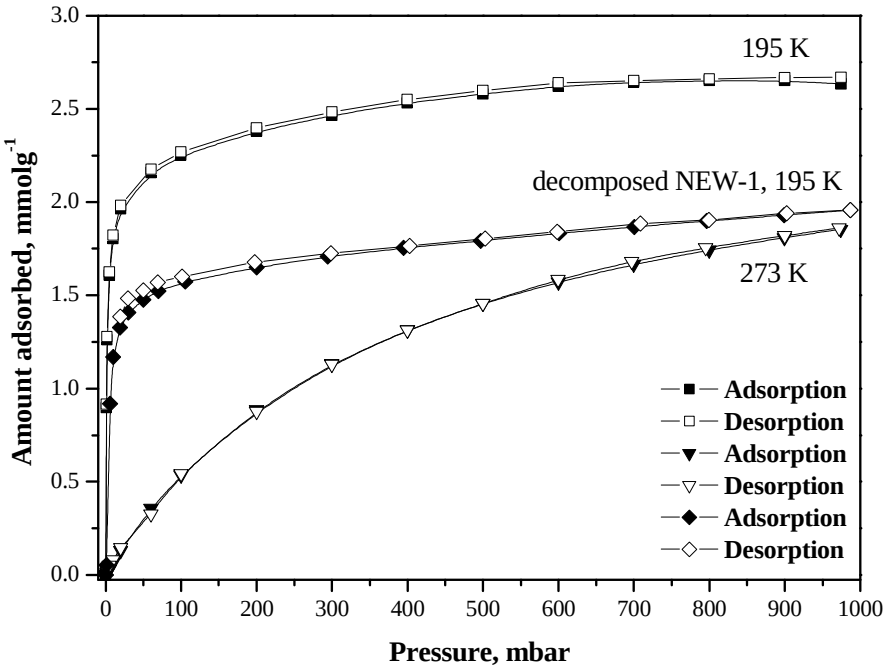

Figure 6.14 Carbon dioxide adsorption/desorption isotherms for NEW-1

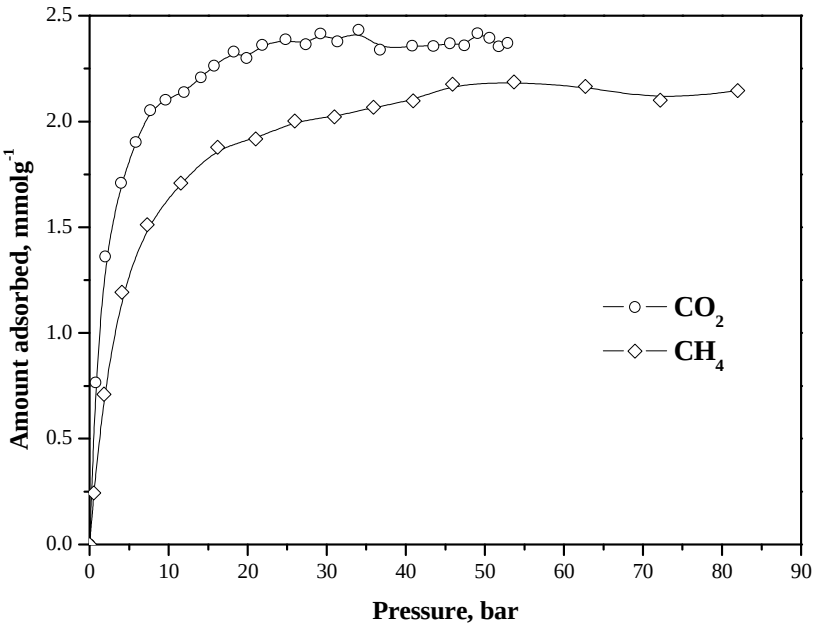

Figure 6.15 Isotherms of CO_2 and CH_4 adsorption on NEW-1 at high pressure

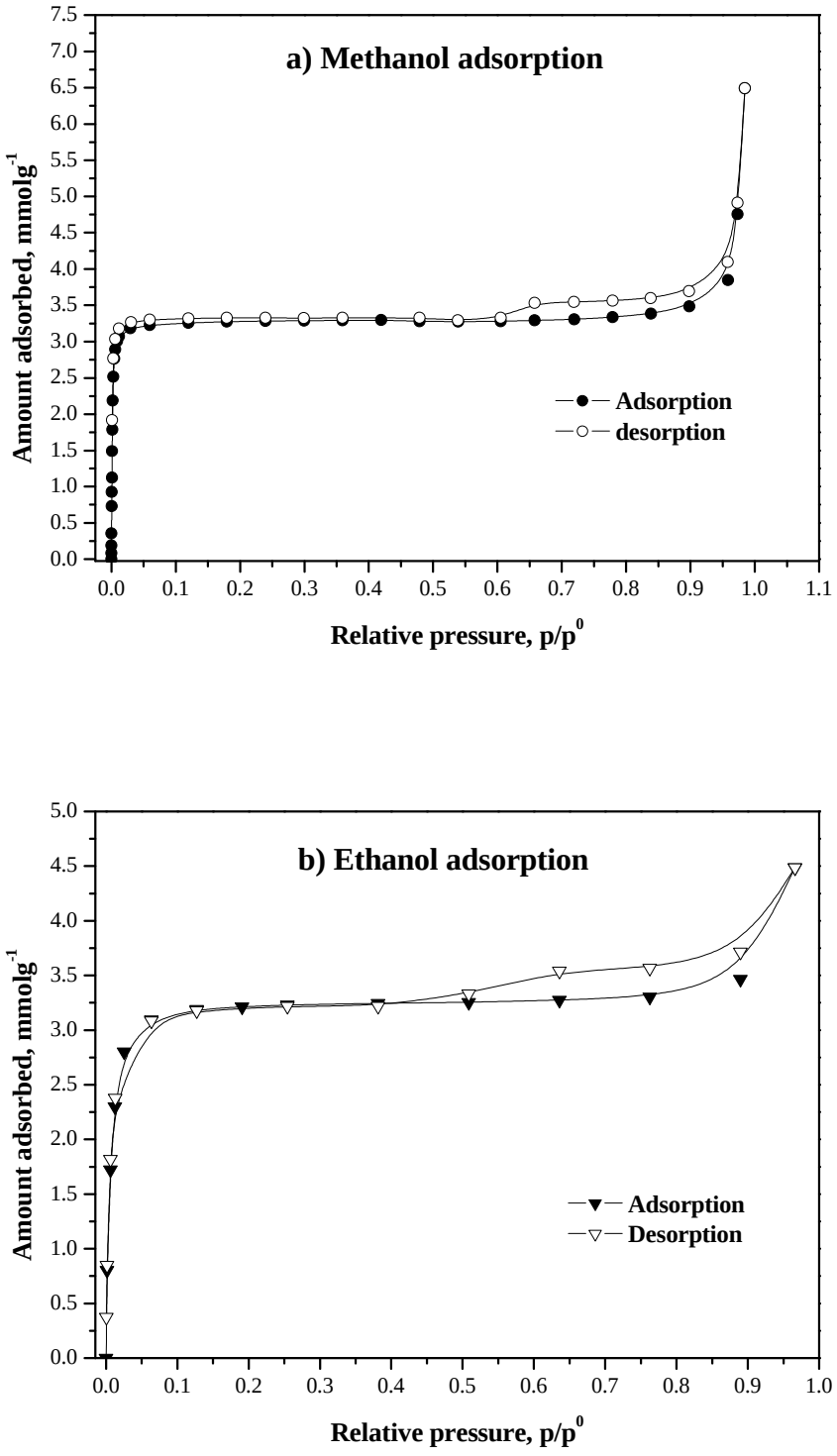

Figure 6.16 Isotherms of a) methanol and b) ethanol adsorption on NEW-1 at 298 K.

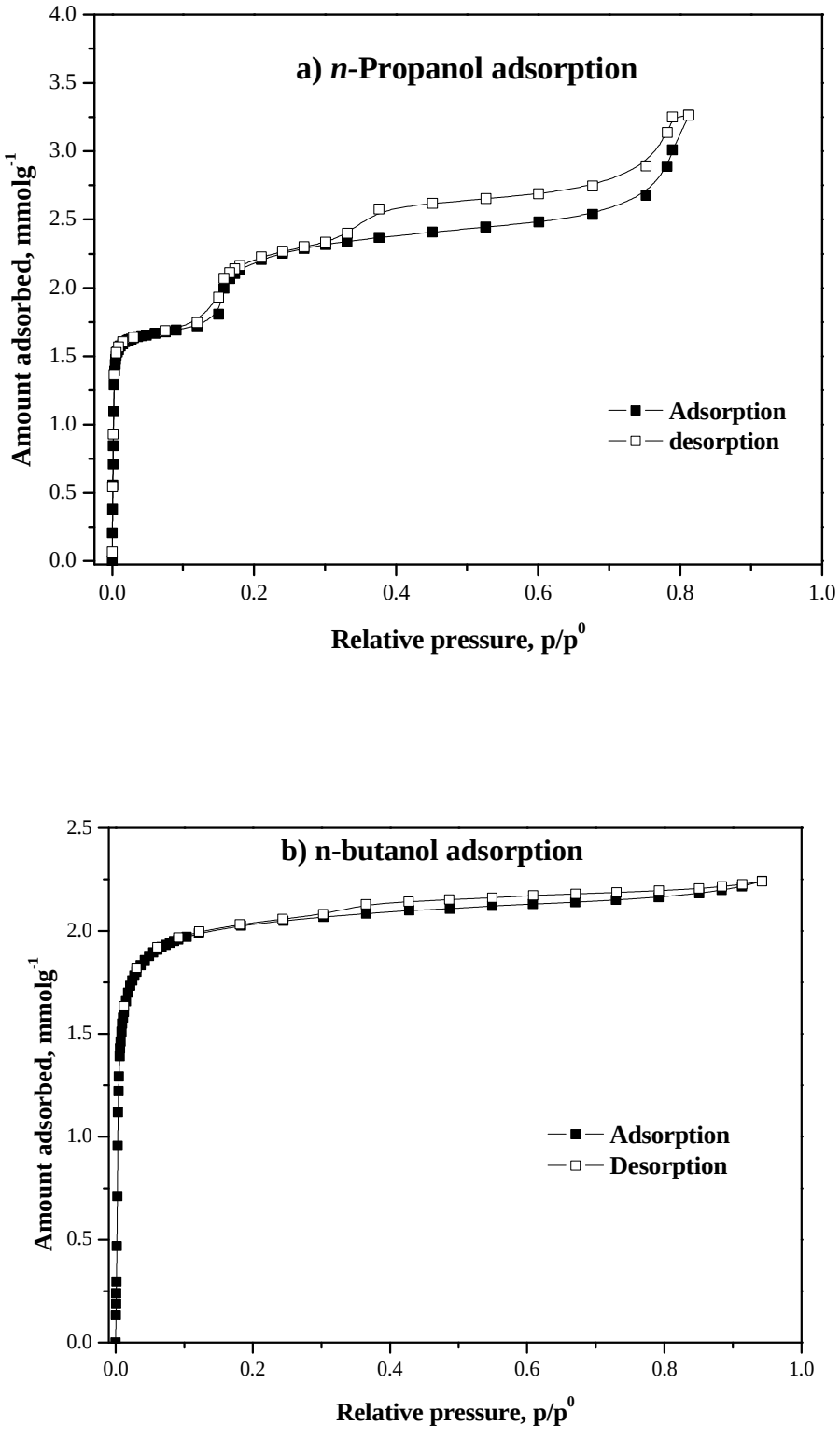

Figure 6.17 Isotherms of a) *n*-propanol and b) *n*-butanol adsorption on NEW-1 at 298 K.

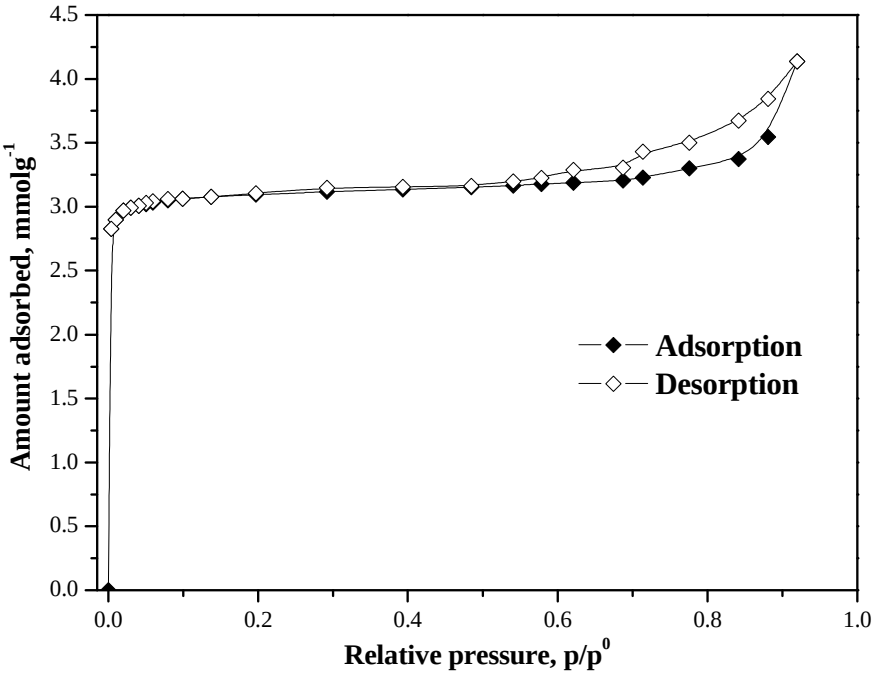

Figure 6.18 Isotherms of methyl chloride adsorption on NEW-1 at 195 K

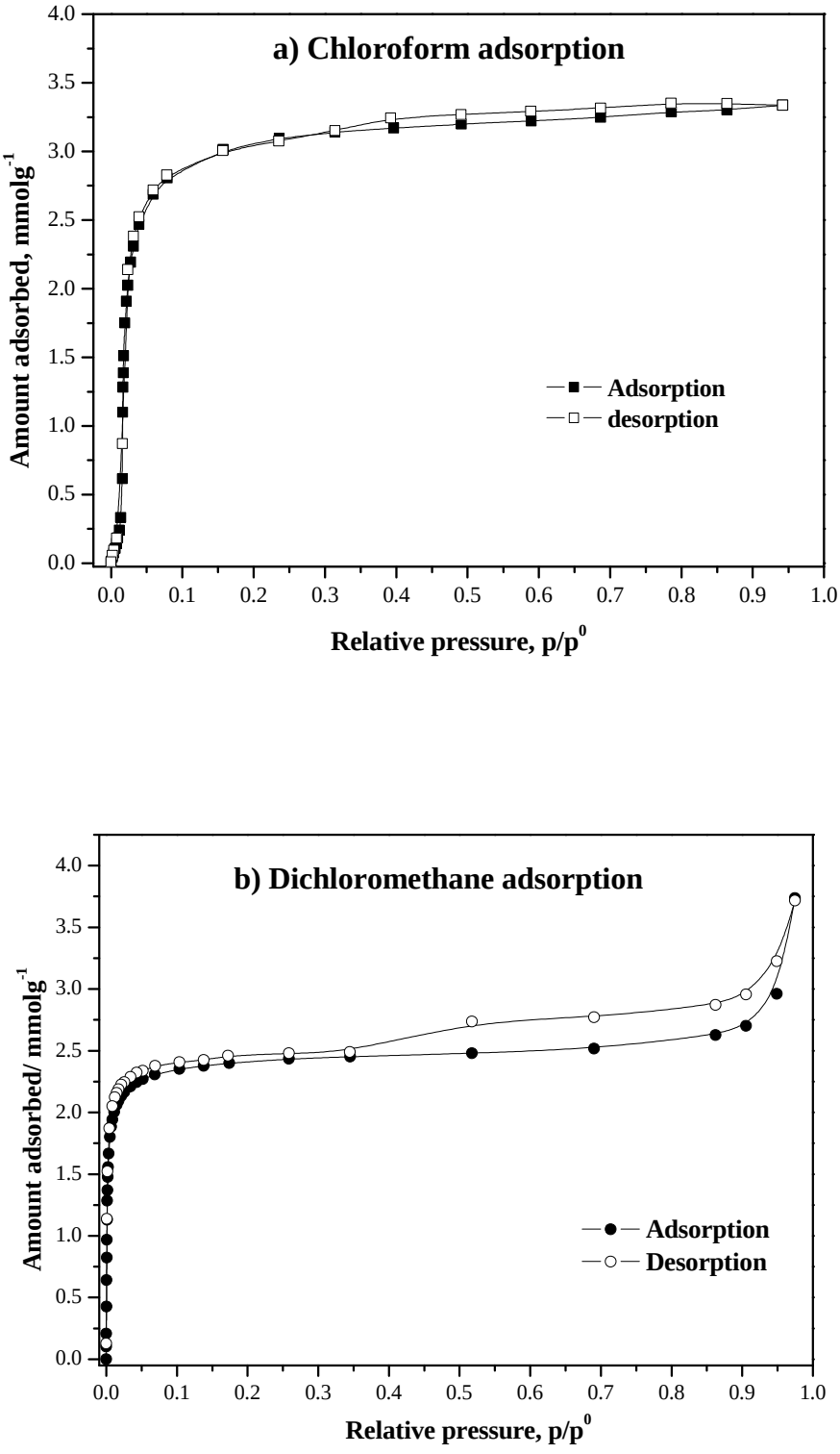

Figure 6.19 Isotherms of a) chloroform and b) dichloromethane adsorption on NEW-1 at 298 K

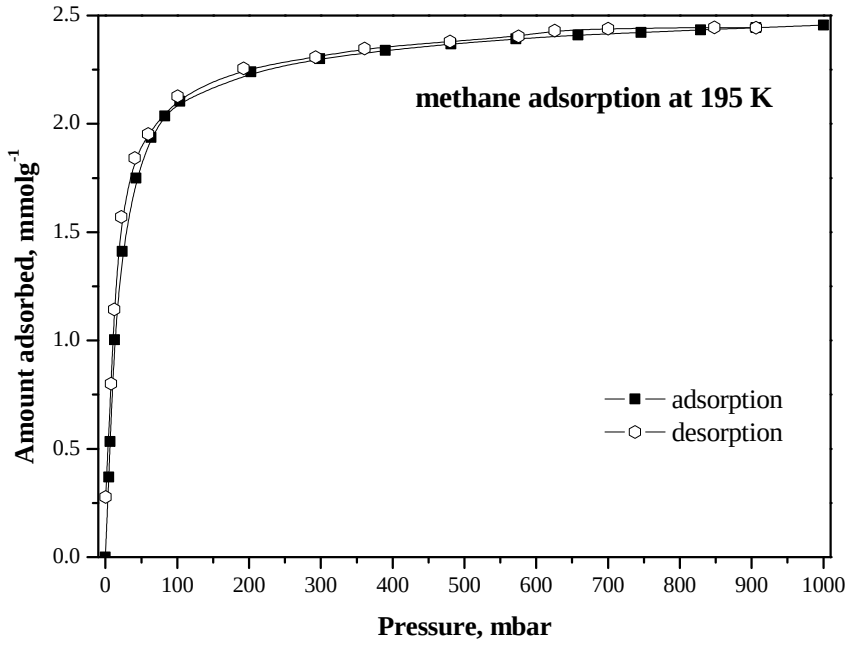

Figure 6.20 Isotherms of methane adsorption/desorption on NEW-1 sample at 195 K.

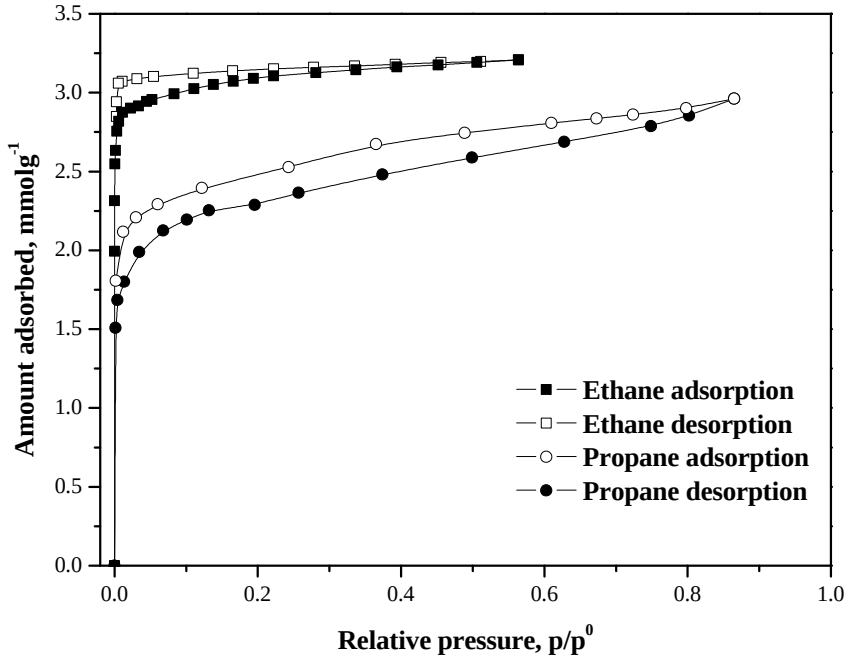

Figure 6.21 Isotherms of ethane and propane adsorption on NEW-1 sample at 195 K.

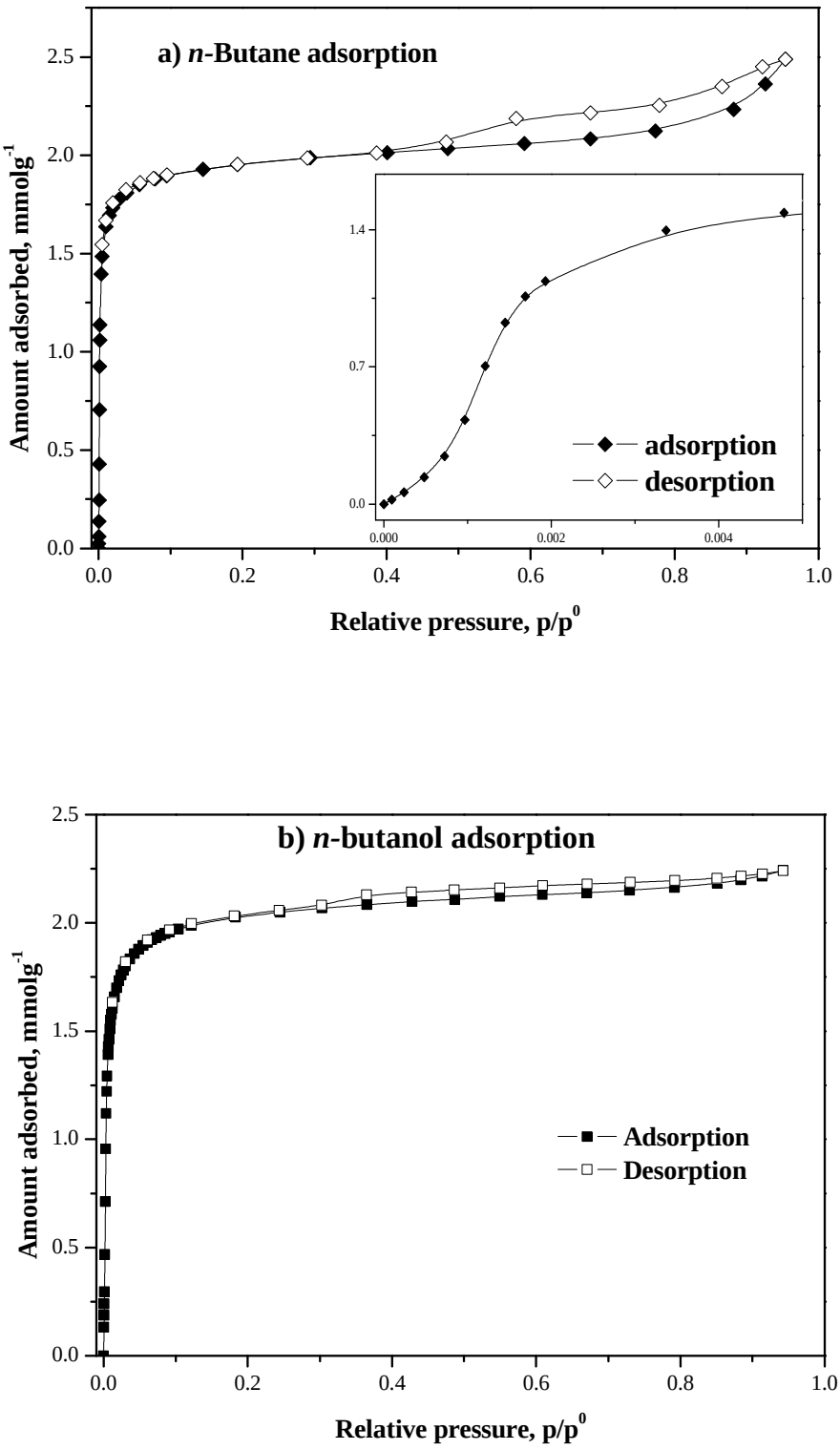

Figure 6.22 Isotherms of a) *n*-butane and b) *n*- pentane alkane adsorption on NEW-1 sample at 273 K and 298 K, respectively, with inset at low relative pressure

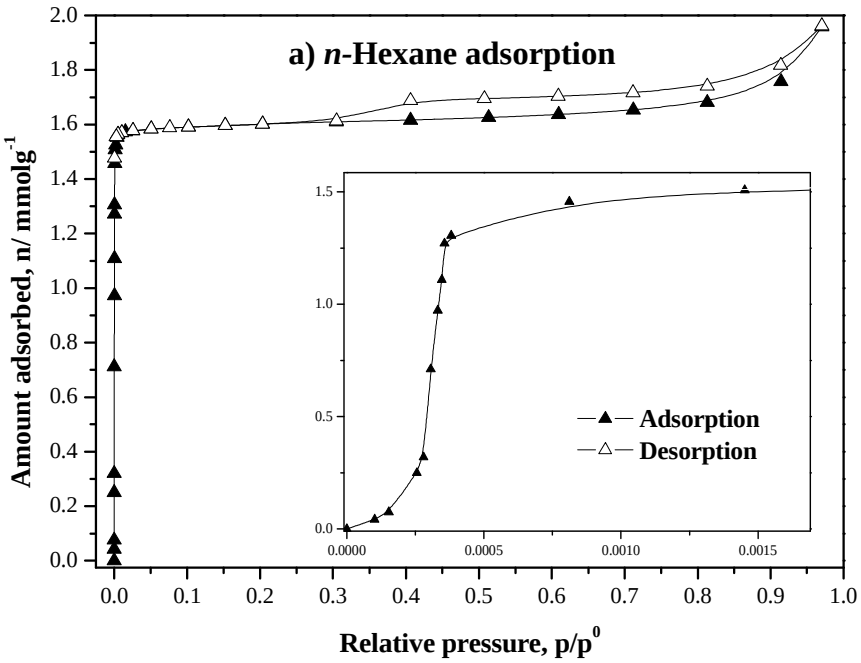

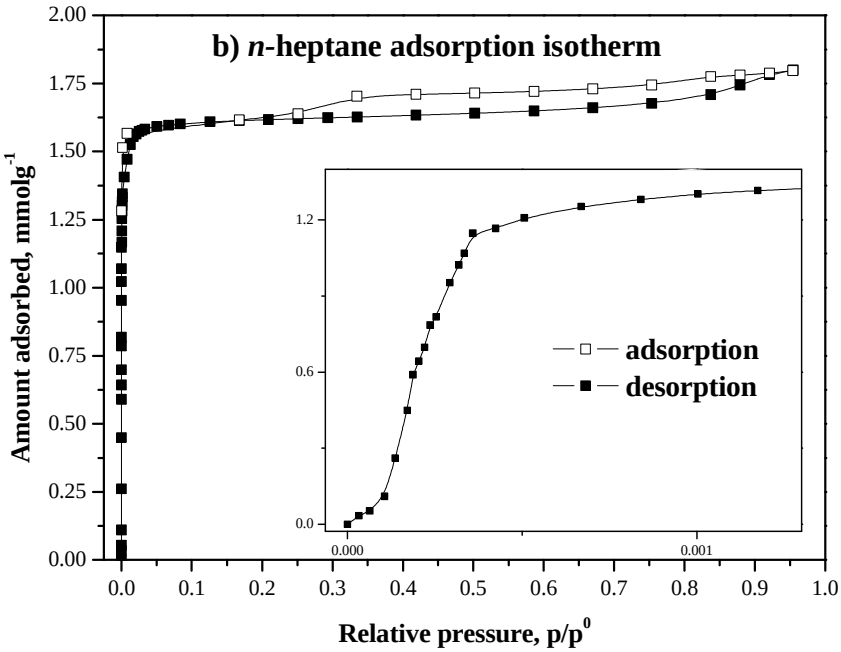

Figure 6.23 Isotherm of Isotherms of alkane adsorption on NEW-1 sample at 298 K a) *n*- hexane and b) *n*-heptane with inset at low relative pressure

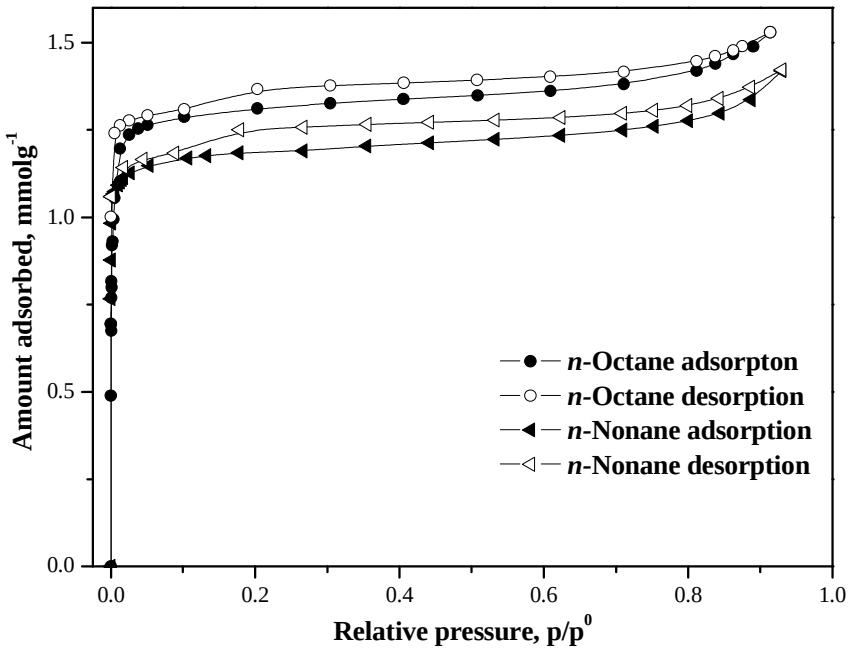

Figure 6.24 Isotherm of *n*-octane and *n*-nonane adsorption on NEW-1 at 298 K.

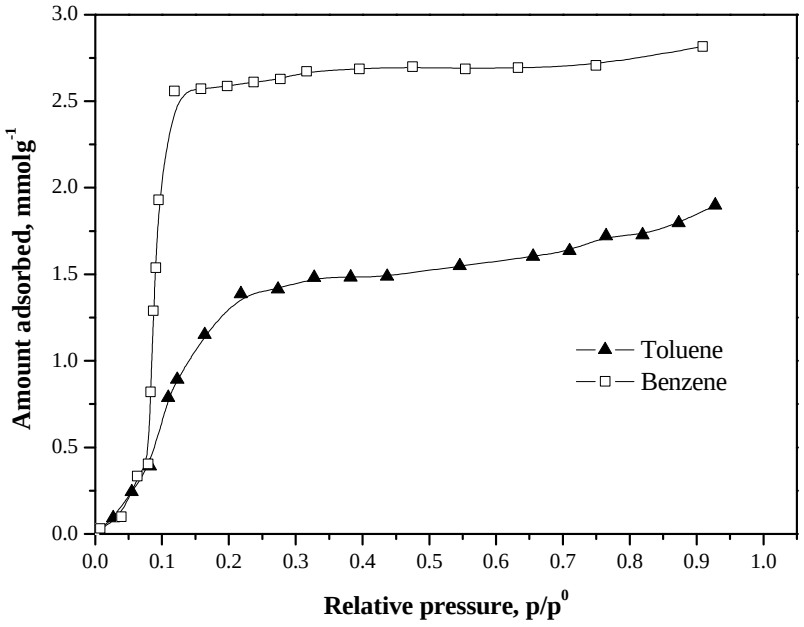

Figure 6.25 Isotherms of benzene and toluene adsorption on NEW-1 at 298 K.

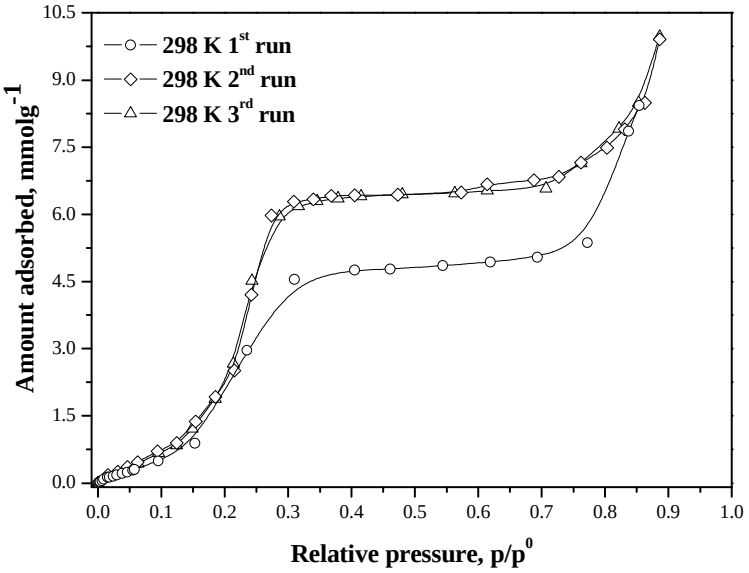

Figure 6.26 Isotherms of water adsorption on NEW-1 sample at 298 K.

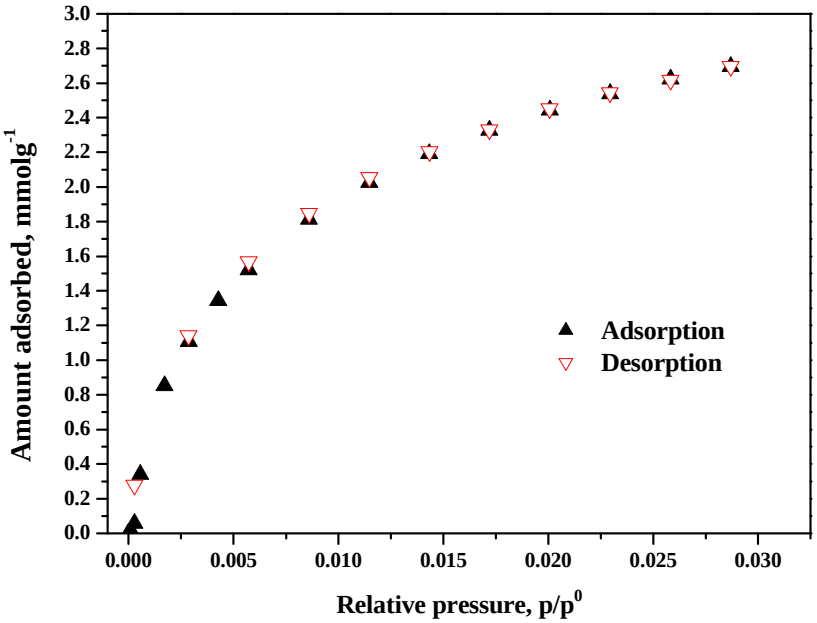

Figure 6.27 Adsorption/desorption isotherm of CO_2 on CMS-40 at 298 K.

6.4 References

1. Tran, D. T.; Fan, X.; Brennan, D. P.; Zavalij, P. Y.; Oliver, S. R. J., Open Metal-Organic Framework Containing Cuprate Chains. *Inorg. Chem.* **2005,** 44, (18), 6192-6.

2. Liu, Y.-H.; Lu, Y.-L.; Tsai, H.-L.; Wang, J.-C.; Lu, K.-L., Hydrothermal Synthesis, Crystal Structure, and Magnetic Property of Copper(II) Coordination Networks with Chessboard Tunnels. *J. Solid State Chem.* **2001,** 158, (2), 315-9.

3. Chui, S. S.-Y.; Lo, S. M.-F.; Charmant, J. P. H.; Orpen, A. G.; Williams, I. D., A Chemically Functionalizable Nanoporous Material $[Cu_3(TMA)_2(H_2O)_3]n$. *Science* **1999,** 283, (5405), 1148-50.

4. Lu, J. Y.; Schauss, V., A novel double-helical-chain coordination polymer constructed from 2,2'-biphenyldicarboxylate-linked binuclear-copper motif. *Inorg. Chem. Commun.* **2003,** 6, (10), 1332-4.

5. Tran, D. T.; Chernova, N. A.; Chu, D.; Oliver, A. G.; Oliver, S. R. J., 3-D Metal Organic Framework Based on Cationic 2-D Cuprate Layers: $Cu_3(OH)_4[C_{10}H_6(SO_3)_2]$. *Cryst. Growth Des.* **2009,** 10, (2), 874-9.

6. Lin, X.; Telepeni, I.; Blake, A. J.; Dailly, A.; Brown, C. M.; Simmons, J. M.; Zoppi, M.; Walker, G. S.; Thomas, K. M.; Mays, T. J.; Hubberstey, P.; Champness, N. R.; Schroder, M., High Capacity Hydrogen Adsorption in Cu(II) Tetracarboxylate Framework Materials: The Role of Pore Size, Ligand Functionalization, and Exposed Metal Sites. *J. Am. Chem. Soc.* **2009,** 131, (6), 2159-71.

7. Jahn, H. A.; Teller, E., Stability of Polyatomic Molecules in Degenerate Electronic States. I. Orbital Degeneracy. *Proceedings of the Royal Society of London. Series A - Mathematical and Physical Sciences* **1937,** 161, (905), 220-35.

8. Tzuoo-Tsair, L.; Hui-Lien, T.; Shang-Li, Y.; Yen-Hsiang, L.; Yadav, R. D.; Chan-Cheng, S.; Chuen-Her, U.; Lee-Gin, L.; Kuang-Lieh, L., Crystal Engineering: Toward Intersecting Channels from a Neutral Network with a bcu-Type Topology13. *Angew. Chem. Int. Ed.* **2005,** 44, (37), 6063-7.

9. Yi, L.; Zhu, L.-N.; Ding, B.; Cheng, P.; Liao, D.-Z.; Zhai, Y.-P.; Yan, S.-P.; Jiang, Z.-H., Synthesis, structures and properties of two novel copper(II) complexes with hydrogen bonding supramolecular networks. *Transition Met. Chem.* **2004,** 29, (2), 200-4.

10. Lu, J. Y.; Babb, A. M., An extremely stable open-framework metal-organic polymer with expandable structure and selective adsorption capability. *Chem. Commun.* **2002**, (13), 1340-1.

11. Xiao, B.; Byrne, P. J.; Wheatley, P. S.; Wragg, D. S.; Zhao, X.; Fletcher, A. J.; Thomas, K. M.; Peters, L.; EvansJohn, S. O.; Warren, J. E.; Zhou, W.; Morris, R. E., Chemically blockable transformation and ultraselective low-pressure gas adsorption in a non-porous metal organic framework. *Nat Chem* **2009,** 1, (4), 289-94.

12. Kiriyama, R.; Ibamoto, H.; Matsuo, K., The crystal structure of cupric formate tetrahydrate, $Cu(HCO_2)_2.4H_2O$. *Acta Cryst.* **1954** 7, 482-3.

13. Martin, R. L.; Waterman, H., Magnetic studies with copper(II) salts. Part IV. Remarkable magnetic behaviour of copper(II) formate and its hydrates. *J. Chem. Soc.* **1959**, 1359 - 70.

14. Macrae, C. F.; Edgington, P. R.; McCabe, P.; Pidcock, E.; Shields, G. P.; Taylor, R.; Towler, M.; van de Streek, J., Mercury: visualization and analysis of crystal structures. *J. Appl. Crystallogr.* **2006,** 39, (3), 453-7.

15. Spek, A., Single-crystal structure validation with the program PLATON. *J. Appl. Crystallogr.* **2003,** 36, (1), 7-13.

16. Wang, Z.; Zhang, B.; Otsuka, T.; Inoue, K.; Kobayashi, H.; Kurmoo, M., Anionic NaCl-type frameworks of $[MnII(HCOO)^{3-}]$, templated by alkylammonium, exhibit weak ferromagnetism. *Dalton Transactions* **2004**, (15), 2209-16.

17. Irena, S.; Stefan, K., Solvent-Induced Pore-Size Adjustment in the Metal-Organic Framework $[Mg_3(ndc)_3(dmf)_4]$ (ndc = naphthalenedicarboxylate). *Eur. J. Inorg. Chem.* **2006,** 2006, (22), 4564-9.

18. Tao, J.; Tong, M.-L.; Chen, X.-M., Hydrothermal synthesis and crystal structures of three-dimensional co-ordination frameworks constructed with mixed terephthalate (tp) and 4,4[prime or minute]-bipyridine (4,4[prime or minute]-bipy) ligands: [M(tp)(4,4[prime or minute]-bipy)] (M = CoII, CdII or ZnII). *J. Chem. Soc., Dalton Trans.* **2000**, (20), 3669-74.

19. Ying, E.-B.; Zheng, Y.-Q.; Zhang, H.-J., Syntheses and crystal structures of $[Mn(H_2O)_4(bpy)]L \cdot 4H_2O$, $[Mn(H_2O)_4(bpy)]L' \cdot 4H_2O$ and $[Zn(H_2O)4(bpy)]L \cdot 4H_2O$ (H_2L = succinic acid, H_2L' = fumaric acid) *J. Coord. Chem.* **2004,** 57, (6), 459 - 67.

20. Xu, J.-Y.; Hurtado, E. J.; Lobkovsky, E. B.; Chen, B., Poly[(2-trans-di-4-pyridylethylene-2N:N')(2-fumarato-2O:O')zinc(II)]. *Acta Cryst. E* **2007,** 63, m2205.

21. Wu, C.-D.; Lu, C.-Z.; Wu, D.-M.; Zhuang, H.-H.; Huang, J.-S., Hydrothermal synthesis of two new zinc coordination polymers with mixed ligands. *Inorg. Chem. Commun.* **2001,** 4, (10), 561-4.

22. Gelfand, L. S.; Pytlewski, L. L.; Mikulski, C. M.; Speca, A. N.; Karayannis, N. M., Copper(II) chloride adducts with nicotinic and isonicotinic acid N-oxides. *Inorg. Chim. Acta* **1979,** 33, 265-8.

23. Gelfand, L. S.; Pytlewski, L. L.; Speca, A. N.; Mikulski, C. M.; Karayannis, N. M., Transition metal acetate reactions with nicotinic and isonicotinic acid N-oxides. *J. Inorg. Nucl. Chem.* **1980,** 42, (2), 209-18.

24. Knuuttila, H., The structure of trinuclear Cu(II) complex with isonicotinic acid N-oxide, pentaaquadi-[mu]-hydroxobis-[mu]-(ionicotinato N-oxide)bis(isonicotinato N-oxide)tricopper(II) dihydrate. *Inorg. Chim. Acta* **1983,** 72, 11-6.

25. Can, N.; Sözerli Can, S. E.; Ataç, A.; Bardak, F., Structural characterization and luminescence properties of an isonicotinic acid N-oxide Mn(II) complex. *Polyhedron* **2004,** 23, (7), 1109-13.

26. Williams, D. H.; Fleming, I., *Spectroscopic Methods in Organic Chemistry* 6ed.; McGraw-Hill Higher Education: 2006; p 304.

27. Jacob, M. M. E.; Arof, A. K., FTIR studies of DMF plasticized polyvinyledene fluoride based polymer electrolytes. *Electrochimica Acta* **2000,** 45, (10), 1701-6.

28. Umadevi, M.; Poornima, R. R., Investigations of molecular interactions in propionic acid-N,N-dimethyl formamide binary system--FTIR study. *Spectrochimica Acta Part A: Molecular and Biomolecular Spectroscopy* **2009,** 73, (5), 815-22.

29. Bardak, F.; Atac, A.; Kurt, M., Infrared and Raman study of some isonicotinic acid metal(II) halide and tetracyanonickelate complexes. *Spectrochim. Acta, Part A* **2009,** 71, (5), 1896-900.

30. Koczon, P.; Dobrowolski, J. C.; Lewandowski, W.; Mazurek, A. P., Experimental and theoretical IR and Raman spectra of picolinic, nicotinic and isonicotinic acids. *J. Mol. Struct.* **2003,** 655, (1), 89-95.

31. Atac, A.; Bardak, F., Synthesis and vibrational spectroscopic study of some metal(II) halide and tetracyanonickelate complexes of isonicotinic acid. *TUrk. J. Chem.* **2006,** 30, (5), 609-18.

32. Cernák, J.; Pavlová, A.; Orendácová, A.; Kajnaková, M.; Kuchár, J., A novel two-dimensional Ni(II) fumarato complex: Solvothermal synthesis, crystal structure and magnetic properties. *Polyhedron* **2009,** 28, (14), 2893-8.

33. Zhu, W.-H.; Wang, Z.-M.; Gao, S., Two 3D Porous Lanthanide Fumarate Oxalate Frameworks Exhibiting Framework Dynamics and Luminescent Change upon Reversible De- and Rehydration. *Inorg. Chem.* **2007,** 46, (4), 1337-42.

34. Téllez, C.; Knudsen, R.; Sala, O., Vibrational spectra of the trans-trans and trans-cis conformers of dimethyl fumarate. *J. Mol. Struct.* **1980,** 67, 189-98.

35. Tranchemontagne, D. J.; Hunt, J. R.; Yaghi, O. M., Room temperature synthesis of metal-organic frameworks: MOF-5, MOF-74, MOF-177, MOF-199, and IRMOF-0. *Tetrahedron* **2008,** 64, (36), 8553-7.

36. Li, Y.; Yang, R. T., Gas Adsorption and Storage in Metal Organic Framework MOF-177. *Langmuir* **2007,** 23, (26), 12937-44.

37. Sing, K. W.; Everett, D. H.; Haul, R. A. W.; Moscou, L.; Pierotti, R. A.; Rouquerol, J.; Siemieniewska, T., Reporting physisorption data for gas/solid systems with special reference to the determination of surface area and porosity. *Pure Appl. Chem.* **1985,** 57, (4), 603-19.

38. F. Rouquerol; Rouquerol, J.; Sing, K. S. W., *Adsorption by Powders, Porous Solids*. Academic Press: London, 1999; p 467.

39. Webster, C. E.; Drago, R. S.; Zerner, M. C., Molecular Dimensions for Adsorptives. *J. Am. Chem. Soc.* **1998,** 120, (22), 5509-16.

40. *Handbook of compressed gases* 3rd ed.; Van Nostrand Reinhold: New York, 1990; p 657.

41. Dean, J. A., Lange's Handbook of Chemistry (15th Edition). In McGraw-Hill: 1999.

42. Sing, J. G., Sixty years in the physical adsorption of gases. *Colloids Surf.* **1986,** 21, 109-24.

43. Sing, K. S. W., The use of gas adsorption for the characterization of porous solids. *Colloids Surf.* **1989,** 38, (1), 113-24.

44. Kaneko, K., Determination of pore size and pore size distribution: 1. Adsorbents and catalysts. *J. Membr. Sci.* **1994,** 96, (1-2), 59-89.

45. Li, J.-R.; Kuppler, R. J.; Zhou, H.-C., Selective gas adsorption and separation in metal-organic frameworks. *Chemical Society Reviews* **2009,** 38, (5), 1477-504.

46. Fletcher, A. J.; Thomas, K. M., Compensation Effect for the Kinetics of Adsorption/Desorption of Gases/Vapors on Microporous Carbon Materials. *Langmuir* **2000,** 16, (15), 6253-66.

47. Sircar, S., Basic Research Needs for Design of Adsorptive Gas Separation Processes. *Industrial & Engineering Chemistry Research* **2006,** 45, (16), 5435-48.

48. Blum, L.; Fawcett, W. R., Dielectric Behavior of Polar-Polarizable Solvents in Generic Mean Spherical Approximations: The Kirkwood gK Factor. *The Journal of Physical Chemistry* **1996,** 100, (24), 10423-7.

49. Kondratyuk, P.; Yates Jr, J. T., Desorption kinetic detection of different adsorption sites on opened carbon single walled nanotubes: The adsorption of n-nonane and CCl4. *Chemical Physics Letters* **2005,** 410, (4-6), 324-9.

CHAPTER 7

Effect of oxygen surface functional groups on gas/vapour adsorption on porous metal organic framework NEW-1

Adsorption studies of a series of vapours varying from hydrophilic to hydrophobic including water, alcohol series (methanol, ethanol, n-propanol, n-butanol), chloromethane series (methyl chloride, chloroform, dichloromethane), alkane series (methane, ethane, propane, n-butane, n-pentane, n-hexane, n-heptane, n-octane, n-nonane), and aromatic series (benzene and toluene) were used to investigate the influence of surface oxygen functional groups present in NEW-1 on the adsorption characteristics. The results show that methanol, ethanol, ethane, propane, methyl chloride and chloroform adsorption isotherm plateaus exhibited the stoichiometric ratio 1:1 for amount adsorbed and crystallographic formula unit of NEW-1, while n-propanol has two plateaus with ratios 0.5:1 and 0.75:1. In comparison, dichloromethane also had a plateau with 0.75:1 ratio. However, n-butane, n-pentane, n-hexane and n-heptane adsorption isotherms had a stoichiometric ratio 0.5:1 for amount adsorbed and formula unit of NEW-1 for the isotherm plateaus. In contrast, n-butanol, n-octane, n-nonane benzene and toluene vapours did not show stoichiometric relationships between the amount adsorbed and crystallographic formula unit of NEW-1 for the isotherm plateaus. The results indicate that 1) specific interactions with oxygen surface functional groups were dominant for small hydrophilic molecules e.g. methanol, ethanol and n-propanol and 2) the importance of the relative size of the adsorbate to the framework repeat pore structure formed by the crystallographic formula unit in determining isotherm plateaus. Here in, the adsorption isotherm, adsorption kinetic parameters, isosteric enthalpies and activation energies obtained from the experiments are discussed in relation to the adsorption characteristics, structural characteristics and dynamic response of the framework to adsorption.

7.1 Introduction

Porous materials have a wide range of applications, for example, gas separation and storage,[1-3] sensors,[4, 5] catalysts and catalysts supports,[6-8] and as adsorbents for the removal of environmentally friendly species from either air or waste water.[9-11] Porous materials are available in four main types a) activated carbon b) inorganic materials (alumino-silicate) c) microporous polymers and d) metal organic framework materials. Traditional porous materials, activated carbon and zeolite have been investigated extensively. However, microporous polymer and metal organic frameworks materials are very recent developments. The first adsorption isotherm for metal organic frameworks materials (MOFs) was reported in 1997.[12] The unique characteristics of MOFs is the capability of rational design of a wide range of structure with different surface chemistry. Therefore, an understanding of fundamental aspects of the adsorption/desorption processes are necessary to aid the design of new materials for specific applications.

Both adsorption and desorption isotherms, adsorption capacity and sorption kinetics are determined by adsorptive properties, adsorbent pore structure and surface functional group, and the experimental conditions. Adsorbents with ultra-microporosity may exhibit size exclusion, molecular sieving and quantum sieving effects during the sorption process (details in Chapter 3). Furthermore, the flexible nature of some porous metal organic framework material structures can also influence the adsorption characteristics.[13, 14]

The role of surface chemistry groups in adsorption on porous materials is a critical part of determining adsorption characterisation. In the case of porous carbon materials, there are two types of surface sites involved in sorption process. The first surface sites are hydrophobic sites on graphene layers in the carbon structure, while the second surface sites, hydrophilic sites, such as hydroxyl, carbonyl, peroxide and aldehyde *etc.*, are located on the edges of the graphene layers formed during either gas or chemical activation process (see section 1.6). For water vapour adsorption, these hydrophilic functional groups play a role as primary adsorption centres and these sites are sites for H-bond formation with water leading to the enhancement of water adsorption.[15-17] The water adsorption on primary adsorption centres is observed at low pressure with the cluster layer formation occurring at higher pressure until filling the porosity occurs at near saturated vapour pressure.[17, 18] Functional groups on the surface of porous carbon have only small effect on adsorption

capacity for some gases and vapours. This is because the adsorption capacity at high relative pressure is determined by the available pore volume.[19]

In the case of porous metal organic framework materials, a wide variety of framework topologies can be obtained by selection of reaction-influencing factors including using different metal coordination geometries, multidentate ligand etc. Transition-metal or lanthanide ions are metal centred secondary building units (SBUs) and mostly used as the nodes in the synthesis of metal organic frameworks to generate 3-dimensional topology. Moreover, by choosing appropriate organic linker, it is possible to control pore sizes and surface functionality of the open frameworks.[20, 21] The results from Samsonenko and co-workers[22] showed that there is no specific interaction except van der Waals interactions between the adsorption of acetylene molecules on the wall of the non-surface functionalised microporous metal formates. While the comparative result from Matsuda *et al.*[23] indicated that acetylene was hydrogen bonded with two non-coordinated oxygen atoms on the pore surface of their $Cu_2(pzdc)_2(pyz)$, where pzdc = 2,3-pyrazinedicarboxylic acid and pyz = pyrazine, yielded a very high acetylene uptake at a density 200 time of acetylene at room temperature. In addition, the amount adsorbed at saturation pressure was one molecule of acetylene per formula unit. Vaidhyanathan *et al.*[24] also reported that their amine-functionalised metal organic framework give high uptake and high isosteric enthalpy of CO_2 adsorption. Recently, synthetic modification approach was introduced in order to substitute the new functional group on the surface of metal organic framework materials. This approach may lead to a wide range of applications of MOFs. For example, Sao *et al.*[25] post modified the pyridyl groups in to the ligand on the MOF surface by alkylation reaction at room temperature. The presence of pyridyl groups on the surface pore allowed the MOF to be used as a catalyst. Tanabe and his coworker[26] reported a post synthetic modification of the amino groups in ligands of isorecticular metal organic framework IROMF-3 by alkyl anhydride. This post synthesis is based on the reaction of the amino functional group with a variety of chemicals at room temperature. The post synthetic structure of IRMOF-3 maintained its crystalline structure and porosity.

Functional groups in the linker ligands on the surface of metal organic framework materials play an important role on the adsorption/desorption processes but unsaturated metal sites also influence the adsorption/desorption processes. For instance, Chen *et al.*[2] and Dinca *etal.*[27] reported that hydrogen can bind more strongly with the unsaturated metal centre within the MOFs and given a very high isosteric enthalpies of hydrogen adsorption.

Recent molecular simulation of the water vapour adsorption showed that the water molecules had a large affinity for the Cu metal centre in the Cu-BTC MOF (HKUST-1, BTC- benzene-1,3,5-tricarboxylate).[28]

Fundamental studies of gas/vapour adsorption on flexible metal organic frameworks are in their infancy stage compare to other porous materials, e.g. activated carbons and zeolites. It is apparently that some metal organic framework materials have a flexible structure, e.g. pore windows of an interpenetration structure of $[Cu(dhbc)_2(4,4'\text{-bpy})].H_2O$ where dhbc = 2,5-dihydroxybenxoic acid and 4,4′-bpy = 4,4′-bipyridine, are opened at specific pressure of the CH_4, N_2 and O_2 but windows were almost closed below the specific gate pressure. The authors suggested that this unique property possibly allows this MOF to be used for gas separation or sensors.[29] Zhao *et al.*[13] reported that pore windows of $Ni_2(bipy)_3(NO_3)_4$ opened at high pressure to allow the hydrogen to be adsorbed in the cavity but the windows remained closed at low pressure. This allowed the hydrogen to be trap in the cavities of the MOF at low pressure.

The structure of NEW-1 with DMF located in the pores has an uncoordinated oxygen in the pore wall at a van der Waals distance from the non-coordinated Cu centre. The DMF is not coordinated directly to the pore surface by specific interactions. The pore structure collapses on desolvation and it is proposed that structure results in the oxygen functionality and/or Cu centre, which are in close proximity being available in the desolvated structure. The objective was to probe these sites in NEW-1(details in section 6.1.1.1) with molecules of varying hydrophilic and hydrophobic character to investigate the dynamic response of the framework to adsorption of gases/ vapours. Hydrophilic vapours include water and four alcohols (methanol, ethanol, 1-propanol and n-butanol) and three polar chloromethane compounds (methyl chloride, dichloromethane and chloroform) were also studied. Nine hydrophobic alkane gases /vapours (methane, ethane, propane, *n*-butane, *n*-pentane, *n*-hexane, *n*-heptanes, *n*-octane and *n*-nonane) and two aromatics (benzene and toluene) were investigated. Adsorption of probe molecules with varying hydrophilic and hydrophobic character and polarity were used to probe the surface chemistry of the MOF and the dynamic response of the MOF to adsorption.

7.2 Alcohols adsorption on NEW-1

7.2.1 Adsorption isotherms of alcohols

Four alcohol vapours methanol, ethanol, 1-propanol and *n*-butanol were used for adsorption/desorption studies of NEW-1 sample. These sorption studies were conducted at temperatures ranging from 298 K to 318 K.

7.2.1.1 Adsorption isotherms of methanol and ethanol

Adsorption isotherms of methanol and ethanol at different five temperatures are shown in Figure 7.1a-b and Figure 7.2a-b, respectively. The isotherms of both methanol and ethanol are all type I in the IUPAC classification scheme, but have deviations at high relative pressure where there is a steep uptake corresponding to the approach to pore filling. The isotherms overlap much more closely when plotted on a relative pressure. All isotherm have a steep uptake at very low relative pressure region (as shown in Figure 7.1b region **I**), followed by a plateau (**II**). The methanol isotherms from five different temperatures reached the plateau at p/p^0 ranging 0.12-0.15 and amount adsorbed corresponding to one molecule of methanol per crystallographic formula unit of the NEW-1 (Figure 7.3a). The ethanol isotherms reach the plateau at p/p^0 ranging 0.19-0.22, and the amount adsorbed on the plateau also corresponds to one molecule of ethanol per crystallographic formula unit (Figure 7.3b). This indicates that one methanol or ethanol is adsorbed per un-coordinated oxygen in the ligand of NEW-1. The isotherms at 298 K and 303 K of both methanol and ethanol exhibited the upward curvature at high relative pressure close to 1 where pores filling occurs (region **III** in Figure 7.3a). The total pore volumes of methanol and ethanol calculated from these upward curvatures were 0.263 cm^3g^{-1} (~p/p^0 0.984) and 0.262 $cm^3\ g^{-1}$ (~p/p^0 0.966), respectively which are consistent with the total pore volume (0.269 $cm^3\ g^{-1}$) obtained from crystallographic calculations using PLATON.

Fletcher *et al.*[30] reported isotherms for ethanol adsorption on both the ethanol (**E**) and methanol (**M**) template phases of $Ni_2(bpy)_3(NO_3)_4$, bpy = 4,4′ bipyridine, exhibits plateaus while the adsorption isotherms for methanol showed a gradually increase without reaching a plateau. The plateau of ethanol isotherms for **E** corresponded to pore filling and coordination of the ethanol to the uncoordinated oxygen of the nitrate group. These

methanol and ethanol adsorption isotherms are similar to that observed for methanol and ethanol adsorption on activated carbon.[31, 32]

7.2.1.2 Adsorption isotherms of *n*-propanol

Figure 7.4a-b shows isotherms of *n*-propanol adsorption on NEW-1 over temperature range 298-318 K based on pressure and relative pressure, respectively. All *n*-propanol isotherms are exhibited step isotherms which can be divided in two five regions (see Figure 7.4b). At very low relative pressure (**I**), the isotherms exhibited very steep uptake followed by an initial plateau at ~ p/p^0 0.048-0.05 (**II**). Then, the isotherms have a step uptake (**III**) before reached the second plateau at ~ p/p^0 0.4 (**IV**). The adsorption isotherms of at 298 K and 303 K exhibited the upward curvature at high relative pressure due to ~ p/p^0 close to 1 (**V**). The total pore volume obtained at ~ p/p^0 0.812, (298 K) was 0.244 $cm^3\ g^{-1}$. Amount adsorbed at the first plateau corresponds to ~0.5 molecules per crystallographic formula unit of NEW-1, as shown in Figure 7.6a. This suggests that the *n*-propanol molecule is coordinated to alternate surface oxygen groups in NEW-1. The second plateau corresponds to ~0.75 molecules per crystallographic formula unit of NEW-1. Furthermore, the pressure at the second step of *n*-propanol adsorption begins increases with increasing temperature. A graph of *ln(pressure)* versus *1/T* was linear (R^2 = 0.9995 (see Figure 7.7). The enthalpy of adsorption was ~ 63.8 ± 0.9 kJ mol^{-1} at this point on the isotherm. It is proposed that it is related to framework flexibility leading to structural change in NEW-1 and rearrangement of the adsorbate in order to increase adsorption.

Framework flexibility is well established as an important property of metal organic frameworks. Fletcher *et al.*[33] showed that adsorption of ethanol and methanol on the ethanol template phase of $Ni_2(bpy)_3(NO_3)_4$, (bpy = 4,4′ bipyridine), the windows were too small to allow the ethanol and methanol to pass through without framework flexibility. A scissoring motion of the crystallographic unit cell was observed during adsorption. Also, the methanol isotherm had a step at 2 methanol molecules per $Ni_2(bpy)_3(NO_3)_4$, corresponding to structural change due to framework flexibility. Cussen *el al.*[34] reported that methanol (**M**) template phases of $Ni_2(bpy)_3(NO_3)_4$, bpy = 4,4′ bipyridine, can accommodate the adsorptive molecules with lager size than pore window due to the flexible sorption of the framework. Uemura *et al.*[35] showed that the metal organic

framework [{Zn_2(1,4-bdc)$_2$(dabco)}$_n$] (where 1,4-bdc=1,4-benzenedicarboxylate and dabco=1,4-diazabicyclo[2.2.2]octane) exhibited an adsorption step for propan-2-ol due to expanding of the structure. Similarly, the metal-organic framework MIL-53[36] also exhibited the opening or breathing of the framework, which leads to a step in the adsorption isotherm. It is evidenced that this breathing effect occurred by rotation of the O-C-O and C-C bonds in the framework which is induced by either adsorption at high pressure or by relatively strong bonding between adsorbate-adsorbent species along the channel of MIL-55. This report also showed that after the breathing phenomenon, the adsorption capacity increases to about 20 wt %. Kepert *et al.*[37] synthesised MOF [$Co(H_2O)_6$]H_2(tc-ttf)·H_2O which constructed by the 3D hydrogen-bonding network between H_2(tc-ttf: tetra(carbonyl)tetrathiafulvalene) ions and [$Co(H_2O)_6$]$_2$. This compound showed a crystal-structure transformation on the removal of two water guest molecules, which is indicated that formation of hydrogen bonds via water molecules play an important role in this transformation. Kitamura *et al.*[38]reported that [Cu_2(pzdc)$_2$(dpyg)]$_n$(pzdc = pyrazine-2,3-dicarboxylate; dpyg = 1,2-di(4-pyridyl)glycol) adsorbed methanol molecules, while excluding methane. This is associated with the hydrogen bonding interaction between the methanol molecules and the OH groups of the dpyg ligands, which is strong enough to transform the channel structure to allow the incorporation of the guest molecules.

7.2.1.3 Adsorption isotherms of *n*-butanol

The adsorption isotherms for *n*-butanol are shown in Figure 7.5 a and 7.5 b based on pressure and relative pressure, respectively. The isotherms are type I in the IUPAC classification scheme. All *n*-butanol isotherms exhibited small upward curvature at very low relative pressure (**I**) up to ~ p/p^0 0.05 then increased (**II**) until reaching the plateau (**III**) and this was followed by the small upward curvatures (**IV**) of the isotherm at p/p^0 close to 1(see Figure 7.5 b for the regions). Unlike the other methanol, ethanol and *n*-propanol isotherms for NEW-1, the small upward curvature is only observed in the adsorption isotherm of the larger *n*-butanol, which is presumably due to structural change, which leads to opening of the desolvated material to allow the vapour of *n*-butanol to be adsorbed. The total pore volume calculated from the uptake was 0.20 cm^3 g^{-1} (~p/p^0 0.942), which is lower than the value obtained from crystallographic data and adsorption of other

alcohols as mentioned previously (See Table 7.2). The amount of *n*-butanol adsorbed at the plateau of adsorption isotherm was 0.65 molecule adsorbed on crystallographic formula unit of the sample as shown in Figure 7.6b. This ratio indicates that there is probably no specific adsorbate-adsorbent interaction related to the crystallographic formula unit.

7.2.2 Effect of oxygen surface functional groups on the isotherms of alcohols adsorption on NEW-1

Adsorption of ethanol and methanol on NEW-1 samples showed the stoichiometric ratio 1:1 between the number of alcohol molecules adsorbed and the formula unit. This result is ascribed to hydrogen bonding between the OH group of alcohols with carboxylate non-coordinated oxygen in the pore wall of the NEW-1 (details of the NEW-1 and its non-coordinated oxygen are described in Section 6.1.1.1). However, the copper is 5 coordinate and this is also in the vicinity of the non-coordinated oxygen. In contrast, adsorption isotherms of *n*-propanol has a stoichiometric ratio 0.5 : 1 of the *n*-propanol per formula unit of NEW-1 due the hydrophilic alkyl chain of *n*-propanol being longer than those methanol and ethanol and restricting the space available for specific interactions between the hydroxyl group and the pore surface (Table7.2). The step in the *n*-propanol isotherm results in a new plateau at a stoichiometric ratio 0.75 : 1 and this step corresponds to a minimum in the isosteric enthalpy of adsorption and the isosteric entropy of adsorption becomes less negative. This indicates that there is an increase in disorder during the step and this is discussed in detail later in the chapter. In case of the *n*-butanol where no stoichiometric relationship is observed, the non-specific interactions of the hydrophobic chains are dominant rather than the hydrophilic OH-surface oxygen interaction.

The crystallographic data indicated that solvated form of NEW-1 has pore dimensions of approximately 7.09 x 5.65 Å. However, the powder X-ray diffractogram of desolvated NEW-1 differed from the solvated form indicating structural flexibility and the total pore volume (N_2 adsorption at 77 K) of the desolvated form was much lower than the PLATON pore volume indicating collapse of pores. So, the window dimension of the desolvated form is expected to be much smaller than 7.09 x 5.65 Å due to framework collapses. A similar result was reported by Kepert *et al.*[37] which is reported that window dimension of desolvated structure of $[Co(H_2O)_6]H_2(tc\text{-}ttf)\cdot H_2O$ where tc-ttf is

tetra(carboxyl)tetrathiafulvalene, reduced from about 9 x 7 to 8 x 5 Å. However, there appears to be evidence indicates the flexibility of the NEW-1 structure, e.g. opening of the pores in the desolvated pore structure as shown by comparison of total pore volumes for alcohols with N_2 total pore volume, step adsorption isotherms of *n*-propanol (region III) and upward curvature at low relative pressure region of the *n*-butanol adsorption.

Table 7.1 Temperature dependence on the step adsorption of *n*-propanol on NEW-1

Temperature (K)	Pressure(mbar) at the beginning of the step isotherms	Relative pressure (p/p^o)
298	~3.9	~0.12
303	~5.9	~0.13
308	~8.9	~0.15
313	~13.0	~0.16
318	~19.9	~0.19

Table 7.2 Summary of adsorption data for plateau regions of isotherm for NEW-1

Sorbates	**Amount adsorbed at plateau (mmol/g^{-1}1)**	**Total pore volume at p/p^0 ~1**	**Relative pressure at start of plateau (p/p^0)**	**Sorbate molecules per formula unit**	**Molecular size (Å)[31, 39]***
Methanol	3.2-3.28	0.263	0.12-0.15	1:1	3.81, 4.18, 4.95
Ethanol	3.2-3.23	0.262	0.19-0.22	01:01	4.16, 4.27, 6.33
n-Propanol	1.5-1.6		0.048-0.05	0.5:1	
n-Propanol	2.1-2.3	0.244	0.4-0.5	0.75:1	6.8[40]**
n-Butanol	2.0-2.03	0.200	0.31-0.32	0.65:1	4.16, 4.46, 8.91

* Minimum dimension; MIN-1, MIN-2, MIN-3

** MIN-3

7.2.3 Adsorption thermodynamic measurements of alcohols

Isosteric enthalpies and entropies of adsorption were calculated at constant surface coverage using the Clausius-Clapeyron equation[31, 41, 42] as shown below;

$$\ln(p) = -\frac{\Delta H_{vap}}{RT} + \frac{\Delta S}{R}$$

where p = the pressure

ΔH_{vap} = isosteric enthalpy of vaporisation (kJ mol^{-1})

ΔS = entropy of adsorption (kJ mol^{-1})

T = temperature (K)

ln (p) values from five temperatures ranging from 298-318 K were plotted against *1/T* (K^{-1}) at fixed surface coverage. Gradients obtained from these straight line graphs were used to calculate the isosteric enthalpy of adsorption (Q_{st}). Also**,** an intercept which equals to *ΔS/R* can be evaluated. Examples of the plots of *ln(p)* against *1/T* at fixed different surface coverage are shown in appendix D. The isosteric enthalpies of adsorption for all alcohols adsorption on NEW-1 are shown in Figure 7.8.

7.2.3.1 Isosteric enthalpy and entropy for methanol and ethanol adsorption

The isosteric enthalpy of adsorption obtained from the methanol and ethanol adsorption decreased with increasing of surface coverage to ~ 0.75 mmol g^{-1} and ~1.0 $mmolg^{-1}$, respectively (See Figure7.1b and 7.2b). In region **II**, the isosteric enthalpy of adsorption of methanol was quite constant while isosteric enthalpy of adsorption of ethanol gradually increased. This plateau region **II** corresponds to the stoichiometric ratio 1:1 between molecules of either methanol or ethanol adsorbed on crystallographic structure of NEW-1. The values obtained for methanol adsorption varied with surface coverage in the range of 57-65 kJ mol^{-1} (value at zero surface coverage 63.95 ± 1.00 kJ mol^{-1}) and were higher than the enthalpy of vaporization of 35.2 kJ mol^{-1}. These values are slightly higher than the values obtained for methanol adsorption on methanol (**M**) template phase of $Ni_2(bpy)_3(NO_3)_4$ as shown in Table 7.3. Ethanol adsorption gave the isosteric enthalpy of

adsorption of 62-74 kJ mol^{-1} (value at zero surface coverage 71.68 ± 2.55 kJ mol^{-1}), which is much higher than its enthalpy of vaporization of 38.6 kJ mol^{-1}. The values of enthalpies obtained from methanol and ethanol adsorption are slightly higher than those values obtained from adsorption on activated carbon. These higher isosteric enthalpy values at zero surface coverage indicate that both methanol and ethanol have stronger bonding with NEW-1 than activated carbon.

Detailed analyses of isosteric entropy of methanol and ethanol adsorption on NEW-1 are shown in Figure 7.9. The highest values of isosteric entropies obtained for both methanol and ethanol adsorption were found at the low surface coverage which is consistent with a very sharp adsorption isotherm at low pressure region. The isosteric entropies adsorptions of methanol and ethanol adsorption become more negative with increasing of the surface coverage showing the increased structural order during the adsorption process.

7.2.3.2 Isosteric enthalpy and entropy for *n*-propanol adsorption

Isosteric enthalpies of *n*-propanol adsorption on NEW-1 decreased with increasing surface coverage until being virtually unchanged in the region of the first isotherm plateau, which is corresponds to ~0.5 molecules adsorbed per formula unit of the NEW-1, while the lowest values were observed at surface coverage in the range ~1.7 -2 mmol g^{-1}, which is the region of the isotherm step. The trough was at ~58 $kJmol^{-1}$. Thereafter, the isosteric enthalpy gradually increases with increasing amount adsorbed. The isosteric heat of adsorption of *n*-propanol is in range of 58-77 $kJmol^{-1}$ and the value at zero surface coverage was (78.55 ± 2.51 $kJmol^{-1}$). These isosteric enthalpies are similar to those values obtained from adsorption of *n*-propanol on activated carbon and Co-formate MOF as shown in Table 7.3.

Isosteric entropy obtained for *n*-propanol adsorption on NEW-1 is shown in Figure 7.9. At low surface coverage, there is a little change of isosteric entropy with surface coverage. It is apparent that the isosteric entropy decreases sharply with increasing of surface coverage from ~1.0 to ~1.6 mmol g^{-1} and followed by a sharp increase with further increase in surface coverage. This sharp decrease corresponds to the plateau of the adsorption isotherm while the later increased corresponds to the step of the adsorption isotherm where structural change occurs in order to accommodate more molecules.

7.2.3.3 Isosteric enthalpy and entropy for *n*-butanol adsorption

The isosteric enthalpy for *n*-butanol adsorption on NEW-1 was high (92.91 ± 3.46 kJ mol^{-1}.) at zero surface coverage and then decreased with increasing amount adsorbed covering the range ~72-92 $kJmol^{-1}$. This high isosteric enthalpy presumably due to the large size of *n*-butanol induced structural change as can be seen on the upward curvature of the adsorption isotherm at very low relative pressure. Even through, the amount adsorbed increased from ~0.75-2.0 mmol g^{-1}, but the isosteric enthalpies were quite steady at ~84 $kJmol^{-1}$. This is corresponds to the amount adsorbed at the plateau of the adsorption isotherm. These values are much higher than the enthalpy of vaporization of 43.3 $kJmol^{-1}$ and the enthalpy of *n*-butanol adsorption on Co-formate MOF[40], but it is similar to the values obtained from adsorption on carbons.[43, 44]

Isosteric entropy obtained for *n*-butanol adsorption on NEW-1 is shown in Figure 7.9. The isosteric entropies obtained for *n*-butanol adsorption become more negative with increasing of the surface coverage. The trend of the isosteric entropy obtained for *n*-butanol adsorption is similar to methanol and ethanol.

7.2.3.4 Effect of oxygen surface functional groups on the thermodynamic of adsorption of a series of alcohols on NEW-1

Figure 7.10a shows the isosteric enthalpies at zero surface coverage obtained from each alcohol adsorption on NEW-1 plotted against the number of carbon atoms in alcohols. The linearity of the plot with correlation 0.998 shows that there is a steady increase in the adsorbent-adsorbate interaction energy with increasing of chain length. It is clear that the order of isosteric enthalpy of adsorption: *n*-butanol > *n*-propanol > ethanol > methanol

Similar results were found in the gas chromatographic studied of Carrott and Sing[45] which reported that, at zero surface coverage, the isosteric enthalpies of adsorption of *n*-alkane, *n*-alkenes and aromatics on various activated carbon increase approximately linearly with increasing of carbon number. A similar trend of the isosteric enthalpy of adsorption was also observed from the adsorption of *n*-alkanes (n= 5-8) on precipitated calcium carbonate.[46] The linear relationship of isosteric enthalpy of adsorption with carbon number also depends on the polarisability of both adsorbent and adsorbate.[47, 48] The isosteric enthalpy for methanol adsorption on NEW-1 is approximately 2.7 times higher

than the enthalpy obtained from methanol adsorption on non-porous natural graphite (See Table 7.3). This is probably due to channel-liked microporous structure of NEW-1 enhancing the adsorbate-adsorbent interactions leading to high isosteric enthalpy of adsorption. Similar results have been reported for the isosteric heats of adsorption of C_1-C_6 alkanes on slit shaped microporous carbon, which are enhanced 1.2-2.0 times compare to non-porous carbon.[45, 47] The isosteric enthalpies for both ethanol and methanol adsorption on NEW-1 were found to be higher ~1.2-1.6 times than those values obtained from activated carbon and ~1.2-1.4 times than the values obtained for the **M** and **E** phases of $Ni_2(bpy)_3(NO_3)_4$, This is presumably due to hydrogen bonding between alcohols and uncoordinated oxygen functional groups on the surface of NEW-1. The isosteric enthalpies for methanol and ethanol are similar to the values obtained from both activated carbons and the **M** and **E** phases of $Ni_2(bpy)_3(NO_3)_4$. The length of the alkane chain is clearly a factor in determining the adsorbate-adsorbent interaction as well as the OH- functional group. The increase in non-specific interactions for alkyl chains in alcohols become increasingly important with increasing chain length and dominate the adsorbate-adsorbent interaction for longer chain lengths. Hence, the change from specific hydrogen bond dominated interactions for *n*-propanol to non-specific interactions of the alkyl chains for *n*-butanol.

Table 7.3 Isosteric enthalpies of adsorption obtained from literatures.

References	Isosteric enthalpy of Adsorbates, Q_{st} (kJmol^{-1})				Adsorbents	Temperature
	Methanol	**Ethanol**	***n*-Propanol**	***n*-Butanol**		
Enthalpy of evaporisation[49, 50]	35.2	38.6	40.45	43.3		*
This study	57-65 (63.95±1.0)**	62-74 (71.68±2.5)	58-77 (78.55±2.5)	72-92 (92.91±3.4)	MOF-NEW-1	298-318 K
Taqvi *et al.*[44]	~45-70	~50-70	~55-86	~61-79	Activated carbon	298-373 K
Herry *et al.*[43]	36.44	54.78	59.47	76.87	Activated carbon	473-626 K
Fletcher *et al.*[30]	39-52	44-63		51-56	Activated carbon	288-313 K
Prasetyo *et al.*[51]		55.2			Activated carbon	303-323 K
Ludwig *etal.*[47]	21.8	42.3			Natural graphite	303-623 K
		42.3			Carbon black	303-623 K
Kunhao *et al.*[40]	58	62	76	56	Co-formate MOF	-
Fletcher *et al.*[33]	39-56	40-58			MOF **M** and **E**[a]	268-288 K
Słoczyński *et al.*[52]	45-49				CuO-ZnO-Al_2O_3	433-493 K

* these values were determined at its boiling point, ** value at zero surface coverage

[a] ethanol (E) and methanol (M) template phases of $Ni_2(bpy)_3(NO_3)_4$ where bpy = 4,4′ bipyridine

7.2.4 Adsorption kinetics of alcohols

In a previous study[30] of the methanol (**M**) and ethanol (**E**) template phases of $Ni_2(bpy)_3(NO_3)_4$ indicated that the adsorption kinetics of both vapours at low surface coverage obey a linear driving force (LDF) model. While, both methanol and ethanol adsorption kinetics follow a combined barrier resistance/diffusion model at high surface coverage. Rao *et al.*[30] reported that there are two processes involved in the adsorption process; a) diffusion along the pores and b) diffusion through the barriers at constrictions in the porosity. The Fickian diffusion model is followed when the former process is rate determining while the LDF model is followed for the latter. A combined barrier resistance/diffusion model is followed when both processes are significantly control the kinetics. The results from Finqueneisel *et al.*[53] also indicated that the kinetics of methanol adsorption on activated carbon obey the LDF model. However, the kinetic results obtained for the adsorption of all alcohols on NEW-1 studied showed that the LDF model does not give a good fit for the experimental data. Therefore, a stretched exponential model (SE) was used for fitting the experimental data and this gives a very good fit and the residual errors obtained from this model being typically about < 2 %. Details on SE model are already discussed in section 2.6.5. Examples of the SE and LDF model fitted on the kinetics of all alcohols are provided in Appendix E. It is clearly that the SE model provides reasonably good fits for all kinetic profiles of alcohols adsorption.

The SE model, the model previously was used to analyse H_2 and D_2 adsorption on carbon molecular sieve (CMS) and a microporous carbon[54], adsorption of organic vapour pollutants on activated carbon[55], ammonia adsorption on porous silicon,[56] and water adsorption in activated carbons.[16] In case of the NEW-1, the structure is flexible with a unidirectional array of pores. However the pore structure collapses as shown by the total pore volumes obtained from Ar (77 K), N_2 (77 K) and CO_2 (195 K) adsorption and is opened by adsorption of alcohols, which involves specific interactions (methanol, ethanol and *n*-propanol) and non-specific interactions in the case of *n*-butanol. The SE model fits the adsorption kinetics for all the isotherm steps. The rate constants change as a function of surface coverage. In the cases of methanol, ethanol and *n*–propanol where specific interactions occur, β values obtained from region **I** and **III** of the adsorption isotherms were in the ranges ~0.75-0.90, ~0.67-0.98, and ~0.66 – 0.85, respectively. In the case of *n*-butanol, where the interactions are non-specific, β values were in the ranges ~0.50 to ~

0.91. When the SE exponent β = 1, this indicates that SE model reduces to the LDF model and is 3-dimentional with a single relaxation time. When the SE model gives β values of ~ 0.75, the adsorption kinetics are a 2-dimensional process and when β = 0.5 it is 1-dimensiolnal with a distribution of relaxation times.[57]

7.2.4.1 Adsorption kinetics of ethanol and methanol

Figure 7.11a and b show the SE kinetic rate constants and exponents for methanol adsorption on NEW-1 at 298 K based on pressure and amount adsorbed, respectively. The isotherm has three regions and the changes in chemical potential gradients in these regions influence the kinetic parameters. In region **I**, initially the SE kinetics rate of constants decreased until reached the minimum value at the pressure step close to ~0.6 mbar (~ 1.0 mmol g^{-1}). The SE adsorption kinetic increased with increasing of the amount adsorbed up to ~ 3.0 mmol g^{-1} as the chemical potential gradient gradually increases. The highest amount adsorbed is corresponds to the isotherm plateau with stoichiometric ratio 1:1 between methanol and crystallographic unit. In region **II**, corresponding to the plateau of the isotherm, the adsorption kinetic parameters were too fast to determine accurately. This region gave fast SE kinetic rate constants in the range of 0.02-0.08 s^{-1}. his upward curvature corresponding to pores filling (region **III**) resulted in slowing adsorption kinetics due to decreasing chemical potential gradient for the SE kinetic exponent, the β were quite constant in ranges ~0.75-0.84 with pressure step just below 1 mbar (see region **I**). In region **III** (~150-165 mbar), the β values were increase with increasing of the amount uptake and reach the maximum value ~0.9, which is close to the LDF model.

Figures 7.12a and b shows the variation of adsorption kinetic parameters for ethanol adsorption on NEW-1 at 298 K based on the pressure and amount adsorbed, respectively. In region **I**, it is apparent that the SE rate constant gradually increased with increasing surface coverage. The rate constants start at ~0.0026 $s^{-1}$and increased to ~0.0125 s^{-1} (~4 mbar) which is corresponded to ~3.0 mmol g^{-1} adsorbed on NEW-1. This increase can be attributed to the change is chemical potential gradient with increasing pressure. Region **II** is the isotherm plateau region (amount adsorbed of ~3.0 $mmolg^{-1}$) and this corresponds to the stoichiometric ration of one ethanol per one crystallographic formula unit. The adsorption kinetics in this region were too fast for accurate measurements in the pressure range > 4 -70 mbar. In region **III** where pore filling is approached, the SE rate

constants were decreased. The exponent β, initially the SE rate constant is very close to LDF then the rate of SE rate constants were gradually decreased with increasing of the surface coverage. The values obtained from region **I** and **III** covered ~0.67-0.98 and ~0.76-0.84.

7.2.4.2 Adsorption kinetics of *n*- propanol

Figure 7.13-7.14 shows the SE kinetic parameters for *n*-propanol adsorption on NEW-1 at 298 K with pressure and amount adsorbed, respectively. Both SE rate constants and exponents change in relation to the five *n*-propanol isotherm regions. In region **I**, the SE rate constants increase from ~0.005 to ~0.01 s^{-1} at pressure ~0.2 mbar. The isotherm step ends at approximately 1.5 mmol g^{-1} and this amount adsorbed corresponds to the stoichiometric ~0.5:1 of *n*-propanol and crystallographic unit. The increase in SE rate constants in isotherm region **I** is consistent with the change in chemical potential gradient. The SE rate constant for the pressure steps ~0.2-0.5 mbar were obtainable due to the very fast adsorption kinetics on the first plateau of adsorption isotherm (region **II**). The trend of SE rate constants in region **III** is exhibited a "U" shape and this follows the trend of the chemical potential gradient. Initially, SE rate constant were sharply decrease with increasing of pressure and surface coverage. This is because the flexible MOF structure changes in order to increase adsorption beyond the 0.5:1 *n*-propanol: Formula Unit ratio. Then the SE rate constants were increased as the isotherm reached plateau (region **IV**). The SE rate constants in isotherm region **IV** (~10-17 mbar) were very fast, which is similar to plateau region **II.** Isotherm region **V** starts at a pressure of ~17.5 mbar with the amount adsorbed ~2.5 mmol g^{-1}. In this region, the SE rate constant decreased from ~0.03 to 0.001 s^{-1} (27.5 mbar) as pore filling takes place. For the SE kinetic exponent (β) the values were in the range ~0.80 – 0.85 up to amount adsorbed ~2.8 mmol g^{-1} (see region **I)**. At region **III** (~7.0-7.8 mbar), the β values were slightly decrease from ~0.82 to 0.66.

7.2.4.3 Adsorption kinetics of *n*- butanol

The variations of SE rate constant with either pressure or amount adsorbed for *n*-butanol adsorption are shown in Figure 7.15a and 7.15b, respectively. Both SE rate constants and exponents are discussed in terms of three regions, which are based on the regions of adsorption isotherm. In region **I**, the SE rate constant tends to increase with

increasing of both pressure and surface coverage as the chemical potential gradient increases. The rate constants obtained for this *n*-butanol adsorption range increased initially from ~0.001 to ~0.005 at ~0.08 mbar. This maximum SE rate constant is corresponded to the amount adsorbed of 1.6 mmol g^{-1} at the plateau of *n*-butanol adsorption isotherm. The SE rate constants were too fast to be measured accurately in the pressure range ~0.09-7.0 mbar in the plateau region **II**. In region **III**, the SE rate constants were decreased with increasing of both pressure and amount adsorbed which related to filling of the pores as can be seen in adsorption isotherm. These changes follow the trends expected from the chemical potential of the isotherm. In the case of SE exponent, the β values for adsorption of *n*-butanol do not change markedly with increasing of surface coverage until the plateau of adsorption isotherm is reached. In contrast, the β values of *n*-butanol obtained beyond the isotherm adsorption plateau decreased markedly from ~0.9 to ~ 0.5 which corresponds to the upward curvature of adsorption isotherm as pore filling takes place. The change of β from 1 to 0.5 indicates a change from a 3-dimensional process with a single relaxation time to a 1-dimensional process with a distribution of relaxation times. It is interesting to note that the structure of NEW-1 is an unidirectional array of pores

7.2.5 Activation energies for alcohol adsorption on NEW-1

The variations of SE rate constant with amount adsorbed obtained at temperature range 289-318 K for adsorption of alcohols on NEW-1 are shown in Figure 7.16-7.19. Typically, the SE rate constants in region **I** correspond to the initial adsorption uptake to the plateau of the adsorption isotherm. The SE rate constants for *n*-propanol adsorption were obtained from both regions **I** and **III** (step adsorption). As expected, the rate constants increase with increasing of the temperature.

The activation energies corresponding to barriers to diffusion of alcohol vapours into the pores of NEW-1 sample were obtained using the Arrhenius equation:[41, 58]

$$\ln k = \ln A - \frac{E_a}{RT}$$

where k is the rate constant, A is the pre-exponential factor, E_a is the activation energy, R is the universal gas constant and T is the temperature (K). The values of ln(k) versus 1/T were plotted and the activation energies for each amount adsorbed were obtained from the gradient $-E_a/R$.[31, 59] The SE rate constants (k) for specific surface coverages were calculate by linear interpolation between adjacent isotherm points for constant surface coverage. The ln(k) values at zero surface coverage were calculated by extrapolation of the ln(k) versus amount adsorbed graphs

7.2.5.1 Activation energy of methanol and ethanol adsorption on NEW-1

Figure 7.20 shows the activation energies for methanol adsorption on NEW-1 for specific amounts adsorbed. It is apparent that the activation energy increases with increasing surface coverage and reached the peak of ~29.7 kJ mol^{-1} at ~1.75 mmol g^{-1}. An increasing of activation energy is probably due to structural change due to framework flexibility leads to an increasing of diffusion barrier and decreasing SE rate of constants. After the peak, the SE rate constants increase and the activation energies decreased dramatically to a minimum value of ~14.0 kJ mol^{-1} (~2.75 mmol g^{-1}) as the pores of the flexible framework open to accommodate more adsorbate molecules. The activation energies for adsorption covered the range 14 – 29 kJ mol^{-1} and the value at zero surface coverage was 14.47 ± 1.15 kJ mol^{-1}.

Figure 7.21 shows the activation energies for ethanol adsorption on NEW-1 based on the amount adsorbed calculated using the SE rate constants. The activation energies for adsorption covered the range 22 – 31 kJ mol^{-1} and the value at zero surface coverage was 24.53 ± 0.64 kJ mol^{-1}. The activation energies obtained for both methanol and ethanol adsorption on NEW-1 are similar to those values obtained for activated carbon and MOF $Ni_2(bpy)_3.(NO_3)_4$ **M** and **E** phases as shown in Table 7.5.

7.2.5.2 Activation energy for *n*-propanol adsorption on NEW-1

The activation energies for *n*-propanol adsorption were obtained from two adsorption regions, from low relative pressure isotherm region (**I**) and from step adsorption region (**III**) as shown in Figure 7.22a and b, respectively. The activation energies obtained from region **I** did not change significantly with increasing amount adsorbed while the SE rate constant decreased slightly. The value of activation energies at this region covered the range 30-38 kJ mol^{-1} with the value at zero surface coverage of 33.33 ± 1.19 kJ mol^{-1}. The activation energy at the step adsorption initially increased with increasing of the amount adsorbed to the steepest part of the isotherm but decreased as the isotherm approaches the adsorption isotherm plateau (region **IV)**. This trend corresponds well with the SE rate constant which initially decreased due to the increased diffusion barrier followed by an increase with decreasing diffusion barrier. The value of activation energies at this step adsorption region covered the range 42-57 $kJmol^{-1}$. It is clear that the activation energies at low relative pressure region are much lower than those activation energy obtained in the step adsorption region. The large value for the activation energy in the step adsorption region (**III**) is presumably due to structural change of NEW-1 in order to increase adsorption and minimise adsorbate-adsorbate interactions.

7.2.5.3 Activation energy for *n*-butanol adsorption on NEW-1

The highest activation energy (75.34 ± 3.19 kJ mol^{-1}) for *n*-butanol adsorption was obtained at the zero surface coverage. This is followed by a decrease in activation energy and reach the lowest value of 41.56 ± 2.38 kJ mol^{-1} at ~ 1.3 mmol g^{-1} adsorbed (Figure 7.23). The initial large value for the activation energy at low relative pressure is due to the initial filling of the narrowest porosity, with the highest energy in the collapsed desolvated structure. This corresponded to the slowest SE rate constant at the initial stage of adsorption process (region **I**). The structure gradually expands with adsorption to give a structure with a pore volume of 0.2 cm^3 g^{-1}, which is slightly lower than the values in the region 0.26 cm^3 g^{-1} obtained for methanol and ethanol.

7.2.5.4 Effect on the oxygen surface functional groups on the activation energy

The literature on the activation energy for alcohols adsorption on materials is very rare. However, some data obtained from the literature are showed in Table 7.5. The activation energies obtained from the methanol and ethanol adsorption on NEW-1 over temperature range 289-318 K show similar values to those obtained for activated carbon and **M** and **E** phases of $Ni_2(bpy)_3.(NO_3)_4$ while the activation energy obtained for *n*-butanol adsorption on NEW-1 was much higher than the values reported for activated carbon.[30] Higher value of activation energy of *n*-butanol compared the other alcohols studied is probably due to high diffusion barrier caused by the larger size compared with the NEW-1 pore structure. Figure 7.24 shows the activation energies at zero surface coverage obtained for alcohols adsorption on NEW-1 with the number of carbon atom of alcohols. Although the linear relationship is relatively weak it still indicates that the activation energy increased with increasing of the number of carbon atom. In comparison, both the activation energies and isosteric enthalpies of adsorption were listed in Table 7.6 and their values at zero surface coverage were plotted as seen in Figure 7.25. It is clear that both isosteric enthalpies and activation energy increased with increasing of number of carbon atom for adsorption of C_1-C_4 alcohols on NEW-1. Additionally, the enthalpies obtained for adsorption of methanol, ethanol and *n*-propanol are much higher than the activation energy. This indicates that the enthalpy of adsorption controls the barrier to diffusion via a site-to-site or hopping mechanism.

Table 7.5 Comparison of activation energies of adsorption of C_1-C_4alcohols obtained from this study and literatures.

References	Activation energy, E_a (kJ mol^{-1})				Adsorbents	Temperature
	Methanol	**Ethanol**	***n*-Propanol**	***n*-Butanol**		
This study	14 – 29	22 – 31	30 – 38 42 – 57*	41-73	NEW-1	298-318 K
Fletcher *et al.*[31]	8-40	10-49		20-38	Activated carbon	288-313 K
Fletcher *et al.*[33]	16-33	10-60			MOF **E**	268-288 K
Fletcher *et al.*[33]	4-24 [a] 5-64 [b]				MOF **M**	268-288 K

* determined at the step adsorption of the isotherm

[a] and [b] represents the values at slow and fast kinetic, respectively, obtained from DE model

Table 7.6 Isosteric enthalpies and activation energies obtained from alcohols adsorption on NEW-1.

Adsorbates	Isosteric enthalpy at zero surface coverage Q_{st} (kJmol^{-1})	Activation energy at zero surface coverage E_a (kJmol^{-1})
Methanol	63.95 ± 1.00	14.47 ± 1.15
Ethanol	71.68 ± 2.55	24.53 ± 0.64
n-propanol	78.55 ± 2.51	33.33 ± 1.19
	63.36 ± 2.17*	49.95 ± 3.05*
n-butanol	92.91 ± 3.46	75.34 ± 3.19

* Mean value determined at the step adsorption of the isotherm

7.3 Adsorption of water vapour

As described in Section 6.3.1, water adsorption studies on NEW-1 were conducted in the temperature ranges 298-303 K. All isotherms at 298 K were type V in IUPAC classification scheme while the adsorption isotherms at 303 K were not repeatable due to irreversible partial structural collapses. Calculated pore volume at the plateau and the maximum uptake of water adsorption isotherm at 298 K was of 0.115 $cm^3 g^{-1}$ and 0.178 cm^3g^{-1} which is lower than total pore volume calculated from PLATON 0.269 $cm^3 g^{-1}$. However, pore volume calculated from water adsorption on NEW-1 are higher than the values obtained from those total pore volume calculated from N_2, Ar and CO_2 adsorption on NEW-1. This indicates that the structure of NEW-1 was partly recovered after water vapour adsorption. Water adsorption on NEW-1 also shows the stoichiometric relationship 2:1 between the molecule adsorbed and crystallographic unit. This stoichiometric relationship indicates that water formed the cluster formation in the pores of NEW-1. After several water adsorption experiments, the isotherm of water adsorption on NEW-1 at 298 K gave the lower uptake and lower pore volume of 4.86 mmol g^{-1} and 0.0920 $cm^3 g^{-1}$, respectively (isotherm is shown in Section 6.3.1). These pore volumes are consistent with the pore volume obtained from CO_2 adsorption isotherm of NEW-1 at 195 K with the values of 0.0835 $cm^3 g^{-1}$. The much lower pore volumes indicate that the structure of NEW-1 was partly collapsed after several water adsorption experiments.

7.4 Methyl chloride, chloroform and dichloromethane adsorption on NEW-1

7.4.1 Adsorption isotherms of methyl chloride, chloroform and dichloromethane

Figure 7.26 a and b shows the adsorption isotherms of methyl chloride on NEW-1 over the temperature range 195-313 K based on pressure and relative pressure, respectively. The adsorption isotherms have a similar shape with type I in IUPAC classification scheme but only the adsorption isotherm at 195 K deviates at high relative pressure. This large upward curvature is observed for methyl chloride adsorption is due to pore filling. In region **I**, the adsorption isotherms had very sharp uptakes presumably due to strong adsorbate-adsorbent interactions. These methyl chloride isotherms reach the plateau at p/p^0 ~0.076-0.095, which corresponds to ~1 molecule of methyl chloride per crystallographic formula unit (Figure 7.27 region **II**).

The isotherms for chloroform adsorption on NEW-1 over the temperature range 298-318 K are shown in Figure 7.28. These adsorption isotherms have a similar shape to type I in IUPAC classification scheme.[60] However, it should be noted that the chloroform adsorption isotherms exhibited a small upward curvature at very low relative pressure (~p/p^0 0.02, region **I**). This upward curvature is due to interaction between adsorbate-adsorbent and this probably results in a structural change lead to expansion or opening of the porous structure of the flexible framework. In region **II** the isotherm showed a very steep uptake. The chloroform isotherms from five different temperatures reached the plateau at p/p^0 ranging from ~0.28-0.32, which corresponds to ~1 molecule of chloroform per crystallographic formula unit of the NEW-1 (see region **III** in Figure 7.30a). The adsorption isotherm also exhibited slight upward curvatures at the relative pressure close to 1, which indicated pores filling occurred (see region **IV**).

Figure 7.29 shows the adsorption isotherms of dichloromethane on NEW-1 over the temperature range 298-318 K. The adsorption isotherms have a similar shape with type I in IUPAC classification scheme but have deviation at high relative pressure. In region **I**, the adsorption isotherms had very sharp uptakes presumably due to strong adsorbate-adsorbent interactions. These dichloromethane isotherms reach the plateau at p/p^0 ~0.29-0.35, which corresponds to ~0.75 molecule of dichloromethane per crystallographic formula unit (Figure 7.30b region **II**). Large upward curvature is observed for

dichloromethane adsorption at high relative pressure close to 1 and this is due to pore filling

It is clear that the adsorption isotherms of methyl chloride and chloroform showed the stoichiometric ratio 1:1 between the adsorbed molecule and the crystallographic formula unit. These results were presumably due hydrogen bonding between the H atom of chloroform with non-coordinated carboxylic oxygen in the pore wall of NEW-1. This stoichiometric ratio is similar to methanol and ethanol adsorption on NEW-1. However, adsorption isotherms of dichloromethane indicated that there is a 0.75:1 stoichiometric relationship between dichloromethane adsorbed and the formula unit of NEW-1. The total pore volumes obtained from methyl chloride adsorption on NEW-1 at 293 K and 195 K were ~0.171 cm^3g^{-1} and 0.232 $cm^3 g^{-1}$, respectively. The total pore volume obtained from chloroform and dichloromethane adsorption on NEW-1 at 298 K were 0.267 and 0.253 cm^3g^{-1}, respectively (see Table 7.7). These total pore volumes are consistent with the total pore volume obtained from alcohols adsorption and crystallographic calculation using PLATON. It should be noted that the NEW-1 had a flexible structure which is evidenced by the upward curvature at region **I** of chloroform adsorption. This is due to the co-operative effect, which is probably caused by chloroform being slightly larger than the pore dimensions with the isotherm curvature being attributed to structure change in the flexible framework which results in pore expansion at low relative pressure.

Table 7.7 Summary of adsorption data for plateau regions of isotherm for NEW-1.

Parameters	Methyl chloride	Chloroform	Dichloromethane
Amount adsorbed at plateau ($mmolg^{-1}$)	3.05-3.07	3.09-3.14	2.43-5.45
Relative pressure at plateau (p/p^0)	0.076-0.079	0.28-0.32	0.29-0.35
Adsorbate molecules per formula unit	1	1	0.75
Total pore volume at (p/p^o ~1) cm^3g^{-1}	0.232**	0.267	0.253
Molecular size (Å)[39, 61]*	4.18***[62]	4.613, 5.713, 6.181	4.14, 4.57, 6.26

* minimum dimension; MIN-1, MIN-2, MIN-3

** determined from the maximum uptake of the adsorption isotherm at 195 K

*** kinetic diameter

7.4.2 Adsorption thermodynamics for dichloromethane, methyl chloride, and chloroform adsorption on NEW-1

The isosteric enthalpy obtained for methyl chloride adsorption on NEW-1 is shown in Figure 7.31. The isosteric enthalpy for methyl chloride adsorption increases with increasing of surface coverage to ~0.5 mmol g^{-1}, which corresponds to region **I** in adsorption isotherm. The isosteric enthalpy increased markedly in this region for ~24 kJ mol^{-1} to ~40 kJ mol^{-1}. Then, the isosteric enthalpies of methyl chloride were quite constant at ~40 kJ mol^{-1} for the isotherm. The isosteric enthalpy of methyl chloride at zero surface coverage was 24.47 ± 1.5 kJ mol^{-1}. This value is higher than the enthalpy of vaporization of 21.4[50] kJ mol^{-1} and also higher than the values obtained from methyl chloride adsorption on Graphon (~10.4 kJ mol^{-1}).[63] However, the isosteric enthalpies of obtained for methyl chloride adsorption on NEW-1 is similar to those values of obtained from the Carbonsieve G[64] and magnesium oxide[65] (Table 7.8). The entropies for methyl chloride adsorption on NEW-1 are shown in Figure 7.32. The highest value of isosteric entropies obtained for methyl chloride adsorption on NEW-1 was observed at low surface coverage and decreased with increasing surface coverage and this coincides with the very sharp increase in the adsorption isotherm at low pressure region.

The isosteric enthalpies for both chloroform and dichloromethane adsorption on NEW-1 are shown in Figure 7.33a and 7.33b, respectively. The isosteric enthalpy of chloroform adsorption decreased with increasing of surface coverage to ~0.2 mmol g^{-1}, which corresponds to region **I** in adsorption isotherm. The isosteric enthalpy decreased remarkably in this region for ~70 kJ mol^{-1} to ~50 kJ mol^{-1}, which is consistent with pore expansion or structural change. Then, the isosteric heats of chloroform were quite constant at ~52.5 kJ mol^{-1} and this corresponds to the plateau of adsorption isotherm. The Q_{st} values obtained for chloroform adsorption were in the range 20 -73 $kJmol^{-1}$ (value at zero surface coverage of 72.54 ± 2.83 kJ mol^{-1}) and were higher than the enthalpy of vaporization of 31.28 kJ mol^{-1}.[49] Isosteric enthalpies of dichloromethane gradually decrease with increasing of the surface coverage. The values obtained for this dichloromethane adsorption were in the range 53-57 kJ mol^{-1} (value at zero surface coverage of 56.69 ± 1.3 kJ mol^{-1}) and were higher than the enthalpy of vaporization of 38.6 kJ mol^{-1}. The isosteric enthalpies of both chloroform and dichloromethane reported in this study are similar to those values of obtained from the other materials (Table 7.8).

The entropies for chloroform and dichloromethane adsorption on NEW-1 are shown in Figure 7.34a and 7.34b, respectively. In case of chloroform, there is a rapid increase in entropy (becomes less negative) to the maximum values at very low surface coverage which can be ascribed to the chloroform molecules opening pores. This is related to the upward curvature of adsorption isotherm at low relative pressure. After the maximum value is reached, the entropy of adsorption of chloroform decreased with increasing surface coverage. The highest value of isosteric entropies obtained for dichloromethane adsorption on NEW-1 was observed at low surface coverage and decreased with increasing surface coverage and this coincides with the very sharp increase in the adsorption isotherm at low pressure region. Methyl chloride showed similar trends.

Table 7.8 Isosteric enthalpies of chlorinated compounds adsorption obtained from this study and literatures.

References	Isosteric enthalpies of Adsorbates, Q_{st} (kJmol^{-1})			Adsorbents	Temperatures
	Methyl chloride	Chloroform	Dichloromethane		
Enthalpy of evaporisation[49, 50]	21.4	31.28	38.6		**
This study	24-40 (22.47±1.5)*	20-73 (72.54±2.83)	53-57 (56.69±1.38)	MOF NEW-1	298-318 K
Chiang *et al* [66]		42.13	31.71	Activated carbon	278-353 K
Reid *et al.*[61*]		44.7		CMS	288-313 K
Diaz *et al.*[67*]		30.8		Carbon nanotubes	473-525 K
		28.5		Carbon nanofibers	473-525 K
Chen *et al.*[68]		30-70		California soil	288-298 K
Giraudet *et al.*[69]			43.2	Norit R3extra[a]	293 K
			48.3	Pica NC60[b]	293 K
Markovic *et al.*[70]		44.5	37.9	SiO_2-H	333-393K
		43.9	39.9	SiO_2-Ni	333-393 K
Mooi *et al.*[63]	~10.6			Graphon	195-448 K
Mariwala *et al.*[64]	~23-39			Carbonsieve G	273-295 K
Sprung *et al.*[65]	~25-33			Magnesium oxide	162-175 K

* The isosteric enthalpies of adsorption (Q_{st}) at zero surface coverage

** These values were determined at its boiling point

[a] and [b] represents the granular activated carbon from Norit and Pica manufacturers

7.4.3 Adsorption kinetics of chloroform and dichloromethane

The kinetic parameters of methyl chloride adsorption on NEW-1 cannot determine accurately because the adsorption kinetics were too fast. The SE kinetic rate constants and exponents of chloroform adsorption on NEW-1 at 298 K are show in Figure 7.35a and b. It is clear that, there are four regions, which are consistent with the adsorption isotherm. In region **I**, the SE rate constant decreased with increasing of the pressure and amount adsorbed until reached a minimum at a pressure ~4 mbar (~0.8 mmol g^{-1}) and the SE rate constants in the range 0.002-0.06 s^{-1}. This is attributed to the opening of the collapsed porous structure resulting in slow diffusion kinetics in upward isotherm curvature region **I**. Then, the adsorption kinetics was gradually increased until pressures close to ~20 mbar (see region **II**). The amount adsorbed in this region was ~ 3.0 mmol g^{-1}, which corresponds with amount adsorbed ~1:1 adsorbate molecule per crystallographic formula unit. The adsorption kinetics between ≥ 20 to 200 mbar were too fast to be determined accurately and this corresponds to the adsorption isotherm plateau. However, the adsorptions kinetics decreased above 200 mbar where pores filling occurs. The kinetic exponent (β) values were in the range ~ 0.65-0.75 in both regions **I** and **II**. The β values slightly increased as the plateau is approached and the β values increased at very close to saturated vapour pressure of chloroform.

Figure 7.36a and 7.36b shows kinetic SE rate constant and exponent graphs of dichloromethane adsorption on NEW-1 at 298 K based on the pressure based and amount adsorbed, respectively. The adsorption kinetics of dichloromethane can be classified in to three regions corresponding to the regions of adsorption isotherm. In region **I**, the SE rate constants slightly decreased with increasing pressure and amount adsorbed until the minimum point is reached at a pressure of ~0.3 mbar (~0.5 mmol g^{-1}) and SE rate constant in the range 0.006-0.011 s^{-1}. In region **I**, the SE rate constants increased until ~3 mbar corresponding to amount adsorbed of ~1.6 mmol g^{-1}. The adsorption kinetics between ≥ 4 to 525 mbar could not be determined accurately due to the changes in the amount adsorbed for pressure steps on the plateau being very small and the very fast kinetics. Beyond pressure 525 mbar, the SE rate constants decrease with increasing of the amount uptake due to pores filling. This is consistent with the change in chemical potential gradient. For the SE kinetic exponents (β) were quite consistent at the low relative pressure region with values in the range ~0.75-0.8. Then the β values were slightly decreased at the plateau and

followed with an increased of the β values at very close to saturated pressure of dichloromethane.

7.4.4 Activation energy for chloroform and dichloromethane adsorption

The variations of SE rate constants with amount of chloroform and dichloromethane adsorbed on NEW-1 obtained over the temperature range 298-318 K are shown in Figure 7.37 and 7.38, respectively. Typically, the SE rate constants shown here were obtained from region **I**, the first pressure step of adsorption to the pressure step at the plateau of the adsorption isotherms. The SE rate constants (k) for both chloroform and dichloromethane adsorption from temperatures range 298-318 K were interpolated from the constant surface coverage and then were plotted versus *1/T*. Therefore, the activation energies are obtained from the slope from these plots. The activation energy profiles for both chloroform and dichloromethane compounds are quite similar as shown in Figure 7.39 and 7.40, respectively. At region I, the activation energies for chloroform adsorption were remarkably increased from 20.51 ± 3.36 to 73.71 ± 3.38 kJ mol^{-1}. An increased of these diffusion barriers caused the adsorption kinetic slowing down, as can be seen on the SE rate constant at region **I**. At the peak, the activation energy obtained from chloroform adsorption is corresponded to ~0.8 mmol g^{-1}. After reaching the peak, the activation energies gradually decreased with increasing of both amount adsorbed and pressure. The activation energies dichloromethane adsorption were gradually increased with increasing of surface coverage until reaching the peak, then the activation energy of both chlorinated compounds trends to decrease with an increasing of surface coverage. The activation energies obtained from dichloromethane adsorption were in the range 10.20 ± 0.79 – 23.52 ± 0.90 kJ mol^{-1} and the amount adsorbed at the peak of the activation energy corresponds to ~0.4 mmol g^{-1}. It is clear that the activation energy of chloroform is much higher than dichloromethane. This is attributed to the larger molecular dimensions of chloroform as compared to dichloromethane. It should be noted that isosteric enthalpies of chloroform and dichloromethane at zero surface coverage are much higher than the activation energy, which indicates that chloroform and dichloromethane diffuse to the pore by a site-to-site surface hopping mechanism.

Table 7.9 Isosteric enthalpies and activation energies obtained from chloroform and dichloromethane adsorptions on NEW-1.

Adsorbates	Isosteric enthalpy at zero surface coverage Q_{st} (kJ mol^{-1})	Activation energy at zero surface coverage E_a (kJ mol^{-1})
Chloroform	72.54 ± 2.83	20.51 ± 3.36
Dichloromethane	56.69 ± 1.38	10.20 ± 0.79

7.5 Adsorption of Alkanes on NEW-1

7.5.1 Adsorption isotherms of alkanes

The adsorption of nine alkanes include methane, ethane, propane, *n*-butane, *n*-pentane, *n*-hexane, *n*-heptane, *n*-octane and *n*-nonane on NEW-1 were studied. Methane, ethane and propane, adsorption studies were conducted at temperature ranging from 195 K to 318 K, *n*-butane at 273-313 K, *n*-pentane, *n*-hexane and *n*-heptane at 298 - 318K, while *n*-octane and *n*-nonane adsorptions studies were conducted only at 298 K.

Adsorption isotherms for methane adsorption on NEW-1 at temperature ranges 195-313 K are shown in Figure 7.41a. The isotherms of methane adsorption at 195 K were type I in the IUPAC classification scheme, while the adsorption isotherms of methane determined from 273 K to 313 K only showed a very small amount of curvature with increasing pressure. The total pore volume obtained for methane adsorption at 195 K was 0.084 cm^2 g^{-1} which consistent with the total pore volumes calculated from N_2 (77 K), Ar (77 K), and CO_2 (195 K), adsorption isotherms. Figure 4.1b showed that methane does not have stoichiometric relationship between molecule adsorbed and crystallographic formula unit.

Adsorption isotherms for ethane and propane adsorption on NEW-1 for temperature range 195-313 K are shown in Figure 7.42a and 7.42b, respectively. The isotherms of methane adsorption at 195 K were type I in the IUPAC classification scheme while the adsorption isotherms in range of 293-313 K were intermediate of type I. The total pore volume obtained for ethane adsorption at 195 K was 0.1685 cm^2 g^{-1} (n = 3.206 mmol

g^{-1}, $\rho(C_2H_6)$ = 0.572, p/p^0 ~0.564), which is much higher than the pore volume obtained for methane adsorption on NEW-1. This indicates that the partial expansion of pore volume of NEW-1 is induced by ethane adsorption.

All isotherms of propane adsorption were type I in the IUPAC classification scheme (see Figure 7.43). Also, the adsorption isotherm at 195 K showed an upward curvature at high relative pressure due to pore filling. The total pore volume calculated from propane adsorption isotherm at 195 K was 0.226 $cm^2\ g^{-1}$(n = 2.961 mmol g^{-1}, $\rho(C_3H_8)$ = 0.5853), which is slightly lower than the value calculated from PLATON calculation. However, these total pore volumes are much higher than the pore volume calculated from N_2, Ar and CO_2 adsorption isotherms which indicates that pore volume of NEW-1 is expanded during adsorption of propane. Figure 7.44a and 7.44b show that both ethane and propane do not have stoichiometric relationships one molecule adsorbed per crystallographic formula unit. The propane adsorption isotherms for 298- 318 K have a steep uptake until 0.5 C_3H_8 per crystallographic formula unit and then increases more gradually as the pressure is increased.

The *n*-butane adsorption isotherms for 298- 318 K had a similar shape to type I shape in the IUPAC classification scheme but with showed some upward curvature at very low relative pressure (see Figure 7.45). This upward curvature is probably due cooperative effects leading to structural change. This upward curvature is followed by a steep uptake until 0.6 C_4H_{10} per crystallographic formula unit and then increases very gradually as the pressure is increased. This increase is less steep than the corresponding propane isotherm.

Adsorption isotherms of *n*-pentane obtained in the temperature range 293- 318K are shown in Figure 7.46 a-b. The isotherms of *n*-pentane had a similar shape to type I shape in the IUPAC classification scheme but with some deviations. The isotherms also showed upward curvature at very low relative pressure (region **I**) probably due cooperative effects leading to structural change. In region **II**, the isotherms exhibited steep uptake, which is indicated high adsorbate-adsorbent interaction. There was also upward curvature close to relative pressure ~ 1. The *n*-pentane isotherms from five different temperatures reached the plateau at p/p^0 ranging from ~0.2 - 0.3. Figure 7.47 showed that the stoichiometric relationship between molecules of n-pentane corresponding to the isotherm plateau per crystallographic formula unit of the NEW-1 was close to 0.5. The adsorption isotherms at 298 K and 303 K of *n*-pentane exhibited the upward curvature at the relative pressure close to 1, which is attributed to pore filling (see region **IV**).

Adsorption isotherms of *n*-hexane and *n*-heptane obtained from different five temperatures are shown in Figure 7.48 and 7.49, respectively. The *n*-hexane and *n*-heptane adsorption isotherms are similar to the isotherms of *n*-pentane. Both *n*-hexane and *n*-heptane adsorption isotherms also showed upward curvature at very low relative pressure (region **I**), which is probably due to the cooperative effect leading to structural change. In region **II**, *n*-hexane and *n*-heptane isotherms exhibited sharp uptake, which indicates high adsorbate-adsorbent interactions.

Figure 7.50a shows the adsorption isotherms of five different alkane vapours on NEW-1 at 298 K. It is clear that all five isotherms are similar to type I in the IUPAC classification. The amount adsorbed at the isotherm plateau of *n*-pentane, *n*-hexane and *n*-heptane are similar, but much higher than *n*-octane and *n*-nonane. The cross-sectional dimensions of *n*-alkanes are similar and only differ in the third (longest) dimension. The amount adsorbed at the plateau of *n*-butane, *n*-pentane, *n*-hexane, *n*-heptane, *n*-octane and *n*-nonane isotherms corresponded to ~0.6 (p/p^0~0.12), ~0.5 (p/p^0~0.14), ~0.5 (p/p^0~ 0.2), ~0.5 (p/p^0~0.2), ~0.4 (p/p^0~0.2), and ~0.38 (p/p^0~0.2) molecule of the adsorbent per crystallographic formula unit of the NEW1 as shown in Figure 7.50a. The particular order of the amount adsorbed on the isotherm plateau is *n*-butane > *n*-pentane ~ *n*-hexane ~ *n*-heptane > *n*-octane > *n*-nonane. The pore volumes calculated for the amount adsorbed at the plateau are *n*-butane 0.201 cm^3g^{-1}, *n*-pentane 0.202 cm^3g^{-1}; *n*-hexane 0.225 cm^3g^{-1}; *n*-heptane 0.243 cm^3g^{-1}; *n*-octane 0.219 cm^3g^{-1} and *n*-nonane 0.218 cm^3g^{-1}. This is possibly related to a relationship between molecular size and the crystallographic repeat unit even for non-specific interactions. Figure 7.50b showed that the stoichiometric relationships between either molecules of *n*-hexane or *n*-heptane per crystallographic formula unit of the NEW-1 existed for the plateau but not for the final uptakes corresponding to the total pore volume.

7.5.2 Thermodynamics of alkane adsorption

Figure 7.51 shows isosteric enthalpies obtained for methane, ethane, propane, *n*-butane, *n*-pentane, *n*-hexane and *n*-heptane adsorption on NEW-1 over temperature range 288-313 K. The isosteric enthalpy of methane slightly decreased from 23.83 ± 1.14 kJ mol^{-1} at zero surface coverage and stabilised at ~20 kJ mol^{-1}. There is no significant change of isosteric enthalpies with pressure obtained for ethane adsorption on NEW-1 and the

isosteric enthalpy at the zero surface coverage was 31.90± 1.34 kJ mol^{-1}. The isosteric enthalpy at zero surface coverage of propane was 48.24 ± 1.52 kJ mol^{-1} and there was no significant change with surface coverage. This enthalpy for methane is similar to the enthalpies of vaporisation within experimental uncertainty while the value for propane is significantly greater as shown in Table 7.10. The isosteric enthalpies obtained for methane and propane adsorption on NEW-1 are similar to those values obtained from activated carbon, microporous polymer and zeolite.[43, 48, 67, 71, 72] The isosteric entropies obtained for methane adsorption on NEW-1 decreased with increasing of the surface coverage. The isosteric entropies for propane adsorption initially decreased with increasing of surface coverage until reached the minimum values at surface coverage ~0.25 mmol g^{-1}. The isosteric enthalpy of n-butane was slightly increased with increasing of surface coverage until reached the maximum value of ~59.33 kJ mol^{-1} at surface coverage ~0.8 mmol g^{-1}. The isosteric enthalpy at zero surface coverage of *n*-butane was 56.07 ± 0.59 kJ mol^{-1} which is similar to those values obtained for porous carbons.

Table 7.10 Isosteric enthalpies of methane and propane adsorption obtained from this study and the literatures.

References	Isosteric enthalpy of Adsorbates, Q_{st} (kJmol^{-1})				Adsorbents	Temperatures
	Methane	Ethane	Propane	*n*-Butane		
Enthalpy of evaporisation[49, 50]	8.2	14.7	18.4	22.4		***
This study	18-24 (23.83 ± 1.14)*	31-32 (31.90 ± 1.34)*	40-51 (48.24 ± 1.52)*	52-59 (56.07 ± 0.59)*	NEW-1	298-318 K
Carrott *et al*	~17	~28	~39	~50	Carbon AX21	293-303 K
	~22	~38	~51	~67	Carbon JF006	293-303 K
Cao *et al.*[48]	22.2	36.6	49.5	62.9	Carbosieve B	413-653 K
	20.9	33.3	44.3	58.6	Charcoal cloths 1	413-653 K
	21.4	33.8	46.2	57.6	Charcoal cloths 2	413-653 K
Wood *et al.*[73]	22**				Dichloroxylene	298 K
	20.8				Dichloroxylene	298 K
Myers alan [74]	21.1	31.1	41.4		ZSM-22	305.75 K
Almazan *et al.*[71]		39.9	45.3	49.6	Activated carbon	463-523 K

* the isosteric enthalpies of adsorption (Q_{st}) at zero surface coverage

** simulated value, *** These values were determined at its boiling point.

Figure 7.51 shows isosteric enthalpies obtained from *n*-pentane adsorption on NEW-1 at 298 K. There is no significant change of isosteric enthalpies with surface coverage. The values obtained covered the range ~62 – 66 kJ mol^{-1} with the value at zero surface coverage of 64.65 ± 1.23 kJ mol^{-1}. These values are much higher than the enthalpy of vaporization of 24.3 kJ mol^{-1}, but similar to those values obtained from *n*-pentane adsorption on activated carbons as shown in Table 7.11.[71, 75] The isosteric enthalpy obtained from *n*-pentane adsorption on NEW-1 is similar to the values obtained from the *n*-pentane adsorption on activated carbons and zeolites[72] while the isosteric enthalpy for *n*-pentane adsorption on NEW-1 are higher than those values obtained from the porous alumina, carbon nanotubes and carbon nanofibers.[67] This is probably due to similarity between the adsorbate and pore sizes of NEW-1, enhancing the non-specific adsorbate-adsorbent interactions leading to high isosteric enthalpy of adsorption. In the same way, Naono *et al.* [76] reported similar results that micro pore size and surface functional group is enhanced the adsorbed-adsorbent interaction on the adsorption. Diaz *et al.*[67, 72] reported that the microporous activated carbons showed that the isosteric enthalpies obtained from vapours adsorption on microporous carbon were ~25 % higher than the values obtained from mesoporous material e.g. alumina, carbon nanotubes and carbon nanofibers. Diaz *et al.* [67, 72, 77] suggested that the high isosteric enthalpies were obtained for vapour adsorption on porous materials with the acid surface functional group on the pore surfaces.

The isosteric enthalpies obtained from *n*-hexane and *n*-heptane adsorption on NEW-1 decreased with increasing of the surface coverage until reached the minimum values at surface coverage ~0.5 mmol g^{-1}. These minimum values correspond to the point on the adsorption isotherm where the plateau is reached. After that, the isosteric enthalpies for *n*-hexane and *n*-heptane adsorption gradually increased, which corresponds to the second uptake on the adsorption isotherm. The values obtained for *n*-hexane adsorption on NEW-1 were covered the range ~65-83 kJ mol^{-1} with the value at zero surface coverage of 76.76 ± 3.51 kJ mol^{-1} while the values obtained for *n*-heptane adsorption were ~54-94 kJ mol^{-1} with the value at zero surface coverage of 89.27 ± 3.48 kJ mol^{-1}. These isosteric enthalpies of *n*-hexane and *n*-heptane were higher than the enthalpy of vaporization of 27.2 kJ mol^{-1} and 31.7 kJ mol^{-1}, respectively. The isosteric enthalpies obtained from *n*-hexane and *n*-heptane adsorption on NEW-1 are slightly lower than those values obtained from Carbosieve B and charcoal cloths 1 and 2 as shown in Table 7.12.[48]

Figure 7.52 showed the isosteric entropies obtained from alkane adsorption on NEW-1 at 288-318 K. The isosteric entropies for methane were dramatically decreased with increasing of surface coverage while the isosteric entropies for ethane, propane and n-butane gradually decreased with increasing of the amount adsorbed. In is apparent that there is no significant change of isosteric entropies with surface coverage. The isosteric entropies obtained from *n*-hexane and *n*-heptane adsorption on NEW-1 decreased slightly with increasing of the surface coverage until reached the maximum values at surface coverage ~0.5 mmol g^{-1}. These maximum values correspond to the point on the adsorption isotherm where the plateau is reached.

Figure 7.53 shows the isosteric enthalpies at zero surface coverage obtained for methane, ethane, propane, *n*-butane, *n*-pentane, *n*-hexane and *n*-heptane adsorption on NEW-1 plotted against the number of carbon atoms in alkane. It is clear that the order of isosteric enthalpies of alkane is methane < ethane < propane < *n*-butane < *n*-pentane < *n*-hexane < *n*-heptane. The linearity of the plot with correlation 0.9948 shows that there is a steady increase in the adsorbate-adsorbent interaction energy with increasing of chain length of alkane. The liner relationship between length of alkane molecules and isosteric enthalpies was also shown in Figure 5.54. Ahsan *et al.*[46] and Dernovaya *et al.*[78] obtained similar results in gas chromatographic studies of isosteric enthalpies at zero surface coverage for *n*-alkane, *n*-alkenes and aromatics adsorption on various porous materials showed an approximately linear increase with increasing of carbon number. [56]

Table 7.11 Isosteric enthalpies of *n*-pentane adsorption obtained from this study and literatures.

References	*n*-Pentane		Adsorbents	Temperatures
	Isosteric enthalpy, Q_{st} (kJmol^{-1})	Activation energy, E_a (kJmol^{-1})		
Enthalpy of evaporisation[49, 50]	24.3			309.15 K
This study	62-66 (64.65 ± 1.23)*	38-75 (29.61 ± 4.51)	NEW-1	298-318 K
Almazan *et al.*[71]*	68.1		Activated carbon A950-4	463-523 K
Herry *et al.*[43]	53.9		Activated carbon A	473-573 K
	58.6		Activated carbon D	473-573 K
Diaz *et al.*[72]*	48.01		Activated carbon	473-543 K
	28.47		Alumina	473-543 K
	52.96		Zeolite 5 A	473-543 K
Diaz *et al.*[67] *	36.9		Carbon nanotubes	473-525 K
	27.5		Carbon nanofibers	473-525 K

* the isosteric enthalpies of adsorption (Q_{st}) at zero surface coverage

Table 7.12 Isosteric enthalpies of *n*-hexane and *n*-heptane adsorption obtained from this study and literatures.

References	Isosteric enthalpy of Adsorbates, Q_{st} (kJmol^{-1})		Adsorbents	Temperatures
	n-Hexane	*n*-Heptane		
Enthalpy of evaporisation[49, 50]	27.2	31.7		341.7, 371.8 K
This study	65-83(76.76 ± 3.51)*	54-94(89.27 ± 3.48)	NEW-1	298-318 K
Cao *et al.*[48]	88.9	100.4	Carbosieve B	413-653 K
	82.1	93.6	Charcoal cloths 1	413-653 K
	82.7	93.4	Charcoal cloths 2	413-653 K
Domingo-Gracia	33.8	39.2	Carbon black V3	606-636 K
et al.[79]	26.7	36.3	Pyrolytic graphite	606-636 K
Dernovaya et al.[78]	37.1	42.4	Porous cellulose	333-383 K
	43.7	52.5	Carbon black	333-383 K
Ahsan *et al.*[46]	36.4	44.1	Calcium carbonate	373-393 K

* the isosteric enthalpies of adsorption (Q_{st}) at zero surface coverage

7.5.3 Adsorption kinetics for *n*-alkanes on NEW-1

Adsorption kinetics of propane, *n*-pentane, *n*-hexane and *n*-heptane followed the stretch exponential model (SE) and some selected fits of the model to the kinetic profiles of the alkanes studied are shown in appendix E. However, the adsorption kinetics of methane and ethane were too fast to determine accurately.

Figure 7.55 a and b show the SE rate constant and kinetic exponent data versus pressure and amount adsorbed for propane adsorption on NEW-1 at 288 K, respectively. Adsorption kinetics data for *n*-pentane were obtained from the low pressure region (**I**) of the adsorption isotherm. The SE rate constant decreased with increasing pressure and stabilised at the amount adsorbed in range of ~0.4-1.4 mmol g^{-1} with the SE rate ~ 0.019-0.022 s^{-1}. The SE rate constant then increased dramatically with increasing of the pressure with the values in range of ~ 0.022-0.043 s^{-1}. This increase in SE rate constant corresponds to the plateau of adsorption isotherm. In the case of SE exponent, the β values for adsorption of propane slightly decreased with increasing of surface coverage until reach the minimum value of ~ 0.65 at an amount adsorbed ~ 1.35 mmol g^{-1}. Then, the β values increased from ~0.65 to ~0.92 with increasing surface coverage on the plateau of the adsorption isotherm. Figure 7.56 shows the SE rate constant versus amount adsorbed graphs for propane adsorption on NEW-1 over the temperature range 288-308 K had a similar trend. The Figure indicates that the SE kinetic constant increased with increasing of the temperature.

Figure 7.57a and b shows the SE kinetic rate constant and exponent of *n*-pentane adsorption on NEW-1 at 298 K. It is clear that, there are four regions of the SE rate constant. Firstly, at the initial adsorption process, the SE rate constant decrease to a minimum point of this step at the pressure step close to ~1.0 mbar and this corresponds to an increase in the barrier (activation energy). The corresponding region **I** of the isotherm also showed the upward curvature, i.e. some cooperative effect resulting in structural change opening the pores resulting in the development of a barrier to diffusion through the pores. The adsorption SE rate constant determined at 298 K increased until the pressure step close to ~25 mbar, which is consistent to the region **II** of the adsorption isotherm. The adsorption kinetics determined at 298 K and over the pressure range between ~26.0-550 mbar were too fast to be determined accurately. The adsorptions kinetics decreased beyond pressure step 550 mbar, which is corresponds to pores filling in region **IV** of the adsorption

isotherm. The amount adsorbed at the minimum SE rate constant was ~ 0.6 mmol g^{-1} and this region gave the rate of adsorption kinetic in range 0.0008-0.010 s^{-1}. While, the amount adsorbed at the peak of region **II** of kinetic was ~ 1.4 mmol g^{-1}. This step gave the rate of adsorption kinetic in rage 0.001-0.012 s^{-1}. For the kinetic exponent, the β were in ranges ~0.6-0.9 with pressure step just below 1 mbar. Then the β values were increase at the pressure step very close to saturated pressure of pentane and reach the maximum value ~0.9. The SE rate constant versus amount adsorbed graphs for *n*-pentane adsorption on NEW-1 over the temperature range 288-308 K is shown in Figure 7.58.

Figure 7.59 and 7.60 shows the SE kinetic rate constant and exponent of *n*-hexane adsorption on NEW-1 at 298 K based on pressure and the amount adsorbed, respectively. The SE kinetic rates constant are taken from two regions which correspond to region **I** and **II** on the adsorption isotherms. At the initial adsorption process, the SE rate constant decrease from ~ 0.0073 s^{-1} to ~ 0.0016 s^{-1} at the pressure step close to ~0.10 mbar (amount adsorbed ~ 0.97 mmol g^{-1}) and this corresponds to an increase in the barrier. The corresponding region **I** of the adsorption isotherm at high temperature also showed the upward curvature. This indicates some cooperative structural change resulting in opening of the pore and the development of a diffusion barrier. In region **II**, the adsorption SE rate constant are relatively constant ~ 0.0016 - 0.017 s^{-1} with the maximum pressure step close to ~0.25 mbar. The adsorption kinetics on the plateau of isotherm (region **III**) were too fast to be measured accurately. In the case of SE exponent, the initial values of β for adsorption of *n*-hexane were in range of ~0.97-0.98 which is very close to LDF. Then, the β values decreased sharply with increasing of surface coverage until reach the minimum value of ~ 0.69 at the amount adsorbed~ 0.9 mmol g^{-1}. Then, the β values increased from ~0.69 to ~0.89 with increasing of the surface coverage. This is related to the changes in the barriers to diffusion into the porous structure. The kinetic profiles of *n*-hexane adsorption on NEW-1 at temperature range 298-318 K also showed that the SE kinetic rate constant is tempereture dependent (see Figure 7.61)

Figure 7.62 and 7.63 shows the SE kinetic rate constant and exponent β for *n*-heptane adsorption on NEW-1 at 298 K based on pressure and the amount adsorbed, respectively. The SE kinetic rates constant are taken from two regions which correspond to region **I** and **II** on the adsorption isotherms. In the initial adsorption region, the SE rate constant slightly decrease from ~ 0.008 s^{-1} to ~ 0.0025 s^{-1} at the pressure step close to ~0.04 mbar. The corresponding region **I** of the adsorption isotherm at high temperature

also showed the upward curvature which indicates some cooperative effective of a structural change after build up in the barrier. In region **II**, the adsorption SE rate constant increased from ~ 0.0025 s^{-1} to ~ 0.016 s^{-1} with the maximum pressure step close to ~0.1 mbar. The adsorption kinetics on the plateau of the isotherm (region **III**) were too fast to be obtained accurately. In the case of SE exponent, the initial values of β for adsorption of *n*-heptane were stabilised in range of ~0.81-0.85 with the amount adsorbed of ~0.3-0.8 mmol g^{-1}. Then, the β values decreased sharply with increasing of surface coverage until reach the minimum value of ~ 0.64 at the amount adsorbed ~ 1.15 mmol. In region **II**, the β values varied in range of 0.62 - 0.78.

7.5.4 Activation energies for alkane adsorption on NEW-1

Activation energy profile of propane adsorption on NEW-1 over the temperature range of 288-308 K is shown in Figure 7.65. It is apparent that the activation energy of propane did not change markedly and stabilises at 20-25 kJ mol^{-1} with the amount adsorbed up to ~1.0 mmol g^{-1}. This was followed by an increased of activation energy with increasing of surface coverage. This increase corresponds to the adsorption steps close to the plateau of the isotherm and there is a small amount of curvature indicative of structural change. This is most visible in the isotherms obtained at higher temperatures. The activation energies obtained from propane adsorption were in the range of 19 to 43 kJ mol^{-1} with the value of zero surface coverage of 19.66 ± 3.3 kJ mol^{-1}.

Activation energy profiles of *n*-pentane, *n*-hexane and *n*-heptane adsorption on NEW-1 over the temperature range of 298-318 K are shown in Figure 7.66, 7.67 and 7.68, respectively. It is apparent that the activation energies of *n*-pentane, *n*-hexane and *n*-heptane have an inverted 'U' shaped trend. Initially, the activation energies were gradually increased with increasing of surface coverage reaching a peak. An increasing activation energy is consistent with a decrease in SE rate constant. This can be ascribed to structural change opening the porosity and increasing the barrier to diffusion into the porous structure. The trends for the activation energies of *n*-pentane, *n*-hexane and *n*-heptane are to decrease with further increasing surface coverage . The activation energies obtained for *n*-pentane adsorption was in the range 29.61 ± 4.5 to 74.27 ± 4.56 kJ mol^{-1} with the values at zero surface coverage 29.61 ± 4.5 kJ mol^{-1}. The activation energies at zero surface

coverage obtained for *n*-hexane and *n*-heptane adsorption on NEW-1 were 27.01 ± 4.10 kJ mol^{-1} and 26.44 ± 2.33 kJ mol^{-1}, respectively. It should be noted that activation energies at zero surface coverage of propane, *n*-pentane, *n*-hexane and *n*-heptane are much lower than their isosteric enthalpies values which indicates that molecules of propane, *n*-pentane, *n*-hexane and *n*-heptane diffuse to the pore by a site-to-site surface hopping mechanism (see Figure7.69).

7.6 Adsorption of aromatic compounds on NEW-1

The adsorption isotherm of both benzene and toluene on NEW-1 at 298 K are shown in Figure 7.70 a (pressure basis) and 7.71 b (relative pressure basis). These adsorption isotherms are similar to type I IUPAC classification scheme but the deviation occurred at very low surface coverage. Both isotherms exhibited the upward curvature at low relative pressure region until p/p^0 ~0.9 which corresponds to the amount adsorbed of both benzene and toluene ~ 0.4 mmol g^{-1}. Thereafter, the benzene isotherm sharply increased while the toluene isotherm is gradually increased until reaching the plateau.

The upward curvatures observed in both benzene and toluene are similar to those observed for larger alkanes and alcohols is probably due to structural change to open up the porosity to accommodate the molecular shapes of benzene and toluene and this leads to an increase in the barrier to diffusion as the structure changes. The amount adsorbed of benzene molecules on NEW-1 is higher than toluene and the total pore volume obtained from the maximum adsorption capacity at high relative pressure (Gurvitsch‘s rule) gave the following values for benzene 0.254 cm^3 g^{-1} and toluene 0.193 cm^3 g^{-1}. The toluene pore volume is significantly lower than both pore volume obtained from benzene adsorption and crystallographic pore volume obtained using PLATON (0.269 cm^3 g^{-1}). This is due to the molecular size toluene being larger than benzene (toluene : 4.012, 6.625 and 8.252 Å and benzene : 3.277, 6.628 and 7.337 Å) [39]. In the case of spherical pores two dimensions are important whereas for slit shaped pores only one dimension is significant. In the case of diffusion of molecules into NEW-1 which has 6.092 x 6.092 Å pores it is apparent that in the case of toluene the smallest dimension is larger than for benzene. Adsorption induces structural changes as is evident from the shape of the isotherm.

The initial upward curvatures convex to the pressure axes observed in both benzene and toluene isotherms are similar to the previous observed of benzene and toluene adsorption on titanium dioxide[80] and activated carbon[81], and also similar to the initial uptake regions for $CHCl_3$ and *n*-alkanes. Figure 7.69 shows the isotherm of both benzene and toluene adsorption on NEW-1 at 298 K based on the stoichiometric ratio of the amount adsorbed. At the plateau, the amount of benzene adsorbed was ~ 0.84 mmol g^{-1} per formula unit of NEW-1 (p/p^0 ~0.23) while the amount adsorbed of toluene was about 0.45 mmol g^{-1} per formula unit of NEW-1 (p/p^0 ~0.27). So, this is reasonable to conclude that there is no relationship between the amount adsorbed of either benzene or toluene and formula unit of the NEW-1.

7.7 Dynamic Response of NEW-1 to Adsorption

The pore structure of NEW-1 undergoes partial collapse on desolvation as shown by the much lower total pore volumes obtained for nitrogen (77K), carbon dioxide (195 K) and argon (77 K) adsorption compared with C_3-C_9 hydrocarbons and the various other adsorptives studied. The latter were usually in good agreement with the crystallographic value obtained from PLATON. Adsorption is driven by the enthalpy of adsorption and since the desolvated structure is most likely more disordered than the solvated structure, the enthalpy also drives the structural change involving ordering and opening of the pore structure. This structural change can be driven by both specific and non-specific interactions.

This study has shown that specific hydrogen bonding interactions occur for methanol, ethanol and *n*-propanol with surface oxygen groups, which are evident from stoichiometric relationships between amounts adsorbed at isotherm plateaus and oxygen present in crystallographic formula unit. Chloroform also has an isotherm plateau where the amount adsorbed corresponds to 1 $CHCl_3$: 1 Formula Unit of NEW-1. In contrast, *n*-butanol, dichloromethane and hydrophobic molecules includes methane, ethane, propane, *n*-butane, *n*-pentane, *n*-hexane, *n*-heptane, *n*-octane, *n*-nonane, benzene and toluene do not have specific interaction with the surface functional groups. The difference between *n*-butanol and the other alcohols is ascribed to the increasing dominance of the interaction of hydrophobic with the surface rather than the hydrophilic OH-surface oxygen interaction.

Adsorption isotherms over a range of temperatures were used to determine the isosteric enthalpies and entropies of adsorption as a function of surface coverage. The adsorption kinetics for each isotherm pressure increment for both hydrophilic and hydrophobic molecules follows the stretched exponential model, which is consistent with a distribution of relaxation times. The rate constants and exponential β parameters were studied as a function of surface coverage.

In the case of the adsorptives with slightly larger cross-sections/lengths the isotherms had an initial upward curvature. The thermodynamics and kinetics barriers of adsorption were investigated in these regions. The isosteric enthalpies of adsorption usually decrease with increasing surface coverage whereas the kinetic rates decrease and the barriers to diffusion increase. These observations for *n*-propanol, chloroform and propane, *n*-butane, *n*-pentane, *n*-hexane and *n*-heptane adsorption are indicative of a cooperative effect involving structural change leading to pore opening.

Isosteric enthalpies and activation energies for adsorption of a range of alcohols at zero surface coverage on NEW-1 over temperature rang 298-318K increase with increasing of number of carbon atoms. It is clear that the order of isosteric enthalpy and activation energy of adsorption is *n*-butanol > *n*-propanol > ethanol > methanol. It is interesting to note that hydrogen bonding between methanol, ethanol and *n*-propanol and surface groups predominates, while *n*-butanol does not show evidence for specific interactions. However, the isosteric enthalpy of adsorption increases approximately linearly with increasing of carbon number, molecular size and longest molecular dimension for alcohols.

Isosteric enthalpies and activation energies at zero surface coverage for methane, ethane, propane, *n*-butane, *n*-pentane, *n*-hexane and *n*-heptane adsorption on NEW-1 over temperature rang 288-318K also increase with increasing of number of carbon atoms. The Q_{st} values are directly proportional to molecule size while the activation energies which represent the barriers to diffusion are much less correlated with size. This can be attributed to the very similar cross-section dimensions of the molecules being very similar and these are the important dimensions for diffusion along rectangular unidirectional pores. Similarly, it is apparent that the orders of isosteric enthalpy and activation energy of adsorption of alkanes at zero surface coverage are in the orders as shown below;

Enthalpies:

methane < ethane < propane < *n*-butane < *n*-pentane < *n*-hexane < *n*-heptane

Activation energies:

propane < *n*-pentane < *n*-hexane <*n*-heptane

The isosteric enthalpies obtained for adsorption of C_1-C_4 alcohols and chloroform, dichloromethane, and C_5-C_6 alkanes adsorption on NEW-1 are much higher than the activation energy. This indicates that the enthalpy of adsorption controls the kinetics and diffusion is a site-to-site hopping mechanism rather than limited by constrictions in the porous structure. In case of adsorptive where there is convex curvature to the pressure axis in the initial adsorption isotherm regions, for example, chloroform, *n*-pentane etc. the situation is more complex. At very low surface coverage the isosteric enthalpy is higher than the activation energy, but changes to a situation where, as a result of structural change (framework flexibility), the activation energy increases to similar values to the enthalpy of adsorption. Here, the factor controlling the adsorption dynamics changes from the site-to-site hopping mechanism to increasing importance of diffusion through barriers at constrictions in the porous structure. A summary of the isosteric enthalpies obtained for alcohols, alkane and aromatic compound vapour adsorption on NEW-1 are shown in Table 7.13.

In general, the adsorption kinetics follows the trends expected from the isotherm chemical potential gradient. The adsorption isotherms of vapours in this study show the upward curvature of the isotherm at the relative pressure close to 1. This results in a slowing down of the adsorption kinetics. Furthermore, the adsorption isotherms of *n*-propanol show the step adsorption isotherm. The slow adsorption kinetics for the isotherm step for 0.5 to 0.75 propanol molecules per formula unit are associated with an increase in the activation barrier to diffusion into the porous structure and the entropy of adsorption increases (becoming less negative), which corresponds to increasing disorder. This can be explained by framework flexibility and the rearrangement of adsorptive molecules coordinated to surface sites in the pores driven by the chemical potential to a more disordered state to accommodate more adsorbed molecules. Initially adsorption occurs in on the surface and in structural defects which are easily accessible to the vapour. The structural change leading to pore expansion or opening is driven by the isosteric enthalpy of adsorption. The largest of the adsorptives in terms of cross-section which does not

expand the pore structure is methane with a cross-section (3.829 x 4.101 x 3.942 Å) can clearly enter the desolvated collapsed pore structure. Some molecules, for example, dichloromethane, barely show any change in isotherm shape or activation energies as evidence for expansion of the pore structure. Adsorptives such as dichloromethane appear to open the porous structure in a uniform manner. However, chloroform, *n*-pentane, *n*-hexane, etc show upward curvature in the isotherm, which is accompanied by a marked increase in activation energy for the barrier to diffusion into the porous structure. This cross-section is smaller than dichloromethane 4.14 Å x 4.57 Å which does open the pore structure. The upward curvature for chloroform adsorption is possibly due to heterogeneous expansion of the pore structure with a distribution of structures changing with changing amount adsorbed.

The dynamic response of unidirectional framework NEW-1 to a range of hydrophilic and hydrophobic adsorptives is complex and framework expansion may be driven by both specific hydrogen bonding and non-specific van der Waals interactions. The size of the adsorbate molecule relative to the pore structure repeat unit and specific interactions are important in changing framework structure. These factors may be useful for gas separation using MOFs.

Table 7.13 Comparison of physical and thermodynamic parameters for the probe molecules used in this study.

Molecule	Kinetic diameter (pm)	Molecular dimensions x, y, z (pm)	Isosteric enthalpy of adsorption on NEW-1 (kJ/mol)
O_2	346.7	298.5, 293.0, 405.2	19.88 ± 0.46**
N_2	368.0	305.4, 299.1, 404.6	20.05 ± 0.86**
Ar	354.2	363, 351	21.86 ± 0.99**
CO_2	330.0	333.9, 318.9, 536.1	27.68 ± 1.45
H_2O	264.1	322.6, 291.7, 388.8	17-45[15, 16, 76]
Alcohol series			
Methanol	362.6	381.0 418.0 495.0	63.39 ± 1.00
Ethanol	453.0	416.0, 427.0, 633.0	71.68 ± 2.55
n-Propanol	498.0	n/a	78.55 ± 2.51
			63.36 ± 2.17*
n-Butanol	540.0	416, 446, 891	92.91 ± 3.46
Chloromethane series			
Methyl chloride	418.2	n/a	24.47± 1.50
Dichloromethane	489.8	n/a	56.69 ± 1.30
Chloroform	538.9	618.1, 571.3, 461.3	72.54 ± 2.83
Alkane series			
Methane	375.8	382.9, 410.1, 394.2	23.83 ± 1.14
Ethane	443	380.9, 407.9, 482.1	31.90 ± 1.34
Propane	430-511	660.6, 451.6, 402.0	48.24 ± 1.52
n-butane	468.7	785.5, 451.9, 401.4	56.07 ± 0.59
n-Pentane	450.0	910.1, 452.2, 401.4	64.54 ± 1.52
n-Hexane	430.0	1034.4, 453.6, 401.4	76.76 ± 3.51
n-Heptane	430.0	1158.9, 452.3, 401.4	89.27 ±3.48
Aromatic series			
Benzene	534.9	662.8, 733.7, 327.7	46-75[82]
Toluene	525.0	662.5, 401.2, 825.2	45-70[83]

Note: * Mean value at the step isotherm of 1-propanol adsorption on NEW-1

** Details in Chapter 8

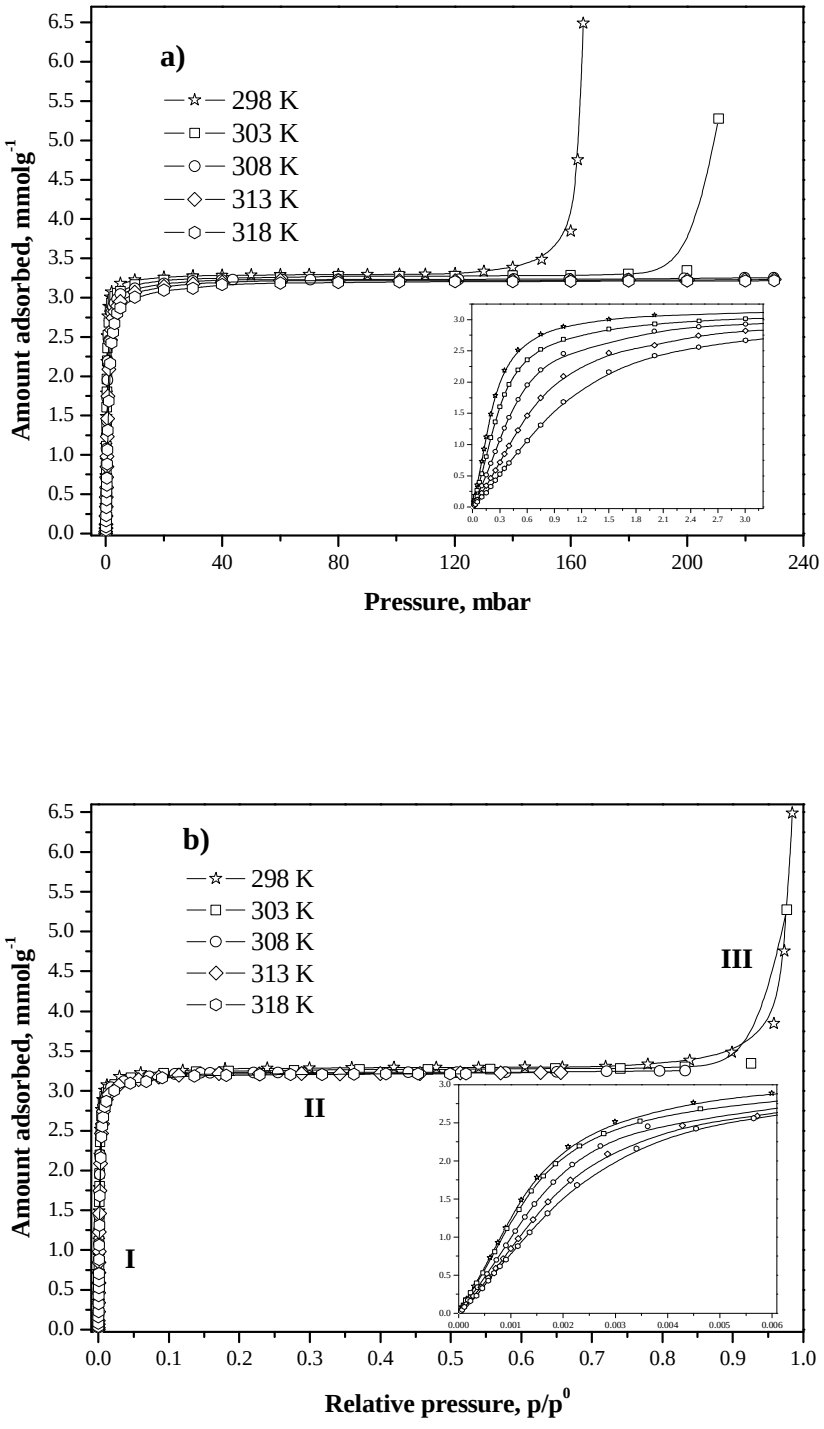

Figure 7.1 Isotherm for methanol adsorption on NEW-1 over the temperature range 298-318 K a) on a pressure basis with an inset in the low pressure region and b) on a relative pressure basis with an inset in the low relative pressure region

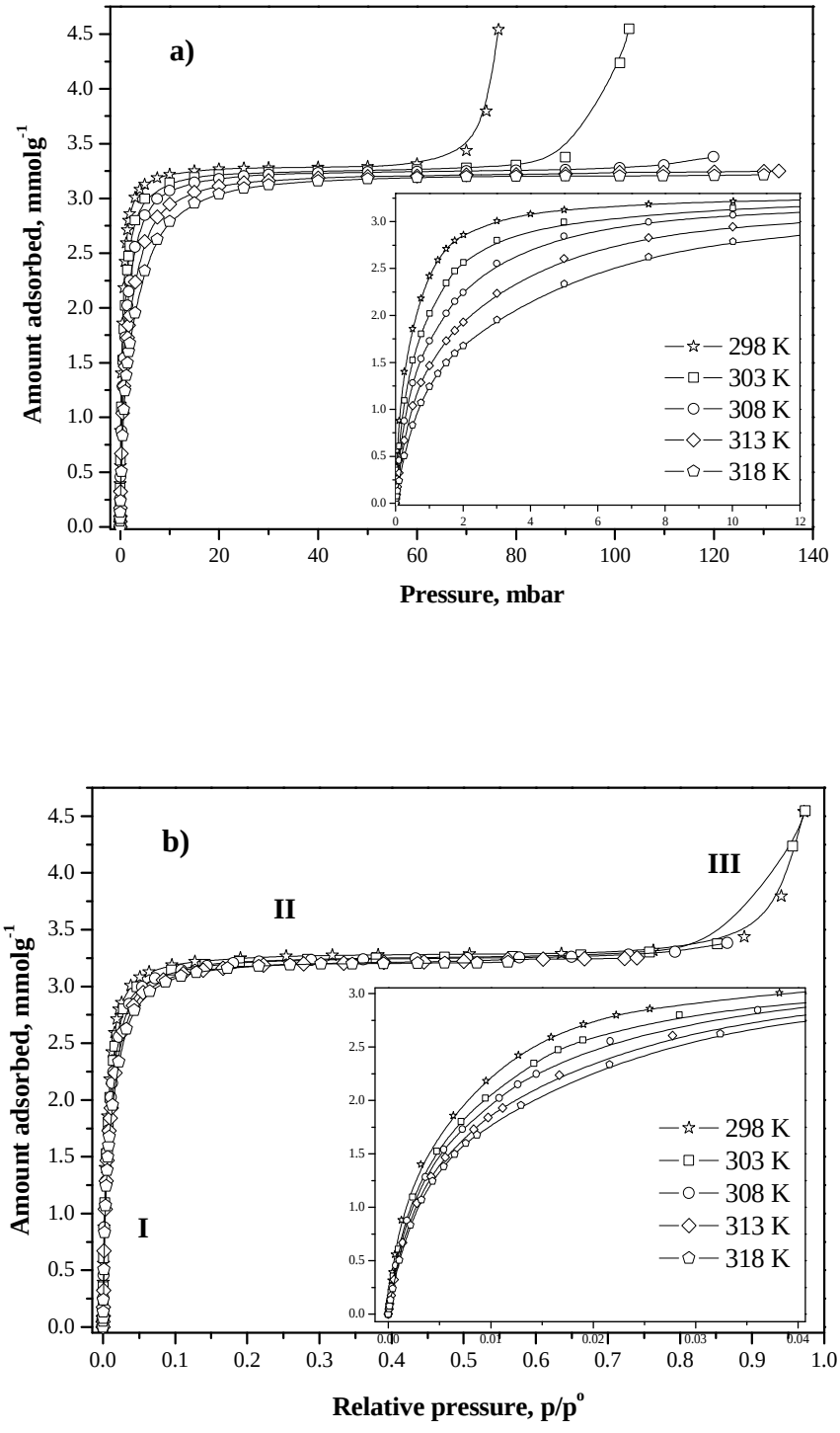

Figure 7.2 Isotherm for ethanol adsorption on NEW-1 over the temperature range 298-318 K a) on a pressure basis with an inset in the low pressure region and b) on a relative pressure basis with an inset in the low relative pressure region

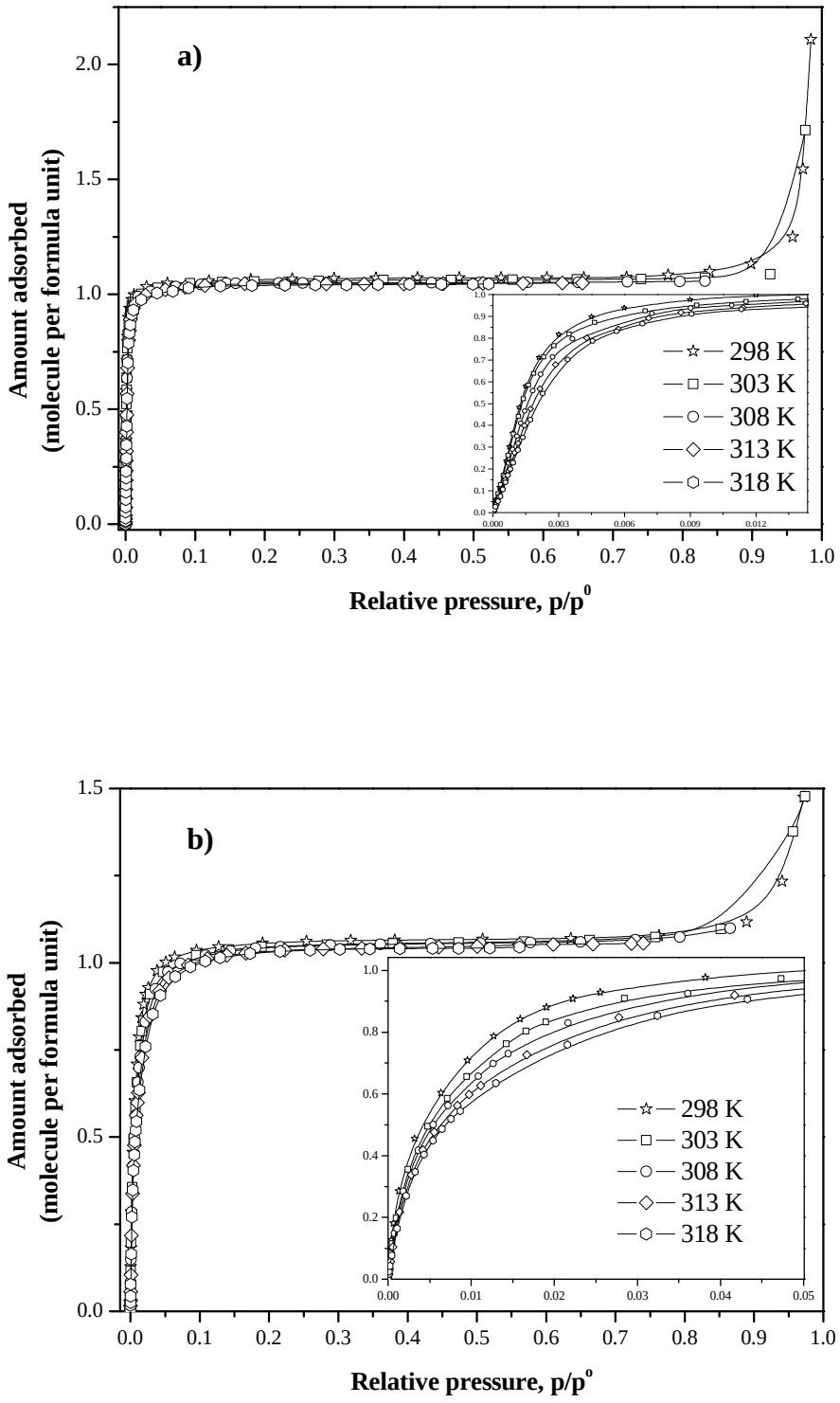

Figure 7.3 Adsorption isotherms for a) methanol and b) ethanol on NEW-1 with showing amount adsorbed on molecule per formula unit with inset in low relative pressure region

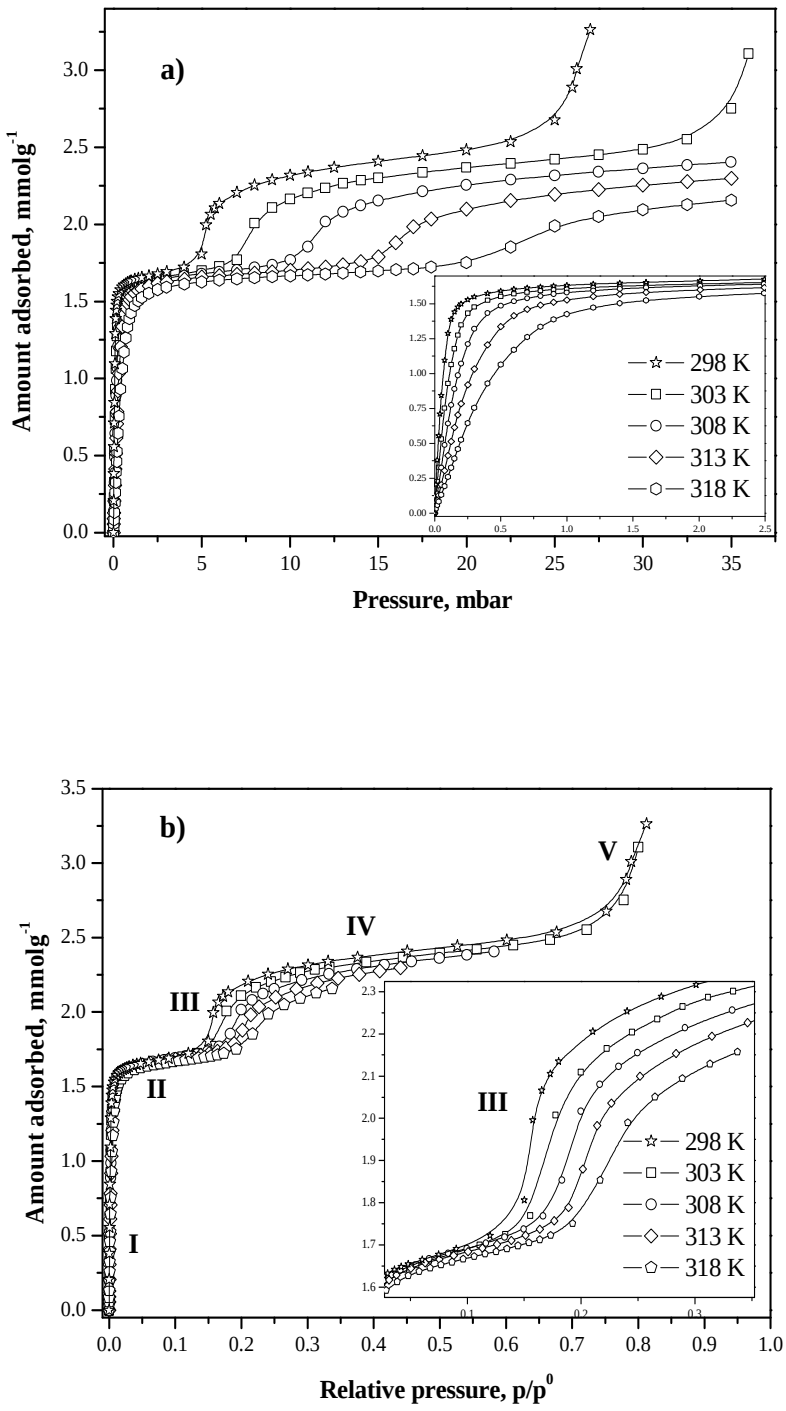

Figure 7.4 Isotherm for *n*-propanol adsorption of NEW-1 over the temperature range 298-318 K a) on a pressure basis with an inset in the low pressure region and b) on a relative pressure basis with an inset magnified the step adsorption.

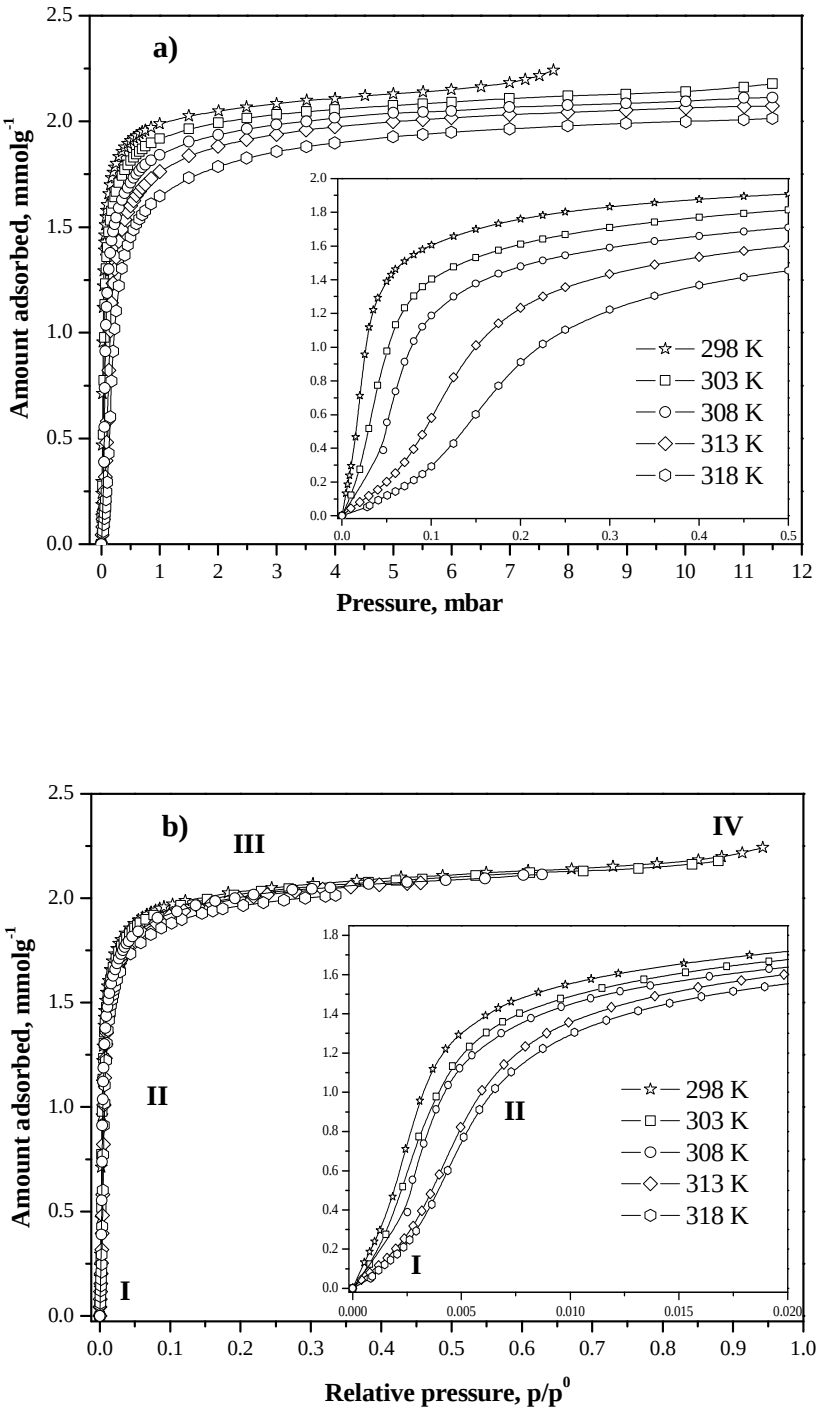

Figure 7.5 Isotherm for *n*-butanol adsorption on NEW-1 over the temperature range 298-318 K a) on a pressure basis with an inset in the low pressure region and b) on a relative pressure basis with an inset in the low relative pressure region

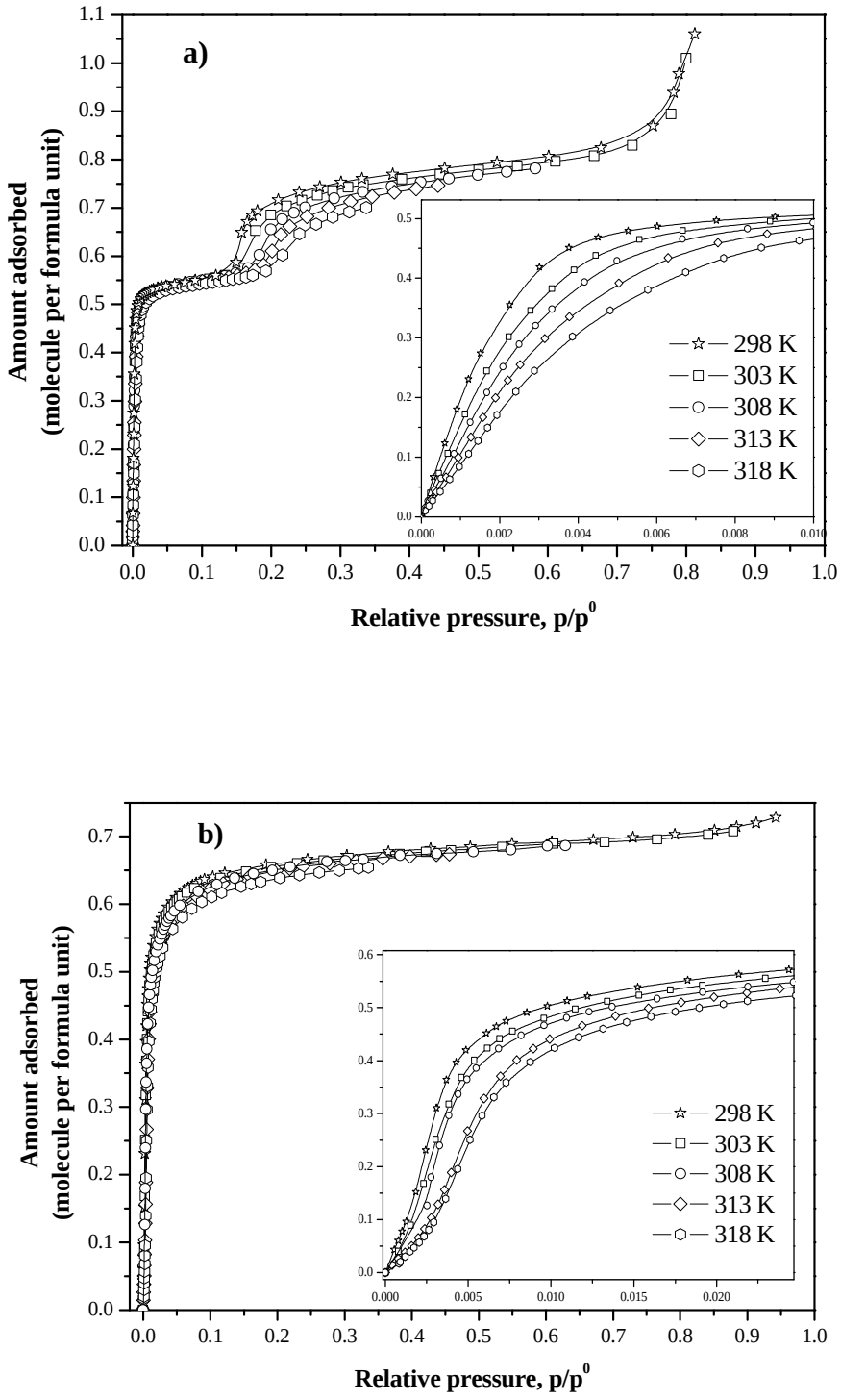

Figure 7.6 Adsorption isotherms for a) *n*-propanol and b) *n*-butanol on NEW-1 showing amount adsorbed on molecule per formula unit with inset in low relative pressure.

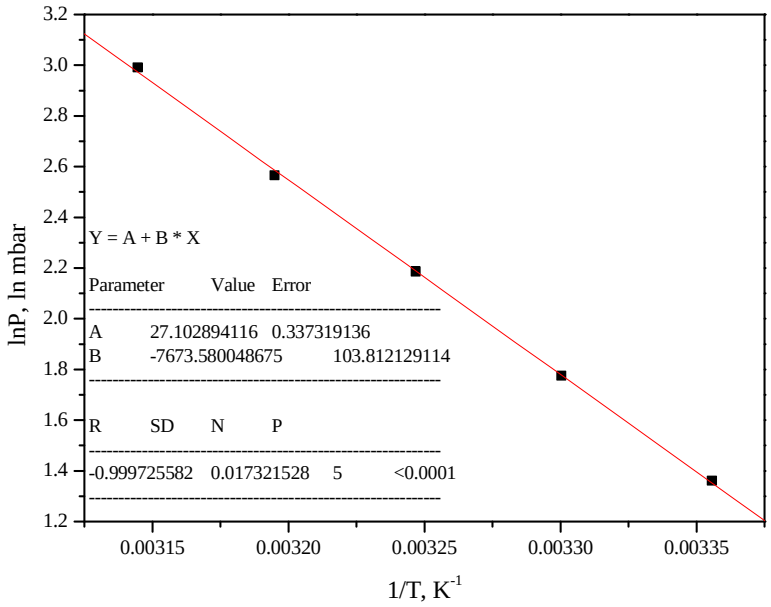

Figure 7.7 Plot of *ln P* at steps adsorptions isotherm of 1-propanol with *1/temperature*.

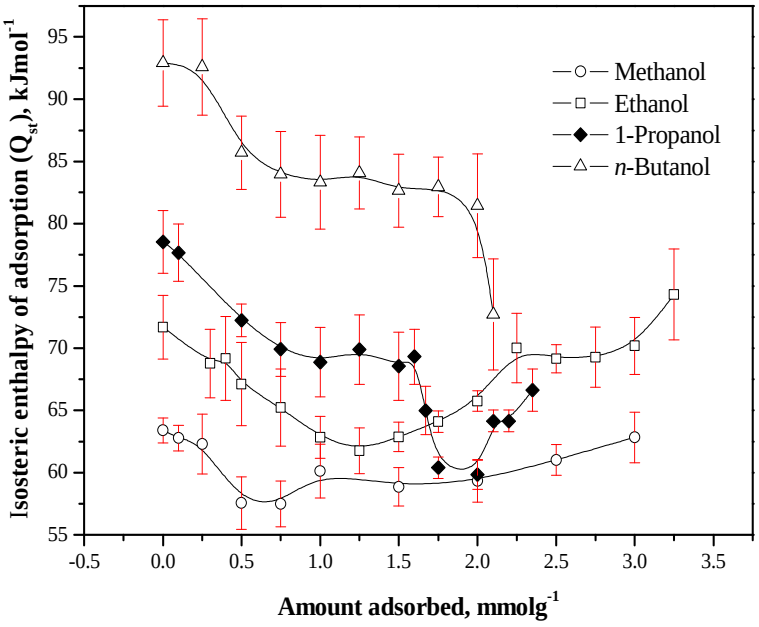

Figure 7.8 Isosteric enthalpies for adsorption of alcohols on NEW-1 as a function of amount adsorbed.

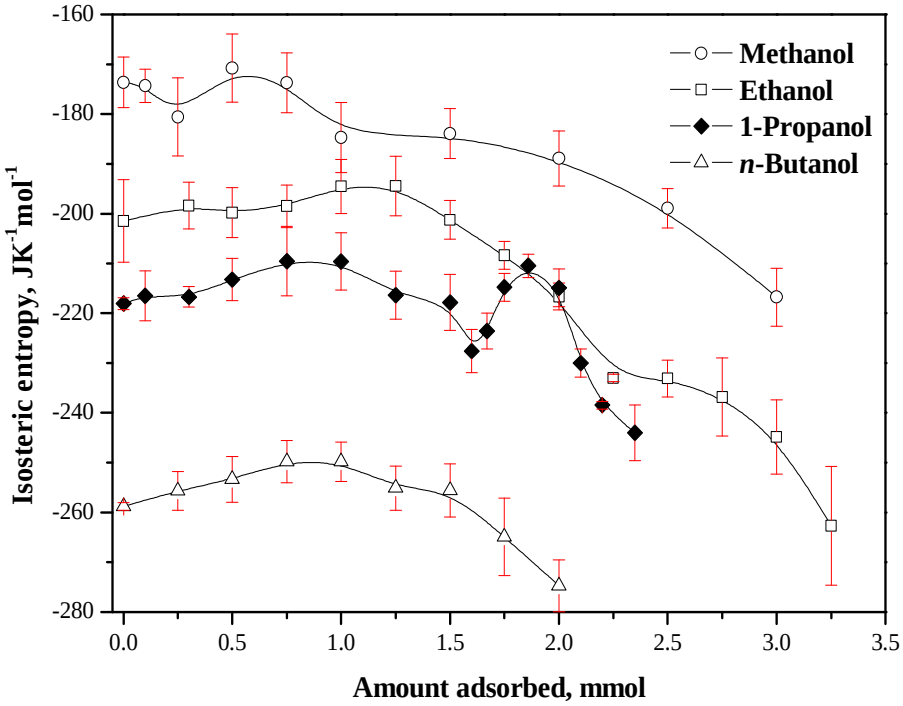

Figure 7.9 Isosteric entropies for adsorption of alcohols on NEW-1 as a function of amount adsorbed.

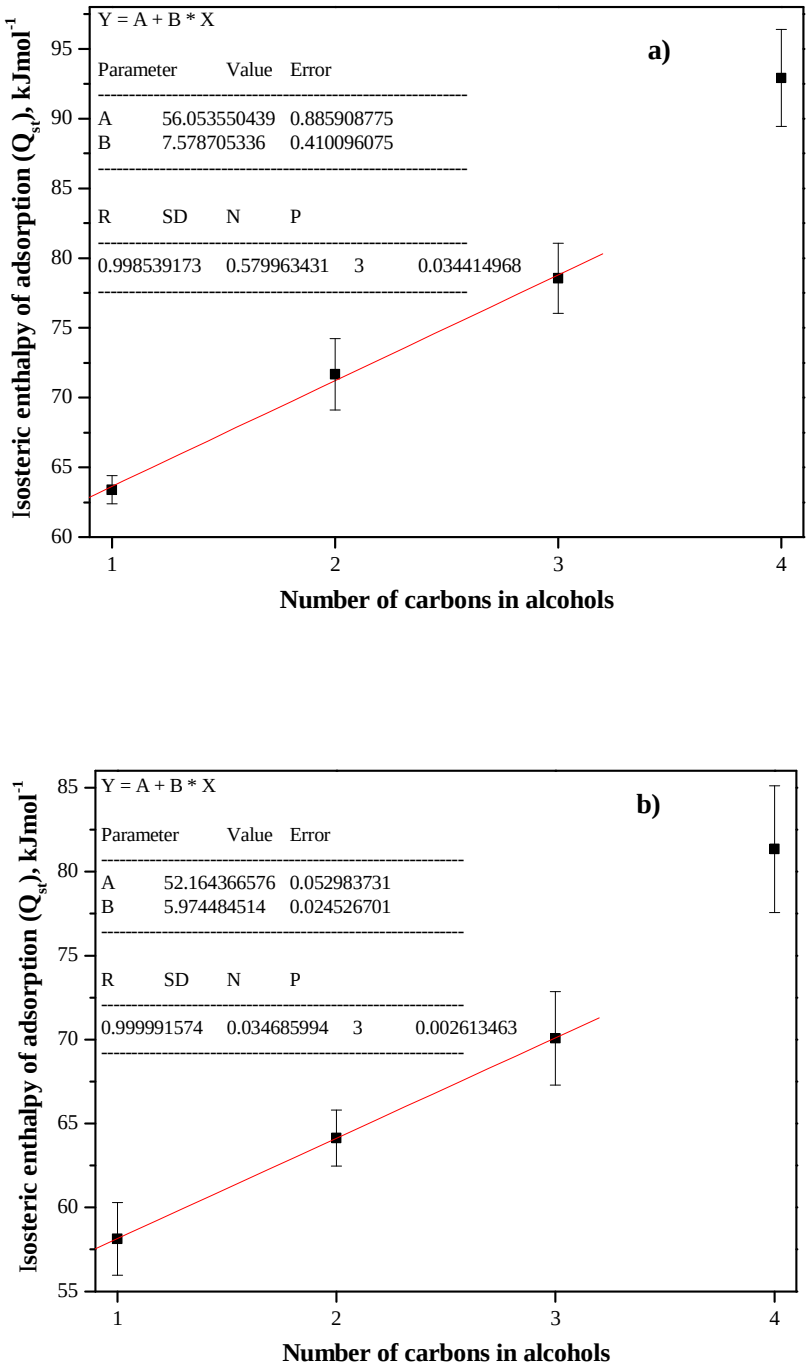

Figure 7.10 Variation of isosteric enthalpies at a) zero surface coverage and b) 1.0 mmol of the amount adsorbed for adsorption of alcohols adsorption on NEW-1 with a number of carbons in alcohols

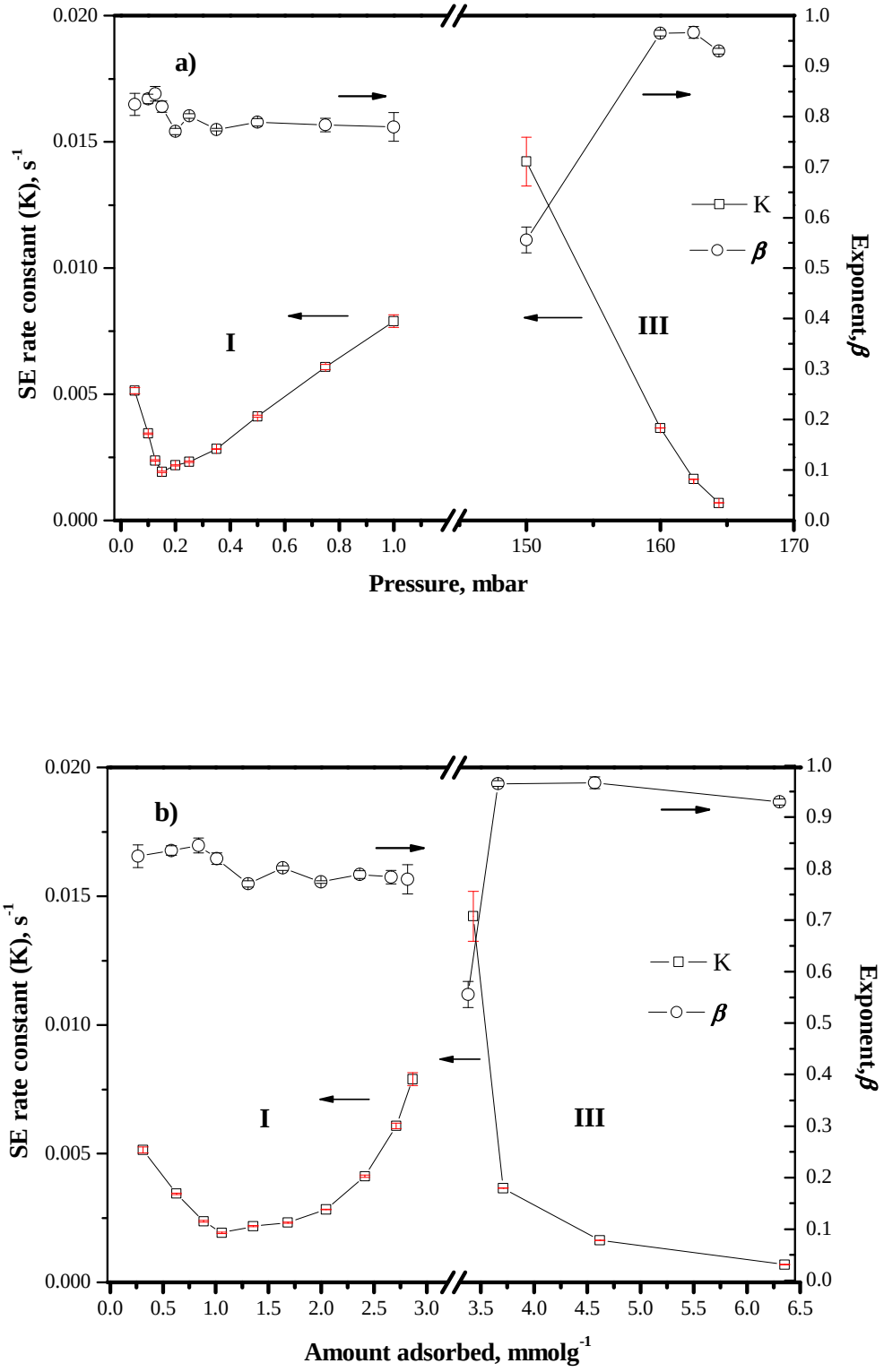

Figure 7.11 Kinetic profiles of methanol adsorption on NEW-1 at 298 K a) pressure based b) amount adsorbed based

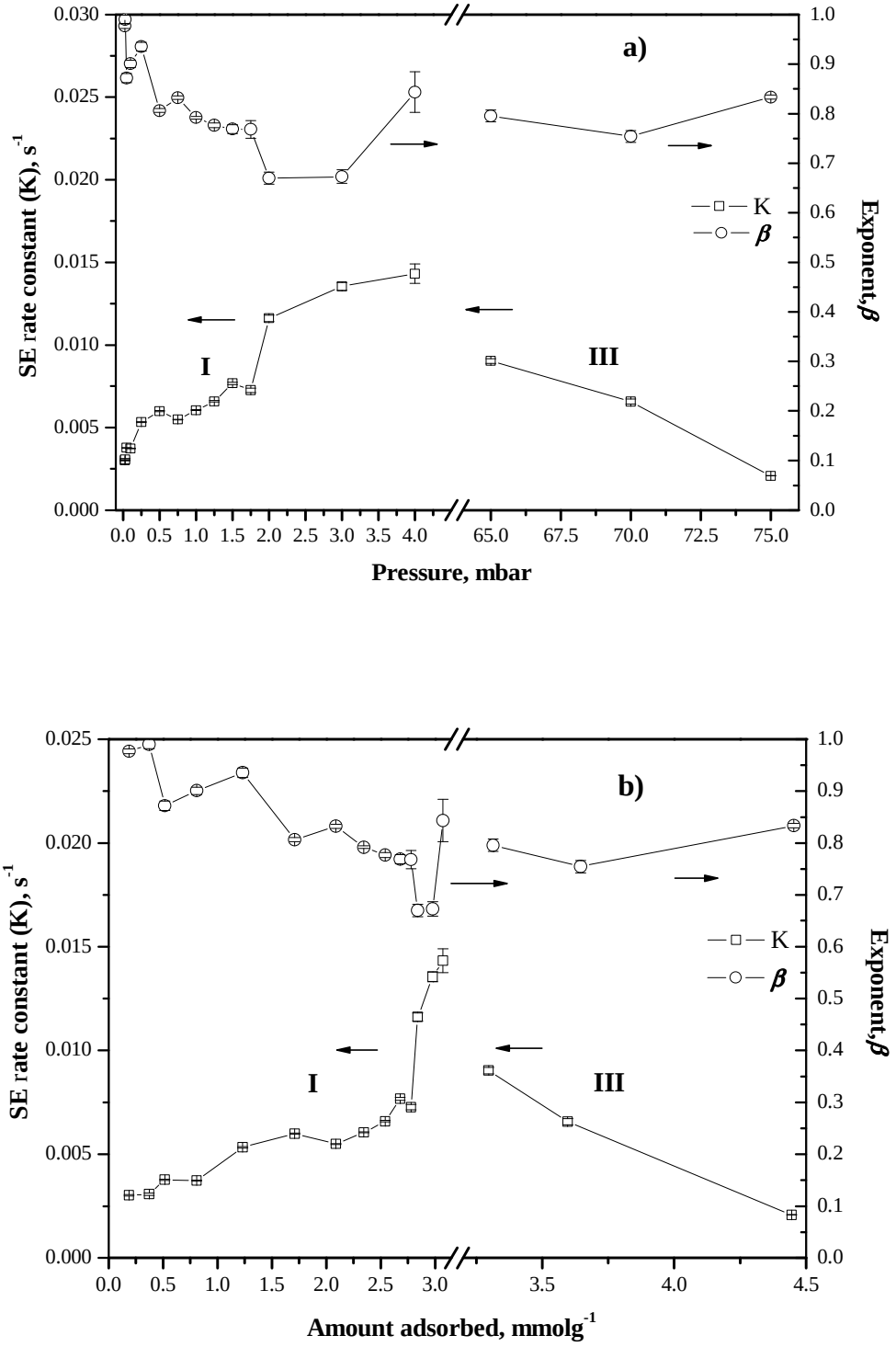

Figure 7.12 Kinetic profiles of ethanol adsorption on NEW-1 at 298 K
a) pressure based b) amount adsorbed based

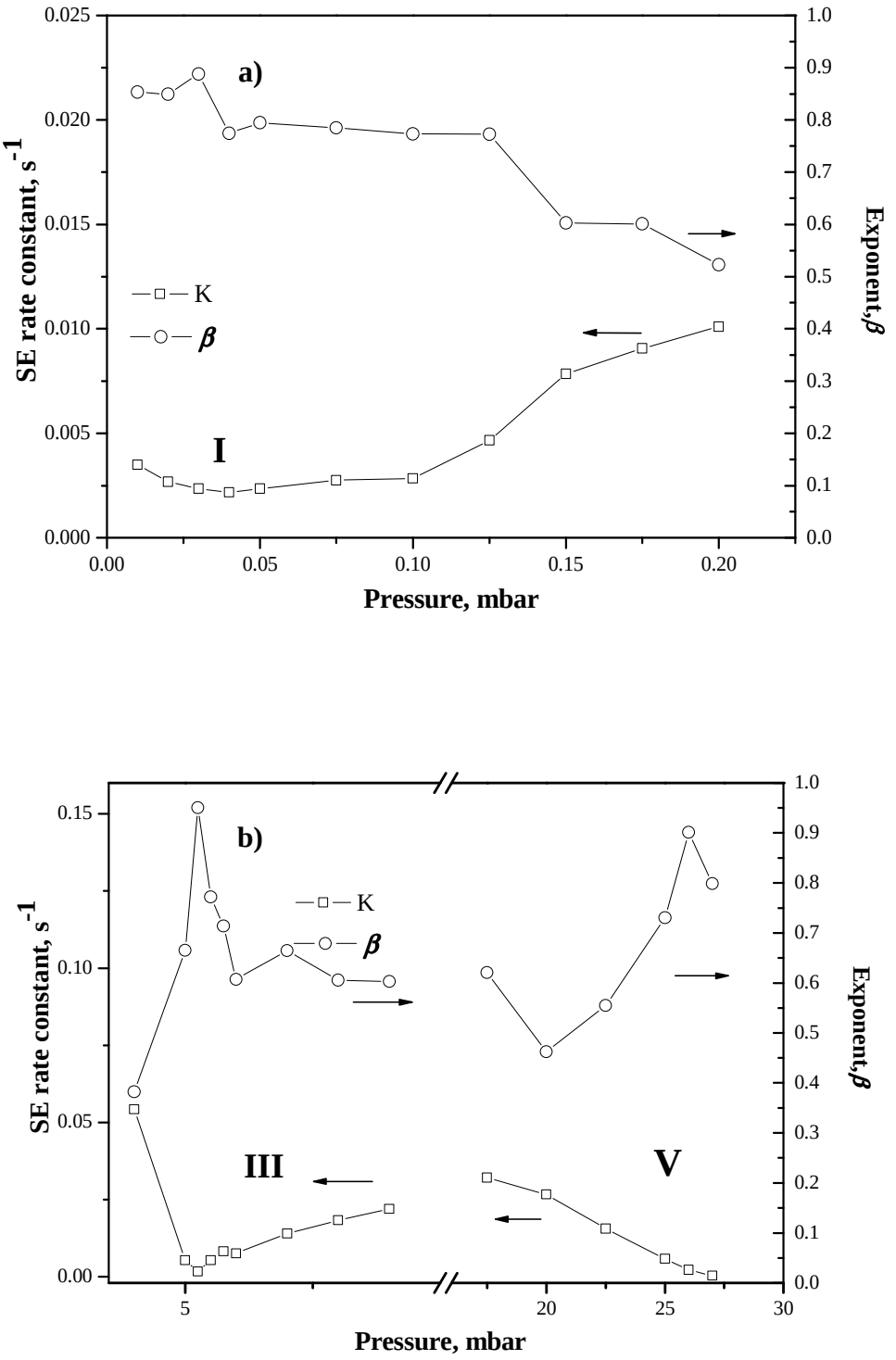

Figure 7.13 Kinetic profiles of 1-propanol adsorption on NEW-1 at 298 K based on the pressure a) region **I** and b) region **III** and **IV**

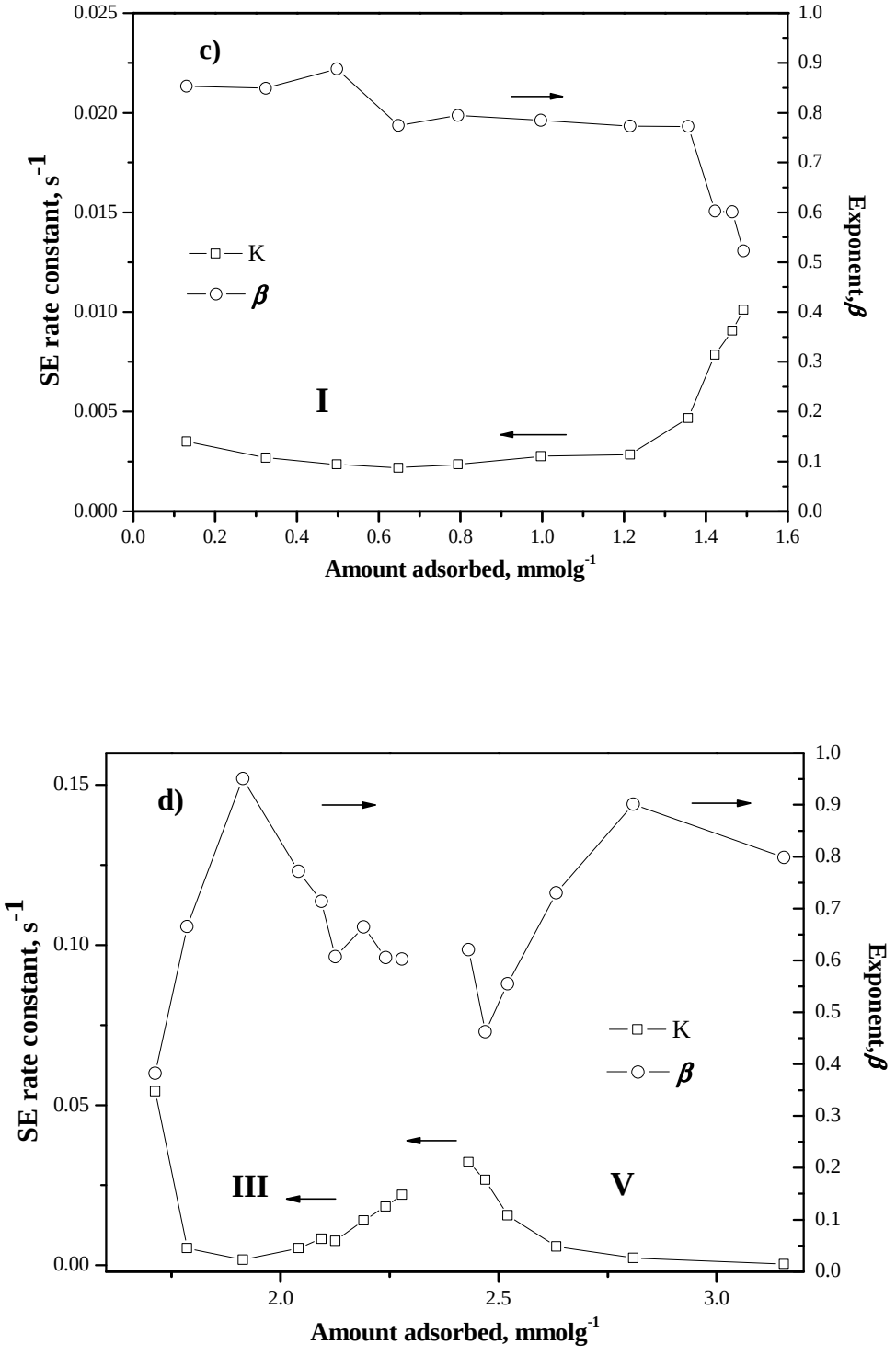

Figure 7.14 Kinetic profiles of 1-propanol adsorption on NEW-1 at 298 K based on the amount adsorbed c) region **I** and d) region **III** and **IV**

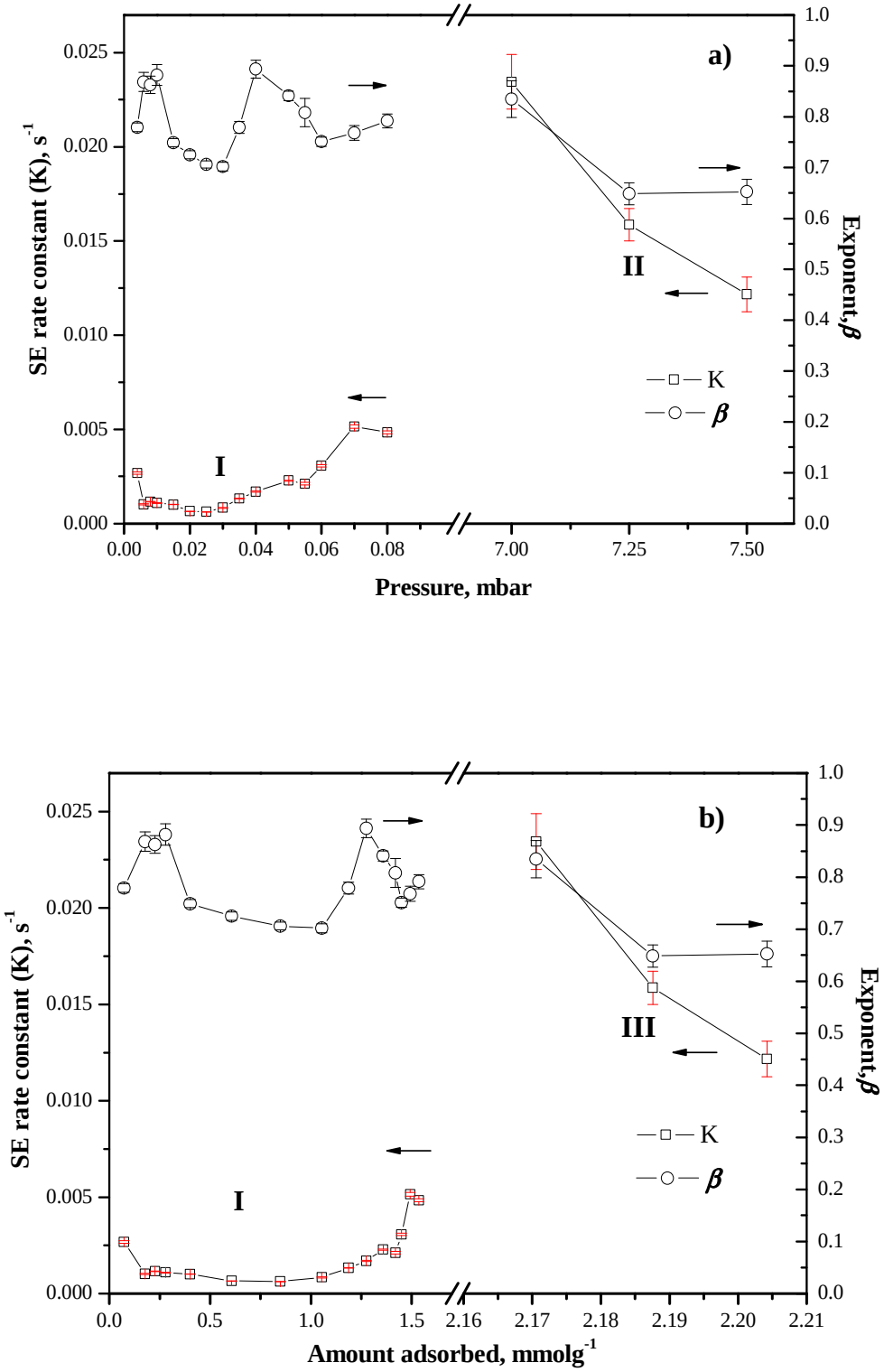

Figure 7.15 Kinetic profiles of *n*-butanol adsorption on NEW 1 at 298 K

a) pressure based b) amount adsorbed based

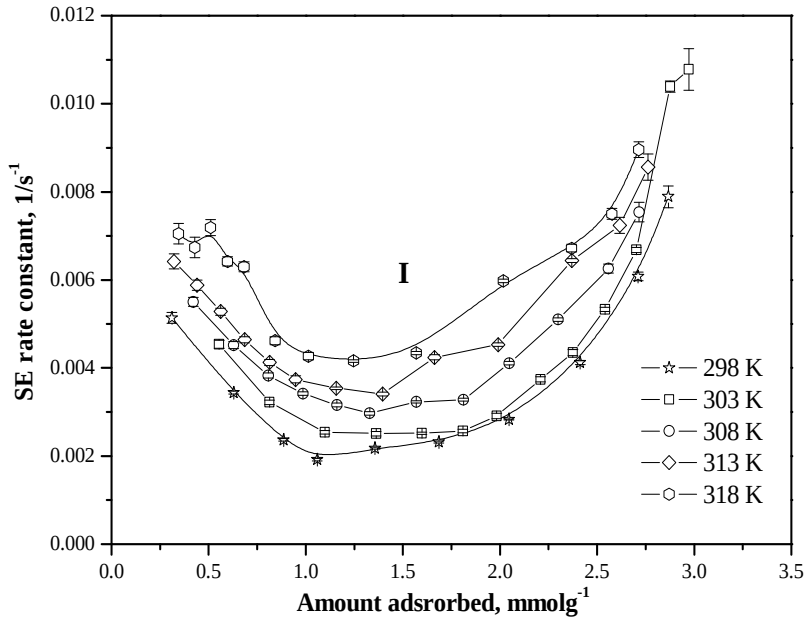

Figure 7.16 Kinetic profiles of methanol adsorption on NEW-1 at temperature range 298-318 K

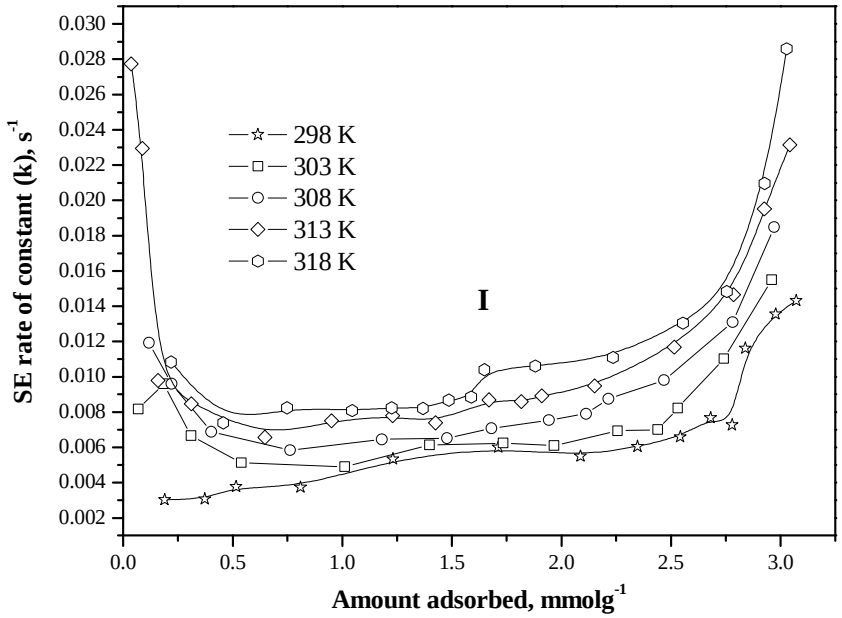

Figure 7.17 Kinetic profiles of ethanol adsorption on NEW-1 at temperature range 298-318 K

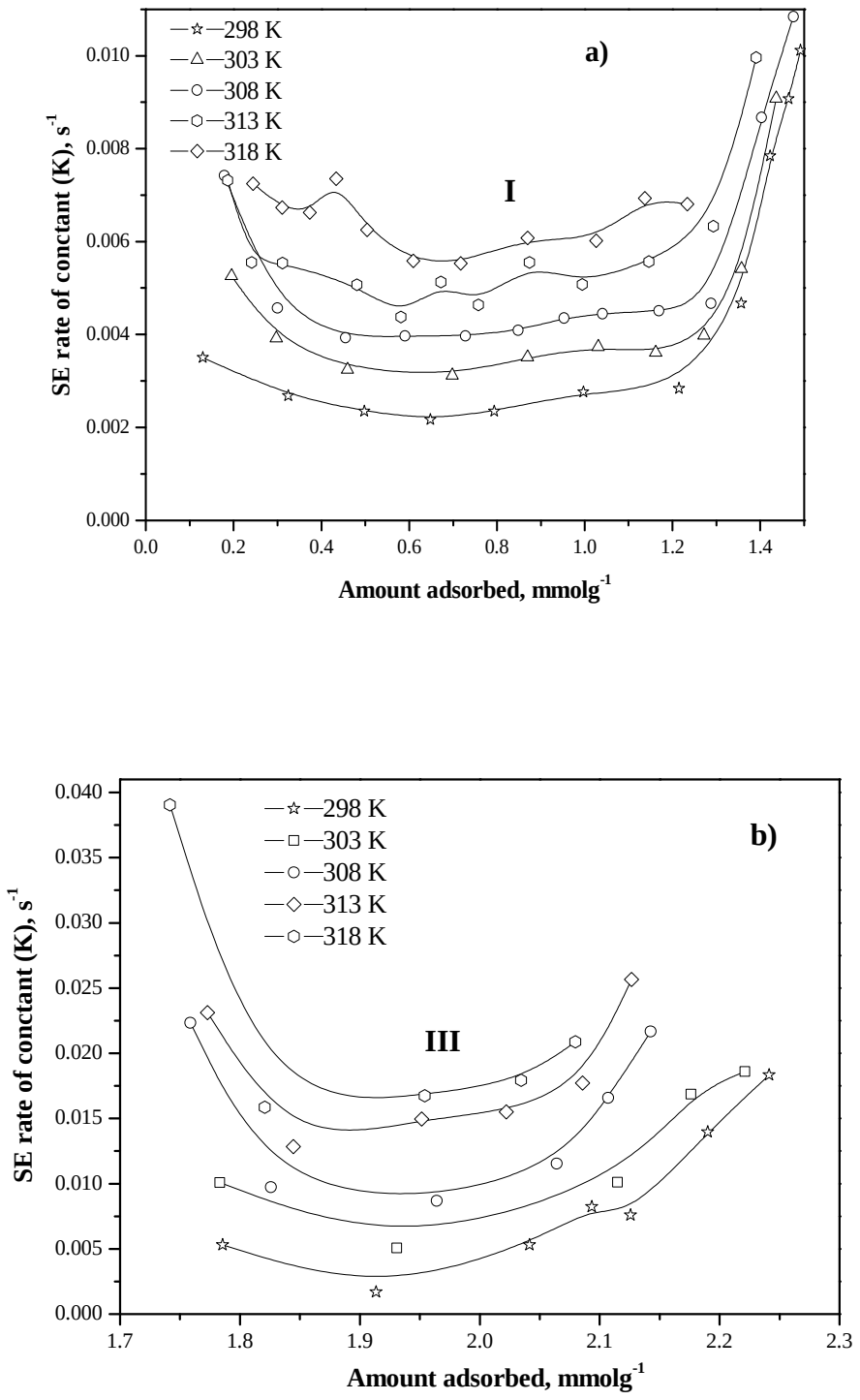

Figure 7.18 Kinetic profiles of 1-propanol adsorption on NEW-1 at temperature range 298-318 K a) at low surface coverage and b) at step adsorption

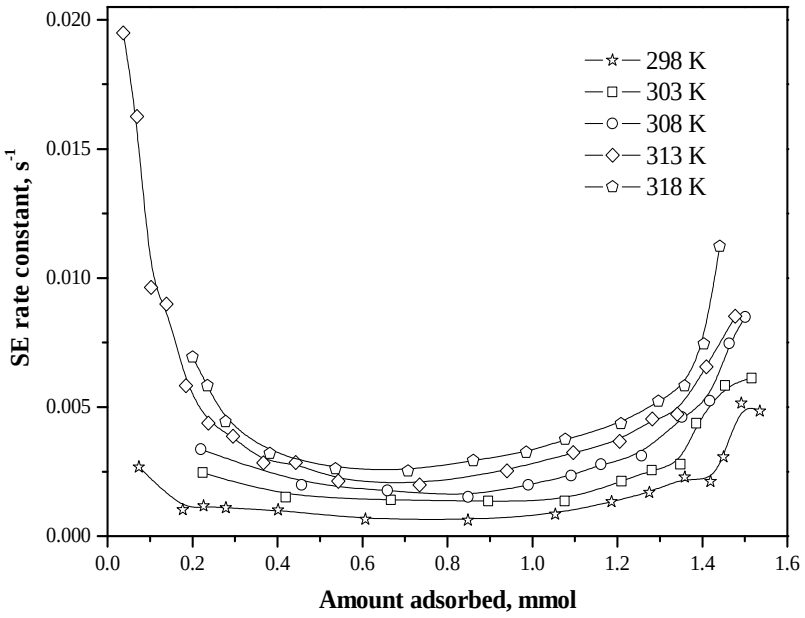

Figure 7.19 Kinetic profiles of *n*-butanol adsorption on NEW-1 at temperature range 298-318 K

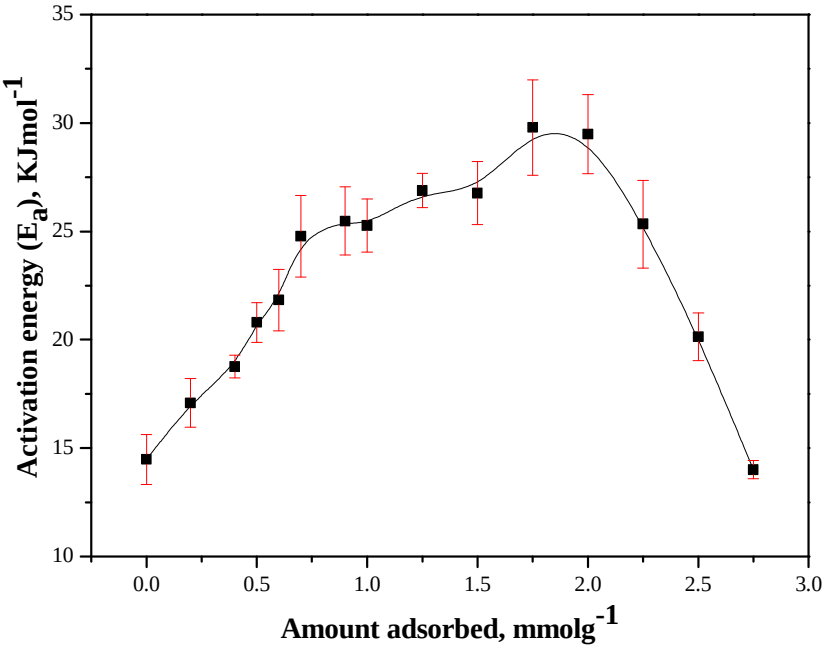

Figure 7.20 Activation energy of methanol adsorption on NEW-1 at temperature range 298-318 K

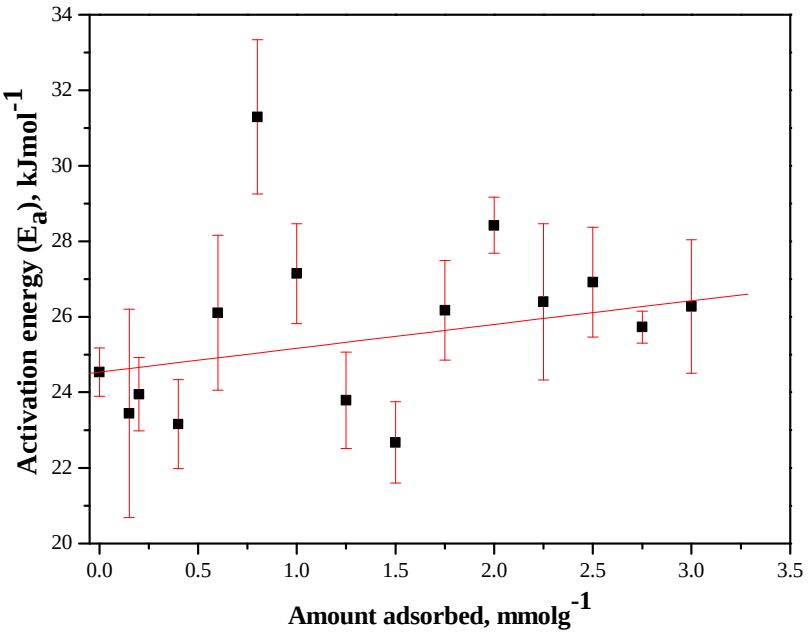

Figure 7.21 Activation energy of ethanol adsorption on NEW-1 at temperature range 298-318 K

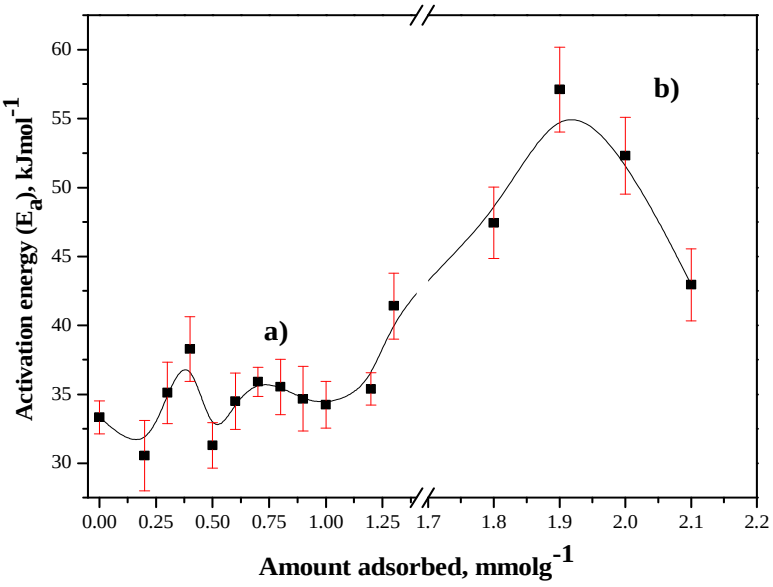

Figure 7.22 Activation energy of *n*-propanol adsorption on NEW-1 at temperature range 298-318 K a) at low surface coverage and b) at step adsorption

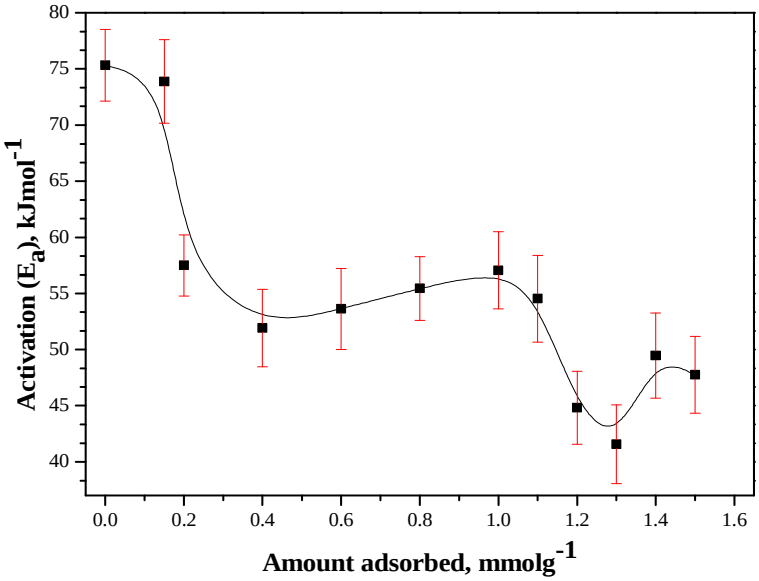

Figure 7.23 Activation energy of *n*-butanol adsorption on NEW-1 at temperature range 298-318 K

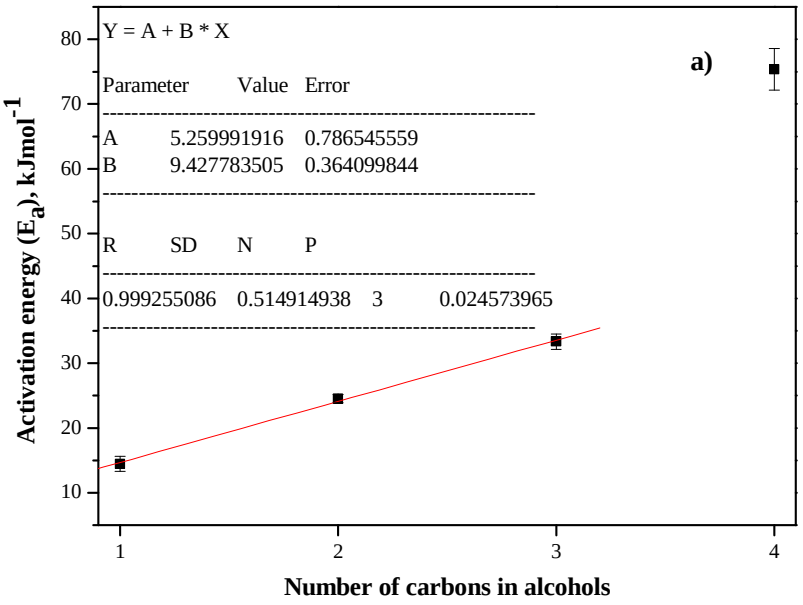

Figure 7.24 Showing the activation energies at a) zero surface coverage and b) 1.0 mmol surface coverage determined from alcohols adsorption on NEW-1with number of carbons in alcohols

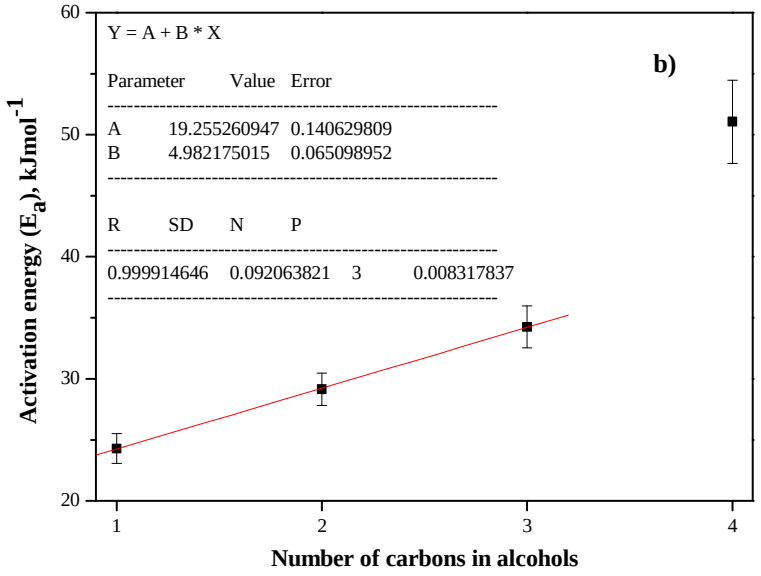

Figure 7.24 (Cont.) Showing the activation energies at a) zero surface coverage and b) 1.0 mmol surface coverage determined from alcohols adsorption on NEW-1with number of carbons in alcohols

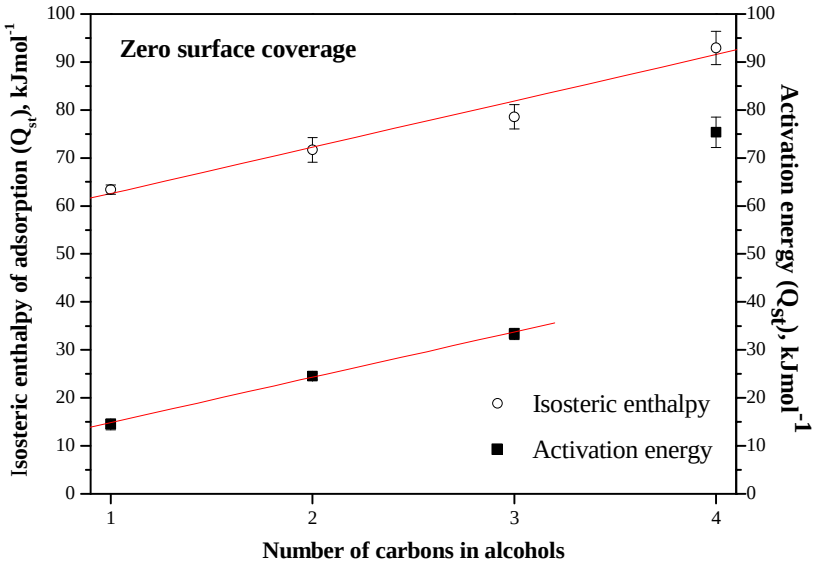

Figure 7.25 Comparing the the activation energies and isosteric enthalpies at zero surface coverage determined from alcohols adsorption on NEW-1with number of carbons in alcohols

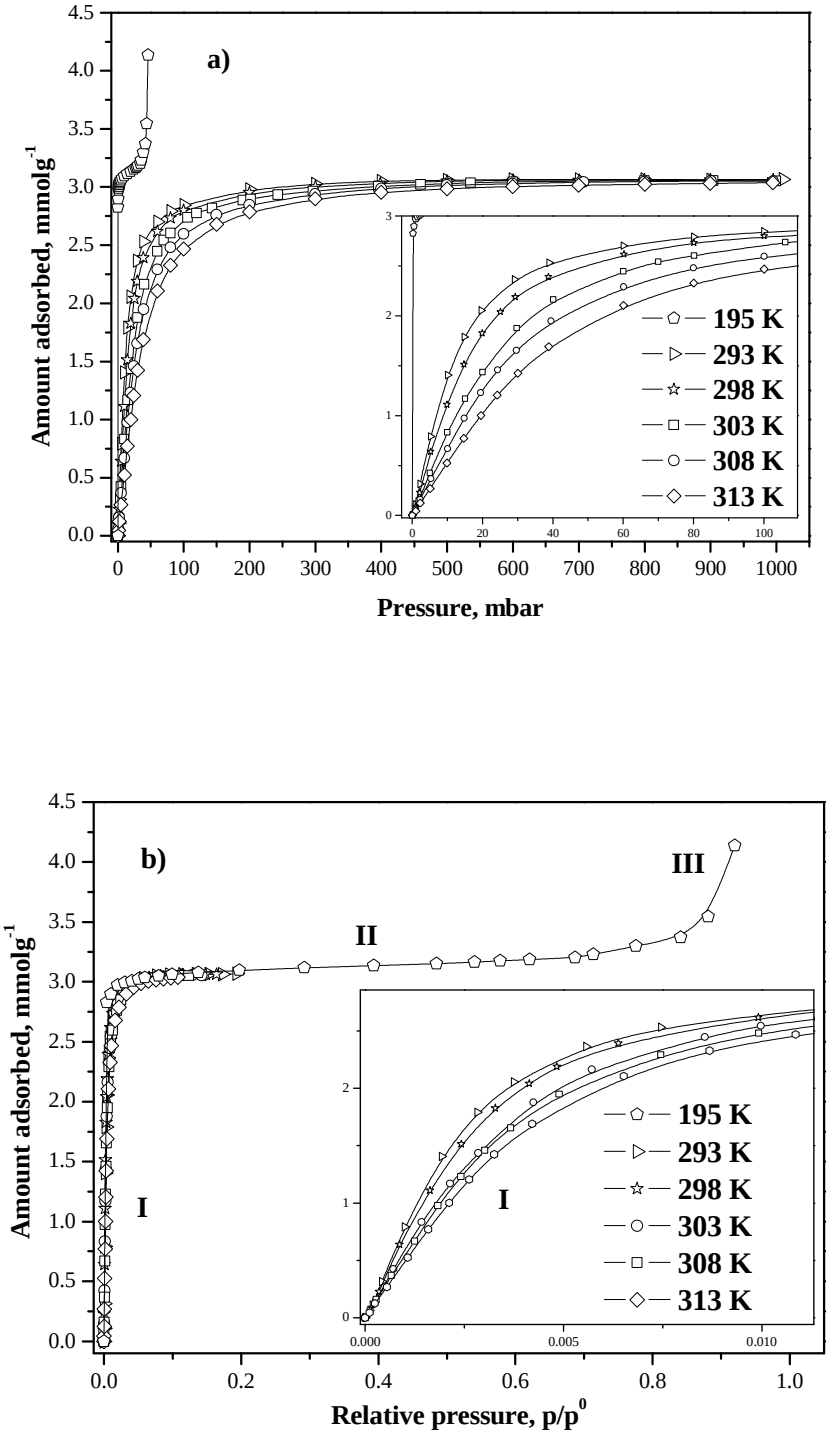

Figure 7.26 Isotherms for methyl chloride adsorption on NEW-1 over the temperature range 195-313 K a) on a pressure basis with an inset in low pressure region and b) on a relative pressure basis with an inset in the low relative pressure region

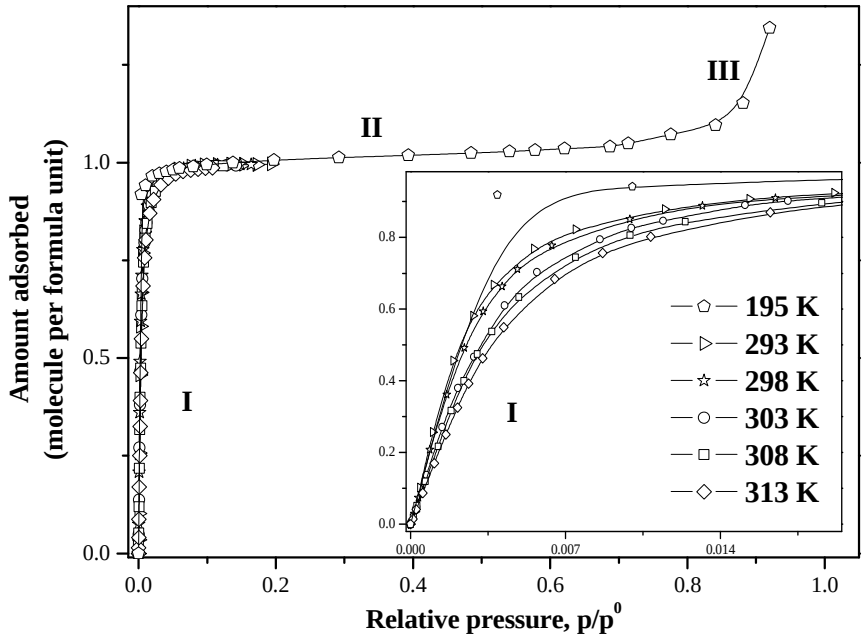

Figure 7.27 Isotherm for methyl chloride adsorption on NEW-1 showing amount adsorbed on molecule per formula unit with inset in low relative pressure.

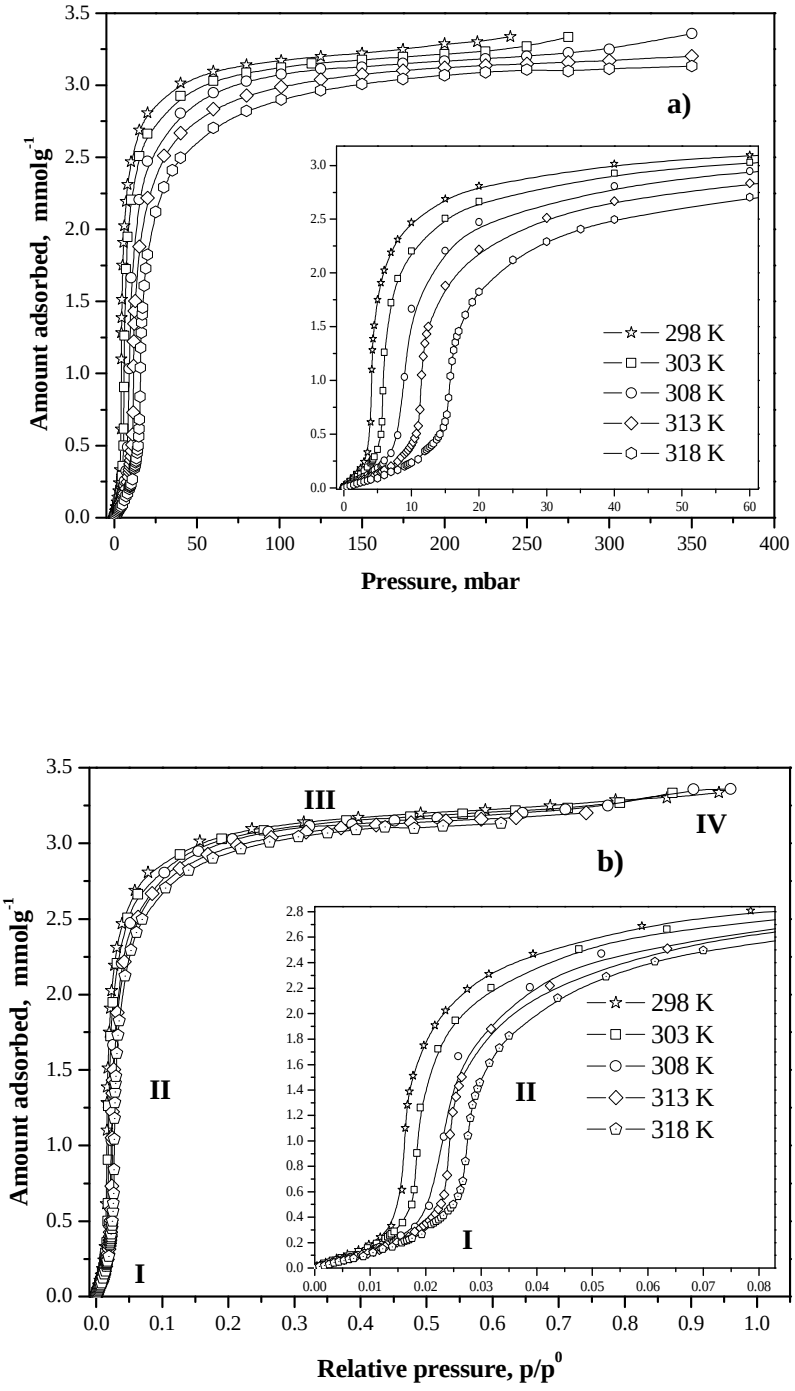

Figure 7.28 Isotherm for chloroform adsorption on NEW-1 over the temperature range 298-318 K a) on a pressure basis with an inset in low pressure region and b) on a relative pressure basis with an inset in the low relative pressure region

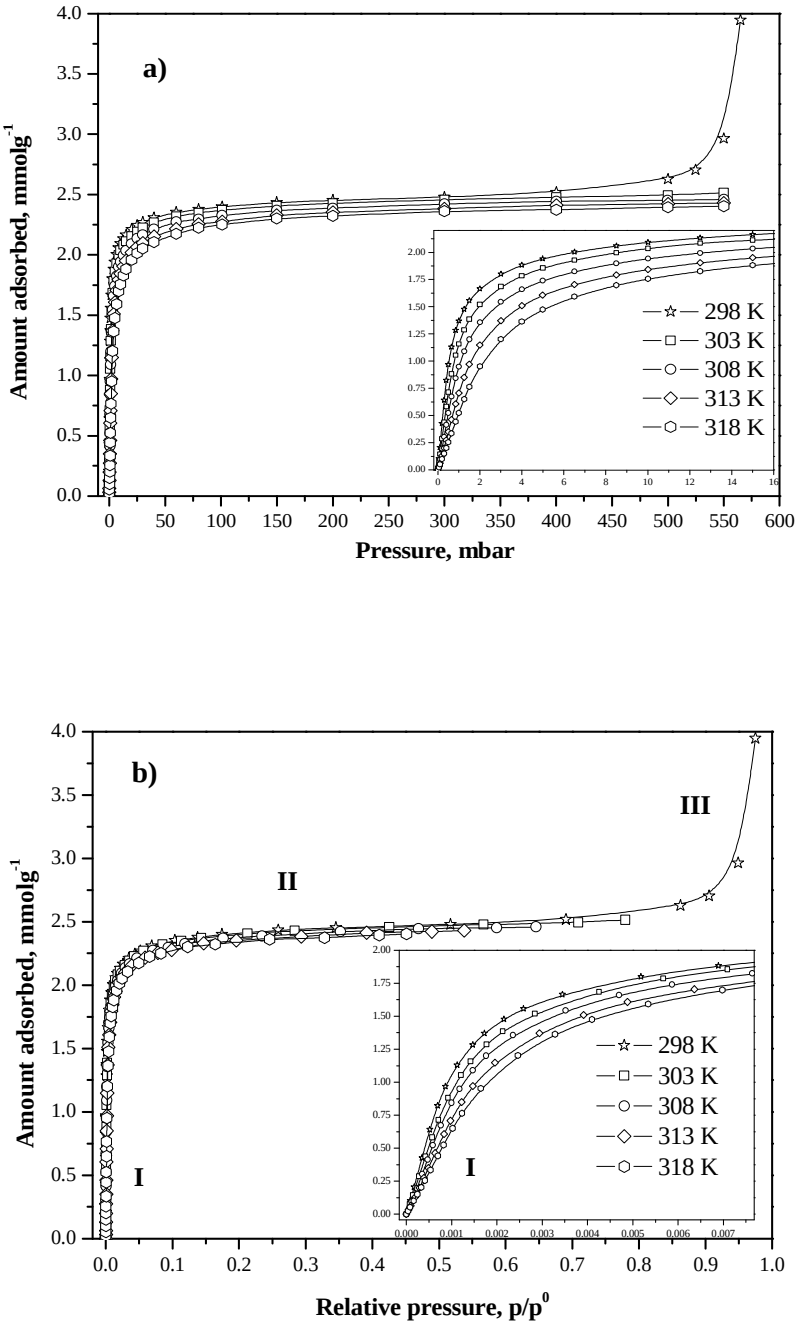

Figure 7.29 Isotherm for dichloromethane adsorption on NEW-1 over the temperature range 298-318 K a) on a pressure basis with an inset in low pressure region and b) on a relative pressure basis with an inset in the low relative pressure region

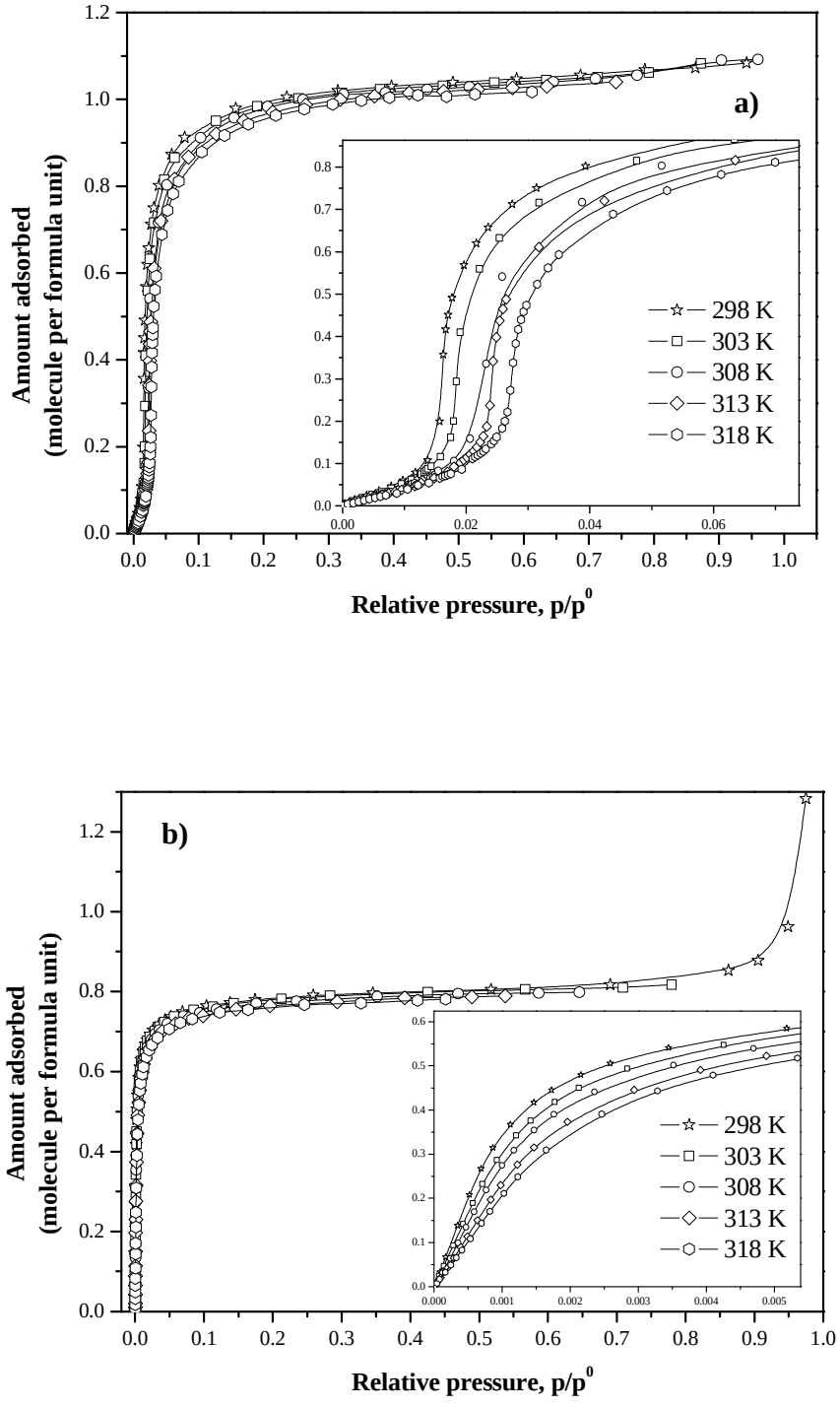

Figure 7.30 Adsorption isotherms for a) chloroform and b) dichloromethane on NEW-1 showing amount adsorbed on molecule per formula unit with inset in low relative pressure.

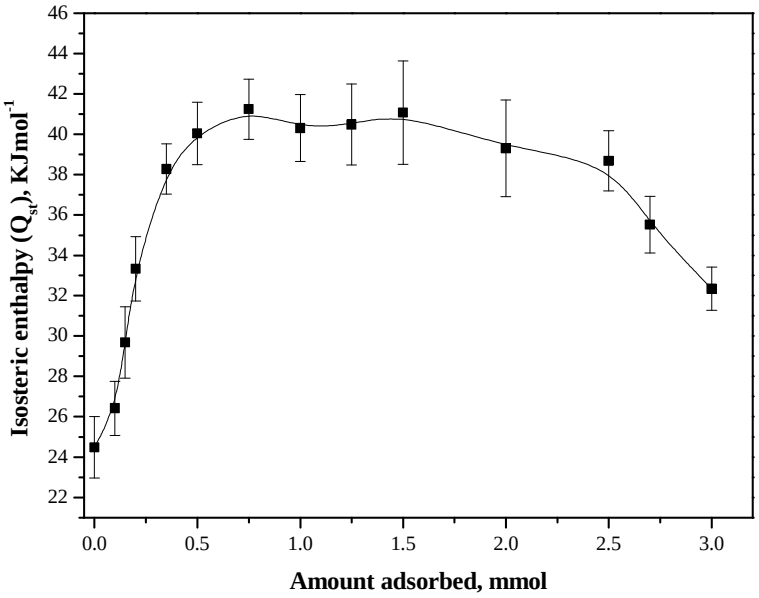

Figure 7.31 Isosteric enthalpies obtained for methyl chloride adsorption on NEW-1 as a function of the surface coverage.

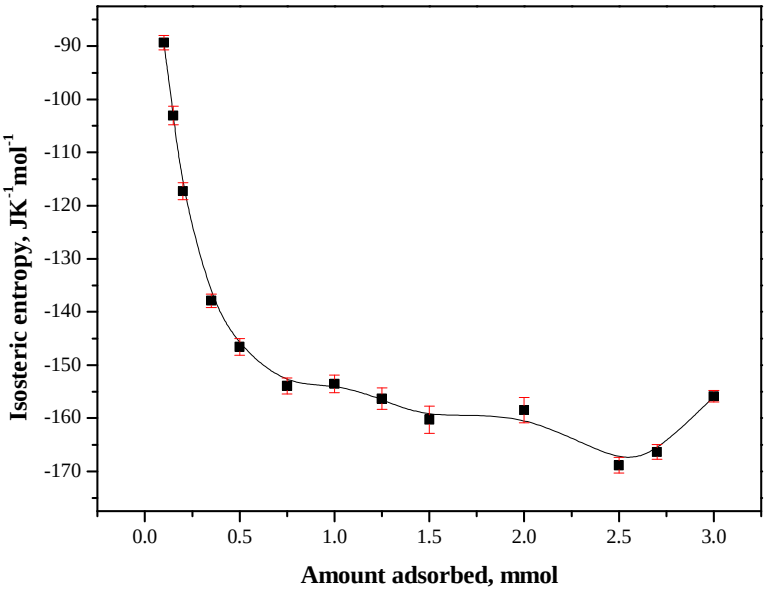

Figure 7.32 Isosteric entropies obtained for methyl chloride adsorption on NEW-1 as a function of the surface coverage.

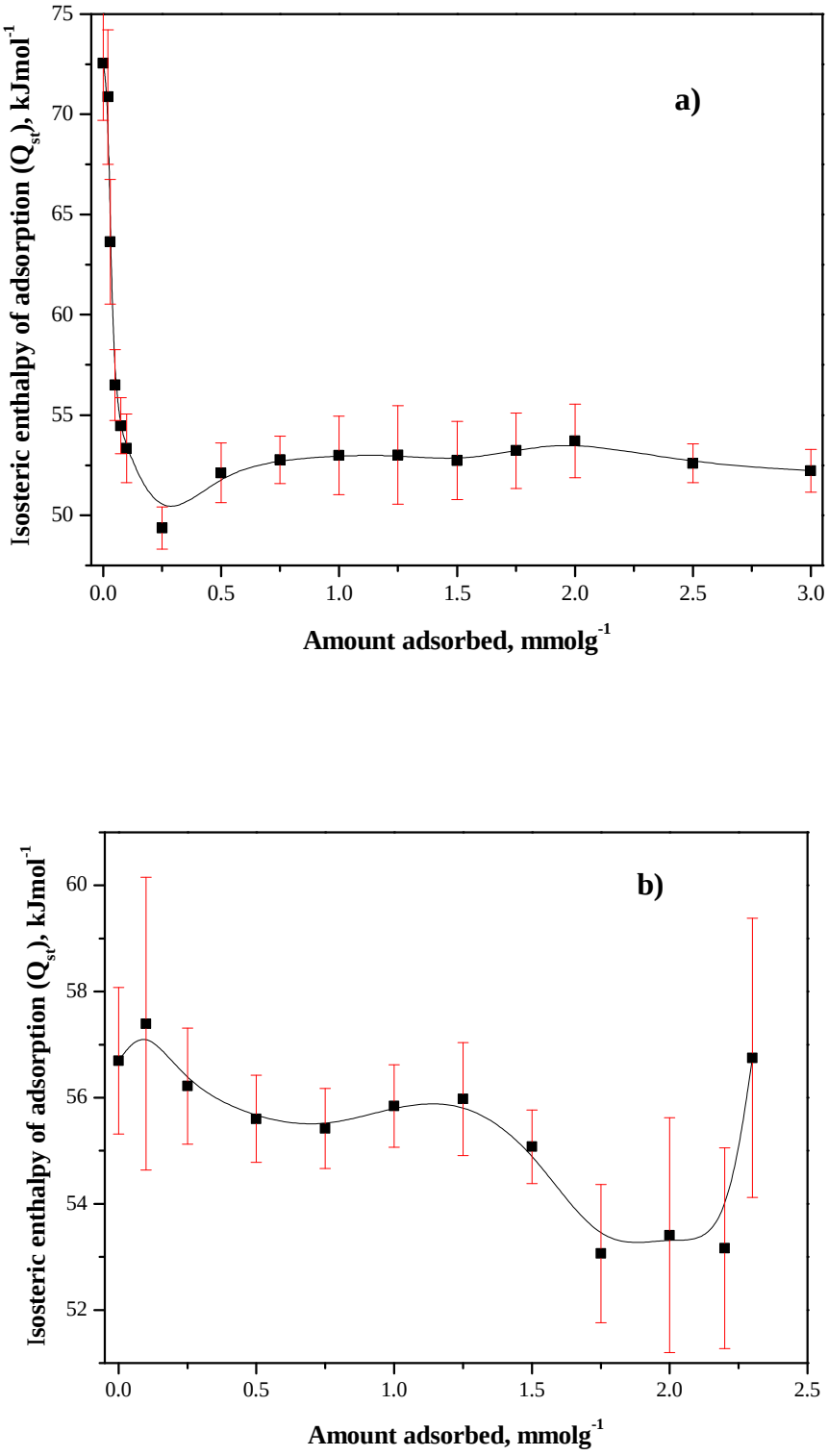

Figure 7.33 Isosteric enthalpies of a) chloroform and b) dichloromethane as a function of the surface coverage.

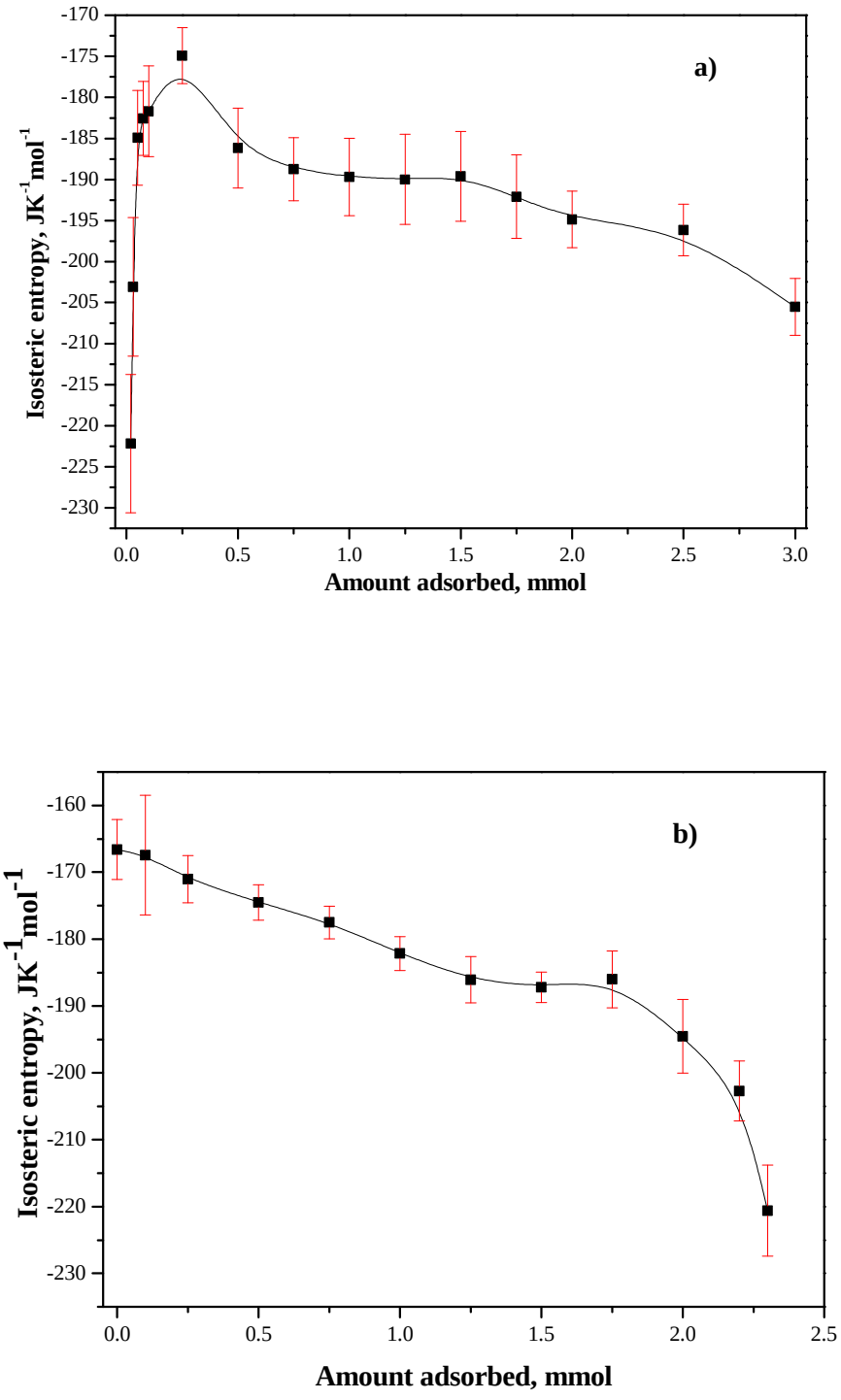

Figure 7.34 Isosteric entropies of a) chloroform and b) dichloromethane as a function of the surface coverage.

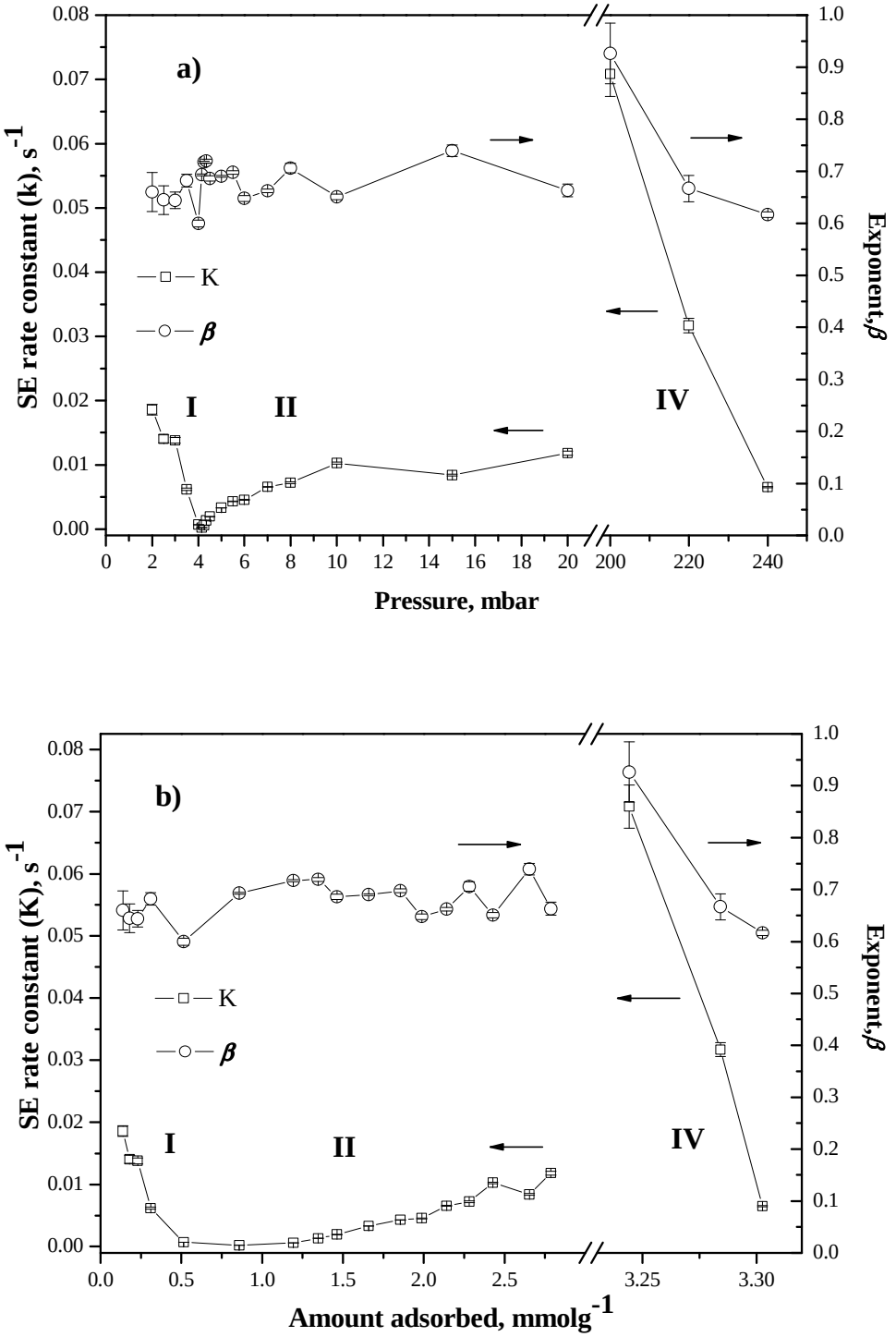

Figure 7.35 Kinetic profiles of chloroform adsorption on NEW-1 at 298 K
a) pressure based b) amount adsorbed based

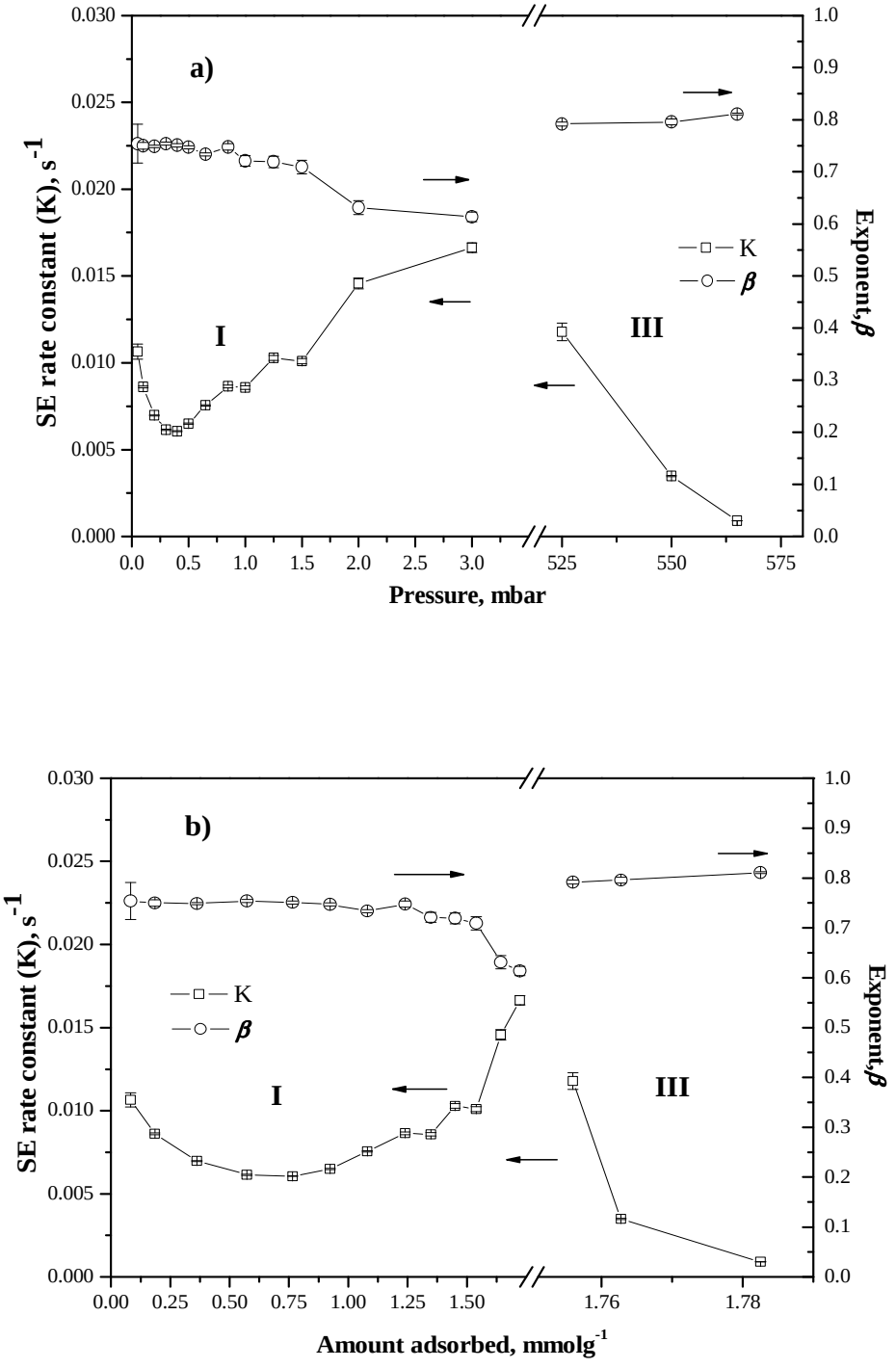

Figure 7.36 Kinetic profiles of dichloromethane adsorption on NEW-1 at 298 K
a) pressure based b) amount adsorbed based

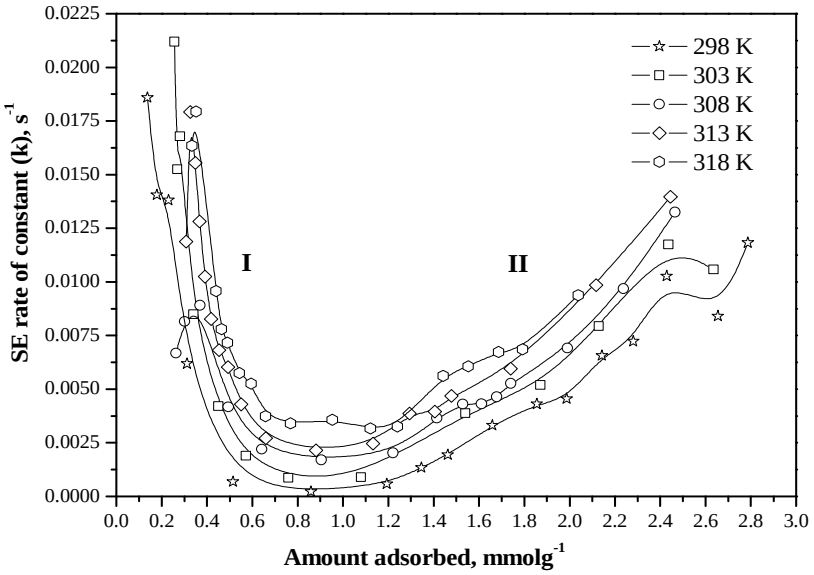

Figure 7.37 Kinetic profiles of chloroform adsorption on NEW-1 over the temperature range 298-318 K

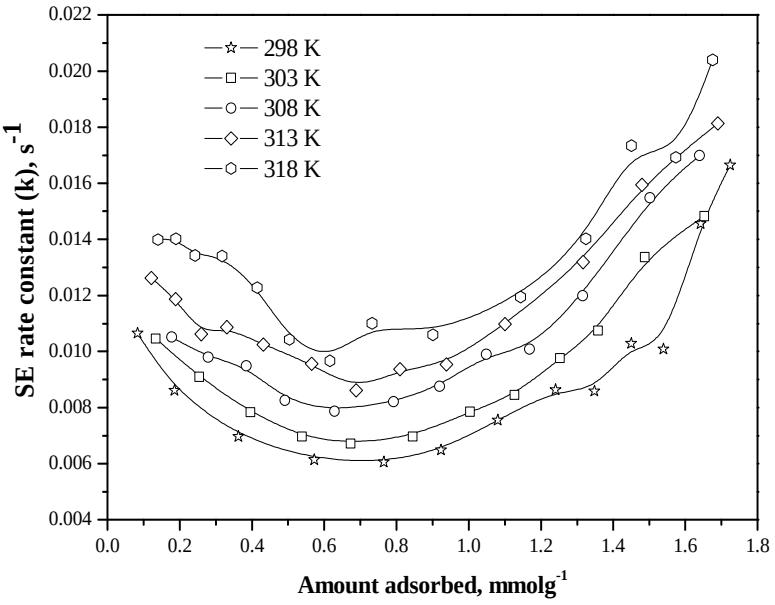

Figure 7.38 Kinetic profiles of dichloromethane adsorption on NEW-1 over the temperature range 298-318 K

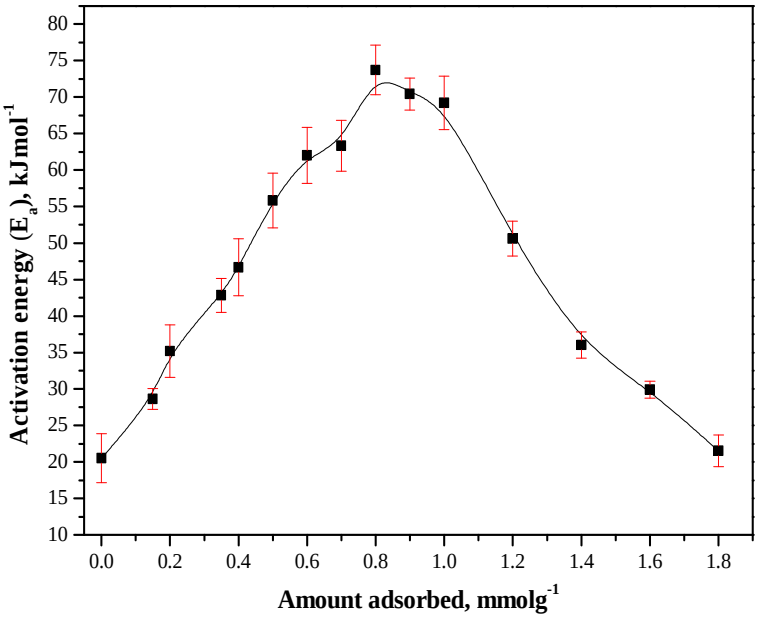

Figure 7.39 Activation energy of chloroform adsorption on NEW-1 over the temperature range 298-318 K

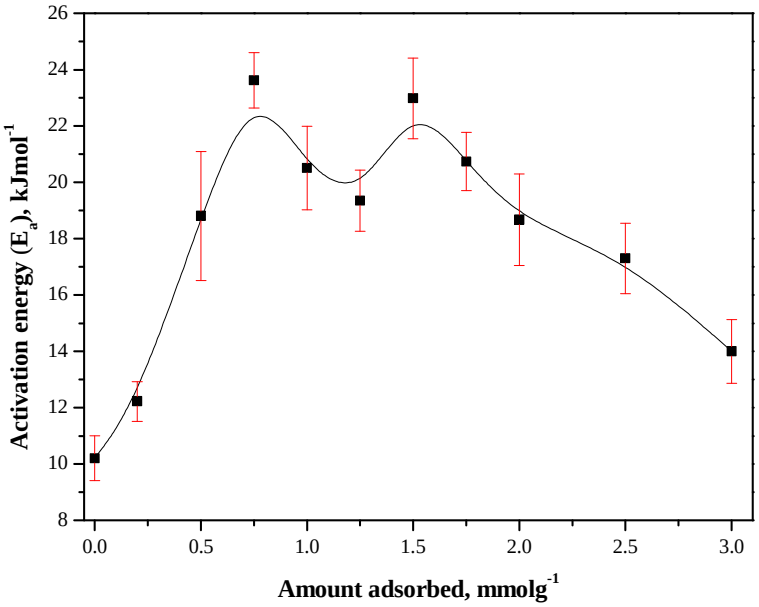

Figure 7.40 Activation energy of dichloromethane adsorption on NEW-1 over the temperature range 298-318 K

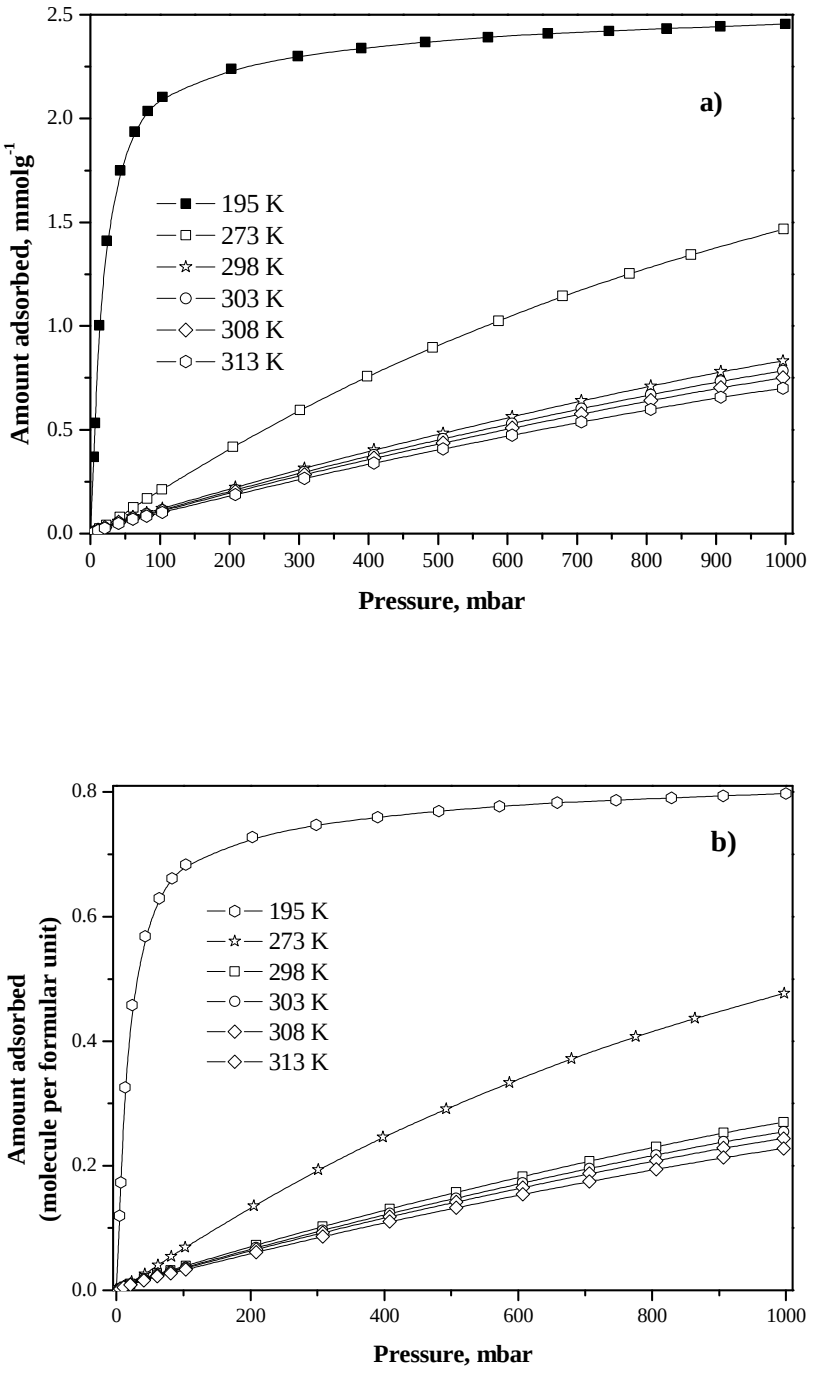

Figure 7.41 Isotherms of methane adsorption on NEW-1 over temperature range 195-313 K showing a) the amount adsorbed and b) amount adsorbed per crystallographic formula unit

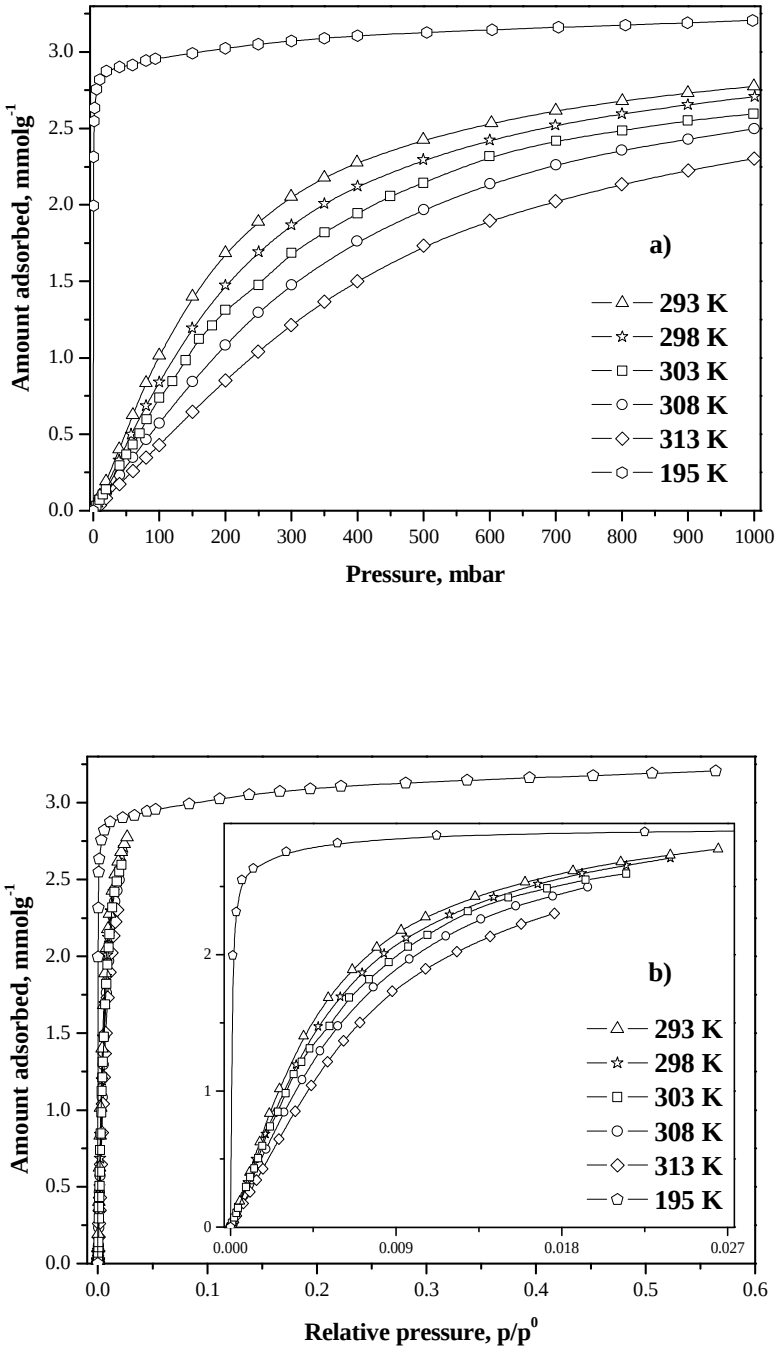

Figure 7.42 Isotherms of ethane adsorption on NEW-1 over temperature range 195-313 K a) based on a pressure basis and b) relative pressure with an inset shows the lower pressure region

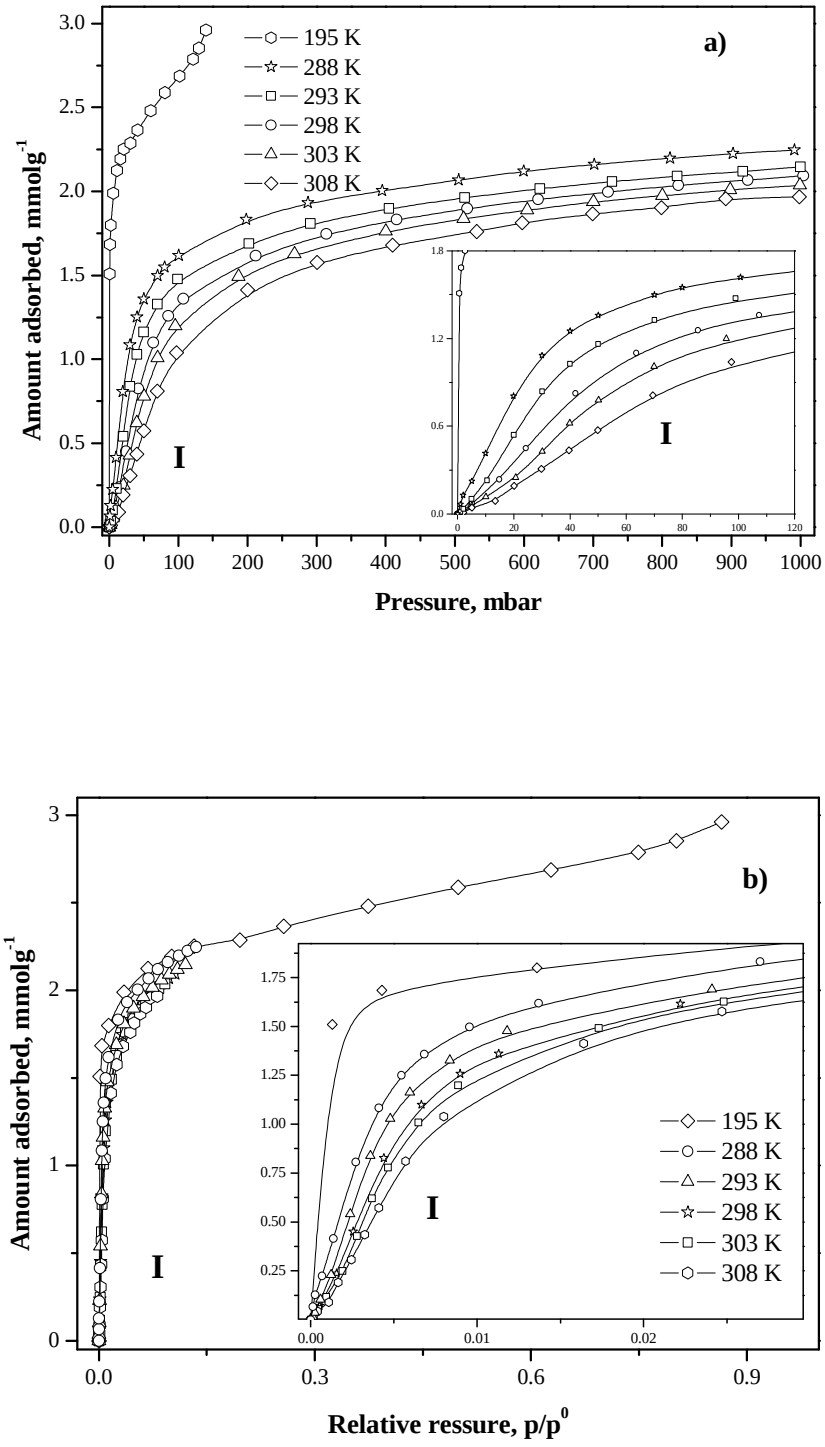

Figure 7.43 Isotherms of propane adsorption on NEW-1 over temperature range 195-308 K a) based on a pressure basis and b) relative pressure with an inset shows the lower pressure region

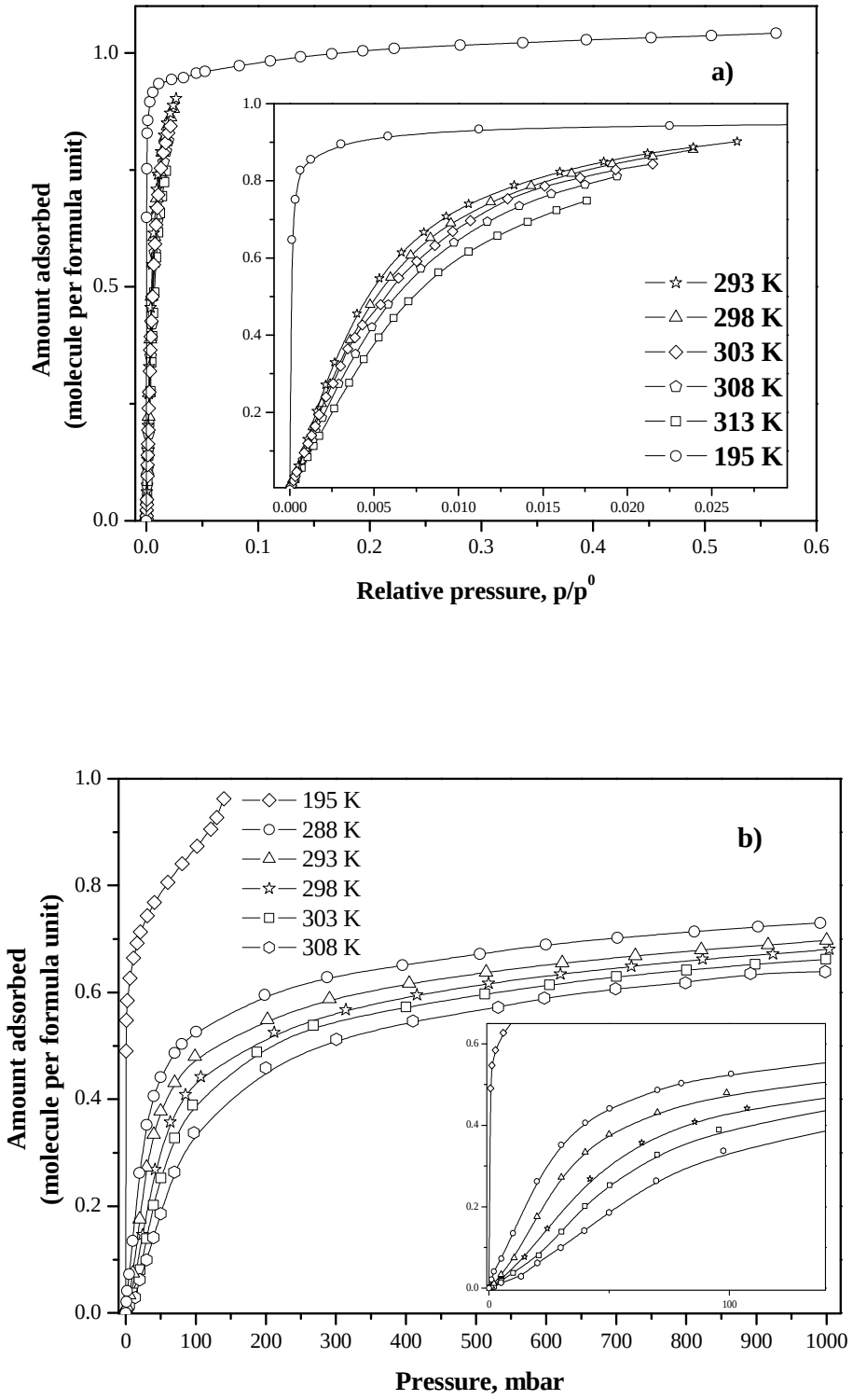

Figure 7.44 Isotherms of a) ethane and b) propane adsorption on NEW-1 over temperature 195-313 K based on amount adsorbed on molecules per formula unit.

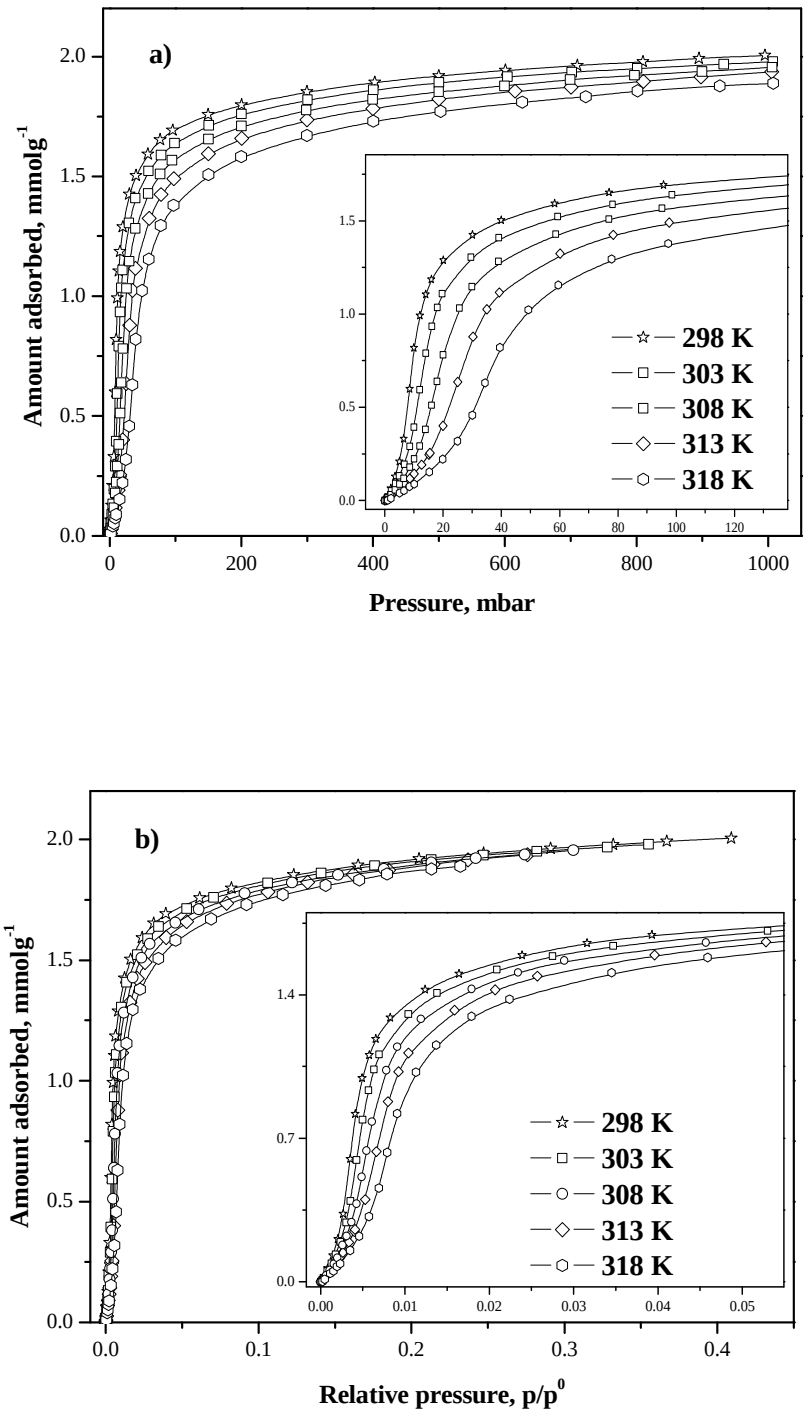

Figure 7.45 Isotherms of *n*-butane adsorption on NEW-1 over temperature range 298-318 K a) on a pressure basis with an inset shows the lower pressure region and b) on a relative pressure basis.

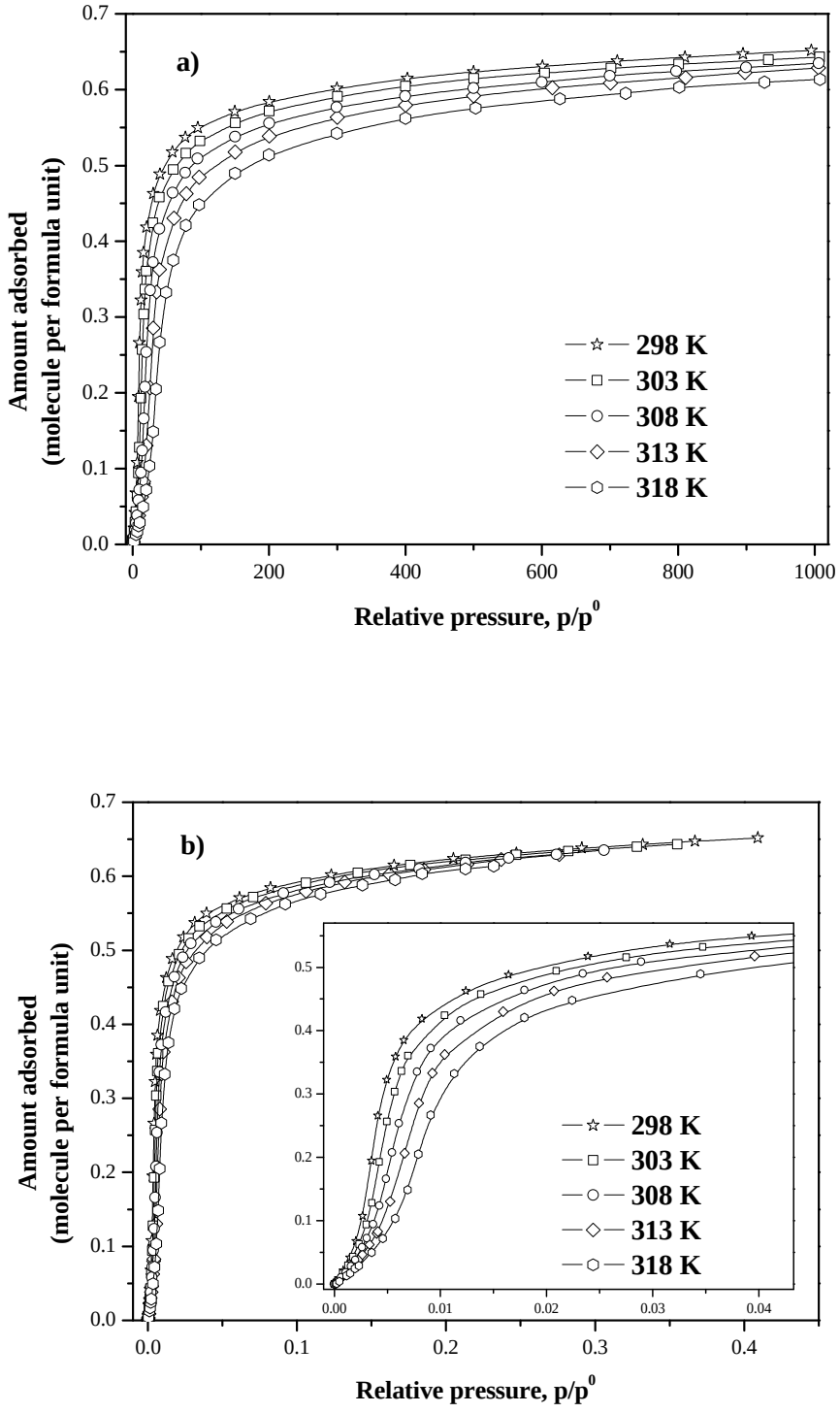

Figure 7.46 Isotherms of *n*-butane adsorption on NEW-1 over temperature 298-318 K based on amount adsorbed on molecules per formula unit and a) pressure and b) relative pressure with an inset at low relative pressure.

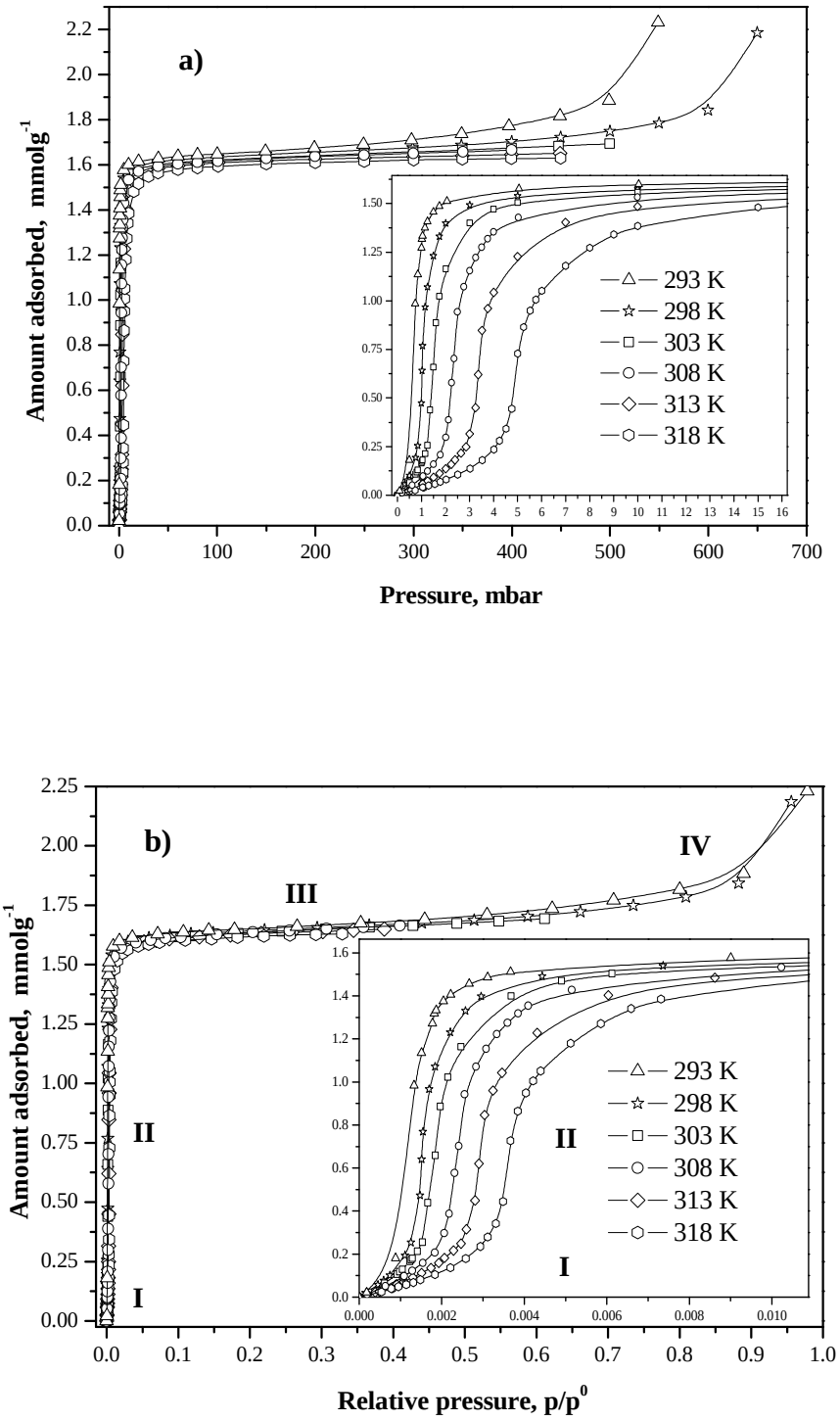

Figure 7.46 Isotherms of *n*-pentane adsorption on NEW-1 over temperature range 293-318 K a) on a pressure basis with an inset shows the lower pressure region and b) on a relative pressure basis.

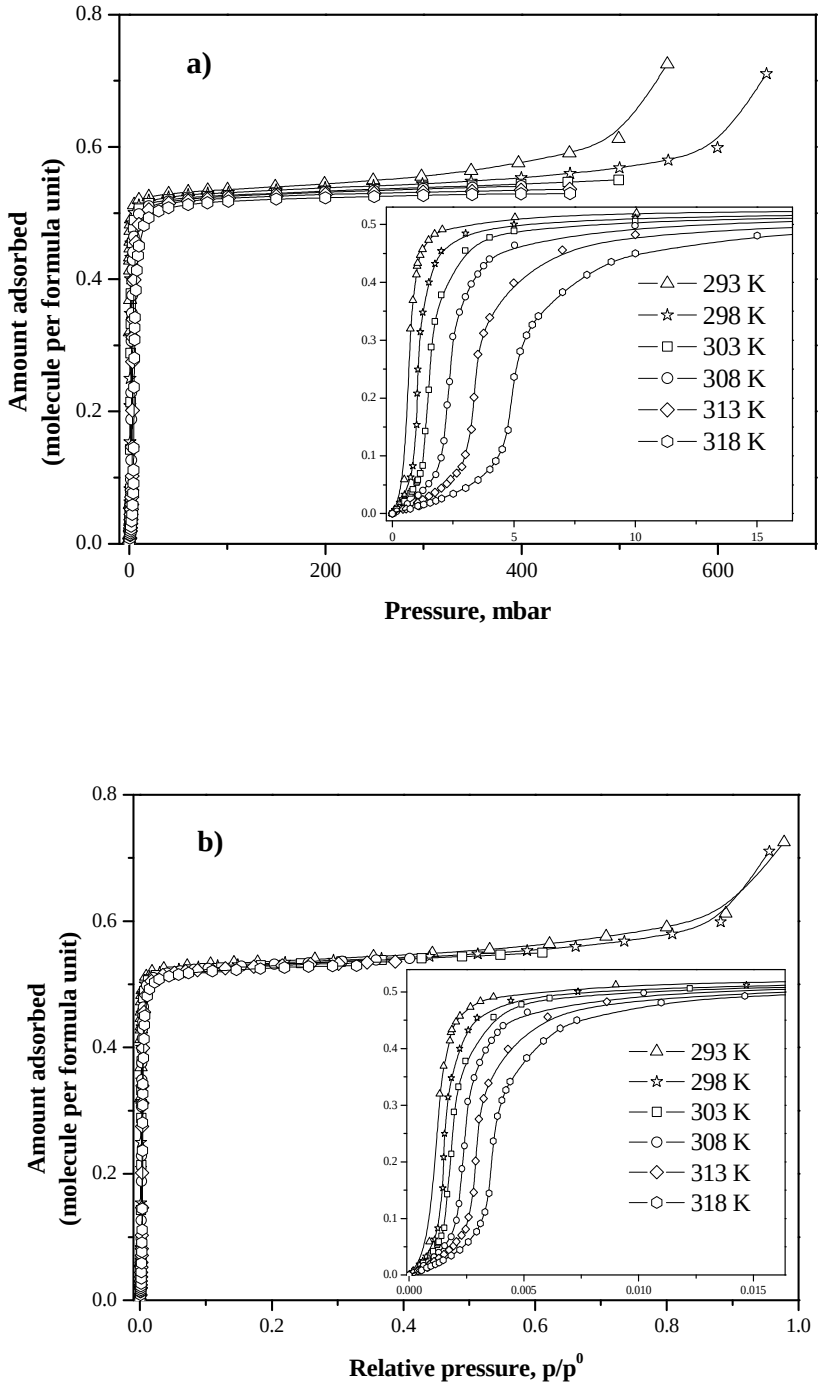

Figure 7.47 Isotherms of *n*-pentane adsorption on NEW-1 over temperature 293-318 K based on amount adsorbed on molecules per formula unit and a) pressure and b) relative pressure.

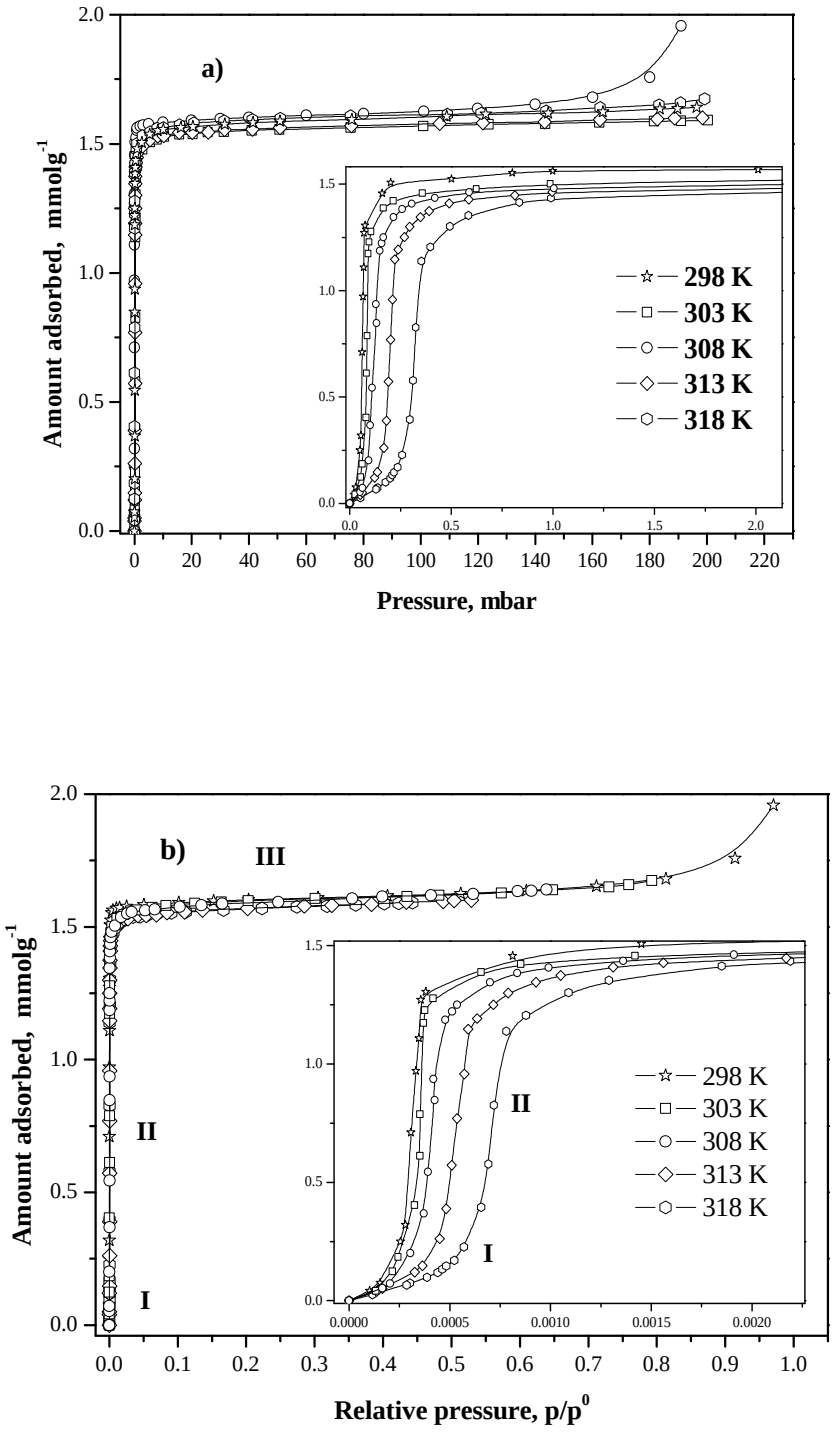

Figure 7.48 Isotherms of *n*-hexane adsorption on NEW-1 over temperature range 298-318 K a) on a pressure basis with an inset shows the lower pressure region and b) on a relative pressure basis.

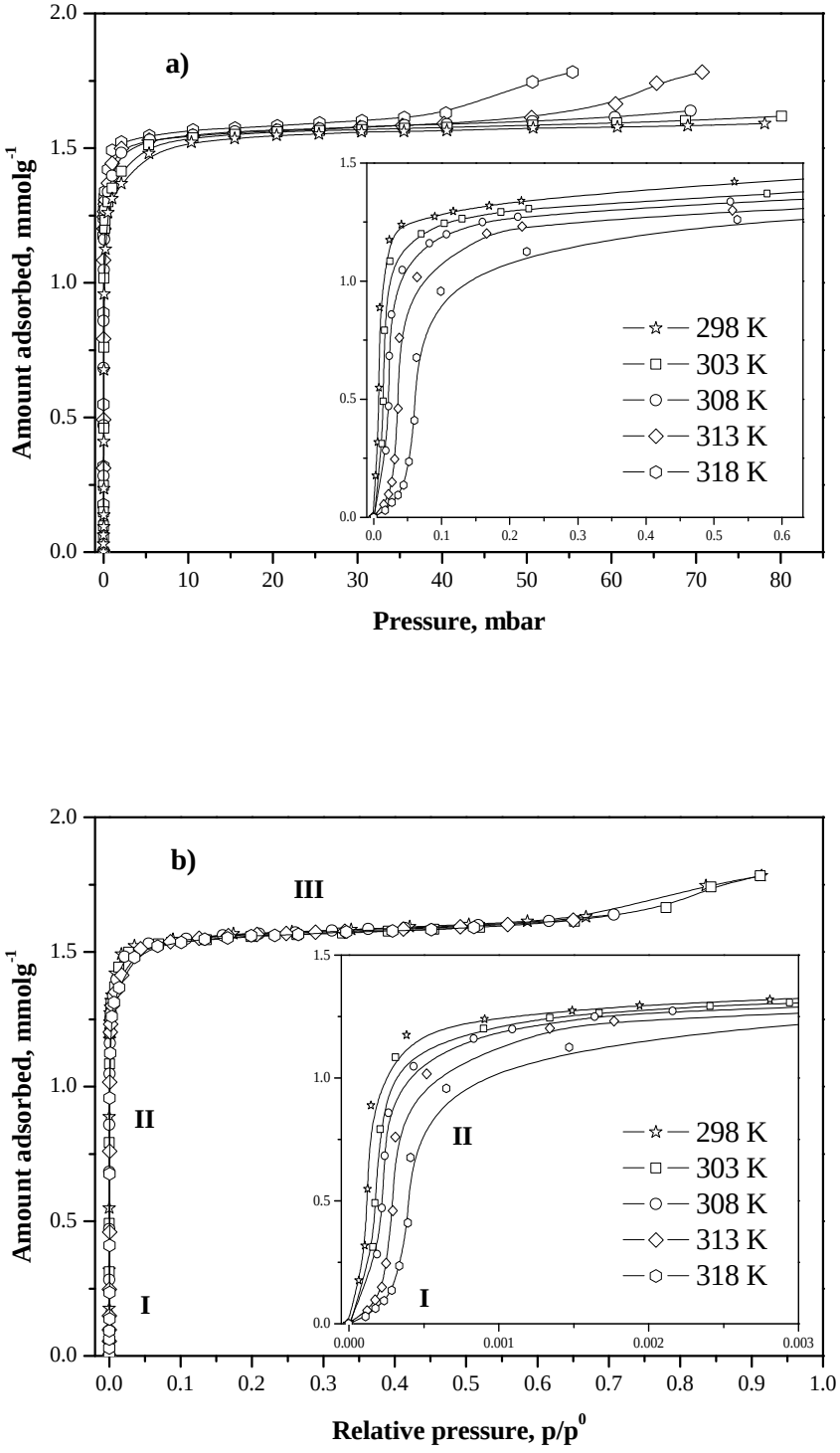

Figure 7.49 Isotherms of *n*-heptane adsorption on NEW-1 over temperature range 298-318 K a) on a pressure basis with an inset shows the lower pressure region and b) on a relative pressure basis.

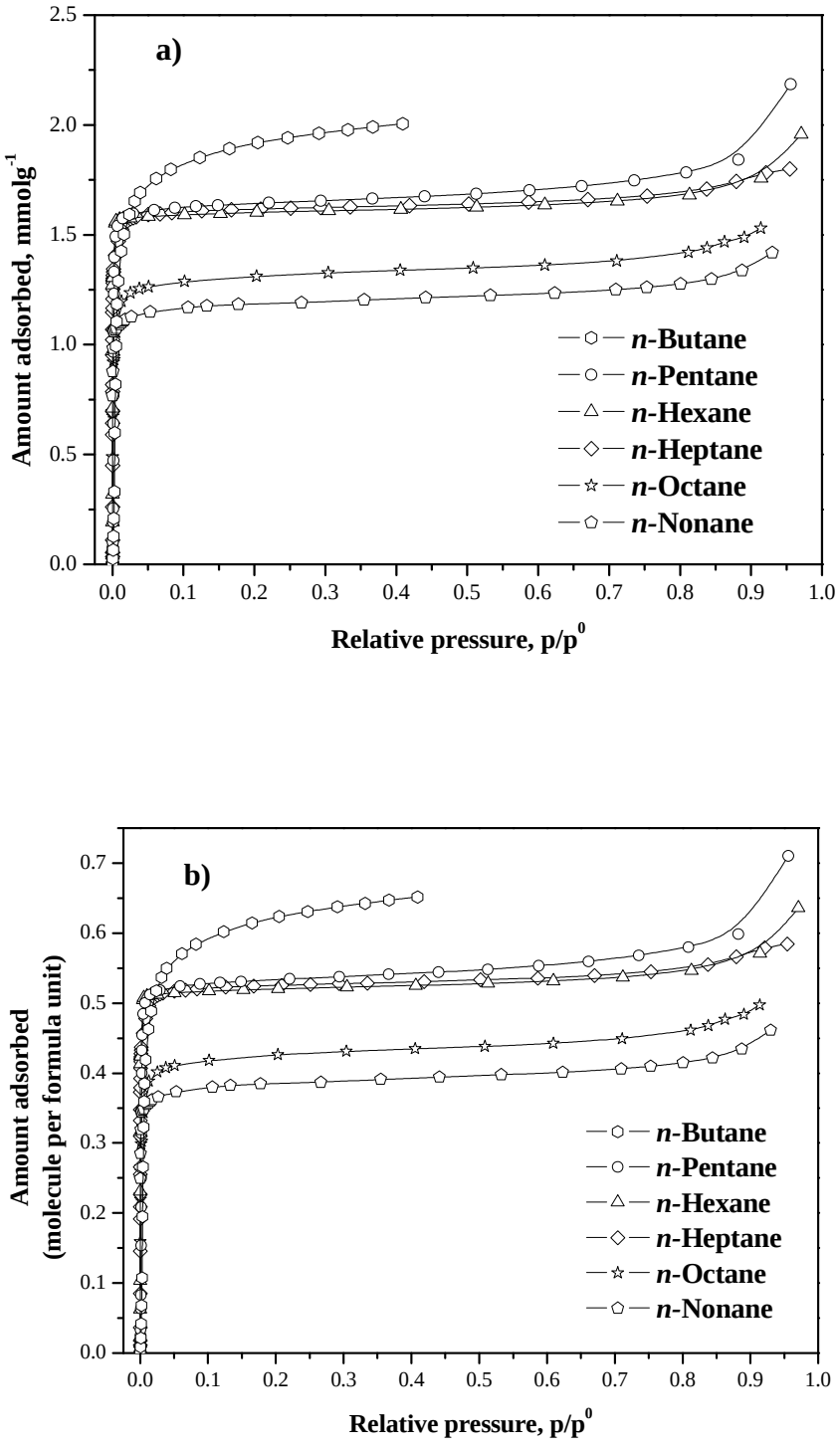

Figure 7.50 Isotherms of alkanes adsorption on NEW-1 at 298 K a) shows amount adsorbed per grams of NEW 1 b) shows amount adsorbed on molecules per formula unit.

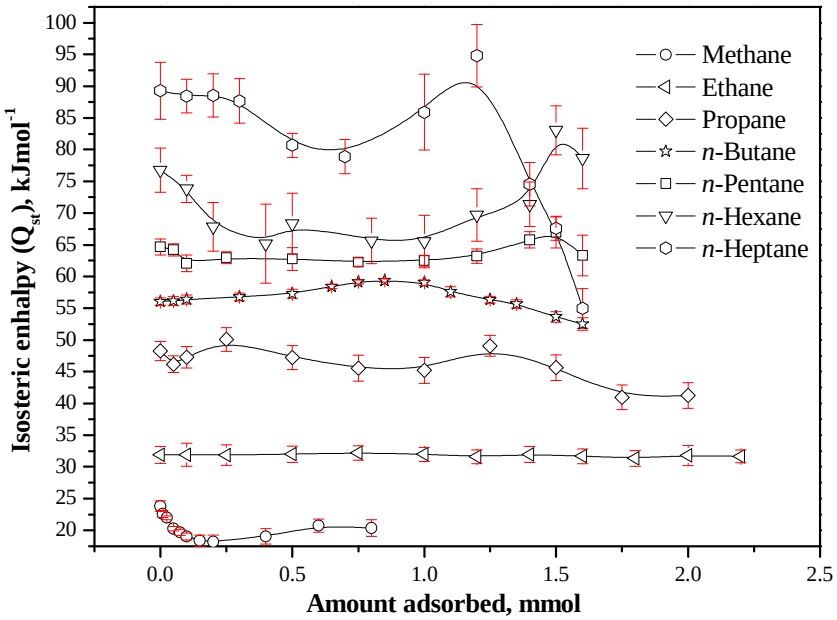

Figure 7.51 Isosteric enthalpies for methane, propane, ethane, *n*-butane, *n*-pentane, *n*-hexane and *n*-heptane adsorption on NEW-1as a function of the surface coverage.

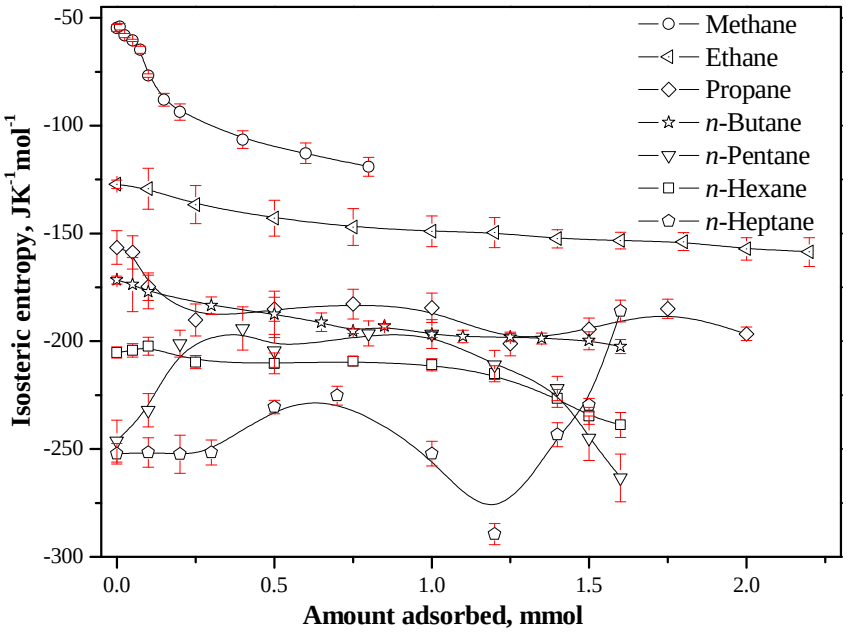

Figure 7.52 Isosteric entropies for methane, propane, ethane, *n*-butane, *n*-pentane, *n*-hexane and *n*-heptane adsorption on NEW-1 as a function of the surface coverage.

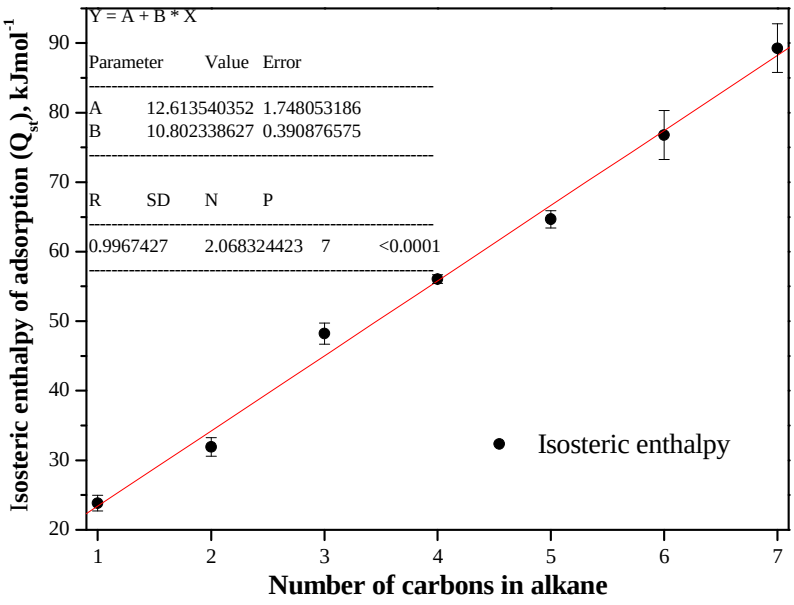

Figure 7.53 Isosteric enthalpies at zero surface coverage for methane, propane, ethane, *n*-butane, *n*-pentane, *n*-hexane and *n*-heptane of adsorption on NEW-1 with a number of carbons in alkanes

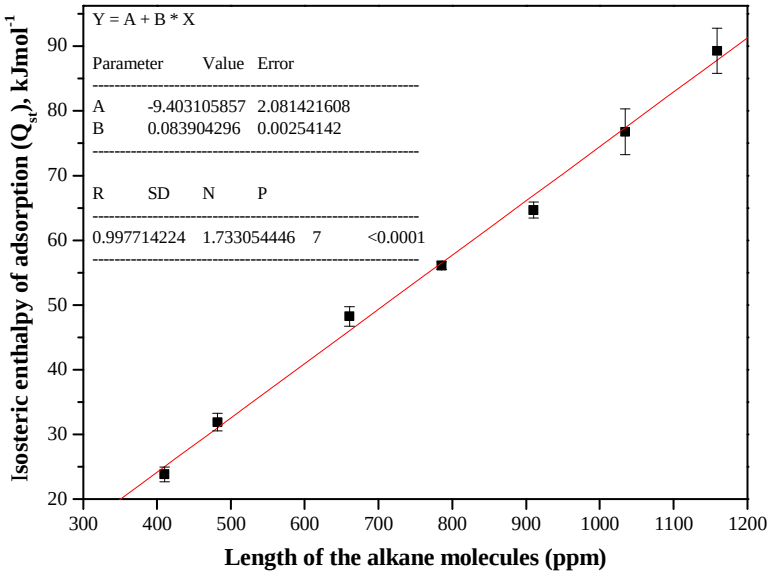

Figure 7.54 Isosteric enthalpies at zero surface coverage for methane, propane, ethane, *n*-butane, *n*-pentane, *n*-hexane and *n*-heptane of adsorption on NEW-1 with length of alkane molecule.

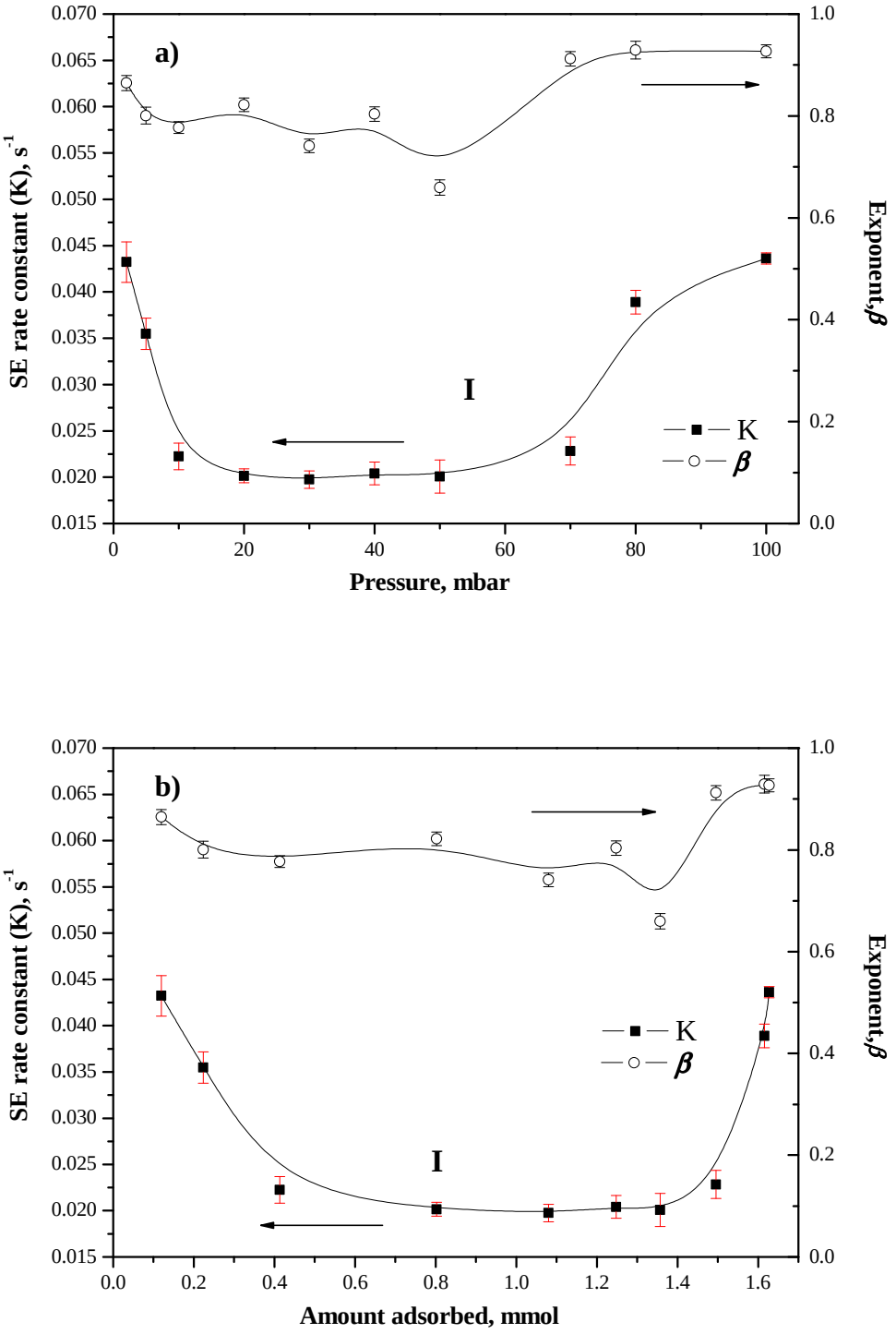

Figure 7. 55 Kinetic profiles of propane adsorption on NEW-1 at 298 K a) pressure basis and b) amount adsorbed basis

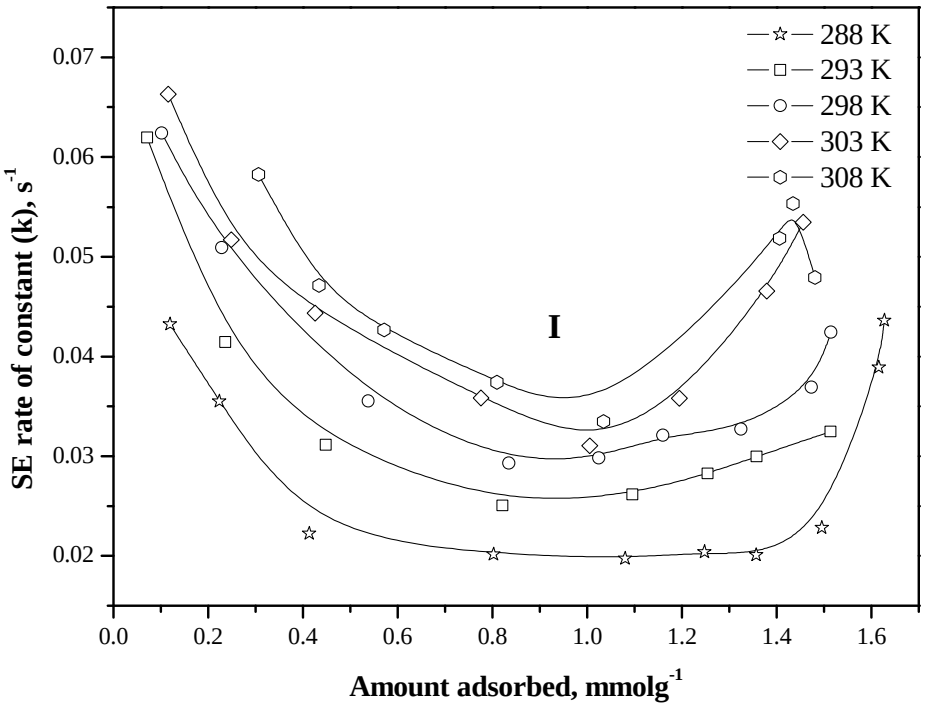

Figure 7.56 Kinetic profiles of propane adsorption on NEW-1 at temperature range 288-308 K

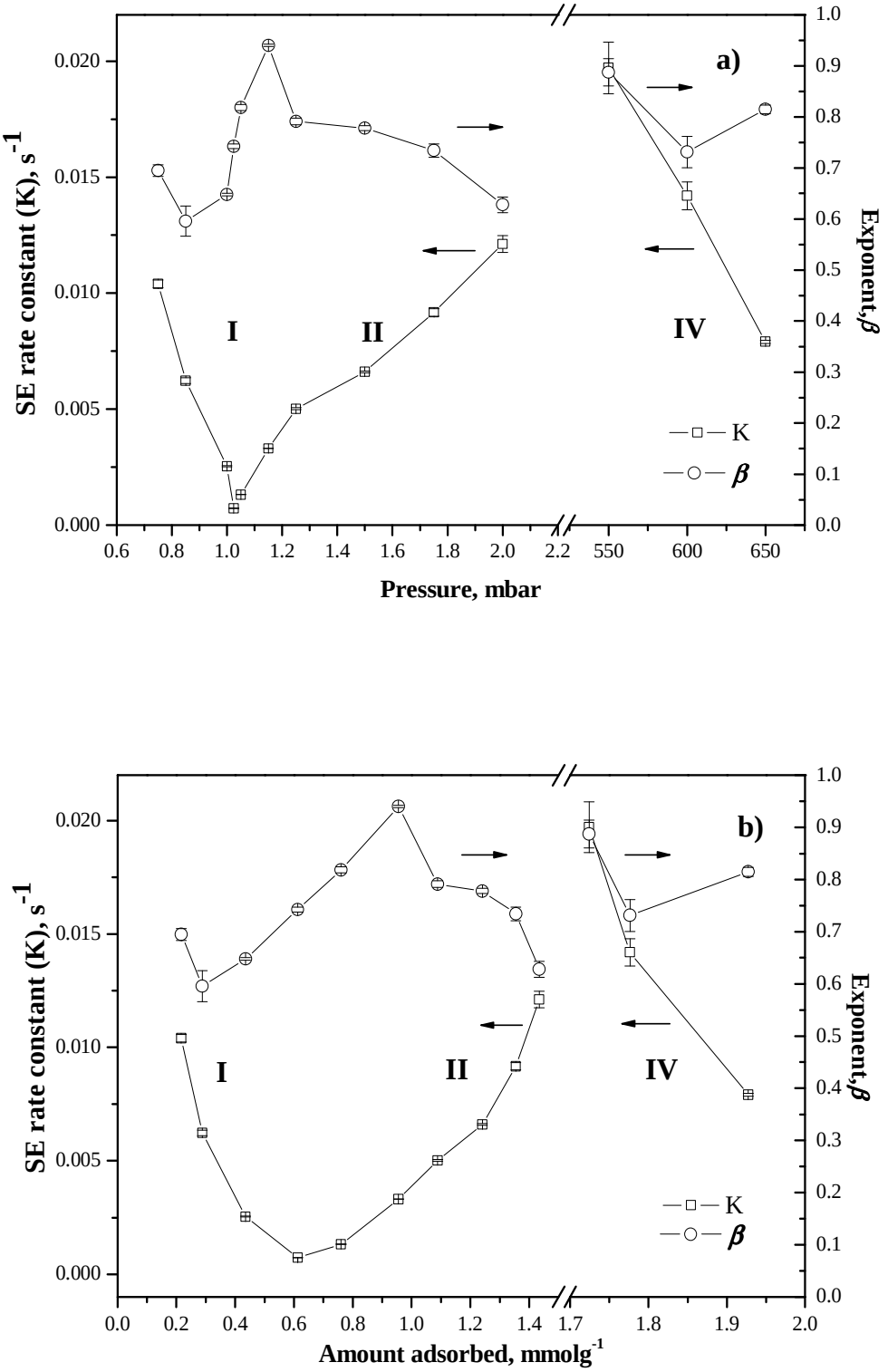

Figure 7.57 Kinetic profiles of *n*-pentane adsorption on NEW-1 at 298 K a) pressure based b) amount adsorbed based

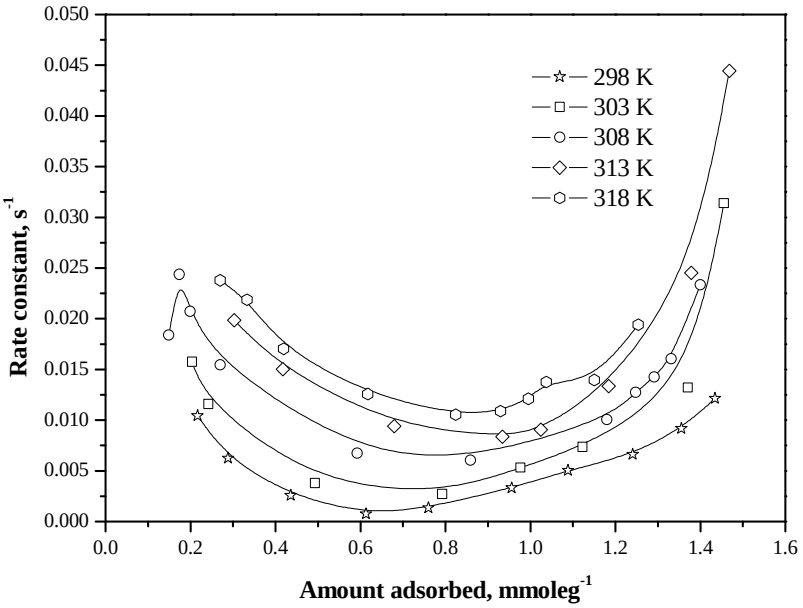

Figure 7.58 Kinetic profiles of *n*-pentane adsorption on NEW-1 at temperature range 298-318 K

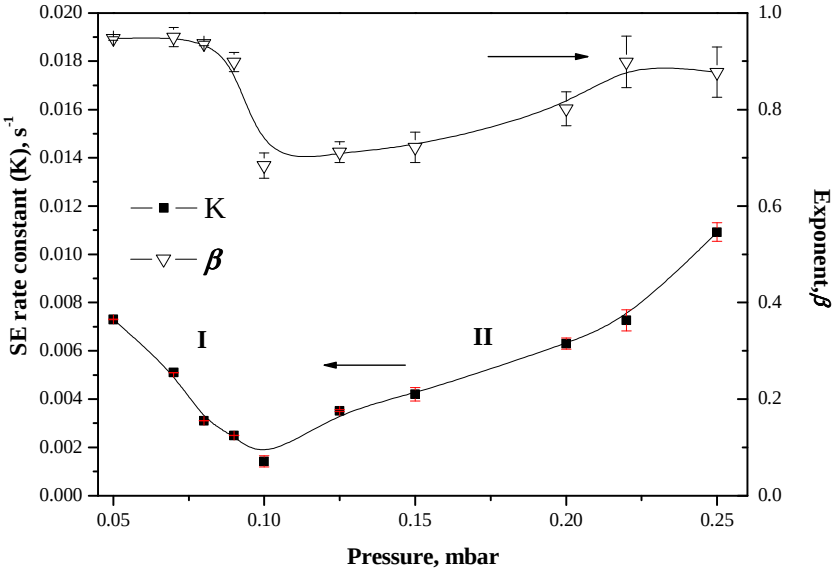

Figure 7.59 Kinetic profiles of *n*-hexane adsorption on NEW-1 at 298 K based on the pressure

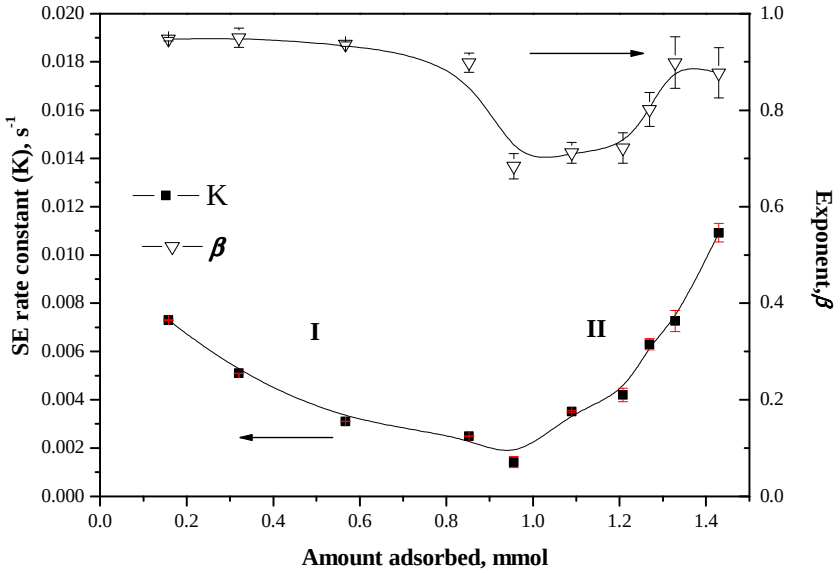

Figure 7.60 Kinetic profiles of *n*-hexane adsorption on NEW-1 at 298 K based on the amount adsorbed

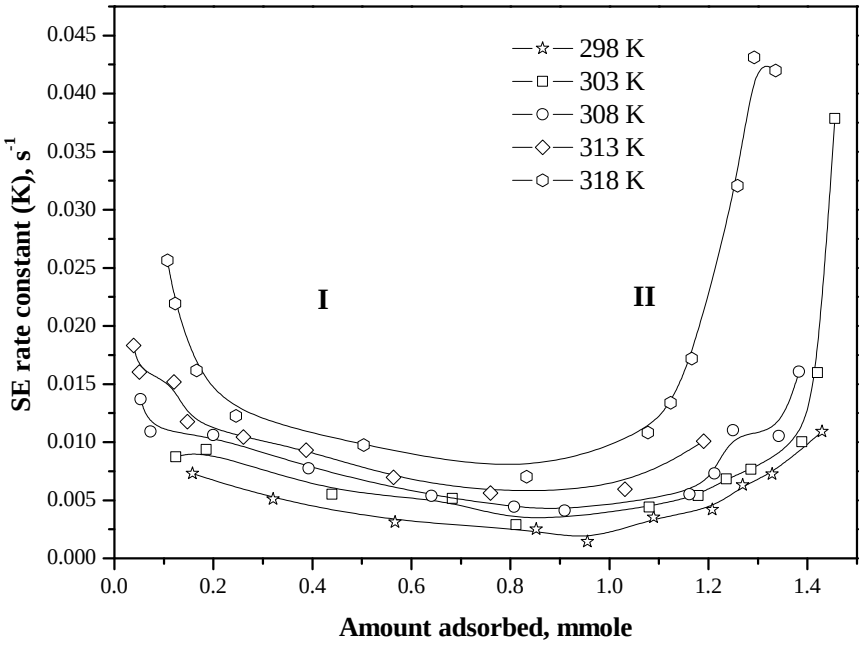

Figure 7.61 Kinetic profiles of *n*-hexane adsorption on NEW-1 at temperature range 298-318 K based on the amount adsorbed

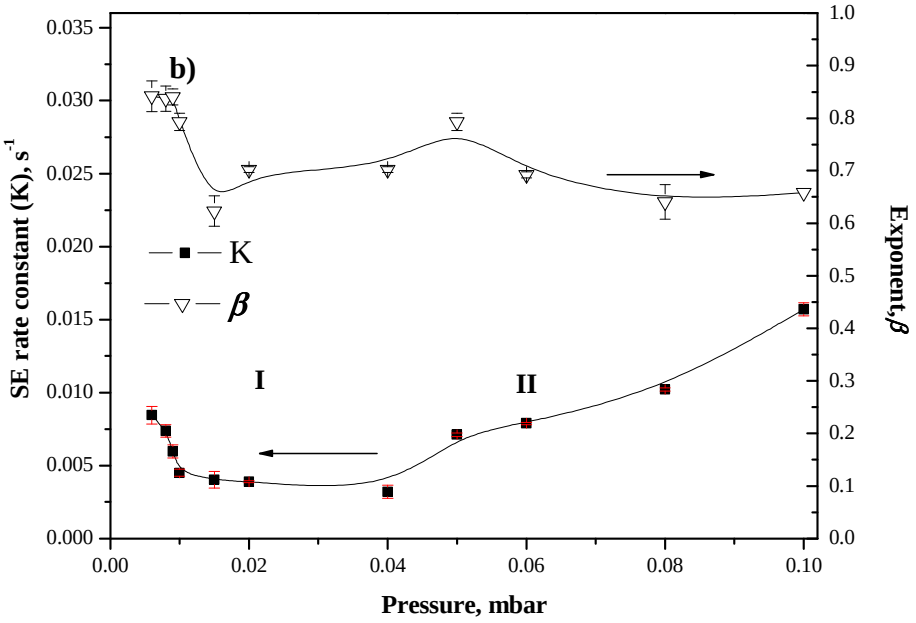

Figure 7.62 Kinetic profiles of *n*-heptane adsorption on NEW-1 at 298 K based on the pressure

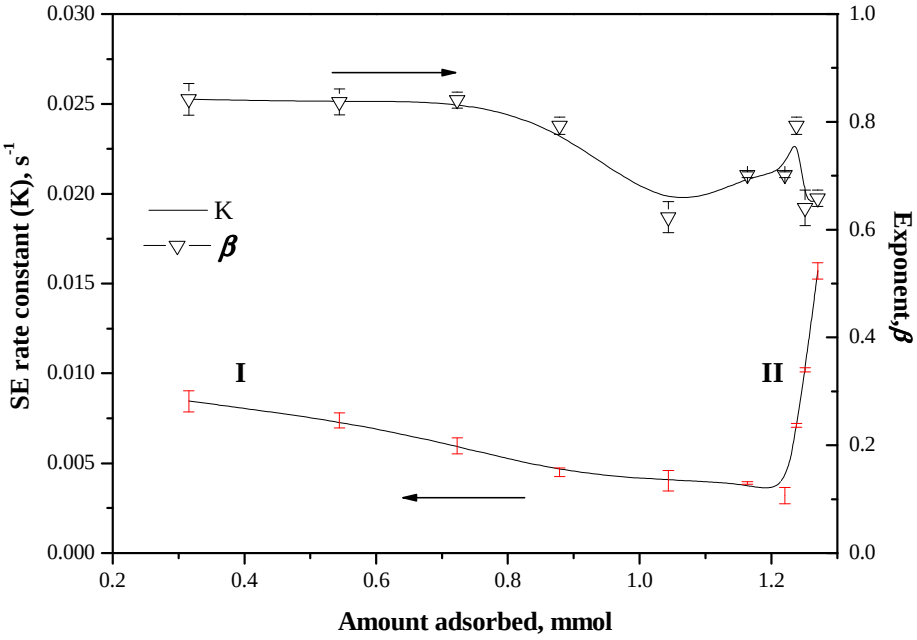

Figure 7.63 Kinetic profiles of *n*-heptane adsorption on NEW-1 at 298 K based on the amount adsorbed

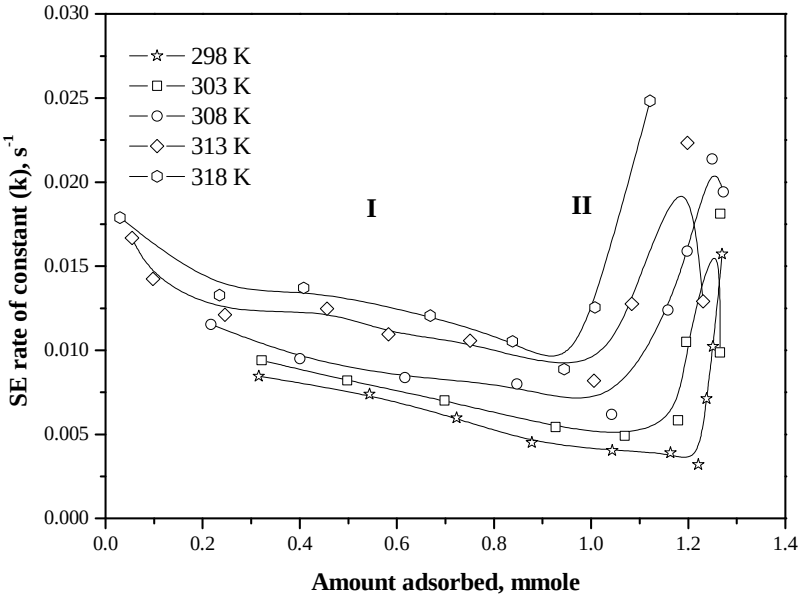

Figure 7.64 Kinetic profiles of *n*-heptane adsorption on NEW-1 over the temperature range 298-318 K based on the amount adsorbed

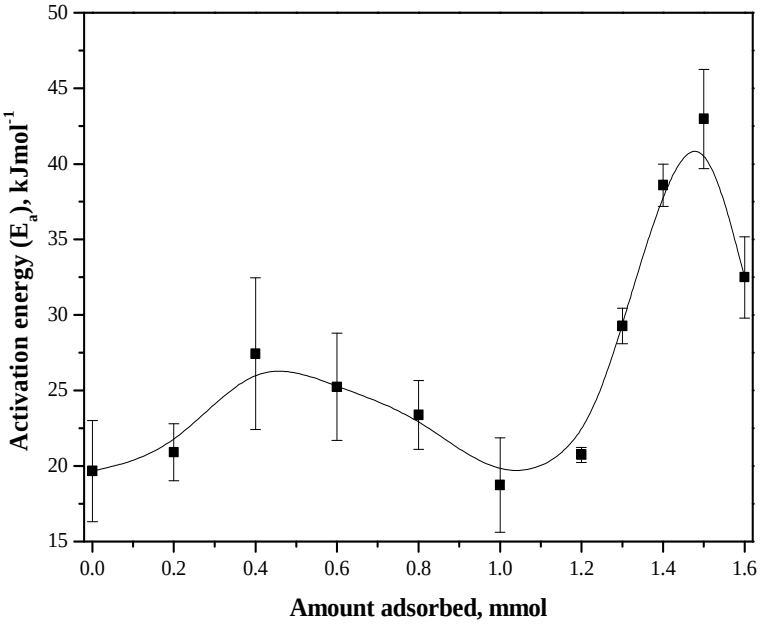

Figure 7.65 Activation energy obtined for of propane adsorption on NEW-1 over the temperature range 298-318 K

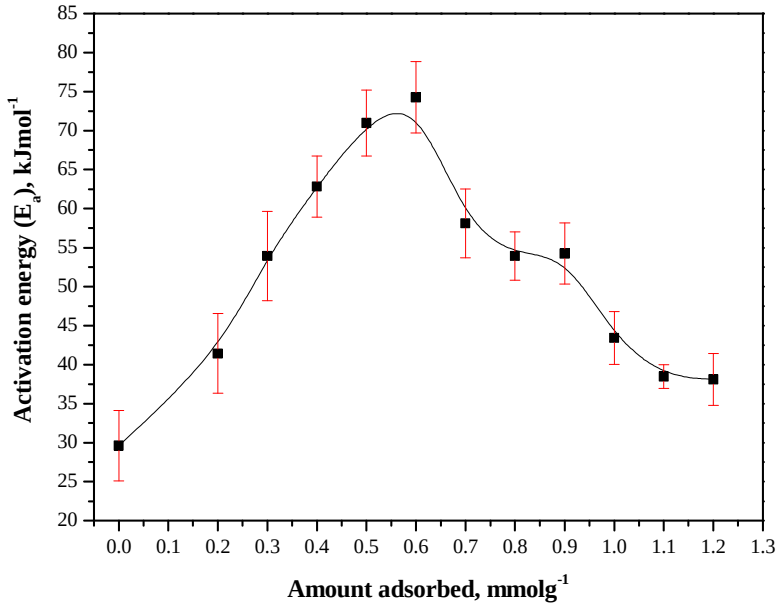

Figure 7.66 Activation energy for *n*-pentane adsorption on NEW-1 over the temperature range 298-318 K

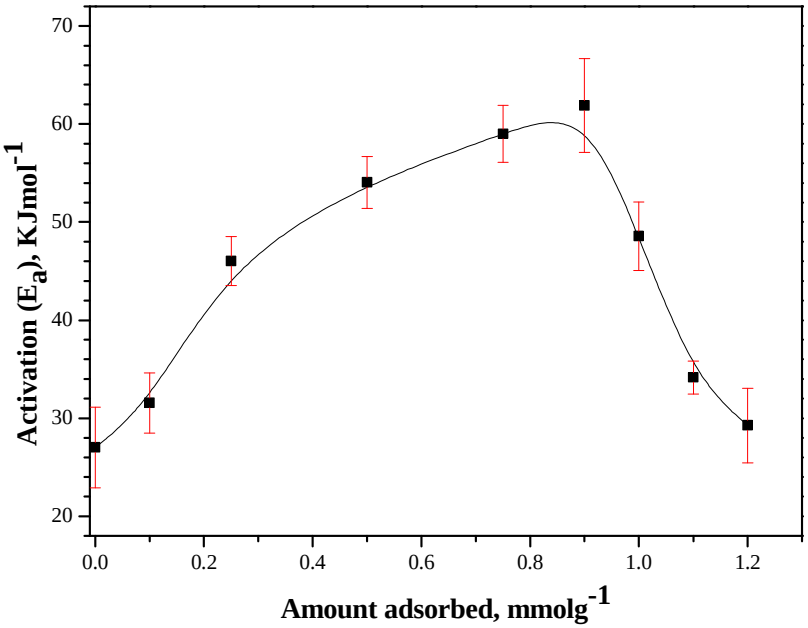

Figure 7.67 Activation energy for *n*-hexane adsorption on NEW-1 over the temperature range 298-318 K

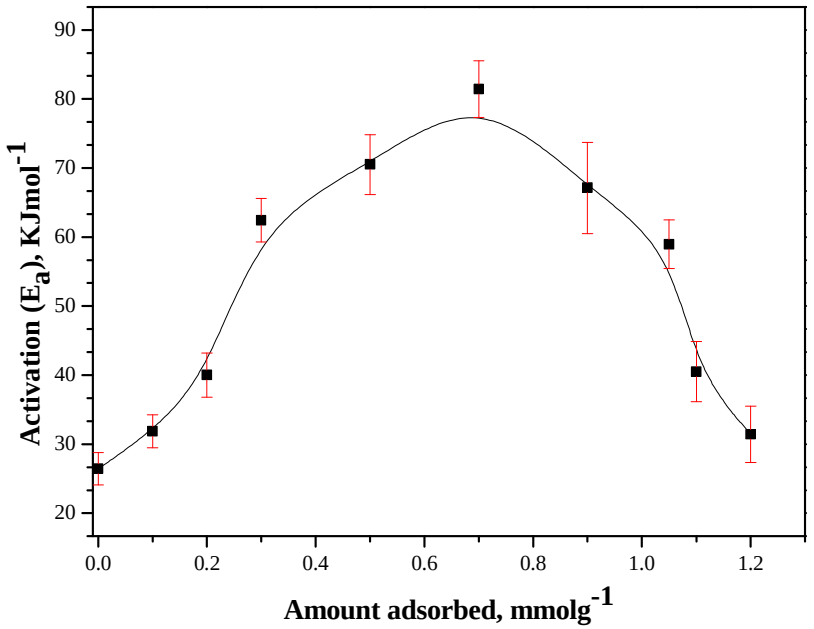

Figure 7.68 Activation energy for *n*-heptane adsorption on NEW-1 over the temperature range 298-318 K

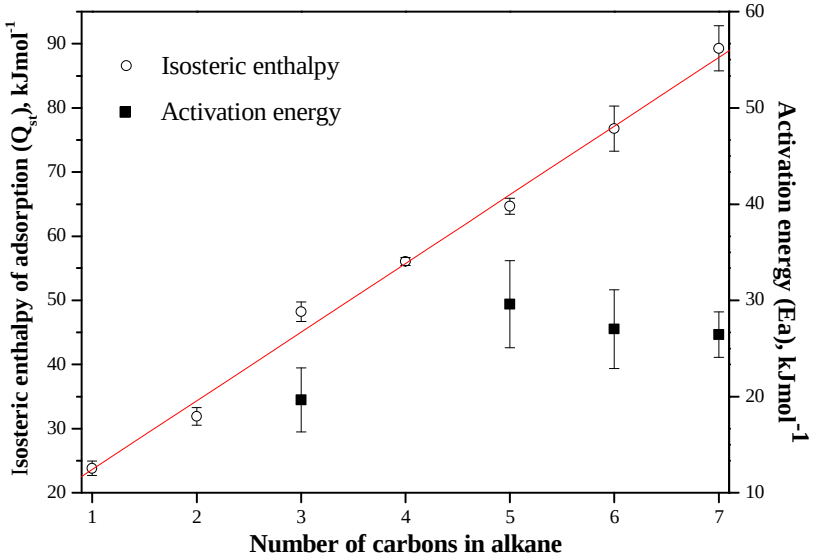

Figure 7.69 Activation energies and isosteric enthalpies at zero surface coverage for alkane adsorption on NEW-1 over the temperature range 298-318 K based on carbon number of alkane.

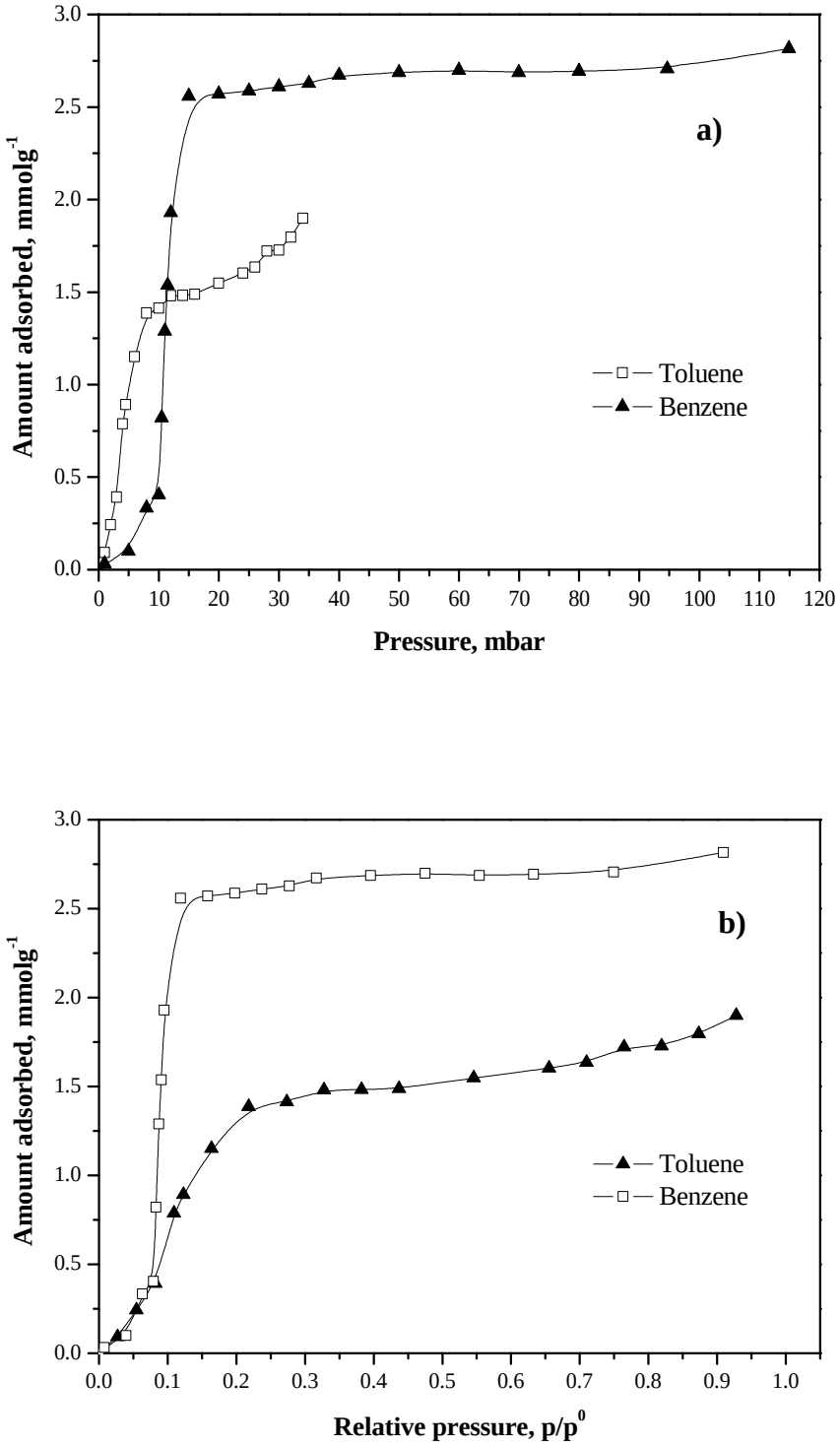

Figure 7.70 Isothems of benzene and toluene adsorption on NEW-1 at 298 K a) based on pressure and b) relative pressure

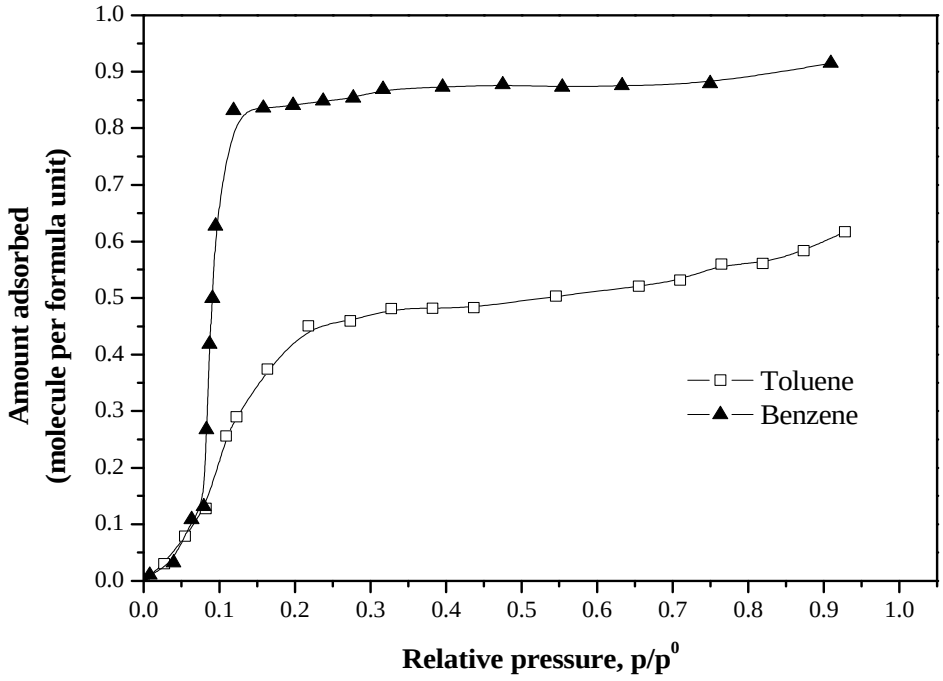

Figure 7.71 Isothems of benzene and toluene adsorption on NEW-1 at 298 K based on molecules per formula unit

7.7 References

1. Rowsell, J. L. C.; Millward, A. R.; Park, K. S.; Yaghi, O. M., Hydrogen Sorption in Functionalized Metal-Organic Frameworks *J. Am. Chem. Soc.* **2004,** 126, (18), 5666 - 7.

2. Chen, B.; Zhao, X.; Putkham, A.; Hong, K.; Lobkovsky, E. B.; Hurtado, E. J.; Fletcher, A. J.; Thomas, K. M., Surface Interactions and Quantum Kinetic Molecular Sieving for H_2 and D_2 Adsorption on a Mixed Metal Organic Framework Material. *J. Am. Chem. Soc.* **2008,** 130, (20), 6411-23.

3. Zhao, X. B.; Xiao, B.; Fletcher, A. J.; Thomas, K. M., Hydrogen Adsorption on Functionalized Nanoporous Activated Carbons *J. Phys. Chem. B* **2005,** 109, (18), 8880 -8.

4. Yeom, J.; Oh, I.; Field, C.; Radadia, A.; Ni, Z.; Bae, B.; Han, J.; Masel, R. I.; Shannon, M. A. In *Enhanced toxic gas detection using a MEMS preconcentrator coated with the metal organic framework absorber*, Micro Electro Mechanical Systems, 2008. MEMS 2008. IEEE 21st International Conference on, 2008; 2008; pp 232-5.

5. B. Chen; Y. Yang; F. Zapata; G. Lin; G. Qian; Lobkovsky, E. B., Luminescent Open Metal Sites within a Metal-Organic Framework for Sensing Small Molecules. *Advanced Materials* **2007,** 19, (13), 1693-6.

6. Zielinski, M.; Wojcieszak, R.; Monteverdi, S.; Mercy, M.; Bettahar, M. M., Hydrogen storage in nickel catalysts supported on activated carbon. *Int. J. Hydrogen Energy* **2007,** 32, (8), 1024-32.

7. Hasegawa, S.; Horike, S.; Matsuda, R.; Furukawa, S.; Mochizuki, K.; Kinoshita, Y.; Kitagawa, S., Three-Dimensional Porous Coordination Polymer Functionalized with Amide Groups Based on Tridentate Ligand; Selective Sorption and Catalysis. *J. Am. Chem. Soc.* **2007,** 129, (9), 2607-14.

8. Zou, R.-Q.; Sakurai, H.; Han, S.; Zhong, R.-Q.; Xu, Q., Probing the Lewis Acid Sites and CO Catalytic Oxidation Activity of the Porous Metal-Organic Polymer [Cu(5-methylisophthalate)]. *J. Am. Chem. Soc.* **2007,** 129, (27), 8402-3.

9. Britt, D.; Tranchemontagne, D.; Yaghi, O. M. In *Metal-organic frameworks with high capacity and selectivity for harmful gases*, Proc. Natl. Acad. Sci. , USA, 2008; USA, 2008; pp 11623-7.

10. Alhamed, Y. A.; Bamufleh, H. S., Sulfur removal from model diesel fuel using granular activated carbon from dates' stones activated by ZnCl2. *Fuel* **2009,** 88, (1), 87-94.

11. Sison, N. F.; Hanaki, K.; Matsuo, T., Denitrification with external carbon source utilizing adsorption and desorption capability of activated carbon. *Water Research* **1996,** 30, (1), 217-27.

12. Mitsuru, K.; Tomomichi, Y.; Hiroyuki, M.; Susumu, K.; Kenji, S., Three-Dimensional Framework with Channeling Cavities for Small Molecules: {[M_2(4, 4′-bpy)$_3$(NO_3)$_4$]·xH_2O}n (M &dbond; Co, Ni, Zn). *Angew. Chem. Int. Ed.* **1997,** 36, (16), 1725-7.

13. Zhao, X.; Xiao, B.; Fletcher, A. J.; Thomas, K. M.; Bradshaw, D.; Rosseinsky, M. J., Hysteretic Adsorption and Desorption of Hydrogen by Nanoporous Metal-Organic Frameworks. *Science* **2004,** 306, (5698), 1012-5.

14. Bae, Y.-S.; Farha, O. K.; Hupp, J. T.; Snurr, R. Q., Enhancement of CO2/N2 selectivity in a metal-organic framework by cavity modification. *J. Mater. Chem.* **2009,** 19, (15), 2131-4.

15. Foley, N. J.; Thomas, K. M.; Forshaw, P. L.; Stanton, D.; Norman, P. R., Kinetics of Water Vapor Adsorption on Activated Carbon. *Langmuir* **1997,** 13, (7), 2083-9.

16. Fletcher, A. J.; Uygur, Y.; Thomas, K. M., Role of Surface Functional Groups in the Adsorption Kinetics of Water Vapor on Microporous Activated Carbons. *J. Phys. Chem. C* **2007,** 111, (23), 8349-59.

17. Brennan, J. K.; Bandosz, T. J.; Thomson, K. T.; Gubbins, K. E., Water in porous carbons. *Colloids Surf., A* **2001,** 187-188, 539-68.

18. Vartapetyan, R. S.; Voloshchuk, A. M.; Isirikyan, A. A.; Polyakov, N. S.; Tarasevich, Y. I., Chemistry of carbon surface and mechanism of water molecule adsorption. *Colloids Surf., A* **1995,** 101, (2-3), 227-32.

19. Zhao, X. B.; Xiao, B.; Fletcher, A. J.; Thomas, K. M., Hydrogen Adsorption on Functionalized Nanoporous Activated Carbons. *J. Phys. Chem. B* **2005,** 109, (18), 8880-8.

20. Yaghi, O. M.; O'Keeffe, M.; Ockwig, N. W.; Chae, H. K.; Eddaoudi, M.; Kim, J., Reticular synthesis and the design of new materials. *Nature* **2003,** 423, 705-14

21. Kim, J.; Chen, B.; Reineke, T. M.; Li, H.; Eddaoudi, M.; Moler, D. B.; O'Keeffe, M.; Yaghi, O. M., Assembly of Metal-Organic Frameworks from Large Organic and Inorganic Secondary Building Units: New Examples and Simplifying Principles for Complex Structures. *J. Am. Chem. Soc.* **2001,** 123, (34), 8239 -47.

22. Denis , G. S.; Hyunuk, K.; Yinyong, S.; Ghyung-Hwa, K.; Heung-Soo, L.; Kimoon, K., Microporous Magnesium and Manganese Formates for Acetylene Storage and Separation. *Chemistry - An Asian Journal* **2007,** 2, (4), 484-8.

23. Matsuda, R.; Kitaura, R.; Kitagawa, S.; Kubota, Y.; Belosludov, R. V.; Kobayashi, T. C.; Sakamoto, H.; Chiba, T.; Takata, M.; Kawazoe, Y.; Mita, Y., Highly controlled acetylene accommodation in a metal-organic microporous material. *Nature* **2005,** 436, (7048), 238-41.

24. Vaidhyanathan, R.; Iremonger, S. S.; Dawson, K. W.; Shimizu, G. K. H., An amine-functionalized metal organic framework for preferential CO2 adsorption at low pressures. *Chem. Commun.* **2009**, (35), 5230-2.

25. Seo, J. S.; Whang, D.; Lee, H.; Jun, S. I.; Oh, J.; Jeon, Y. J.; Kim, K., A homochiral metal-organic porous material for enantioselective separation and catalysis. *Nature* **2000,** 404, (6781), 982-6.

26. Tanabe, K. K.; Wang, Z.; Cohen, S. M., Systematic Functionalization of a Metal Organic Framework via a Postsynthetic Modification Approach. *J. Am. Chem. Soc.* **2008,** 130, (26), 8508-17.

27. Dinca, M.; Dailly, A.; Liu, Y.; Brown, C. M.; Neumann, D. A.; Long, J. R., Hydrogen Storage in a Microporous Metal Organic Framework with Exposed Mn^{2+} Coordination Sites. *J. Am. Chem. Soc.* **2006,** 128, (51), 16876-83.

28. Castillo, J. M.; Vlugt, T. J. H.; Calero, S. a., Understanding Water Adsorption in CuBTC Metal Organic Frameworks. *J. Phys. Chem. C* **2008,** 112, (41), 15934-9.

29. Ryo, K.; Kenji, S.; George, A.; Susumu, K., Porous Coordination-Polymer Crystals with Gated Channels Specific for Supercritical Gases. *Angew. Chem. Int. Ed.* **2003,** 42, (4), 428-31.

30. Fletcher, A. J.; Cussen, E. J.; Bradshaw, D.; Rosseinsky, M. J.; Thomas, K. M., Adsorption of Gases and Vapors on Nanoporous Ni2(4,4-Bipyridine)$_3$(NO_3)$_4$ Metal Organic Framework Materials Templated with Methanol and Ethanol: Structural Effects in Adsorption Kinetics. *J. Am. Chem. Soc.* **2004,** 126, (31), 9750-9.

31. Fletcher, A. J.; Thomas, K. M., Compensation Effect for the Kinetics of Adsorption/Desorption of Gases/Vapors on Microporous Carbon Materials. *Langmuir* **2000,** 16, (15), 6253-66.

32. Tamon, H.; Okazaki, M., Influence of acidic surface oxides of activated carbon on gas adsorption characteristics. *Carbon* **1996,** 34, (6), 741-6.

33. Fletcher, A. J.; Cussen, E. J.; Prior, T. J.; Rosseinsky, M. J.; Kepert, C. J.; Thomas, K. M., Adsorption Dynamics of Gases and Vapors on the Nanoporous Metal Organic Framework Material Ni_2(4,4'-Bipyridine)$_3$(NO_3)$_4$: Guest Modification of Host Sorption Behavior. *J. Am. Chem. Soc.* **2001,** 123, (41), 10001-11.

34. Cussen, E. J.; Claridge, J. B.; Rosseinsky, M. J.; Kepert, C. J., Flexible Sorption and Transformation Behavior in a Microporous Metal-Organic Framework. *J. Am. Chem. Soc.* **2002,** 124, (32), 9574-81.

35. Kazuhiro, U.; Yukari, Y.; Yuki, K.; Kazuhiro, T.; Hidetoshi, K., Two-Step Adsorption/Desorption on a Jungle-Gym-Type Porous Coordination Polymer13. *Angew. Chem. Int. Ed.* **2007,** 46, (35), 6662-5.

36. Vincent, F.; Christine, E. A. K.; Gill, V.; Michael, M.; Luc, A.; Dirk , E. De V.; Gino , V. B.; Joeri , F. M. D., Framework Breathing in the Vapour-Phase Adsorption and Separation of Xylene Isomers with the Metal-Organic Framework MIL-53. *Chem. Eur. J.* **2009,** 15, (31), 7724-31.

37. Kepert, C. J.; Hesek, D.; Beer, P. D.; Rosseinsky, M. J., Desolvation of a Novel Microporous Hydrogen-Bonded Framework: Characterization by In Situ Single-Crystal and Powder X-ray Diffraction. *Angew. Chem. Int. Ed.* **1998,** 37, (22), 3158-60.

38. Kitaura, R.; Fujimoto, K.; Noro, S.-i.; Kondo, M.; Kitagawa, S., A Pillared-Layer Coordination Polymer Network Displaying Hysteretic Sorption: $[Cu_2(pzdc)_2(dpyg)]_n$ (pzdc= Pyrazine-2,3-dicarboxylate; dpyg=1,2-Di(4-pyridyl)glycol). *Angew. Chem. Int. Ed.* **2002,** 41, (1), 133-5.

39. Webster, C. E.; Drago, R. S.; Zerner, M. C., Molecular Dimensions for Adsorptives. *J. Am. Chem. Soc.* **1998,** 120, (22), 5509-16.

40. Kunhao, L.; David, H. O.; Jeong Yong, L.; Wenhua, B.; Ke, W.; Tan, Y.; Qiang, X.; Jing, L., Multifunctional Microporous MOFs Exhibiting Gas/Hydrocarbon Adsorption Selectivity, Separation Capability and Three-Dimensional Magnetic Ordering. *Adv. Funct. Mater.* **2008,** 18, (15), 2205-14.

41. Do, D. D., *Absorption Analysis: Equilibria and Kinetics*. Imperial College Press: 1998; p 892.

42. F. Rouquerol; Rouquerol, J.; Sing, K. S. W., *Adsorption by Powders, Porous Solids*. Academic Press: London, 1999; p 467.

43. Herry, C.; Baudu, M.; Raveau, D., Estimation of the influence of structural elements of activated carbons on the energetic components of adsorption. *Carbon* **2001,** 39, (12), 1879-89.

44. Taqvi, S. M.; Appel, W. S.; LeVan, M. D., Coadsorption of Organic Compounds and Water Vapor on BPL Activated Carbon. 4. Methanol, Ethanol, Propanol, Butanol, and Modeling. *Ind. Eng. Chem. Res.* **1998,** 38, (1), 240-50.

45. Carrott, P. J. M.; Sing, K. S. W., Gas chromatographic study of microporous carbons. *J. Chromatogr. A* **1987,** 406, 139-44.

46. Ahsan, T.; Colenutt, B. A.; Sing, K. S. W., Gas chromatography of pure and surface-modified precipitated calcium carbonate. *J. Chromatogr. A* **1989,** 479, 17-25.

47. Ludwig, S.; Schmidt, H. D., Determination of heats of adsorption on graphite and on a microporous carbon black by gas--solid chromatography. *J. Chromatogr. A* **1990,** 520, 69-74.

48. Cao, X. L.; Colenutt, B. A.; Sing, K. S. W., Study of microporous carbons by gas chromatographic determination of heats of physisorption. *J. Chromatogr. A* **1991,** 555, (1-2), 183-90.

49. *CRC Handbook of Chemistry and Physics* 74th ed.; CRC Press: Boca Ratan, FL, 1993.

50. Dean, J. A., Lange's Handbook of Chemistry (15th Edition). In McGraw-Hill: 1999.

51. Prasetyo, I.; Do, H. D.; Do, D. D., Surface diffusion of strong adsorbing vapours on porous carbon. *Chem. Eng. Sci.* **2002,** 57, (1), 133-41.

52. Sloczynski, J.; Grabowski, R.; Janas, J.; Skrzypek, J., Adsorption model of methanol synthesis reactants on CuO---ZnO---Al2O3 catalyst--I. Adsorption on the catalyst. *Chem. Eng. Sci.* **1991,** 46, (10), 2599-610.

53. Finqueneisel, G.; Vagner, C.; Zimny, T.; Weber, J. V., Comparison of the kinetics of methanol adsorption in static and continuous flow conditions on activated carbons with different burn-off degree. *Colloids Surf., A* **2004,** 232, (2-3), 175-81.

54. Zhao, X.; Silvia, V.-R.; Fletcher, A., J. ; Thomas, K. M., Kinetic Isotope Effect for H_2 and D_2 Quantum Molecular Sieving in Adsorption/Desorption on Porous Carbon Materials. *J. Phys. Chem. B* **2006,** 110, (20), 9947-55.

55. Fletcher, A. J.; Kennedy, M. J.; Zhao, X. B.; Bell, J. B.; Thomas, K. M., Adsorption of Organic Vapour Pollutants on Activated Carbon. In *Recent Advances in Adsorption Processes for Environmental Protection and Security*, 2008; pp 29-54.

56. Borini, S., Experimental observation of glassy dynamics driven by gas adsorption on porous silicon. *Journal of Physics: Condensed Matter* **2008,** 20 385207.

57. Klafter, J.; Shlesinger, M. F., On the relationship among three theories of relaxation in disordered systems. *Proc. Natl. Acad. Sci. U. S. A.* **1986,** 83, (4), 848-51.

58. Laidler, K. J., The development of the Arrhenius equation. *Journal of Chemical Education* **1984,** 61, (6), 494.

59. Fletcher, A. J.; Thomas, K. M., Adsorption and Desorption Kinetics of n-Octane and n-Nonane Vapors on Activated Carbon. *Langmuir* **1999,** 15, (20), 6908-14.

60. Sing, K. W.; Everett, D. H.; Haul, R. A. W.; Moscou, L.; Pierotti, R. A.; Rouquerol, J.; Siemieniewska, T., Reporting physisorption data for gas/solid systems with special reference to the determination of surface area and porosity. *Pure Appl. Chem.* **1985,** 57, (4), 603-19.

61. Reid, C. R.; Thomas, K. M., Adsorption Kinetics and Size Exclusion Properties of Probe Molecules for the Selective Porosity in a Carbon Molecular Sieve Used for Air Separation. *J. Phys. Chem. B* **2001,** 105, (43), 10619-29.

62. Li, J.-R.; Kuppler, R. J.; Zhou, H.-C., Selective gas adsorption and separation in metal-organic frameworks. *Chemical Society Reviews* **2009,** 38, (5), 1477-504.

63. Mooi, J.; Pierce, C.; Smith, R. N., Heats and Entropies of Adsorption on a Homogeneous Carbon Surface. *J. Phys. Chem.* **1953,** 57, (7), 657-9.

64. Mariwala, R. K.; Foley, H. C., Calculation of Micropore Sizes in Carbogenic Materials from the Methyl Chloride Adsorption Isotherm. *Ind. Eng. Chem. Res.* **1994,** 33, (10), 2314-21.

65. Sprung, M.; Larese, J. Z., Adsorption isotherm studies of methyl chloride on MgO. *Physical Review B* **2000,** 61, (19), 13155.

66. Chiang, Y.-C.; Chiang, P.-C.; Huang, C.-P., Effects of pore structure and temperature on VOC adsorption on activated carbon. *Carbon* **2001,** 39, (4), 523-34.

67. Díaz, E.; Ordóñez, S.; Vega, A., Adsorption of volatile organic compounds onto carbon nanotubes, carbon nanofibers, and high-surface-area graphites. *J. Colloid Interface Sci.* **2007,** 305, (1), 7-16.

68. Chen, C.-H.; Dural, N. H., Chloroform Adsorption on Soils. *J. Chem. Eng. Data* **2002,** 47, (5), 1110-5.

69. Giraudet, S.; Pré, P.; Tezel, H.; Le Cloirec, P., Estimation of adsorption energies using the physical characteristics of activated carbons and the molecular properties of volatile organic compounds. *Carbon* **2006,** 44, (12), 2413-21.

70. Markovic, M.; Kopečni, M.; Milonjić, S.; Ceranić, T., Thermodynamics of adsorption of organic liquids on Ni-modified solid obtained from collodal silica. *Chromatographia* **1988,** 26, (1), 387-92.

71. Almazán-Almazán, M. C.; Pérez-Mendoza, M.; Domingo-García, M.; Fernández-Morales, I.; del Rey-Bueno, F.; García-Rodríguez, A.; López-Garzón, F. J., The role of the porosity and oxygen groups on the adsorption of n-alkanes, benzene, trichloroethylene and 1,2-dichloroethane on active carbons at zero surface coverage. *Carbon* **2007,** 45, (9), 1777-85.

72. Díaz, E.; Ordóñez, S.; Vega, A.; Coca, J., Adsorption characterisation of different volatile organic compounds over alumina, zeolites and activated carbon using inverse gas chromatography. *J. Chromatogr. A* **2004,** 1049, (1-2), 139-46.

73. D. Wood, C.; Tan, B.; Trewin, A.; Su, F.; J. Rosseinsky, M.; Bradshaw, D.; Sun, Y.; Zhou, L.; I. Cooper, A., Microporous Organic Polymers for Methane Storage. *Advanced Materials* **2008,** 20, (10), 1916-21.

74. Myers, A. L., Characterization of nanopores by standard enthalpy and entropy of adsorption of probe molecules. *Colloids and Surfaces A: Physicochemical and Engineering Aspects* **2004,** 241, (1-3), 9-14.

75. Wood, C. D.; Bien, T.; Abbie, T.; Fabing, S.; Rosseinsky, M. J.; Bradshaw, D.; Sun, Y.; Zhou, L.; Cooper, A. I., Microporous Organic Polymers for Methane Storage. *Advanced Materials* **2008,** 20, (10), 1916-21.

76. Naono, H.; Hakuman, M.; Shimoda, M.; Nakai, K.; Kondo, S., Separation of Water and Ethanol by the Adsorption Technique: Selective Desorption of Water from Micropores of Active Carbon. *J. Colloid Interface Sci.* **1996,** 182, (1), 230-8.

77. Diaz, E.; Ordóñez, S.; Vega, A.; Coca, J., Comparison of adsorption properties of a chemically activated and a steam-activated carbon, using inverse gas chromatography. *Microporous Mesoporous Mater.* **2005,** 82, (1-2), 173-81.

78. Dernovaya, L. I.; Eltekov, Y. A., Retention and heats of adsorption of hydrocarbons and aliphatic alcohols on cellulose. *J. Chromatogr. A* **1988,** 455, 263-9.

79. Domingo-García, M.; Fernandez-Morales, I.; López-Garzón, F. J.; Moreno-Castilla, C., Adsorption of hydrocarbons on graphites and graphitized carbon black at zero surface coverage. *J. Chromatogr. A* **1984,** 294, 41-50.

80. Nagao, M.; Suda, Y., Adsorption of benzene, toluene, and chlorobenzene on titanium dioxide. *Langmuir* **2002,** 5, (1), 42-7.

81. Yun, J.-H.; Hwang, K.-Y.; Choi, D.-K., Adsorption of Benzene and Toluene Vapors on Activated Carbon Fiber at 298, 323, and 348 K. *J. Chem. Eng. Data* **1998,** 43, (5), 843-5.

82. McCullen, S. B.; Reischman, P. T.; Olson, D. H., Hexane and benzene adsorption by aluminophosphates and SSZ-24: The effect of pore size and molecular sieve composition. *Zeolites* **1993,** 13, (8), 640-4.

83. Russo, P.; Ribeiro Carrott, M.; Carrott, P., Adsorption of toluene, methylcyclohexane and neopentane on silica MCM-41. *Adsorption* **2008,** 14, (2), 367-75.

CHAPTER 8

Applications of NEW-1 for hydrogen storage and air separation

Adsorption of H_2, N_2, O_2 and Ar were studied in order to investigate the possible applications of metal organic framework NEW-1 for gas storage and separation. The adsorption isotherm of hydrogen on NEW-1 at 77 K is classified as a type I isotherm in the IUPAC classification scheme and no hysteresis was observed during the desorption process. The highest hydrogen uptake at ~1 bar and 77 K was 2.98 ± 0.0016 mmolg^{-1} which corresponds to ~0.6 % by weight, which is quite low compared to the 6 % target set by the US Department of energy (DOE). The adsorption characteristics of O_2, N_2, and Ar on a metal organic framework NEW-1, mixed-zinc/copper organic framework (M'MOF1) and a carbon based molecular sieve (CMS-40) were also determined over the temperature range 195-298 K. The kinetics profiles obtained for gases adsorption on M'MOF-1 and CMS-40 followed the stretched exponential model (SE) and double stretched exponential model (DSE), respectively. The adsorption kinetics of gases on NEW-1 were too fast to be determined properly. The kinetic selectivities for fast and slow components of O_2/N_2 obtained for gas adsorption on M'MOF-1 were in the ranges 0.8-4.7 and 0.9-4.3, respectively. While, kinetic selectivity of O_2/N_2 obtained for gas adsorption on CMS-40 was in the range of 33-35. Higher isosteric enthalpies were observed for gas adsorption on both NEW-1 and M'MOF-1, which is indicative of stronger adsorbate-adsorbent interactions compared to CMS-40.

8.1 Hydrogen storage on NEW-1

Hydrogen is a possible energy source for powering cars due to its pollutant-free combustion. Most hydrogen is extracted by processing methane at oil refineries and chemical plants. However, in the future hydrogen can be potentially produced from ethanol and methanol via steam reforming process.[1, 2] However, the great challenge for commercialising hydrogen powered vehicles is hydrogen storage.[3] Methods of hydrogen storage which are currently under consideration include high pressure gas, liquid hydrogen, and adsorption on porous materials, complex hydrides and hydrogen intercalation in metals. None of these methods satisfy the criteria for the amount of hydrogen that can be

supplied from a given weight or volume of tank for vehicles for the refueling ranges required.[4-6] Hydrogen is being developed for use in fuel cell electric vehicles, which potentially have higher efficiency. The use of hydrogen physisorption on porous materials is one of the main methods being considered for vehicle applications. These materials would also need to satisfy the requirements of reasonable volume, weight and realistic kinetics for charging and discharging the gas. The US department of energy (DOE) has set targets for the amount of hydrogen adsorbed as 6% wt by 2010 and 9% wt by 2015.[7] Various types of porous materials have been investigated. It is now generally accepted that there are limitations for the amounts of hydrogen that can be adsorbed on carbon materials at ambient temperatures and high pressure. This is related to the low enthalpy of hydrogen adsorption on carbon materials. Metal organic framework materials are capable of being designed and synthesized using systematic methods to include specific adsorption sites with stronger interactions for hydrogen adsorption.[8-10] In this study, the metal organic framework NEW-1 was used in hydrogen adsorption in order to determine hydrogen storage characteristics.

Hydrogen adsorption/desorption isotherms for NEW-1 at 77 K and pressures up to 1000 mbar are shown in Figure 8.1a and 8.1b. The adsorption isotherm of hydrogen on NEW-1 is classified as type I isotherm in IUPAC classification scheme. It is well established that the sharp hydrogen uptake at low pressure region is enhanced by micropores while the adsorption uptake at high pressure region is controlled by the total pore volume.[11, 12] Hydrogen adsorption was reversible and no hysteresis occurred during the desorption process. The highest hydrogen uptake at ~1000 mbar and 77 K was 2.98 ± 0.0016 mmol g^{-1}, which corresponded to ~ 0.6 % by weight. The amount of hydrogen adsorbed at this temperature and pressure corresponds to ~ 1 molecule of hydrogen per crystallographic formula unit of NEW-1. The maximum amount of hydrogen adsorbed (2.98 mmol g^{-1}) and the liquid density of hydrogen of 0.077 g cm^{-3} at the triple point (–259.35°C) can be used to calculate the volume of hydrogen adsorbed on NEW-1. The calculated volume of hydrogen adsorbed on NEW-1 was 0.0774 cm^3 g^{-1}, which corresponds to 29 % filling of the total pore calculated from the PLATON (0.269 cm^3 g^{-1}). The porous structure of NEW-1 collapsed after degassing to remove the solvent to activate the porous structure. The volumes of hydrogen adsorbed on NEW-1 after pore collapse were 86 %, 78 % and 63% of filling of the total pore volume as determined by N_2 (0.099 cm^3 g^{-1} at 77 K), Ar (0.090 cm^3 g^{-1} at 77 K) and CO_2 (0.116 cm^3 g^{-1} at 195 K), respectively.

Chen *et al.*[13] reported that the kinetics of H_2 and D_2 adsorption on M'MOF-1, $Zn_3(BDC)_3[Cu(Pyen)]\cdot(DMF)_5(H_2O)_5$, where H_2BDC = 1,4 benzenedicarboxylic acid and $PyenH_2$ = 5-methyl-4-oxo-1,4-dihydro-pyridine-3-carbaldehyde and showed that the adsorption kinetics obey a double exponential (DE) model. This DE model describes two diffusion processes during adsorption, diffusion along two types of cavities of M'MOF-1 (5.6 x 12.0 Å and irregular ultramicropores, details in section 1.3.1). However, the adsorption kinetics for hydrogen adsorption on NEW-1 were too fast and could not be measured accurately. The faster adsorption kinetics of hydrogen adsorption on NEW-1 is due to the larger pore size in NEW-1 (6.092 x 6.092 Å) compared with the hydrogen molecule (2.4 x 2.4 x 3.14 Å).

8.2 Air separation

Nitrogen and Oxygen are two of the most widely used chemicals in the world *e.g.* manufacture of steel, welding of material, hospitals and laboratories.[14, 15] The recovery of either nitrogen or oxygen from air is a commercially important consideration. Carbon molecular sieves (CMS) are a unique class of material where the selective porosity is incorporated by carbon deposition on a nanoporous carbon substrate with pore sizes is approximately 0.5 nm. The kinetic selectivity of these materials for oxygen and nitrogen is controlled by the extent of carbon deposition and the experiment conditions. These materials are used commercially for nitrogen and oxygen separation from air by pressure swing adsorption (PSA).[16, 17] Recently, some novel porous framework materials also known as metal-organic coordination networks or metal organic frameworks (MOFs) have attracted the attention for applications in catalysis and gas storage particularly for hydrogen storage. Some possible advantages of the metal organic frameworks are the pore sizes and functionality of the open frameworks can be controlled by choosing appropriate organic linkers and metals. In the case of carbon molecular sieves the selective carbon deposit and the microporous substrate are amorphous and it is only possible to establish the size of the selectivity by probe molecule studies.[18, 19] In contrast, in the case of MOF materials, detailed structural information is available from X-ray crystallographic studies. Therefore, more detailed information is available on pore size and surface structure. In this study, adsorption characteristics of O_2, N_2 and Ar on NEW-1, M'MOF-1 and CMS-40 over the temperature range 195 K – 298 K were investigated. Also, the adsorption kinetics and adsorption enthalpies for these gases were determined.

8.2.1 Isotherms of O_2, N_2 and Ar adsorption on porous materials

Figure 8.2 shows the uptake of all gases on NEW-1 at 195 K. It is apparent that the gases adsorption isotherms at 195 K on NEW-1 can be classified as Type I in the IUPAC classification scheme. These adsorption isotherms were approximately linear at low pressure regions but deviated from linearity at higher pressure. The uptakes of all gas adsorption at 273 K and 298 K were linear with increasing pressure as shown in Figure 8.3 and 8.4, respectively. It is apparent that the adsorption capacities of both oxygen and argon on NEW-1 over the temperature range of 195-298 K were similar, while the adsorption capacity of nitrogen was slightly lower than both oxygen and argon. The adsorption capacities of oxygen and nitrogen at 1000 mbar over the temperature range 195-298 K are shown in Table 8.1. It can be seen that the equilibrium oxygen adsorbed on NEW-1 was higher than nitrogen with highest pure component selectivity of O_2/N_2 of 1.47 at 298 K. The smallest differences in the amount adsorbed for oxygen and nitrogen adsorbed were observed at 195 K.

Figure 8.5-8.7 shows the adsorption isotherms of gases on M'MOF-1 at 195, 273 and 298 K, respectively. The adsorption isotherms of gases at 195 K showed that the amount of gas adsorbed in the low pressure region increased approximately linearly with increasing pressure. However, the amount gases adsorbed diverted from linearity in the high pressure region. The adsorption isotherms at both 273 and 298 K showed the amount of gas adsorbed was linear with increasing pressure as shown in Figure 8.6 and 8.7, respectively. It is apparent that both oxygen and argon were adsorbed to a greater extent than nitrogen on M'MOF-1 and the equilibrium selectivity of O_2/N_2 of 1.50 was observed at 195 K.

Figure 8.8-8.10 shows the adsorption isotherms of gases on CMS-40 over the temperature range 273-298 K. It is clear that the amount of gas adsorbed on CMS-40 increased approximately linearly with increasing pressure. The amount of oxygen and nitrogen adsorbed is similar to that of argon.

Table 8.1 Equilibrium amount of gases adsorbed on porous materials at 1000 mbar

Samples	Window dimension (Å)	O_2 uptake (mmol/g)	N_2 uptake (mmol/g)	O_2/N_2 selectivity	Temperatures (K)
Metal organic frameworks					
NEW-1	7.09 x 5.65	1.37	1.12	1.22	195
		0.20	0.14	1.43	273
		0.11	0.07	1.57	298
M'MOF-1	5.6 x 12.0 and irregular shaped ultra-micropore	1.32	0.88	1.50	195
		0.07	0.05	1.40	273
		0.04	0.03	1.33	298
MOF-177[20]	7.1~ 7.6	0.18	0.10	1.80	298
Carbon molecular sieves					
CMS-C600[21]	-	-	-	1.04	298
CMS-C900[21]	-	-	-	1.80	298
G-1, G-2[22]				1.70	300
Zeolites[23]					
NaX		0.16	0.23	0.25	295
CeX#10		0.15	0.59	0.68	295

It should be noted that the amount of nitrogen adsorbed was lower than amount of oxygen adsorbed on both NEW-1 and M'MOF-1. This is probably due to the lack of electric charge on the surface of both NEW-1 and M'MOF-1 unlike zeolites, where the quadrupole of nitrogen strongly interacts with cations in the pores of zeolites.[11, 23-25] The pure component selectivities of O_2/N_2 obtained from gas adsorption on both NEW-1 and M'MOF-1 at 278 K are comparable to values obtained for MOF-177 and carbon molecular sieve C900 both having a selectivity of 1.80. It would be expected that the higher pure component selectivity of O_2/N_2 could be obtained at higher pressure. Hence, oxygen and nitrogen are kinetically separated since the equilibrium component separation ratio is possibly too small for air separation using porous materials.[22, 24]

8.2.2 Kinetic selectivity of O_2, N_2 and Ar

In term of the adsorption kinetics, previous studies revealed that the kinetics of oxygen, nitrogen and argon adsorption on carbon molecular sieve[18, 26, 27] and zeolites[28] follow the linear driving force model (LDF). However, the kinetic constants for oxygen, nitrogen and argon adsorption on NEW-1 at temperatures above 195 K could not be obtained accurately due to the fast kinetic profiles for gas adsorption as shown in Appendix F. This is due to a larger window dimension of NEW-1 compare to the molecular size of the adsorptive leading to the fast adsorption kinetics. The kinetic profiles for gas adsorption on M'MOF-1 at 195 K were fitted with the double stretched exponential model (DSE). Examples of the fitted DSE model on the kinetics profile of M'MOF-1 are shown in Appendix F. There are two set of DES rate constant for oxygen, nitrogen and argon adsorption on M'MOF-1 which are fast and slow DSE rate constants. The lager pores are expected to give the fast DSE rate constants (k_1) while slow DSE rate constant (k_2) is due to diffusion through the irregular shaped ultramicropores.

Figure 8.11 shows the fast DSE rate constant for gas adsorption on M'MOF-1 at 195 K. It is clear that the DSE rate constant of oxygen > nitrogen ≥ argon with the selectivity of O_2/N_2 and O_2/Ar in range 1.2-2.0 and 1.5-1.9, respectively. Figure 8.12 shows that the slow DSE rate constant tends to decrease with increasing pressure then reach a plateau. The DSE rate constant of both nitrogen and argon tends to be constant, which is probably due to constricted diffusion in the ultramicropores. The order of DSE rate constants were oxygen > nitrogen ≈ argon with the selectivity of O_2/N_2 and O_2/Ar in range 0.8-4.7 and 0.9-4.3, respectively. Figure 8.13 shows the DSE exponents β_1 and β_2 obtained for fast (k_1) and slow (k_2) DSE rate constant, respectively. The DSE exponents β_1 and β_2 obtained for argon, nitrogen and oxygen adsorption on M'MOF-1 at 195 K were in range 1.2-1.6 and 0.5-1.0, respectively. The values of DSE exponent β_1 were higher than the recommended values $0 < \beta < 1$. These high values of DSE exponent β_1 are presumably due to the diffusion of gases through the large pores size of M'MOF-1 which made the adsorption kinetics very difficult to measure accurately.

For CMS-40, the kinetics of gas adsorption on CMS-40 at 273 K follow the stretched exponential model (SE) which is indicative of diffusion through a distribution of pore sizes. Some selected kinetic profile for oxygen, nitrogen and argon adsorption on CMS-40 are shown in Appendix F. The SE rate constants of gas adsorption on CMS-40 at 273 K are shown in Figure 8.14. It is clear that the order of the SE rate constant of oxygen >> nitrogen > argon. This shows that the slightly smaller oxygen molecule diffuses more rapidly in the pore of CMS-40 compared to nitrogen and argon molecules. This is often attributed to the reverse order of the molecular width of oxygen (2.8 Å) < nitrogen (3.0 Å) < argon (3.8 Å) as shown in Table 8.2. However the cross-sectional dimensions of the molecules obtained from ZINDO calculations do not show such a clear trend. The pure component selectivity of O_2/N_2 was in the range of 33-55 which is similar to the values obtained for other CMS materials (25-45).[18, 26] The SE exponents (β) obtained for argon, nitrogen and oxygen adsorptions on CMS-40 at 273 K were quite constant and were in range ~0.90-0.94, ~0.82-0.92 and ~0.73-0.81, respectively (see Figure 8.15). The β values obtained for Ar adsorption were very close to the LDF (β =1).

Table 8.2 Comparison of structural and physical parameters for the probe molecules

Parameters	Oxygen	Nitrogen	Argon
Lennard-Jones (1ó) (pm)[19]	346	364	340
Critical dimension minimum cross section (pm) [29]	280	300	384
Molecular dimensions x, y, z (pm)[30]	298.5, 293.0, 405.2	305.4, 299.1, 404.6	363, 351,-
Dipole Moment (D)[27]	0	0	0
Quadrupole moment 10^{40} θ (Cm^2)[27]	1.3	4.7	0
Polarizability ($Å^3$)[31]	1.6	1.76	1.66

In summary, the kinetics profiles obtained for gas adsorption on M'MOF-1 followed a double stretched exponential model due to the presence of 2 types of pores while the CMS-40 followed a stretched exponential model, corresponding to a narrow distribution of pore sizes in the carbon deposit. Fast adsorption kinetics obtained for gas adsorption on NEW-1 were not analysed in detail with mathematical models because of their limited accuracy but the results suggest that the kinetics follow the pore size of the selective structural regions in the materials: NEW-1 > M'MOF-1 > CMS-40. The sizes of pores in M'MOF 1 are very small but the temperature still had to be reduced to 195 K to show kinetic differences. The DSE rate constant obtained for gas adsorption on both M'MOF-1 and CMS-40 indicated that O_2 has the fastest kinetics while the rate constants obtained for N_2 adsorption are slightly higher than Ar. Critical minimum cross section appears to give a better prediction of adsorption kinetics which is similar to the previous results reported by Reid *et. al.*[18, 19], Vyas *et. al.*[22] and Rutherford *et. al.*[32]. Comparison of the adsorption kinetics of N_2, O_2 and Ar on NEW-1, M'MOF-1 and CMS-40 shows that MOFs must have extremely narrow pores to give kinetics separation characteristics similar to CMS-40 which is used commercially for air separation.

8.2.3 Thermodynamic of O_2, N_2 and Ar adsorption on porous materials

The isosteric enthalpies of adsorption at zero surface coverage were calculated using virial equation.[18, 19, 23, 26] Kiselev *et al*[33]. firstly introduced the virial equation by modifying the Henry's law equation and then Cole *et. al.*[34] proposed that the virial equation can be expressed in a linear form as shown below (details in section 2.5.1);

$$\ln(n/p) = A_0 + A_1 n + A_2 n^2 + ... \qquad (1)$$

Where the A_0 and A_1 parameters represent the adsorbate-adsorbent interaction at zero surface coverage and adsorbate-adsorbate interaction, respectively. Values of A_0 can be obtained from the graphs of $\ln(n/p)$ versus n at different temperatures T. The isosteric enthalpy of adsorption at zero surface coverage can be determined from the slope of the plot of A_0 against $1/T$.[12, 18, 26]

The adsorption temperature used in this study was above the critical temperatures of argon, nitrogen and oxygen and therefore, it is not possible to express the pressures in terms of relative pressure since the saturated vapour pressure (p^o) does not exist. The virial plots for both NEW-1 and M'MOF-1 are obtained from the adsorption isotherms of gases over the temperature range 195-298 K (see Figure 8.16-8.21) while the virial plots for CMS-40 were obtained from the adsorption isotherm of gases over temperature range 273-298 K as shown in Figures 8.22-8.24. The virial plots obtained from gas adsorption on NEW-1, M'MOF-1 and CMS-40 are linear over a major part of the pressure range but deviate from linearity at low-pressure where the uncertainties in the measurement of small amounts adsorbed and pressures lead to higher uncertainties in the virial graphs (see Figure 8.25-8.32).

The first and the second virial coefficients obtained from gas adsorption on metal organic framework and carbon molecular sieve are shown in Table 8.3 and 8.4, respectively. Good agreement was obtained for values of A_0 and A_1 for the adsorption of gases on both metal organic frameworks and carbon molecular sieve. However, the data showed that the higher terms (A_1, etc.) in the virial equation could be ignored at low uptakes/pressures.

In Table 8.3, the A_0 obtained for gas adsorption on metal organic frameworks and CMS-40 decreased with increasing of temperature as expected for a physisorption mechanism. The values of the first virial coefficient A_0 for nitrogen, oxygen and argon adsorption on both NEW-1 and M'MOF-1 at temperature range 195-298 K were similar. While, the values of the first virial coefficient for nitrogen, oxygen and argon adsorption on CMS-40 over the temperature range 273-298 K were slightly higher than those values obtained for both MOF-1 and M'MOF-1 as a result of the amount of gases adsorbed on CMS-40 being slightly higher. These higher values of A_0 of CMS-40 are also indicative of larger pore volumes/surface areas for CMS-40 than for both MOF-1 and M'MOF-1. The pore structure of NEW-1 is in its collapsed form which has a low total pore volume. The A_0 values of both metal organic frameworks obtained from the adsorption of gases at 195 K were much higher than those values obtained at 273 and 298 K. In case of the CMS-40, the adsorption of oxygen, nitrogen and argon at 195 K or lower temperature cannot be done due to activated diffusion at this temperature.

Table 8.3 First virial coefficient ($A_{0,}$ mol g^{-1} Pa^{-1}) for gases adsorption on porous materials

Gases	195 K	273 K	288	298 K
NEW-1				
O_2	-16.51 ± 0.052	-20.08 ± 0.005		-20.71 ± 0.006
Ar	-16.06 ± 0.076	-20.05 ± 0.004		-20.64 ± 0.007
N_2	-16.88 ± 0.015	-20.54 ± 0.014		-21.09 ± 0.002
M'MOF-1				
O_2	-17.05 ± 0.004	-20.89 ± 0.004		-21.42 ± 0.004
Ar	-17.06 ± 0.002	-21.00 ± 0.001		-21.51 ± 0.004
N_2	-17.51 ± 0.002	-21.31 ± 0.007		-21.67 ± 0.008
CMS-40				
O_2		-18.46 ± 0.004	-18.83 ± 0.014	-18.98 ± 0.021
Ar		-18.49 ± 0.011	-18.93 ± 0.013	-19.07 ± 0.013
N_2		-18.32 ± 0.010	-18.72 ± 0.014	-18.95 ± 0.014

O'koye *et al.*[26] reported A_0 values for oxygen and nitrogen adsorption on carbon molecular sieve at 298 K of -736 ± 7 and -921 ± 25 g mol^{-1}, respectively. Reid *et al.*[18, 19] investigated the adsorption of nitrogen, oxygen and argon on various carbon molecular sieves over the temperature range 273-343 K. The values of A_0 for nitrogen, oxygen and argon adsorption were in the range of -19.3 to -20.3, -18.50 to -19.8 and -19.8 to -20.4 mol g^{-1} Pa^{-1}, respectively. While the values of the A_1 values for nitrogen, oxygen and argon adsorption carbon molecular sieve were in the range of -648 to -1077, -507 to -1079 and -549 to -20.4 g mol^{-1}, respectively. Comparison of these literature values for A_0 and A_1 with the values obtained in this study shows that they are similar.

Table 8.4 Second virial coefficient (A_1, g mol^{-1}) for gases adsorption on porous materials

Gases	195 K	273 K	288	298 K
NEW-1				
O_2	-1125.2 ± 48.3	-1374.1 ± 48.0		-1111.3 ± 94
Ar	-1641.1 ± 69.5	-1436.5 ± 35.5		-1070.9 ± 112.4
N_2	-1132.5 ± 20.1	-1482.7 ± 186.4		-929.3 ± 67.1
M'MOF-1				
O_2	-812.9 ± 5.3	-1281.2 ± 102.2		-1160.2 ± 154.3
Ar	-858.4 ± 3.7	-1211.7 ± 48.5		-934.9 ± 192.0
N_2	-1186.16 ± 12.3	-1670.6 ± 30.7		-1052.7 ± 423.3
CMS-40				
O_2		-810.5 ± 11.7	-1013.4 ± 50.2	-1206.4 ± 81.2
Ar		-930.89 ± 30.9	-993.59 ± 49.37	-1225.9 ± 52.9
N_2		-1084.2 ± 27.0	-1226.25 ± 52.1	-1245.5 ± 56.0

The values for the isosteric enthalpies of adsorption (Q_{st}) for the gases studied were obtained from graphs of A_0 versus $1/T$ as shown in Figure 8.33-8.35 and isosteric enthalpy values are listed in Table 8.5. The values of Q_{st} at zero surface coverage for oxygen, nitrogen and argon obtained for both NEW-1 and M'MOF-1 were in range 19-22 kJ mol^{-1} and were similar. While, the values of Q_{st} at zero surface coverage for oxygen, nitrogen and argon obtained for CMS-40 were 14-17 kJ mol^{-1} and were lower than the values obtained for those two metal organic frameworks. These low values of isosteric enthalpies obtained for gases adsorption on CMS-40 indicating weaker adsorbate-adsorbent interaction compare to both NEW-1 and M'MOF-1. However, Q_{st} for CMS-40 is similar to the values obtained for adsorption of nitrogen, argon and oxygen on other CMS and porous carbons (see Table 8.5).[18, 19, 35, 36]

Table 8.5 Isosteric enthalpies of adsorption for O_2, N_2 and Ar on porous materials

Gases	NEW-1 (kJ/mol)	M'MOF 1 (kJ/mol)	CMS-40 (kJ/mol)	Microporous carbon and CMS (kJ/mol)
O_2	19.88 ± 0.46	20.89 ± 1.09	14.28 ± 1.35	11.7-22.0[18, 19, 35, 36]
N_2	20.05 ± 0.86	20.16 ± 1.71	17.08 ± 0.20	14.7-21.5 [19, 35, 36]
Ar	21.86 ± 0.99	21.35 ± 1.20	16.00 ± 2.34	14.9-17.7 [18, 19, 35, 36]

a)

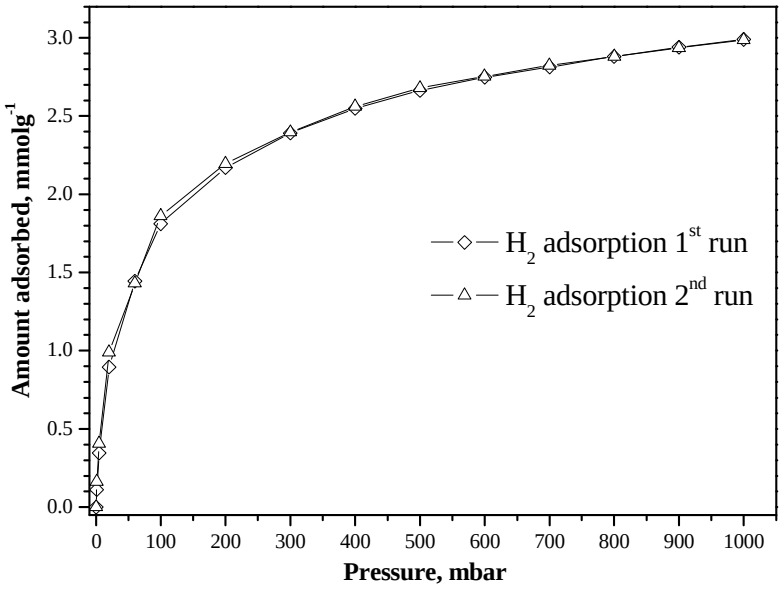

b)

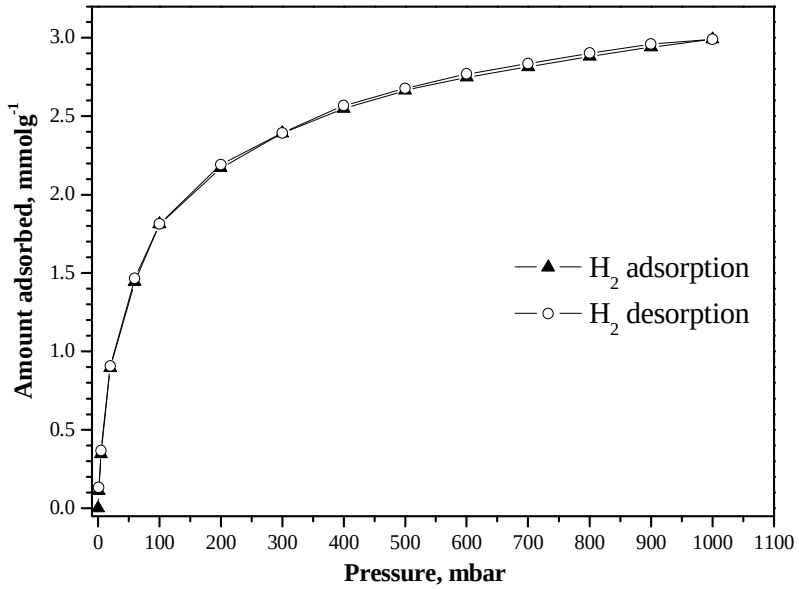

Figure 8.1 a) Repeatability measurements for hydrogen adsorption isotherms on NEW-1 at 77 K b) hydrogen adsorption/desorption isotherms for NEW-1 at 77 K

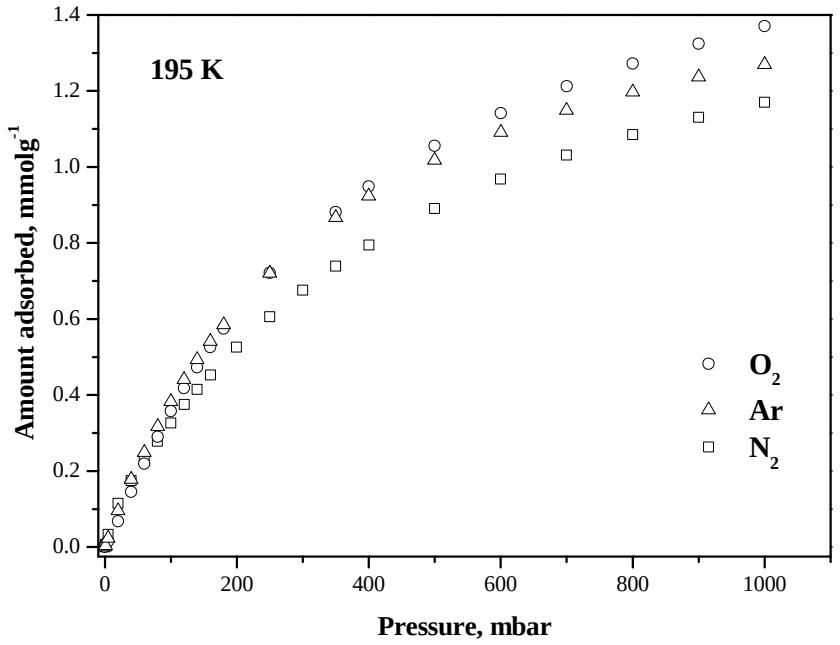

Figure 8.2 Adsorption isotherms for O_2, N_2 and Ar on NEW-1 at 195 K

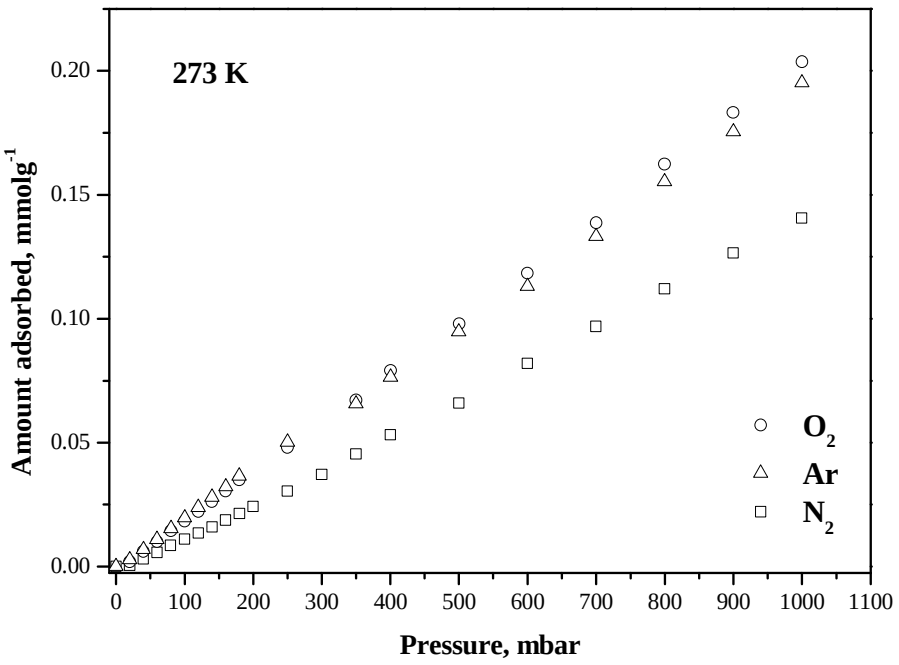

Figure 8.3 Adsorption isotherms for O_2, N_2 and Ar on NEW-1 at 273 K

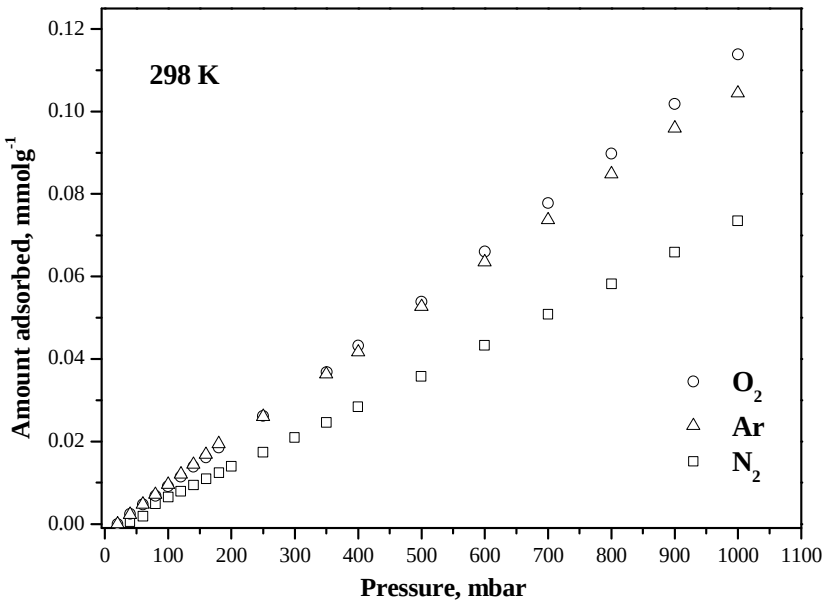

Figure 8.4 Adsorption isotherms for O_2, N_2 and Ar on NEW-1 at 298 K

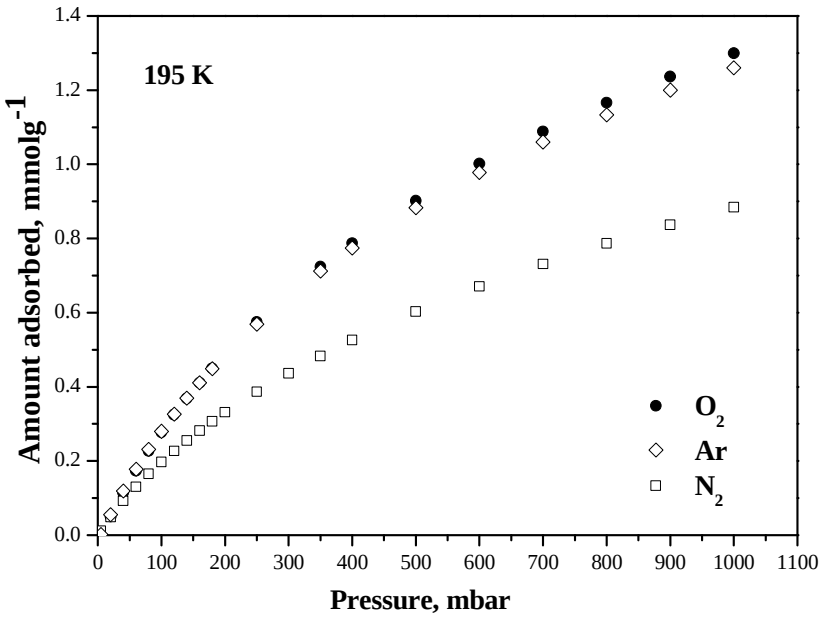

Figure 8.5 Adsorption isotherms for O_2, N_2 and Ar on M'MOF-1 at 195 K

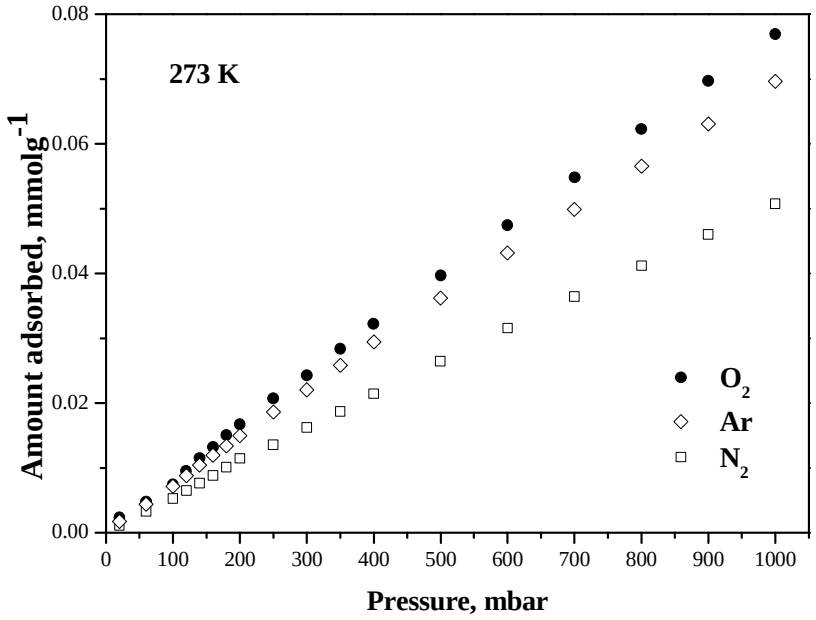

Figure 8.6 Adsorption isotherms for O_2, N_2 and Ar on M'MOF-1 at 273 K

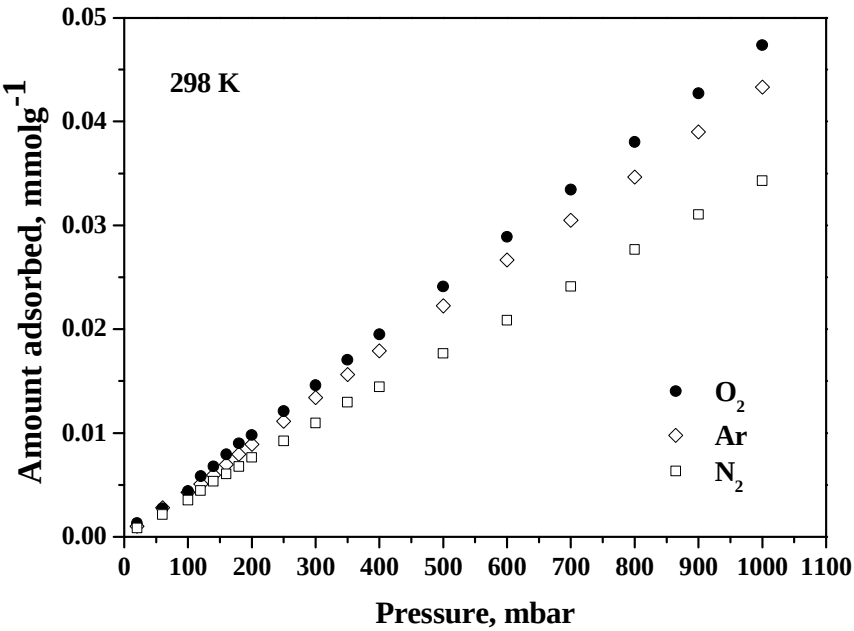

Figure 8.7 Adsorption isotherms for O_2, N_2 and Ar on M'MOF-1 at 298 K

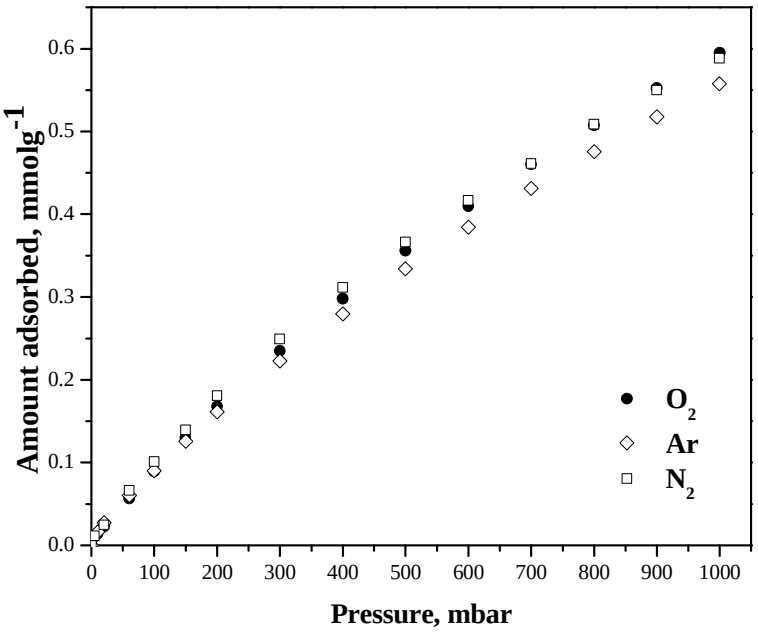

Figure 8.8 Adsorption isotherms for O_2, N_2 and Ar on CMS-40 at 273 K

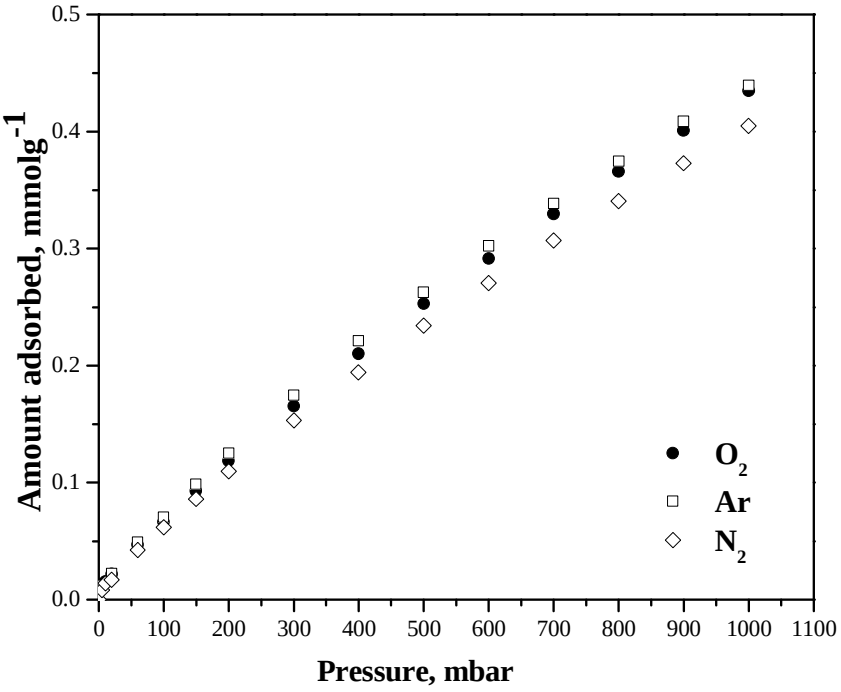

Figure 8.9 Adsorption isotherms for O_2, N_2 and Ar on CMS-40 at 288 K

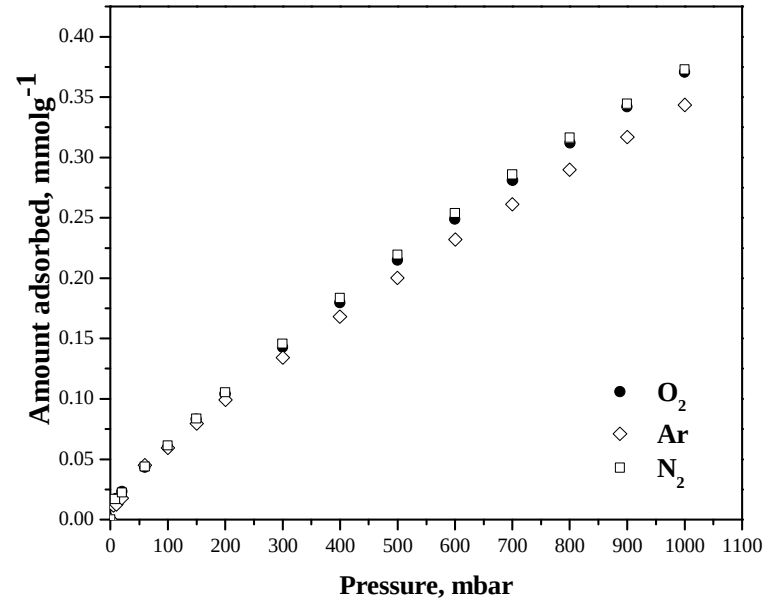

Figure 8.10 Adsorption isotherms for O_2, N_2 and Ar on CMS-40 at 298 K.

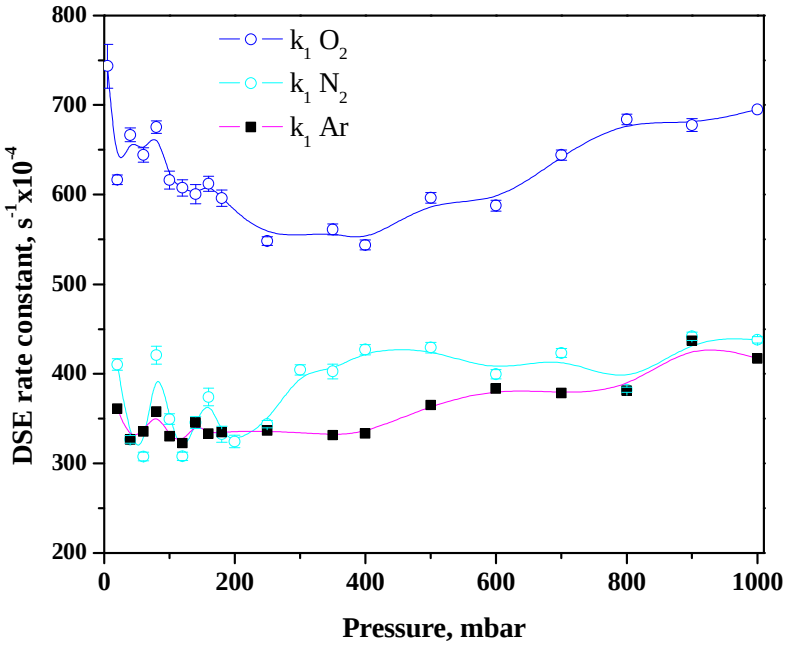

Figure 8.11 The fast DSE rate constants versus pressure for O_2, N_2 and Ar adsorption on M'MOF-1 at 195 K.

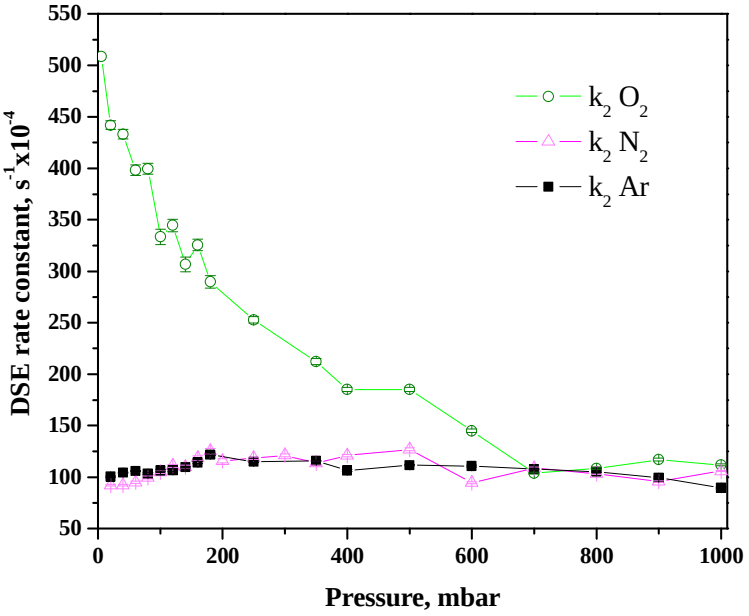

Figure 8.12 The slow DSE rate constants versus pressure for O_2, N_2 and Ar adsorption on M'MOF-1 at 195 K.

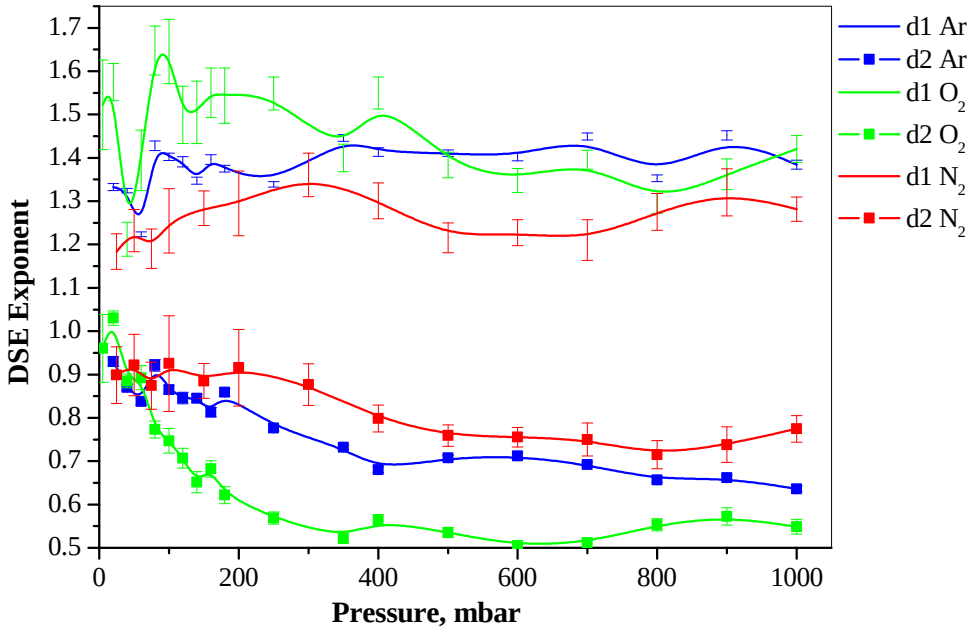

Figure 8.13 DSE exponents versus pressure for O_2, N_2 and Ar adsorption on M'MOF-1 at 195 K.

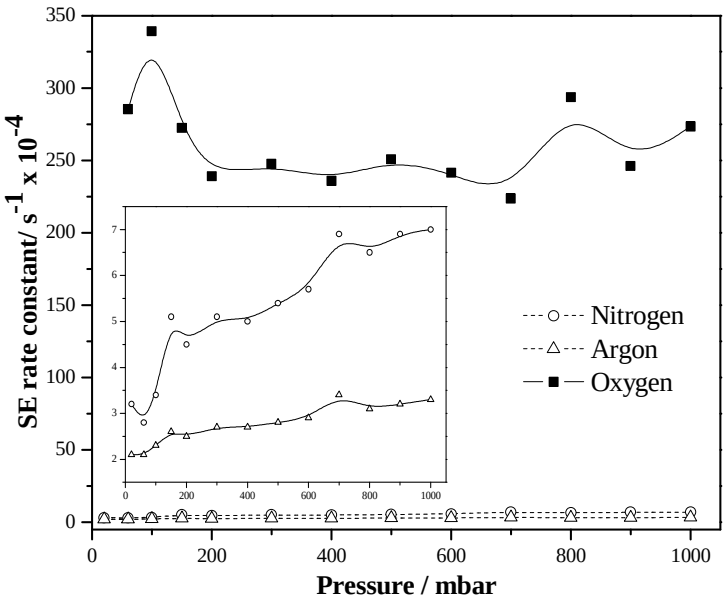

Figure 8.14 The SE rate constants versus pressure for O_2, N_2 and Ar adsorption on CMS-40 at 273 K, inset magnified SE rate constants for nitrogen and argon

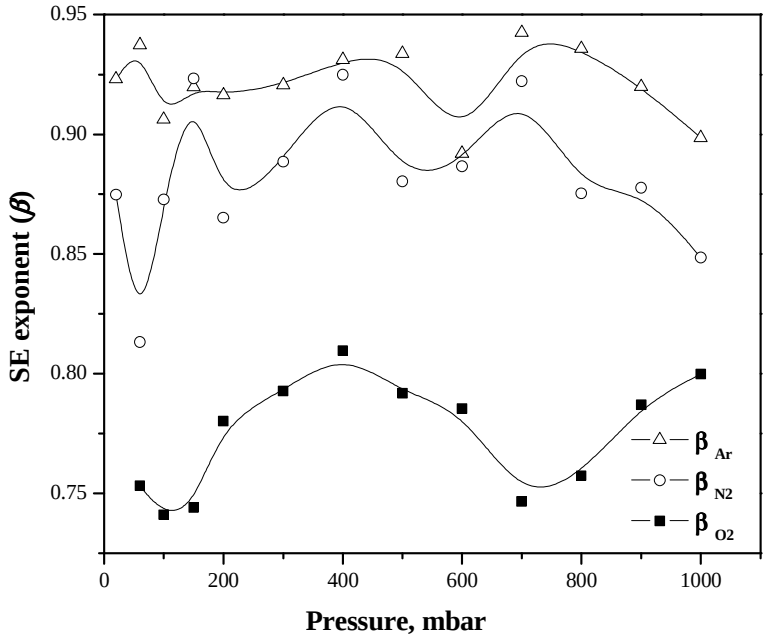

Figure 8.15 The SE exponent versus pressure for O_2, N_2 and Ar adsorption on CMS-40 at 273 K.

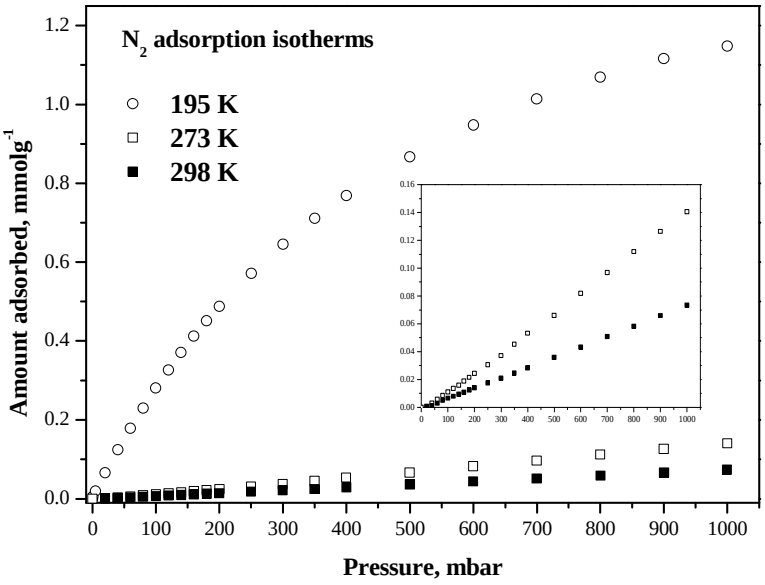

Figure 8.16 Nitrogen adsorption isotherms for NEW-1 over the temperature range 195-298 K

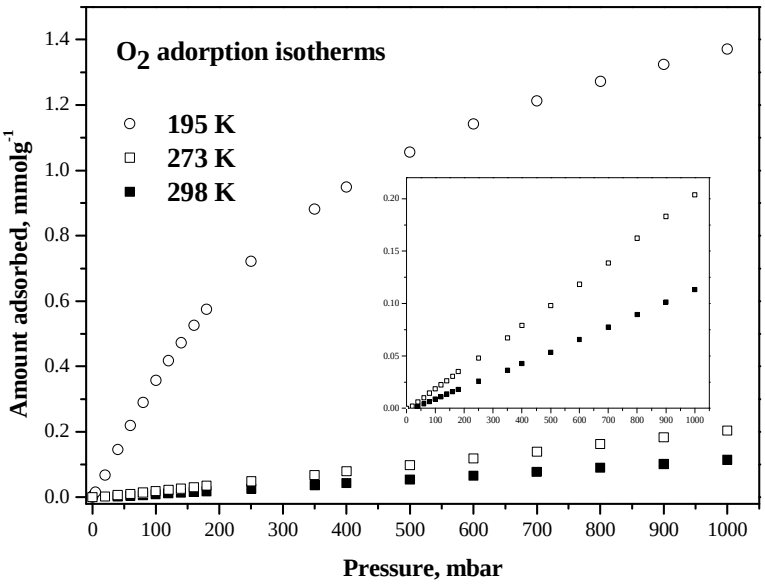

Figure 8.17 Oxygen adsorption isotherms for NEW-1 over the temperature range 195-298 K

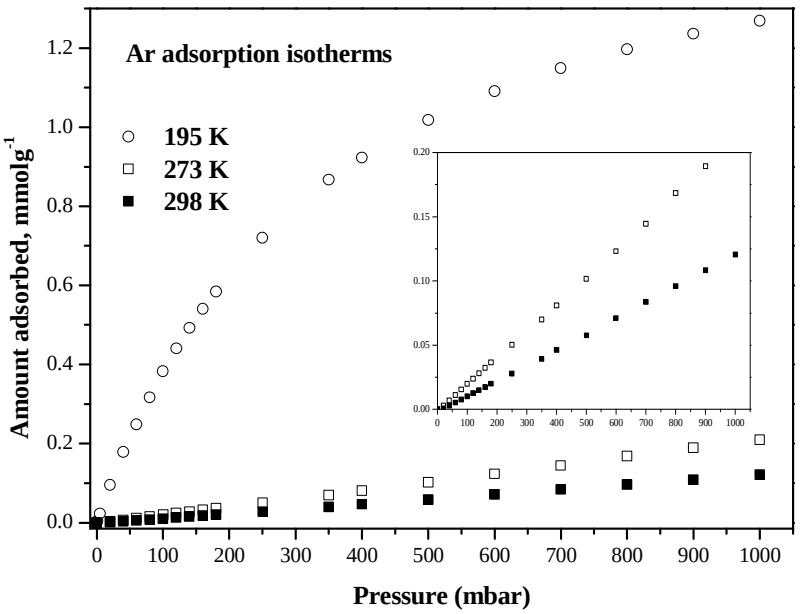

Figure 8.18 Argon adsorption isotherms for NEW-1 over the temperature range 195-298 K

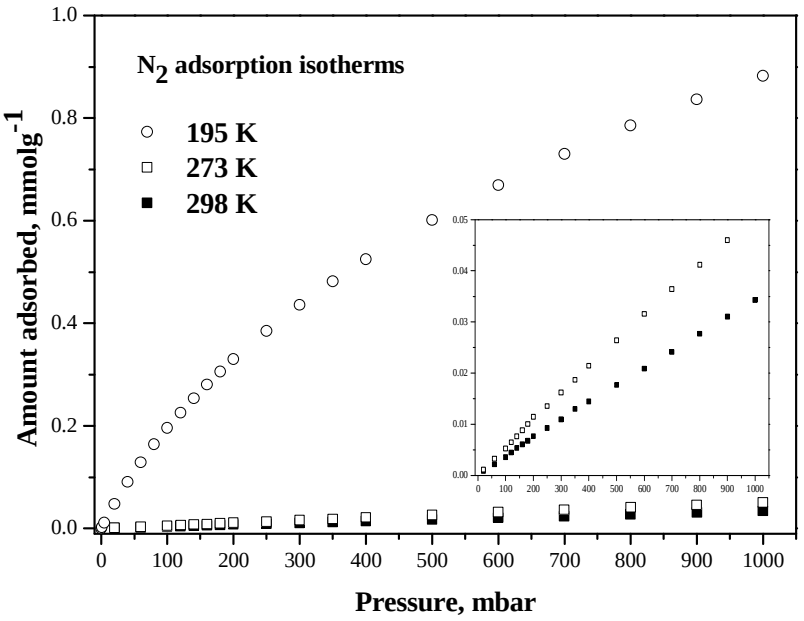

Figure 8.19 Nitrogen adsorption isotherms for M'MOF-1 over the temperature range 195-298 K

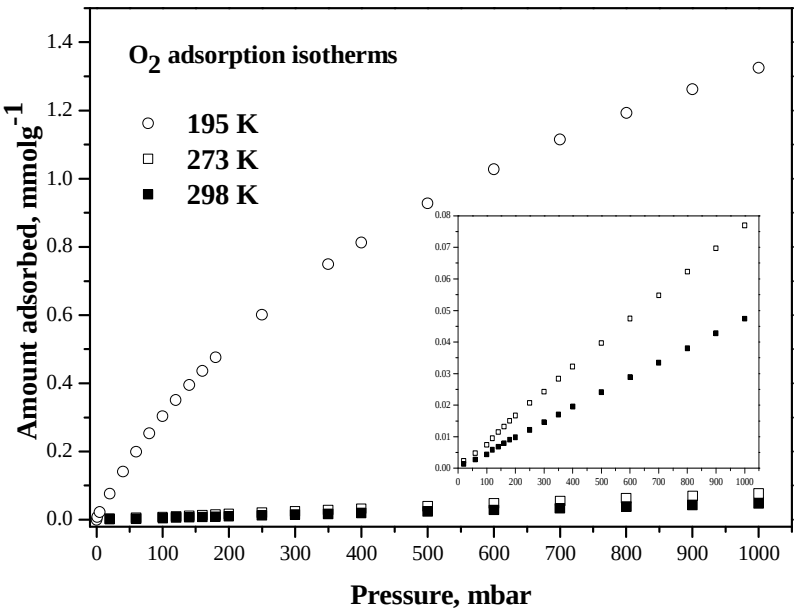

Figure 8.20 Oxygen adsorption isotherms for M'MOF-1 over the temperature range 195-298 K

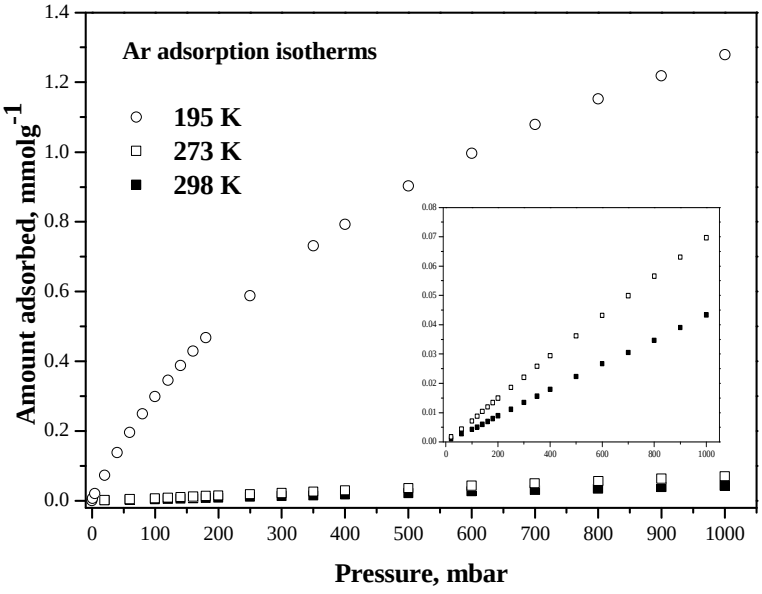

Figure 8.21 Argon adsorption isotherms for M'MOF-1 over the temperature range 195-298 K

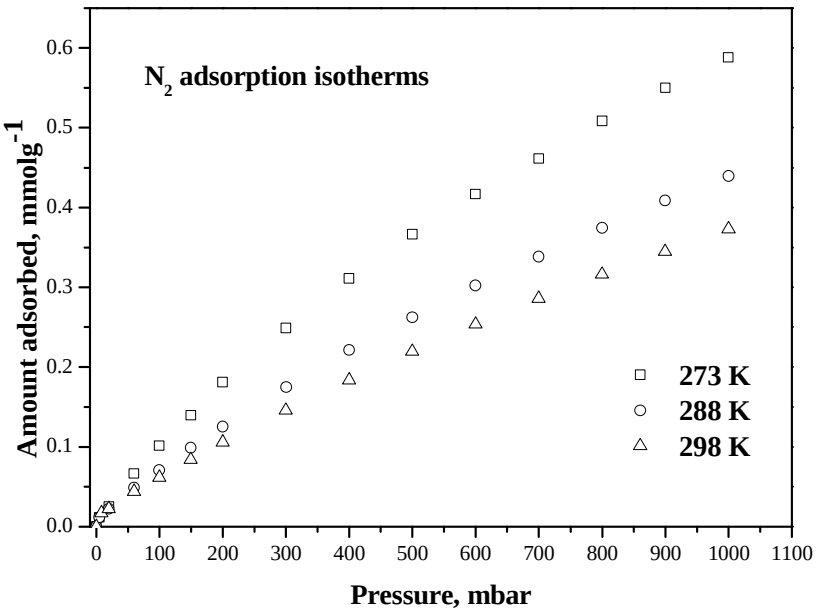

Figure 8.22 Nitrogen adsorption isotherms for CMS-40 over the temperature range 273-298 K

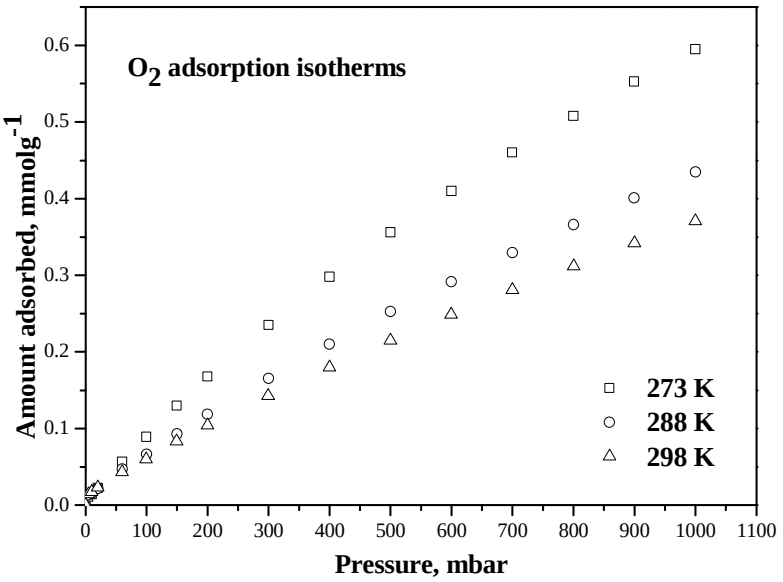

Figure 8.23 Oxygen adsorption isotherms for CMS-40 over the temperature range 273-298 K

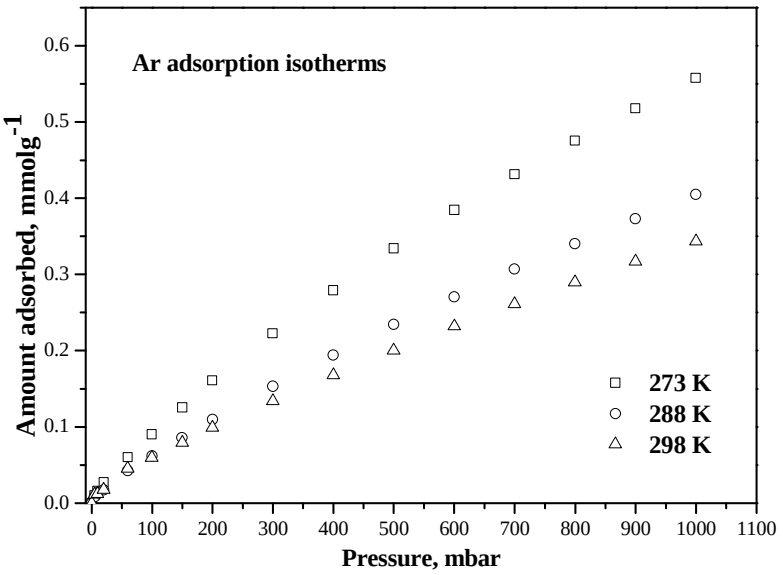

Figure 8.24 Argon adsorption isotherms for CMS-40 over the temperature range 273-298 K

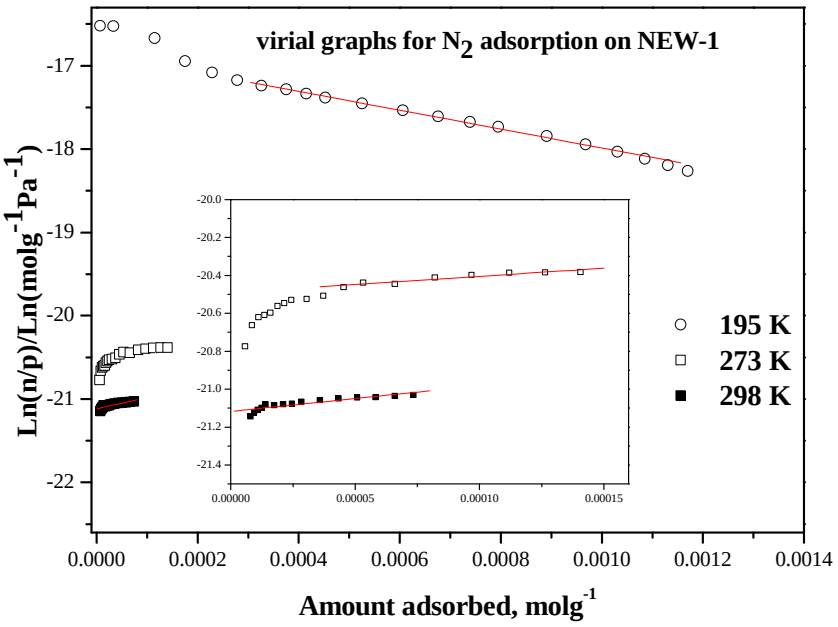

Figure 8.25 Virial plots for nitrogen adsorption on NEW-1 over the temperature range 195-298 K

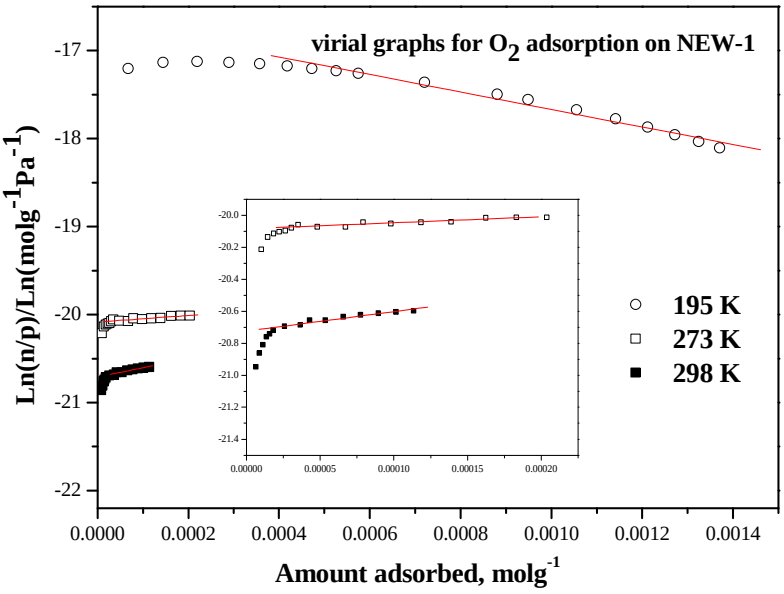

Figure 8.26 Virial plots for oxygen adsorption on NEW-1 over the temperature range 195-298 K

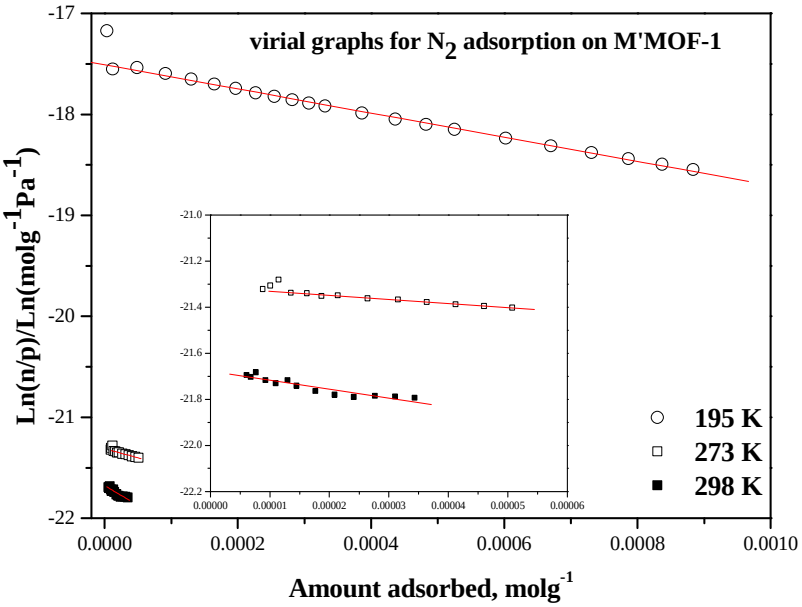

Figure 8.27 Virial plots for nitrogen adsorption on M'MOF-1 over the temperature range 195-298 K

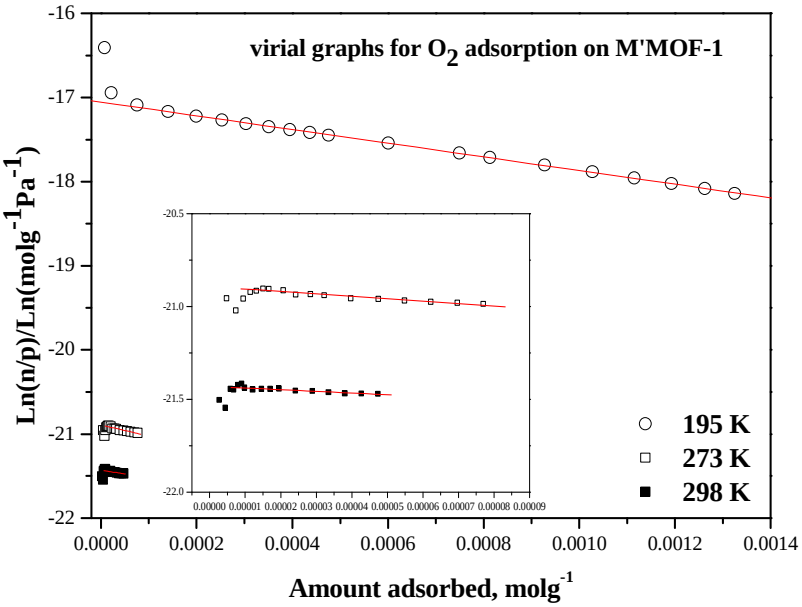

Figure 8.28 Virial plots for oxygen adsorption on M'MOF-1 over the temperature range 195-298 K

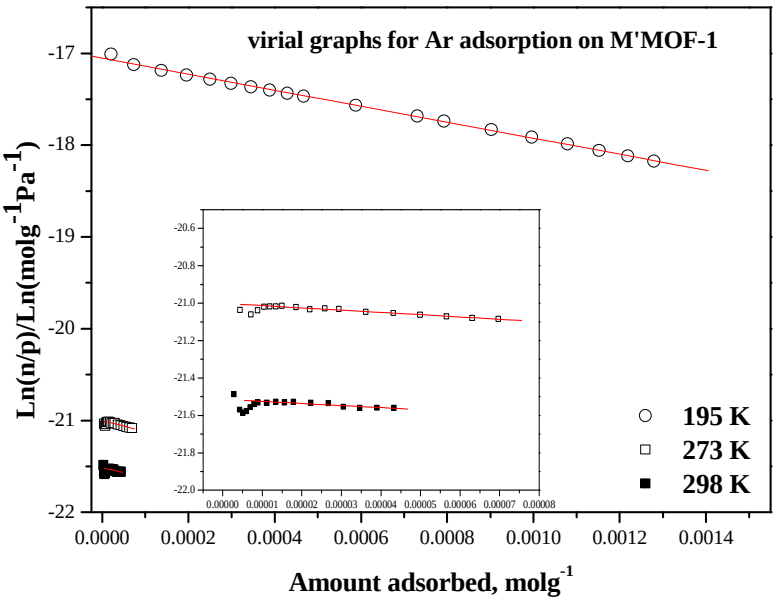

Figure 8.29 Virial plots for argon adsorption on M'MOF-1 over the temperature range 195-298 K

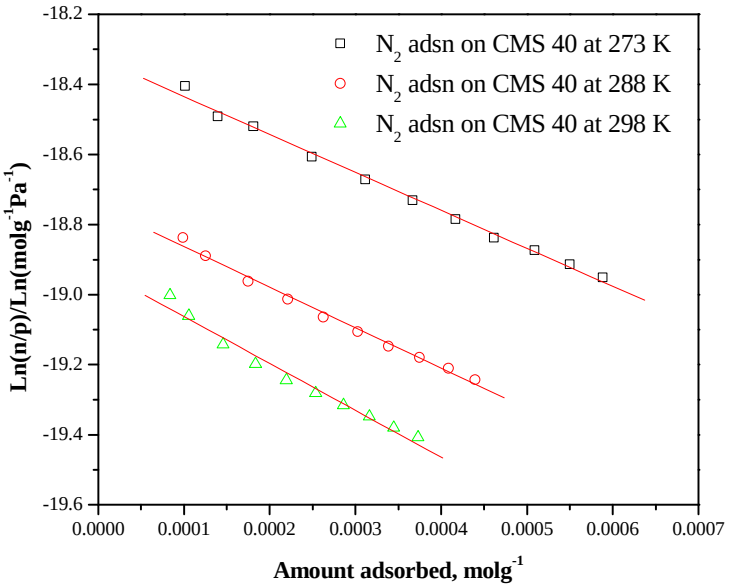

Figure 8.30 Virial plots for nitrogen adsorption on CMS-40 over the temperature range 273-298 K

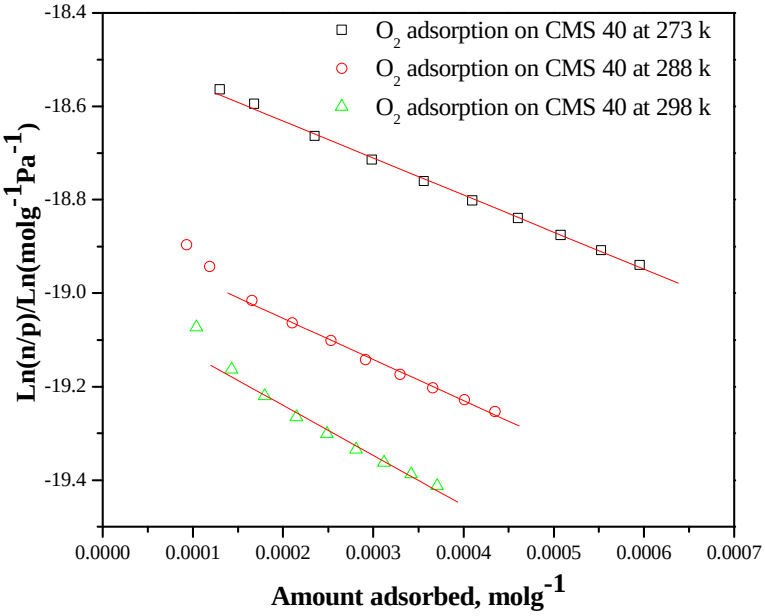

Figure 8.31 Virial plots for oxygen adsorption on CMS-40 over the temperature range 273-298 K

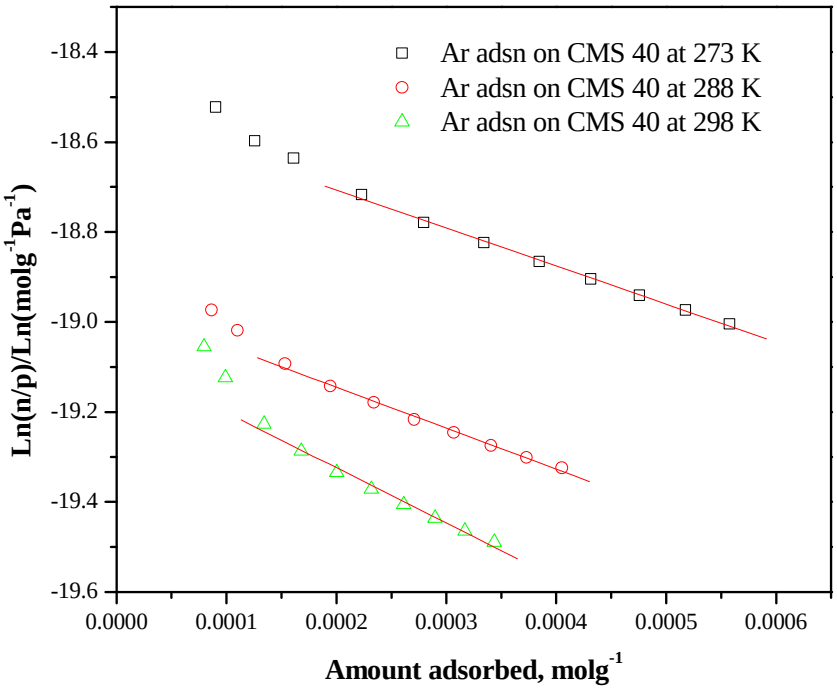

Figure 8.32 Virial plots for argon adsorption on CMS-40 over the temperature range 273-298 K

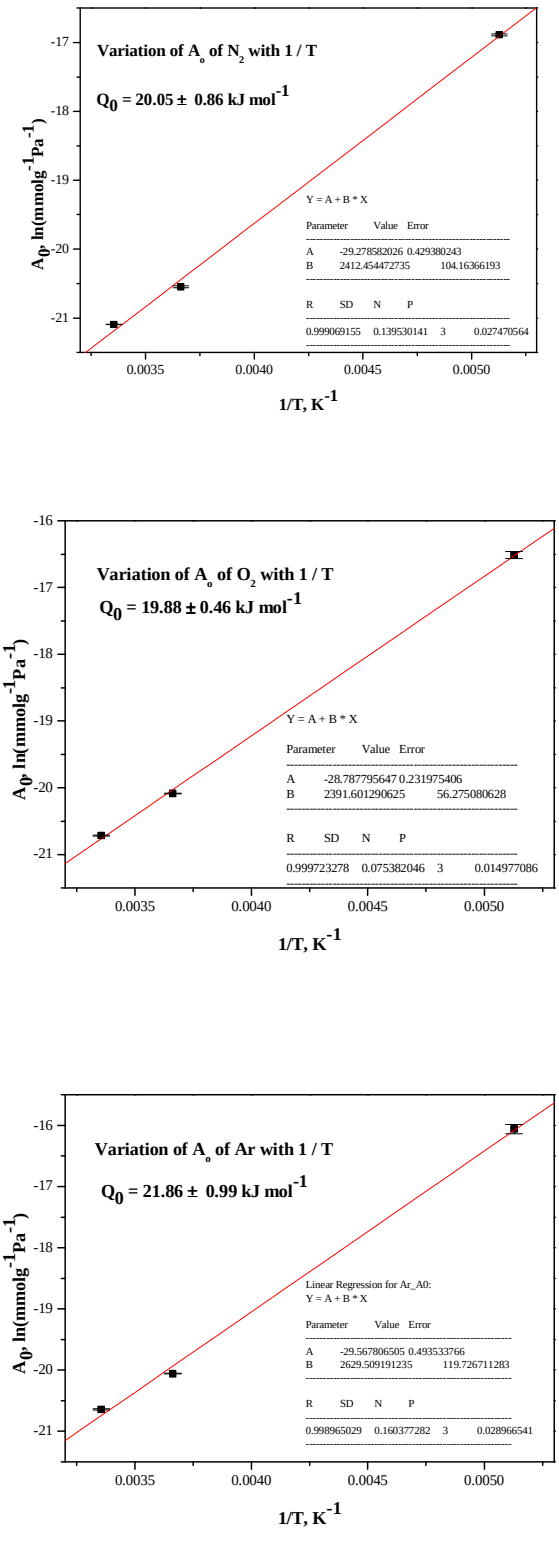

Figure 8.33 Variation of A_0 versus $1/T$ for gases adsorption on NEW-1 over the temperature range 195-298 K

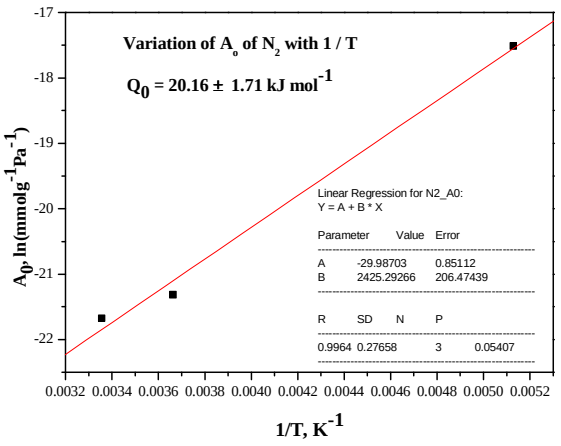

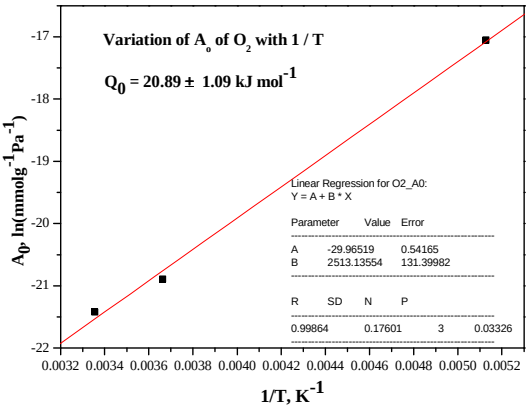

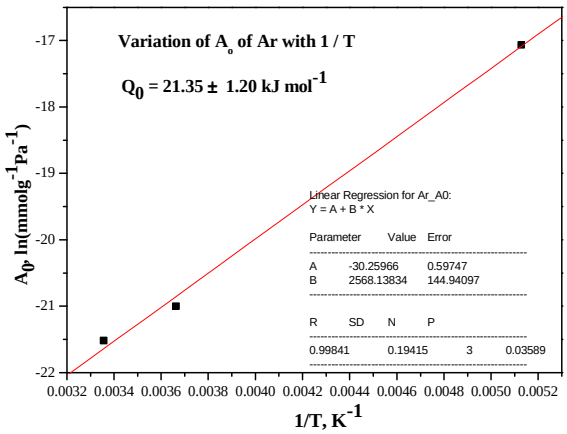

Figure 8.34 Variation of A_0 versus $1/T$ for gases adsorption on M'MOF-1 over the temperature range 195-298 K

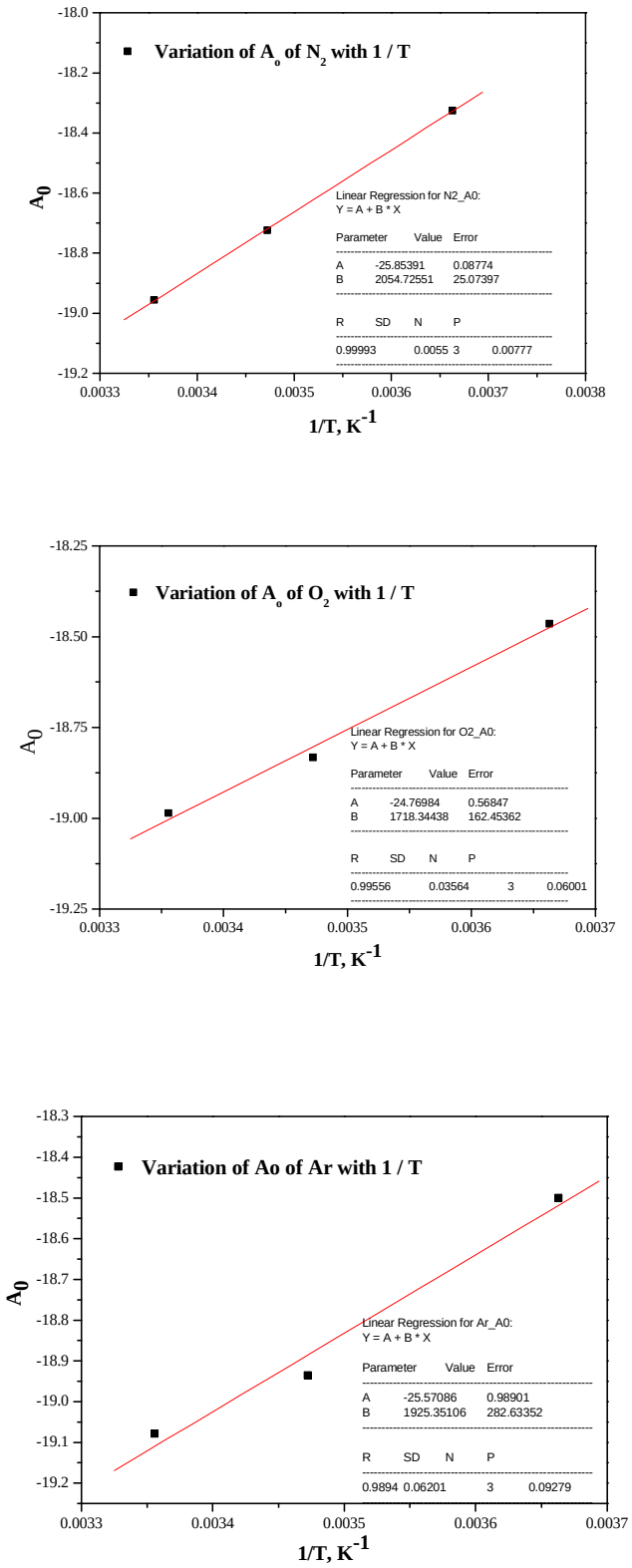

Figure 8.35 Variation of A_0 versus $1/T$ for gases adsorption on CMS-40 over the temperature range 273-298 K

8.3 References

1. Lin, Y.-M.; Rei, M.-H., Study on the hydrogen production from methanol steam reforming in supported palladium membrane reactor. *Catalysis Today* **2001,** 67, (1-3), 77-84.

2. de Wild, P. J.; Verhaak, M. J. F. M., Catalytic production of hydrogen from methanol. *Catalysis Today* **2000,** 60, (1-2), 3-10.

3. Schlapbach, L.; Zuttel, A., Hydrogen-storage materials for mobile applications. *Nature* **2001,** 414, (6861), 353-8.

4. Zhou, L., Progress and problems in hydrogen storage methods. *Renew. Sust. Energ Rev.* **2005,** 9, (4), 395-408.

5. Fichtner, M., Nanotechnological Aspects in Materials for Hydrogen Storage. *Adv. Eng. Mater.* **2005,** 7, (6), 443-55.

6. David, E., An overview of advanced materials for hydrogen storage. *J. Mater. Process. Technol.* **2005,** 162-163, 169-77.

7. Nijkamp, M. G.; Raaymakers, J. E. M. J.; van Dillen, A. J.; de Jong, K. P., Hydrogen storage using physisorption – materials demands. *Appl. Phys. A* **2001,** 72, (5), 619-23.

8. Texier-Mandoki, N.; Dentzer, J.; Piquero, T.; Saadallah, S.; David, P.; Vix-Guterl, C., Hydrogen storage in activated carbon materials: Role of the nanoporous texture. *Carbon* **2004,** 42, (12-13), 2744-7.

9. Jesse, L. C. R.; Omar, M. Y., Strategies for Hydrogen Storage in Metal-Organic Frameworks. *Angew. Chem. Int. Ed.* **2005,** 44, (30), 4670-9.

10. Fletcher, A. J.; Thomas, K. M.; Rosseinsky, M. J., Flexibility in metal-organic framework materials: Impact on sorption properties. *J. Solid State Chem.* **2005,** 178, (8), 2491-510.

11. Yang, R. T., *Adsorbents: Fundamentals and Applications*. Wiley-Interscience 2003; p 424.

12. Rouquerol, F.; Rouquerol, J.; Sing, K. S. W., *Adsorption by Powders, Porous Solids*. Academic Press: London, 1999; p 467.

13. Chen, B.; Zhao, X.; Putkham, A.; Hong, K.; Lobkovsky, E. B.; Hurtado, E. J.; Fletcher, A. J.; Thomas, K. M., Surface Interactions and Quantum Kinetic Molecular

Sieving for H2 and D2 Adsorption on a Mixed Metalâˆ'Organic Framework Material. *J. Am. Chem. Soc.* **2008,** 130, (20), 6411-23.

14. Thorogood, R. M., Developments in air separation. *Gas Sep. Purif.* **1991,** 5, (2), 83-94.

15. Castle, W. F., Air separation and liquefaction: recent developments and prospects for the beginning of the new millennium. *Int. J. Refrig* **2002,** 25, (1), 158-72.

16. Golden, T. C.; Battavio, P. J.; Chen, Y. C.; Farris, T. S.; Armor, J. N., Carbon-based oxygen selective desiccants for use in nitrogen PSA. *Gas Sep. Purif.* **1993,** 7, (4), 274-8.

17. Hassan, M. M.; Ruthven, D. M.; Raghavan, N. S., Air separation by pressure swing adsorption on a carbon molecular sieve. *Chem. Eng. Sci.* **1986,** 41, (5), 1333-43.

18. Reid, C. R.; O'Koy, I. P.; Thomas, K. M., Adsorption of Gases on Carbon Molecular Sieves Used for Air Separation. Spherical Adsorptives as Probes for Kinetic Selectivity. *Langmuir* **1998,** 14, (9), 2415-25.

19. Reid, C. R.; Thomas, K. M., Adsorption of Gases on a Carbon Molecular Sieve Used for Air Separation: Linear Adsorptives as Probes for Kinetic Selectivity. *Langmuir* **1999,** 15, (9), 3206-18.

20. Li, Y.; Yang, R. T., Gas Adsorption and Storage in Metal Organic Framework MOF-177. *Langmuir* **2007,** 23, (26), 12937-44.

21. Tan, J. S.; Ani, F. N., Carbon molecular sieves produced from oil palm shell for air separation. *Sep. Purif. Technol.* **2004,** 35, (1), 47-54.

22. Vyas, S. N.; Patwardhan, S. R.; Vijayalakshmi, S.; Ganesh, K. S., Adsorption of Gases on Carbon Molecular Sieves. *J. Colloid Interface Sci.* **1994,** 168, (2), 275-80.

23. Jayaraman, A.; Yang, R. T.; Cho, S.-H.; Bhat, T. S. G.; Choudary, V. N., Adsorption of Nitrogen, Oxygen and Argon on Na-CeX Zeolites. *Adsorption* **2002,** 8, (4), 271-8.

24. Gaffney, T. R., Porous solids for air separation. *Curr. Opin. Solid State Mater. Sci.* **1996,** 1, (1), 69-75.

25. De Stefanis, A.; Perez, G.; Semprini, E.; Stefani, F.; Tomlinson, A. A. G., Air separation on H-mordenite. *Microporous Mesoporous Mater.* **2004,** 71, (1-3), 103-8.

26. O'Koye, I. P.; Benham, M.; Thomas, K. M., Adsorption of Gases and Vapors on Carbon Molecular Sieves. *Langmuir* **1997,** 13, (15), 4054-9.

27. Bae, Y. S.; Lee, C. H., Sorption kinetics of eight gases on a carbon molecular sieve at elevated pressure. *Carbon* **2005,** 43, (1), 95-107.

28. Berenguer-Murcia, A.; Fletcher, A. J.; Garcia-Martinez, J.; Cazorla-Amoros, D.; Linares-Solano, A.; Thomas, K. M., Probe Molecule Kinetic Studies of Adsorption on MCM-41. *J. Phys. Chem. B* **2003,** 107, (4), 1012-20.

29. Ainscough, A. N.; Dollimore, D., Adsorption capacity of molecular sieve type carbons. *Langmuir* **2002,** 3, (5), 708-13.

30. Webster, C. E.; Drago, R. S.; Zerner, M. C., Molecular Dimensions for Adsorptives. *J. Am. Chem. Soc.* **1998,** 120, (22), 5509-16.

31. Golden, T. C.; Sircar, S., Gas Adsorption on Silicalite. *J. Colloid Interface Sci.* **1994,** 162, (1), 182-8.

32. Rutherford, S. W.; Do, D. D., Characterization of Carbon Molecular Sieve 3A. *Langmuir* **2000,** 16, (18), 7245-54.

33. Avgul, N. N.; Bezus, A. G.; Dobrova, E. S.; Kiselev, A. V., The similarity of gas adsorption by nonporous and microporous crystalline adsorbents. *J. Colloid Interface Sci.* **1973,** 42, (3), 486-95.

34. Cole, J. H.; Everett, D. H.; Marshall, C. T.; Paniego, A. R.; Powl, J. C.; Rodriguez-Reinoso, F., Thermodynamics of the high temperature adsorption of some permanent gases by porous carbons. *J. Chem. Soc., Faraday Trans.* **1974,** 70, 2154 - 69.

35. Kazuyuki, C.; Motoyuki, S.; Kunitaro, K., Adsorption rate on molecular sieving carbon by chromatography. *AIChE Journal* **1978,** 24, (2), 237-46.

36. Verma, S. K., Development of molecular sieving properties in microporous carbons. *Carbon* **1991,** 29, (6), 793-803.

CHAPTER 9

Conclusions

9.1 Overall conclusion

Two new three-dimensional metal organic frameworks, named NEW-1 and NEW-2, were successfully synthesised from $Cu(NO_3)_2$ with isonicotinic acid and $Zn(NO_3)_2$ with fumaric acid, respectively. Physical, chemical and gas/vapour adsorption/desorption characterisation results indicate that NEW-1 is a unidirectional nano-porous material with non-coordinated oxygen surface functional groups and square pyramidal copper centres in close proximity in the pore walls. NEW-1 has high thermal stability and the framework is flexible. NEW-2 is non-porous material due to template methanol molecules strongly bonded with Zn. The NEW-2 framework decomposes when air dried.

NEW-1 changes structure on desolvation. The unidirectional pore system with surface oxygen functional groups and copper centres periodically located along the surface of pores of NEW-1 provides a well defined structure to investigate the adsorption interactions with surface functional groups and the dynamic response of the flexible framework to adsorption. Oxygen surface functional groups and copper centres in NEW-1 dominate the adsorption characteristics of small molecules such as water, methanol, ethanol, *n*-propanol and also, chloroform. Studies of isosteric enthalpies and activation energies for C_1-C_3 alcohol adsorption on NEW-1 demonstrate a linear relationship with the number of carbon atoms in alcohols and also demonstrate stoichiometric relationships between isotherm plateaus and the crystallographic formula unit.

The adsorption interaction for alkanes involves non-specific dispersions forces and the isotherms also showed some evidence for stoichiometric relationships between isotherm plateaus and the crystallographic formula unit. This is attributed to the response of the repeat unit in the MOF structure under the influence of molecules with different sizes. These relationships are not observed for longer ($>C_7$) chain alkanes.

The adsorption kinetics were analysed using a stretched exponential model for each isotherm step, which provided kinetic parameters that allowed the activation energies to be determined as a function of surface coverage. In the case of the species studied the

isosteric enthalpies of adsorption were always higher than the activation energies. This implies that the diffusion mechanism is dominated by a site-to-site hopping mechanism rather than diffusion through constrictions in pores.

The kinetics profiles obtained for nitrogen, argon and oxygen adsorption on M'MOF-1 followed a double stretched exponential model due to the presence of 2 types of pores while the CMS-40 followed a stretched exponential model corresponding to a narrow distribution of pore sizes in the carbon deposit. The adsorption kinetics of nitrogen, argon and oxygen on NEW-1 were too fast to determine accurately under ambient temperature conditions. Adsorption of nitrogen, argon and oxygen on both NEW-1 and M'MOF-1 needs to be done at very low temperature in order to determine adsorption kinetics. Comparison of the adsorption characteristics of NEW-1, M'MOF-1 and CMS-40 shows that MOFs must have extremely narrow pores to give kinetic separation characteristics similar to CMS-40, which is used commercially for air separation.

9.2 Specific conclusions

9.2.1 Synthesis and characterise the porous metal organic frameworks

Three dimensional metal organic frameworks NEW-1 ($C_{12}H_8CuN_2O_4 \cdot C_3H_7NO$) and NEW-2 ($C_6H_{10}O_6Zn$) were synthesised via solvothermal and room temperature method, respectively. It is apparent that NEW-1 is a nanoporous material while NEW-2 is a non-porous framework material. Solvothermal synthesis of NEW-1 using DMF as a template molecule produced framework topology with larger pore volume rather than the framework synthesised with water template. The results from single X-ray diffraction revealed that NEW-1 has a channel-like porous material with window dimension of 6.092 x 6.092 Å. The pore volume obtained from a PLATON calculation was 0.269 $cm^3\ g^{-1}$. NEW-1 is thermally stable up to ~290 ºC. The N_2 (77 K) and CO_2 (195 and 273 K) adsorption isotherms for NEW-1 were typical type I as defined by the IUPAC classification scheme while the Ar adsorption isotherms were intermediate between types I and type II. Both nitrogen and argon isotherms exhibited small hysteresis while CO_2 was virtually completely reversible.

The total pore volumes calculated from adsorption isotherms of both N_2 and Ar at 77 K, and CO_2 195 K were 0.099 cm^3g^{-1} and 0.090 cm^3g^{-1} and 0.116 cm^3g^{-1}, respectively. These total pore volumes are much lower than pore volume calculated from PLATON indicating pore structure of NEW-1 are partly collapses on desolvation. This is consistent with the XRD profile of the desolvated form of NEW-1. Measurements of total pore volume for CO_2 adsorption at 303 K and 55 bar gave a pore volume 0.101 $cm^3\ g^{-1}$ (2.384 mmol g^{-1}). Similarly the amounts of methane adsorbed at 195/K/1bar and 303 K/80bar are equivalent to pore volumes of 0.084 and 0.074 $cm^3\ g^{-1}$, respectively. However, there is uncertainty over the density of adsorbed methane above the critical temperature. These results indicate that there is no thermally activate phase transition of the desolvated NEW-1 structure at temperatures up to 303 K.

Total pore volumes obtained from the maximum adsorption capacity at high relative pressure gave the following values similar to the crystallographic pore volume, for example, methanol 0.263 cm^3g^{-1}, ethanol 0.262 cm^3g^{-1}; *n*-propanol 0.244 cm^3g^{-1}; *n*-butanol 0.200 cm^3g^{-1}; methyl chloride 0.227 cm^3g^{-1}, dichloromethane 0.253 cm^3g^{-1}, chloroform 0.267 cm^3g^{-1}; methane 0.084 cm^3g^{-1}, ethane 0.168 cm^3g^{-1}, propane 0.225 cm^3g^{-1}, *n*-butane 0.238 cm^3g^{-1}, *n*-pentane 0.253 cm^3g^{-1}; *n*-hexane 0.257 cm^3g^{-1}; benzene 0.254 cm^3g^{-1} and toluene 0.202 cm^3g^{-1}. It is apparent that these total pore volumes, with the exceptions of toluene and *n*-butanol, are consistent with Gurvitsch's rule and agree well with the PLATON pore volume obtained from crystallographic data. It is evident that the adsorption data for NEW-1 are consistent with NEW-1 being flexible with total pore volumes ranging from ~ 0.07-0.26 cm^3g^{-1}.

The adsorption process is driven by the enthalpy of adsorption since when the MOF is desolvated structural disorder is increased. Therefore, the enthalpy of adsorption drives both the adsorption processes and the structural change from the desolvated structure to the expanded structure. Molecules such as N_2, Ar, CO_2 and CH_4 do not expand the structure since the enthalpies of adsorption are low. Adsorptives which have high enthalpies of adsorption by virtue of either a hydrogen bonding interaction with surface of oxygen functional group or dispersion interactions as in the case of *n*-pentane etc. have sufficient enthalpy to open the structure of desolvated porous structure of NEW-1.

The hydroxyl groups in alcohols hydrogen bond probably to surface oxygen functional groups as shown by stoichiometric relationships between amounts adsorbed and oxygen present in crystallographic formula unit. It is proposed that framework collapse leads to the Cu (1)-O(3)-C(12)-O(4) planar region in solvated NEW-1 becoming non-planar leading to O(4) pointing into the pore thereby providing surface sites for hydrogen bonding. However, the adjacent five coordinate Cu is also a possible site. Strong interactions allow expansion of the porous structure to the maximum pore volume. The length of the alkyl chain in the alcohol clearly has a major influence. As the chain length increases i) it decreases the availability of oxygen surface sites by occupying more space ii) the isosteric enthalpy of adsorption increases and iii) it increases the hydrophobic character.

9.2.2 Effect of surface chemistry on adsorption characteristics of MOF NEW-1

In order to increase the understanding of role of surface chemistry on adsorption characteristics, a series of adsorption isotherms of gases/vapours of varying size, shape and hydrophobic/hydrophilic characteristics were studied over the temperature range 298-318 K. Most of these adsorption isotherms were type I in the IUPAC classification scheme but some had deviations from the standard isotherm shape. Additionally, all desorption isotherms of these vapour exhibited only a small amount of hysteresis at high relative pressure. The adsorption isotherm of *n*-propanol on NEW-1 is type VI. The *n*-propanol isotherms exhibit steps corresponding to stoichiometric relationships between the amount adsorbed and the crystallographic formula unit. The adsorption isotherms of small hydrophilic molecules e.g. methanol and ethanol also exhibited plateaus that correspond to stoichiometric ratios for amount adsorbed and the formula unit of NEW-1. This suggests that specific adsorbate-adsorbent interactions occur. It is proposed that hydrogen bonding occurs between the OH group of alcohols and carboxylate non-coordinated oxygen in the pore wall of the NEW-1.

Isosteric enthalpies for C_1-C_3 alcohol adsorption at zero surface coverage on NEW-1 over temperature rang 298-318 K increase with increasing of number of carbon atoms. The isosteric enthalpies obtained for alcohols initially decreased with increasing of surface coverage stabilising at amounts adsorbed in the range 1.0-1.5 mmol g^{-1}. A decrease in isosteric enthalpy for *n*-propanol adsorption is observed in the amount adsorbed range 1.5-

2.0 mmol g^{-1}, which corresponds to the step in the adsorption isotherm. It is clear that the order of isosteric enthalpy of adsorption is *n*-propanol > ethanol > methanol where hydrogen bonding between alcohol and surface groups predominates and the isosteric enthalpy of adsorption increases approximately linearly with increasing of carbon number. The isotherm of *n*-butanol adsorption does not have a stoichiometric relationship with the crystallographic formula unit. This is ascribed to dispersion interactions of the hydrocarbon chain dominating the adsorbate-adsorbent interaction.

The effect of surface interactions between adsorbate and adsorbent NEW-1 can be summarised as below;

1) It is proposed that adsorption characteristics of hydrophilic molecules (R-OH, R= H, CH_3, C_2H_5, C_3H_7) depends on oxygen surface functional groups in NEW-1 for smaller molecules while *n*-butanol does not have the specific stoichiometric interactions indicating that the hydrophobic interactions dominate the specific hydrophilic interactions with surfaces for *n*-butanol and other factors are influencing the adsorption process.
2) The isotherm plateaus for *n*-alkane adsorption on NEW-1 show evidence for stoichiometric relationships with the crystallographic structural formula unit. Hydrophobic *n*-alkanes do not have a specific interaction with the surface groups of NEW-1. The stoichiometric trends are attributed to the systematic repeat of the framework structure and the ability of molecules to fit into the framework repeat unit. A particularly interesting observation is the change of the isotherm plateau from a stoichiometric 1:1 adsorbate: crystallographic formula unit for ethane to 0.5: 1 for *n*-butane, *n*-pentane, *n*-hexane, and *n*-heptane. Calculations based on the known densities of the adsorbate show that the pores are not fully for the smaller alkanes in the C_4-C_7 series. In the case of propane, a high chemical potential is required to drive the adsorption to the 1:1 stoichiometry which has a pore volume corresponding to total pore filling.
3) Isosteric enthalpies at zero surface coverage and activation energies for C_1-C_3 alcohols adsorption on NEW-1 over temperature rang 298-318K demonstrate a linear relationship with the number of carbon atom in alcohols. Similar trends are observed for the C_1-C_7 *n*-alkane series. This illustrates the effect of size on thermodynamic parameters

4) The adsorption kinetics of both hydrophilic and hydrophobic molecules follows the stretch exponential (SE) model and the rates, SE rate constants and exponent β values change with surface coverage, pressure and temperature. These changes are attributed to the change in chemical potential gradient in the isotherm. The β exponent values from the SE model are close 1 i.e. LDF model, correspond to diffusion through high barriers to diffusion of molecules into or along narrow porosity. The increase in rate constant is related to the increase in chemical potential gradient in the isotherm.
5) In some cases the isosteric enthalpy of adsorption is much higher than the corresponding activation energy for diffusion into the porous structure. This indicates that the diffusion mechanism is a site-to-site hopping mechanism. When the barrier to diffusion is higher than the isosteric enthalpy of adsorption the adsorbate molecule and pore sizes are similar. Examples of former are systems where this is observed are alcohols, larger alkanes (C_5 and above) and CH_2Cl_2. The latter is observed as the pore structure expands during the adsorption of $CHCl_3$.
6) Framework flexibility is driven by the enthalpy of adsorption and occurs irrespective of the types of adsorption interaction i.e. framework structural change can occur due to both non-specific dispersion and specific H-bonded interactions. Adsorption of probe molecules provides evidence in support of stoichiometric relationships between the isotherm plateaus and the crystallographic formula unit emphasising the role of the repeat nature of the porous structure in MOFs.
7) In most cases the framework expansion occurs at high relative pressure when pore filling occurs. However, in the case of $CHCl_3$ adsorption, the isotherm, thermodynamic and kinetic studies are consistent with expansion occurring at low pressure low pressure and this is driven by a high enthalpy of adsorption at low surface coverage.
8) The *n*-propanol isotherm has two isotherm steps. The first step corresponds to a plateau with stoichiometry 0.5 C_3H_7OH per crystallographic formula unit. This is related to the fact that *n*-propanol is too long to fit into the space available if 1:1 stoichiometry occurred in the unidirectional pores. The second step occurs at higher chemical potential and is accompanied by an increase in

both enthalpy and entropy of adsorption and, also, a slowing of the adsorption kinetics with an increase in the barrier to diffusion. These observations are presumably related to structural change in the flexible framework and the need to break H-bonding interactions to accommodate more molecules leading to pore filling.

9) The dynamic response of the framework to adsorption is complex and it is likely that there are a range of structural confirmations of NEW-1, which may be taken during the adsorption process and only low energy changes allow these to be driven by the adsorption process. Results based on the adsorbate: crystallographic formula unit stoichiometry for isotherm plateaus indicates that conformations corresponding to pore volumes ~0.16-0.18 cm^3 g^{-1} are relatively stable. However, the results for the plateaus for C_4-C_7 alkanes suggest that arrange of conformations or distributions of several conformations may be present during adsorption.

9.2.3 Gas storage and separation

The adsorption isotherm of hydrogen on NEW-1 at 77 K is classified as type I isotherm in IUPAC classification scheme and no hysteresis occurred during the desorption process. The highest hydrogen uptake at ~ 1 bar and 77 K was 2.98 ± 0.0016 $mmolg^{-1}$ which is corresponded to ~ 0.6 % by weight which is quite low compare to 6 % target of the US DOE. In case of air separation, it is apparent that the nitrogen, argon and oxygen adsorption isotherms at 195 K on NEW-1 and M'MOF-1 can be classified as type I in the IUPAC classification scheme. While the amount of nitrogen, argon and oxygen adsorbed on CMS-40 over temperature range 273-298 K increased approximately linear with increasing of the pressure. Selectivity ratio (O_2/N_2) obtained for gases adsorptions on M'MOF-1 were in range 0.8-4.7 and 0.9-4.3, respectively. While, kinetic selectivity ratios (O_2/N_2) obtained for gases adsorption on CMS-40 were in range 33-35. Critical dimension minimum cross section appears to give a better prediction of adsorption kinetics than kinetic diameter. High isosteric enthalpies were observed in gases adsorption on both NEW-1 and M'MOF-1 which is indicated stronger adsorbate-adsorbent interaction compare to CMS-40.

Table 6.2 Bond lengths around pyramidal copper in NEW-1 structure compare with selected framework structures reported in the literatures

Formulae	**$C_{15}H_{14}CuN_3O_5$ (NEW-1)**	**$C_{12}H_{12}CuN_2O_6$ Lu *et. al*[10]**	**$C_6H_7CuNO_4$ Tran *et. al.*[1]**	**$C_{18}H_{12}O_{15}Cu_3$ (HKUST-1)[3]**	**$Cu(BPDC)(H_2O)$ Lu *et. al.*[4]**	**$C_{13}H_{10}Cu_2NO_9S$ (Cu-SIP-3-pyridine)[11]**	**$C_{35}H_{43}Cu_2N_3O_{16}$ NOTT103[6]**
Space group	momoclinic,$P2_1/c$	momoclinic, Cc	momoclinic, $P2_1/n$	Cubic crystal, Fm-3m	Orthorhombic, Cmca	momoclinic,$P2_1/n$	Rhombohedral,R -3 m
Metal-SBU	Square pyrimedal	Square pyrimedal	Square pyrimedal	Octahedral	Octahedral	Square pyrimedal and Octahedral	Octahedral
Void volume A^3(%)	551.4 (35.6%)	37.1 (2.7%)	130 (17.8%)				
Cu-Cu	4.596	4.958	2.965(2) 3.107(2)	2.628(2)	2.601	2.947(2)	2.664(2)
Cu-O1	2.2578(16) 1.9889(15) 1.9702(15)	2.275(2) 1.987(2) 1.965(2)	2.2671(18) 2.0036(16) 1.9931(19) 1.9705(17) 1.9358(16)	2.165(8) 1.952(3)	2.251(5) 1.958(3) 1.948(3)	1.995(5) 1.987(5) 1.963(5) 1.957(5) 1.957(4) 1.910(4)	2.148(11) 2.286(11) 1.970(5) 1.969(5)
Cu-N	2.0017(18) 1.9946(18)	2.026(3) 2.021(3)	1.991(19)			2.014(5)	

Table 6.2 Bond lengths around pyramidal copper in NEW-1 structure compare with selected framework structures reported in the literatures

Formulae	**$C_{35.50}H_{47.50}Cu_2N_{2.50}O_{17.50}$** **NOTT101**	**$C_{35}H_{43}Cu_2N_3O_{16}$** **NOTT103**	**$C_{74}H_{70}Cu_4N_2O_{28}$** **NOTT104**	**$C_{32}H_{42}Cu_2F_2N_2O_{18}$** **NOTT105**	**$C_{24.75}H_{21.75}Cu_2N_{0.25}O_{11.25}$** **NOTT106**	**$C_{25}H_{19}Cu_2F_4NO_{12}$** **NOTT108**	**$C_{44}H_{66}Cu_2N_6O_{20}$** **NOTT109**
Space group	Rhombohedral,R -3 m	Rhombohedral,R -3 m	Trigonal,R -3 m	Rhombohedral, R -3 m	Rhombohedral, R -3 m	Rhombohedral, R -3 m	Tetragonal, I 4/mmm
Metal-SBU	Octahedral	Octahedral	Octahedral	Octahedral	Octahedral	Octahedral	Octahedral
Void voulme A^3(%)							
Cu-Cu	2.1388(19)	2.664(2)	2.657(4)	2.6597(7)	2.6439(10)	2.664(2)	2.660(2)
Cu-O1	2.148(11)	2.148(11)	2.199(16)	2.125(3)	2.146(4)	2.130(3)	2.141(6)
	1.9525(12)	2.286(11)	1.984(13)	1.9538(16)	1.961(2)	1.9552(19)	1.933(5)
	1.9492(11)	1.970(5)	1.935(10)	1.9528(16)	1.942(2)	1.950(2)	1.951(4)
		1.969(5)	1.903(13)				

Table 6.8 Langmuir and BET parameters for gas adsorption on NEW-1 sample

Adsorbents	BET. Parameters					Langmuir Parameters				Total pore volume			
	n_m ($molg^{-1}$)	Surface area (m^2g^{-1})	p/p^0	C	R^2	n_m ($molg^{-1}$)	Surface area (m^2g^{-1})	Pore Volume (cm^3g^{-1})	R^2	Pressure (mbar)	p/p^0	n ($mmolg^{-1}$)	Pore Volume (cm^3g^{-1})
Ar (77K)	0.00177	147	0.03-0.30	1633	0.9986	0.00332	267	0.0931	0.9993	288	0.934	3.112	0.090±0.0009
N_2 (77K)	0.00179	174	0.01-0.04	1983	0.9999	0.00215	210	0.0728	0.9994	978	0.977	2.876	0.099±0.0005
CO_2 (195K)	0.00205	241	0.01-0.10	745	0.9999	0.00273	321	0.1160	0.9998			n/a	
CO_2 (273K)	0.00244	308	0.005-0.02	98	0.9999	n/a	n/a	0.2055*	0.9988*			n/a	
CO_2 (195K)**			n/a			n/a	n/a	0.0835	0.9990			n/a	
CO_2 (303K)			n/a					n/a		40-55 bar		2.384	0.979±0.0012
CH_4 (303K)			n/a					n/a		50-80 bar		2.146	0.074±0.0013

* Micro pore volume calculated by D-R equation.

** The NEW-1was used in water adsorption prior the CO_2 adsorption at 195 K was conducted.

List of liquid densities (ρ, g cm^{-3}) used to calculate total pore volumes;[39-41] Ar =1.380, N_2=0.808, CO_2=1.107, CH_4 = 0.4660, methanol=0.7918, ethanol=0.7893, *n*-propanol=0.803, *n*-butanol=0.809, methyl chloride=0.917, dichloromethane=1.326, chloroform= 1.489, benzene=0.865, toluene=0.8669, water=0.997, methane=0.466, ethane=0.572, propane=0.5853, *n*-butane=0.6011, *n*-pentane=0.6262, *n*-hexane=0.6603, *n*-heptane=0.684, *n*-octane=0.7025 and *n*- nonane=0.7176.

Table 6.9 Langmuir parameters for alcohols chloromethane and aromatic species adsorption on NEW-1 sample

Adsorbents	Langmuir Parameters					Total pore volume			
	n_m ($molg^{-1}$)	Surface area (m^2g^{-1})	n, at plateau ($mmolg^{-1}$)	Pore Volume* (cm^3g^{-1})	R^2	Pressure (mbar)	p/p^0	n ($mmolg^{-1}$)	Pore Volume (cm^3g^{-1})
Alcohols									
Methanol	0.00330	436	3.283 (p/p^0, 0.239)	0.115	0.9999	164	0.984	6.489	0.263±0.0012
Ethanol	0.00331	564	3.229 (p/p^0, 0.254)	0.193	0.9999	76	0.966	4.487	0.262±0.0011
n-Propanol	0.00271	536	1.673 (p/p0, 0.060)	0.203	0.9997	27	0.812	3.263	0.244±0.0010
n-Butanol	0.002197	468	2.084 (p/p0, 0.365)	0.201	0.9997	7.74	0.942	2.241	0.200±0.0010
Chloromethane									
Methyl Chloride	n/a	n/a	3.09 (p/p0, 0.197)	0.181	0.9997	45.9	0.919	4.136	0.227±0.0002
Chloroform	0.00332	550	3.140 (p/p^0, 0.314)	0.265	0.9999	239	0.942	3.335	0.267±0.0005
Dichloromethane	0.00250	598	2.451 (p/p^0, 0.345)	0.160	0.9998	565	0.974	3.946	0.253±0.0010
Aromatics									
Benzene	0.00281	555	2.586 (p/p^0, 0.197)	0.253	0.994	114	0.909	2.816	0.254±0.0013
Toluene	0.00182	505	1.454 (p/p^0, 0.362)	0.193	0.9986	34	0.936	1.899	0.202±0.0010

Table 6.10 Langmuir parameters for alkanes and water adsorption on NEW-1 sample

Adsorbents	Langmuir Parameters					Total pore volume			
	n_m (molg^{-1})	Surface area (m^{2}g^{-1})	n, at plateau (mmolg^{-1})	Pore Volume (cm^{3}g^{-1})	R^2	Pressure (mbar)	p/p^0	n (mmolg^{-1})	Pore Volume (cm^{3}g^{-1})
Alkanes									
Methane(195K)	n/a	n/a	2.301 (p, 298.2mbar)	n/a	n/a	1000	n/a	2.455	0.084±0.0008
Ethane(195K)	0.00319	436	2.992 (p/p^0, 0.083)	0.171	0.9998	1000	0.564	3.206	0.168±0.0003
Propane(195K)	0.00261	503	2.253 (p/p^0, 0.132)	0.196	0.9982	139	0.839	2.961	0.225±0.0022
n-Butane(273K)	0.00212	508	1.948 (p/p^0, 0.139)	0.201	0.9997	950	0.918	2.481	0.238±0.0019
n-Pentane	0.00181	509	1.722 (p/p^0, 0.088)	0.202	0.9994	649	0.955	2.185	0.252±0.0013
n-Hexane	0.00172	530	1.601 (p/p^0, 0.203)	0.225	0.9996	191	0.970	1.969	0.257±0.0013
n-Heptane	0.00165	572	1.626 (p/p^0, 0.334)	0.243	0.9999	56.9	0.954	1.799	0.264±0.0024
n-Octane	0.00135	496	1.287 (p/p^0, 0.101)	0.219	0.9999	18	0.943	1.529	0.250±0.0003
n-Nonane	0.00122	450	1.722 (p/p^0, 0.088)	0.218	0.9998	5.23	0.930	1.418	0.252±0.0013
Water									
1st run	n/a	n/a	4.756 (p/p^0, 0.239)	0.085*	n/a	27.99	0.851	8.431	0.151
2nd-3rd run	n/a	n/a	6.411 (p/p^0, 0.239)	0.115*	n/a	28.06	0.886	9.937	0.178±0.0007

* Pore volume calculated from the amount adsorbed at the plateau of isotherm

Table A1. Crystal data and structure refinement for NEW-1

Identification code	NEW-1	
Chemical formula (moiety)	$C_{12}H_8CuN_2O_4 \cdot C_3H_7NO$	
Chemical formula (total)	$C_{15}H_{15}CuN_3O_5$	
Formula weight	380.84	
Temperature	120(2) K	
Radiation, wavelength	synchrotron, 0.69430 Å	
Crystal system, space group	monoclinic, $P2_1/c$	
Unit cell parameters	a = 11.579(2) Å	α = 90°
	b = 12.292(3) Å	β = 117.871(2)°
	c = 12.318(3) Å	γ = 90°
Cell volume	1549.8(6) $Å^3$	
Z	4	
Calculated density	1.632 g/cm^3	
Absorption coefficient μ	1.441 mm^{-1}	
F(000)	776	
Crystal colour and size	blue, 0.02 × 0.02 × 0.00 mm^3	
Reflections for cell refinement	977 (θ range 2.5 to 27.1°)	
Data collection method	Bruker APEX2 CCD diffractometer thin-slice ω scans	
θ range for data collection	2.5 to 29.8°	
Index ranges	h −15 to 16, k −17 to 17, l −16 to 17	
Completeness to θ = 26.0°	99.6 %	
Reflections collected	15631	
Independent reflections	4515 (R_{int} = 0.0453)	
Reflections with $F^2>2\sigma$	3521	
Absorption correction	semi-empirical from equivalents	
Min. and max. transmission	0.9718 and 0.9986	
Structure solution	direct methods	
Refinement method	Full-matrix least-squares on F^2	
Weighting parameters a, b	0.0512, 0.1354	
Data / restraints / parameters	4515 / 0 / 230	
Final R indices [$F^2>2\sigma$]	R1 = 0.0399, wR2 = 0.0920	
R indices (all data)	R1 = 0.0564, wR2 = 0.0985	
Goodness-of-fit on F^2	1.031	
Extinction coefficient	0.0047(14)	
Largest and mean shift/su	0.000 and 0.000	
Largest diff. peak and hole	0.42 and −0.85 e $Å^{-3}$	

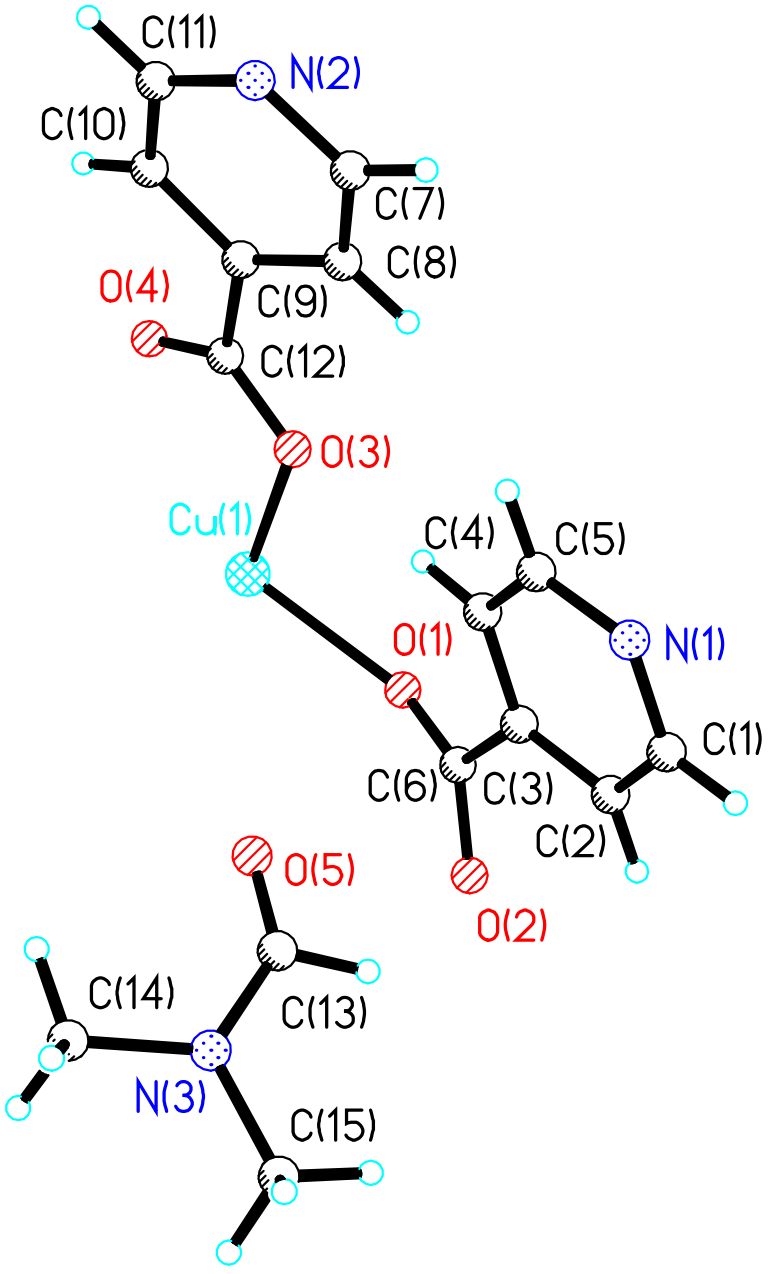

Figure A1 ORTP view of coordination environment of NEW-1 and a DMF molecule in the pore is shown

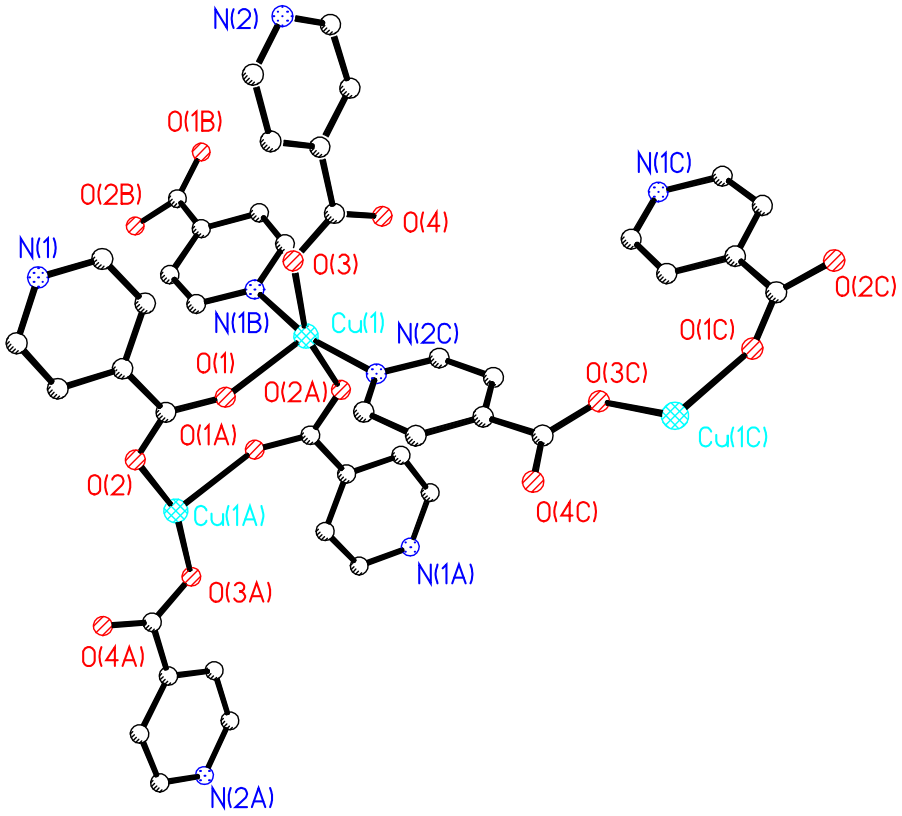

Figure A2 ORTP view of coordination environment of NEW-1. The SBU of NEW-1 is formed by two square pyramidal copper atoms bonding with eight isonicotinate ligands.

Table A2. Atomic coordinates and equivalent isotropic displacement parameters ($Å^2$) for NEW 2. U_{eq} is defined as one third of the trace of the orthogonalized U^{ij} tensor.

	x	y	z	U_{eq}
Cu(1)	–0.70961(2)	0.036754(19)	–0.03629(2)	0.01634(9)
O(1)	–0.58101(15)	0.03715(12)	–0.12870(15)	0.0226(3)
O(2)	–0.37957(14)	0.05773(12)	–0.10874(14)	0.0211(3)
O(3)	–0.84287(14)	0.12999(12)	–0.16662(14)	0.0208(3)
O(4)	–0.96842(16)	0.10130(13)	–0.07592(15)	0.0264(4)
O(5)	–0.4227(8)	0.3914(8)	–0.0265(7)	0.077(4)
O(5A)	–0.3349(5)	0.3732(4)	–0.0942(5)	0.096(2)
N(1)	–0.63827(17)	0.33283(14)	–0.42772(17)	0.0194(4)
N(2)	–1.19387(17)	0.40472(14)	–0.37193(17)	0.0187(4)
N(3)	–0.2416(3)	0.4897(2)	0.0571(3)	0.0506(7)
C(1)	–0.5257(2)	0.2823(2)	–0.3990(2)	0.0291(5)
C(2)	–0.4778(2)	0.1998(2)	–0.3127(2)	0.0284(5)
C(3)	–0.5486(2)	0.16532(16)	–0.2551(2)	0.0190(4)
C(4)	–0.6666(2)	0.2165(2)	–0.2868(3)	0.0340(6)
C(5)	–0.7065(2)	0.2999(2)	–0.3712(3)	0.0345(6)
C(6)	–0.5010(2)	0.07882(16)	–0.15659(19)	0.0187(4)
C(7)	–1.1079(2)	0.35914(17)	–0.4028(2)	0.0203(4)
C(8)	–1.0275(2)	0.27373(18)	–0.3360(2)	0.0212(4)
C(9)	–1.0373(2)	0.23200(16)	–0.2356(2)	0.0193(4)
C(10)	–1.1297(2)	0.2773(2)	–0.2076(2)	0.0268(5)
C(11)	–1.2046(2)	0.36377(19)	–0.2762(2)	0.0257(5)
C(12)	–0.9440(2)	0.14642(17)	–0.1526(2)	0.0204(4)
C(13)	–0.3319(4)	0.4200(4)	–0.0173(4)	0.0662(11)
C(14)	–0.2553(4)	0.5498(3)	0.1505(4)	0.0741(12)
C(15)	–0.1256(4)	0.5083(3)	0.0449(4)	0.0632(10)

Table A3. Bond lengths [Å] and angles [°] for NEW-1.

Cu(1)–O(1)	2.2579(16)	Cu(1)–O(2A)	1.9702(15)
Cu(1)–O(3)	1.9888(15)	Cu(1)–N(1B)	2.0019(18)
Cu(1)–N(2C)	1.9950(18)	O(1)–C(6)	1.239(3)
O(2)–Cu(1A)	1.9702(15)	O(2)–C(6)	1.272(2)
O(3)–C(12)	1.277(3)	O(4)–C(12)	1.237(3)
O(5)–C(13)	1.063(8)	O(5A)–C(13)	1.095(5)
N(1)–Cu(1D)	2.0019(18)	N(1)–C(1)	1.334(3)
N(1)–C(5)	1.337(3)	N(2)–Cu(1E)	1.9950(18)
N(2)–C(7)	1.343(3)	N(2)–C(11)	1.340(3)
N(3)–C(13)	1.330(5)	N(3)–C(14)	1.438(5)
N(3)–C(15)	1.438(5)	C(1)–H(1A)	0.950
C(1)–C(2)	1.384(3)	C(2)–H(2A)	0.950
C(2)–C(3)	1.378(3)	C(3)–C(4)	1.385(3)
C(3)–C(6)	1.511(3)	C(4)–H(4A)	0.950
C(4)–C(5)	1.377(3)	C(5)–H(5A)	0.950
C(7)–H(7A)	0.950	C(7)–C(8)	1.389(3)
C(8)–H(8A)	0.950	C(8)–C(9)	1.390(3)
C(9)–C(10)	1.385(3)	C(9)–C(12)	1.512(3)

C(10)–H(10A)	0.950	C(10)–C(11)	1.382(3)
C(11)–H(11A)	0.950	C(13)–H(13A)	0.950
C(13)–H(13B)	0.950	C(14)–H(14A)	0.980
C(14)–H(14B)	0.980	C(14)–H(14C)	0.980
C(15)–H(15A)	0.980	C(15)–H(15B)	0.980
C(15)–H(15C)	0.980		

O(1)–Cu(1)–O(2A)	105.59(6)	O(1)–Cu(1)–O(3)	92.14(6)
O(1)–Cu(1)–N(1B)	99.88(7)	O(1)–Cu(1)–N(2C)	92.45(7)
O(2A)–Cu(1)–O(3)	162.10(6)	O(2A)–Cu(1)–N(1B)	89.35(7)
O(2A)–Cu(1)–N(2C)	87.23(7)	O(3)–Cu(1)–N(1B)	90.00(7)
O(3)–Cu(1)–N(2C)	89.64(7)	N(1B)–Cu(1)–N(2C)	167.66(8)
Cu(1)–O(1)–C(6)	153.54(15)	Cu(1A)–O(2)–C(6)	122.53(14)
Cu(1)–O(3)–C(12)	113.37(14)	Cu(1D)–N(1)–C(1)	126.64(15)
Cu(1D)–N(1)–C(5)	115.50(15)	C(1)–N(1)–C(5)	117.61(19)
Cu(1E)–N(2)–C(7)	118.16(14)	Cu(1E)–N(2)–C(11)	123.11(15)
C(7)–N(2)–C(11)	118.59(18)	C(13)–N(3)–C(14)	122.5(4)
C(13)–N(3)–C(15)	120.2(4)	C(14)–N(3)–C(15)	117.4(3)
N(1)–C(1)–H(1A)	118.8	N(1)–C(1)–C(2)	122.4(2)
H(1A)–C(1)–C(2)	118.8	C(1)–C(2)–H(2A)	120.0
C(1)–C(2)–C(3)	120.0(2)	H(2A)–C(2)–C(3)	120.0
C(2)–C(3)–C(4)	117.5(2)	C(2)–C(3)–C(6)	123.25(19)
C(4)–C(3)–C(6)	119.2(2)	C(3)–C(4)–H(4A)	120.4
C(3)–C(4)–C(5)	119.3(2)	H(4A)–C(4)–C(5)	120.4
N(1)–C(5)–C(4)	123.2(2)	N(1)–C(5)–H(5A)	118.4
C(4)–C(5)–H(5A)	118.4	O(1)–C(6)–O(2)	126.5(2)
O(1)–C(6)–C(3)	118.31(18)	O(2)–C(6)–C(3)	115.15(18)
N(2)–C(7)–H(7A)	119.1	N(2)–C(7)–C(8)	121.8(2)
H(7A)–C(7)–C(8)	119.1	C(7)–C(8)–H(8A)	120.2
C(7)–C(8)–C(9)	119.7(2)	H(8A)–C(8)–C(9)	120.2
C(8)–C(9)–C(10)	117.79(19)	C(8)–C(9)–C(12)	121.93(19)
C(10)–C(9)–C(12)	120.1(2)	C(9)–C(10)–H(10A)	120.2
C(9)–C(10)–C(11)	119.6(2)	H(10A)–C(10)–C(11)	120.2
N(2)–C(11)–C(10)	122.4(2)	N(2)–C(11)–H(11A)	118.8
C(10)–C(11)–H(11A)	118.8	O(3)–C(12)–O(4)	125.7(2)
O(3)–C(12)–C(9)	115.39(19)	O(4)–C(12)–C(9)	118.88(19)
O(5)–C(13)–O(5A)	96.0(6)	O(5)–C(13)–N(3)	134.9(7)
O(5)–C(13)–H(13A)	112.6	O(5)–C(13)–H(13B)	19.5
O(5A)–C(13)–N(3)	129.1(5)	O(5A)–C(13)–H(13A)	16.6
O(5A)–C(13)–H(13B)	115.4	N(3)–C(13)–H(13A)	112.6
N(3)–C(13)–H(13B)	115.4	H(13A)–C(13)–H(13B)	132.0
N(3)–C(14)–H(14A)	109.5	N(3)–C(14)–H(14B)	109.5
N(3)–C(14)–H(14C)	109.5	H(14A)–C(14)–H(14B)	109.5
H(14A)–C(14)–H(14C)	109.5	H(14B)–C(14)–H(14C)	109.5
N(3)–C(15)–H(15A)	109.5	N(3)–C(15)–H(15B)	109.5
N(3)–C(15)–H(15C)	109.5	H(15A)–C(15)–H(15B)	109.5
H(15A)–C(15)–H(15C)	109.5	H(15B)–C(15)–H(15C)	109.5

Symmetry operations for equivalent atoms

A −x−1,−y,−z B x,−y+1/2,z+1/2 C −x−2,y−1/2,−z−1/2

D x,−y+1/2,z−1/2 E −x−2,y+1/2,−z−1/2

Table A4. Anisotropic displacement parameters (Å^2) for NEW-1. The anisotropic displacement factor exponent takes the form: $-2\pi^2[h^2a^{*2}U^{11} + ...+ 2hka^*b^*U^{12}]$

	U^{11}	U^{22}	U^{33}	U^{23}	U^{13}	U^{12}
Cu(1)	0.01508(13)	0.01090(13)	0.01880(14)	–0.00029(9)	0.00438(10)	–0.00005(9)
O(1)	0.0212(7)	0.0203(7)	0.0262(8)	0.0061(6)	0.0109(6)	0.0021(6)
O(2)	0.0154(7)	0.0184(7)	0.0231(8)	0.0041(6)	0.0037(6)	0.0012(5)
O(3)	0.0183(7)	0.0168(7)	0.0246(8)	0.0040(6)	0.0077(6)	0.0027(6)
O(4)	0.0276(8)	0.0236(8)	0.0309(9)	0.0102(7)	0.0162(7)	0.0078(7)
O(5)	0.064(6)	0.113(8)	0.065(6)	–0.030(5)	0.039(5)	–0.048(5)
O(5A)	0.120(4)	0.114(4)	0.081(3)	–0.057(3)	0.071(3)	–0.073(3)
N(1)	0.0189(8)	0.0151(8)	0.0205(9)	0.0012(7)	0.0061(7)	–0.0004(7)
N(2)	0.0185(8)	0.0128(8)	0.0220(9)	0.0008(7)	0.0070(7)	–0.0006(6)
N(3)	0.0391(13)	0.0378(14)	0.0602(18)	–0.0005(12)	0.0109(13)	–0.0075(11)
C(1)	0.0267(11)	0.0274(12)	0.0372(14)	0.0135(10)	0.0183(11)	0.0074(9)
C(2)	0.0239(11)	0.0272(12)	0.0356(14)	0.0118(10)	0.0151(10)	0.0086(9)
C(3)	0.0173(9)	0.0142(9)	0.0212(10)	0.0011(8)	0.0054(8)	–0.0005(7)
C(4)	0.0259(12)	0.0367(14)	0.0425(15)	0.0206(12)	0.0186(11)	0.0112(10)
C(5)	0.0272(12)	0.0371(14)	0.0440(15)	0.0215(12)	0.0207(12)	0.0158(10)
C(6)	0.0192(9)	0.0133(9)	0.0185(10)	–0.0018(7)	0.0046(8)	0.0008(7)
C(7)	0.0217(10)	0.0158(10)	0.0221(11)	0.0026(8)	0.0090(9)	0.0026(8)
C(8)	0.0207(10)	0.0188(10)	0.0230(11)	0.0000(8)	0.0093(9)	0.0017(8)
C(9)	0.0170(9)	0.0137(9)	0.0239(11)	0.0020(8)	0.0068(8)	0.0000(7)
C(10)	0.0244(11)	0.0271(12)	0.0301(12)	0.0100(10)	0.0138(10)	0.0072(9)
C(11)	0.0222(10)	0.0263(12)	0.0303(12)	0.0087(9)	0.0138(10)	0.0081(9)
C(12)	0.0186(9)	0.0144(10)	0.0244(11)	0.0004(8)	0.0070(8)	0.0013(7)
C(13)	0.064(2)	0.073(3)	0.057(2)	–0.009(2)	0.024(2)	–0.031(2)
C(14)	0.053(2)	0.061(2)	0.096(3)	–0.026(2)	0.025(2)	–0.0039(18)
C(15)	0.0469(19)	0.055(2)	0.074(3)	0.0105(19)	0.0160(18)	–0.0108(16)

Table A5. Hydrogen coordinates and isotropic displacement parameters (Å^2) NEW-1.

	x	y	z	U
H(1A)	–0.4766	0.3037	–0.4394	0.035
H(2A)	–0.3961	0.1670	–0.2931	0.034
H(4A)	–0.7195	0.1944	–0.2506	0.041
H(5A)	–0.7864	0.3358	–0.3903	0.041
H(7A)	–1.1019	0.3861	–0.4723	0.024
H(8A)	–0.9662	0.2440	–0.3587	0.025
H(10A)	–1.1415	0.2490	–0.1417	0.032
H(11A)	–1.2660	0.3954	–0.2546	0.031
H(13A)	–0.3102	0.3885	–0.0758	0.079
H(13B)	–0.4039	0.4095	–0.0014	0.079
H(14A)	–0.3403	0.5336	0.1460	0.111
H(14B)	–0.2494	0.6279	0.1378	0.111
H(14C)	–0.1855	0.5290	0.2315	0.111
H(15A)	–0.1236	0.4576	–0.0156	0.095
H(15B)	–0.0484	0.4968	0.1244	0.095

H(15C)	−0.1258	0.5832	0.0175	0.095

Table A6. Torsion angles [°] for NEW-1.

O(2A)–Cu(1)–O(1)–C(6)	−105.1(3)	O(3)–Cu(1)–O(1)–C(6)	77.4(3)
N(1B)–Cu(1)–O(1)–C(6)	−13.0(3)	N(2C)–Cu(1)–O(1)–C(6)	167.1(3)
O(1)–Cu(1)–O(3)–C(12)	176.28(14)	O(2A)–Cu(1)–O(3)–C(12)	4.0(3)
N(1B)–Cu(1)–O(3)–C(12)	−83.83(15)	N(2C)–Cu(1)–O(3)–C(12)	83.84(15)
Cu(1D)–N(1)–C(1)–C(2)	172.86(19)	C(5)–N(1)–C(1)–C(2)	−1.1(4)
N(1)–C(1)–C(2)–C(3)	1.6(4)	C(1)–C(2)–C(3)–C(4)	−0.4(4)
C(1)–C(2)–C(3)–C(6)	−177.7(2)	C(2)–C(3)–C(4)–C(5)	−1.3(4)
C(6)–C(3)–C(4)–C(5)	176.1(2)	Cu(1D)–N(1)–C(5)–C(4)	−175.3(2)
C(1)–N(1)–C(5)–C(4)	−0.6(4)	C(3)–C(4)–C(5)–N(1)	1.9(4)
Cu(1)–O(1)–C(6)–O(2)	102.9(3)	Cu(1)–O(1)–C(6)–C(3)	−75.7(4)
Cu(1A)–O(2)–C(6)–O(1)	−7.3(3)	Cu(1A)–O(2)–C(6)–C(3)	171.39(13)
C(2)–C(3)–C(6)–O(1)	−165.1(2)	C(2)–C(3)–C(6)–O(2)	16.1(3)
C(4)–C(3)–C(6)–O(1)	17.6(3)	C(4)–C(3)–C(6)–O(2)	−161.1(2)
Cu(1E)–N(2)–C(7)–C(8)	173.61(16)	C(11)–N(2)–C(7)–C(8)	−2.2(3)
N(2)–C(7)–C(8)–C(9)	1.4(3)	C(7)–C(8)–C(9)–C(10)	1.0(3)
C(7)–C(8)–C(9)–C(12)	−174.20(19)	C(8)–C(9)–C(10)–C(11)	−2.4(3)
C(12)–C(9)–C(10)–C(11)	172.8(2)	Cu(1E)–N(2)–C(11)–C(10)	−174.93(18)
C(7)–N(2)–C(11)–C(10)	0.6(3)	C(9)–C(10)–C(11)–N(2)	1.7(4)
Cu(1)–O(3)–C(12)–O(4)	−7.9(3)	Cu(1)–O(3)–C(12)–C(9)	169.75(14)
C(8)–C(9)–C(12)–O(3)	12.4(3)	C(8)–C(9)–C(12)–O(4)	−169.8(2)
C(10)–C(9)–C(12)–O(3)	−162.7(2)	C(10)–C(9)–C(12)–O(4)	15.2(3)
C(14)–N(3)–C(13)–O(5)	−1.9(11)	C(14)–N(3)–C(13)–O(5A)	176.5(6)
C(15)–N(3)–C(13)–O(5)	178.8(9)	C(15)–N(3)–C(13)–O(5A)	−2.7(8)

Symmetry operations for equivalent atoms
A −x−1,−y,−z B x,−y+1/2,z+1/2 C −x−2,y−1/2,−z−1/2
D x,−y+1/2,z−1/2 E −x−2,y+1/2,−z−1/2

Table B1. Crystal data and structure refinement for NEW-2.

Identification code	NEW-2	
Chemical formula (moiety)	$C_6H_{10}O_6Zn$	
Chemical formula (total)	$C_6H_{10}O_6Zn$	
Formula weight	243.51	
Temperature	150(2) K	
Radiation, wavelength	MoKα, 0.71073 Å	
Crystal system, space group	monoclinic, C2/c	
Unit cell parameters	a = 15.747(7) Å	α = 90°
	b = 7.047(6) Å	β = 116.31(8)°
	c = 8.266(3) Å	γ = 90°
Cell volume	822.3(8) $Å^3$	
Z	4	
Calculated density	1.967 g/cm^3	
Absorption coefficient μ	2.982 mm^{-1}	
F(000)	496	
Crystal colour and size	colourless, 0.20 × 0.20 × 0.10 mm^3	
Reflections for cell refinement	54 (θ range 2.5 to 27.5°)	
Data collection method	Nonius KappaCCD diffractometer	
	ϕ and ω scans	
θ range for data collection	4.6 to 27.5°	
Index ranges	h −20 to 20, k −9 to 8, l −10 to 10	
Completeness to θ = 26.0°	99.6 %	
Reflections collected	7363	
Independent reflections	944 (R_{int} = 0.0247)	
Reflections with $F^2>2\sigma$	845	
Absorption correction	semi-empirical from equivalents	
Min. and max. transmission	0.5869 and 0.7547	
Structure solution	direct methods	
Refinement method	Full-matrix least-squares on F^2	
Weighting parameters a, b	0.0212, 1.5563	
Data / restraints / parameters	944 / 0 / 81	
Final R indices [$F^2>2\sigma$]	R1 = 0.0171, wR2 = 0.0428	
R indices (all data)	R1 = 0.0219, wR2 = 0.0451	
Goodness-of-fit on F^2	1.036	
Largest and mean shift/su	0.000 and 0.000	
Largest diff. peak and hole	0.44 and −0.20 e $Å^{-3}$	

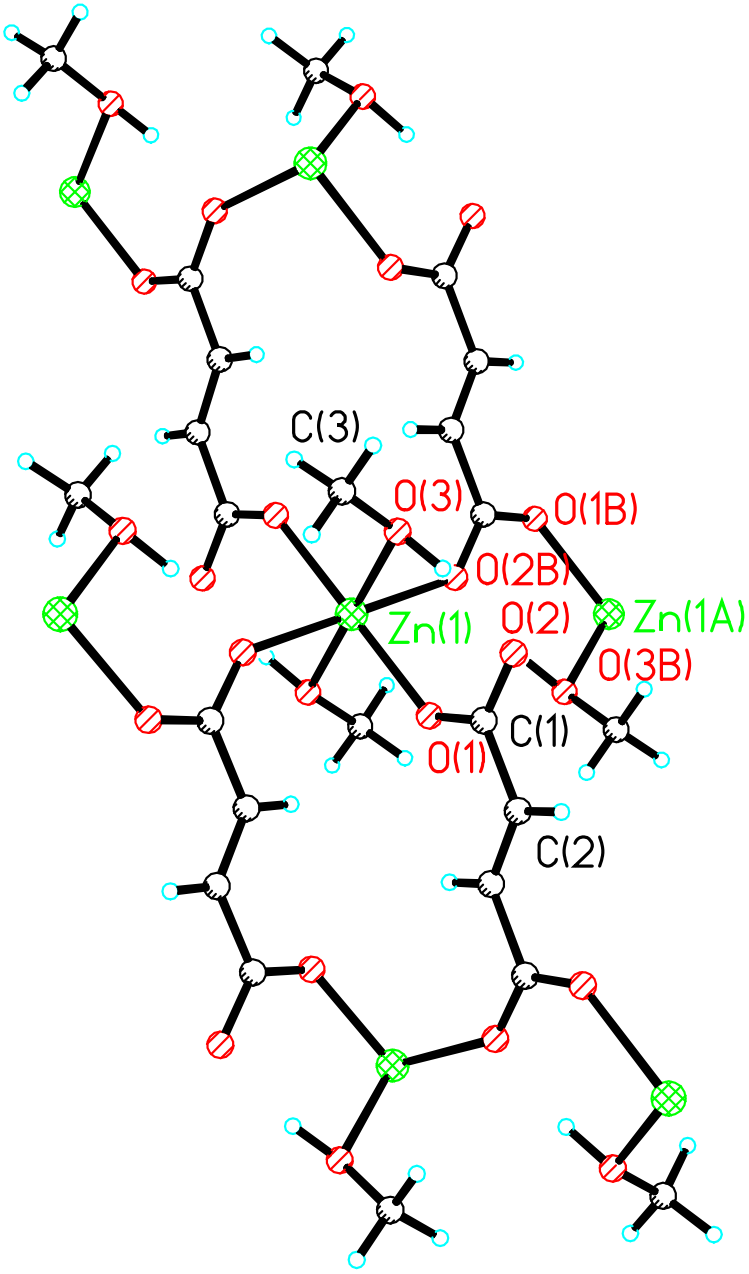

Figure B1 ORTP view of coordination environment of NEW-2.

Table B2. Atomic coordinates and equivalent isotropic displacement parameters ($Å^2$) for NEW-2 U_{eq} is defined as one third of the trace of the orthogonalized U^{ij} tensor.

	x	y	z	U_{eq}
Zn(1)	0.7500	0.7500	0.5000	0.00984(9)
O(1)	0.86084(8)	0.65443(16)	0.74257(15)	0.0128(2)
O(2)	0.79123(8)	0.43625(17)	0.84017(15)	0.0139(2)
O(3)	0.66104(8)	0.54348(17)	0.51678(17)	0.0146(2)
C(1)	0.86423(10)	0.5219(2)	0.8476(2)	0.0105(3)
C(2)	0.95966(11)	0.4599(2)	0.9899(2)	0.0122(3)
C(3)	0.61961(18)	0.3981(3)	0.3852(3)	0.0332(5)

Table B3. Bond lengths [Å] and angles [°] for NEW-2.

Zn(1)–O(1)	2.102(2)	Zn(1)–O(1A)	2.102(2)
Zn(1)–O(2B)	2.1563(14)	Zn(1)–O(2C)	2.1564(14)
Zn(1)–O(3)	2.0669(15)	Zn(1)–O(3A)	2.0669(15)
O(1)–C(1)	1.260(2)	O(2)–Zn(1D)	2.1563(14)
O(2)–C(1)	1.2754(19)	O(3)–C(3)	1.424(3)
O(3)–H(3A)	0.73(3)	C(1)–C(2)	1.505(3)
C(2)–C(2E)	1.332(3)	C(2)–H(2)	0.88(2)
C(3)–H(3)	0.95(4)	C(3)–H(3B)	0.95(3)
C(3)–H(3C)	0.99(3)		

O(1)–Zn(1)–O(1A)	180.000(1)	O(1A)–Zn(1)–O(2B)	92.36(6)
O(1)–Zn(1)–O(2B)	87.64(6)	O(1A)–Zn(1)–O(2C)	87.64(6)
O(1)–Zn(1)–O(2C)	92.36(6)	O(1)–Zn(1)–O(3)	90.65(7)
O(1A)–Zn(1)–O(3A)	90.65(7)	O(1A)–Zn(1)–O(3)	89.35(7)
O(1)–Zn(1)–O(3A)	89.35(7)	O(2B)–Zn(1)–O(2C)	180.0
O(2B)–Zn(1)–O(3A)	90.55(7)	O(2B)–Zn(1)–O(3)	89.45(7)
O(2C)–Zn(1)–O(3A)	89.45(7)	O(2C)–Zn(1)–O(3)	90.55(7)
O(3)–Zn(1)–O(3A)	180.00(5)	Zn(1)–O(1)–C(1)	131.17(10)
Zn(1D)–O(2)–C(1)	140.19(11)	Zn(1)–O(3)–C(3)	123.35(12)
Zn(1)–O(3)–H(3A)	102.4(19)	C(3)–O(3)–H(3A)	111.1(19)
O(1)–C(1)–O(2)	123.75(15)	O(1)–C(1)–C(2)	118.43(14)
O(2)–C(1)–C(2)	117.82(14)	C(1)–C(2)–C(2E)	122.8(2)
C(1)–C(2)–H(2)	115.3(14)	C(2E)–C(2)–H(2)	121.9(14)
O(3)–C(3)–H(3)	112(2)	O(3)–C(3)–H(3B)	108.1(15)
O(3)–C(3)–H(3C)	106.6(16)	H(3)–C(3)–H(3B)	115(3)
H(3)–C(3)–H(3C)	107(3)	H(3B)–C(3)–H(3C)	108(2)

Symmetry operations for equivalent atoms
A –x+3/2,–y+3/2,–z+1 B –x+3/2,y+1/2,–z+3/2
C x,–y+1,z–1/2 D –x+3/2,y–1/2,–z+3/2 E –x+2,–y+1,–z+2

Table B4. Anisotropic displacement parameters ($Å^2$) for NEW-2. The anisotropic displacement factor exponent takes the form: $-2\pi^2[h^2a^{*2}U^{11} + ...+ 2hka^*b^*U^{12}]$

	U^{11}	U^{22}	U^{33}	U^{23}	U^{13}	U^{12}
Zn(1)	0.00897(13)	0.01070(14)	0.00833(13)	0.00089(10)	0.00247(10)	0.00010(10)
O(1)	0.0096(5)	0.0154(6)	0.0109(5)	0.0043(5)	0.0024(4)	0.0010(4)
O(2)	0.0099(5)	0.0169(6)	0.0127(5)	0.0031(5)	0.0031(4)	−0.0022(4)
O(3)	0.0149(6)	0.0158(6)	0.0109(6)	0.0028(5)	0.0037(5)	−0.0017(5)
C(1)	0.0106(7)	0.0115(7)	0.0092(7)	−0.0014(6)	0.0042(6)	0.0008(6)
C(2)	0.0120(7)	0.0129(8)	0.0105(7)	0.0026(6)	0.0038(6)	0.0019(6)
C(3)	0.0412(12)	0.0345(12)	0.0206(10)	−0.0056(9)	0.0106(9)	−0.0236(10)

Table B5. Hydrogen coordinates and isotropic displacement parameters ($Å^2$) for NEW-2.

	x	y	z	U
H(3)	0.666(3)	0.313(5)	0.385(5)	0.079(11)
H(2)	0.9587(15)	0.365(3)	1.059(3)	0.022(5)
H(3A)	0.6893(17)	0.503(3)	0.606(3)	0.026(6)
H(3B)	0.5696(18)	0.342(4)	0.403(3)	0.036(6)
H(3C)	0.5909(18)	0.462(4)	0.266(4)	0.045(7)

Table B6. Torsion angles [°] for NEW-2.

O(1A)–Zn(1)–O(1)–C(1)	−141(100)	O(2B)–Zn(1)–O(1)–C(1)	89.12(15)
O(2C)–Zn(1)–O(1)–C(1)	−90.88(15)	O(3)–Zn(1)–O(1)–C(1)	−0.30(14)
O(3A)–Zn(1)–O(1)–C(1)	179.70(14)	O(1)–Zn(1)–O(3)–C(3)	−118.41(17)
O(1A)–Zn(1)–O(3)–C(3)	61.59(17)	O(2B)–Zn(1)–O(3)–C(3)	153.96(16)
O(2C)–Zn(1)–O(3)–C(3)	−26.04(16)	O(3A)–Zn(1)–O(3)–C(3)	0(100)
Zn(1)–O(1)–C(1)–O(2)	−13.0(2)	Zn(1)–O(1)–C(1)–C(2)	166.72(10)
Zn(1D)–O(2)–C(1)–O(1)	−165.00(11)	Zn(1D)–O(2)–C(1)–C(2)	15.2(2)
O(1)–C(1)–C(2)–C(2E)	0.6(3)	O(2)–C(1)–C(2)–C(2E)	−179.6(2)

Symmetry operations for equivalent atoms
A −x+3/2,−y+3/2,−z+1 B −x+3/2,y+1/2,−z+3/2
C x,−y+1,z−1/2 D −x+3/2,y−1/2,−z+3/2 E −x+2,−y+1,−z+2

Table B7. Hydrogen bonds for NEW-2 [Å and °].

D–H...A	d(D–H)	d(H...A)	d(D...A)	<(DHA)
O(3)–H(3A)...O(2)	0.73(3)	1.95(3)	2.658(3)	165(3)

Symmetry operations for equivalent atoms

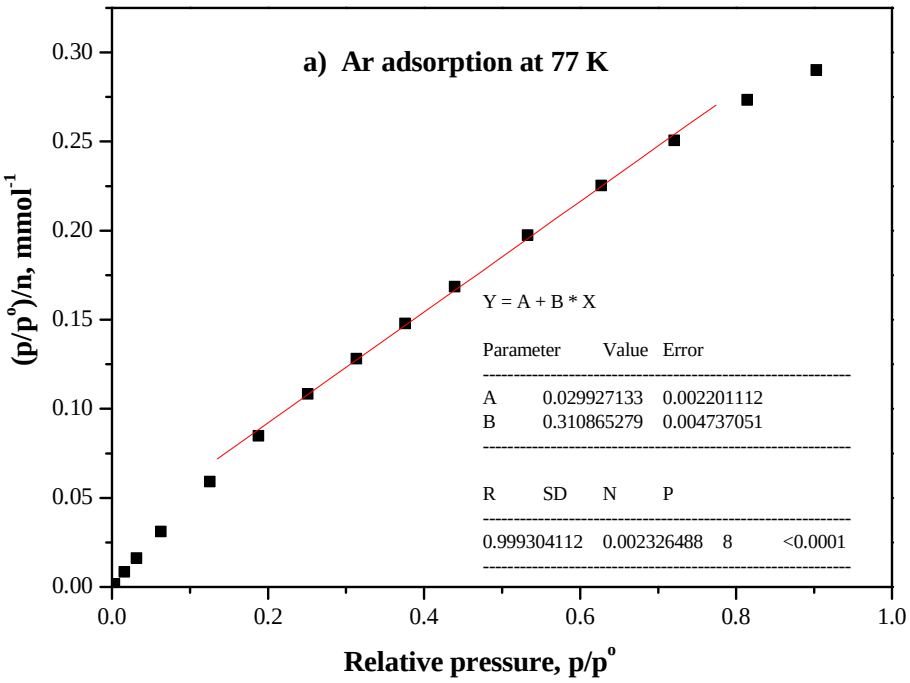

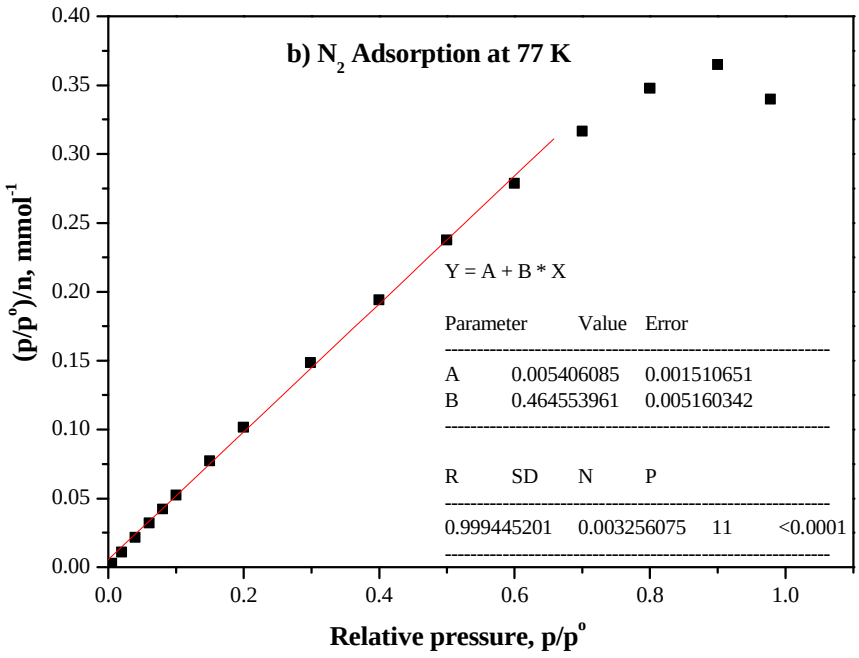

Figure C1 Langmuir plots of a) Ar and b) N_2 adsorption on NEW-1 at 77 K

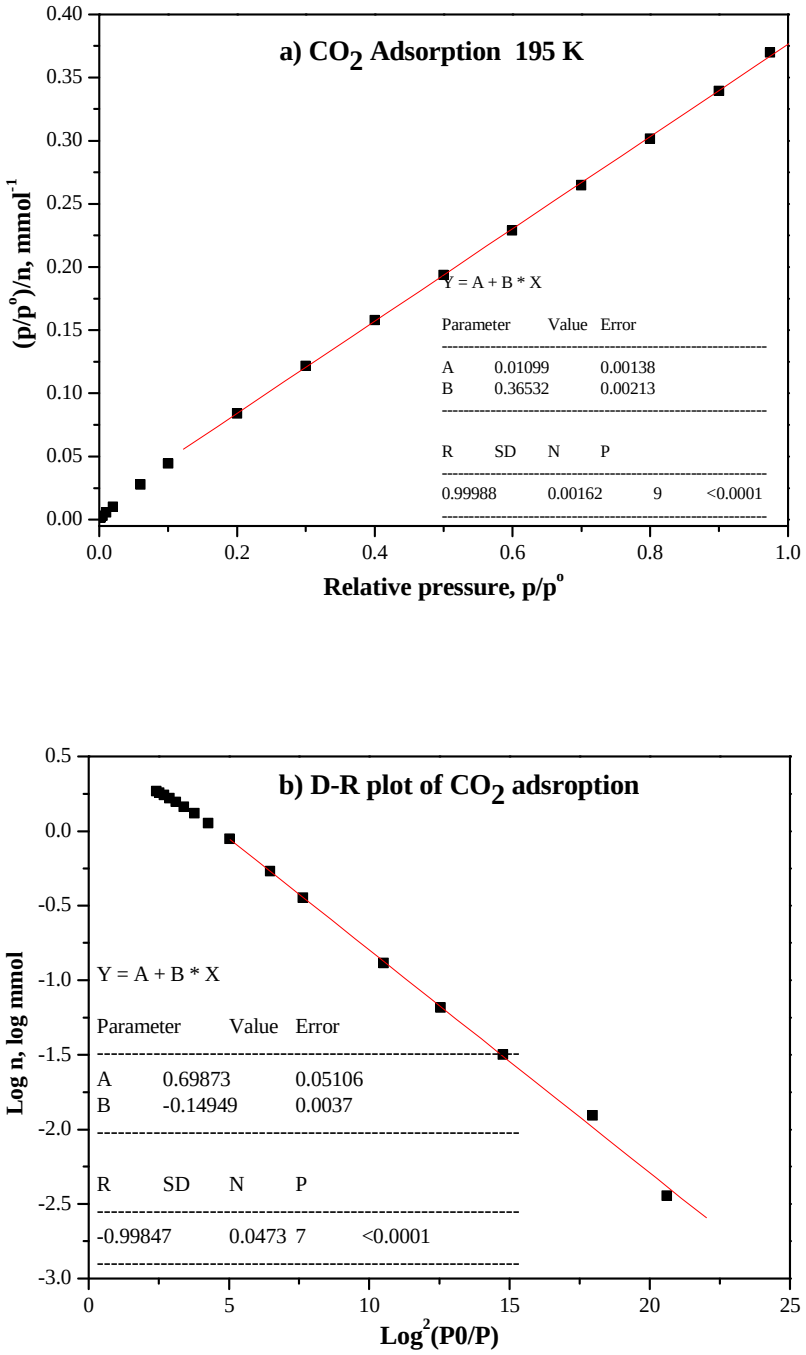

Figure C2 Langmuir plots and D-R plot of CO_2 adsorption on NEW-1 at 195 K and b) 298 K, respectively.

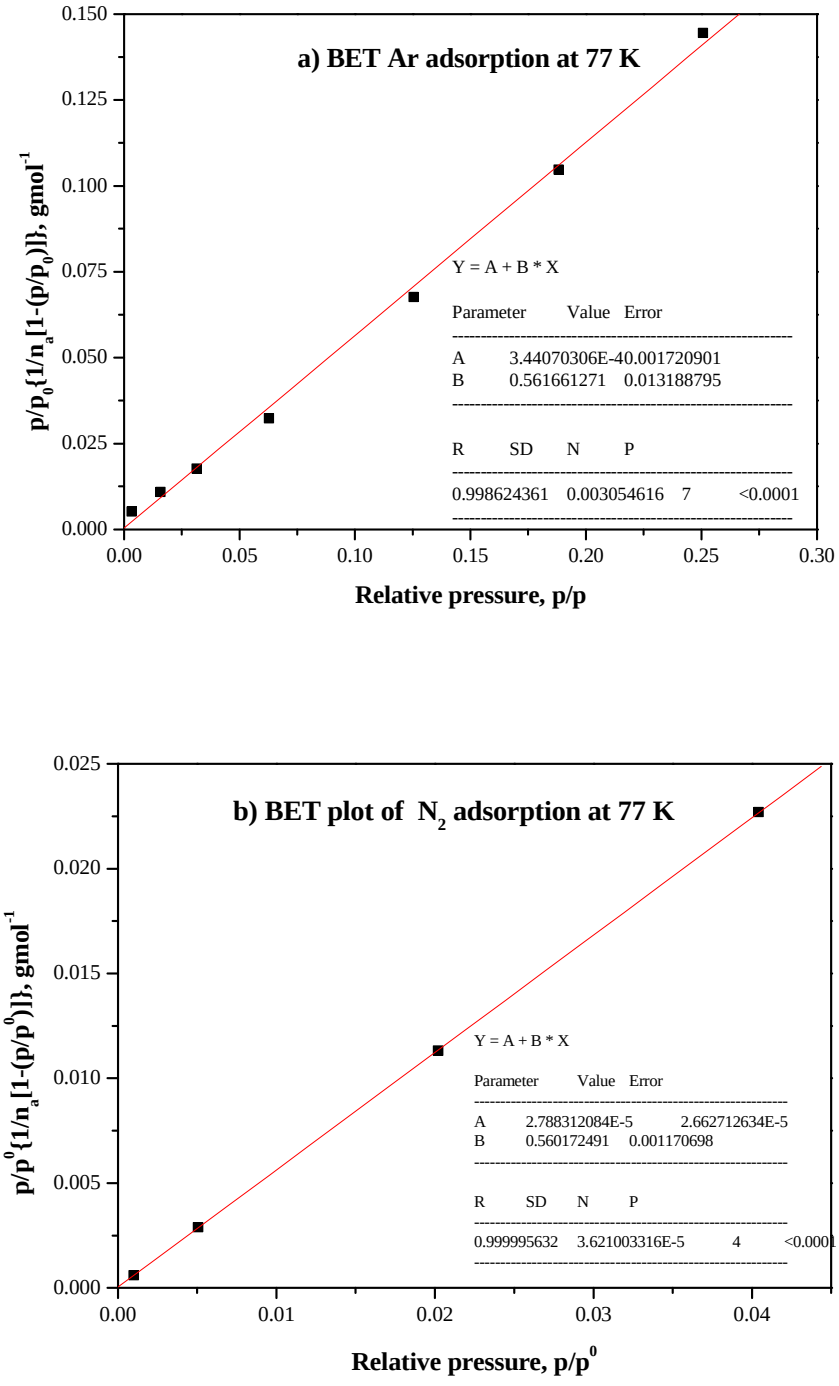

Figure C3 B.E.T plots of a) argon and b) N_2 adsorption on NEW-1

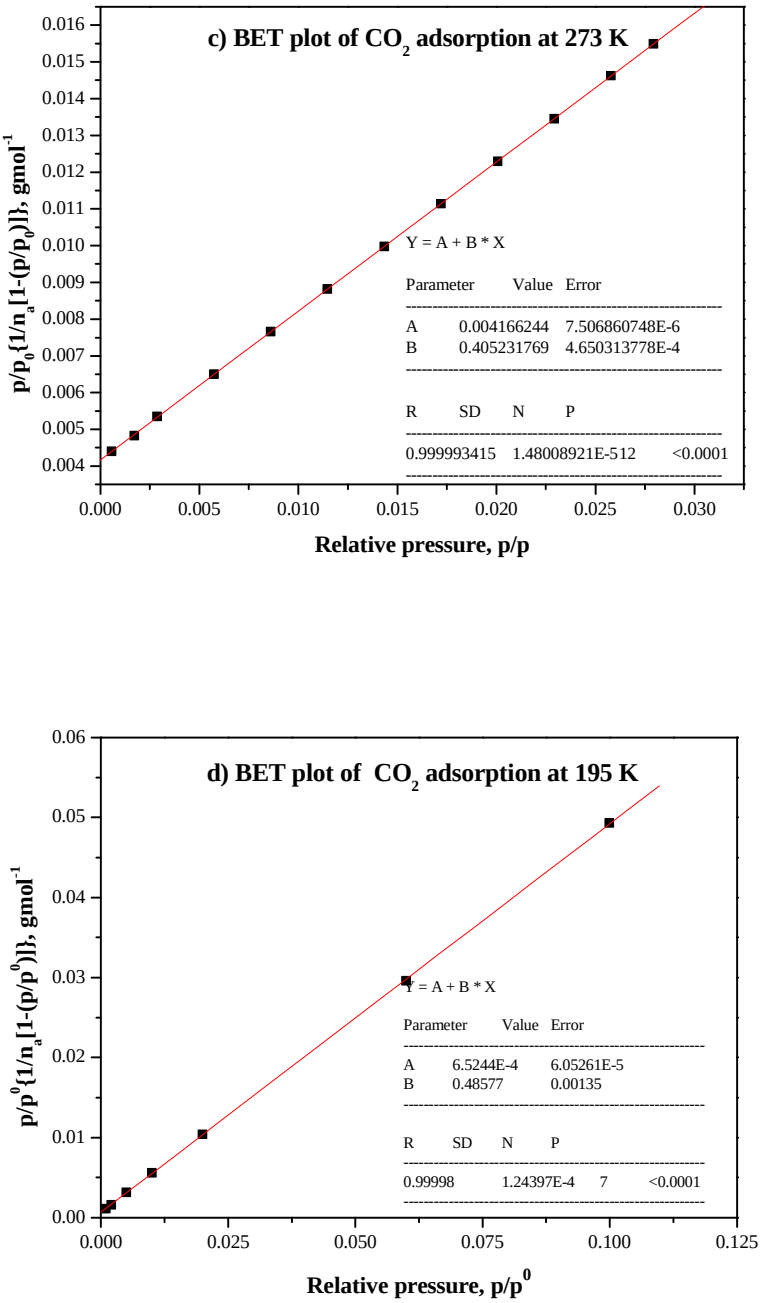

Figure C4 B.E.T plots of CO_2 adsorption on NEW-1 at c) 273 K and d) 195 K, respectively.

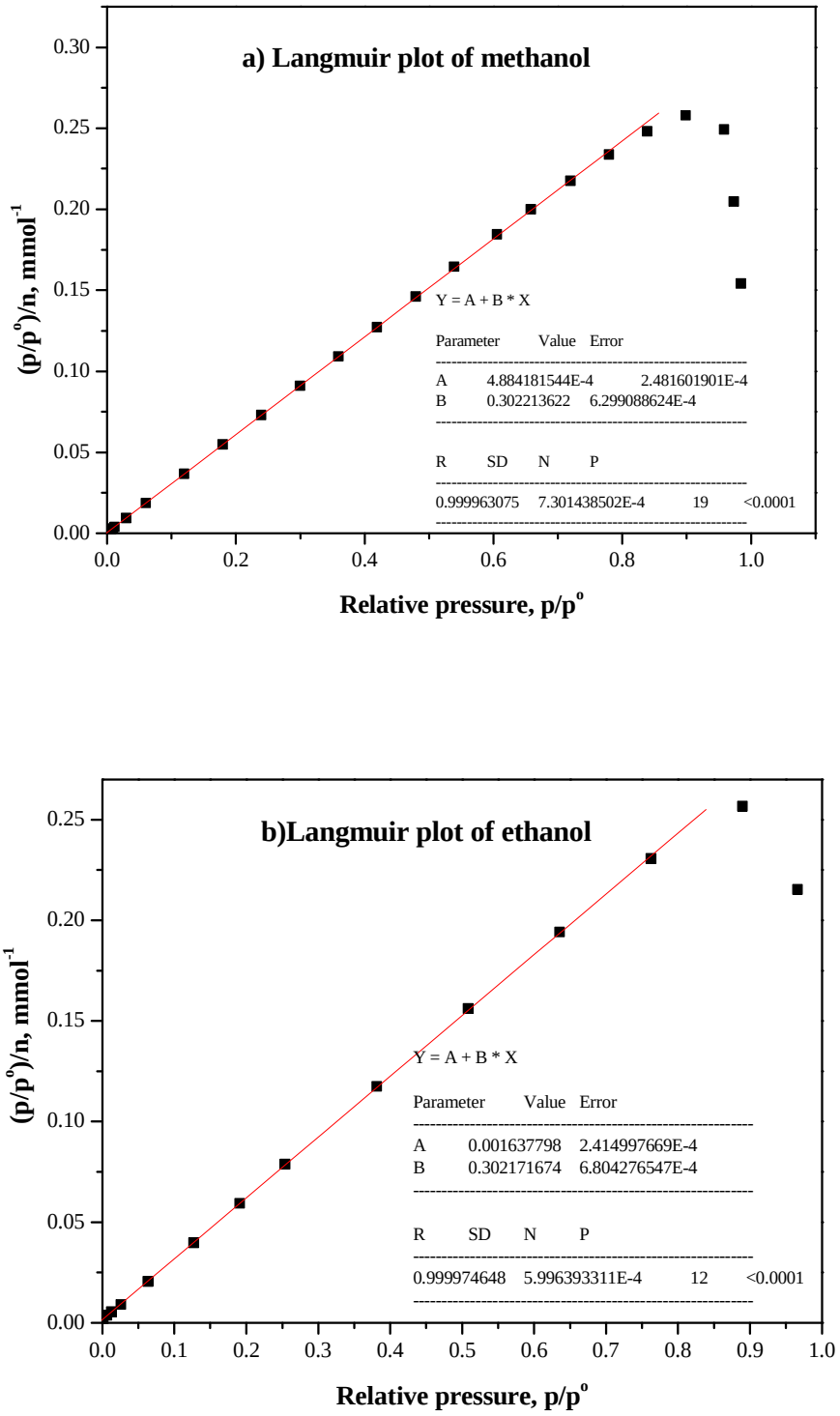

Figure C5 Langmuir plots of a) methanol and b) ethanol adsorption on NEW-1 sample at 298 K.

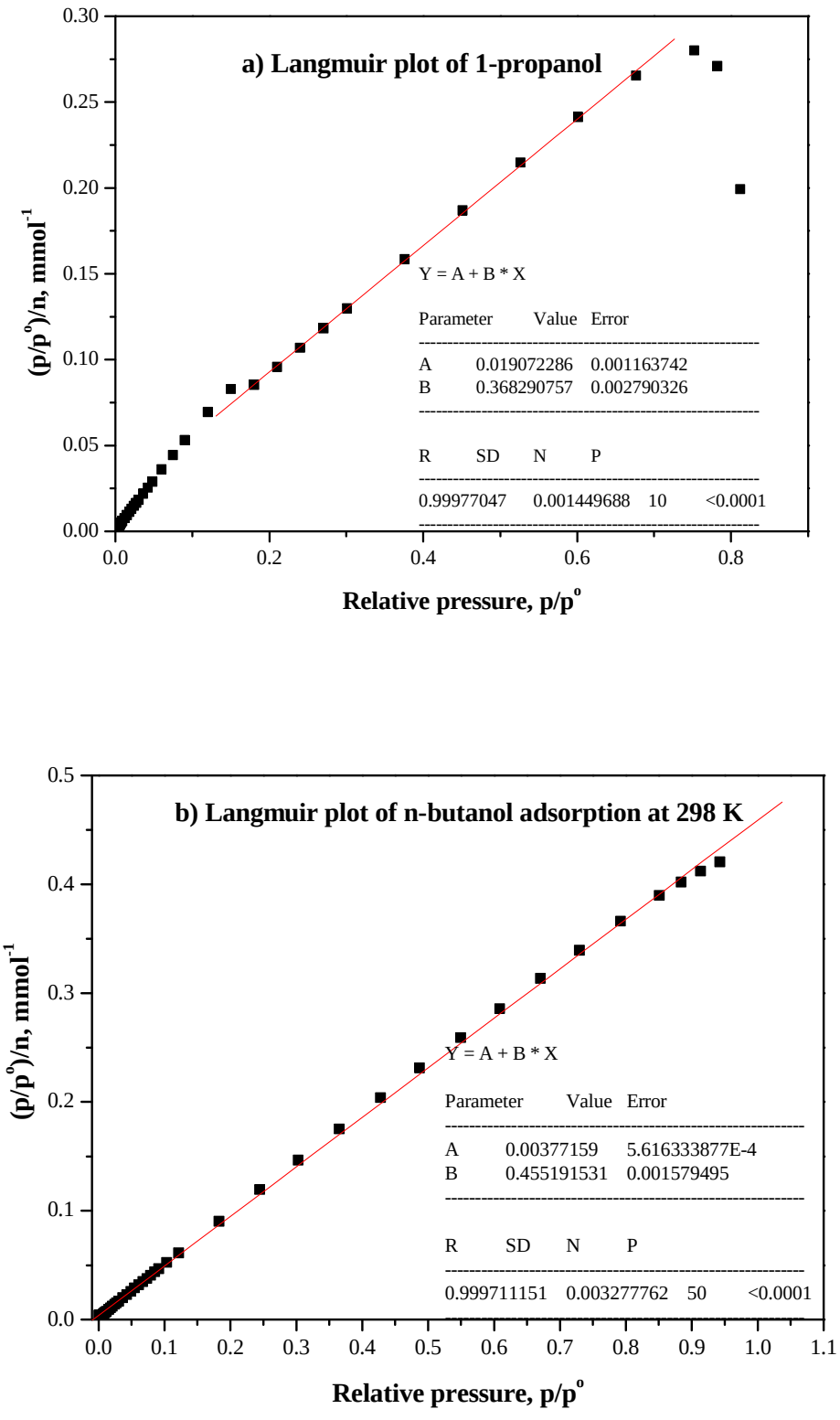

Figure C6 Langmuir plots of a) *n*-propanol and b) *n*-butanol adsorption on NEW-1 sample at 298 K.

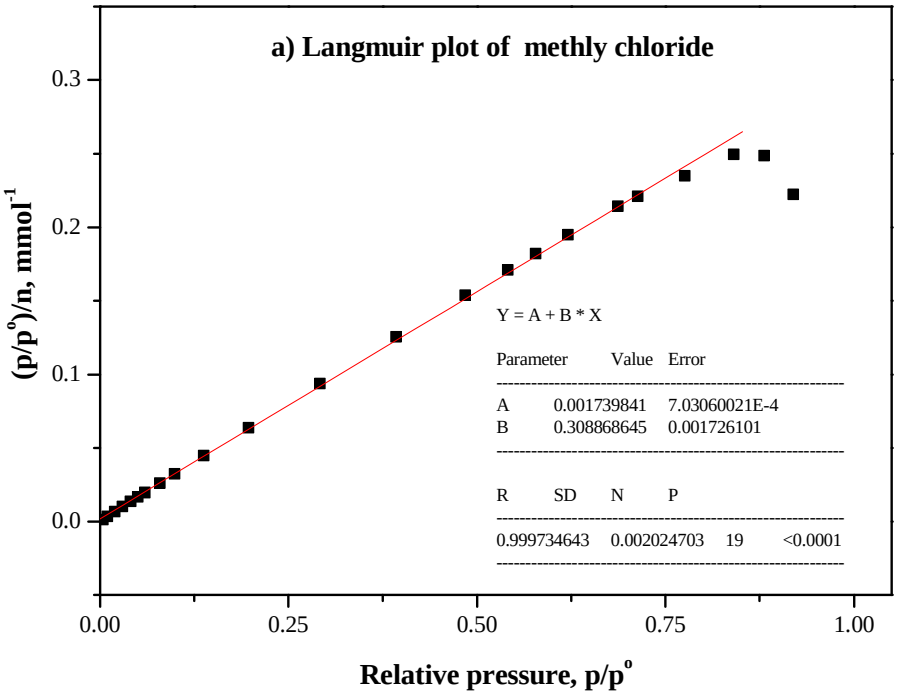

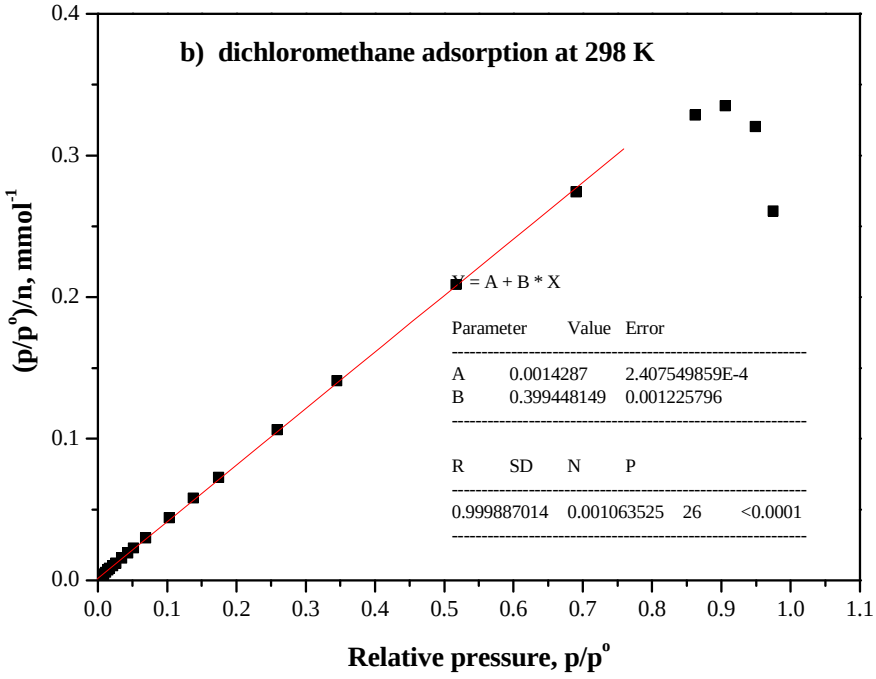

Figure C7 Langmuir plots of a) chloromethane and b) dichloromethane adsorption on NEW-1 sample at 298 K.

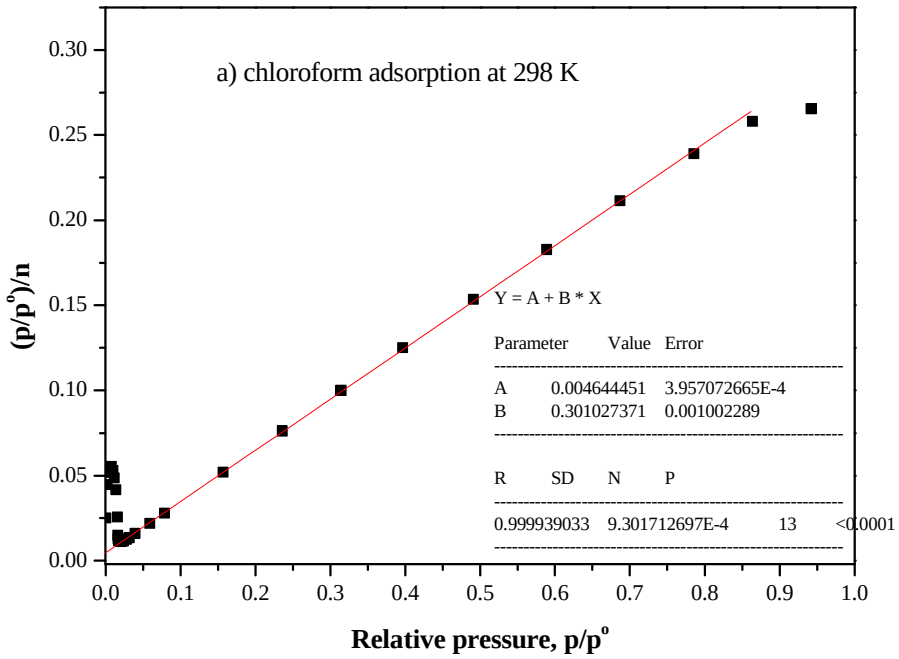

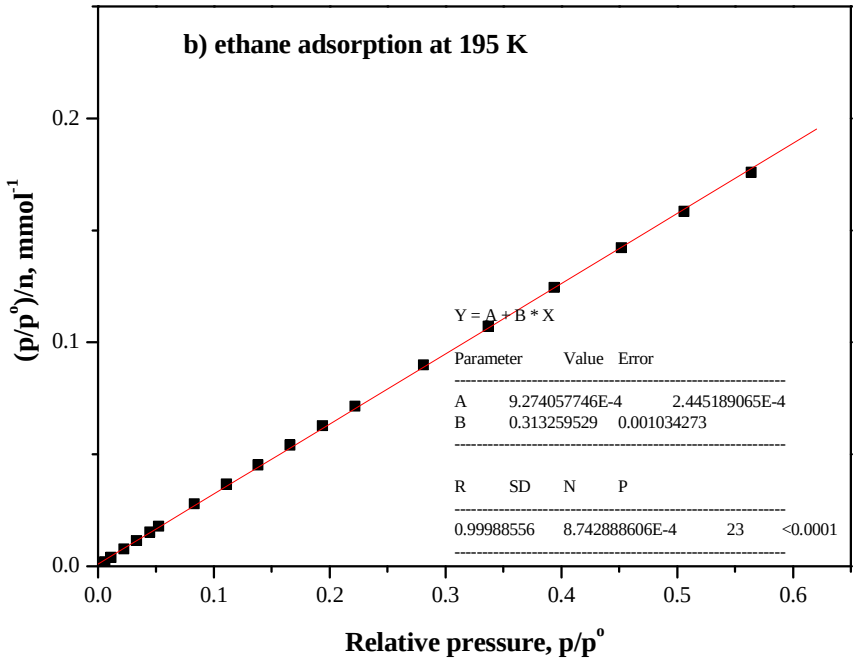

Figure C8 Langmuir plots of a) chloroform and b) ethane adsorption on NEW-1 sample at 298 K and 195 K, respectively.

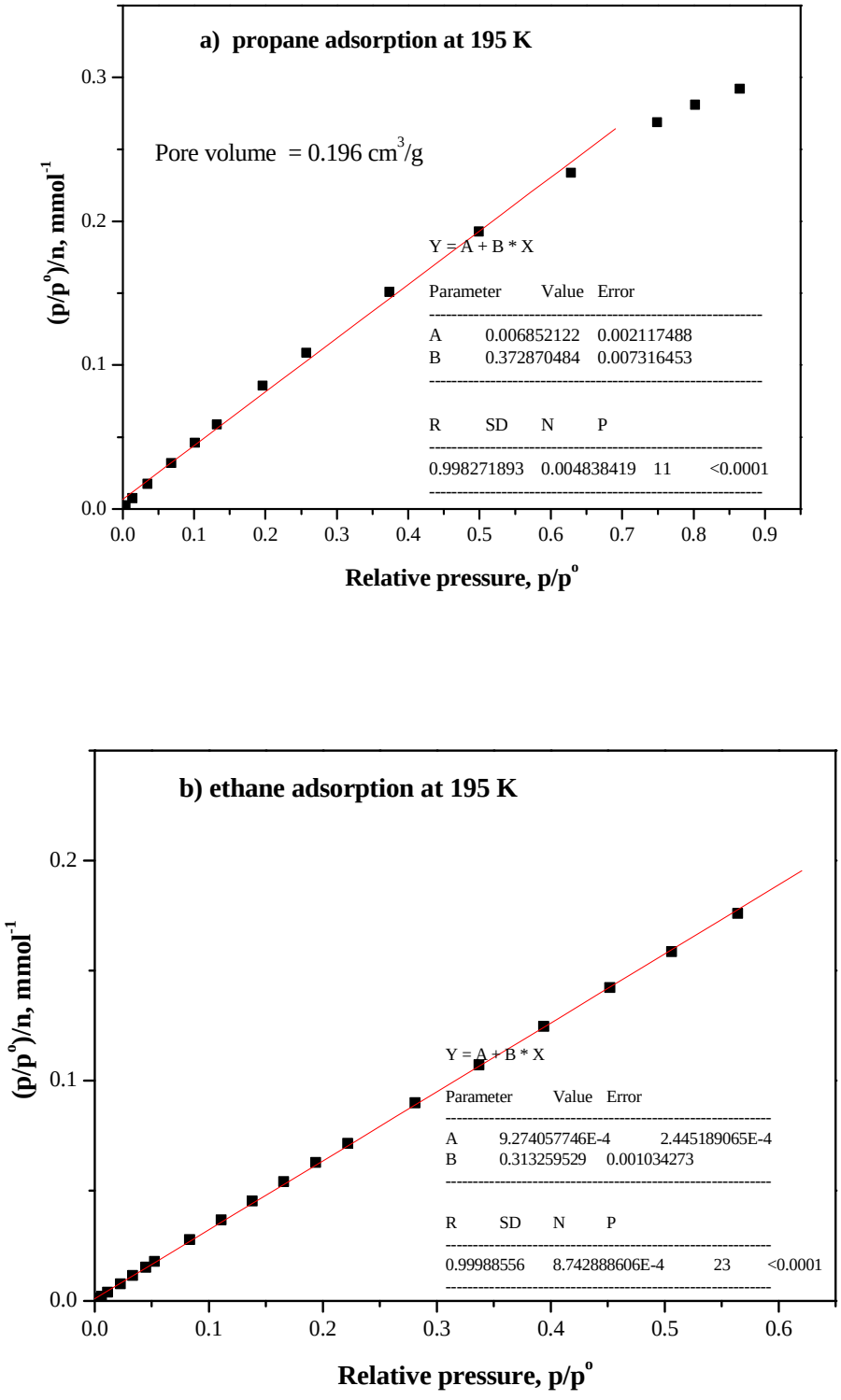

Figure C9 Langmuir plots of a) propane and b) *n*-butane adsorption on NEW-1 sample at 195 K.

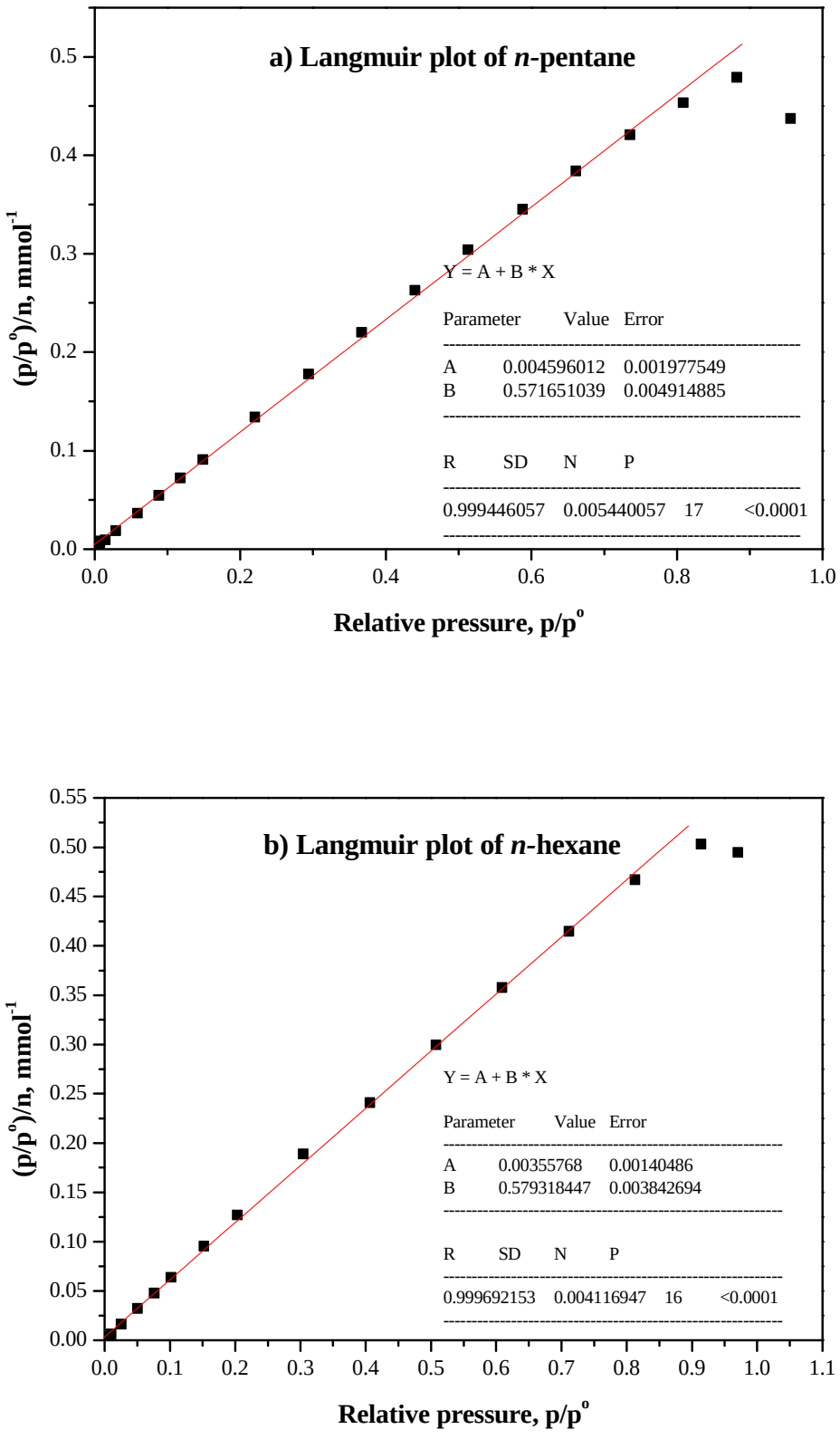

Figure C10 Langmuir plots of a) *n*-pentane and b) *n*-hexane adsorption on NEW-1 sample at 298 K.

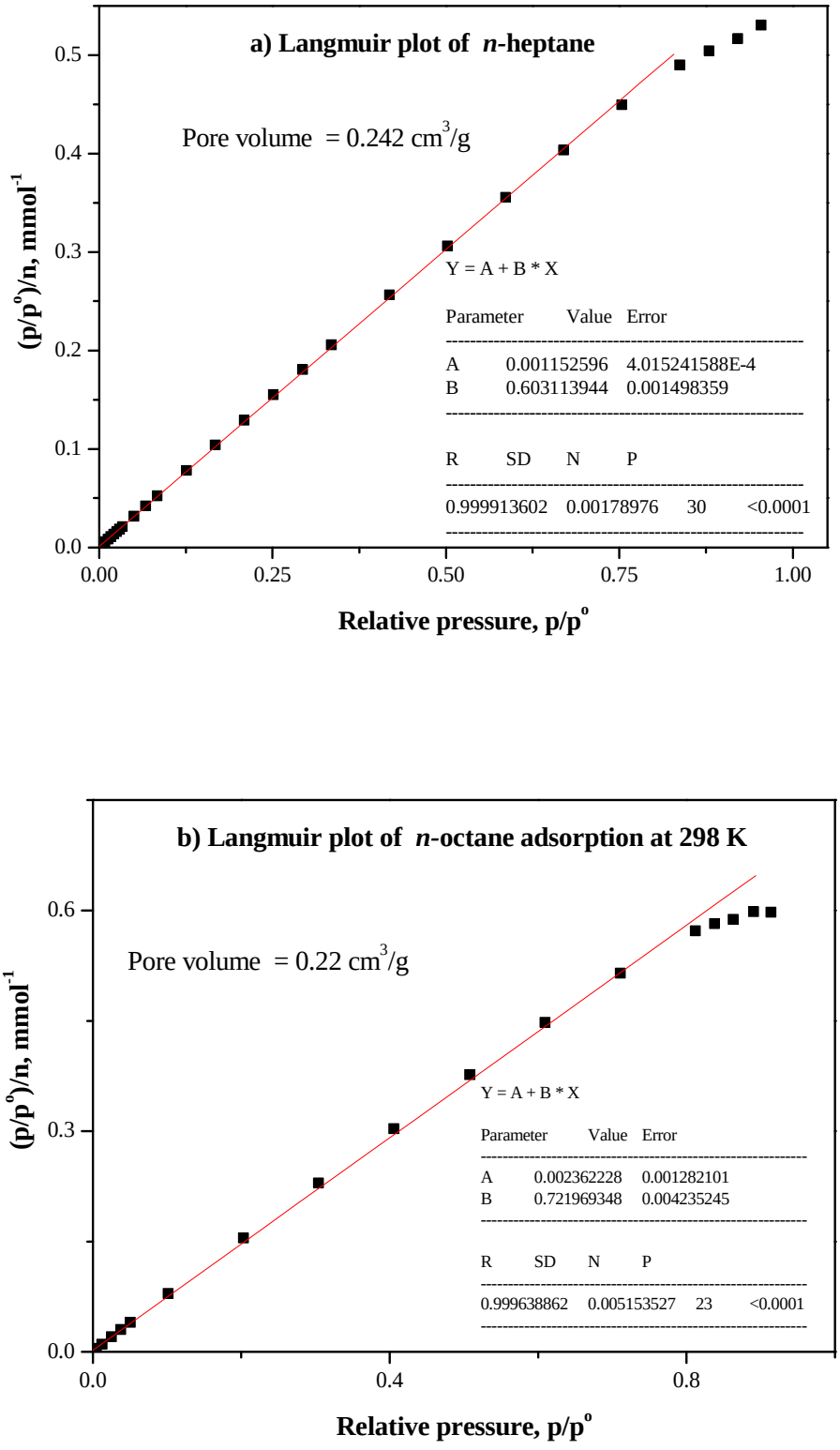

Figure C11 Langmuir plots of a) *n*-heptane and b) *n*-octane adsorption on NEW-1 sample at 298 K.

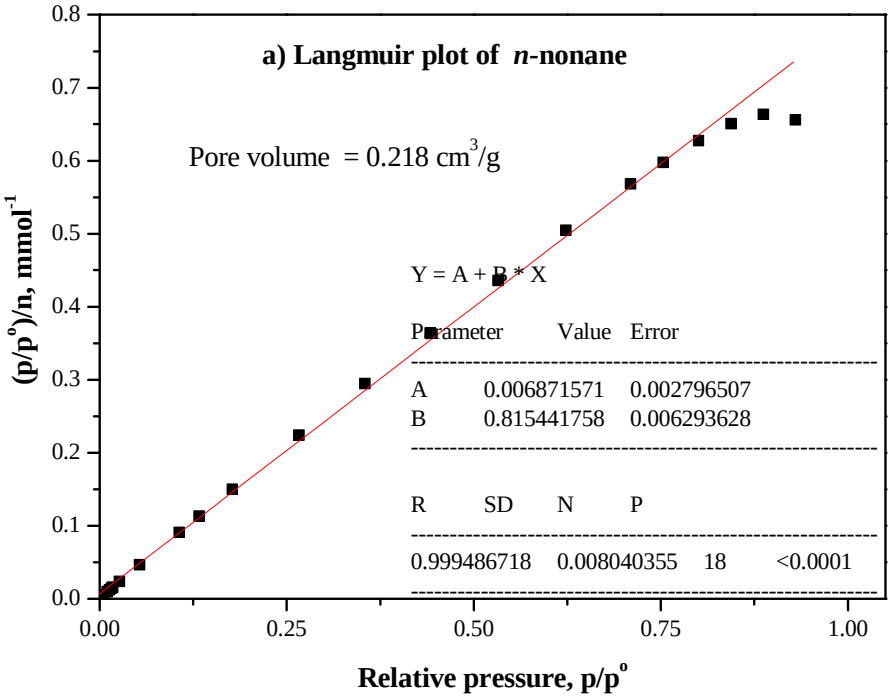

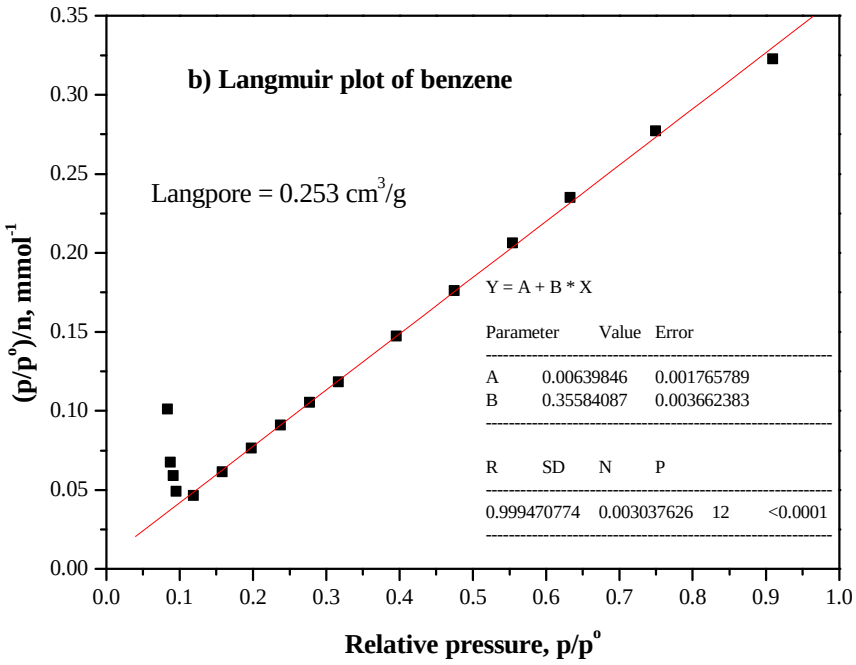

Figure C12 Langmuir plots of a) *n*-nonane and b) benzene adsorption on NEW-1 sample at 298 K.

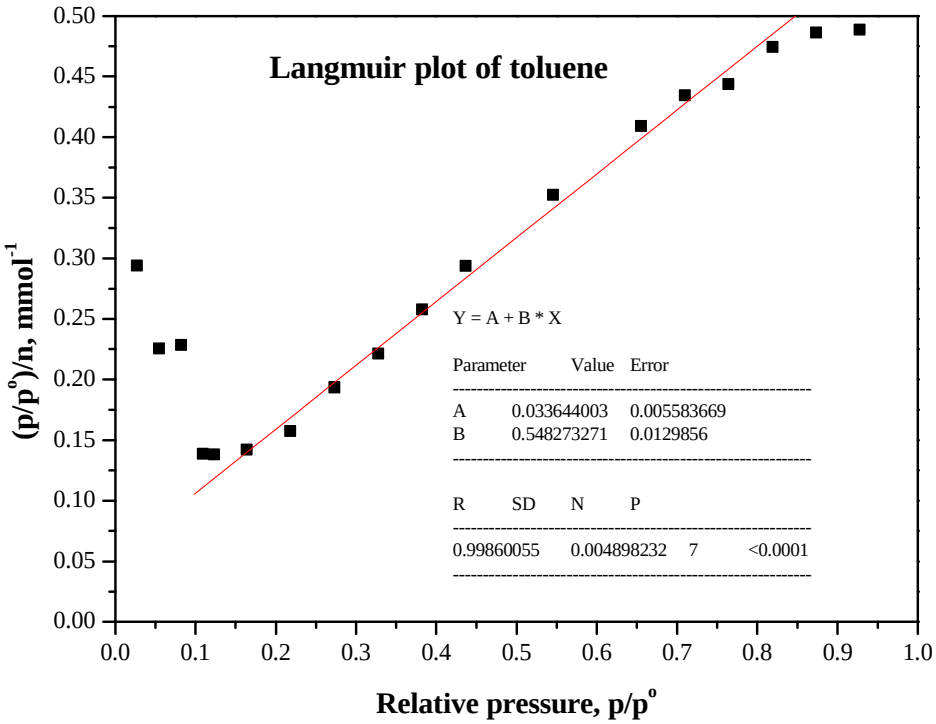

Figure C13 Langmuir plots of toluene adsorption on NEW-1 sample at 298 K.

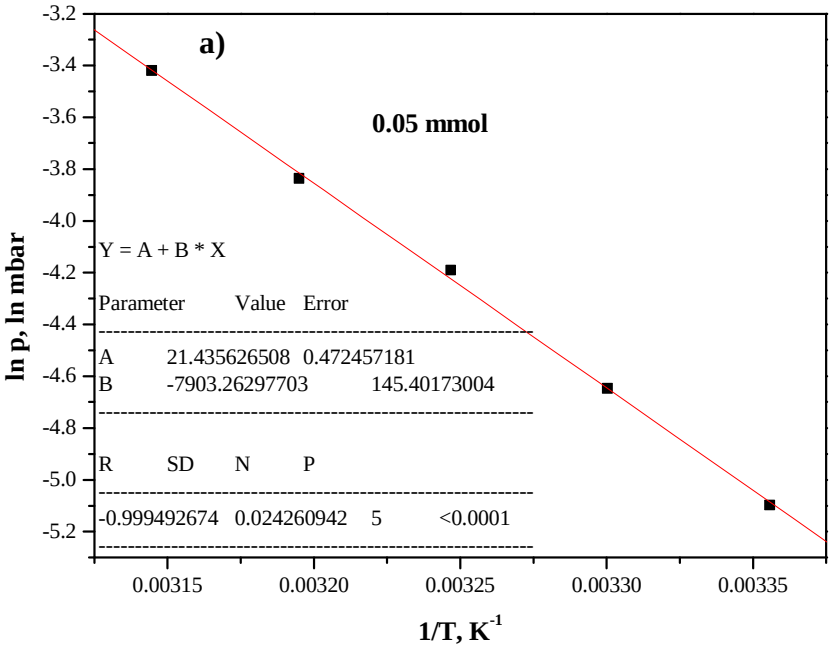

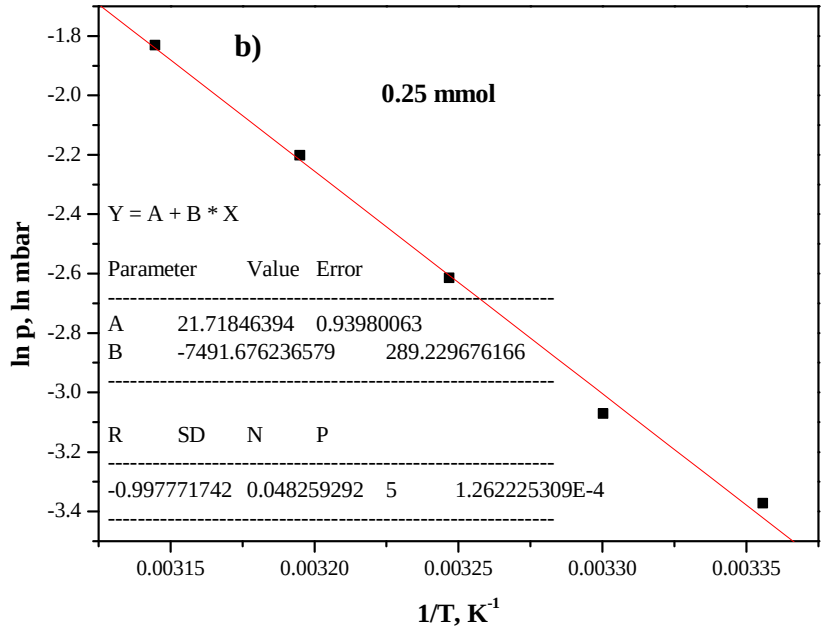

Figure D1 Plots of *In p* vs. *l/T* for the different surface coverage for methanol adsorption on NEW-1

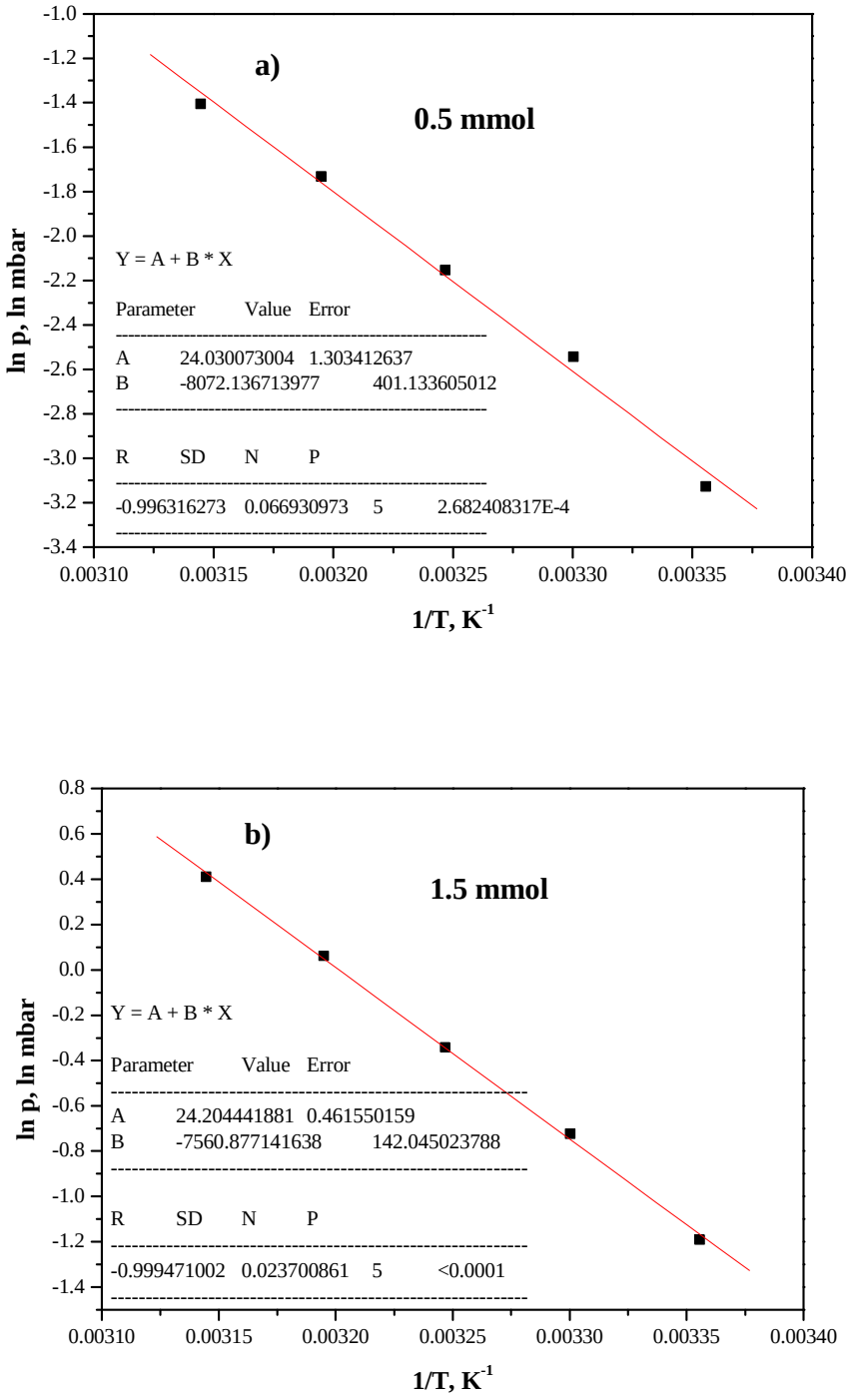

Figure D2 Plots of *In p* vs *l/T* for the different surface coverage for ethanol adsorption on NEW-1

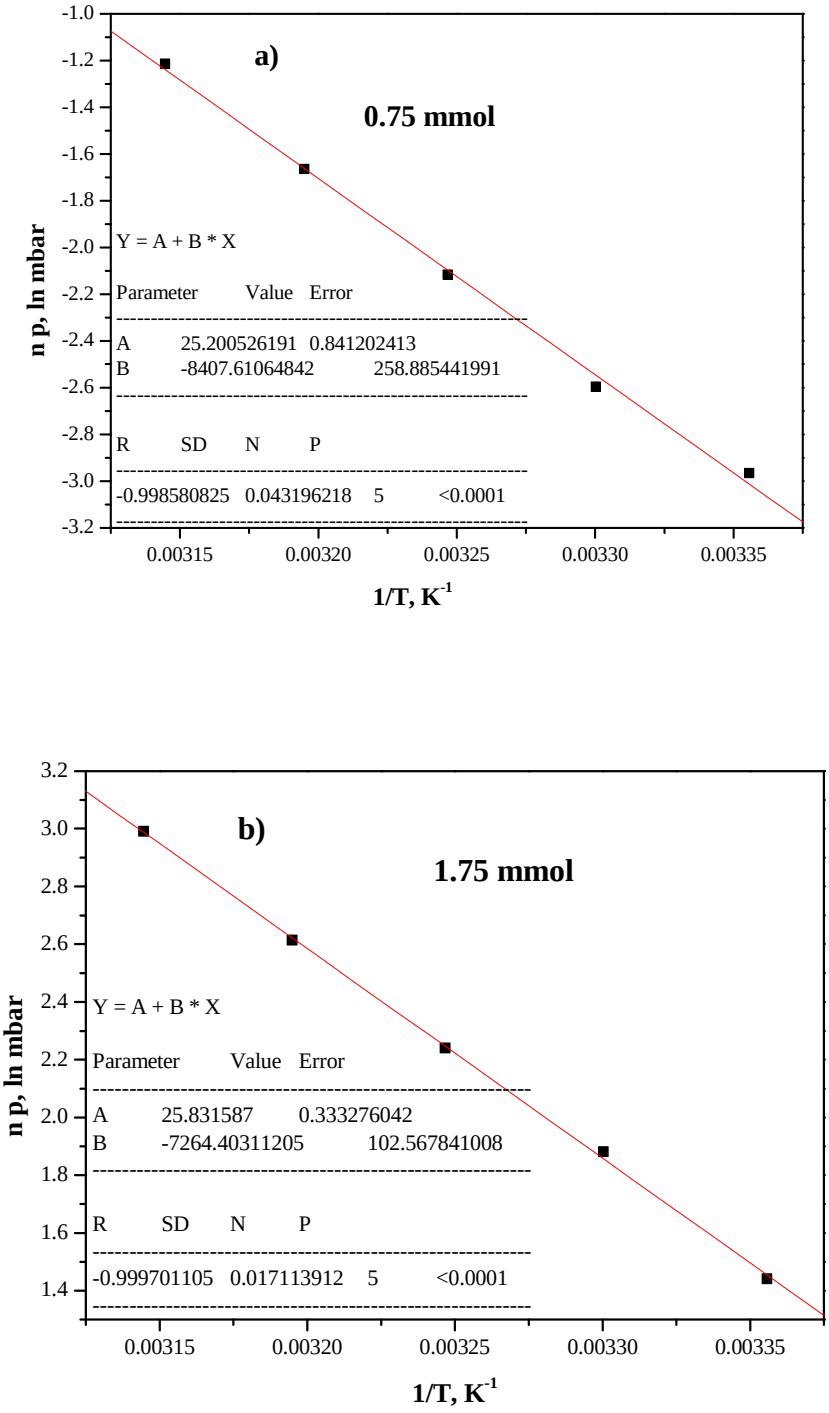

Figure D3 Plots of *In p* vs *l/T* for the different surface coverage for 1-propanol adsorption on NEW-1

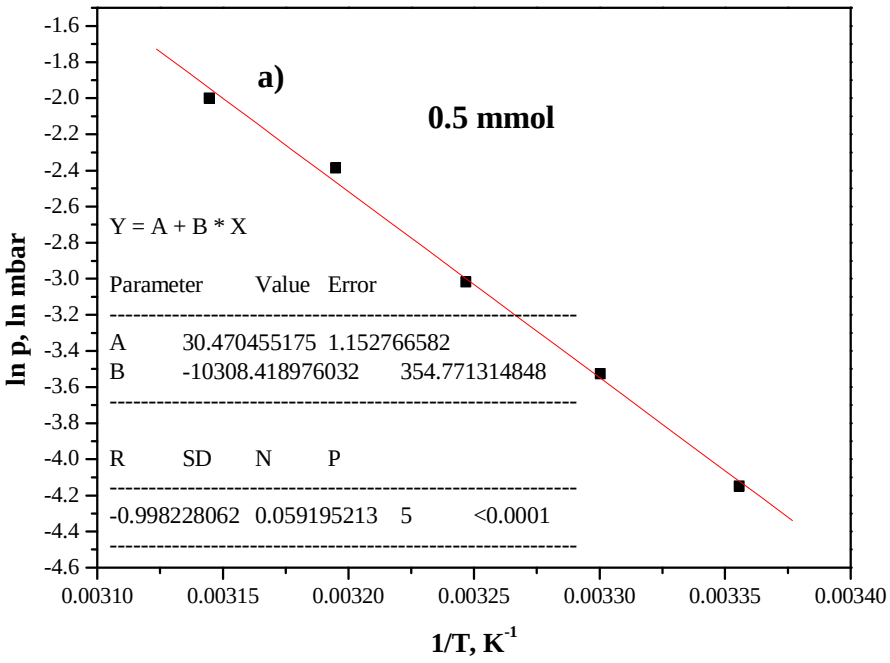

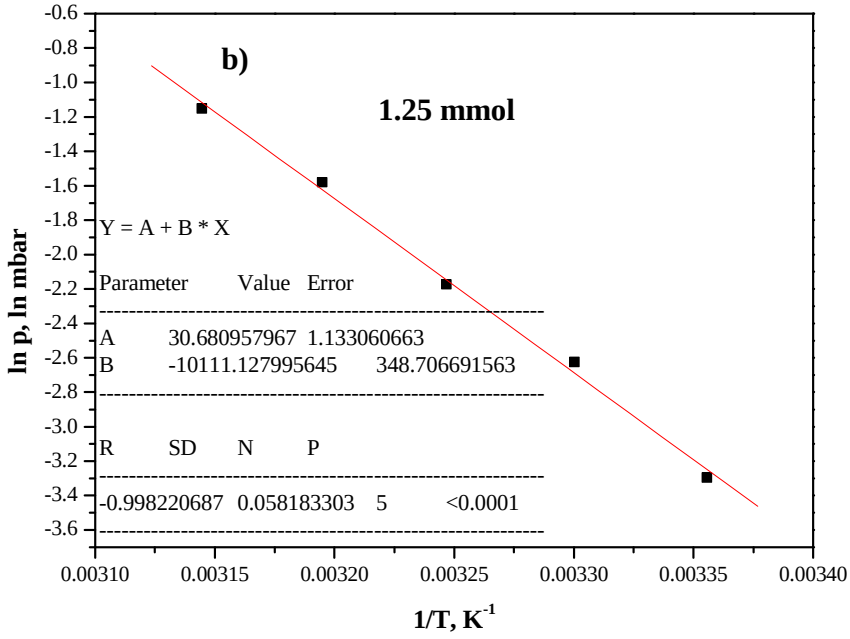

Figure D4 Plots of *In p* vs *l/T* for the different surface coverage for *n*-butanol adsorption on NEW-1

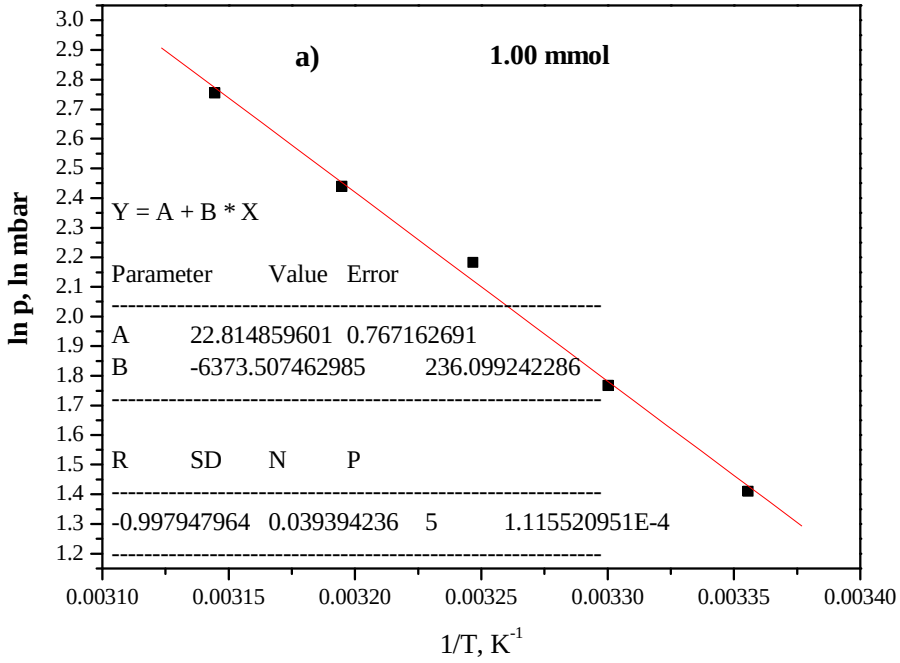

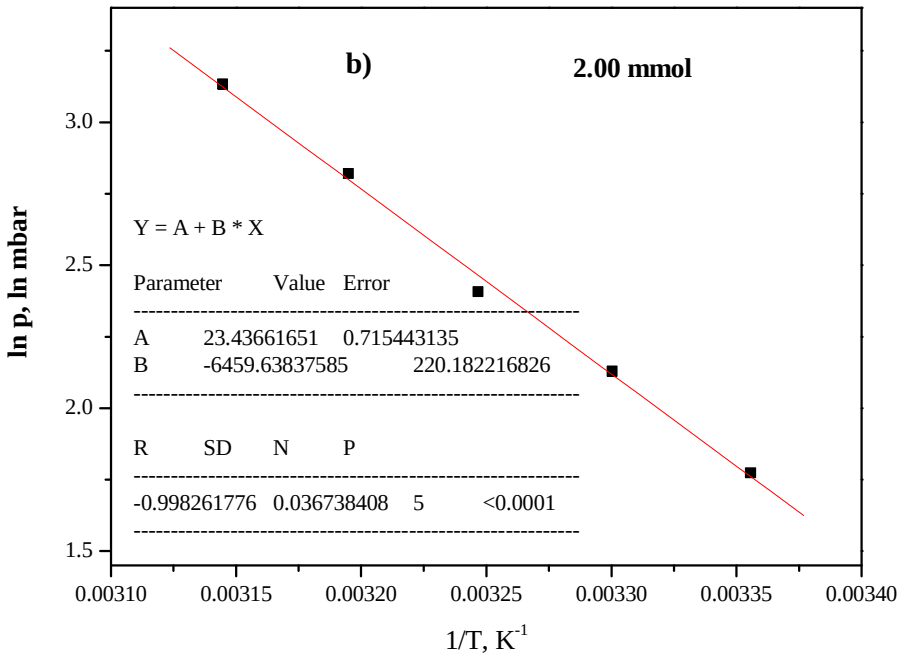

Figure D5 Plots of *In p* vs *l/T* for the different surface coverage for chloroform adsorption on NEW-1

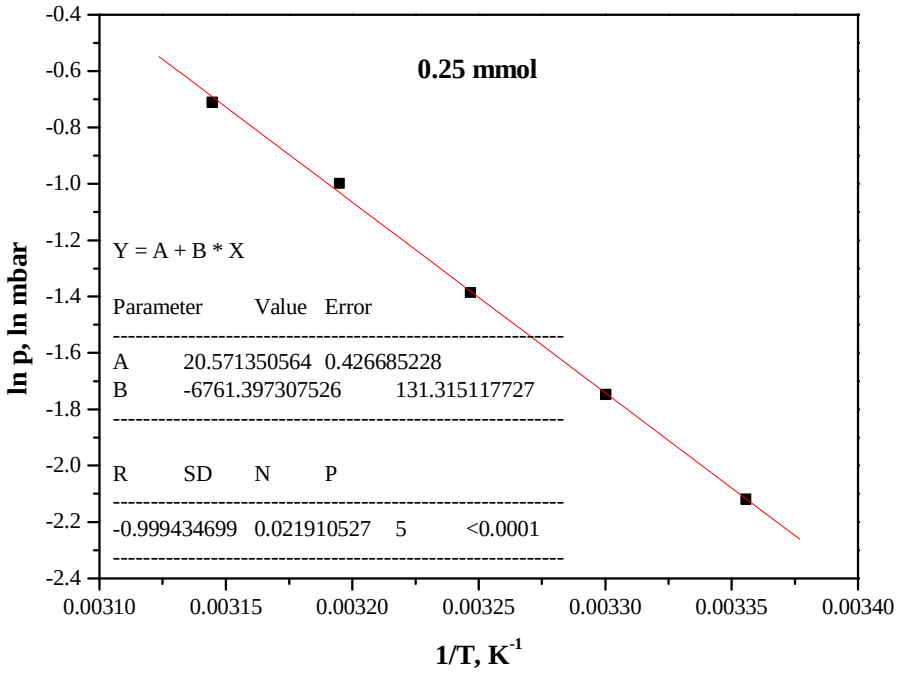

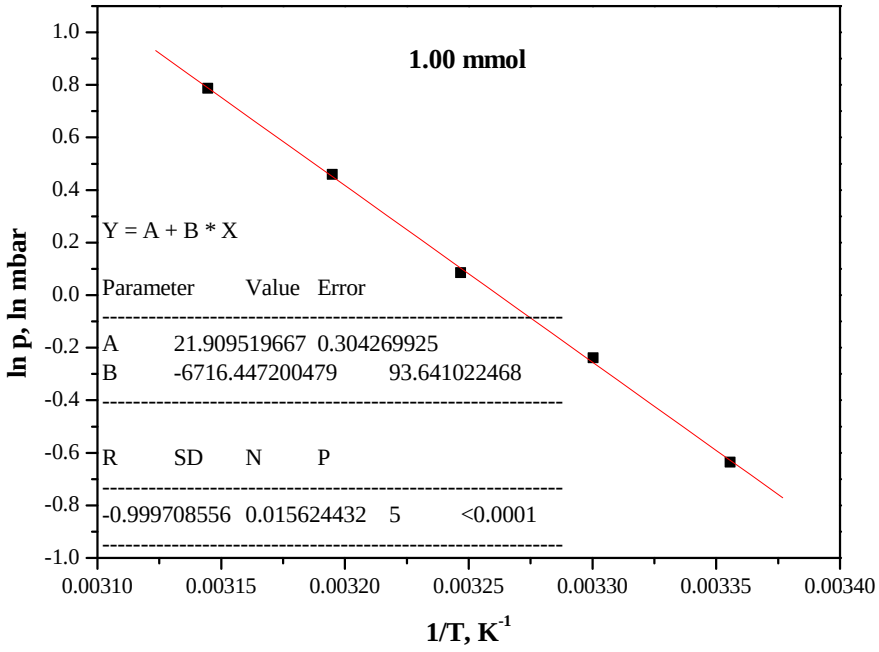

Figure D6 Plots of *In p* vs *l/T* for the different surface coverage for dichloromethane adsorption on NEW-1

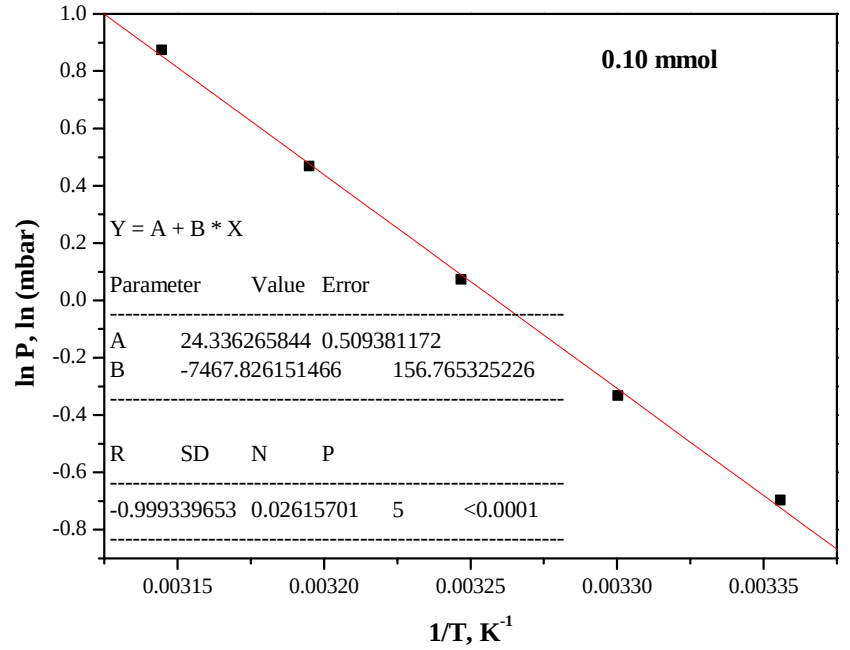

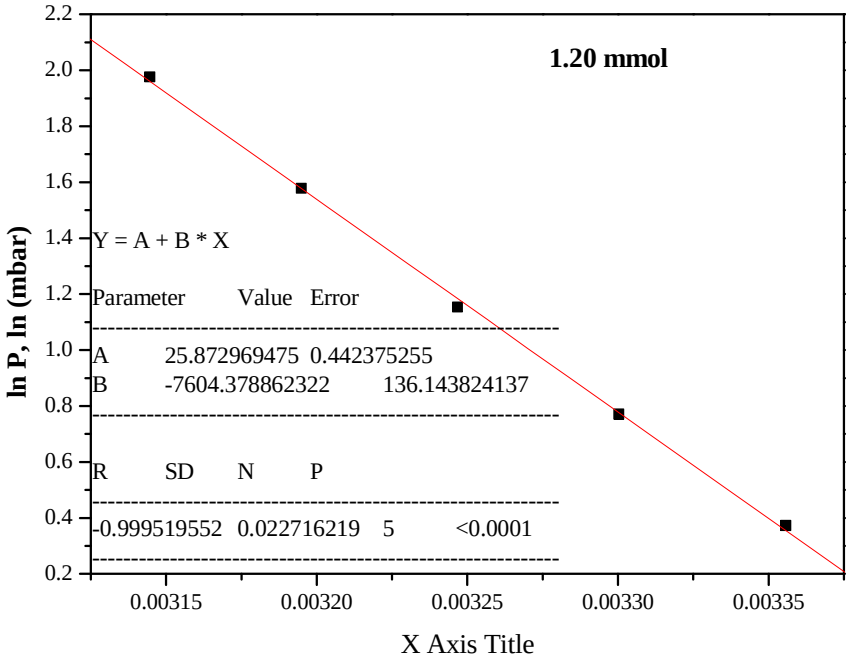

Figure D7 Plots of *In p* vs *l/T* for the different surface coverage for *n*-pentane adsorption on NEW-1

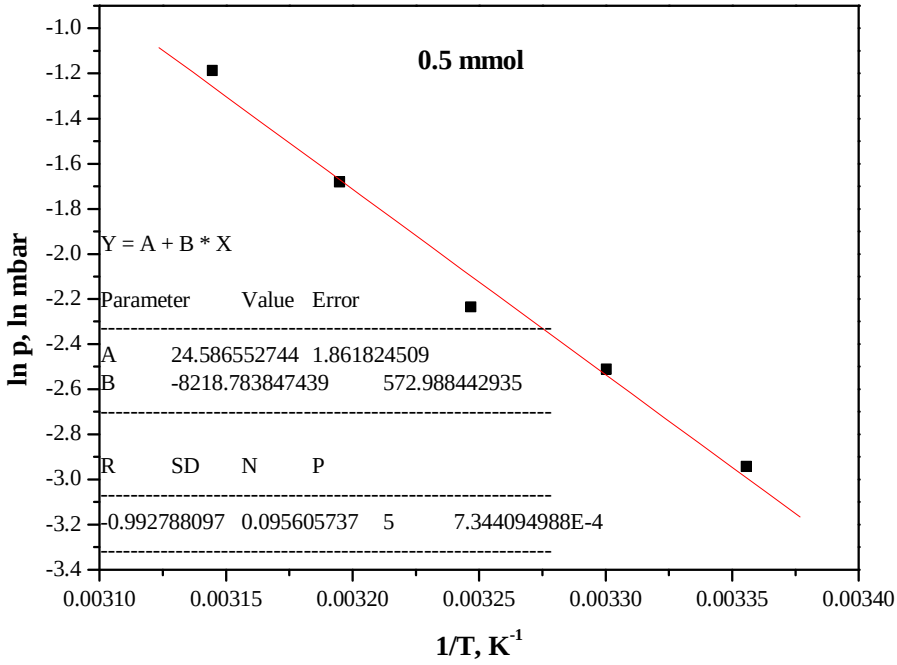

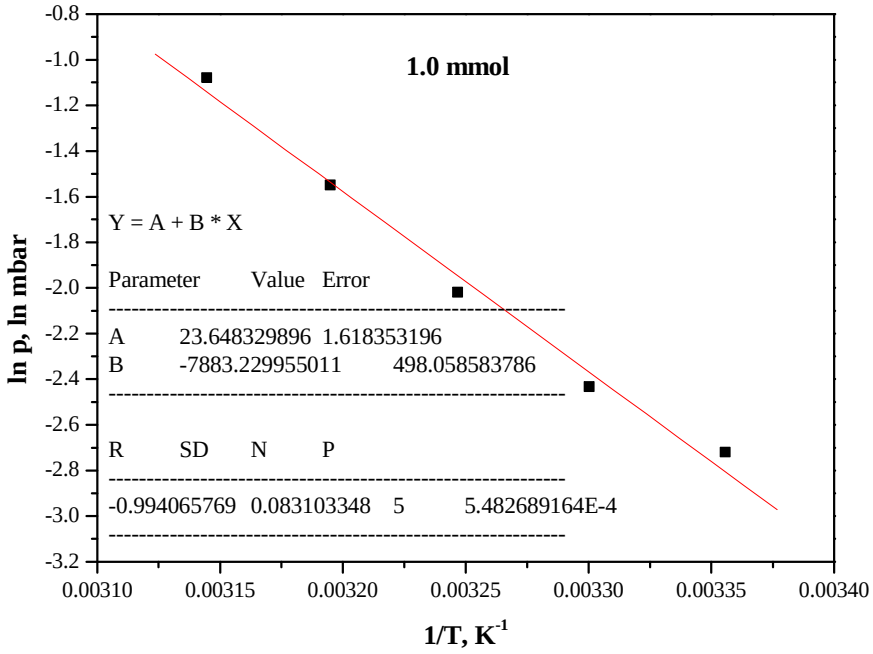

Figure D8 Plots of *In p* vs *l/T* for the different surface coverage for *n*-hexane adsorption on NEW-1

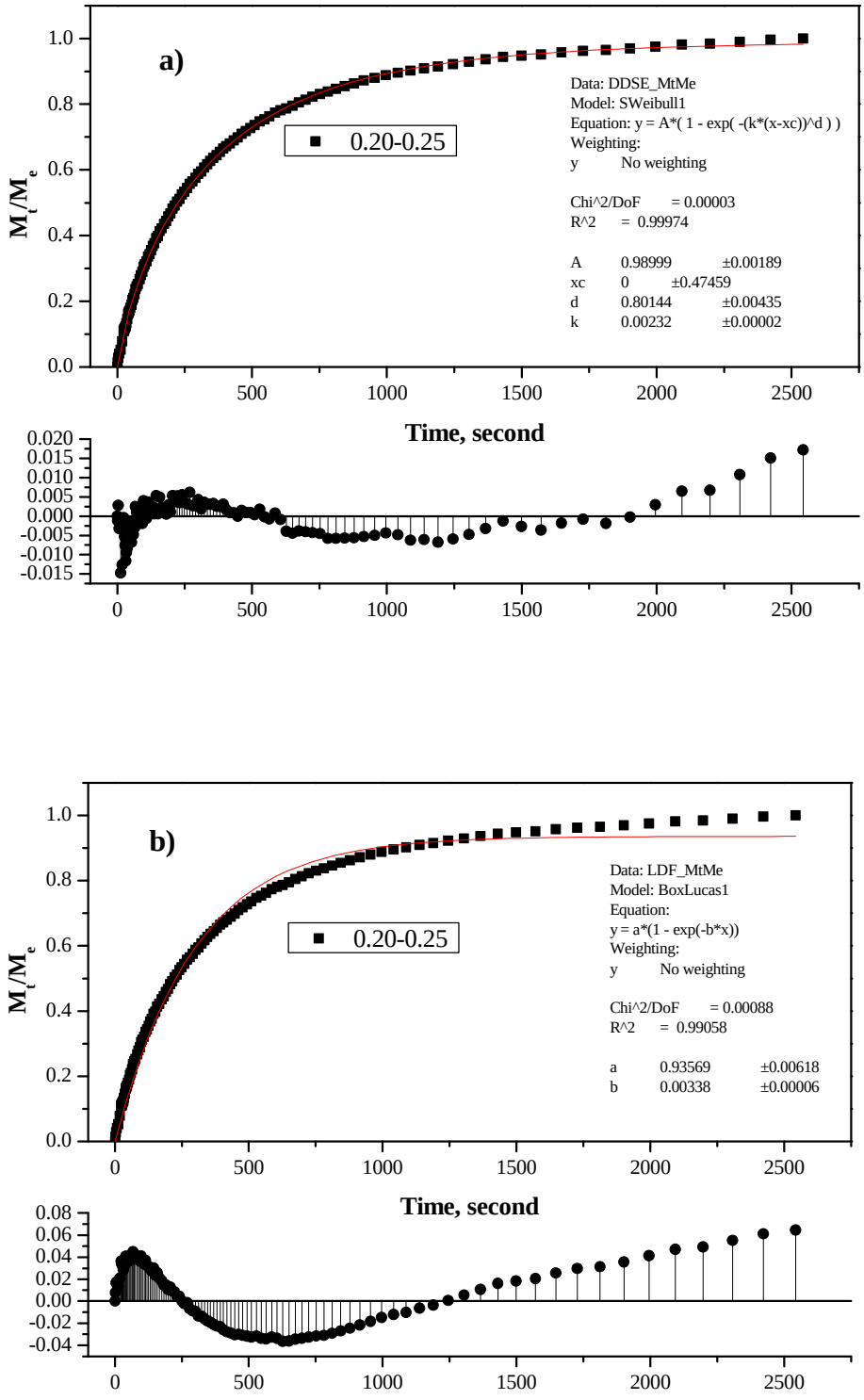

Figure E1 a) SE and b) LDF Model fit for the kinetic profiles of methanol adsorption on NEW-1 at 298 K, p/p0 =0.20-0.25

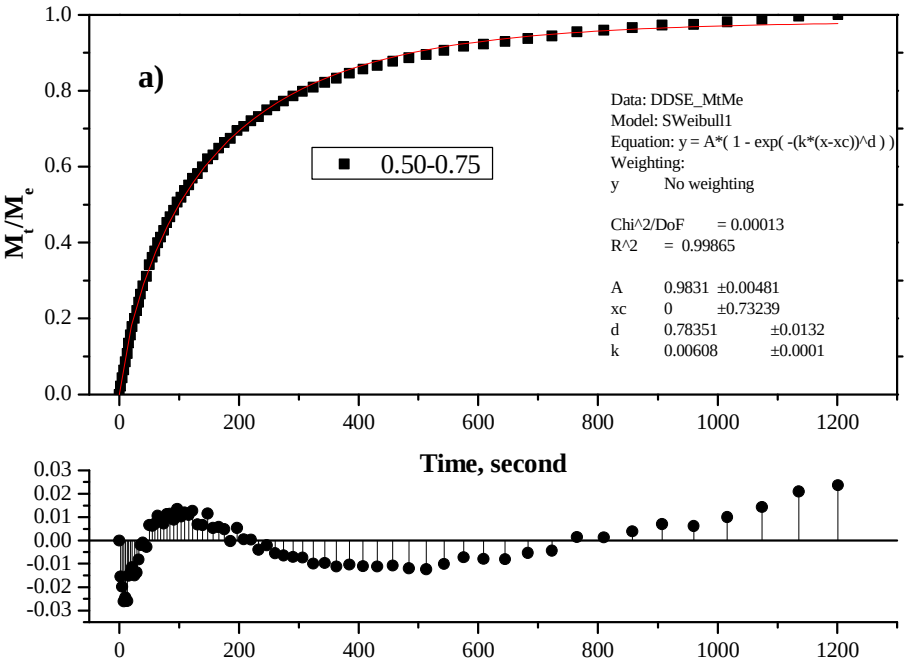

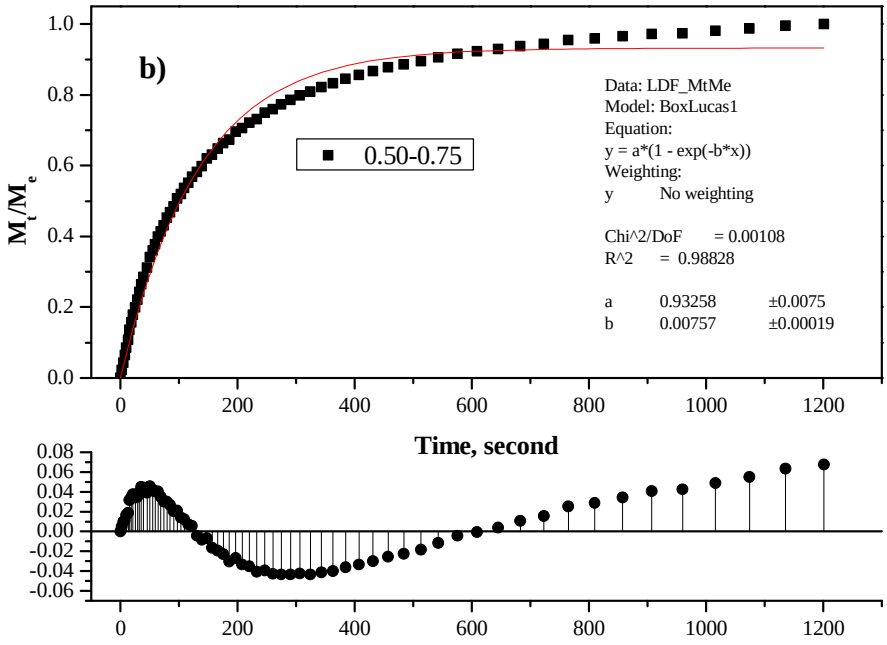

Figure E2 a) SE and b) LDF Model fit for the kinetic profiles of methanol adsorption on NEW-1 at 298 K, p/p0 =0.50-0.75

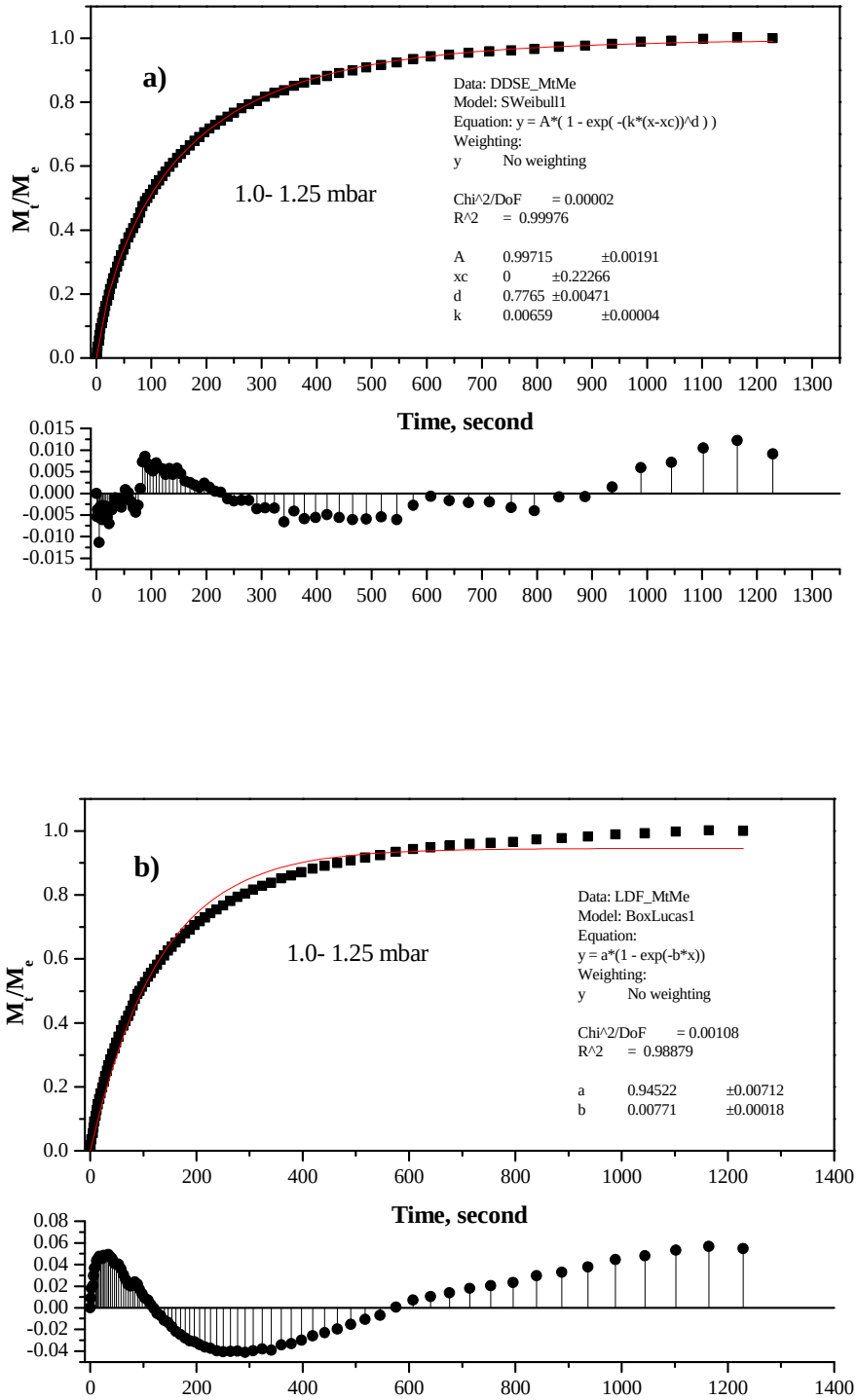

Figure E3 a) SE and b) LDF Model fit for the kinetic profiles of ethanol adsorption on NEW-1 at 298 K, p/p0 =1.0-1.25

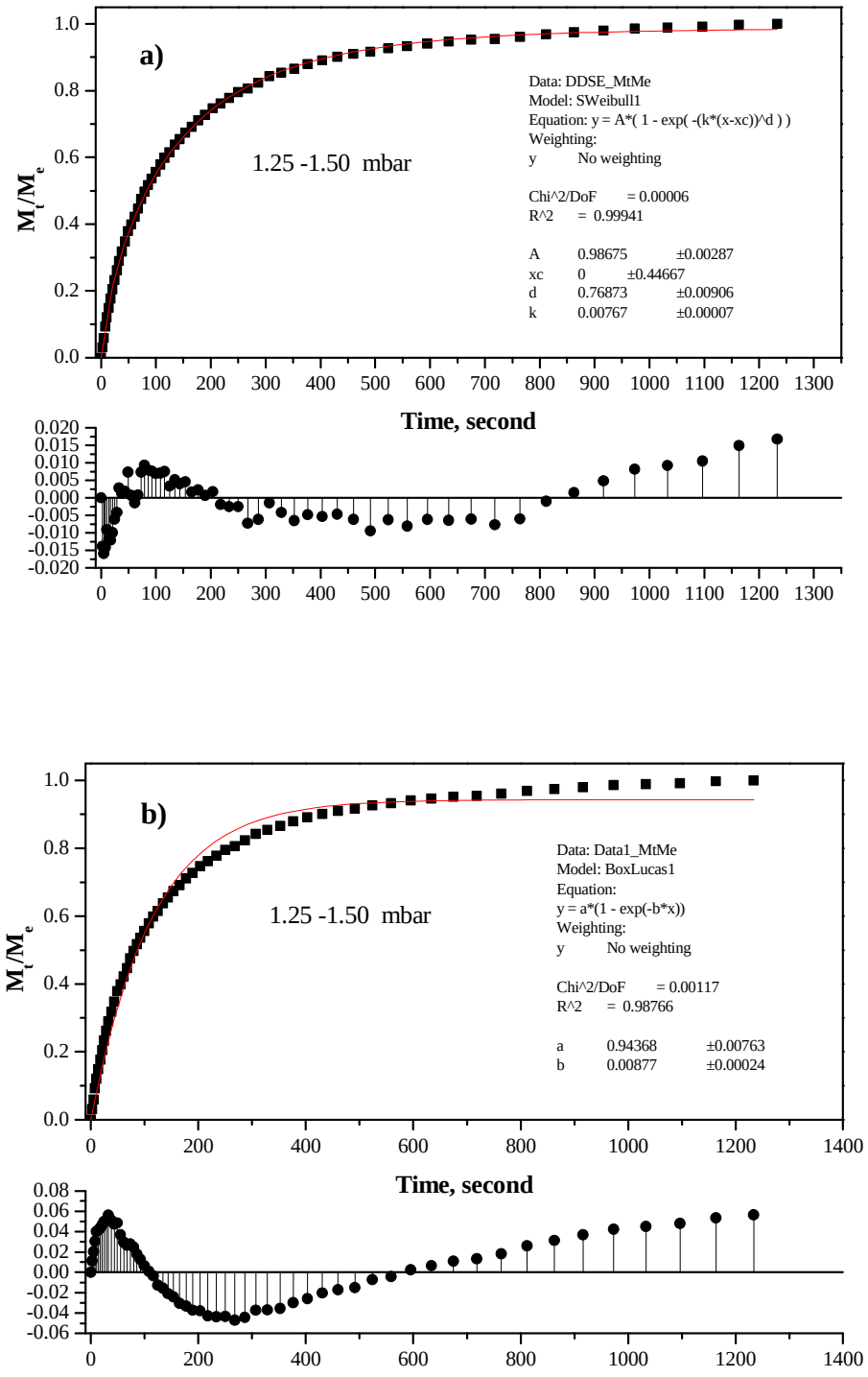

Figure E4 a) SE and b) LDF Model fit for the kinetic profiles of ethanol adsorption on NEW-1 at 298 K, p/p0 =1.25-1.50

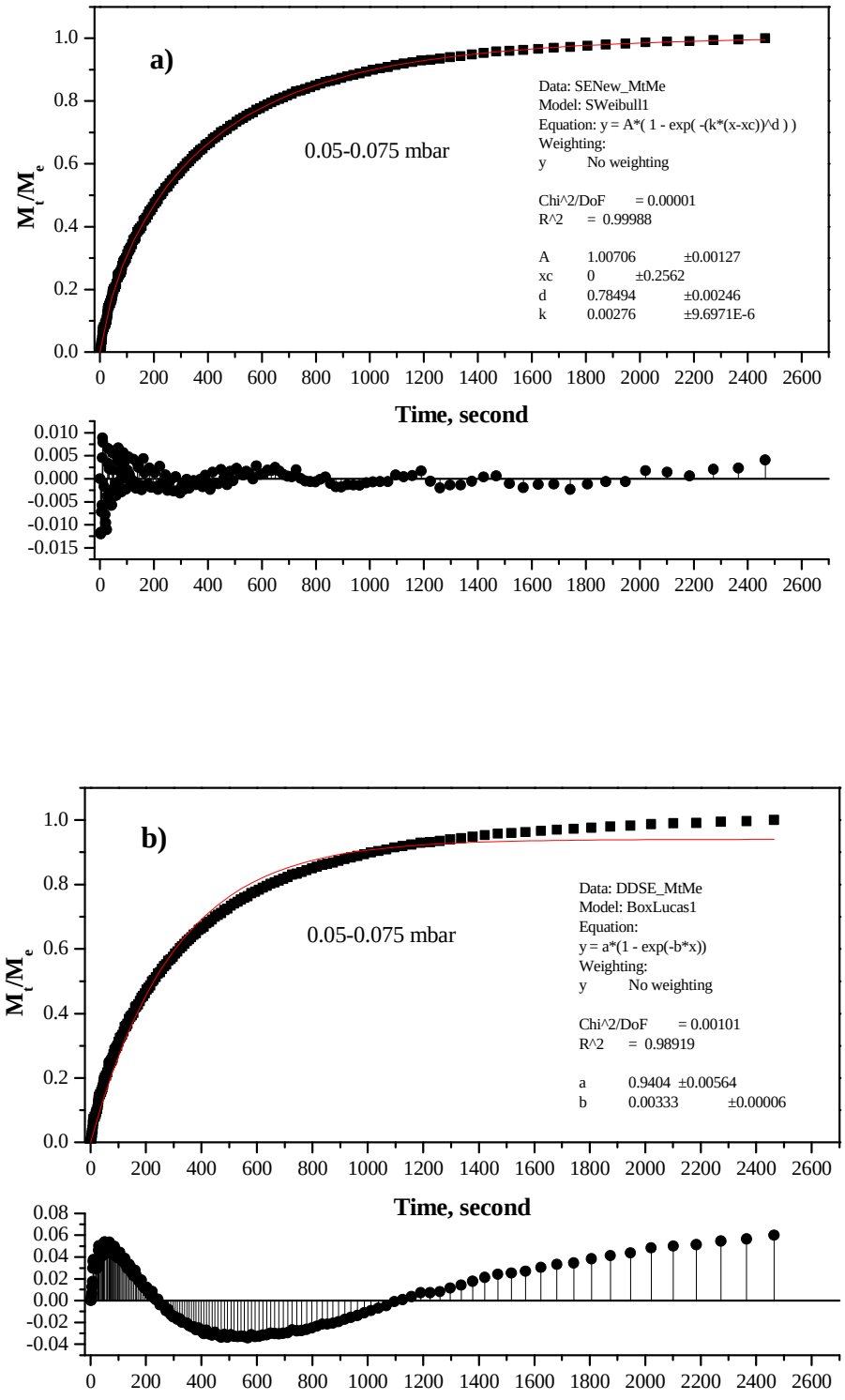

Figure E5 a) SE and b) LDF Model fit for the kinetic profiles of 1-propanol adsorption on NEW-1 at 298 K, p/p0 =0.05-0.075

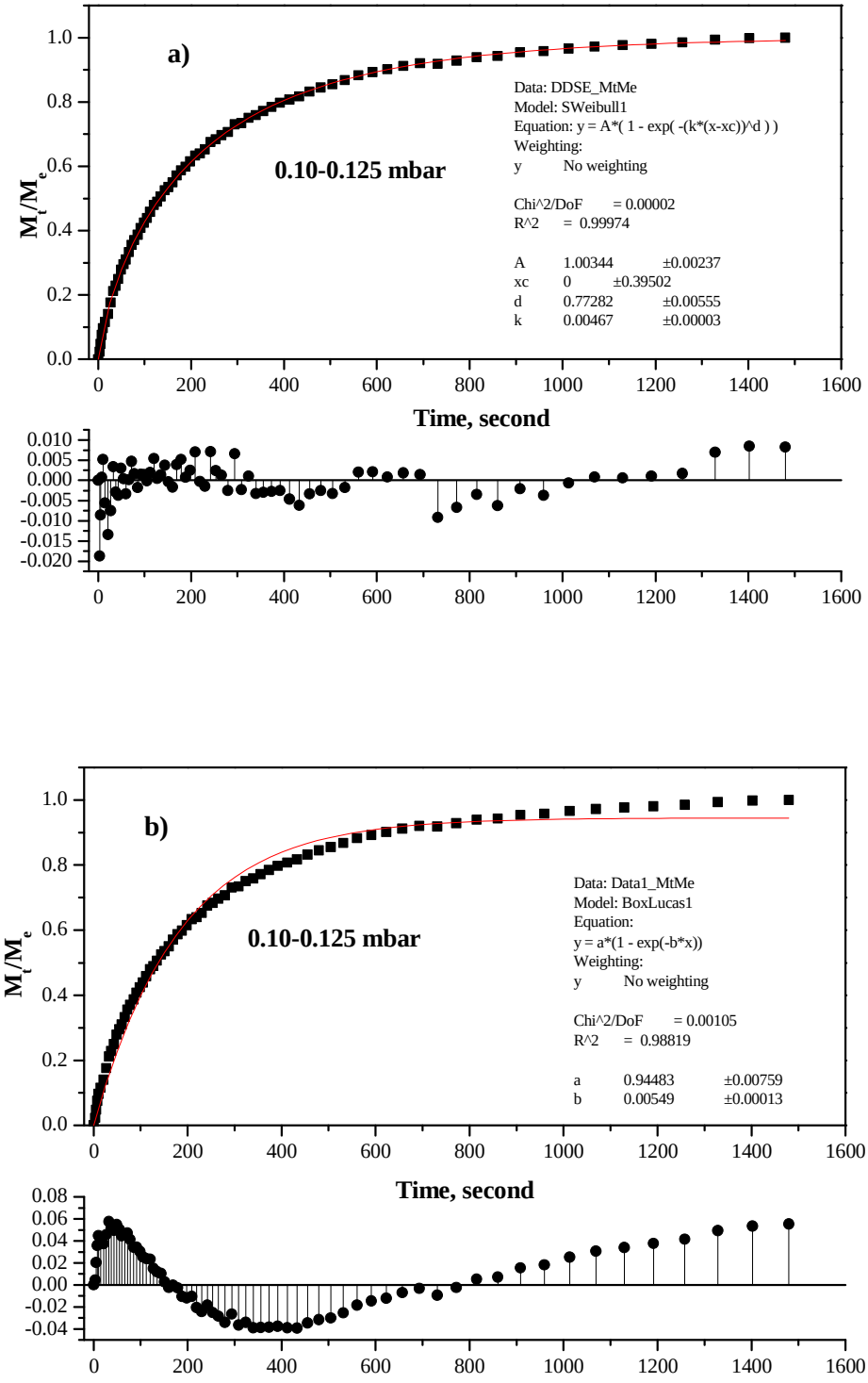

Figure E6 a) SE and b) LDF Model fit for the kinetic profiles of 1-propanol adsorption on NEW-1 at 298 K, p/p0 =0.10-0.125

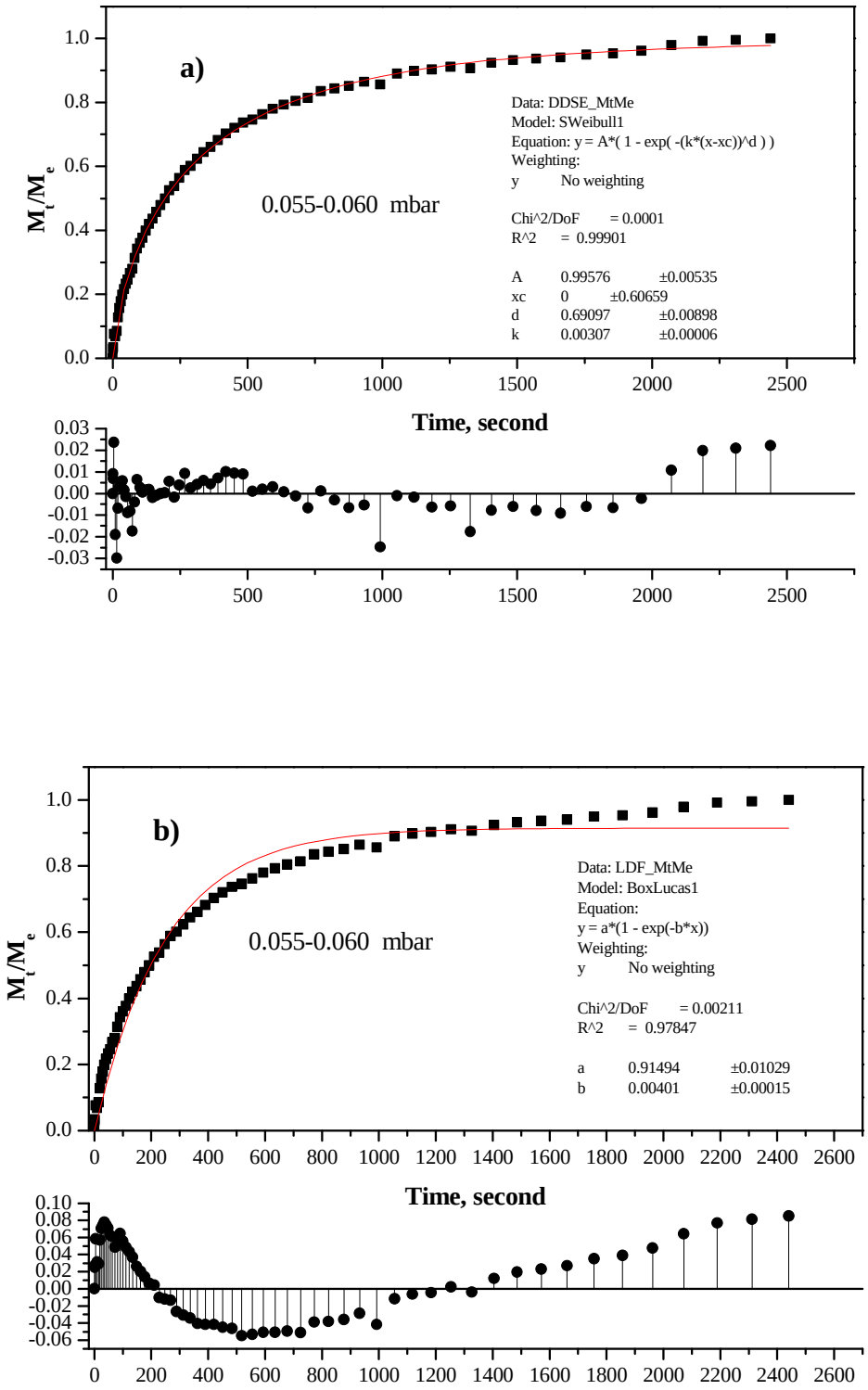

Figure E7 a) SE and b) LDF Model fit for the kinetic profiles of *n*-butanol adsorption on NEW-1 at 298 K, p/p0 =0.055-0.060

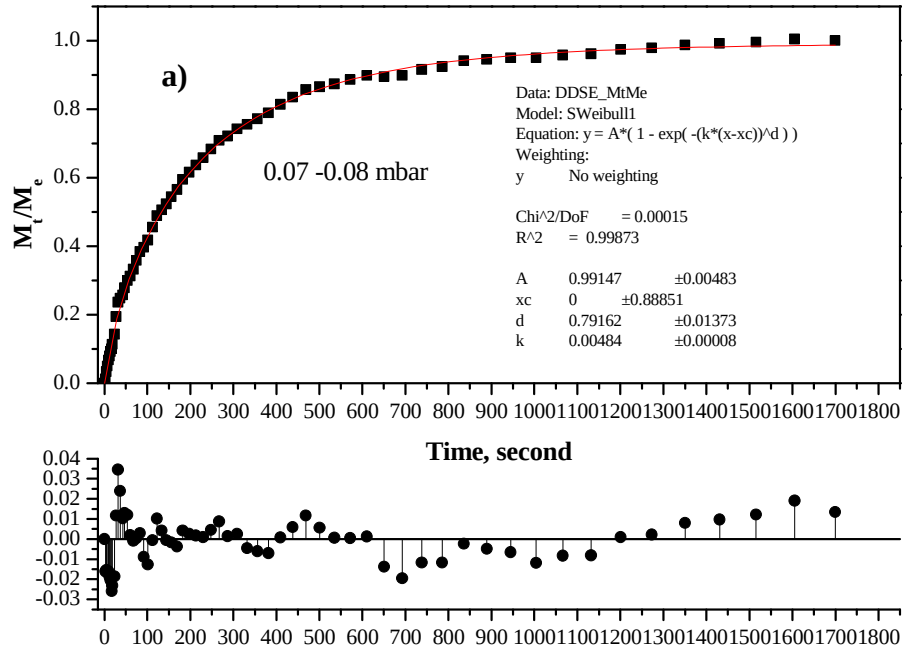

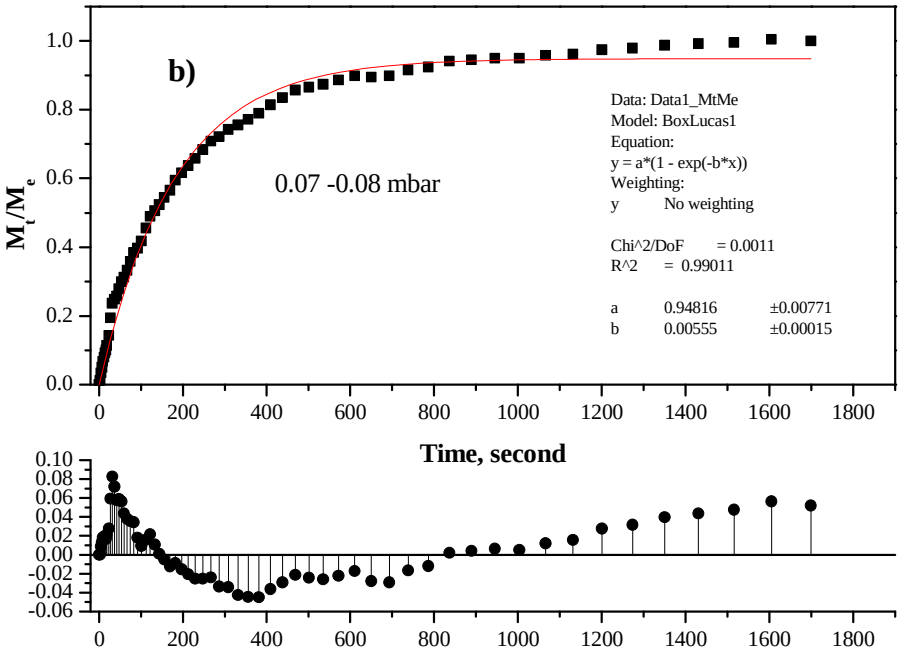

Figure E8 a) SE and b) LDF Model fit for the kinetic profiles of *n*-butanol adsorption on NEW-1 at 298 K, p/p0 =0.07-0.08

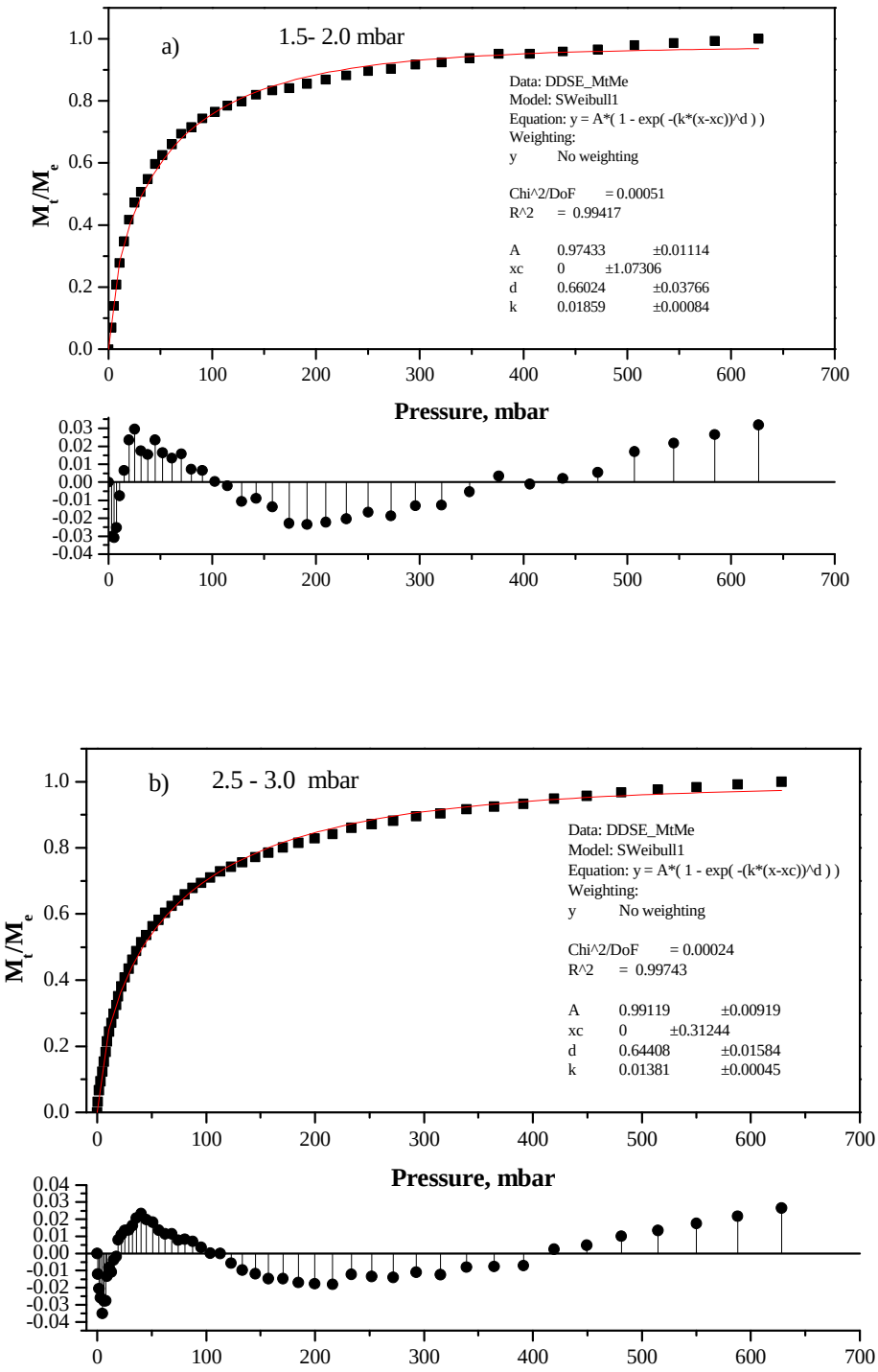

Figure E9 SE Model fit for the kinetic profiles of chloroform adsorption on NEW-1 at 298 K , a) p/p0 =0.0001-0.0003 and b) p/p0 =0.0004-0.002

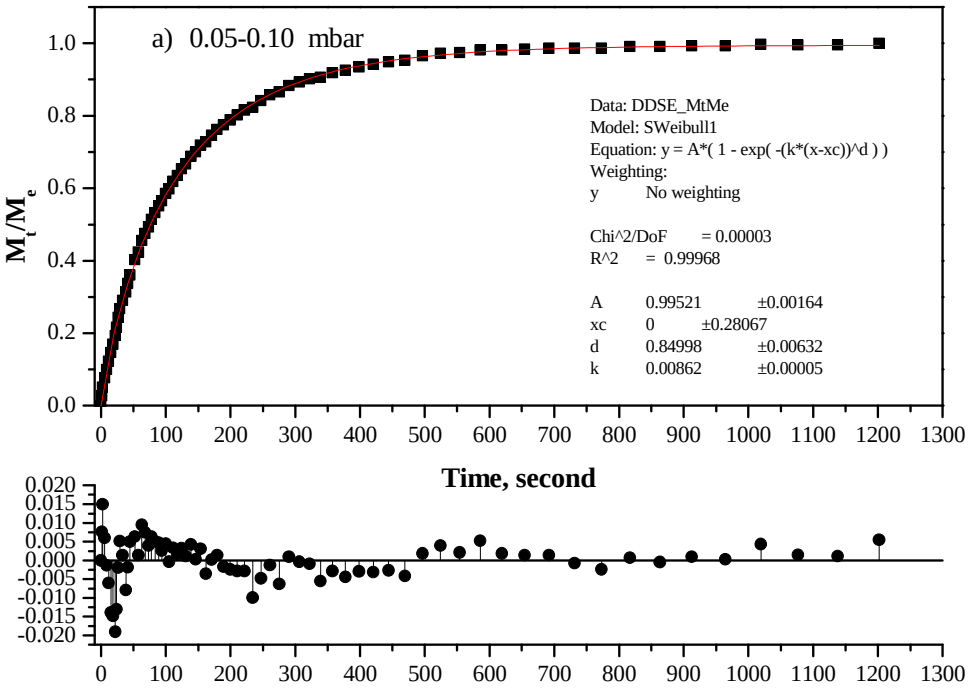

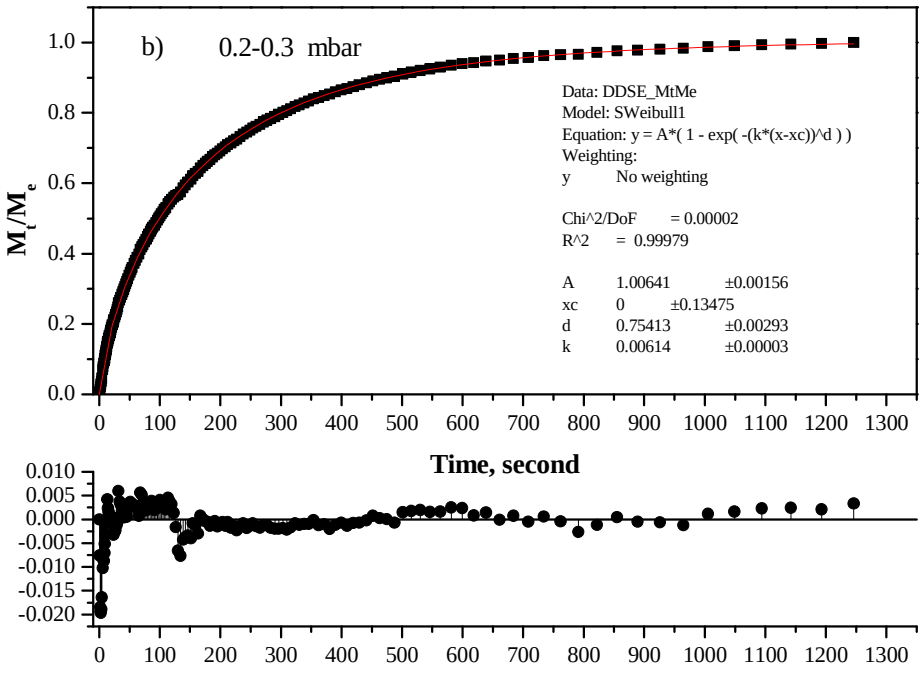

Figure E10 SE Model fit for the kinetic profiles of dichloromethane adsorption on NEW-1 at 298 K , a) p/p0 =0.00008-0.00017 and b) p/p0 =0.003-0.005

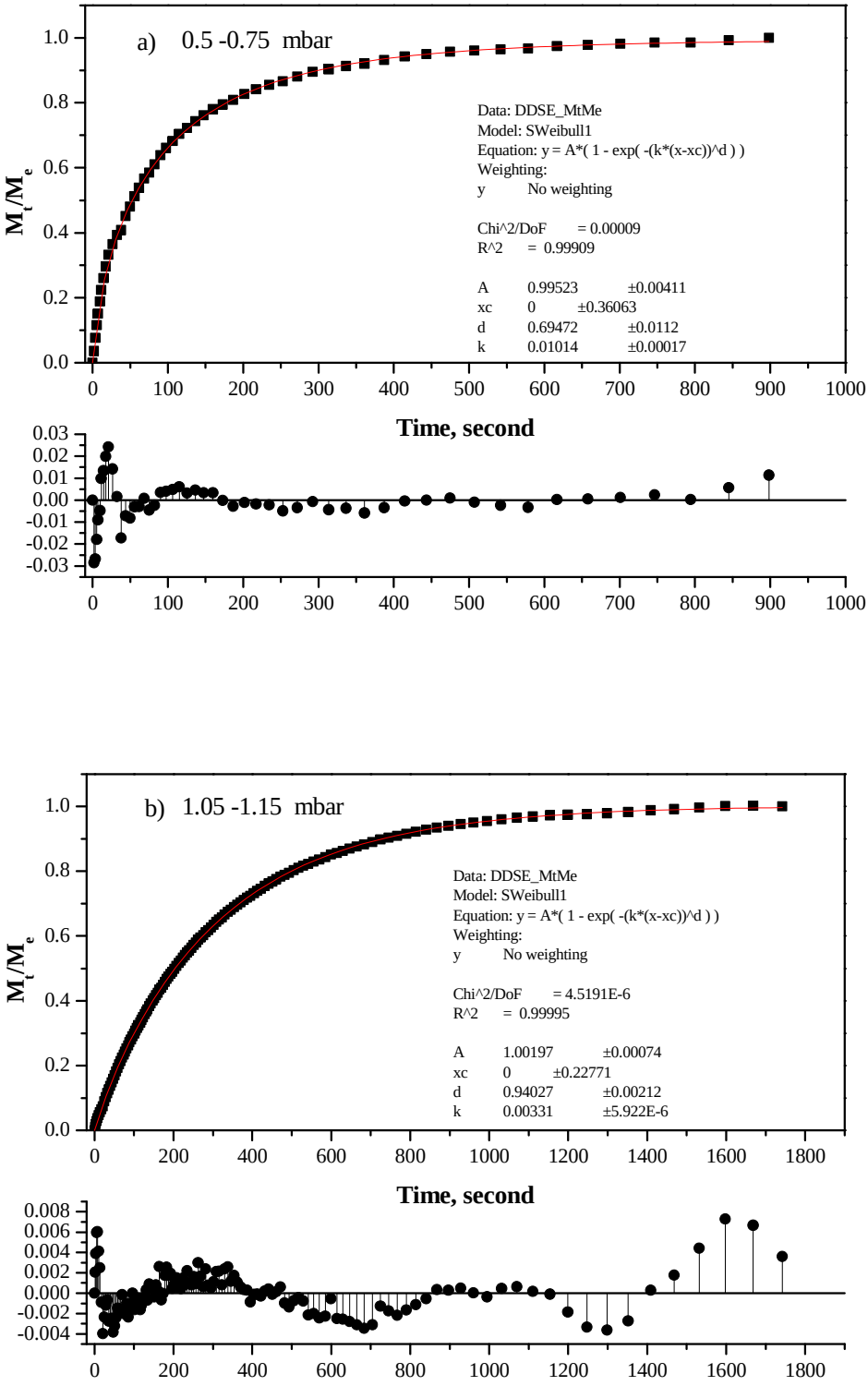

Figure E11 SE Model fit for the kinetic profiles of *n*-pentane adsorption on NEW-1 at 298 K , a) p/p0 =0.00074-0.0011 and b) p/p0 =0.0015-0.0016

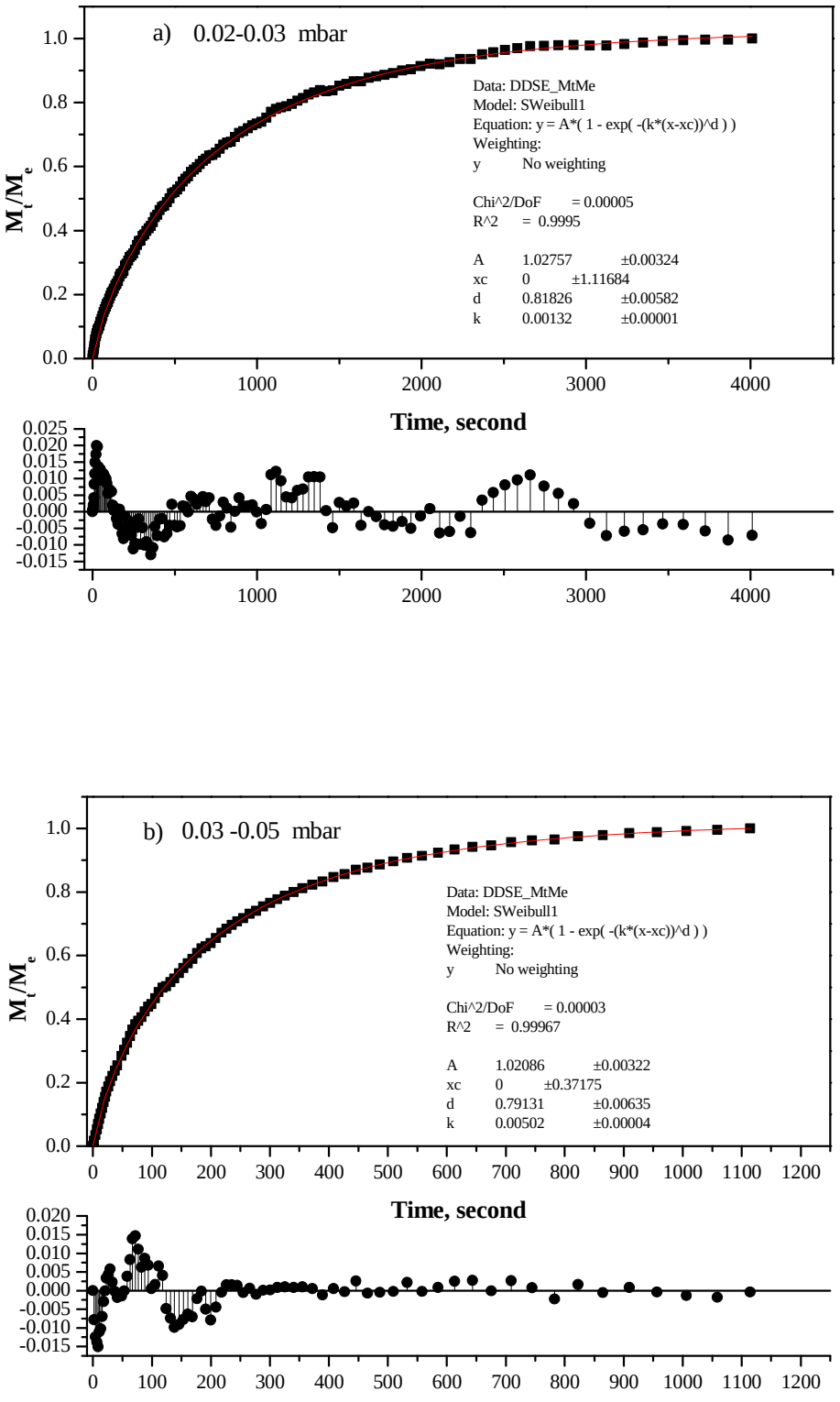

Figure E12 SE Model fit for the kinetic profiles of *n*-hexane adsorption on NEW-1 at 298 K , a) p/p0 =0.0001-0.00015 and b) p/p0 =0.00015-0.00025

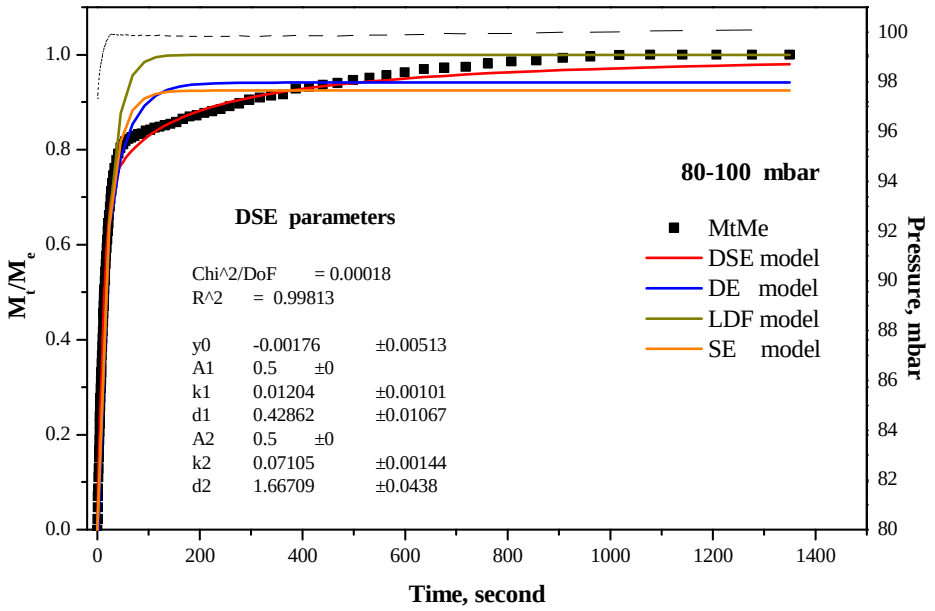

Figure F1 Various models fitted for the kinetic profiles of N_2 adsorption on NEW-1 at 195 K, 80-100 mbar

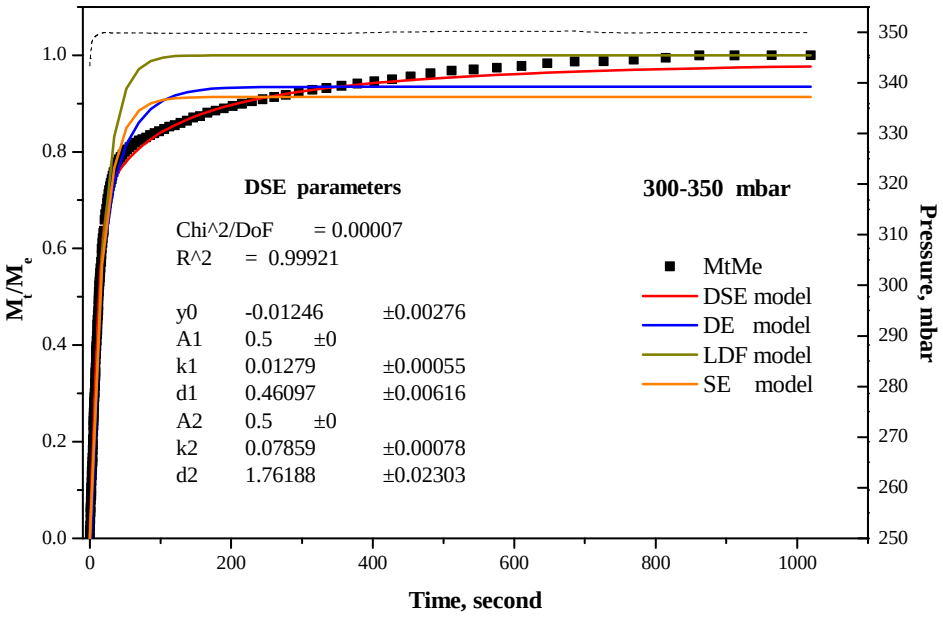

Figure F2 Various models fitted for the kinetic profiles of N_2 adsorption on NEW-1 at 195 K, 300-350 mbar

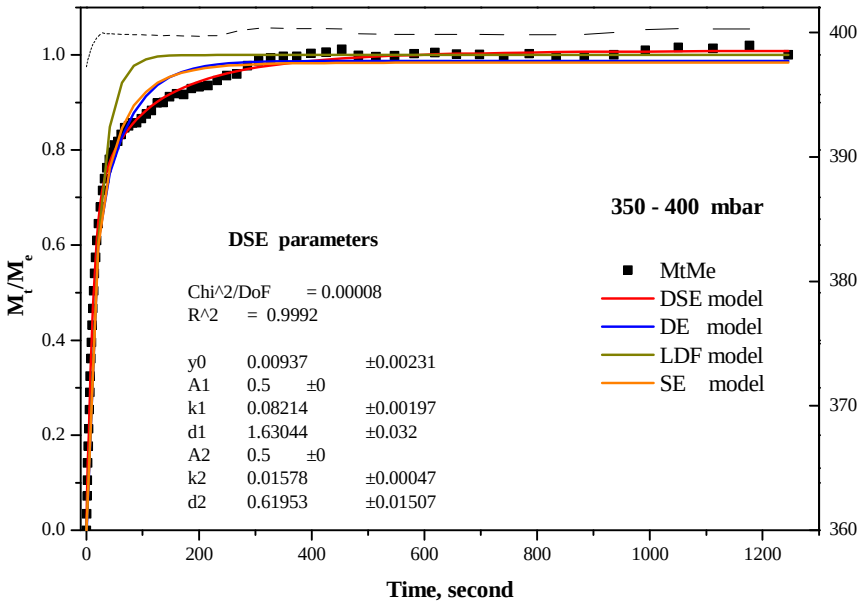

Figure F3 Various models fitted for the kinetic profiles of O_2 adsorption on NEW-1 at 195 K, 350-400 mbar

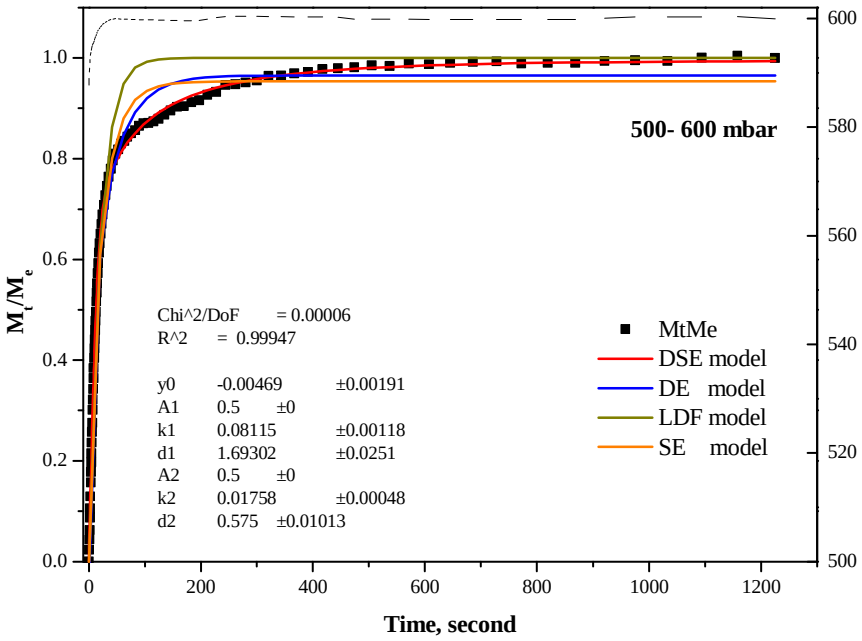

Figure F4 Various models fitted for the kinetic profiles of O_2 adsorption on NEW-1 at 195 K, 500-600 mbar

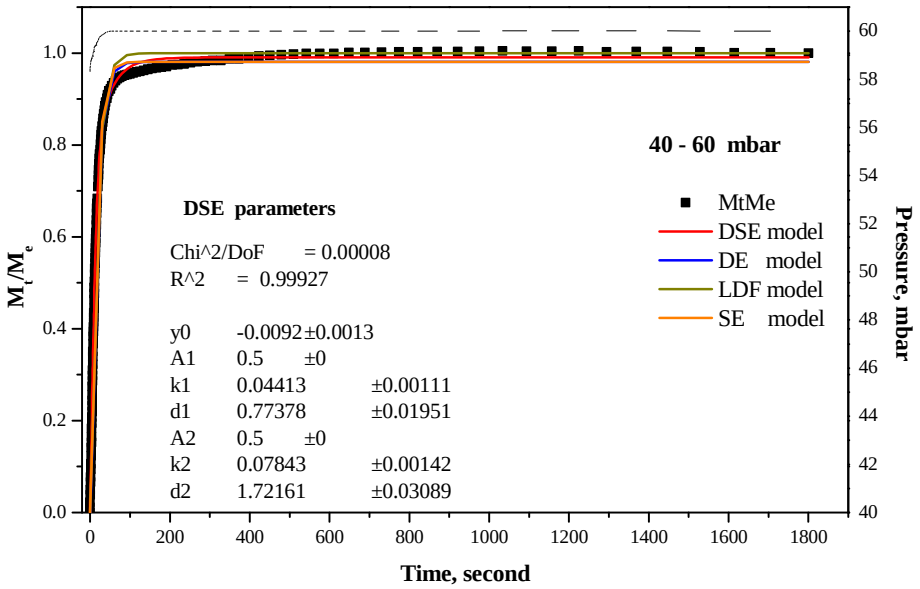

Figure F5 Various models fitted for the kinetic profiles of Ar adsorption on NEW-1 at 195 K, 40-60 mbar

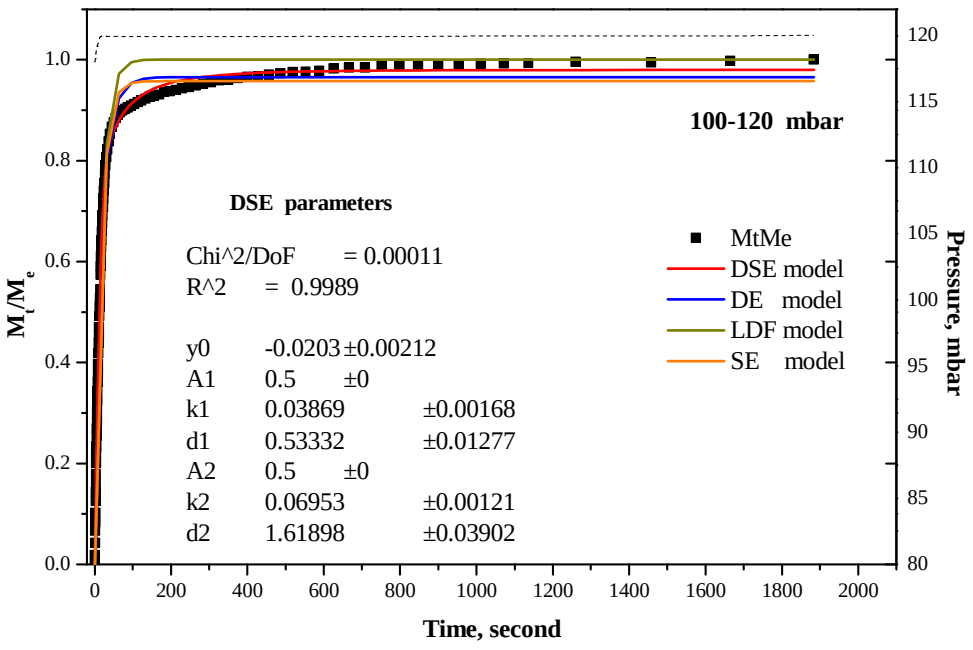

Figure F6 Various models fitted for the kinetic profiles of Ar adsorption on NEW-1 at 195 K, 100-120 mbar

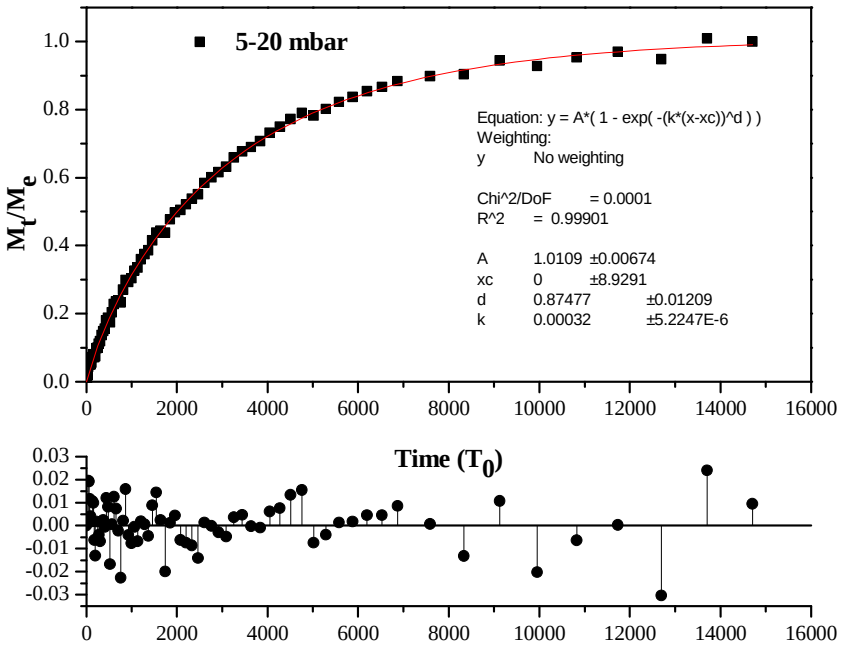

Figure F7 SE Model fit for the kinetic profiles of N_2 adsorption on CMS-40 at 273 K, 5-20 mbar

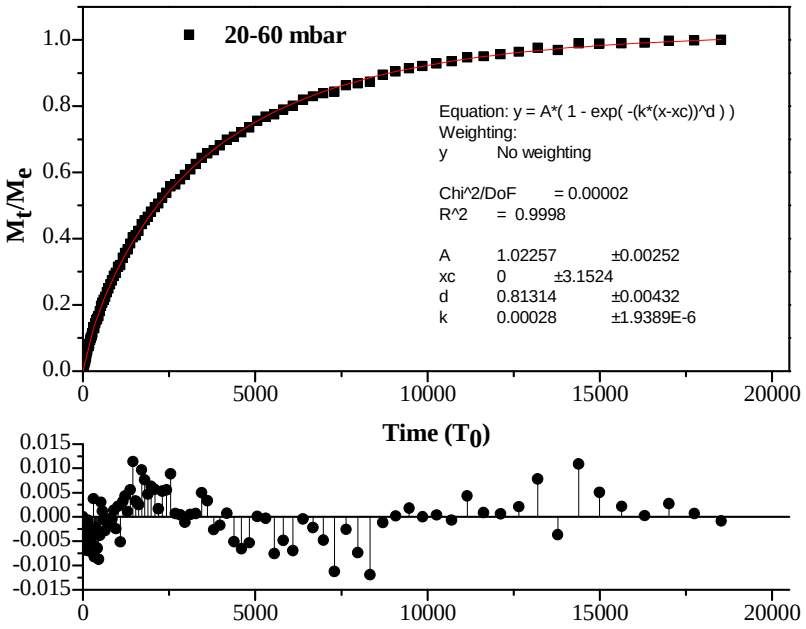

Figure F8 SE Model fit for the kinetic profiles of N_2 adsorption on CMS-40 at 273 K, 20-60 mbar

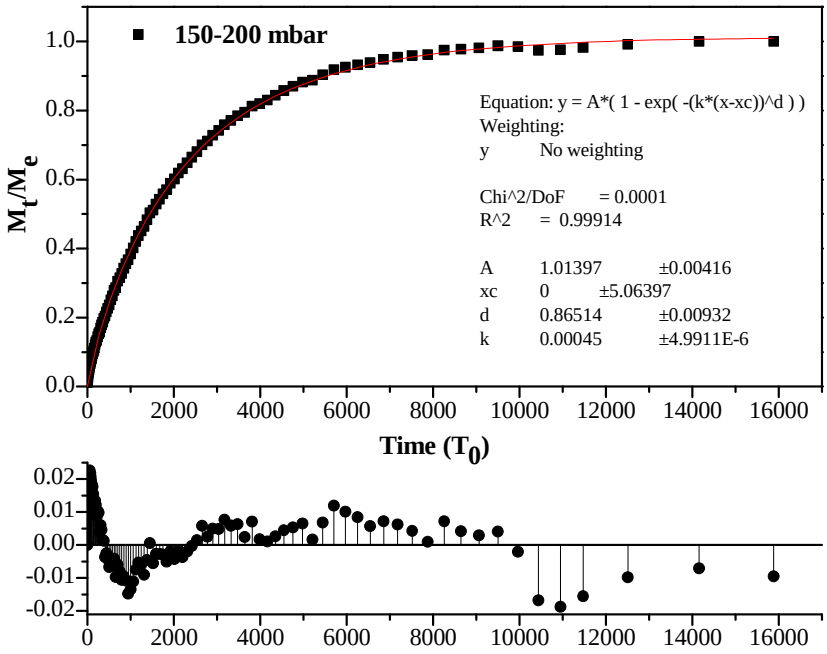

Figure F9 SE Model fit for the kinetic profiles of N_2 adsorption on CMS-40 at 273 K, 150-200 mbar

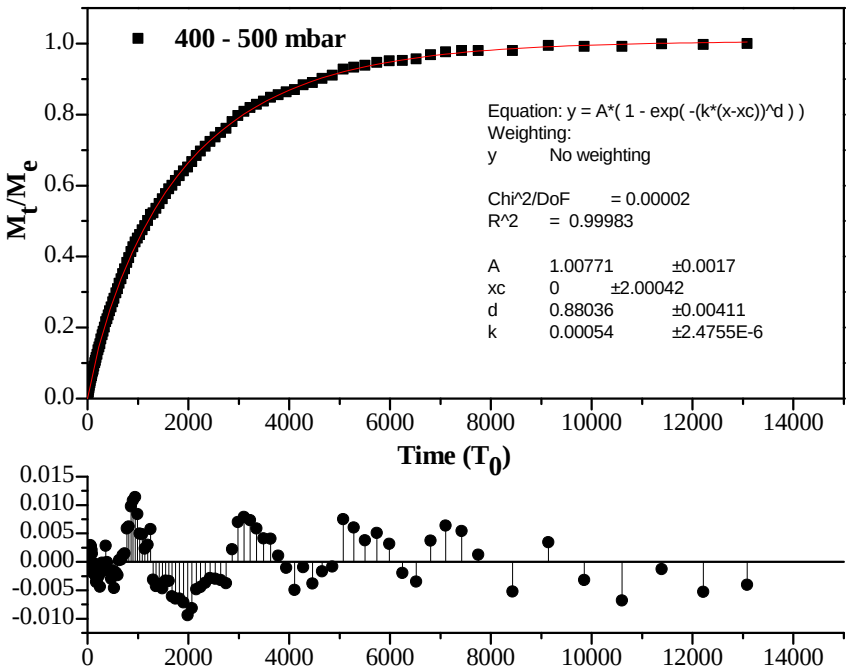

Figure F10 SE Model fit for the kinetic profiles of N_2 adsorption on CMS-40 at 273 K, 400-500 mbar

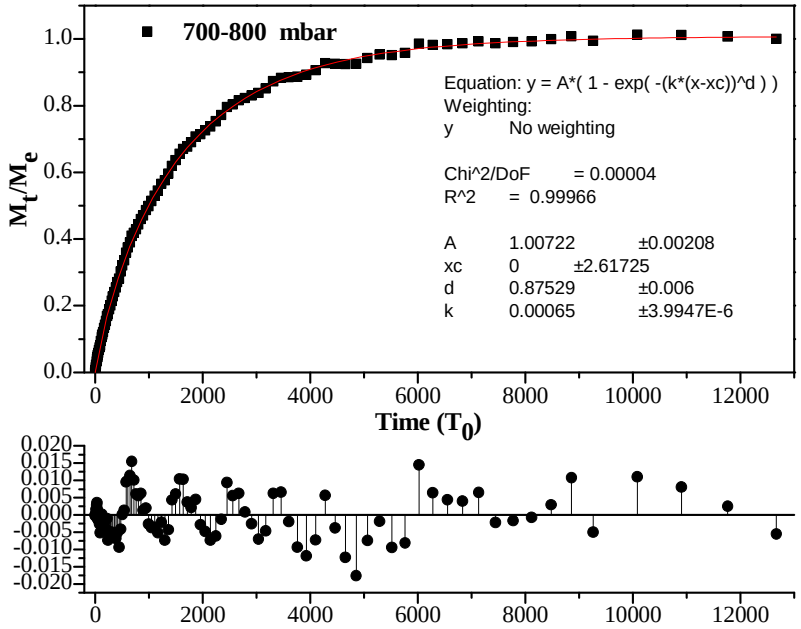

Figure F11 SE Model fit for the kinetic profiles of N_2 adsorption on CMS-40 at 273 K, 700-800 mbar

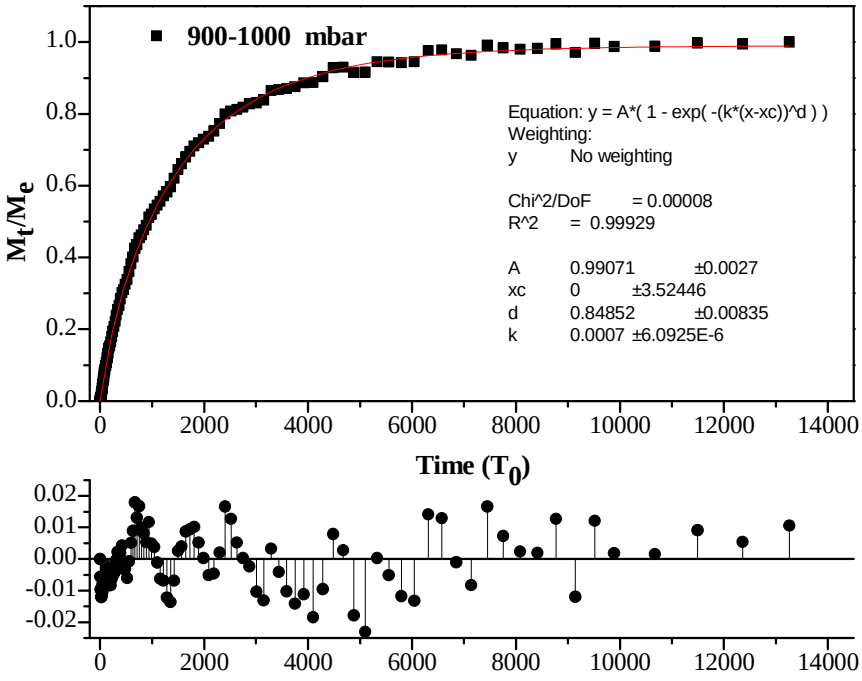

Figure F2 SE Model fit for the kinetic profiles of N_2 adsorption on CMS-40 at 273 K, 900-1000 mbar

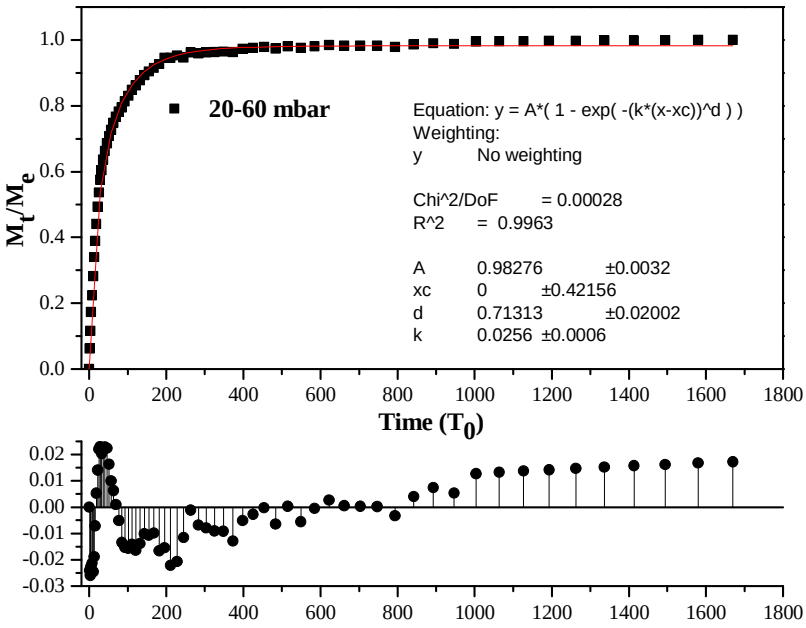

Figure F13 SE Model fit for the kinetic profiles of O_2 adsorption on CMS-40 at 273 K, 20-60 mbar

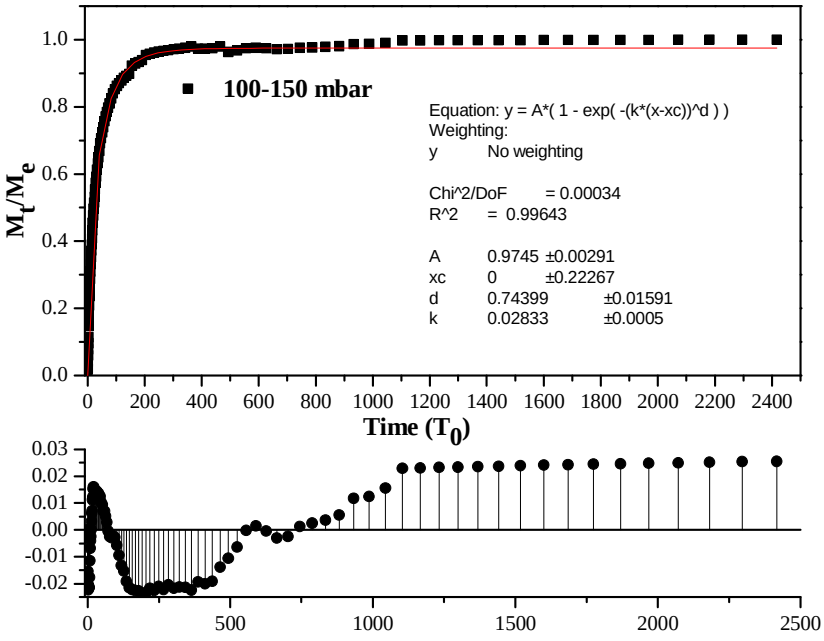

Figure F14 SE Model fit for the kinetic profiles of O_2 adsorption on CMS-40 at 273 K, 100-150 mbar

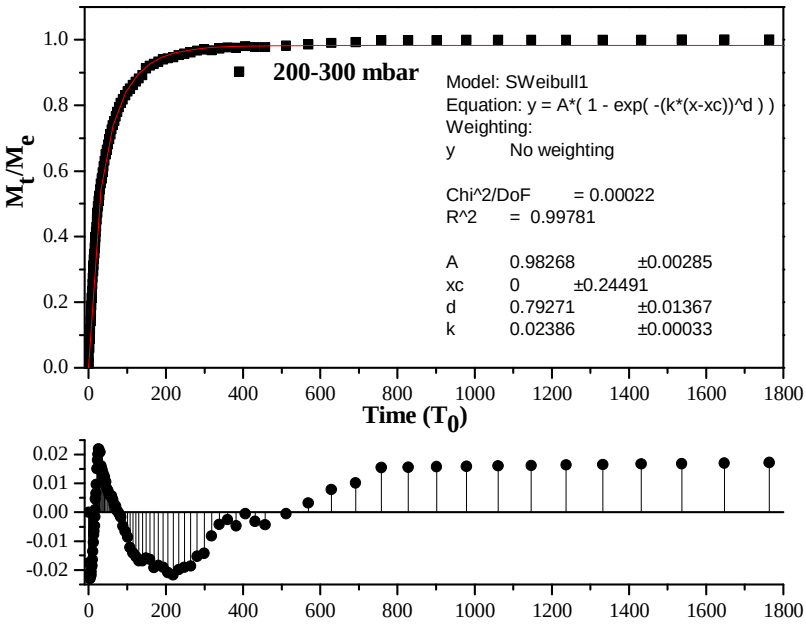

Figure F15 SE Model fit for the kinetic profiles of O_2 adsorption on CMS-40 at 273 K, 200-300 mbar

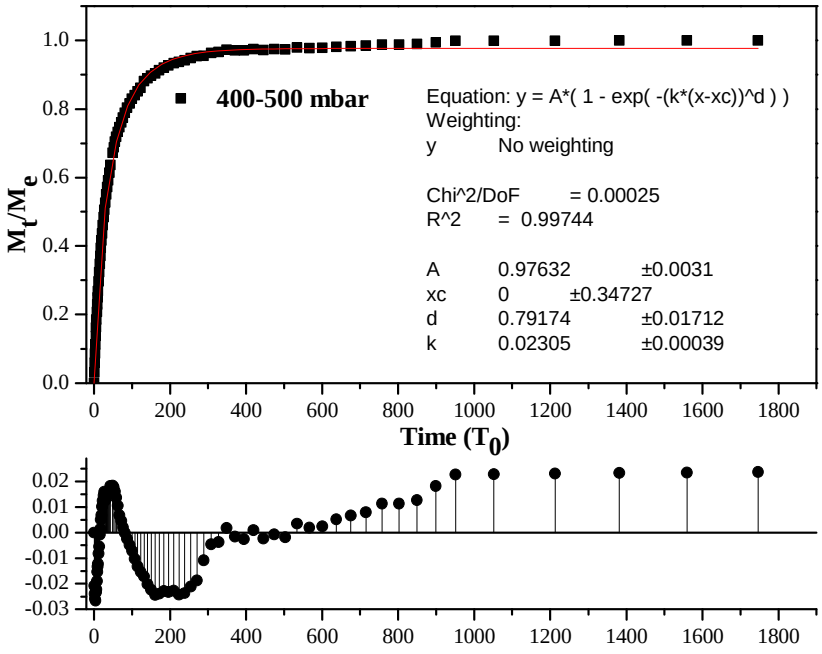

Figure F16 SE Model fit for the kinetic profiles of O_2 adsorption on CMS-40 at 273 K, 400-500 mbar

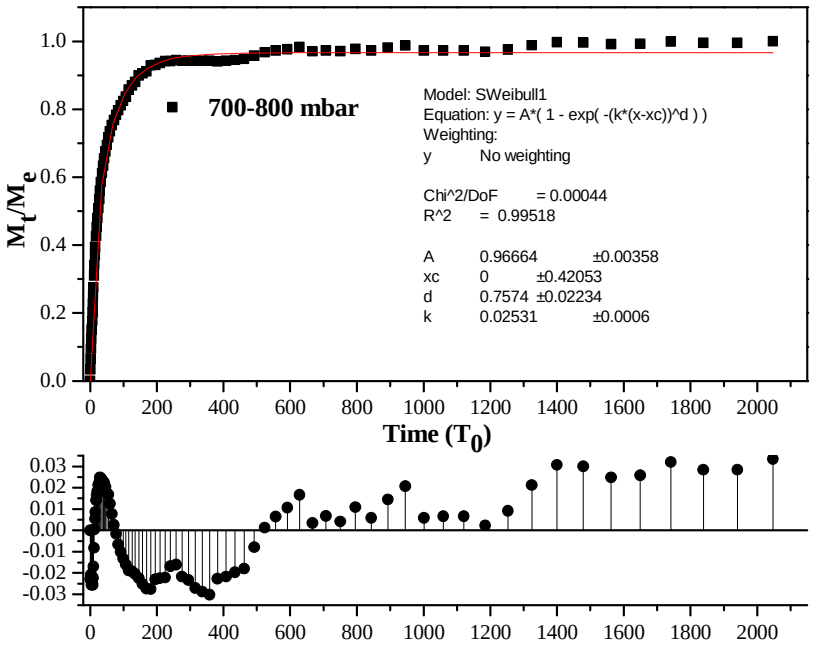

Figure F17 SE Model fit for the kinetic profiles of O_2 adsorption on CMS-40 at 273 K, 700-800 mbar

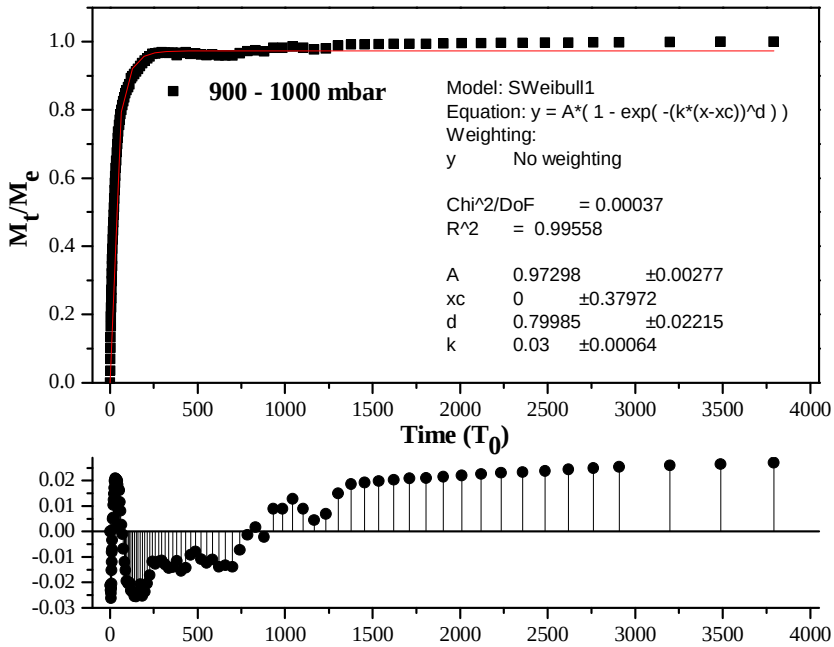

Figure F18 SE Model fit for the kinetic profiles of O_2 adsorption on CMS-40 at 273 K, 900-1000 mbar

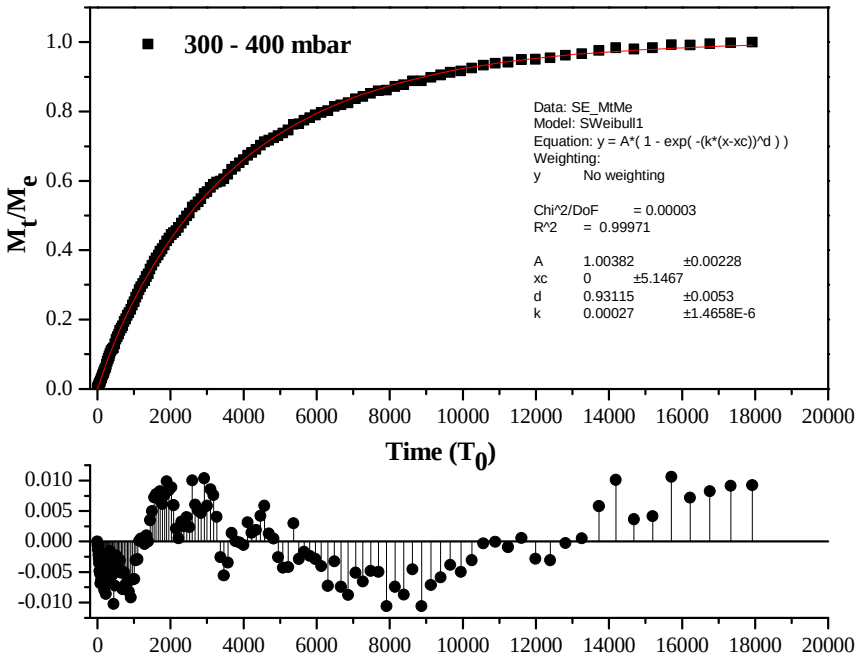

Figure F19 SE Model fit for the kinetic profiles of Ar adsorption on CMS-40 at 273 K, 300-400 mbar

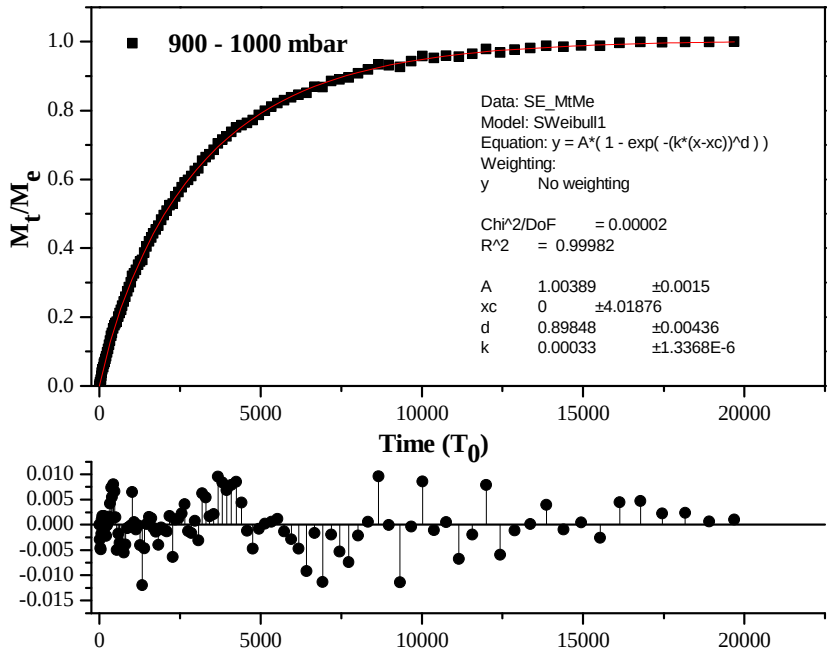

Figure F20 SE Model fit for the kinetic profiles of Ar adsorption on CMS-40 at 273 K, 900-1000 mbar

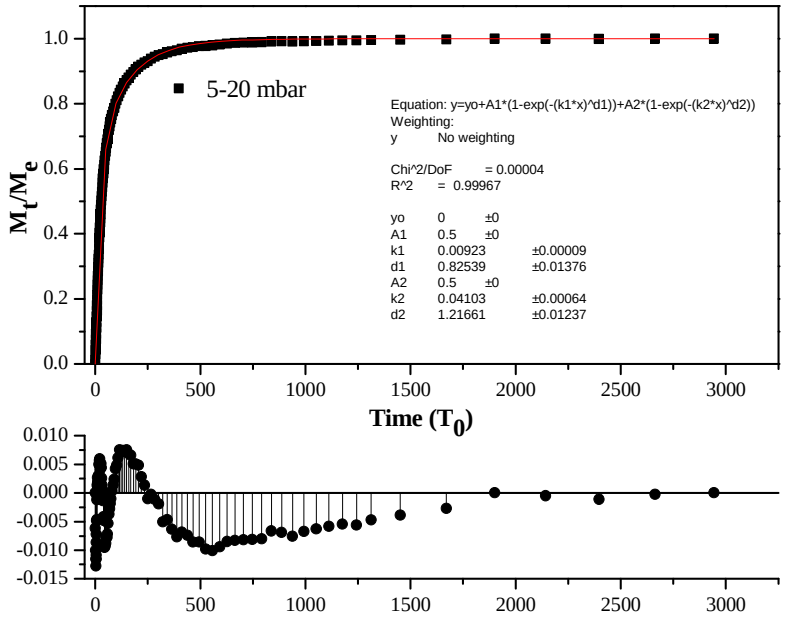

Figure F21 DSE Model fit for the kinetic profiles of N_2 adsorption on M'MOF-1 at 195 K, 5-20 mbar

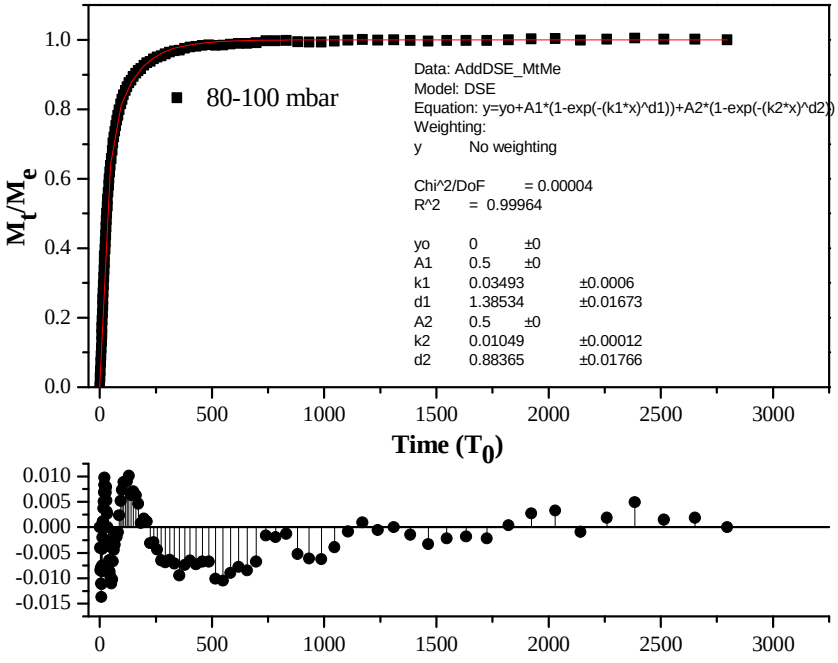

Figure F22 DSE Model fit for the kinetic profiles of N_2 adsorption on M'MOF-1 at 195 K, 80-100 mbar

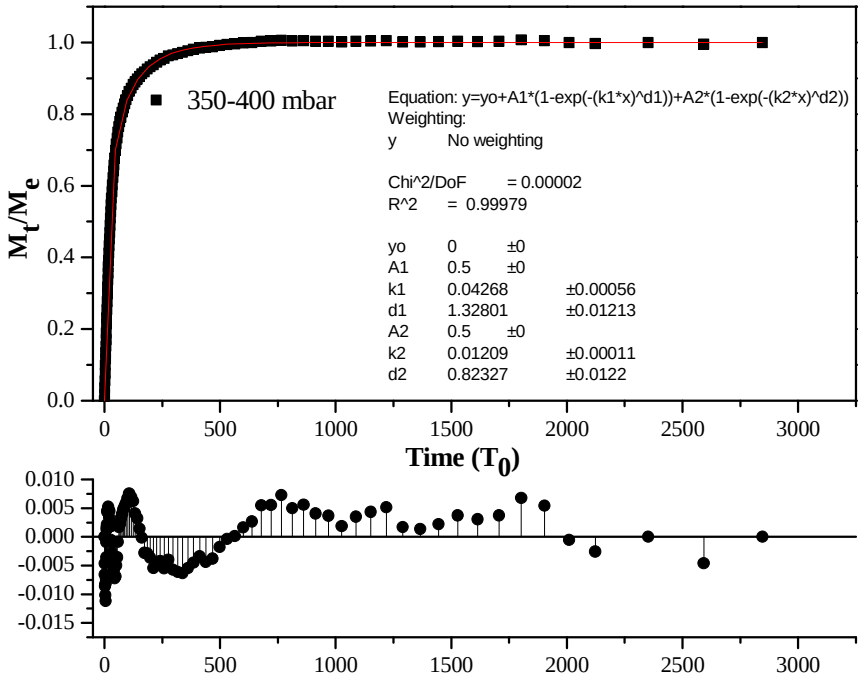

Figure F23 DSE Model fit for the kinetic profiles of N_2 adsorption on M'MOF-1 at 195 K, 350-400 mbar

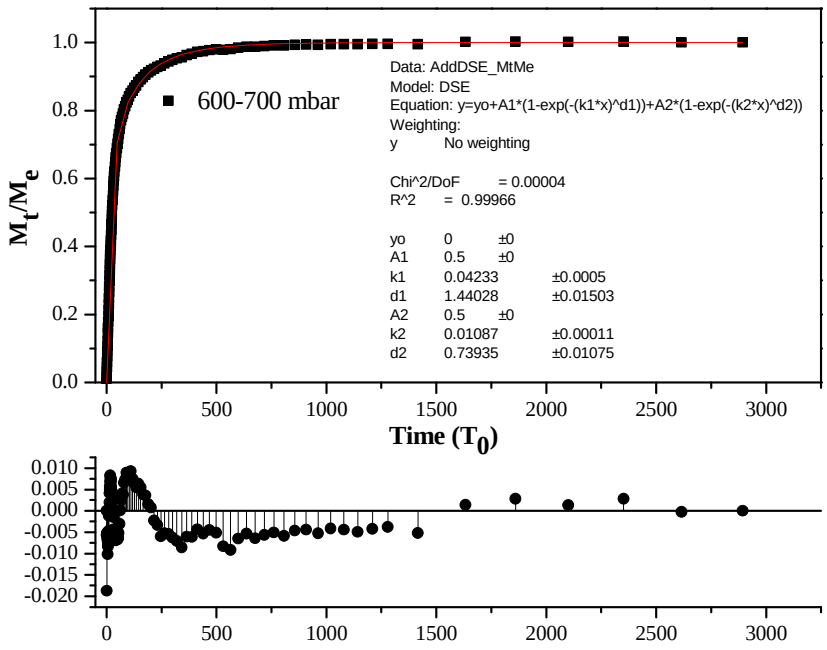

Figure F24 DSE Model fit for the kinetic profiles of N_2 adsorption on M'MOF-1 at 195 K, 600-700 mbar

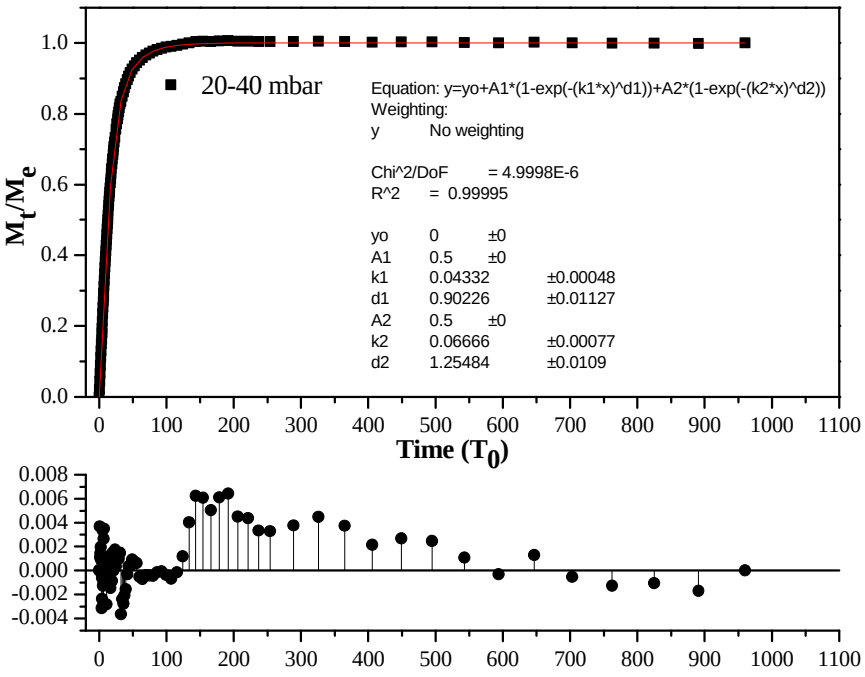

Figure F25 DSE Model fit for the kinetic profiles of O_2 adsorption on M'MOF-1 at 195 K, 20-40 mbar

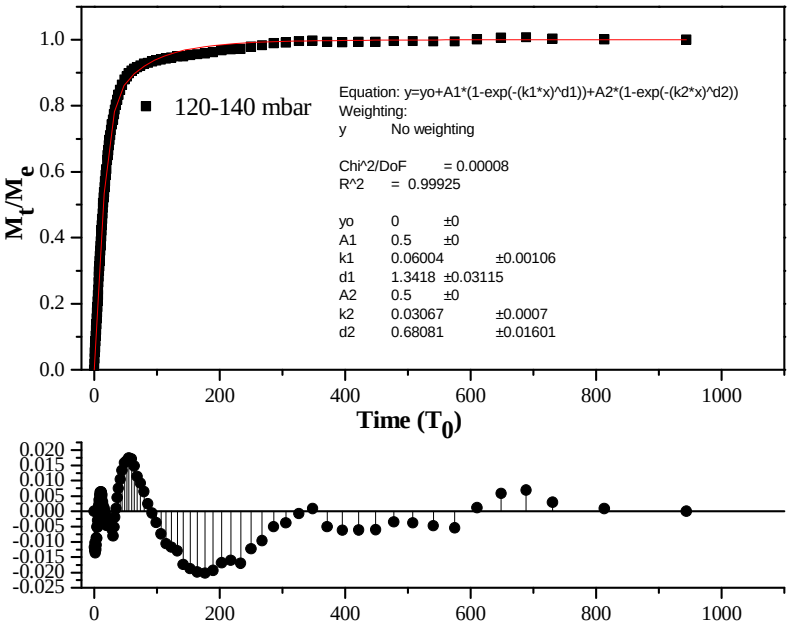

Figure F26 DSE Model fit for the kinetic profiles of O_2 adsorption on M'MOF-1 at 195 K, 120-140 mbar

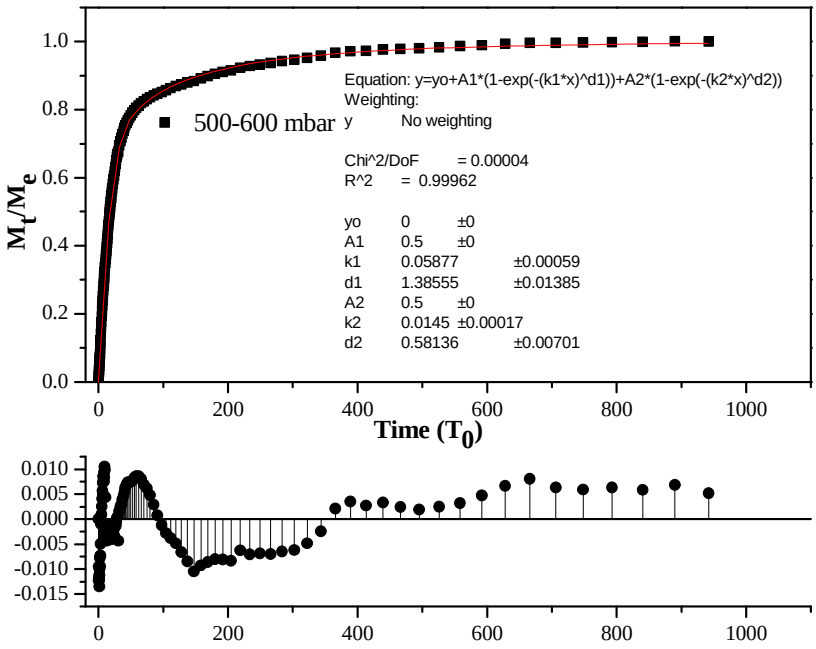

Figure F27 DSE Model fit for the kinetic profiles of O_2 adsorption on M'MOF-1 at 195 K, 500-600 mbar

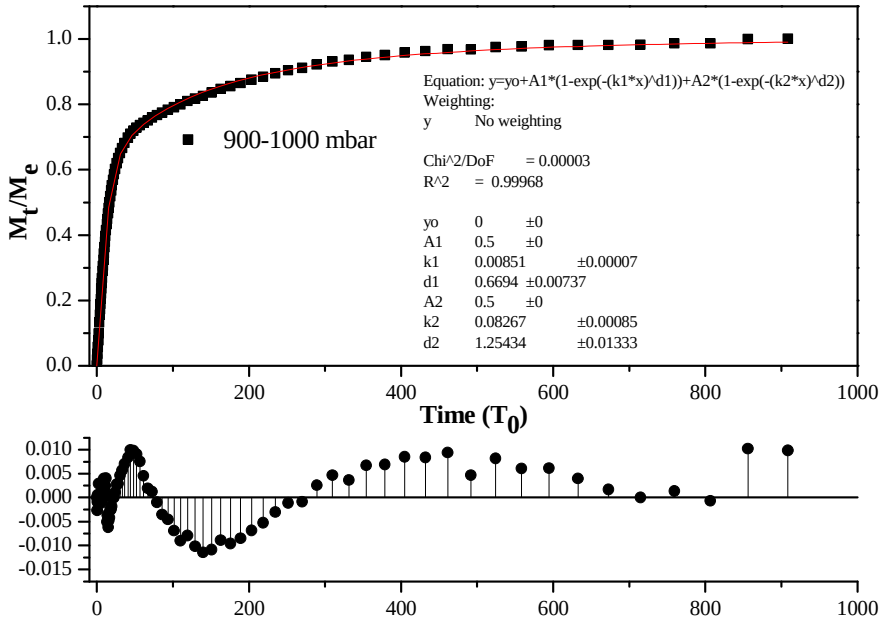

Figure F28 DSE Model fit for the kinetic profiles of O_2 adsorption on M'MOF-1 at 195 K, 900-1000 mbar

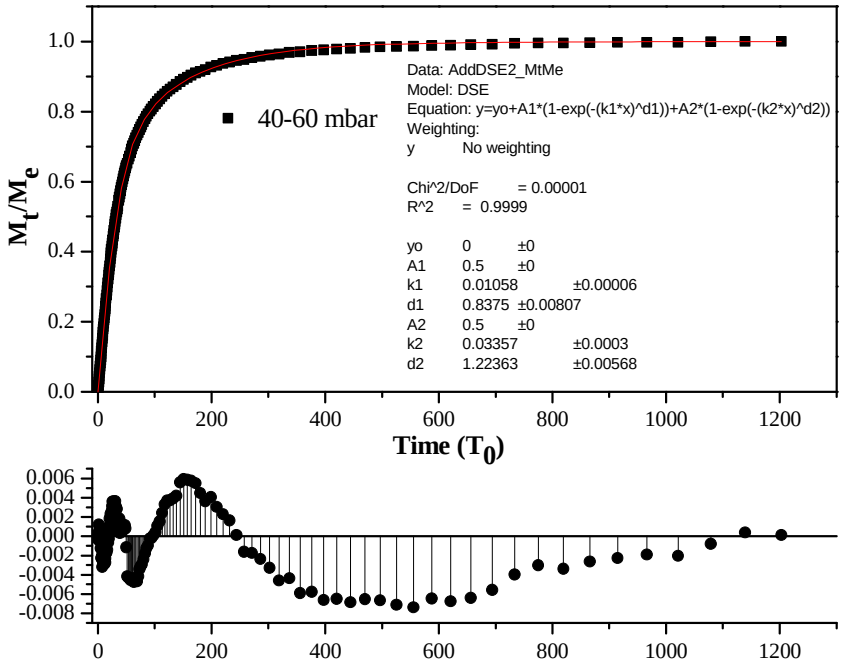

Figure F29 DSE Model fit for the kinetic profiles of Ar adsorption on M'MOF-1 at 195 K, 40-60 mbar

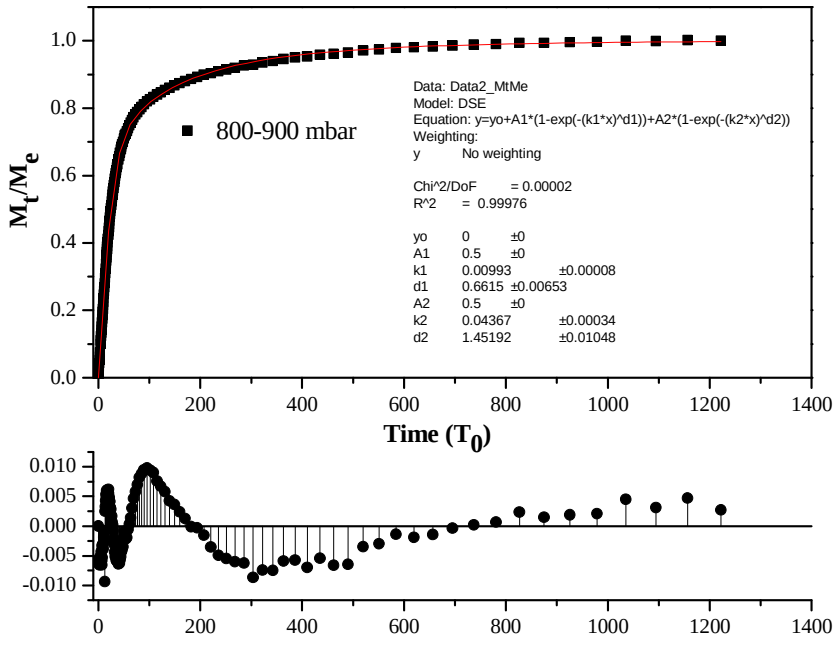

Figure F30 DSE Model fit for the kinetic profiles of Ar adsorption on M'MOF-1 at 195 K, 800-900 mbar